USGS
science for a changing world

Documentation for the 2014 Update of the United States National Seismic Hazard Maps

Mark D. Petersen, Morgan P. Moschetti, Peter M. Powers, Charles S. Mueller, Kathleen M. Haller, Arthur D. Frankel, Yuehua Zeng, Sanaz Rezaeian, Stephen C. Harmsen, Oliver S. Boyd, Ned Field, Rui Chen, Kenneth S. Rukstales, Nico Luco, Russell L. Wheeler, Robert A. Williams, and Anna H. Olsen

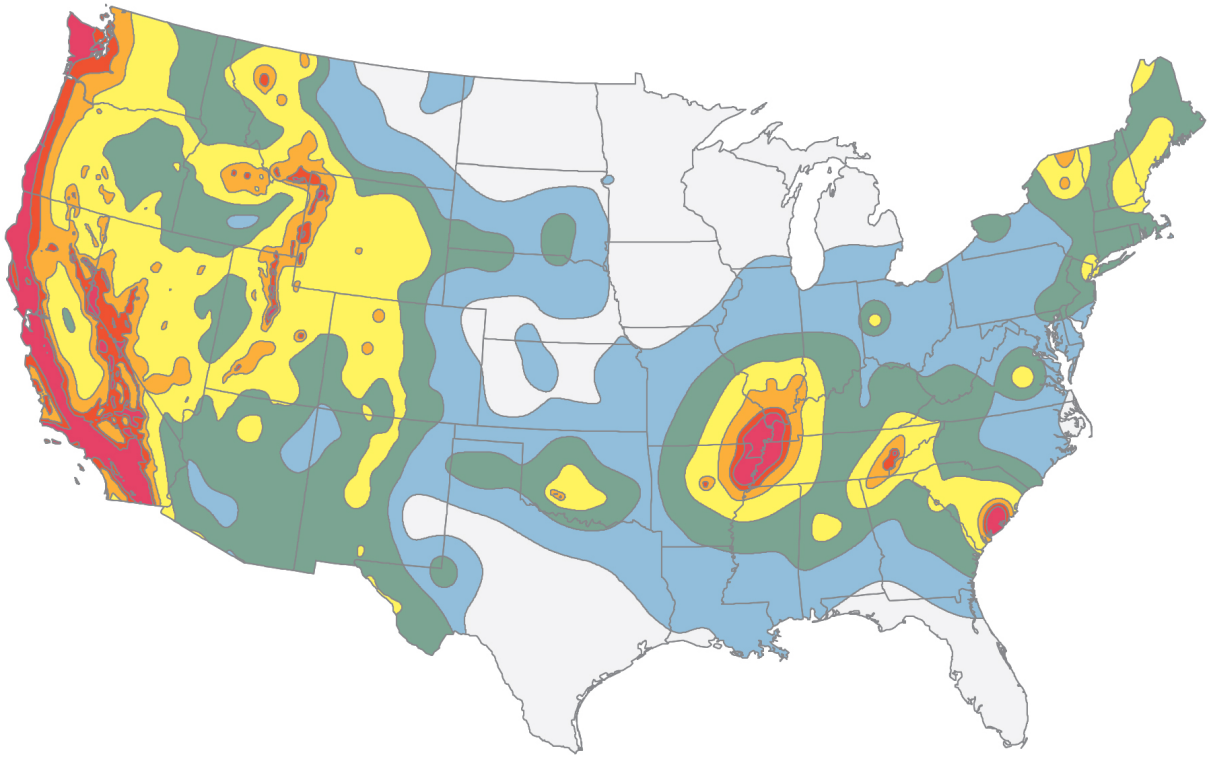

Open-File Report 2014–1091

U.S. Department of the Interior
U.S. Geological Survey

U.S. Department of the Interior
SALLY JEWELL, Secretary

U.S. Geological Survey
Suzette M. Kimball, Acting Director

U.S. Geological Survey, Reston, Virginia: 2014

For more information on the USGS—the Federal source for science about the Earth, its natural and living resources, natural hazards, and the environment—visit *http://www.usgs.gov* or call 1–888–ASK–USGS

For an overview of USGS information products, including maps, imagery, and publications, visit *http://www.usgs.gov/pubprod*

To order this and other USGS information products, visit *http://store.usgs.gov*

Suggested citation:
Petersen, M.D., Moschetti, M.P., Powers, P.M., Mueller, C.S., Haller, K.M., Frankel, A.D., Zeng, Yuehua, Rezaeian, Sanaz, Harmsen, S.C., Boyd, O.S., Field, Ned, Chen, Rui, Rukstales, K.S., Luco, Nico, Wheeler, R.L., Williams, R.A., and Olsen, A.H., 2014, Documentation for the 2014 update of the United States national seismic hazard maps: U.S. Geological Survey Open-File Report 2014–1091, 243 p., *http://dx.doi.org/10.3133/ofr20141091*.

ISSN: 2331-1258 (online)

Any use of trade, firm, or product names is for descriptive purposes only and does not imply endorsement by the U.S. Government.

Although this information product, for the most part, is in the public domain, it also may contain copyrighted materials as noted in the text. Permission to reproduce copyrighted items must be secured from the copyright owner.

Contents

Figures

Tables

Conversion Factors

Inch/Pound to SI

Multiply	By	To obtain
	Length	
inch (in.)	2.54	centimeter (cm)
inch (in.)	25.4	millimeter (mm)
foot (ft)	0.3048	meter (m)
mile (mi)	1.609	kilometer (km)
mile, nautical (nmi)	1.852	kilometer (km)
yard (yd)	0.9144	meter (m)

Initialisms and Abbreviations

BRPEWG	Basin and Range Province Earthquake Working Group
CEUS	Central and Eastern United States
CEUS–SSCn	Central and Eastern United States Seismic Source Characterization for nuclear facilities
CSZ	Cascadia subduction zone
EPRI	Electric Power Research Institute
g	Gravitational acceleration constant equal to 9.81 meters per second squared
GMM	Ground Motion Model

Subduction interface and deep intraslab models:
- AB03—Atkinson and Boore (2003)
- AM09—Atkinson and Macias (2009)
- BC Hydro—Addo and others (2012)
- ZHAO—Zhao and others (2006)

Shallow crustal ground motion models for tectonically active regions:
- ASK13 Abrahamson and others (2013, 2014)
- CB08 Campbell and Bozorgnia (2008)
- CB13 Campbell and Bozorgnia (2013, 2014)
- CY08 Chiou and Youngs (2008)
- CY13 Chiou and Youngs (2013, 2014)
- I13 Idriss (2013, 2014)

Shallow crustal ground motion models for stable continental regions:
- A08' Atkinson (2008, 2011)
- AB06 Atkinson and Boore (2006)
- AB06' Atkinson and Boore (2011)
- C03 Campbell (2003)
- F96 Frankel and others (1996)
- S02 Silva and others (2002)
- P11 Pezeshk and others (2011)
- T02 Toro and others (1997, 2002)
- TP05 Tavakoli and Pezeshk (2005)
- S01 Somerville and others (2001)

GPS	Global Positioning System, measurements used as geodetic data in this report
GridSrc	Background gridded sources
GS	Geometric spreading
HAZUS	Standardized software program that estimates losses from potential earthquakes
IMW	Intermountain West
Kappa	Site attenuation of high frequencies
MFD	Magnitude frequency distribution
Mmax	Maximum magnitude considered in a region—typically limits the earthquake magnitude-frequency distribution applied in the seismic source models
M_w	Moment magnitude, also **M**
m_{blg}	Body-wave magnitude based on guided surface waves
NEHRP	National Earthquake Hazards Reduction Program
NGA	Next Generation Attenuation models, ground motion models
NSHMP	National Seismic Hazard Mapping Project
PDF	Probability Density Function
PEER	Pacific Earthquake Engineering Research center
PNW	Pacific Northwest
Q	Frequency dependent attenuation term used in ground motion models
RLME	Repeated large magnitude earthquake
Rx and Rjb	Distances used in ground motion models
R^{-1} or $R^{-1.3}$	Geometric spreading parameters used in ground motion models
SCRs	Stable continental regions
SA	Spectral acceleration (horizontal) 5% damping

Ground motion intensity measures:

PGA	Peak ground acceleration
SA	Spectral acceleration 5% damping at 5 hertz (0.2 second) and 1 hertz (1.0 second)
UCERF	Uniform California Earthquake Rupture Forecast Model (with 2 or 3 to denote version)
USGS	U.S. Geological Survey
UTC	Coordinated Universal Time
V_{S30}	Shear wave velocity (time-averaged) in the upper 30 meters—used to define National Earthquake Hazards Reduction Program (NEHRP) A,B,C,D soil types, boundary between soil B and C and is defined as V_{S30} = 760 meters/second, which is uniformly applied in maps in this report
WGCEP	Working Group on California Earthquake Probabilities
WUS	Western United States

Documentation for the 2014 Update of the United States National Seismic Hazard Maps

By Mark D. Petersen, Morgan P. Moschetti, Peter M. Powers, Charles S. Mueller, Kathleen M. Haller, Arthur D. Frankel, Yuehua Zeng, Sanaz Rezaeian, Stephen C. Harmsen, Oliver S. Boyd, Ned Field, Rui Chen, Kenneth S. Rukstales, Nico Luco, Russell L. Wheeler, Robert A. Williams, and Anna H. Olsen

Abstract

The national seismic hazard maps for the conterminous United States have been updated to account for new methods, models, and data that have been obtained since the 2008 maps were released (Petersen and others, 2008). The input models are improved from those implemented in 2008 by using new ground motion models that have incorporated about twice as many earthquake strong ground shaking data and by incorporating many additional scientific studies that indicate broader ranges of earthquake source and ground motion models. These time-independent maps are shown for 2-percent and 10-percent probability of exceedance in 50 years for peak horizontal ground acceleration as well as 5-hertz and 1-hertz spectral accelerations with 5-percent damping on a uniform firm rock site condition (760 meters per second shear wave velocity in the upper 30 m, V_{S30}). In this report, the 2014 updated maps are compared with the 2008 version of the maps and indicate changes of plus or minus 20 percent over wide areas, with larger changes locally, caused by the modifications to the seismic source and ground motion inputs.

Introduction

During the past several decades, the U.S. Geological Survey (USGS) national seismic hazard maps (NSHM, Algermissen and Perkins, 1976; Frankel and others, 1996, 2002; Petersen and others, 2008; Petersen and others, 2012) have provided the basis for many public and private policies regarding earthquakes, including seismic-design regulations for buildings, bridges, highways, railroads, and other structures. The maps are used in building codes (for example, Building Seismic Safety Council, 2009) to identify areas where built structures are likely to experience large seismic loads and to allow for prudent allocation of resources by reducing waste resulting from over-built structures. In addition, structures can be built to a standard that will enable critical activities and resources (such as availability of energy resources, accessibility of transportation corridors, and sustainability of medical care) to continue with less disruption following an earthquake. Seismic hazard assessments also affect insurance rate structures (for example, those based on California Earthquake Authority models; Working Group on California Earthquake Probabilities, 2013), governmental disaster management and mitigation strategies (such as those based on HAZUS, *http://www.fema.gov/hazus/*), planning and seismic safety applications (for example, the California Seismic Hazards Mapping Act, Nuclear Regulatory Commission), and many site-specific engineering analyses by industries and governments (such as those applied by the U.S. Department of Defense and the U.S. Bureau of Reclamation).

The USGS updates these time-independent hazard maps to produce the latest science-based information on future earthquake ground motions. The hazard models described in this report incorporate more than 100 years of global earthquake observations, widely accepted seismology-based principles, and a long history of scientific analyses in the science and engineering communities. These communities are expanding the geological, geophysical, geodetic, and engineering observational base and, in the process, improving our understanding of seismic hazard. Therefore, the National Seismic Hazard Mapping Project (NSHMP) maps are updated regularly as new data, methods, and models are acquired and analyzed.

The results of this assessment will be considered by structural design communities, including the Building Seismic Safety Committee, the American Society of Civil Engineers, and the International Code Council, for inclusion in future building codes that generally are adopted by most states and local jurisdictions across the United States. In addition, they are applied for risk assessments, and for other public policy applications. Because these maps affect public safety and economic vitality, the USGS national seismic hazard maps include only earthquake science that is accepted by the science community. The maps represent the NSHMP's assessment of best-available data, models, and methods for seismic hazard assessment at the time of this update (Independent Expert Panel, 2011). The USGS relies on the science and engineering communities for input to this process.

To acquire new hazard information, the NSHMP convened workshops and meetings across the country to identify models available for consideration, and worked in partnerships with other organizations to develop and evaluate the available science and its impact on the seismic hazard. The NSHMP held regional workshops in 2012 and 2013 for the Central and Eastern United States (CEUS) in Memphis, Tenn.; the Pacific Northwest in Seattle, Wash.; the Intermountain West in Salt Lake City, Utah; and in Newark and Menlo Park, California (Calif.). In addition, the NSHMP held topical workshops to discuss Cascadia subduction processes (in Eugene and Corvallis, Oregon [Oreg.]), geodetic models and their use in the USGS NSHMP maps (in Newark and Menlo Park, Calif., and Hood River, Oreg.), Basin and Range hazard (in Salt Lake City, Utah, and Reno, Nev.), and earthquake ground-shaking models (in Berkeley, Calif.). Several hundred earthquake scientists and engineers participated in these workshops. Many presentations from these workshops are available at *http://earthquake.usgs.gov/hazmaps/*.

Several organizations provided essential information for this update. The Pacific Earthquake Engineering Research Center (PEER) provided new ground motion equations and data across the United States, the Central and Eastern United States Seismic Source Characterization for Nuclear Facilities (CEUS–SSCn) project provided a new seismic source model, Earthquake Power Research Institute (EPRI) provided ground motion weighting information, BC Hydro project (Addo and others, 2012) contributed a new subduction zone ground-shaking model, Working Group on California Earthquake Probabilities (2013) contributed a new source model for California (UCERF3), and several working groups met to discuss other hazard issues for this map update. The USGS external-grants investigators provided additional data and models for these maps, as well as new ways to test the results. State and Federal agencies as well as participants from academia and industry provided new models and data in the published literature.

The NSHMP steering committee composed of nine seismic hazard experts from academia, industry, and government, was assembled to guide the review of the input models and provide advice on the best methodologies, data, and input parameter values. This committee met in two separate review periods during May (before the release of the draft maps for public review) and August 2013 (following the public review and before finalizing the 2014 USGS NSHMP maps). This committee provided critical

advice on developing the final maps and insights on how the model should be revised for this version and future updates.

Inputs to the USGS NSHMP maps are based on time-independent scientific estimates of locations and sizes of future earthquakes. These estimates do not consider the time since the last earthquake. We model rates of earthquakes on known faults or as seismicity-based background earthquakes, which account for unknown faults or the incomplete fault inventory. We assume that future, damaging earthquakes generally will occur near past earthquakes or on known faults with evidence of past surface rupture; therefore, we model fault ruptures for the hazard assessment to account for large earthquakes on such structures. However, we also know that there will be future earthquakes that are not associated with mapped Quaternary faults and these earthquakes are modeled using historical seismicity (Frankel, 1995) and physics based principles. We model the magnitude-frequency distribution for earthquakes with a preferred maximum size (characteristic earthquake model) or with a truncated exponential recurrence based on a truncated Gutenberg and Richter (1944) magnitude-frequency distribution.

In this update, we include many new earthquake sources and ground motion models that are based on the abundant new data and studies that have been generated since 2008. The NSHMP developed some of these models, external organizations (listed below) developed others in coordination with the NSHMP for use in this update of the maps, and the NSHMP adopted or adapted other models originally developed by external organizations for applications other than the NSHMP. The following bullets summarize major changes from the 2008 to the 2014 update of the USGS NSHMP maps.
The NSHMP revised the models for the Central and Eastern United States in the following ways:

- Developed a moment magnitude-based earthquake catalog through 2012, replacing the 2008 body wave magnitude that is based on guided surface waves (m_{blg}) based catalog;
- Updated earthquake catalog completeness estimates, catalog of statistical parameters, treatment of nontectonic seismicity, and treatment of magnitude uncertainty;
- Updated the distribution for maximum magnitude (Mmax) for background earthquakes based on a new analysis of global earthquakes in stable continental regions;
- Updated the zonation for Mmax, keeping the two-zone model that distinguishes craton and margin zones used in previous maps, and adding a new four-zone model based on the Central and Eastern United States seismic source characterization for nuclear facilities project (CEUS–SSCn, 2012) delineating the craton, Paleozoic margin, Mesozoic margin, and Gulf Coast;
- Updated the smoothing algorithms for background seismicity, keeping the previous fixed-length Gaussian smoothing model (Petersen and others, 2008), and adding a nearest-neighbor-type adaptive smoothing model;
- Updated the New Madrid source model, including fault geometry, recurrence rates of large earthquakes, and alternative magnitudes from M_w6.6 to 8.0 (maintaining the average weighted magnitude at about M_w7.5);
- Adapted seismic sources such as Charleston, Wabash, Charlevoix, Commerce lineament, East Rift Margin, and Marianna based on the CEUS–SSCn (2012) model; and
- Updated the treatment of earthquakes that potentially are induced by underground fluid injection.

For the Intermountain West and Pacific Northwest crustal sources we made the following changes:

- Considered suggestions from the Basin and Range Province Earthquake Working Group on magnitude-frequency distributions for fault sources, smoothing parameters, comparison of historical and modeled seismicity rates, treatment of magnitude uncertainty, assessment of maximum magnitude, modeling of antithetic fault pairs, slip rate uncertainties, and dip uncertainty for normal faults (Lund, 2012);

- Updated the earthquake catalog and treatment of magnitude uncertainty in rate calculations;
- Incorporated dips for normal faults of 35 degrees (°), 50°, and 65° but applied the fault earthquake rate using only the 50° dip to the three alternatives;
- Updated fault parameters for faults in Utah, based on new datasets and models supplied by the Utah Geological Survey and the Working Group on Utah Earthquake Probabilities (Lund, 2013), and other faults across this part of the country;
- Introduced new combined geologic and geodetic combined-inversion models for assessing fault slip rates on fault sources (Petersen and others, 2013) to account for uncertainty in activity rates on faults;
- Implemented new models for Cascadia earthquake-rupture geometries and rates based on onshore (paleotsunami) and offshore (turbidite) studies;
- Updated the model for deep (intraslab) earthquakes along the coasts of Oregon and Washington, including a new depth distribution for intraslab earthquakes;
- Allowed for an Mmax up to M_w8.0 for crustal and intraslab earthquakes; and
- Added the Tacoma fault source and updated the South Whidbey Island fault source in Washington.

For California sources we implemented new models:

- The NSHMP worked in cooperation with the Southern California Earthquake Center and the State of California to develop a new seismic source model based on the Uniform California Earthquake Rupture Forecast, Version 3 (UCERF3, *www.scec.org/ucerf/*; Working Group on California Earthquake Probabilities, 2013), which include many more multi-segment ruptures than in previous versions of the maps (Frankel and others, 1996, 2002; Petersen and others, 2008). These models were developed over the past several years and involved a major update of the methodology for calculating earthquake recurrence;

For calculating hazard we revised the ground motion models in the following ways:

- Included new earthquake ground motion models for active shallow crustal earthquakes and subduction zone-related interface and intraslab earthquakes;
- Adjusted the additional epistemic uncertainty model to account for regional variability and data availability;
- Updated ground motion prediction equation weights using the Next Generation Attenuation (NGA) ground motion database, reevaluated model weights for the Central and Eastern United States in light of a preliminary Electric Power Research Institute (EPRI) ground motion study, and included newly published ground motion prediction equations for stable continental regions;
- Incorporated new and evaluated older ground motion models: 5 equations for the applied for the Western United States (WUS), 9 for the CEUS, and 4 for the subduction interface and intraslab earthquakes; and
- Increased the maximum distance from 200 kilometers (km) to 300 km when calculating ground motion from WUS crustal sources.

In this update of the hazard maps, the NSHMP accounts for broader aleatory variability (random variability in a given model) and epistemic uncertainty (uncertainty in which model is most correct) than in previous updates. Although the models include the types of earthquakes we would expect in the next 50 years, the seismic hazard models probably do not explicitly include all possible earthquakes. Extremely rare or low probability events that have not been captured in studies of the historical or geologic record may not be represented in this hazard assessment. For this reason, we evaluate the range of uncertainty to capture expected, and some unexpected, earthquakes that are consistent with global observations as well as earthquake physics and statistics.

The USGS NSHMP maps depict time-independent earthquake ground-shaking exceedance levels at specified probabilities over a 50-year time period at several hundred thousand sites across the United States. The models only apply time-independent models and do not consider the time since the last earthquake in the calculations. The seismic hazard maps for this update and the 2008 maps are shown for peak horizontal ground acceleration, 5-hertz (0.2-second) and 1-hertz (1-second) spectral accelerations for a 2-percent and 10-percent probability of exceedance in 50 years on a uniform firm-rock site condition (V_{S30}=760 meters per second) in figures 1–6. Differences (2014 minus 2008 values at each site) and ratios (2014 divided by 2008 values at each site) are shown in figures 7–12. The 2014 and 2008 USGS NSHMP maps generally have similar appearance; however, the new maps differ from the prior maps by plus or minus 20 percent over broad regions and can reach plus or minus 40 percent at some sites.

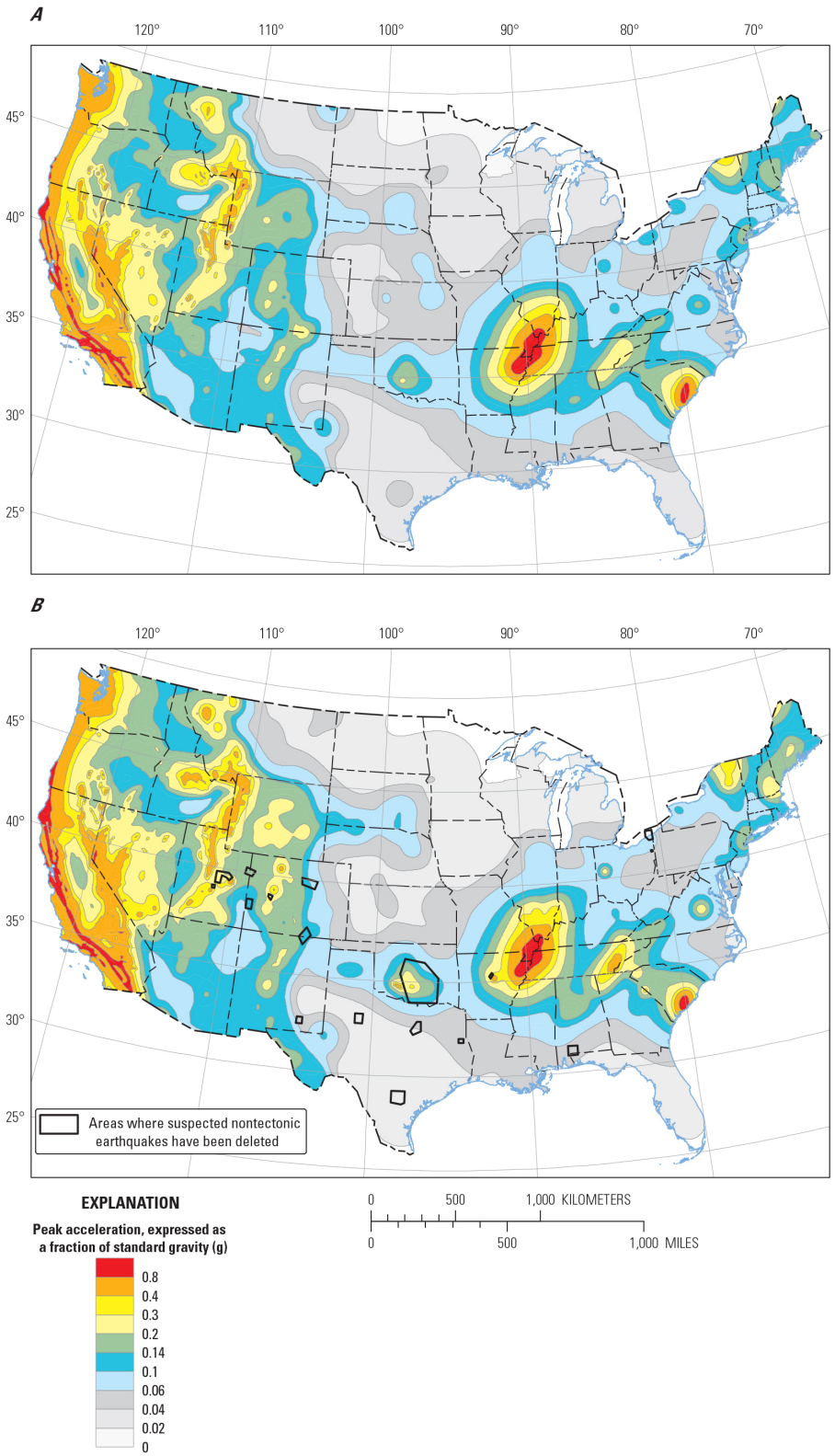

Figure 1. Maps showing peak ground acceleration for 2-percent probability of exceedance in 50 years and V_{S30} site condition of 760 meters per second. *A*, 2008 version of the national seismic hazard maps and *B*, 2014 version.

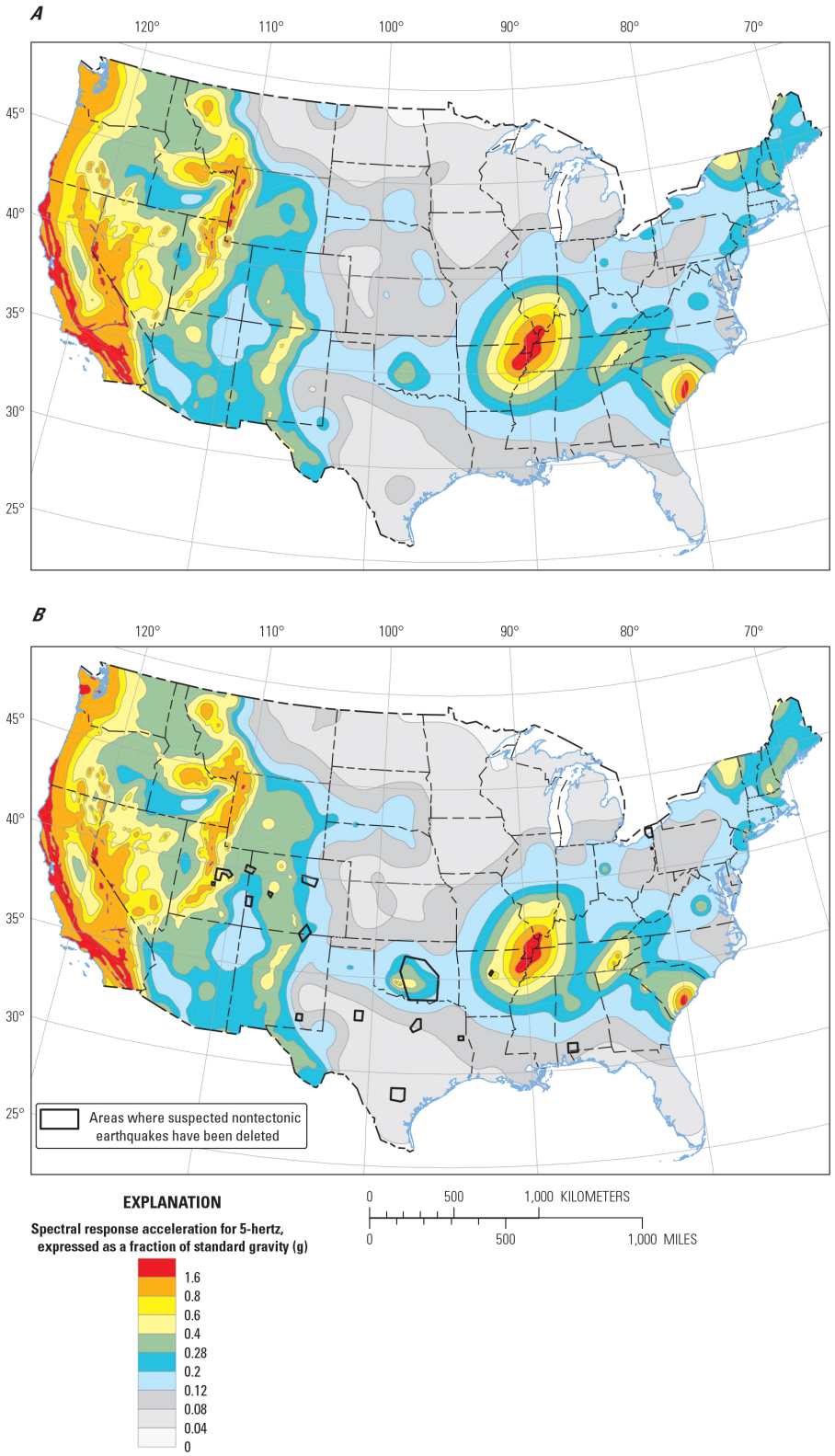

Figure 2. Maps showing 5-hertz (0.2-second) spectral acceleration for 2-percent probability of exceedance in 50 years and V_{S30} site condition of 760 meters per second. *A*, 2008 version of the national seismic hazard maps and *B*, 2014 version.

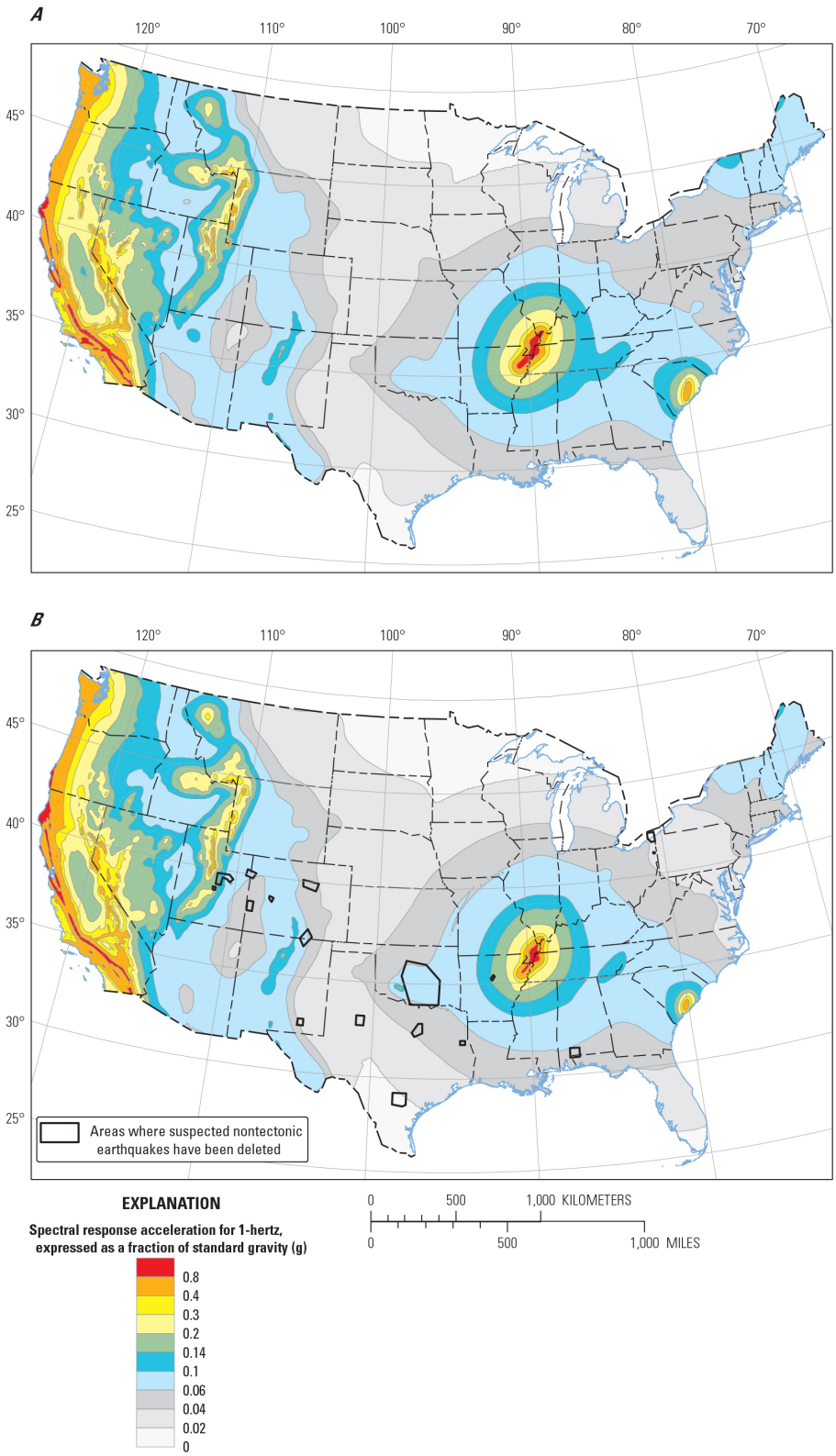

Figure 3. Maps showing 1-hertz (1-second) spectral acceleration for 2-percent probability of exceedance in 50 years and V_{S30} site condition of 760 meters per second. *A*, 2008 version of the national seismic hazard maps and *B*, 2014 version.

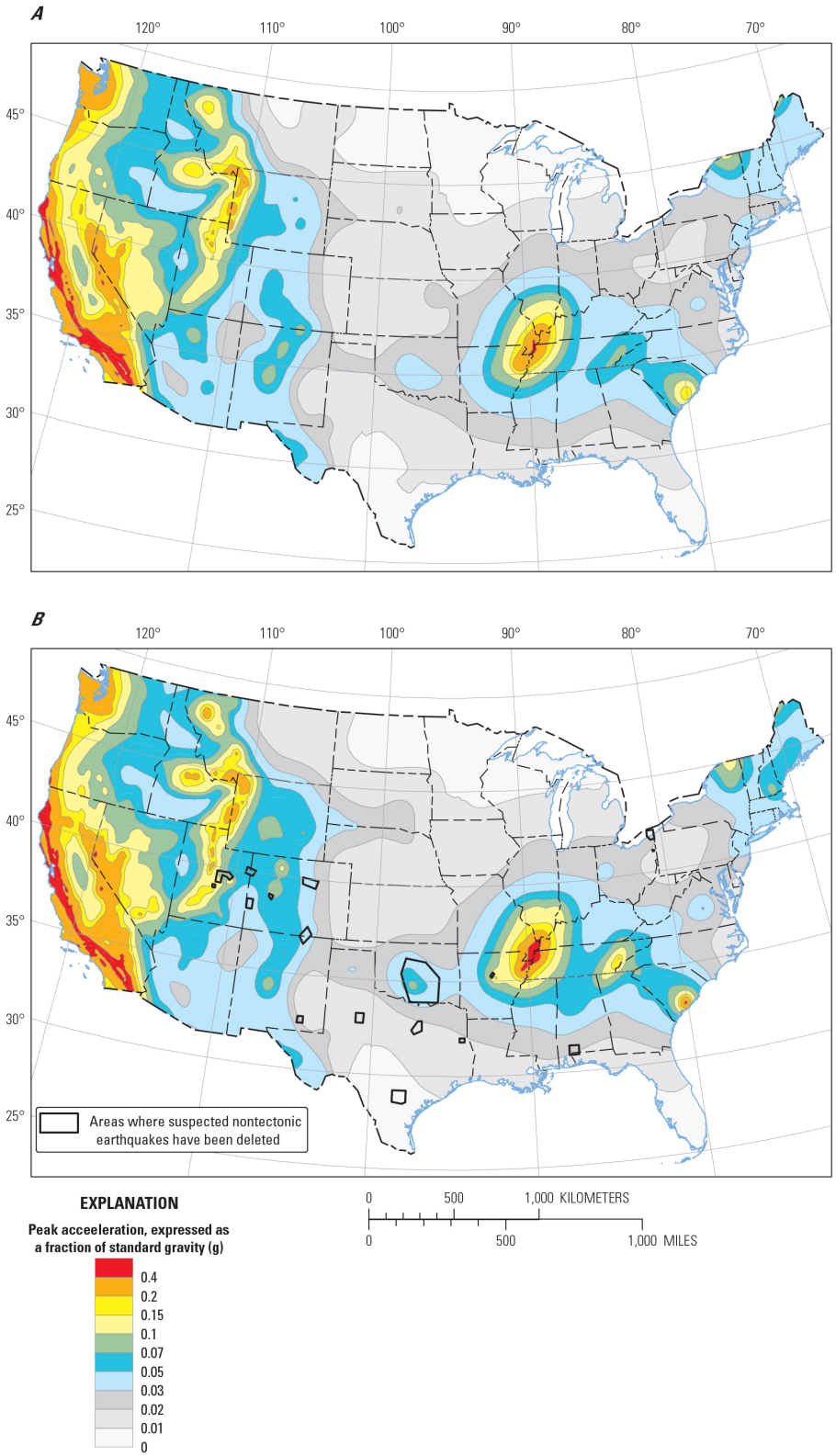

Figure 4. Maps showing peak ground acceleration for 10-percent probability of exceedance in 50 years and V_{S30} site condition of 760 meters per second. *A*, 2008 version of the national seismic hazard maps and *B*, 2014 version.

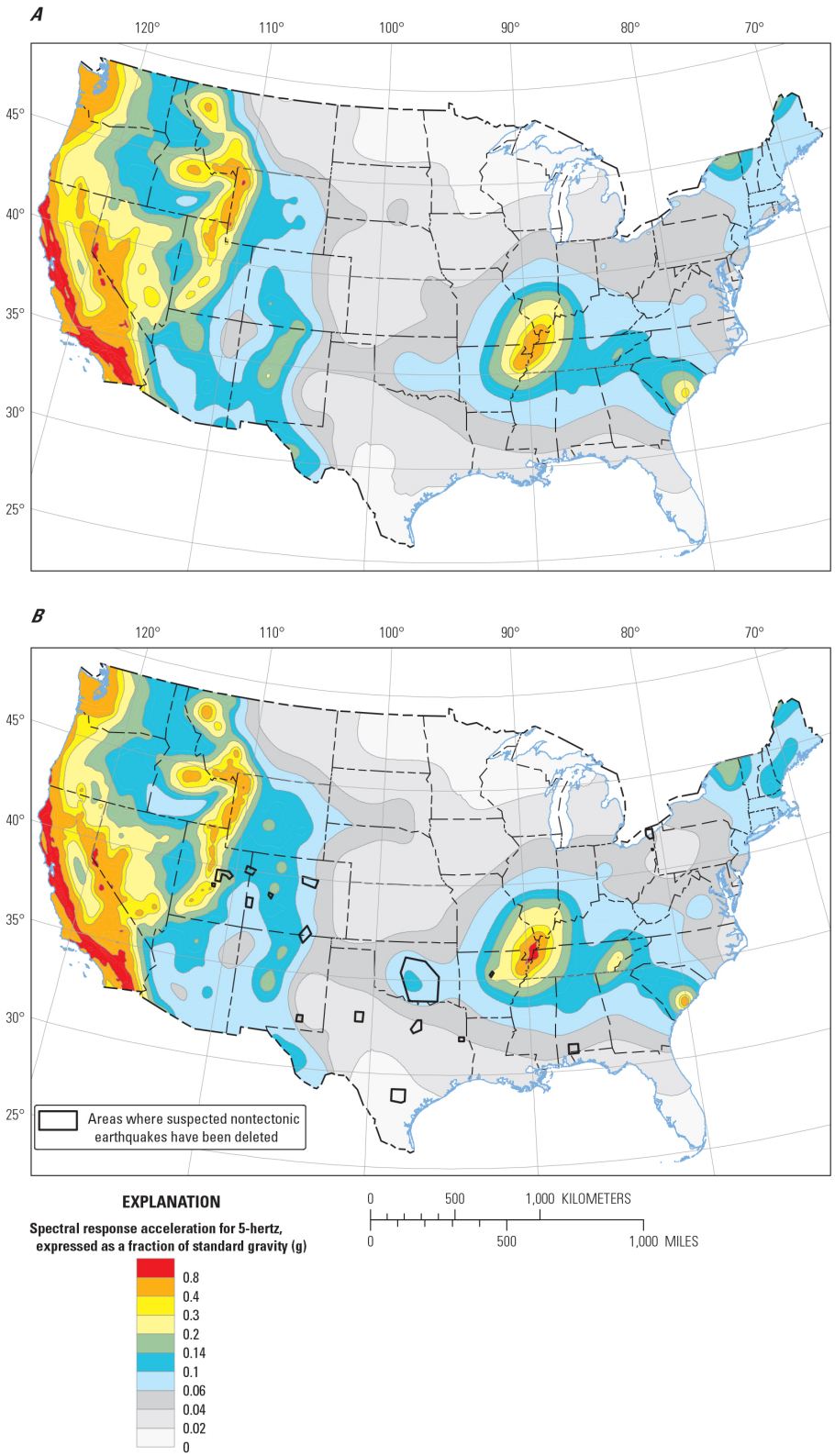

Figure 5. Maps showing 5-hertz (0.2-second) spectral acceleration for 10-percent probability of exceedance in 50 years and VS30 site condition of 760 meters per second. *A*, 2008 version of the national seismic hazard maps and *B*, 2014 version of the maps.

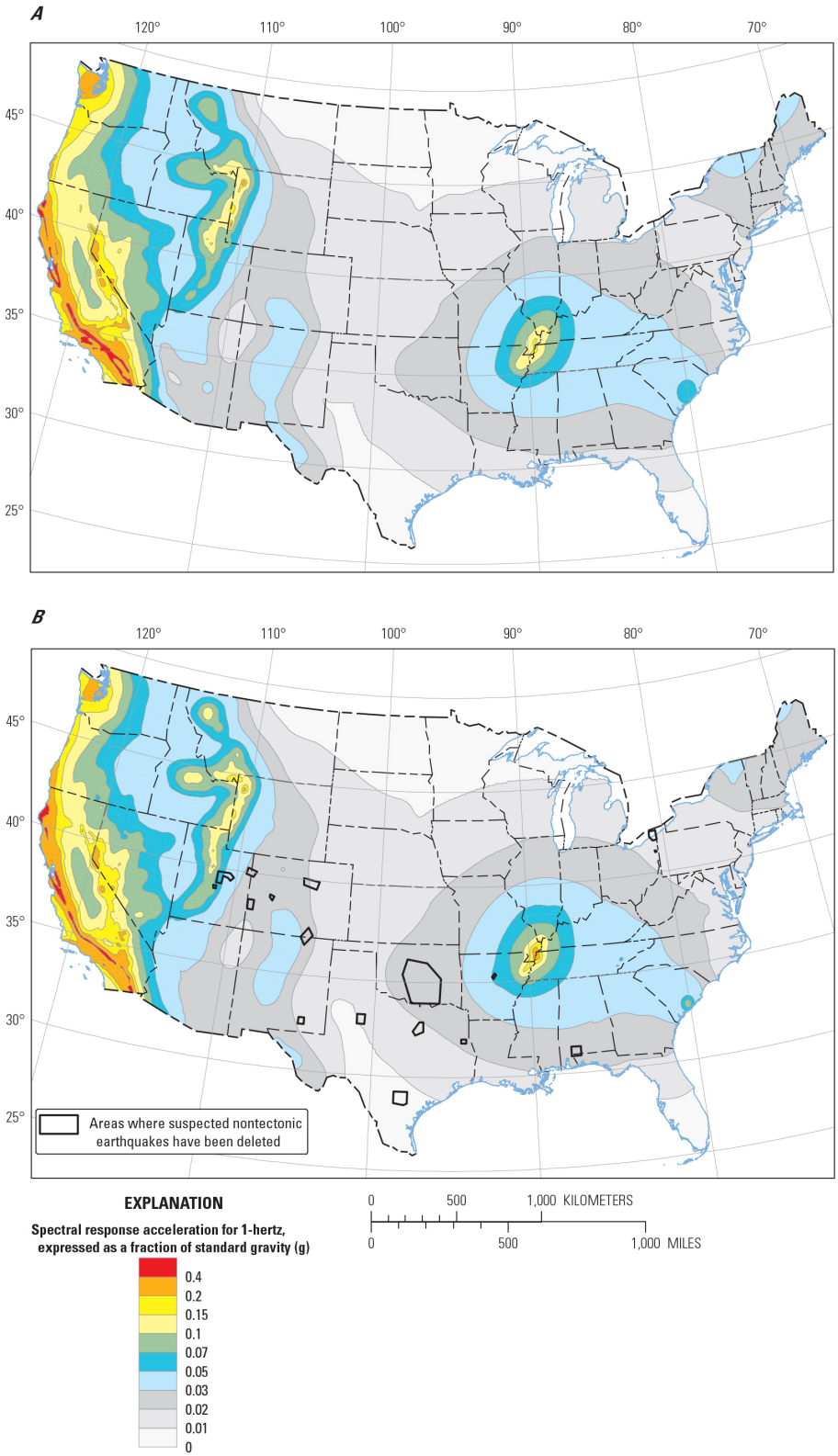

Figure 6. Maps showing 1-hertz (1-second) spectral acceleration for 10-percent probability of exceedance in 50 years and V_{S30} site condition of 760 meters per second. *A*, 2008 version of the national seismic hazard maps and *B*, 2014 version.

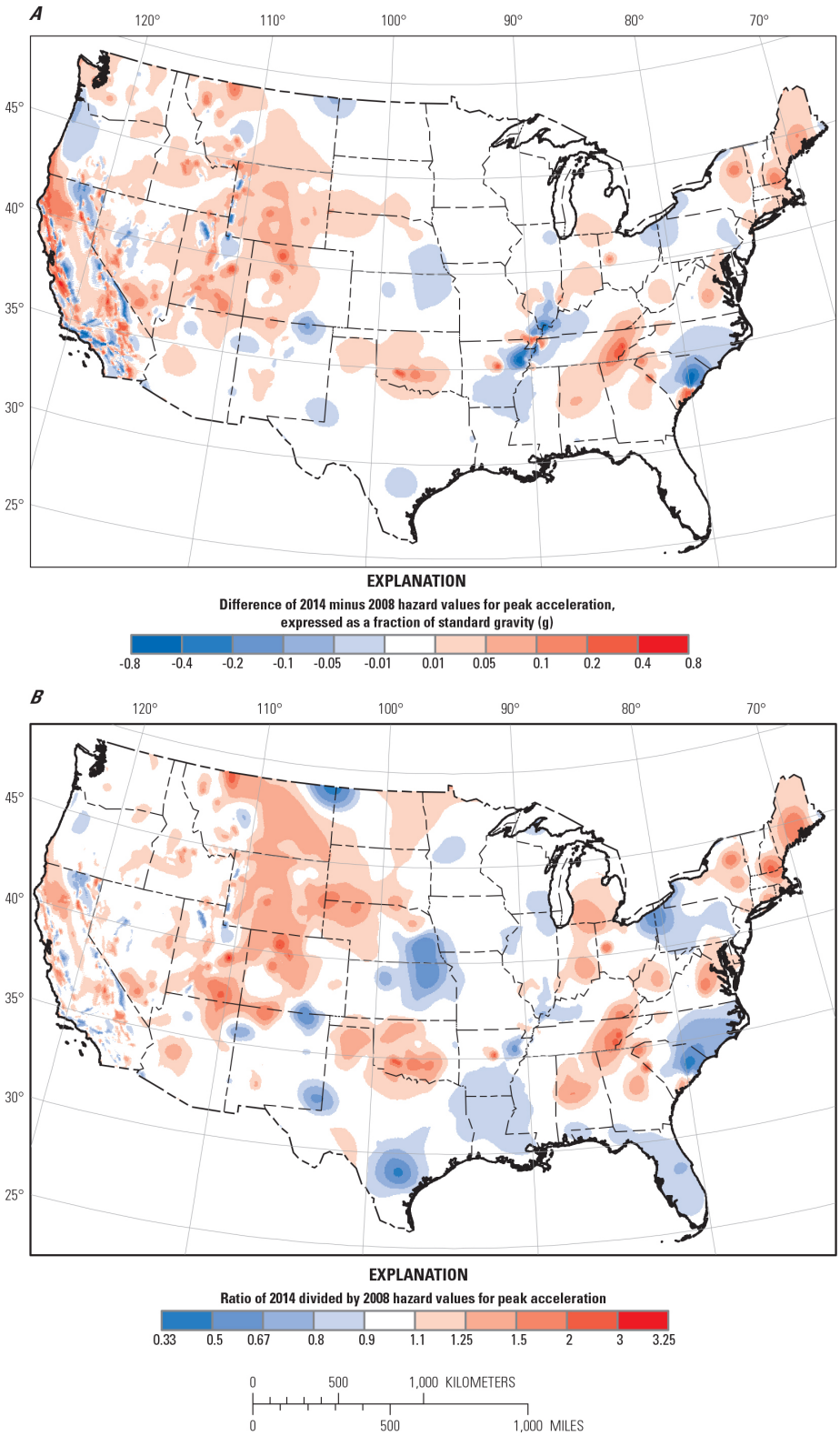

Figure 7. Maps comparing change in peak ground acceleration for 2-percent probability of exceedance in 50 years and V_{S30} site condition of 760 meters per second. *A*, Difference between the 2014 and 2008 versions of the national seismic hazard maps and *B*, ratio between the 2014 and 2008 versions.

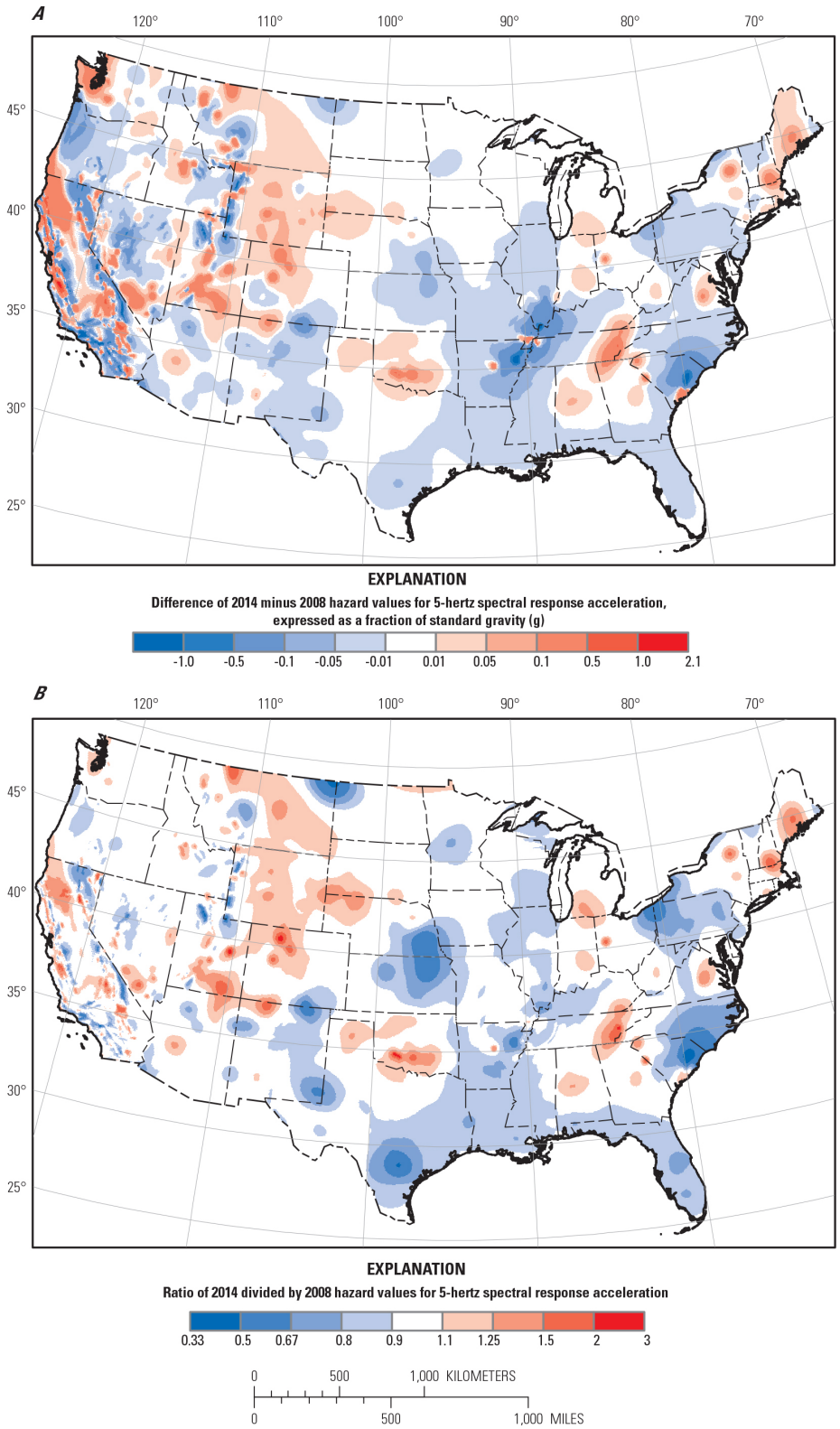

Figure 8. Maps comparing change in 5-hertz (0.2-second) spectral acceleration for 2-percent probability of exceedance in 50 years and V_{S30} site condition of 760 meters per second. *A*, Difference between the 2014 and 2008 versions of the national seismic hazard maps and *B*, ratio between the 2014 and 2008 versions.

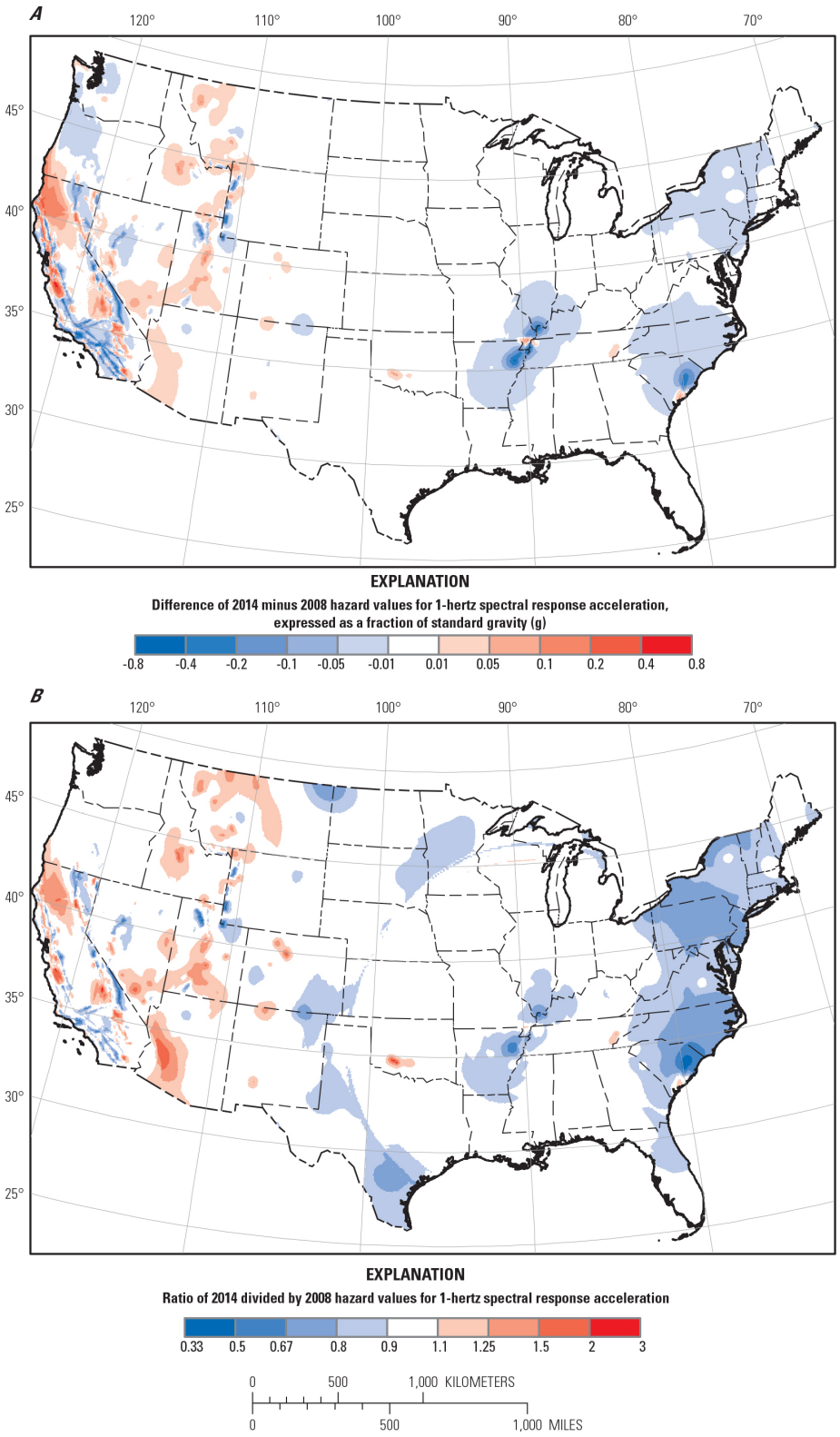

Figure 9. Maps comparing change in 1-hertz (1-second) spectral acceleration for 2-percent probability of exceedance in 50 years and V_{S30} site condition of 760 meters per second. *A*, Difference between the 2014 and 2008 versions of the national seismic hazard maps and *B*, ratio between the 2014 and 2008 versions.

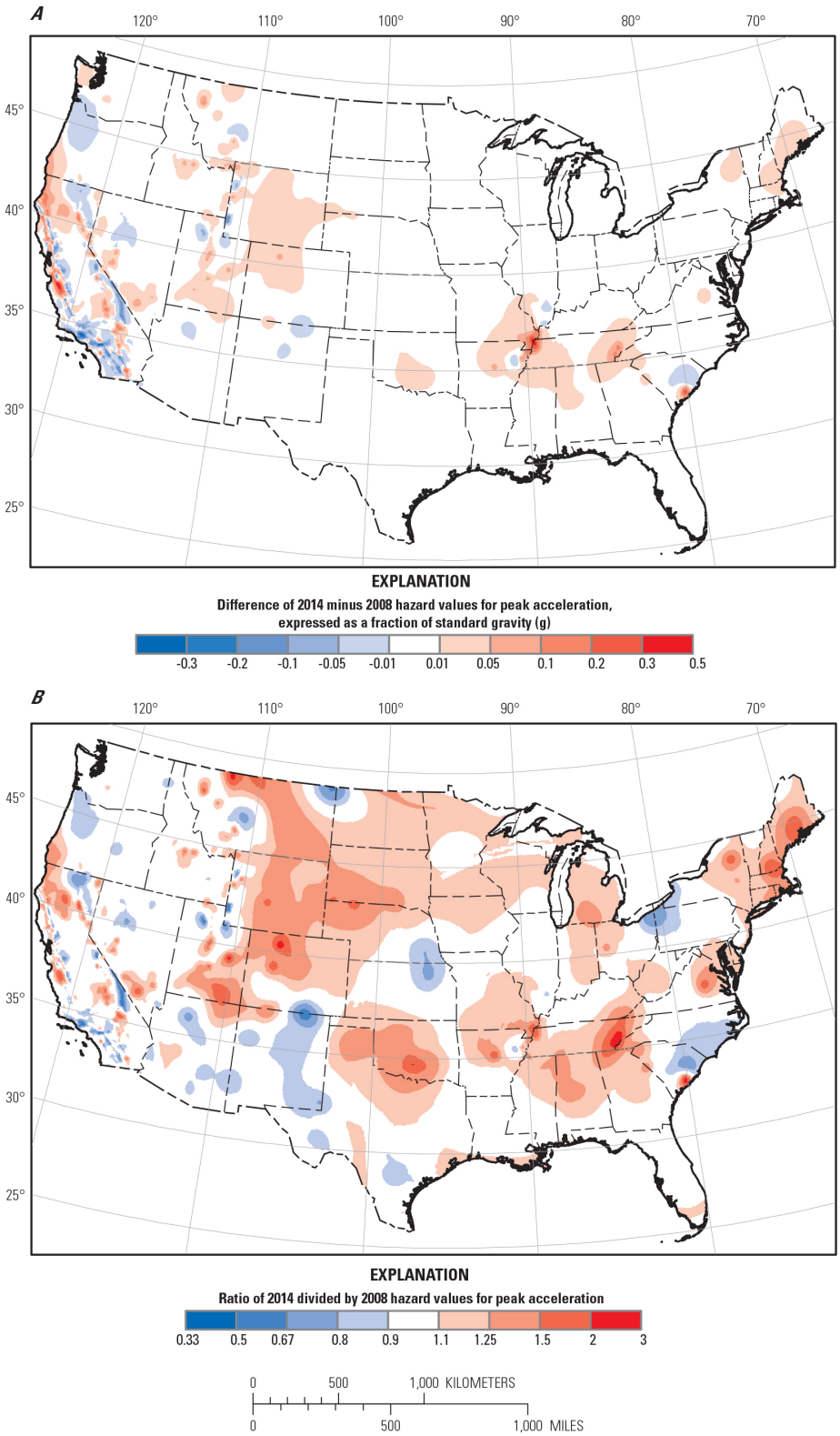

Figure 10. Maps comparing change in peak ground acceleration for 10-percent probability of exceedance in 50 years and V_{S30} site condition of 760 meters per second. *A*, Difference between the 2014 and 2008 versions of the national seismic hazard maps and *B*, ratio between the 2014 and 2008 versions.

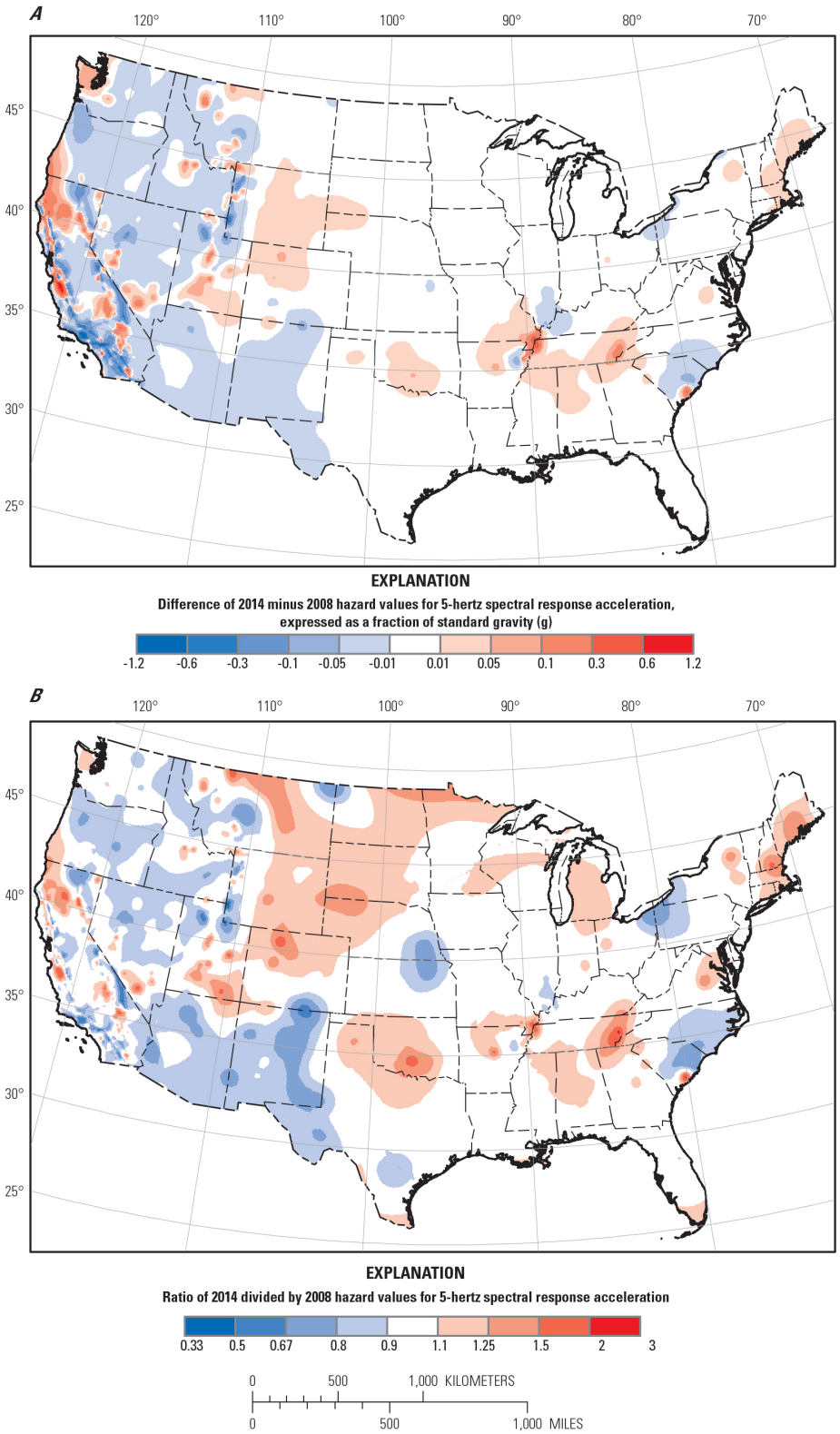

Figure 11. Maps comparing change in 5-hertz (0.2-second) spectral acceleration for 10-percent probability of exceedance in 50 years and V_{S30} site condition of 760 meters per second. *A*, Difference between the 2014 and 2008 versions of the national seismic hazard maps and *B*, ratio between the 2014 and 2008 versions.

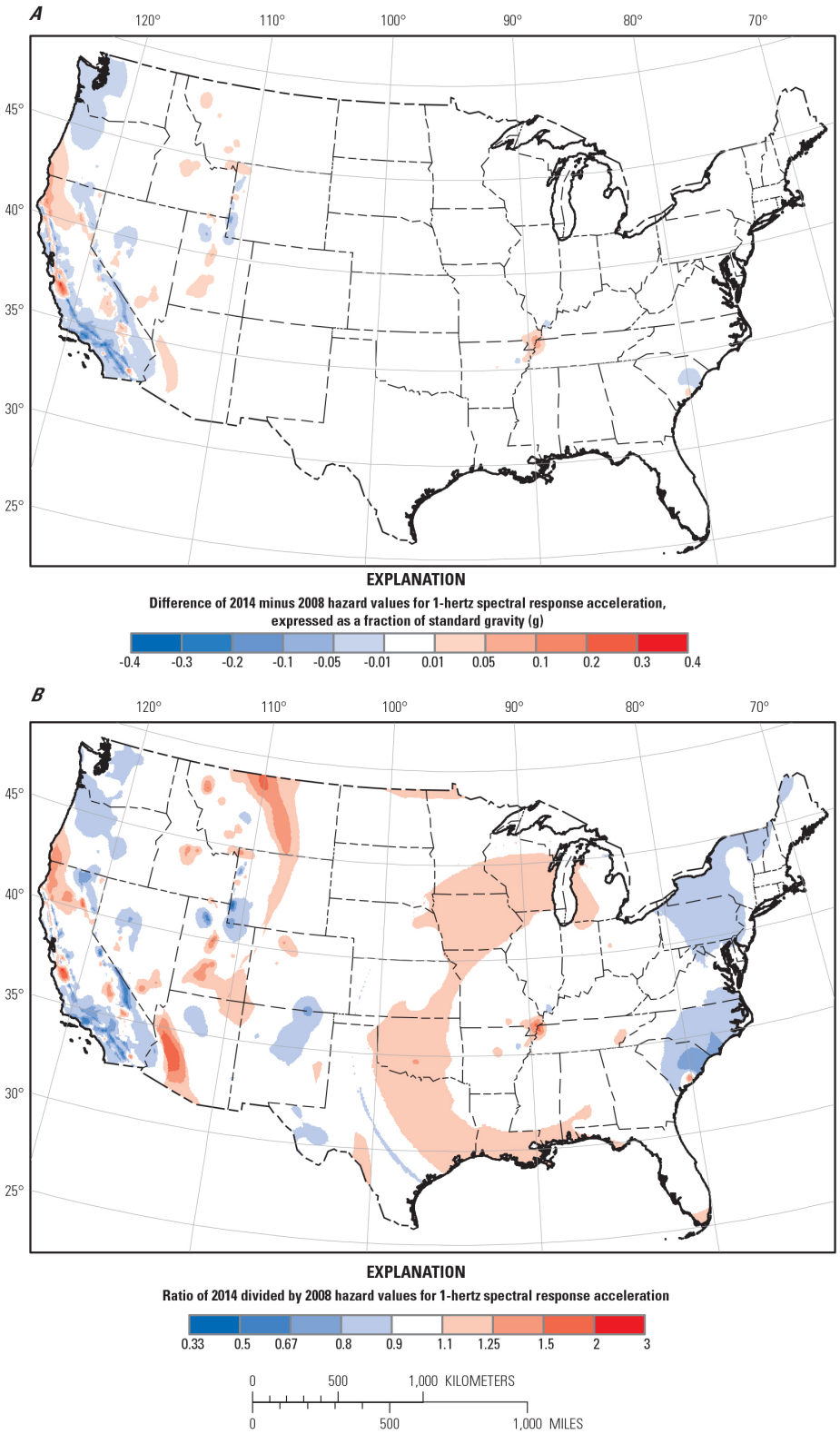

Figure 12. Maps comparing change in 1-hertz (1-second) spectral acceleration for 10-percent probability of exceedance in 50 years and V_{S30} site condition of 760 meters per second. *A*, Difference between the 2014 and 2008 versions of the national seismic hazard maps and *B*, ratio between the 2014 and 2008 versions.

This report describes the changes shown in figures 1–12 and their impacts on hazard for Central and Eastern United States sources, Western United States sources (Intermountain West and Pacific Northwest crustal sources, Cascadia subduction zone, California sources), combined geologic and geodetic inversion sources, and ground motion models (including models for stable crustal, active shallow crustal, subduction interface, and subduction in-slab). The "Results" section of this report describes details of these differences and quantifies the contributions of the fault models, earthquake source models, and ground motion models.

Central and Eastern United States Earthquake Source Models

We derive the probabilistic seismic hazard for the Central and Eastern United States (CEUS) from (1) an earthquake catalog, which records rates and patterns of past earthquakes; (2) geologic studies, which identify faults and their associated slip rates capable of generating earthquakes and liquefaction features caused by prehistoric earthquakes; and (3) ground motion models for stable continental regions (SCRs). This section describes updates of the USGS seismic hazard model (Petersen and others, 2008, 2012) for the seismicity-based background source model and the fault-based source zones. Ground motion models applied in the CEUS are discussed in a separate section. We discuss the impact of these new catalogs and seismic source models in the results section.

The CEUS Seismic Source Characterization Project recently compiled and reanalyzed earthquake catalogs and Quaternary deformation studies in eastern North America to improve earthquake hazard assessments for nuclear power plants. This project, hereafter referred to as CEUS–SSCn (the 'n' signifies that this seismic source characterization is intended for use in seismic hazard assessments for nuclear power plants), followed the Level-3 guidelines of the Senior Seismic Hazard Analysis Committee (Kammerer and Ake, 2012) to develop models that represent the center, body, and range of technically defensible interpretations of the available data, models, and methods. The intention of these models is to account for broader uncertainties and replace older seismic source models. The NSHMP considered the CEUS–SSCn models and adopted some of them in part or with modifications to define new source models and broader epistemic uncertainty in the 2014 update.

Seismicity-Based Background Source Model

The NSHMP has used the seismicity-based background source model, with some variations, since 1996 (Frankel and others, 1996, 2002; Petersen and others, 2008). Sources derived from seismicity account for two types of earthquakes in the CEUS: seismicity that is distributed randomly across the region and large earthquakes that are not associated with identified faults. The seismicity-based background source model assumes that future large earthquakes are more likely to nucleate near previous earthquakes with moment magnitude (M_w) greater than or equal to ($\geq$) 2.7. We generate a new M_w catalog to produce the seismicity-based background source model. Previous versions of the map applied an earthquake catalog based on body-wave magnitude (m_{blg}, from crustal guided surface waves, Lg) greater than or equal to 3.0. This body-wave magnitude of 3.0 converts to an M_w of 2.7. The logic tree for combining seismic-hazard models is shown in figure 13. The logic tree includes an updated earthquake catalog, new tectonic and seismicity-based zonations, alternative smoothing algorithms, and nine published ground motion models.

For the hazard calculations, the source geometry associated with the ruptures in the seismicity-based background source model is a virtual fault centered on grid points, which sample latitude and longitude at 0.1-degree increments. Earthquakes from M_w4.7 to the maximum magnitude (Mmax) are considered, with rates obtained from the smoothed seismicity-based source model. Rupture on a vertical

fault with area, A, are determined from the Somerville relation, $A=10^{M-4.366}$ square kilometers (km^2). The virtual fault width is the lesser of 20 km and square root of A divided by 1.618. In contrast to the CEUS–SSCn (2012), we do not model uncertainty in seismogenic width. Several alternative ground motion models (GMMs) are used to calculate probabilities of ground motion exceedance.

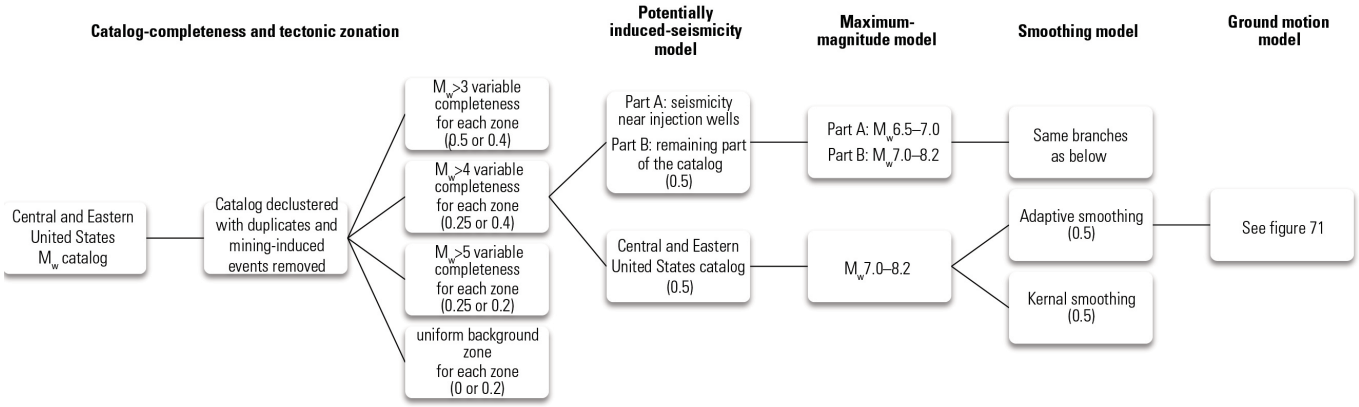

Figure 13. Logic tree for the seismicity-based background source model in the Central and Eastern United States. Assigned branch weights shown in parentheses.

Earthquake Catalog for the Central and Eastern United States

The NSHMP developed an earthquake catalog to estimate the rates of future earthquakes across the CEUS. A major change from the 2008 to the 2014 catalog is the transition from m_{blg} to M_w. This change eliminates uncertain conversions between magnitude scales that formerly were used at several stages of the hazard computations. This change is also consistent with recent CEUS ground motion equations, which require moment magnitude estimates of earthquake size.

We developed a uniform seismicity catalog for central and eastern North America through 2012, generally following the approach used by the CEUS–SSCn (2012). For each earthquake, the catalog lists fields for expected moment magnitude, $E[M_w]$, hypocenter location, and origin time derived from a preferred source that is listed in a comment field. Each entry also lists an estimate of magnitude uncertainty and a counting factor (a function of the b value and the magnitude uncertainty), which is used to compute unbiased seismicity rates.

We combined published catalogs and characterize them by the method used to assign M_w:

- Catalogs from the Global CMT (Centroid Moment Tensor) project (Dziewonski and others, 1981; Ekström and others, 2012), St Louis University (R. Herrmann, written commun., 2013), and table B-2 in CEUS–SSCn (2012) list earthquakes with moment magnitudes from inversions of long-period waveforms or surface-wave spectra ("observed" or "measured" M_w). We adjust magnitudes to $E[M_w]$ and estimate the magnitude uncertainty following CEUS–SSCn (2012).
- Atkinson (2004a, b), Boatwright (1994), and Macherides (2002) cataloged earthquakes with moment magnitudes from analyses of local or regional waveforms or spectra ("approximate" M_w). Table B-3 in CEUS–SSCn (2012) lists $E[M_w]$ and magnitude uncertainty for these earthquakes, which we adopted without modification.

- Johnston and others (1994), Bakun and others (2003), and Bakun and Hopper (2004a, b) cataloged significant historical earthquakes with moment magnitude and magnitude uncertainty derived from special studies of intensity data.
- The sources for most earthquakes are published catalogs:
    - National Center for Earthquake Engineering Research (NCEER) (Seeber and Armbruster, 1991)
    - USGS Preliminary Determination of Epicenters (PDE) online catalog (*neic.usgs.gov/neis/epic/epic_global.html*, accessed April 2007 and January 2013)
    - Geological Survey of Canada (GSC) online catalog (2013)
    - Stover and Coffman (1993)
    - Stover and others (1984)
    - CEUS–SSCn (2012)

Source catalogs in this group generally list traditional instrumental magnitudes, original intensity measures, or both. CEUS–SSCn (2012) developed new empirical conversion relations to M_w from many common magnitude and intensity scales, short-period surface-wave magnitude, local magnitude, duration and coda magnitudes, epicentral intensity, and felt area. We estimate $E[M_w]$ and magnitude uncertainty following the CEUS–SSCn (2012) guidance.

We also maintain a manually edited, "special-case" catalog of suspected erroneous or nontectonic events (explosions, mining-related events, etc.) identified from special studies. For the 2014 update, nontectonic events compiled by the CEUS–SSCn are added to this file. These special-case events are deleted from the final catalog.

The NSHMP combines the source catalogs following the method of Mueller and others (1997). The source catalogs overlap in time and space; a preferred entry is selected when an earthquake is listed in more than one catalog. Original data sources are preferred over compilations. For consistency, observatory magnitudes or original intensities that we can convert to M_w are preferred over published magnitudes that have been converted elsewhere. Catalogs with "observed/measured" M_w, "approximate" M_w, and M_w derived from special studies (the first three bullets above) rank highest. For the remaining sources the preference order is (1) National Center for Earthquake Engineering Research–NCEER (Seeber and Armbruster, 1991), (2) USGS Preliminary Determination of Epicenters (2013), (3) Geological Survey of Canada (2013), (4) Stover and Coffman (1993), (5) Stover and others (1984), and (6) CEUS–SSCn (2012). Rather than combining all size measures for an earthquake, we instead adopt a single estimate of M_w and uncertainty from the preferred catalog; this is done in consideration of catalog maintenance and future updates. Comparisons with the CEUS–SSCn (2012) catalog show some M_w differences, but no obvious systematic biases.

After removing duplicates, the NSHMP declusters the combined catalog (removes events considered to be foreshocks or aftershocks) using the Gardner and Knopoff (1974) algorithm. Early versions of the declustered catalog contained some events that were, judging by their locations and times, probably aftershocks of the 1886 Charleston earthquake. Old, poorly located aftershocks can evade the Gardner and Knopoff (1974) distance filter, which was developed from modern data and intended for modern applications. We implement a stronger filter pre-1900, a bilinear function of distance as compared to magnitude hinged at M_w5 that approximately doubles the Gardner and Knopoff (1974) filter radii for all magnitudes. The final declustered catalog includes 6,259 earthquakes from 1700 through 2012 with M_w greater than or equal to 2.5 (fig. 14). The number of earthquakes that contributed to the declustered catalog from each source catalog is listed in table 1.

Table 1. Contributions to the declustered catalog (1700–2012, M_w2.5 and greater).

[CEUS–SSCn, Central and Eastern United States seismic source characterization for nuclear facilities; M_w, moment magnitude]

Source catalog	Number of earthquakes
Special cases	6
M_w (observed/measured)	233
M_w (approximate)	332
M_w (intensity special studies)	75
National Center for Earthquake Engineering Research, NCEER Seeber and Armbruster (1991)	2,094
USGS Preliminary Determination of Epicenters (2013)	1,311
Geological Survey of Canada (2013)	183
Stover and Coffmann (1993)	10
Stover and others (1984)	446
CEUS–SSCn (2012)	1,569
Total	6,259

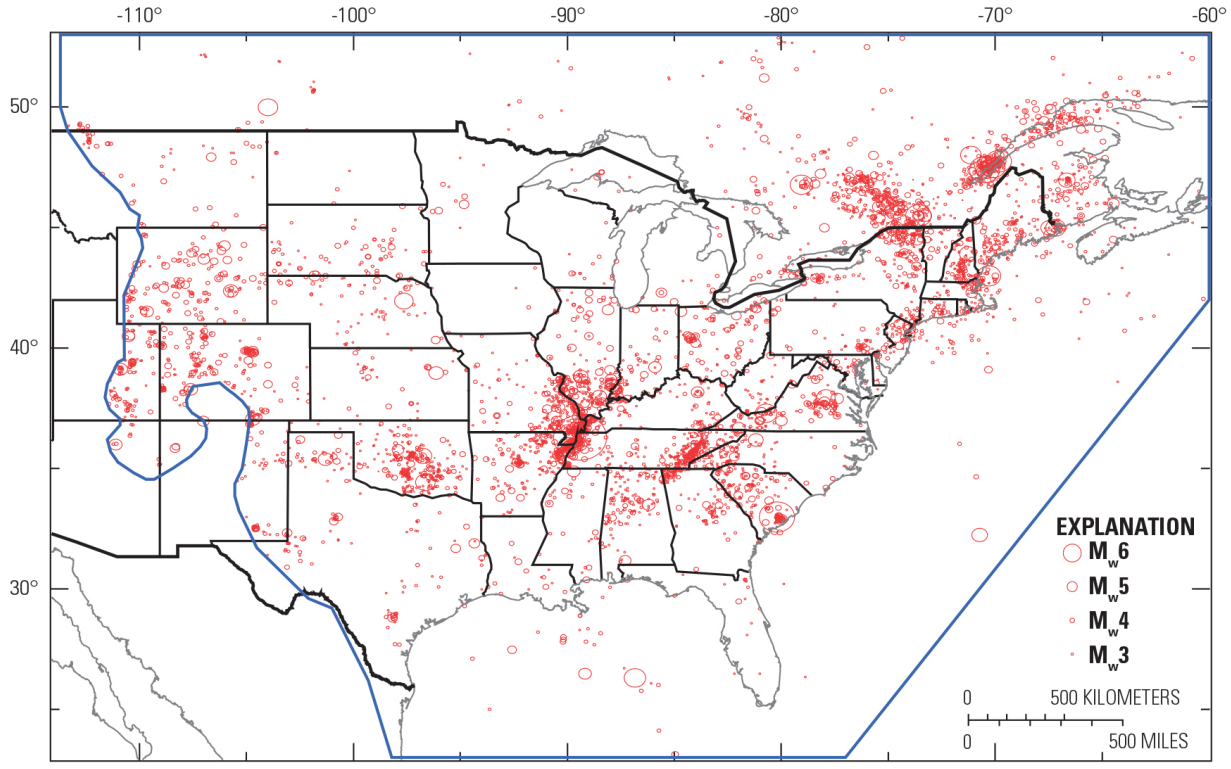

Figure 14. Declustered catalog for the Central and Eastern United States including M_w2.5 and greater earthquakes occurring since 1700, including potentially induced earthquakes.

Some CEUS earthquakes may be causally related to industrial fluid processes such as hydrocarbon production or wastewater disposal. This is a well-known phenomenon (McGarr, 2002), and previous versions of the maps routinely took out such earthquakes; however, the importance of this phenomenon has increased since the 2008 map update because, since that update, there has been a dramatic increase in the earthquake count within the CEUS (Ellsworth, 2013). More than 300 earthquakes with magnitude greater than 3 occurred from 2010 through 2012, compared with an average rate of 21 earthquakes per year observed from 1967 to 2000 across the CEUS. Proper treatment of these earthquakes in probabilistic seismic-hazard analysis is complicated and a topic of active research. The NSHMP is considering several different approaches to account for the hazard from induced earthquakes in a consistent way. Based on current literature (Frohlich, 2012; Horton, 2012; Ellsworth, 2013; Frohlich and Brunt, 2013) and on unusual patterns of seismicity, we identify and separate localized swarms of earthquakes potentially induced by fluid injection from the declustered catalog. These swarms, listed with the starting year of their suspect seismic activity, are Rocky Mountain Arsenal, Colorado (Colo.) (1962–1979); Rangely, Colo. (1957–present); Fashing, Texas (Tex.) (1973–present); Cogdell, Tex. (1976–present); Ashtabula, Ohio (1987–2007); Paradox Valley, Colo. (1991–present); Brewton, Alabama (1997–present); Dagger Draw, New Mexico (N. Mex.) (1998–present); Raton Basin, Colo.–N. Mex. (2001–present); central Oklahoma (2006–present); Dallas–Ft. Worth Airport, Tex. (2008–present); Guy-Greenbrier, Arkansas (Ark.) (2009–present); Youngstown, Ohio (2010–present); and Timpson, Tex. (2011–present) (fig. 15). The NSHMP uses the declustered catalog with these swarms removed for the hazard analysis. The swarm areas are delineated as zones to show where earthquakes have been extracted and where the hazard may vary from what is depicted on the maps based on various models for activity. We will consider alternative models for including potentially induced seismicity in future versions of the map. Users of the current hazard information should consider that hazard might be higher in these zones of potentially induced seismicity than are presently shown on the map. In addition, we suggest reexamination of hazard in other places with the potential for increased rates of earthquakes.

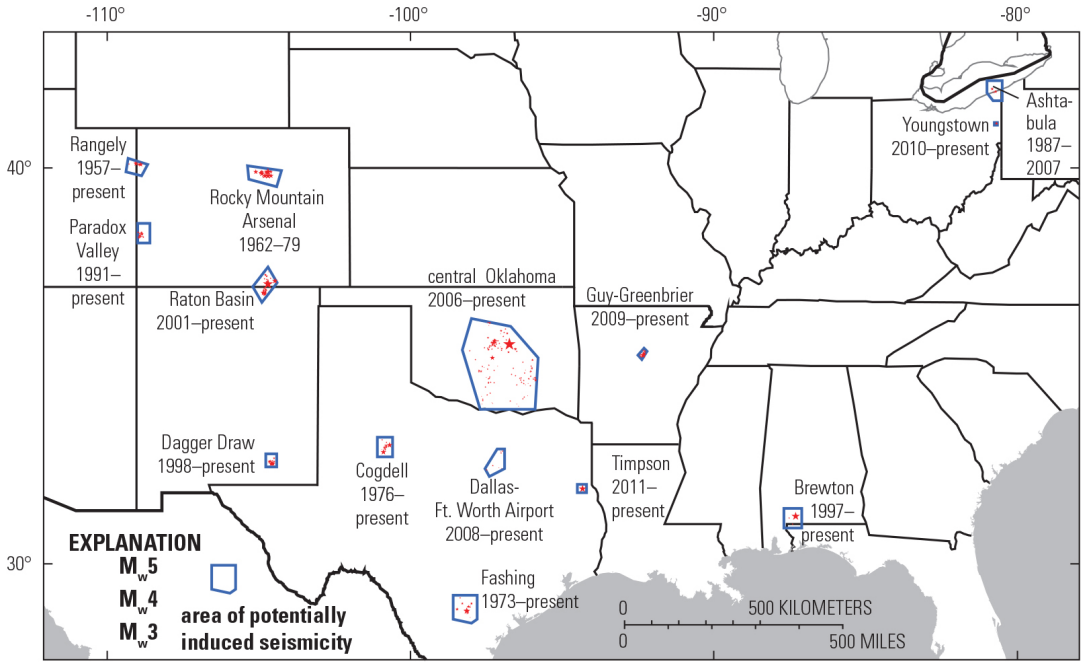

Figure 15. Map showing areas of potentially induced seismicity in the Central and Eastern United States.

Seismotectonic Zones

The 2008 NSHMP distinguished four broad seismotectonic zones in the CEUS with distinct seismicity and Mmax: craton, extended margin, Colorado Plateau, and Rocky Mountains (Petersen and others, 2008). The boundary between the craton and extended-margin zones is based partly on the location of the Iapetan rift margin (Wheeler, 1995), which separates the older craton from younger Mesozoic and Paleozoic terranes (fig. 16*A*). CEUS–SSCn (2012) subdivided the CEUS east of longitude -105° into 12 seismotectonic zones. We generalize this zonation of the craton and extended margin by aggregating the CEUS–SSCn zones into four broader zones (fig. 16*B*): craton, Mesozoic extended terrane, Paleozoic extended terrane, and the Gulf Coast region, which mostly is composed of Paleozoic age crust overlain by up to several kilometers of Mesozoic and younger sediments.

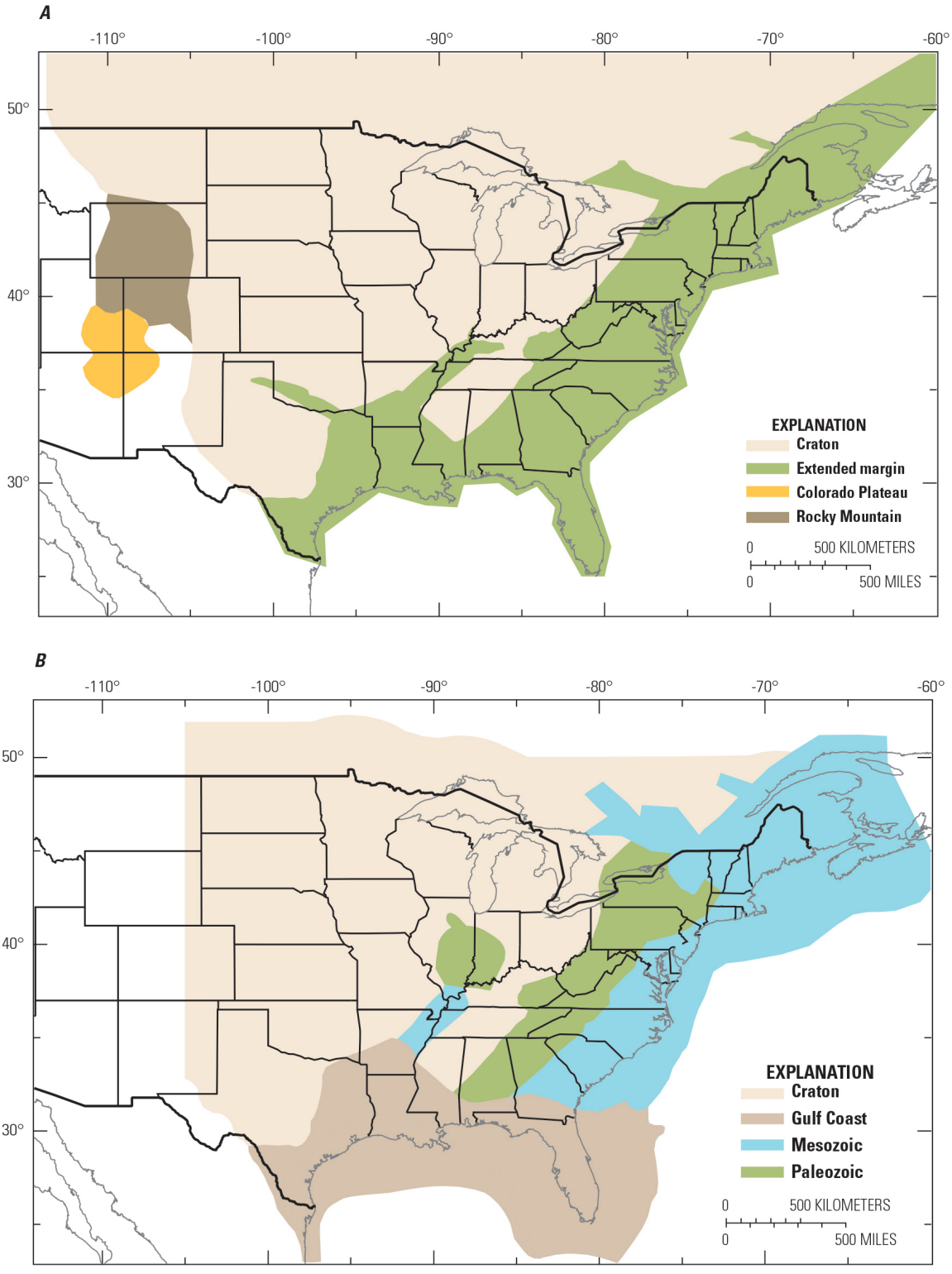

Figure 16. Alternative seismotectonic zonation models used to assign floor *a*-values and Mmax. Map of zonation model based on *A*, 2008 NSHMP model and *B*, generalized CEUS–SSCn (2012) models.

We use seismicity rate floors within the background seismicity model to account for potential activity in areas with very few or no observed earthquakes, as described in the "Calculating a-Grids" section below. Only the NSHMP zonation model (not the generalized CEUS–SSCn model) is used for this implementation. The NSHMP and generalized CEUS–SSCn zonation models are used to develop maximum magnitude models, as described in the "Maximum Magnitude" section below.

Calculating a-Grids

In the 2014 update, the NSHMP has two approaches to calculating seismicity rate grids (a-grids) from the declustered catalog. The first approach computes rate grids for three magnitude levels and uses a fixed-length smoothing algorithm. The second approach uses a single magnitude level and an adaptive smoothing algorithm that allows variable length smoothing depending on the distances to the nearest earthquakes. Both approaches assume b=1.0, incorporate variable completeness times, estimate a-values over the CEUS grid, and spatially smooth the a-values. Thus, we do not change the overall methodology for modeling background seismicity in the CEUS (Frankel, 1995; Frankel and others, 1996), but we add the new approach to account for spatially variable smoothing lengths.

Both approaches share the following components. The NSHMP superimposes a 0.1-degree by 0.1-degree grid on the CEUS. We assign b=1.0 to each grid cell based on a statistical analysis (following Weichert, 1980) of the declustered M_w catalog; however, the analysis of the subcatalog near Charlevoix yields a smaller b-value, so we use b=0.9 in the hazard analysis for the first approach. The historical seismicity rate in each grid cell is compared to the corresponding zone-average rate from the NSHMP seismotectonic zonation (defined in the "Seismotectonic Zonation" section), and a rate floor is implemented if needed. As in past updates, we assign uniform, average background seismicity rates for the eastern Tennessee and New Madrid seismic zones (Petersen and others, 2008). Both methods use a new magnitude completeness zonation (fig. 17), a generalization of the completeness scheme used by the CEUS–SSCn (2012), to account for historical patterns of human settlement and seismic instrumentation. Based on discussions with our steering committee, we weight the fixed-smoothing model 0.6 and the adaptive-smoothing model 0.4. We assigned the adaptive-smoothing model lower weight because it is new and because it tends to tightly smooth some clusters. We describe two methods of smoothing the seismicity below.

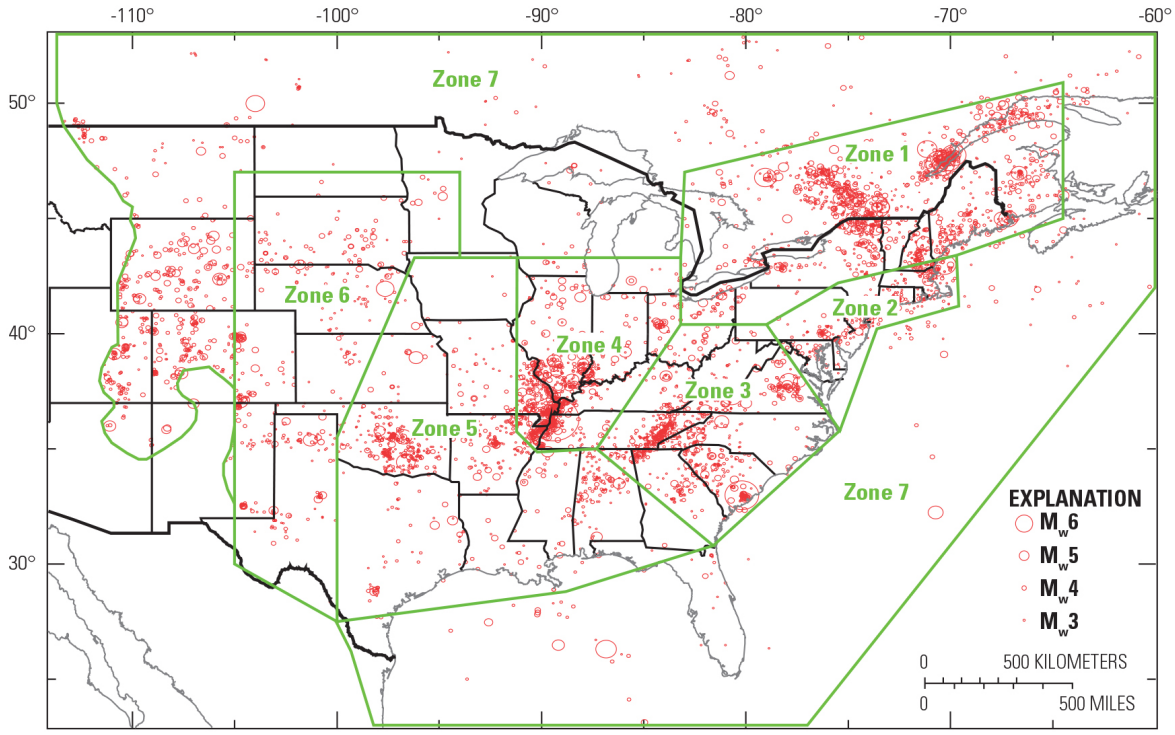

Figure 17. Map of the seven completeness zones for M_w2.7 and greater, M_w3.7 and greater, and M_w4.7 and greater in the Central and Eastern United States. See table 2 for years of variable catalog completeness.

Table 2. Year of catalog completeness for M_w2.7 and greater, M_w3.7 and greater, and M_w4.7 and greater for zones in the Central and Eastern United States shown in figure 17.

[M_w, moment magnitude]

Zone	$M_w \geq 2.7$	$M_w \geq 3.7$	$M_w \geq 4.7$
1	1800	1880	1970
2	1700	1750	1930
3	1800	1885	1975
4	1800	1880	1980
5	1850	1920	1980
6	1850	1900	1960
7	1850	1920	1980

First Approach

In the first approach, separate a-grids are computed for three magnitude levels, accounting for variable catalog completeness (table 2). Model 1 counts earthquakes with M_w greater than or equal to 2.7 (similar to m_{blg} 3 and greater used in previous USGS NSHMP maps updates, Petersen and others, 2008); Model 2 counts earthquakes with M_w greater than or equal to 3.7 (m_{blg} 4 and greater); and Model

3 counts earthquakes with M_w greater than or equal to 4.7 (m_{blg} 5 and greater). Following CEUS–SSCn (2012), we use the counting factor N* to adjust rates to account for magnitude uncertainty. Cumulative rates are adjusted to incremental rates (Herrmann, 1977). Rate grids are spatially smoothed to account for uncertainties in the locations of future earthquakes: we apply a two-dimensional, isotropic, Gaussian function with a fixed correlation distance of 50 km for Model 1 or 75 km for Models 2 and 3. This spatial smoothing remains unchanged from past NSHMP updates. In addition, a seismicity rate floor, Model 4, is implemented to account for future earthquakes in grid cells with little or no historical earthquakes. This model consists of a grid with uniform average seismicity rates computed for each NSHMP seismotectonic zone (defined in the "Seismotectonic Zonation" section).

The historical seismicity rate in each grid cell is defined as a weighted average of Models 1–3, with weights 0.5, 0.25, and 0.25, respectively. If the historical rate exceeds the zone-average rate (Model 4), then the final model rate is simply equal to the historical rate. Otherwise, the final model rate is a weighted average of Models 1–4 with weights 0.4, 0.2, 0.2, and 0.2, respectively. The final rate in a grid cell is never less than the historical rate, and the rate of seismicity in seismically active areas is not reduced to make a floor in quiet areas. The total model-seismicity rate across the CEUS exceeds the historical rate by about 10 percent using this method (Frankel and others, 1996).

For this first approach, figure 18*A* shows the incremental a-grid assuming the NSHMP seismotectonic model and fixed smoothing. The incremental *a*-value represents the annual rate of earthquakes with -0.05 less than M_w less than 0.05 in each grid cell.

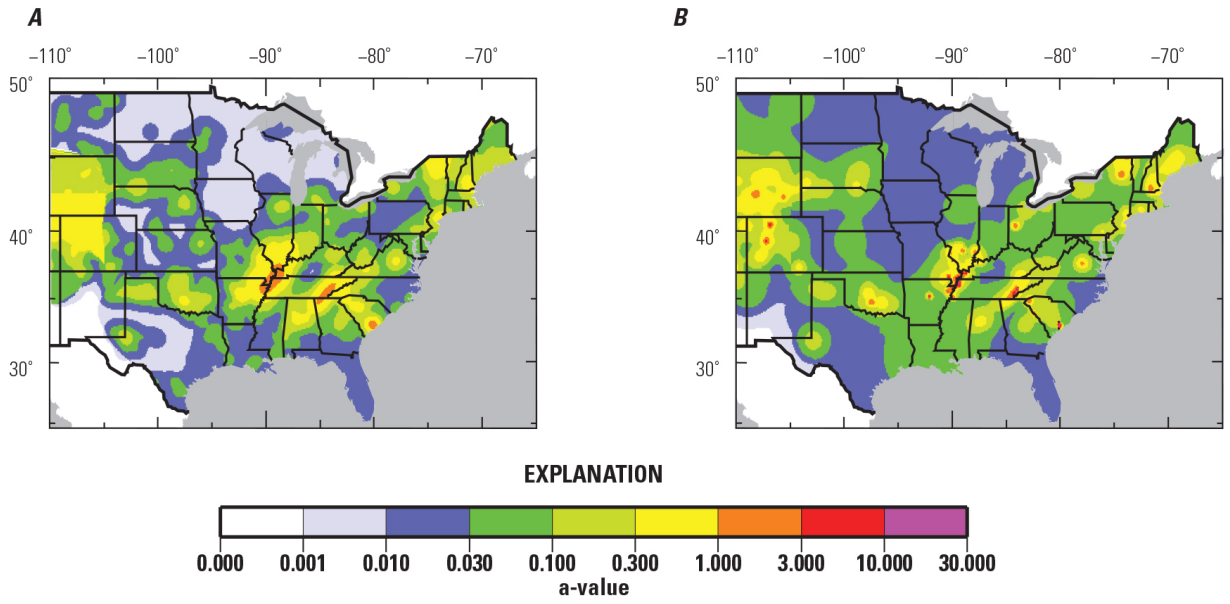

Figure 18. Maps showing cumulative seismicity-rate grids from alternative smoothing methods for 5-hertz spectral acceleration at 2-percent in 50 years probability of exceedance and V_{S30} site conditions of 760 meters per second. *A*, fixed-correlation-length and *B*, adaptive-correlation-length smoothing methods.

Second Approach

The second approach to estimate the background rate in the 2014 NSHMP update uses an adaptive, nearest-neighbor-type smoothing procedure, in which the smoothing distance for each epicenter is determined by the distance to the *n*th nearest epicenter, and the neighbor number (*n*) is optimized by likelihood calculations. Adaptive smoothing techniques were implemented by the USGS for a seismic hazard assessment of Afghanistan (Boyd and others, 2007), but have not been used in previous versions of the USGS NSHMP model. In this report, we follow the approach of Helmstetter and others (2007) and Werner and others (2011). This approach to calculating historical a-grids optimizes the neighbor number and completeness level that maximize the likelihood function.

To calculate the completeness level and neighbor number, the NSHMP uses the likelihood testing methods described by previous authors (for example, Helmstetter and others, 2007; Werner and others, 2011). For the purposes of optimizing the adaptive smoothing parameters, we divide the CEUS earthquake catalog into a "forecasting" subcatalog of older events and a "testing" subcatalog of recent events. We smooth seismicity rates calculated from the forecast catalog for all completeness levels (M_w2.7–5.2) and neighbor number to produce a set of forecast models and calculate the likelihood of observing earthquakes from the testing catalog, assuming a Poisson distribution for earthquake occurrence. The completeness levels and lateral variation in completeness investigated for the adaptive smoothing are a super-set of those used for the fixed-radius smoothing and were developed by the same methods. The completeness level and neighbor number that maximize the likelihood of observing the testing catalog are M_w=3.2 and n=4. In other words, assuming a completeness level of M_w=3.2, with spatially varying year and a neighbor number of four, best characterizes the recent spatial distribution of earthquakes in the CEUS.

We return to the full CEUS declustered earthquake catalog and recalculate the rate for each earthquake using a completeness level of M_w=3.2 and smooth this rate geographically over the distance to its fourth nearest-neighboring earthquake using a two-dimensional, isotropic, Gaussian function. In this way, we smooth the seismicity rates using a unique smoothing distance for the Gaussian function and convert from cumulative seismicity rates to incremental seismicity rates using the Herrmann (1977) relation.

The differences in the a-grids calculated from the fixed- and adaptive-smoothing approaches vary with epicenter density. In regions with high seismicity rates, the adaptive method yields smaller smoothing distances (correlation lengths) and locally higher seismicity rates. In regions with sparse seismicity, smoothing distances from the adaptive method are larger than those from the fixed-smoothing method, and the corresponding seismicity rates are decreased relative to rates from fixed smoothing. A comparison of the historical a-grids from the two approaches, and the differences in seismic hazard calculated between the two approaches are shown in figure 18*B*.

Maximum Magnitude for Background Seismicity

The background-seismicity model serves a dual purpose in the hazard model—it models seismicity from known faults or in places where there is no known fault. Throughout most of the CEUS, there is little geological or geodetic information about the presence or absence of active faults; the few well-studied seismic zones are areas with documented, unusually large earthquakes. Some areas have evidence of paleoearthquakes, but this evidence is insufficient to assign a magnitude or rate to an earthquake consistent with the observations. The background-seismicity model accounts for the uncertainties in these areas until there is enough evidence to define a more certain fault source.

If we assume (for lack of better evidence) that the Mmax of all possible earthquakes is uniform within a seismotectonic zone, then prehistoric and historical earthquakes in each zone provide a lower

bound on Mmax. That is, Mmax must be at least as large as the largest observed earthquake. We cannot know, however, if the largest observed earthquake is the largest possible earthquake. Thus, we rely on observations from other SCRs to define possible Mmax values for the CEUS. We represent the uncertainty in Mmax by assigning weights to four plausible Mmax values.

The New Madrid and Charleston seismic zones lie in the Mesozoic extended margin. For this zone, Mmax must be at least as large as the 1811–1812 New Madrid and 1886 Charleston earthquakes; however, the magnitudes of these historical earthquakes are not well constrained. As described later in this section, the lowest magnitude estimate among these nineteenth century earthquakes is 6.8 (Hough and Page, 2011); it is plausible, but unlikely, that the CEUS cannot produce an earthquake with magnitude greater than or equal to 6.8 (we have observed such earthquakes in other analogous regions and we have paleoseismic evidence for such earthquakes in the CEUS). Thus, we assign a weight of 0.1 to this Mmax. Most estimates for the New Madrid and Charleston earthquakes are in the magnitude range of 7.1–7.5. Given this current evidence, Mmax is more likely to be greater than 7.1 and possibly greater than 7.5. We represent these possibilities with a 0.3 weight at Mmax=7.2 and 0.5 weight at Mmax=7.6. Analogous extended margin regions, such as in northwestern India, have ruptured in similar size earthquakes (for example, 2001 M_w7.7 Bhuj earthquake, Hough and others, 2002). Earthquakes larger than M_w8.0 are not known in the prehistoric and historical SCR record. The low seismicity of SCR crust (Johnston and others, 1994; Mueller and others, 1997) indicates, however, that M_w8.0 and larger earthquakes have long recurrence intervals and might not appear in the record even if they are possible. For this reason, we assign Mmax=8.0 a weight of 0.1. This distribution of uncertainty has a weighted average Mmax of 7.44.

From the 2008 model, we slightly modify the weights of the Mesozoic extended margin to define Mmax weights in the Paleozoic extended margin. Johnston (1989) and Johnston and others (1994) observed in SCRs worldwide that earthquakes occurred preferentially in areas of young extension (Mesozoic or Paleogene, past 252 million years), but the data were insufficient to determine if there is a similar correlation for Paleozoic extension (540–252 million years ago). For the Paleozoic extension in the four-zone seismotectonic model, we assign equal weight (0.4) to Mmax of 7.2 and 7.6. This modification reduces the weighted average to M_w7.40 from M_w7.44 in the Mesozoic extended margin.

To inform but not constrain the Mmax distribution, we add prehistoric earthquakes to the catalog of large historical SCR earthquakes used in the 2008 update. Figure 19 shows magnitudes for prehistoric earthquakes with M_w greater than or equal to 6.0 in the SCRs of North America, Australia, and Western Europe. If two or more paleoearthquakes are close enough together geographically to possibly have broken the same fault or fault system, then we include only the single largest event. If a historical earthquake had size and location similar to those of one or more prehistoric earthquakes, then the historical earthquake is the best characterized, and is the only earthquake included. Note that, in this way, the catalog does not include all observed large-magnitude earthquakes but rather the best single estimate of the largest magnitude at a location. The historical catalog has 138 earthquakes with M_w greater than or equal to 6.0 on their original magnitude scales, which includes earthquakes from all continents. There are 78 prehistoric or historical earthquakes in cratons and 51 in extended margins.

The Mmax distribution for Mesozoic and Paleozoic extended margins is compared to a histogram of large earthquakes in SCRs worldwide in figure 19, which also includes the Mmax distribution for the extended margin in the 2008 update. Although the observed magnitudes of the largest known earthquakes in the CEUS are uncertain, they are consistent with the largest earthquakes observed in other SCRs. Note that we assume that Mmax in the CEUS may differ from Mmax in other SCRs. If we assumed instead that all SCRs share a common Mmax, then the lower bound for Mmax

would have to be larger than the M_w7.7 earthquake in Bhuj, India, since that is the largest observed earthquake in an extended margin (Hough and others, 2002).

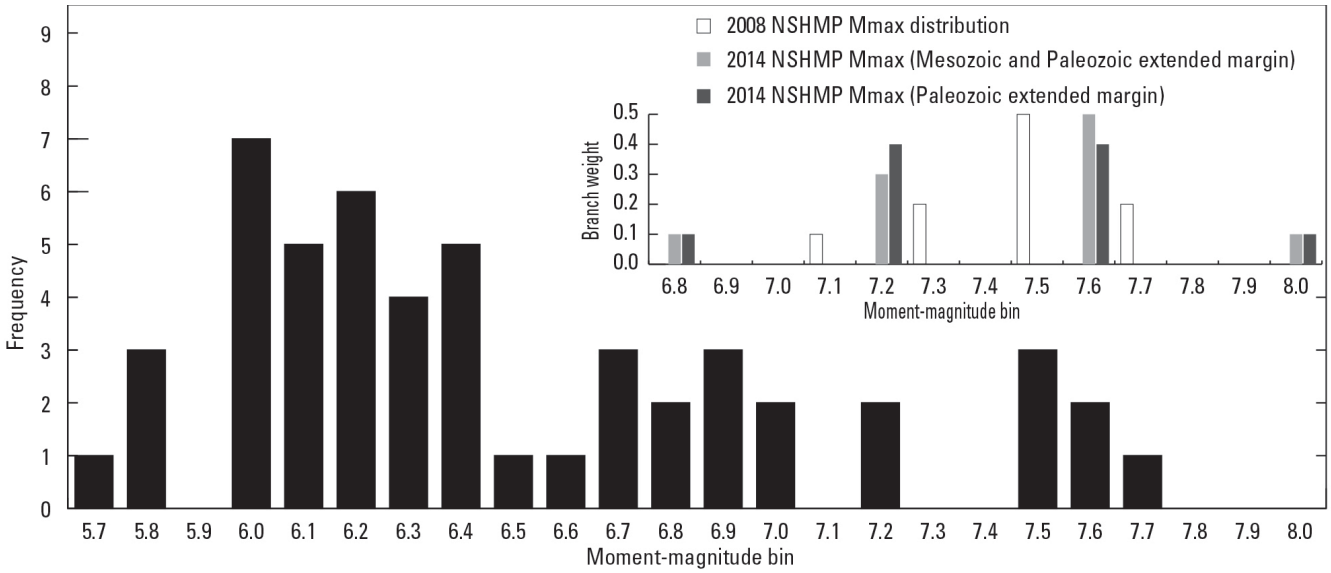

Figure 19. Distribution of large earthquake magnitudes (51 earthquakes) for extended margins in stable continental regions, worldwide. Mmax distributions used in the 2008 and 2014 updates shown in inset.

The Mmax distribution for 79 global cratonic earthquakes along with the 2014 and 2008 Mmax distributions are shown in figure 20. We broaden the Mmax distribution considerably compared to the 2008 distribution, extending both to higher and lower magnitudes than applied in the previous model. The CEUS–SSCn project also allowed for a similar range of Mmax in their hazard models. The prehistoric Cheraw fault earthquake ruptured in the craton of eastern Colorado and was assigned M_w7.0 based on the Wells and Coppersmith (1994) magnitude-scaling relation (all slip types). This magnitude is very uncertain, so we also allow for a possibility that it is an overestimate of the true magnitude. We observe dozens of earthquakes with M_w between 6.5 and 7.8 in the global dataset for cratonic regions (fig 20). Therefore, it is reasonable to expect that such an earthquake could happen in the craton of the CEUS. We weight the lower Mmax of 6.5 with a lower weight because most participants at our workshops agreed that earthquakes larger than M_w6.5 could be generated in this region. We assign one-half weight for an Mmax equal to the expected magnitude of the Cheraw fault earthquake, M_w7. The observed or inferred magnitude distribution of cratonic earthquakes worldwide extends up to M_w7.8, so we also allow for the potential of earthquakes up to M_w7.5 and M_w8.0 (with lower weight) to account for these global analogs.

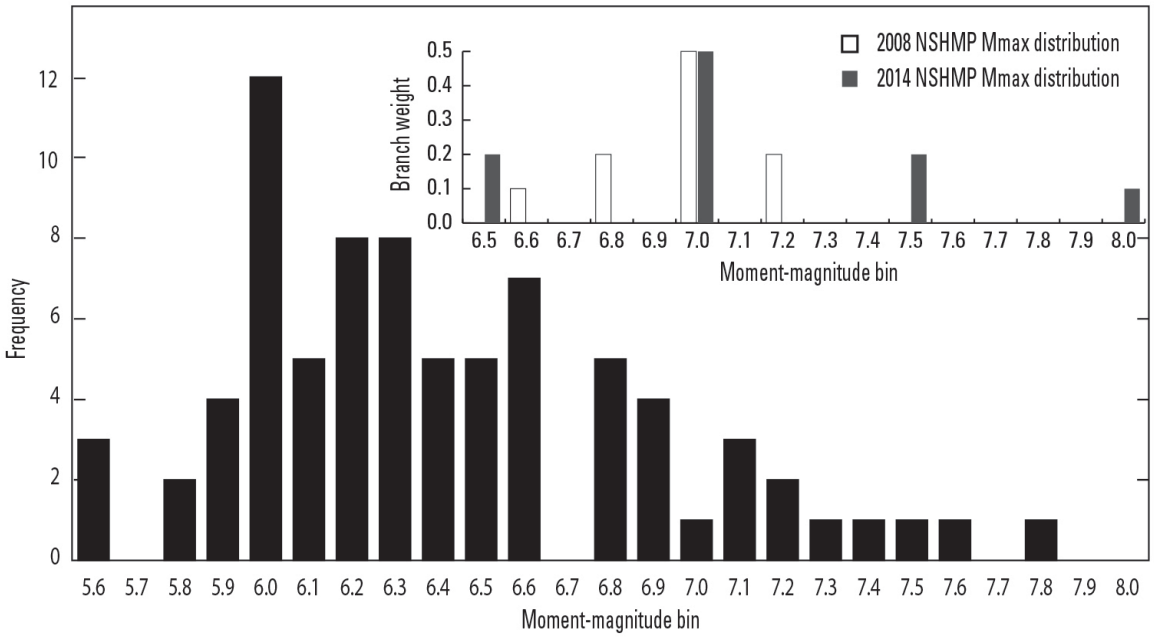

Figure 20. Distribution of large earthquake magnitudes (79 earthquakes) for cratons in stable continental regions, worldwide. Mmax distributions used in the 2008 and 2014 updates shown in the inset.

Fault-Based Source Models in the Central and Eastern United States

For the 2014 NSHM, we update the fault-based source models in the CEUS, relying heavily on the work of the CEUS–SSCn (2012). The 2008 USGS NSHMP maps included four fault-based sources in the CEUS: the Meers (Okla.) and Cheraw (Colo.) faults, and the New Madrid (Missouri [Mo.]) and Charleston (South Carolina [S.C.]) seismic zones (fig. 21). The 2014 model updates these sources and includes an additional six fault-based characteristic or repeating large magnitude earthquake (RLME) sources from the CEUS–SSCn (2012): the Wabash Valley (Ill.–Ind.), Commerce Geophysical Lineament (Ark.–Ind.), Eastern Rift Margin (western Tennessee), Marianna (east-central Arkansas), and Charlevoix (eastern Canada) areal source zones and New Madrid (Ark.–Ky.) fault source (see fig. 22). These new sources have characteristic magnitudes ranging from 6.7 to 7.9 and effective return periods from less than 400 years in New Madrid to nearly 10,000 years for the Commerce Geophysical Lineament and the northern extent of the Eastern Rift Margin. The New Madrid, Charleston, Charlevoix, and Meers faults are the main contributors to ground motion hazard, when considering a 2-percent chance of exceeding defined levels of ground motion in a 50-year time window. Other fault sources contribute to ground motion hazard at longer return periods (greater than 2,475 years).

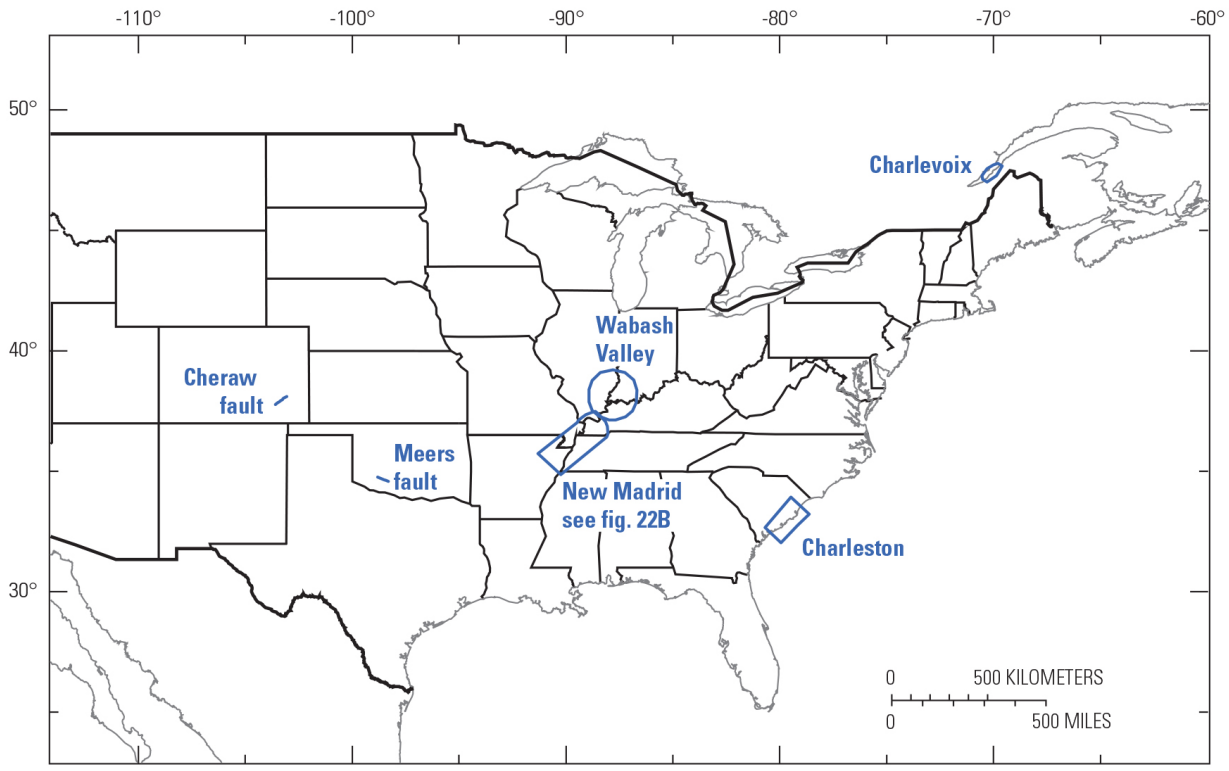

Figure 21. Location of fault sources in the Central and Eastern United States.

Source geometry associated with fault sources in the CEUS is either characterized as a mapped fault or a virtual fault. If the latter, rupture of magnitude, M, on a vertical fault is used to calculate length, L, from the Wells and Coppersmith (1994) relation, $L=10^{-3.22+0.69M}$ km. The NSHMP models faults closely spaced as individual (set of) mapped fault(s) or as a virtual set of faults that span the faulted area. Virtual faults are always centered on grid points, which sample latitude and longitude at 0.1-degree increments.

New Madrid Seismic Zone

The New Madrid seismic zone (NMSZ, fig. 22) contributes significantly to hazard in the CEUS (Petersen and others, 2008). In the 2014 USGS NSHMP maps, we update the 2008 NMSZ model and add a separate branch for the simplified CEUS–SSCn model (fig. 23). We assign equal weight to these alternative models.

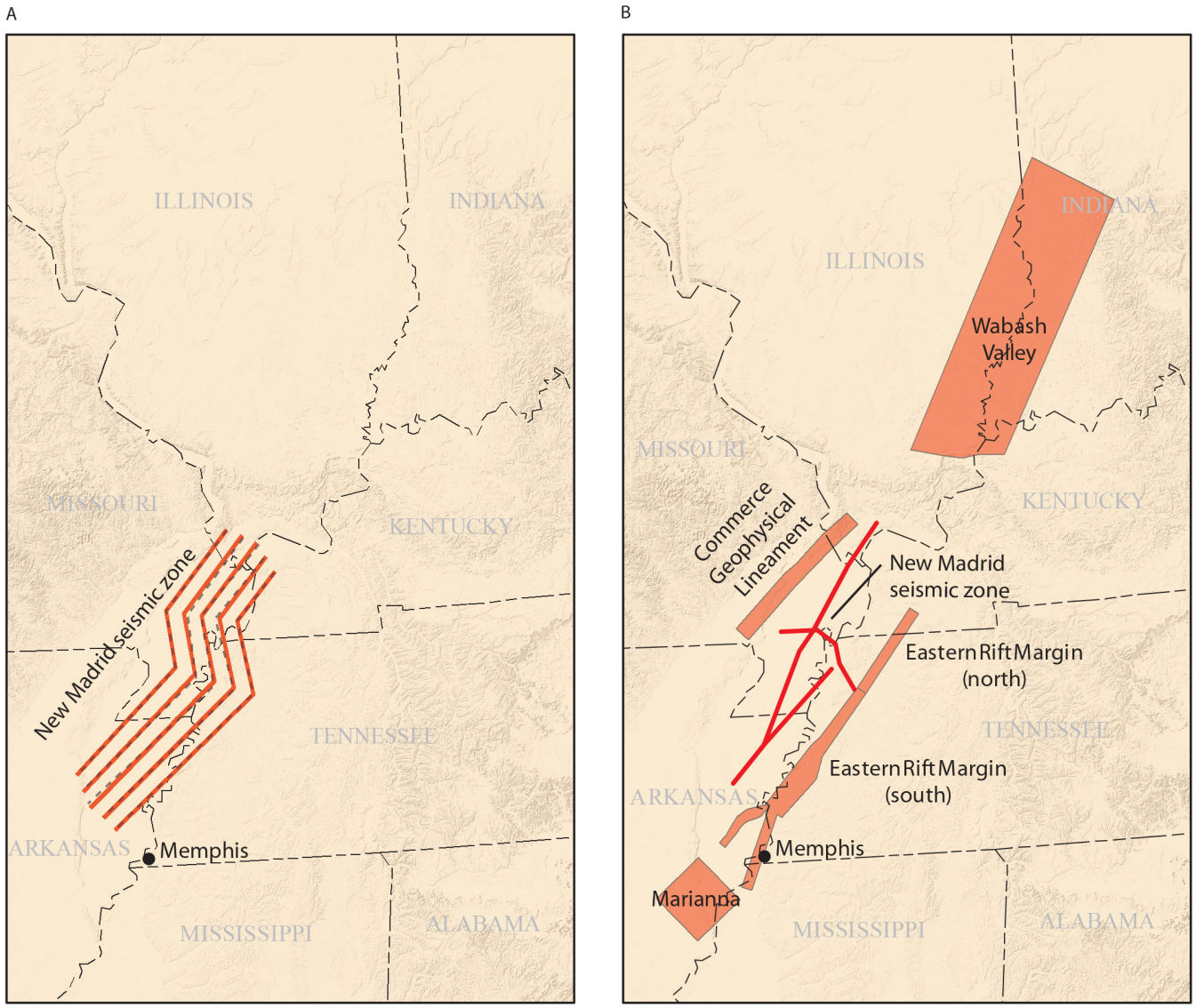

Figure 22. Representations of fault sources near the New Madrid seismic zone. *A*, USGS representation from the 2008 update (dashed lines) and 2014 update (solid lines) and *B*, CEUS–SSCn (2012) project representation.

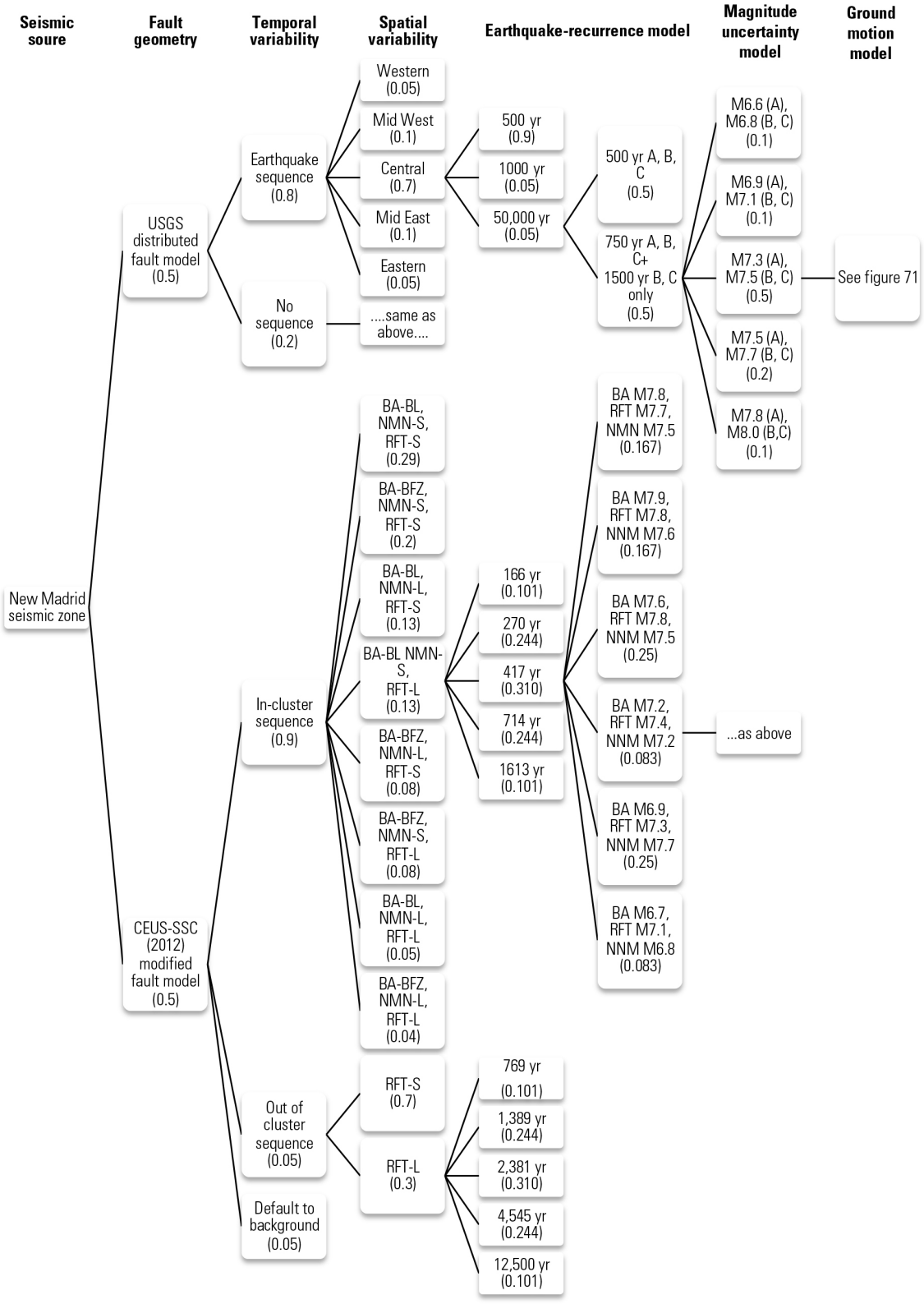

Figure 23. Logic tree for the New Madrid seismic zone (NMSZ). A, B, and C in the "Earthquake-recurrence model" and "Magnitude-uncertainty model" branches for the USGS representation refer to the northern, central, and southern segments of the NMSZ, respectively. Assigned weight for branches shown in parentheses.

For the 2014 update of the 2008 NMSZ model, we (1) maintain the five spatially distributed faults (fig. 22*A*), with minor geographic modifications, and their weights; and (2) update the magnitudes and earthquake recurrence models with new information. In particular, we update the magnitudes based on new estimates for the 1811–1812 sequence and update the rates based on recent geodetic studies. Hough and Page (2011) reexamined macroseismic intensity data and estimated magnitudes lower than any previously reported (table 3). Hough and Page (2011) also suggested that postglacial rebound is sufficient to produce a sequence with a moment release equivalent to one M_w6.8 earthquake in 500 years, which is different than the magnitude assumed in the 2008 version of the maps, an average M_w7.6 in 500 years. In contrast, Frankel and others (2012) examined geodetic baselines across the New Madrid seismic zone and inferred that the current rate of deformation can support one M_w7.3 earthquake in 500 years. To account for all published studies, we update the distribution of epistemic uncertainty in the magnitude. For the central and southern fault segments (denoted B and C, respectively, in the logic tree), the magnitudes (and weights) are M_w6.8 (0.1), M_w7.1 (0.1), M_w7.5 (0.5), M_w7.7 (0.2), and M_w8.0 (0.1). The range of this distribution (M_w6.8–8.0) is wider than the corresponding distribution in the 2008 USGS NSHMP model (M_w7.3–8.0, Petersen and others, 2008). The weighted average, M_w7.47, is smaller than the previous USGS NSHMP maps, which was M_w7.63. For the northern fault segment (A), the magnitudes are 0.2 magnitude units smaller than for the other segments, with the same weights. This reduction is consistent with the paleoliquefaction data described in Petersen and others (2008).

Table 3. Magnitude estimates for the 1811–1812 New Madrid earthquakes.

[M_w, moment magnitude; m_b, body-wave magnitude]

Event	Rupture segment	Hough and Page (2011) M_w	Hough and others (2000) Hough and Martin (2002) M_w	Bakun and Hopper (2004a) M_w	Johnston (1996) M_w	Nuttli (1973) m_b
December 16, 1811	southern	6.8	7.2–7.3	7.6	8.1	7.2
December 16, 1811 aftershock	southern	6.6	7.0	Not applicable	Not applicable	Not applicable.
January 23, 1812	northern	6.9	7.0	7.5	7.8	7.1
February 7, 1812	central	7.2	7.4–7.5	7.8	8.0	7.4

Several models were developed to account for variation in the recurrence times of large earthquakes on the New Madrid Seismic Zone. Calais and Stein (2009) examined available data on coseismic slip and geodetic-based strain rates. These data indicate that, in the past couple of decades, there have been low surface strain rates across the zone. Calais and Stein (2009) determined that the recent Global Positioning System (GPS) based strain rates are consistent with a 10,000- to 100,000-year recurrence for large New Madrid earthquakes. We add a logic-tree branch for a recurrence rate of 50,000 years with a weight of 0.05 to reflect this possibility. From the previous version of the maps (Petersen and others, 2008), we maintain the logic-tree branch for the 500-year recurrence interval, which is obtained from paleoseismic data and includes the possibility that the northern fault branch ruptures with either a 500-year or 750-year recurrence interval, with a weight of 0.9, and reduces the weight on the 1,000-year recurrence branch, obtained from sedimentary studies (Holbrook and others,

2006), to 0.05. This new weighting model gives most weight to the possibility that ruptures will continue with about a 500 year recurrence (based on feedback from our CEUS workshop) but accounts for ruptures with longer recurrences that are consistent with the GPS data and sedimentary studies that have been proposed in the literature.

CEUS–SSCn (2012) developed a new model for the NMSZ that consists of several alternative magnitude and earthquake rates on individual fault strands. We have simplified this model by removing the branches of the CEUS–SSCn logic tree that account for alternative time-dependent and depth-of-rupture distributions.

Faults Near the New Madrid Seismic Zone

The CEUS–SSCn Project comprehensively reviewed the existing literature on paleoseismic studies and paleoliquefaction features near the New Madrid seismic zone. The CEUS–SSCn defined four areal source zones: Wabash Valley, Commerce Geophysical Lineament or Commerce fault zone, Eastern Rift Margin, and Marianna (fig. 22*B*). The NSHMP adopts the CEUS–SSCn sources with the modifications described in the following sections. For example, we assume a single value for the depth of rupture, and we do not include the low-weighted time-dependent branches. The CEUS–SSCn (2012) documentation provides a detailed discussion of the research supporting these sources and logic-tree branches.

Wabash Valley

The 2008 update of the USGS NSHMP maps defined a separate seismicity zone for the Wabash region (fig. 22*B*). The NSHMP used the background seismicity model with a single Mmax value of M_w7.5 to account for the rates and magnitudes of paleoearthquakes identified before 2008. For the 2014 update, we maintain this model for fixed smoothing only, as well as adopt the CEUS–SSCn Wabash Valley RLME source. The CEUS–SSCn (2012) project collected studies of paleoearthquakes in this area, which indicate that there were at least eight Holocene and latest Pleistocene earthquakes with M_w between 6 and 7.8. The CEUS–SSCn seismic zone explicitly models RLMEs, as opposed to assuming a larger Mmax than the surrounding region as was implemented in the 2008 NSHMP maps (Petersen and others, 2008). The CEUS–SSCn project defined a polygonal zone oriented northeast to southwest as a leaky source of earthquakes with possible M_w between 6.7 and 7.5 (fig. 24). In leaky sources, the rupture centroid is constrained to lie within the areal source zone, but the rupture may extend outside the zone. They modeled this source as vertical strike-slip and dipping thrust faults with three distinct orientations. We simplify their model by defining vertical strike-slip faults oriented parallel to the long axis of the zone and do not account for potential dipping structures.

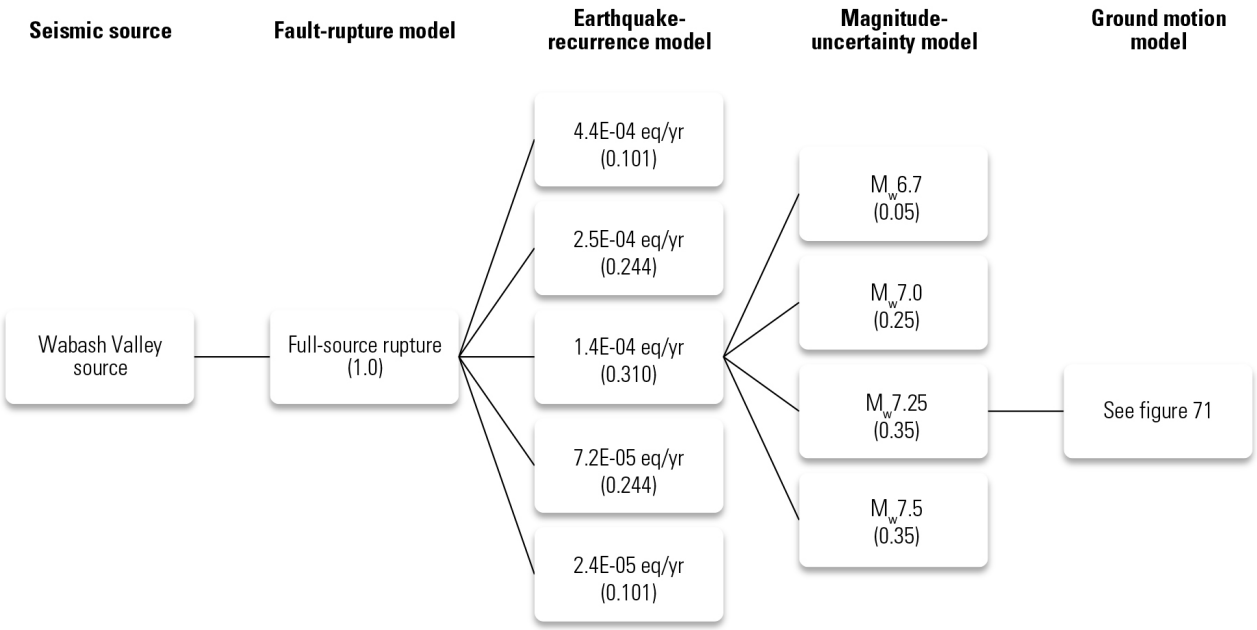

Figure 24. Logic tree for the Wabash Valley source. Value given in "Earthquake-recurrence model" branch is number of earthquakes per year (eq/yr). Assigned branch weight shown in parentheses.

Although eight large-magnitude earthquakes occurred in this region since latest Pleistocene (Obermeier, 1998), the CEUS–SSCn associated only two with the Wabash Valley source and treated the rest as background seismicity. The two earthquakes considered for this source happened in the last 11 to 13 thousand years ago (Hajic and others, 1995; Obermeier, 1998). After accounting for the uncertainty in these dates, the return periods consistent with this observation range from 2,300 to 42,000 years, with an effective return period of 5,900 years. We use the effective return period in our updated model.

Commerce Geophysical Lineament

The Commerce Geophysical Lineament (CGL), or Commerce Fault zone, is a northeasterly trending geophysical anomaly that is located west of and roughly parallel to the southern and northern arms of the New Madrid seismic zone (fig. 22*B*). The CEUS–SSCn (2012) compiled observations and reports that indicate the CGL is seismically active. Along the CGL in southeast Missouri, these observations include anomalously flowing drainages, displaced Tertiary and Pleistocene to Holcene deposits, and paleoliquefaction features.

Following the CEUS–SSCn (2012) Project, we model this seismic source with leaky, vertical strike-slip fault sources oriented parallel to the long axis of the zone, though we implement a single depth to the top of rupture (5 km). The length of the Commerce Geophysical Lineament allows a broad range of possible magnitudes; we adopt, without modification, the CEUS–SSCn's set of magnitudes from 6.7 to 7.7. The CEUS–SSCn presented evidence for two or three earthquakes in the past 20 thousand years. Return periods from 3,000 to 72,000 years are consistent with this observation; the effective return period is 9,300 years (fig. 25).

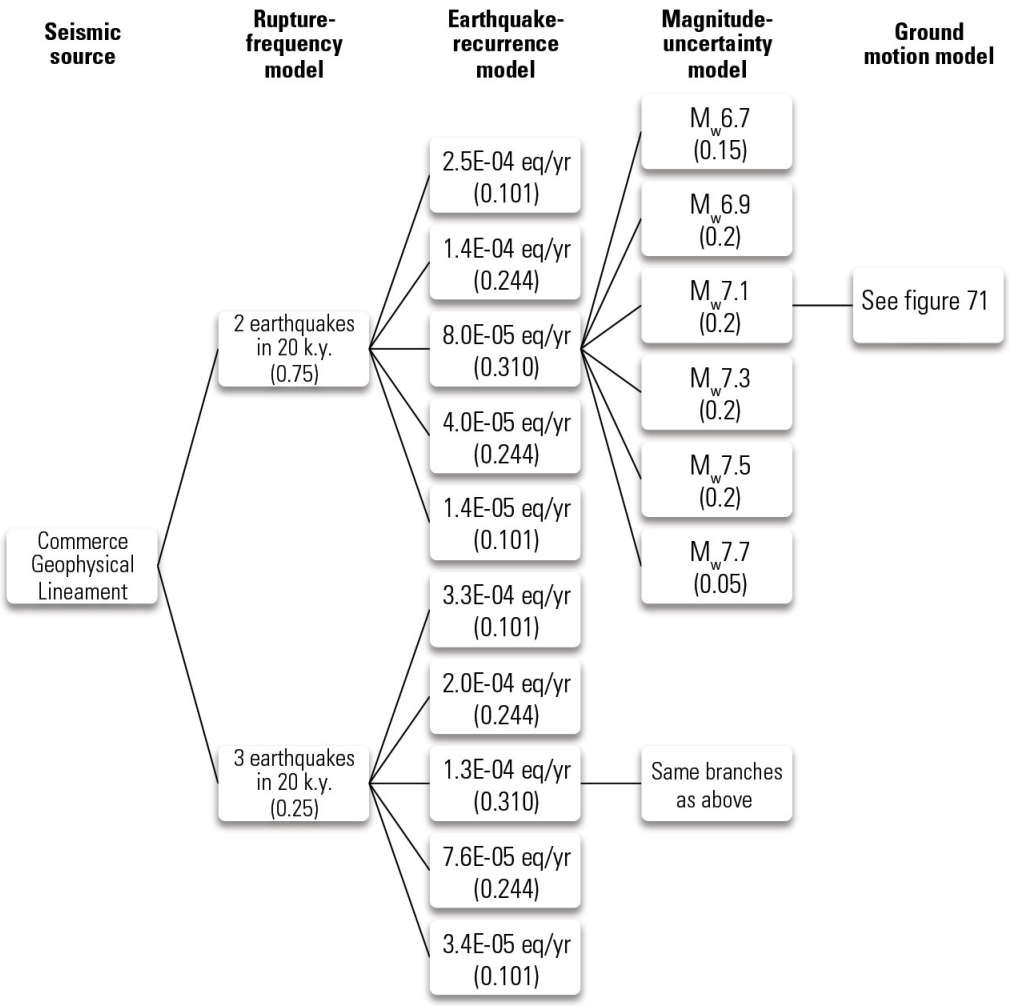

Figure 25. Logic tree for the Commerce Geophysical Lineament source. Value given in "Earthquake-recurrence model" branch is number of earthquakes per year (eq/yr). Assigned branch weight shown in parentheses.

Eastern Rift Margin

The CEUS–SSCn (2012) reviewed studies in the areas of the Eastern Rift Margin (ERM). Seismic imaging along the margin and paleoseismic trenching (fig. 22*B*) revealed repeated movement on Quaternary faults. These studies reported several meters of right-lateral and vertical offset in the north, which increased to the south, and reported evidence that the offsets occurred in the past 20 to 60 thousand years. Following the CEUS–SSCn, we model the ERM source as leaky, vertical strike-slip ruptures parallel to the long axis of the zone.

The CEUS–SSCn divided the ERM into northern and southern zones (fig. 22*B*) to account for the higher rates of deformation in the south. In the northern zone, the CEUS–SSCn assumed magnitudes of 6.7 to 7.4 based on the potential fault length and observations in paleoseismic trenches. The paleoseismic observations also indicated that one or two earthquakes may have happened in the past 12–35 thousand years. This information gives a range of return periods from 2,500 to 71,000 years, with an effective return period of 9,300 years. We adopt the CEUS–SSCn model for the northern zone but use a single depth to the top of rupture (5 km) (fig. 26).

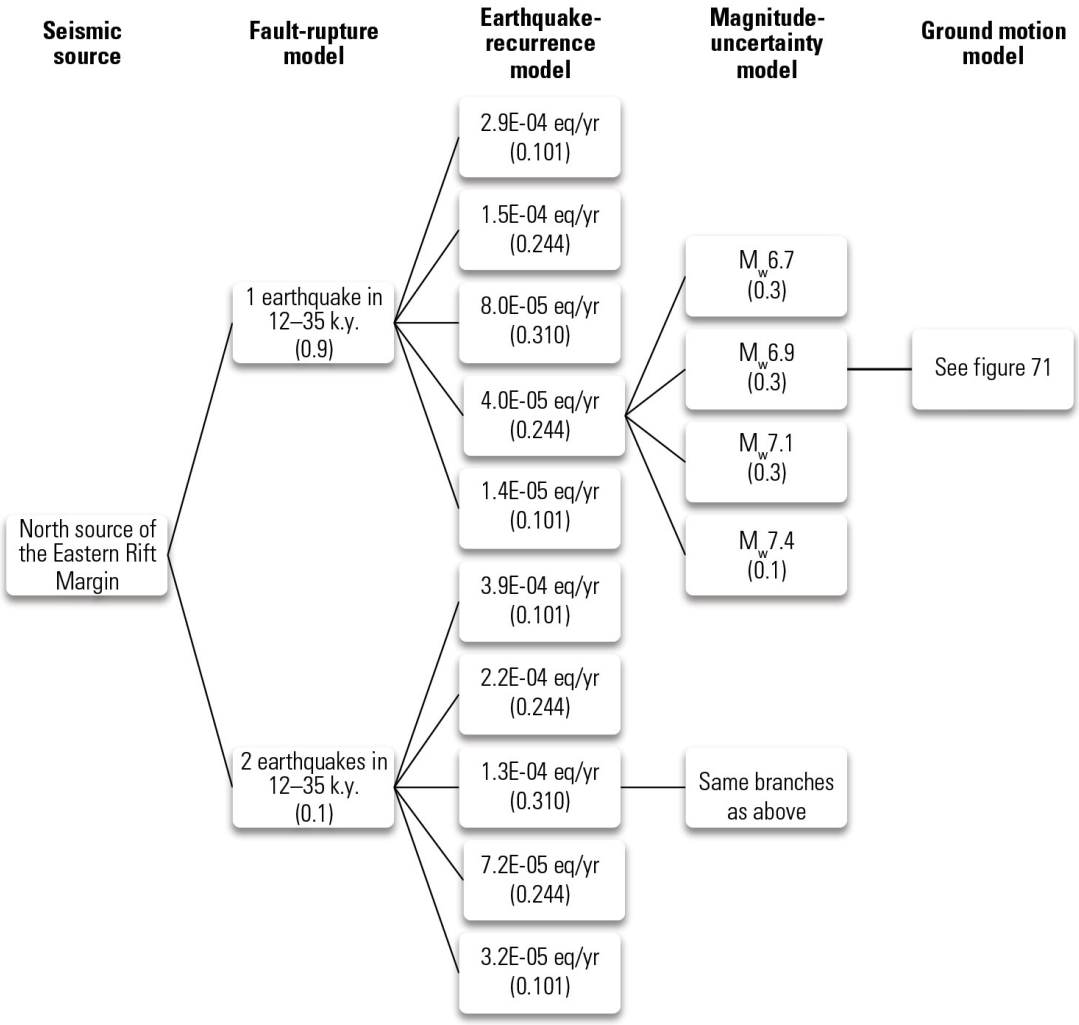

Figure 26. Logic tree for the north source of the Eastern Rift Margin. Value given in "Earthquake-recurrence model" branch is number of earthquakes per year (eq/yr). Assigned branch weight shown in parentheses.

The CEUS–SSCn (2012) further divided the southern zone to account for recent deformation in the along the Mississippi River just west of Memphis, Tenn. (fig 22). Using observations in the south like those in the north, the CEUS–SSCn assumed that a set of magnitudes ranging from 6.7 to 7.7 are possible. The CEUS–SSCn (2012) project conclude that 2–4 earthquakes may have occurred over the past 20 thousand years. This uncertainty yields a range of return periods from 2,000 to 30,000 years with an effective return period of 4,900 years (fig. 27).

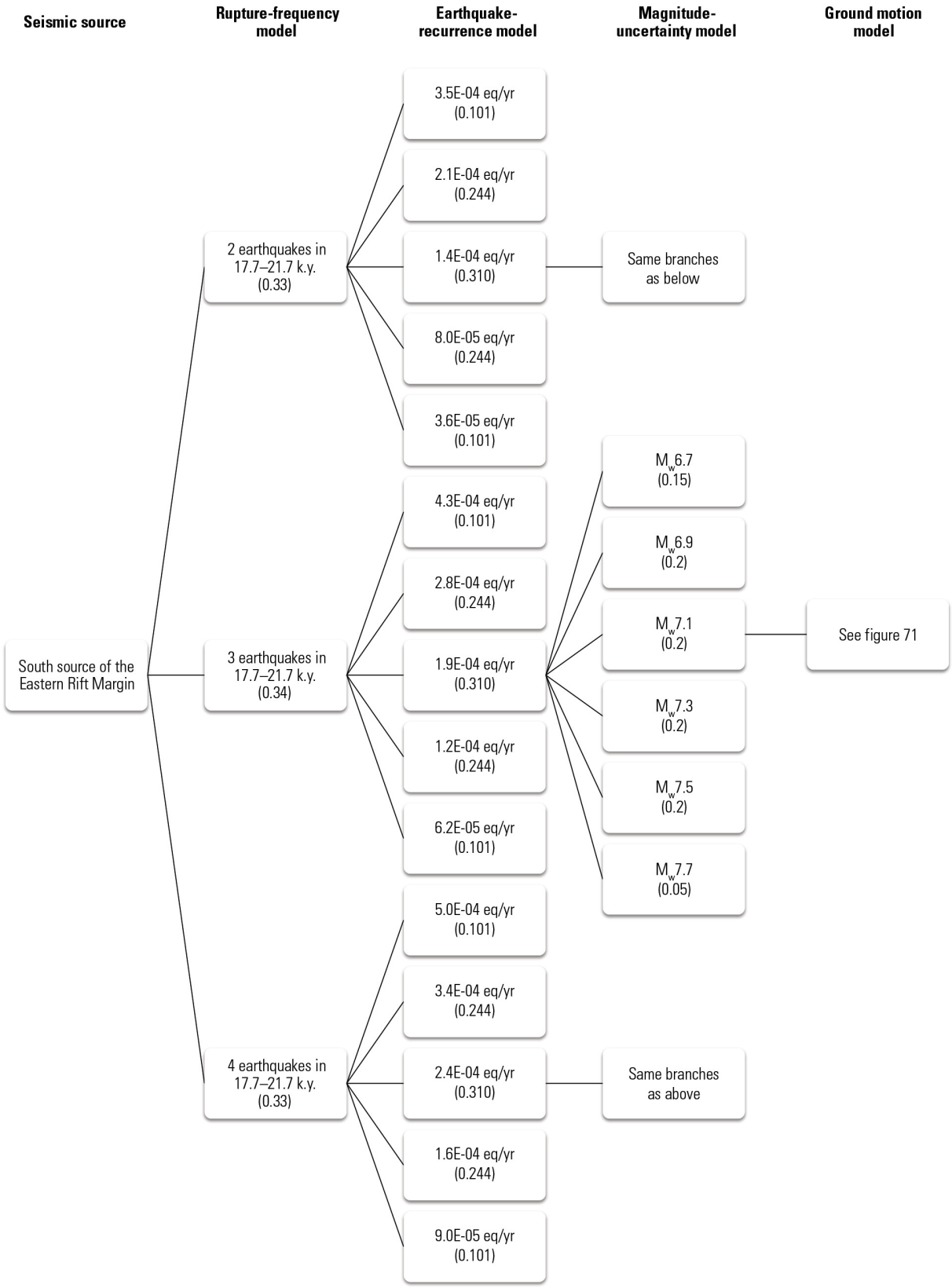

Figure 27. Logic tree for the south source of the Eastern Rift Margin. Value given in "Earthquake-recurrence model" branch is number of earthquakes per year (eq/yr). Assigned branch weight shown in parentheses.

Marianna

Marianna, Ark., is about 80 km southwest of Memphis, Tenn. (fig. 22*B*). The CEUS–SSCn (2012) reviewed studies in this region, which document several very large sand blows, and they define a seismic zone with two fault orientations parallel to the zone's boundaries. We adopt a N. 45° E. orientation of leaky (faults extend outside of zone), vertical strike-slip faults. The size of the Marianna source zone and the size of the sand blows suggest that it could produce earthquakes with magnitudes between 6.7 and 7.7. We adopt magnitudes and assigned weights based on the CEUS-SSC model (fig. 28). Paleoliquefaction studies collected in the CEUS–SSCn (2012) suggest that the sand blows in the Marianna region were associated with three or four events and formed about 5 to 10 thousand years ago, predating those in the New Madrid seismic zone. These observations are consistent with return periods from 1,200 to 14,000 years, with an effective return period of 2,800 years. The CEUS–SSCn (2012) acknowledged that this source zone may be inactive and gave 0.5 weight to an out-of-cluster, inactive, branch, which we adopt.

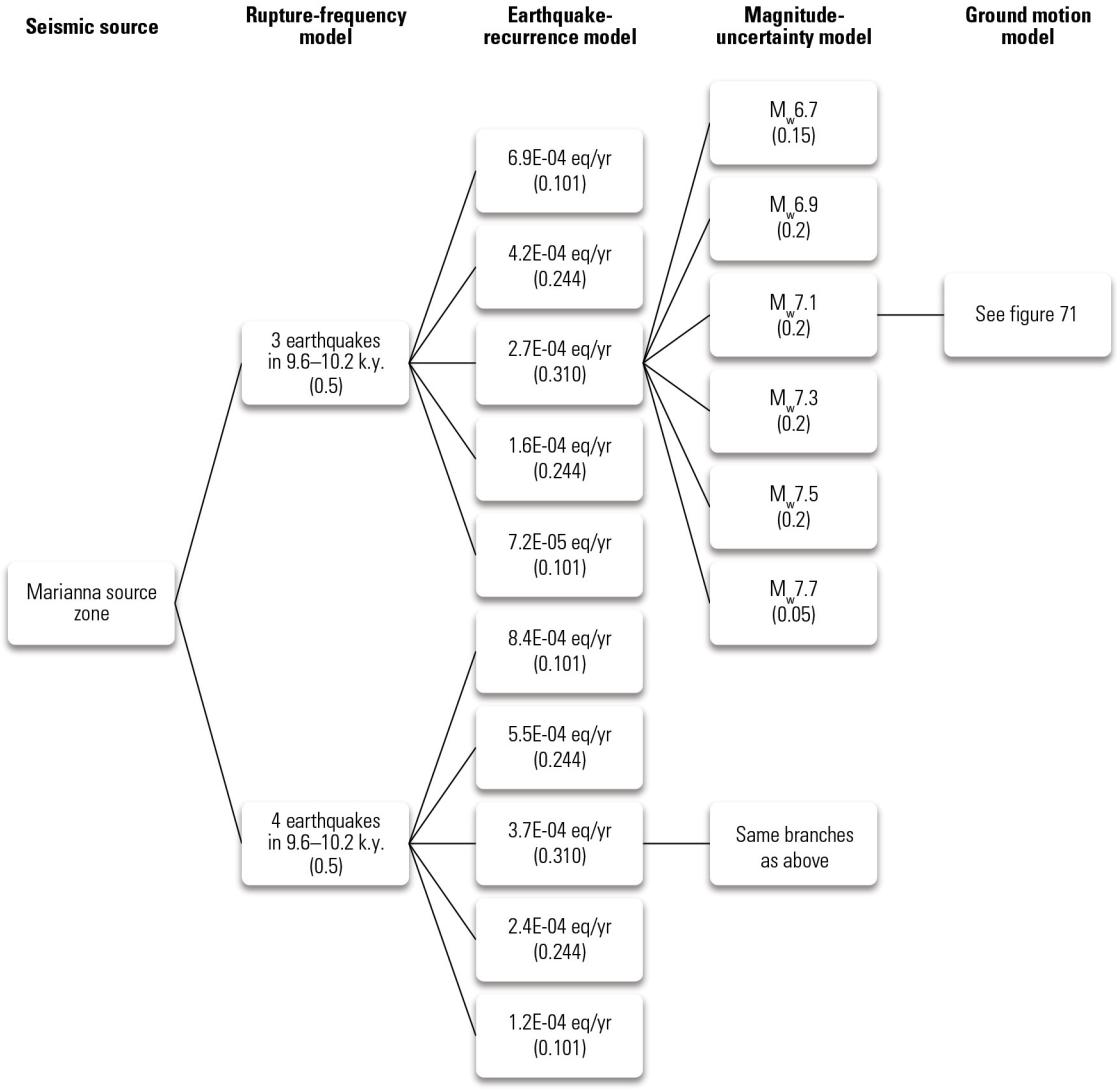

Figure 28. Logic tree for the Marianna source. Value given in "Earthquake-recurrence model" branch is number of earthquakes per year (eq/yr). Assigned branch weight shown in parentheses.

Charleston Seismic Zone

Like the New Madrid seismic zone in the central United States, the Charleston, S. C., seismic zone (fig. 21) contributes significantly to hazard in the Southeast. In 2008, the NSHMP defined two regions within the Charleston seismic zone. A narrow zone was entirely onshore, following the Woodstock lineament and an area of river anomalies. The second zone was broader and extended offshore, encompassing known liquefaction features and offshore faults (Petersen and others, 2008). The scientists at the CEUS regional workshop (Memphis, Tenn., 2012) identified needed modifications in the narrow zone for the 2014 update and the NSHMP steering committee suggested we consider the CEUS–SSCn (2012) results. As a consequence, we adopt the regional, local, and narrow seismic zones, and the wider range of epistemic uncertainty in earthquake magnitudes and rates defined by the CEUS–SSCn (2012; table 4) for the 2014 update of the USGS NSHMP maps (fig. 29).

Table 4. Seismic zones in the Charleston area (see fig. 29).

Zone	Mapped faults	Virtual fault strike	Recurrence model	Weight
Narrow	Woodstock	N. 17.5˚ E.	Poisson	0.3
Local	Various onshore	N. 50˚ E.	Poisson	0.5
Regional	Various, including Helena Banks	N. 50˚ E.	Poisson	0.2

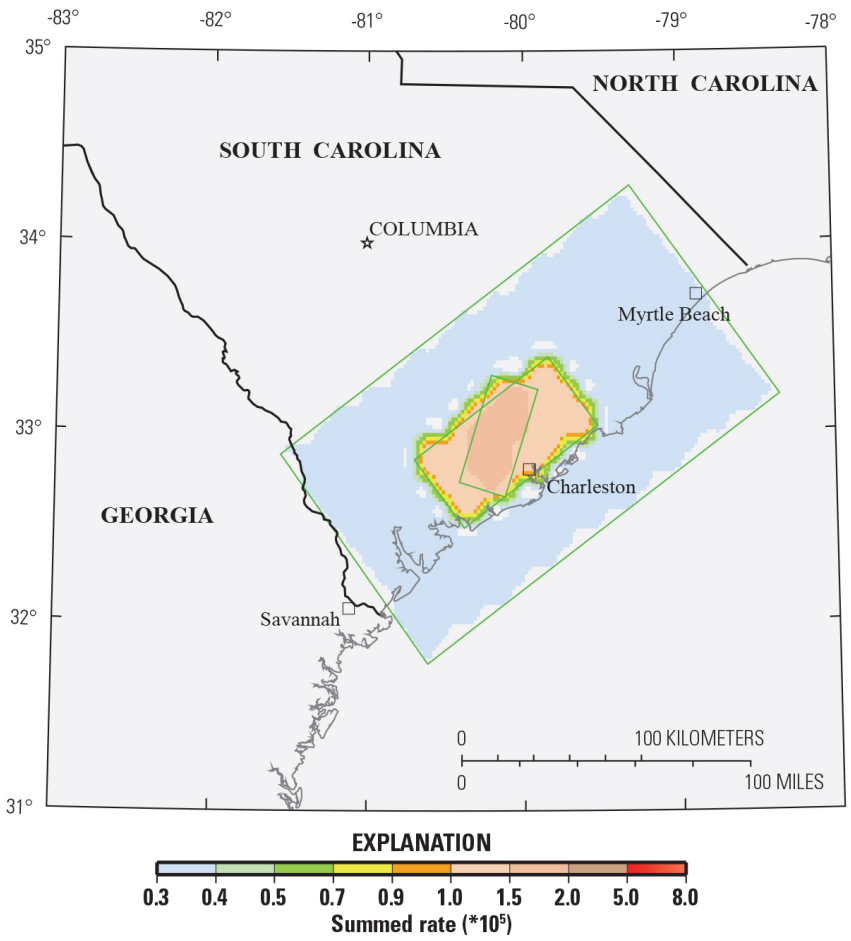

Figure 29. Summed a-grid rates for the local, narrow, and regional Charleston sources. The rate shown is per 0.1- by 0.1-degree cell per year, and is scaled by 10^5.

The southwestern edge of the 2014 regional Charleston zone extends farther southwest than the southwest edge of the 2008 broad zone. Five or more paleoearthquake-liquefaction features near the South Carolina–Georgia border supported the extension of the southwestern edge (CEUS–SSCn, 2012). In our current implementation, finite faults can extend outside the zone boundary in the strike direction but not in the perpendicular direction. In contrast, the CEUS–SSCn (2012) constrained the virtual faults to rupture entirely within the zone boundaries of the regional and local zones, whereas they implemented leaky boundaries along the northeast and southwest edges of the narrow zone. Some of the virtual faults in the 2014 USGS NSHMP model are now very close to Savannah, Ga., which impacts hazard in Savannah and elsewhere in eastern Georgia.

We adopt, without modification, the CEUS–SSCn set of five magnitudes and weights (fig. 30). The new distribution of magnitudes is compared to that in the 2008 update in table 5; the weighted average magnitude was 7.19 in 2008 and is now 7.1. Within each of the 3 zones, the mean return period is 529 years, which is the average of the in-cluster (0.9 weight) and out-of-cluster branches (0.1).

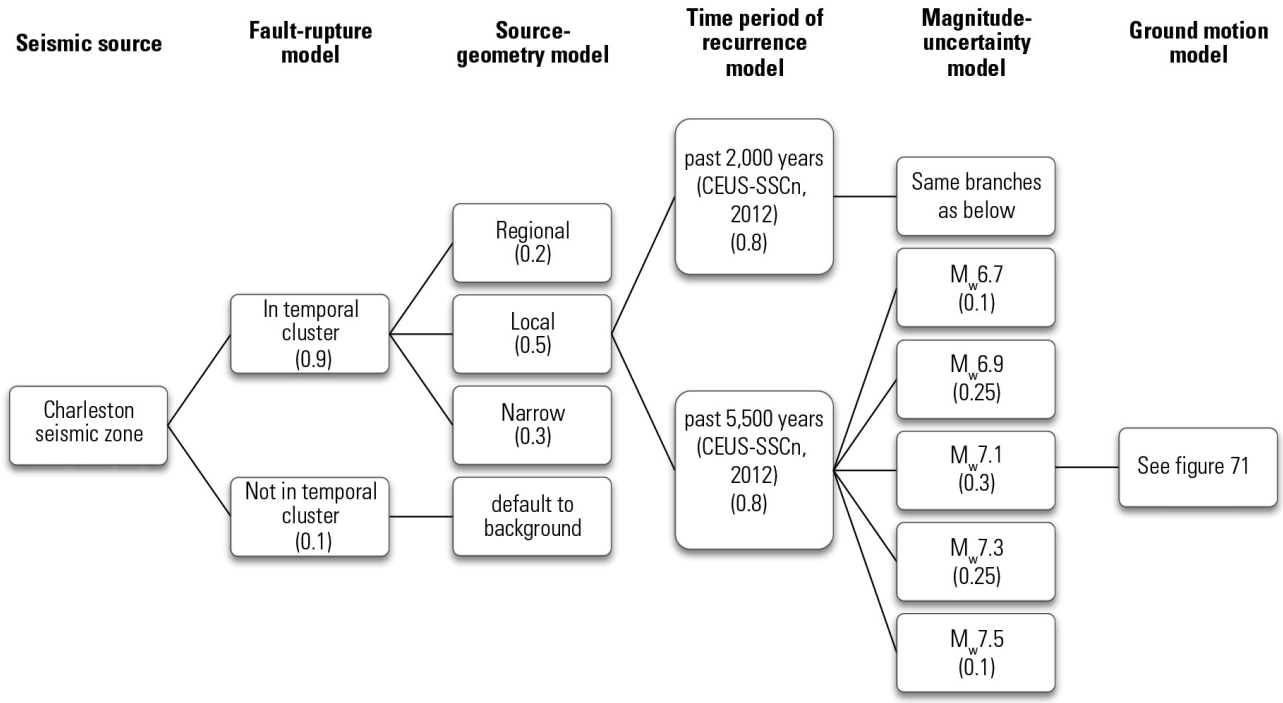

Figure 30. Logic tree for the Charleston source. Value given in "Earthquake-recurrence model" branch is number of earthquakes per year (eq/yr). Assigned branch weight shown in parentheses.

Table 5. Magnitude distribution for Charleston source.

[CEUS–SSCn, Central and Eastern United States seismic source characterization for nuclear facilities; NSHMP, National Seismic Hazard Mapping Project; M_w, moment magnitude]

CEUS–SSCn M_w	CEUS–SSCn weight	2008 NSHMP M_w	2008 NSHMP weight
6.7	0.10		
6.9	0.25	6.8	0.20
7.1	0.30	7.1	0.20
7.3	0.25	7.3	0.45
7.5	0.10	7.5	0.15

The CEUS–SSCn defined time-dependent branches in the narrow zone, but the NSHMP does not adopt these models because the recurrence models for all zones in the 2014 NSHMP maps are time independent (as advocated by workshop participants). In the CEUS–SSCn (2012) time-dependent model, the relatively recent 1886 Charleston earthquake (compared to the mean return period of 500 to 550 years) results in a slightly lower probability of a similar event in the next 50 years relative to the time-independent model. The CEUS–SSCn assigns a total weight of 0.1 to these time-dependent branches.

Meers Fault

Previous updates of the USGS NSHMP maps include the Meers fault in southwestern Oklahoma (fig. 21). In the 2008 update, the NSHMP assigned a characteristic M_w7.0 and a return period of 4,500 years, based on 2 surface-faulting events in the past 3,000 years (Crone and Luza, 1990; Kelson and Swan, 1990) and a lack of evidence of additional surface-rupturing events over the past 100,000 or more years.

The CEUS–SSCn (2012) developed a set of alternative models that account for a much broader range of earthquake magnitudes and rates than the single magnitude and rate assumed in the 2008 NSHMP model. For example, the CEUS–SSCn model includes return periods from 476 to 500,000 years. The CEUS–SSCn model also gives 10-percent weight to the possibility of an extended fault length, but we do not adopt this branch in the 2014 update. We weight the modified CEUS–SSCn model 0.5 and the 2008 NSHMP model 0.5, because they are alternatives based on different interpretations of the same published data (fig. 31).

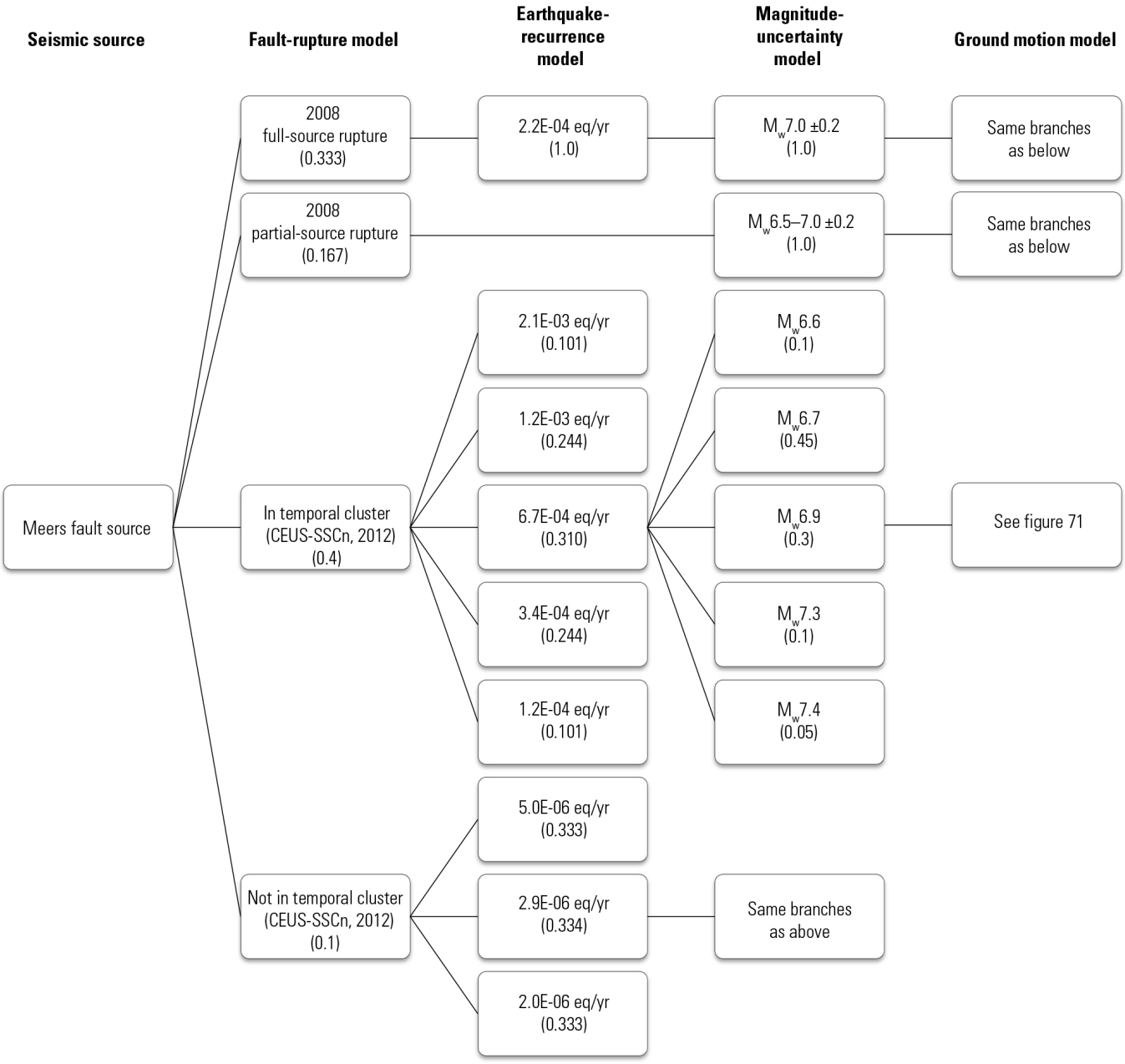

Figure 31. Logic tree for the Meers fault source. Value given in "Earthquake-recurrence model" branch is number of earthquakes per year (eq/yr). Assigned branch weight shown in parentheses.

Cheraw Fault

Previous USGS NSHMP map updates defined the Cheraw fault in eastern Colorado (fig. 21) based on existing information (Petersen and others, 2008). Crone and others (1997) showed evidence of Holocene and earlier faulting, and inferred surface ruptures about 8, 12, and 20–25 thousand years ago. The NSHMP modeled the fault using a slip rate of 0.15 millimeters per year (mm/yr) based on data from the last two events and a maximum magnitude of M_w7.0 plus or minus (±) 0.2 determined from the Wells and Coppersmith (1994) fault length relation for all slip types combined.

The CEUS–SSCn (2012) defined a set of alternative magnitudes, rates, and fault lengths, and we include some of the important alternatives in the 2014 update. For example, the CEUS–SSCn model accounted for a broader range of magnitudes and rates, which we adopt (fig. 32). We do not adopt the extended fault alternative that the CEUS–SSCn considers because these models are not well constrained and further research is needed to verify the new model.

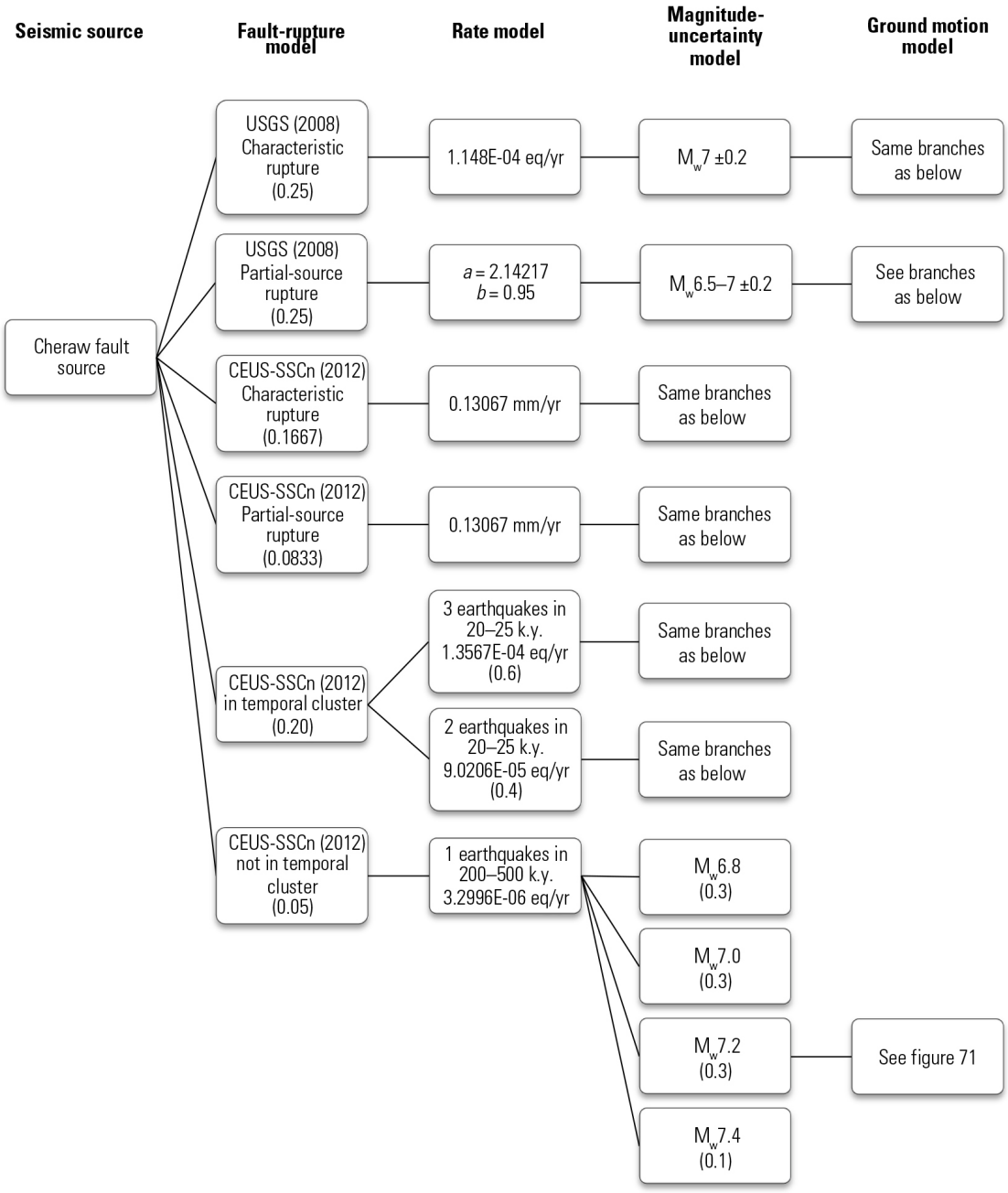

Figure 32. Logic tree for the Cheraw fault source. Value given in "Earthquake-recurrence model" branch is number of earthquakes per year (eq/yr). Assigned branch weight shown in parentheses.

Charlevoix Seismic Zone

The 2008 USGS NSHMP maps included the Charlevoix seismic zone, an area in Canada (fig. 21) that contributes to seismic hazard in the northeastern United States. The NSHMP modeled this zone with the background-seismicity model having a spatially uniform seismicity rate and a *b* value of 0.76. We continue to include the Charlevoix background source zone in the 2014 update; however, because of the new implementation of moment magnitudes, the *b* value is now 0.9 for the fixed-smoothing model and the *b* value is 1.0 for the adaptive smoothing model (accounting for additional epistemic uncertainty). In addition to our model of the source zone, we also include the CEUS–SSCn (2012) model for the Charlevoix seismic zone. We recognize that there is some overlap between the magnitudes in the two models; however, the rates of the seismicity-based background source are much lower than the rates associated with the RLME so this overlap may not be important.

Of the five M_w5.5 and larger earthquakes in the Charlevoix region over the last 350 years, the CEUS–SSCn considers the two largest, the 1963 M_w7.00 and 1870 M_w6.55, to be in the source zone. The remaining events are considered part of the background source zone. Paleoseismic investigations reveal at least three Holocene paleoearthquakes of M_w6.2 and larger (Tuttle and Atkinson, 2010); therefore, the CEUS–SSCn (2012) considers a range of return periods from 100 to 5,600 years with an effective return period of 730 years. The CEUS–SSCn assigns a range of moment magnitudes from 6.75 to 7.5 with greatest weight given to M_w7.0 because of the estimates and uncertainty in the size of the historical and paleoseismic events and the potential size earthquakes within the source zone (fig. 33).

We simplify the CEUS–SSCn (2012) model by modeling sources within this zone as vertical strike-slip ruptures with random strike having a constant depth to the top of rupture (5 km). The CEUS–SSCn modeled these sources as random strike thrust events dipping between 40° and 60° in crust with a seismogenic thickness of 25 or 30 km.

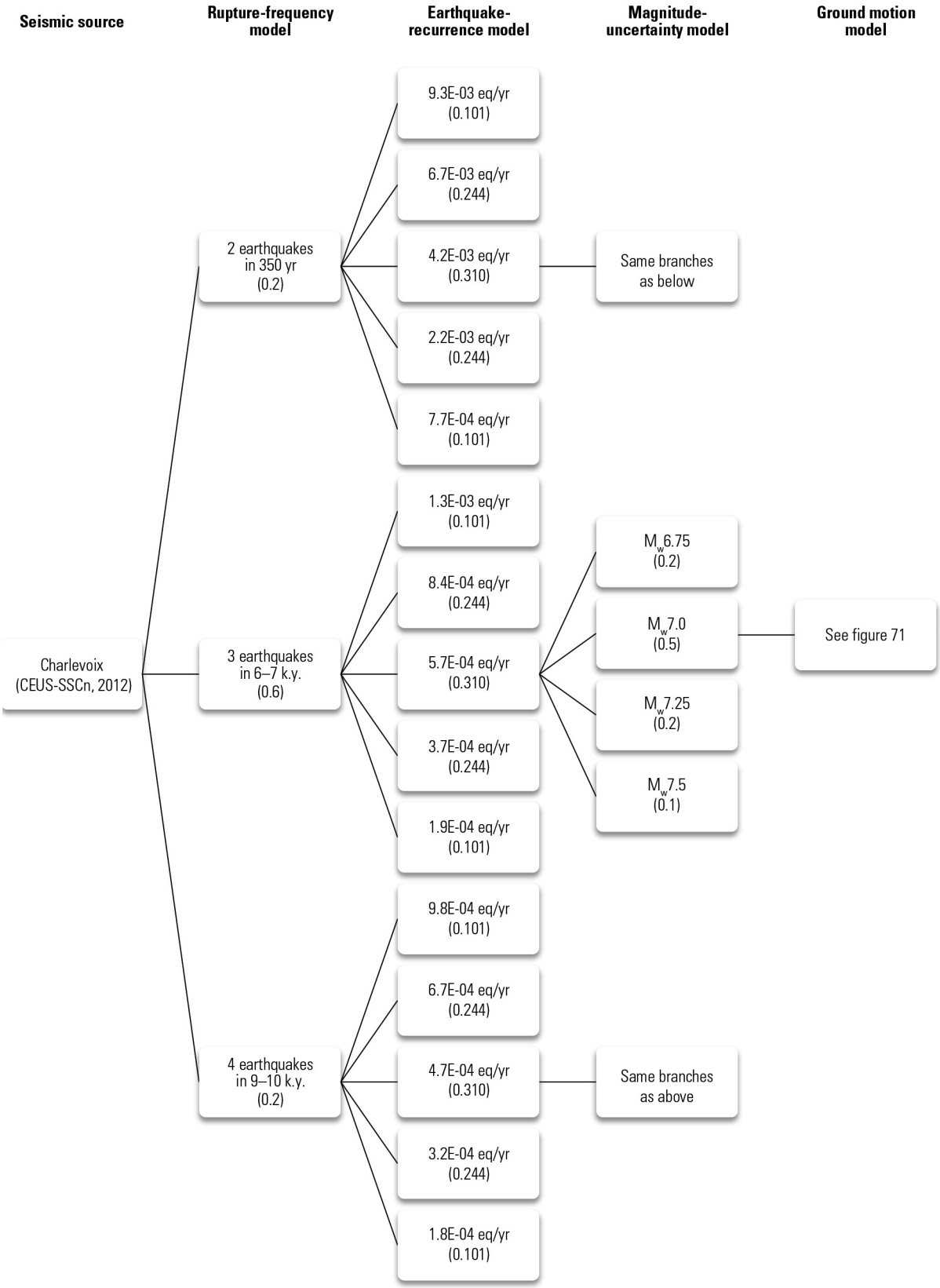

Figure 33. Logic tree for the Charlevoix source. Value given in "Earthquake-recurrence model" branch is number of earthquakes per year (eq/yr). Assigned branch weight shown in parentheses.

Western United States Earthquake Source Models

The overall approach to modeling seismic hazard in the Western United States (WUS) is similar to past USGS NSHMP maps, documented in Frankel and others (1996, 2002) and Petersen and others (2008) that is based on seismicity-based background models and fault models. The models, data, and methods can also be accessed at *http://earthquake.usgs.gov/hazmaps/*. As in previous models, we use historical seismicity (gridded and smoothed spatially) to estimate the hazard from earthquakes on unidentified or uncharacterized faults (seismicity-based background sources). These models account for random earthquakes by using the rate and distances of nearby historical earthquakes above a certain size threshold to estimate the rate of future events. In addition, we apply geologic and geodetic data to estimate slip rates on faults. This additional fault input allows for broader uncertainty in the activity rates on faults. Fault-based models are dependent on a slip rate that is based on a dated offset feature or on multiple measurements of geodetic strain rates across the region. In past models, the geologic data were mostly used exclusively to estimate slip rates and annual recurrence rates on faults; geodetic (GPS) data were used primarily to constrain the regional slip rates or to define rates within designated zones. However, in this update, we include combined geologic and geodetic inversion methods to estimate slip rates on faults (see the section "Combined Geodetic- and Geologic-Based Slip-Rate Models" for more details). These models were incorporated in the 2014 hazard assessment for sites across the WUS.

Earthquake-rate data are used with an earthquake magnitude-frequency distribution (with a defined slope or *b*-value) to estimate the rate of earthquakes at any particular place. As in previous models we apply an exponential magnitude-frequency distribution with a doubly truncated exponential recurrence based on a Gutenberg-Richter curve (Gutenberg and Richter, 1944) to estimate hazard from random sizes of earthquakes on faults as well as in background seismic source models. For the background seismicity, we consider earthquakes from M_w5.0 to the maximum magnitude obtained from global and regional analogs (the Mmax distribution allows for the highest weight at about M_w7.5). For most of the fault sources, we consider earthquakes from M_w6.5 up to the maximum magnitude expected for the fault, which is obtained from published magnitude scaling relations that predict magnitude from fault area or length constraints. We also consider a preferred earthquake magnitude distribution that ruptures the entire source (Schwartz and Coppersmith, 1984). These two distributions form the basis for defining the different sizes of earthquakes on faults.

This update of the USGS NSHMP maps includes several new seismic source and ground motion models. The California fault sources are addressed separately in this report, with sources defined by the Uniform California Earthquake Rupture Forecast Model (UCERF ver. 3.3; Working Group on California Earthquake Probabilities, 2013). The Pacific Northwest update is focused on new information concerning the sizes and rupture sources of earthquakes along the Cascadia subduction zone, the addition of the Tacoma fault source, and modifications to some other fault sources in the region. The Intermountain West update is based on new recommendations on fault modeling from the Basin and Range Province Earthquake Working Group (BRPEWG, Lund, 2012) and the Utah Geological Survey. Both regions incorporate a new earthquake catalog and background seismicity models as well as combined new geologic and geodetic inversion slip-rate models. Several new ground motion models have also been included to account for uncertainty (epistemic) in this analysis.

Seismicity-Based Background Source Model

The logic tree for the seismicity-based background source model, which accounts for the hazard from earthquakes that are located away from modeled faults, is shown in figure 34. Statistical parameters of the seismicity model are derived from the earthquake catalog (Frankel, 1995). A catalog

for the Western United States is updated for this analysis. This analysis defines a truncated-exponential magnitude-frequency distribution for the estimation of rates of different sized earthquakes. The epicenters are spatially smoothed using both fixed length (50 km correlation length) and adaptive smoothing methods (described below). Models for estimating background earthquake rates from (1) shallow crustal background seismicity and (2) deep background seismicity are discussed in this section.

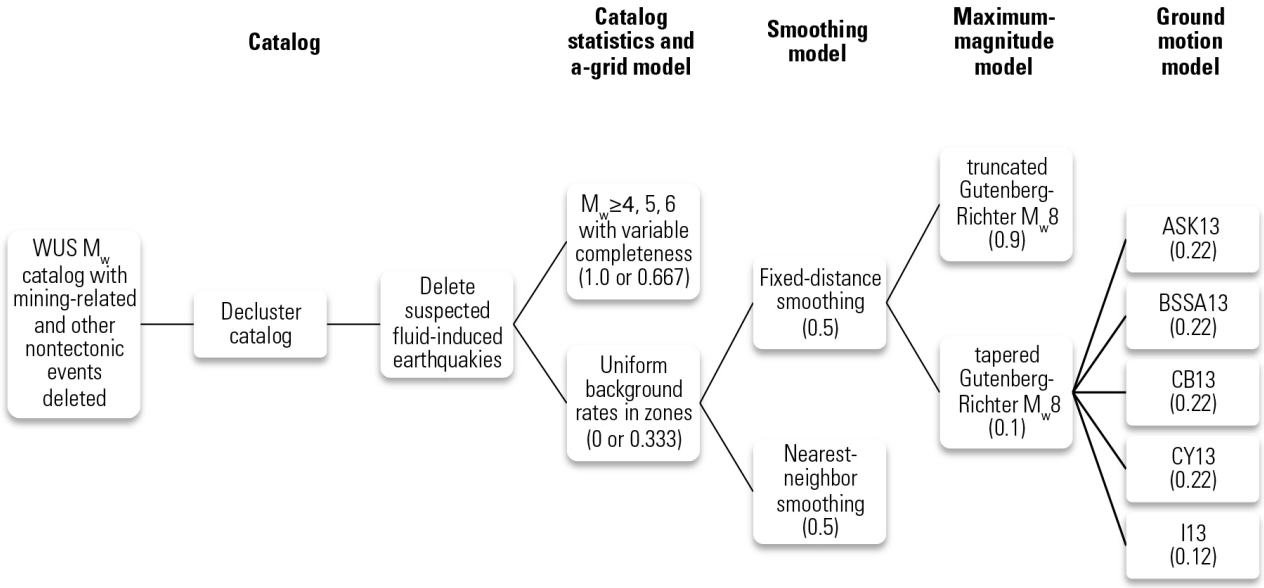

Figure 34. Logic tree for the seismicity-based background source model in the Western United States. Assigned branch weight shown in parentheses.

Earthquake Catalog for the Western United States

Several published source catalogs are combined (Mueller and others, 1997) to develop a composite, uniform seismicity catalog for western North America through 2012. The updated catalog is a 6-year extension of the 2006 catalog used for the 2008 hazard maps. The catalog lists each earthquake with M_w, hypocenter, and origin time derived from a preferred source catalog. A comment field summarizes information from the original source catalog for each entry. We consider magnitude uncertainty in deriving an expected M_w value ($E[M_w]$) for each earthquake after many discussions with seismic hazard experts. In this analysis we distinguish earthquakes that have (1) "observed" M_w (typically from inversions of long-period waveforms or surface-wave spectra), (2) magnitudes that are assumed to be equivalent to M_w (for example, local magnitude m_L and duration magnitude m_d), and (3) M_w formally converted from another magnitude or intensity measure, generally following the formalism described by CEUS–SSCn (2012). Magnitudes are adjusted for saturation and scaling effects using empirical relations from Sipkin (2003) for body-wave magnitude (m_b) and Utsu (2002) for local magnitude (m_L) and surface-wave magnitude (M_S). Magnitude uncertainty is either taken from the original source catalog or estimated following Felzer (2008). Each entry in the catalog lists $E[M_w]$,

magnitude uncertainty, and a counting factor (a function of *b* and magnitude uncertainty) that is used to compute unbiased rates (see below).

Sources contributing to the 2006 catalog included Stover and others (1984), Engdahl and Rinehart (1991), Stover and Coffman (1993), Engdahl and Villaseñor (2002), Pancha and others (2006), California Geological Survey–UCERF2 Project (Felzer and Cao, 2008), USGS Preliminary Determination of Epicenters (2013), and Petersen and others (2008). Information concerning new earthquakes since 2006 comes from several sources. The Global Centroid Moment Tensor Project catalog (2013) and the St. Louis University catalog (Herrmann, 2013) list earthquakes with "observed" moment magnitudes. Catalogs from the UCERF3 project (K. Felzer, written commun., 2013) and the USGS Comprehensive Catalog (2013) contribute earthquakes with various types of size measures. We also maintain a hand-edited "special-case" catalog from special studies and personal communications, including suspected erroneous events and nontectonic events.

Source catalogs are reformatted, concatenated, and sorted chronologically. They overlap in time and space, and when an earthquake is listed in more than one catalog a preferred source is chosen based on our best judgment. In the case of duplicates, entries from new catalogs generally supersede old entries. Known explosions, mining-related events, and erroneous events are deleted. The catalog with duplicates removed is declustered using the algorithm from Gardner and Knopoff (1974). The declustered catalog lists 5,622 earthquakes between 1850 and 2012 with M_w greater than or equal to 3.5 (fig. 35). The contributions from individual source catalogs are listed in table 6.

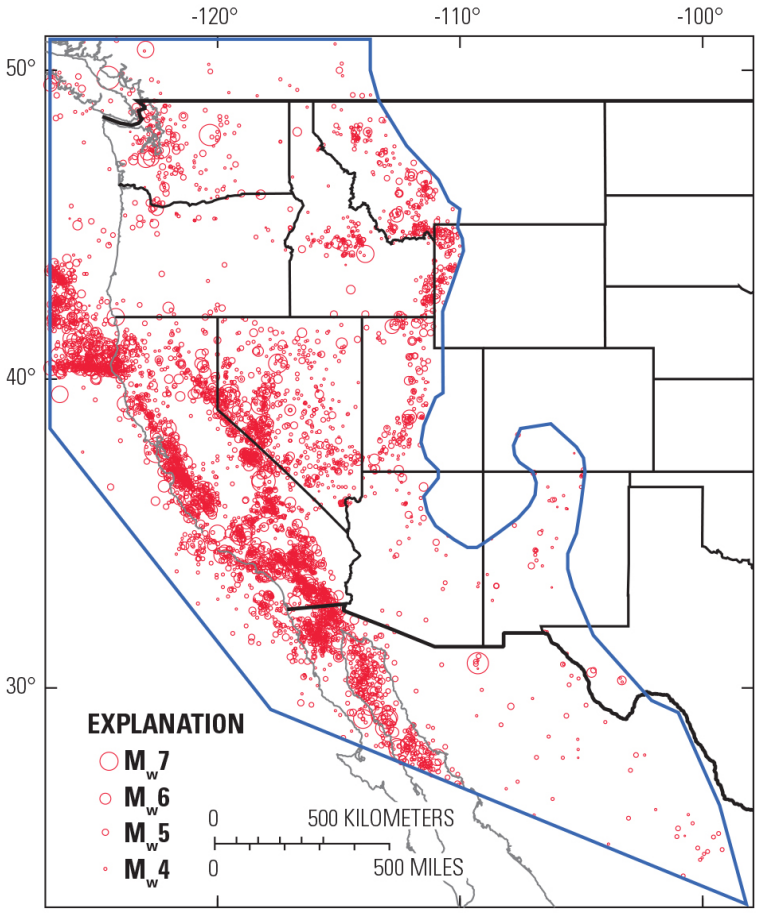

Figure 35. Declustered catalog for outlined region of the Western United States with earthquakes M_w3.5 and greater since 1850.

Table 6. Contributions to the declustered catalog, M_w3.5 and greater, 1850–2012.

[PDE, Preliminary determination of epicenters; UCERF2, Uniform California Earthquake Rupture Forecast version 2; UCERF3, Uniform California Earthquake Rupture Forecast version 3]

Source catalog	Number of earthquakes
Special Cases	16
UCERF2	100
Engdahl and Villaseñor (2002)	27
USGS Preliminary Determination of Epicenters—PDE (2013)	419
Stover and Coffman (1993)	198
Stover and others (1984)	235
Pancha and others (2006)	76
Engdahl and Rinehart (1991)	33
M_w from Centroid Moment Tensor Project (2013) and St. Louis University (Herrmann, 2013)	163
UCERF3	2,867
USGS Comprehensive Catalog (2013)	1,488
Total	**5,622**

Modeling Shallow Crustal Background Seismicity

The overall approach to modeling background seismicity in the WUS was not changed from Petersen and others (2008), but we incorporated a new catalog and adaptive smoothing methods in this version. Magnitude-dependent catalog completeness levels are the same as 2008. Statistical analysis (Weichert, 1980) of the declustered Mw catalog yields a *b* value of about 0.8, and *b*=0.8 is adopted for the hazard analysis. A grid 0.1 degree in latitude by 0.1 degree in longitude is superimposed on the region. Earthquakes with M_w greater than or equal to 4.0 that pass a completeness test are counted in each grid cell, and rates are adjusted for variable completeness (Weichert, 1980). Counting is adjusted for magnitude uncertainty to give unbiased rates (CEUS–SSCn, 2012). To account for future random earthquakes in places with little or no historical seismicity, a seismicity-rate floor is implemented based on average seismicity rates computed from the catalog for several broad regions. The historical rate is compared with the regional average rate for each grid cell. If the historical rate exceeds the regional average, the final modeled rate simply equals the historical rate; however, if the regional average exceeds the historical rate, the models are combined with branch weights of 0.667 (historical) and 0.333 (regional). The final cell rate is never smaller than the historical rate, and active areas are not penalized to compensate for the rate floor in quiet areas. Incremental 10^a (Herrmann, 1977) is computed from the cumulative count. The resulting "a-grid" represents the annual rate of earthquakes with M_w plus or minus 0.05 magnitude units in each grid cell.

As in past models, a two-dimensional spatial Gaussian function with a fixed, uniform correlation distance of 50 km is implemented to smooth the a-grid to account for uncertainties in the locations of future earthquakes. For the 2014 update, a procedure that adaptively derives smoothing lengths using a nearest-neighbor algorithm also has been implemented based on work by Helmstetter and others (2007) and Werner and others (2011). The smoothing distance is unique to each earthquake and is set equal to

the distance to the *n*th nearest neighboring epicenter (neighbor-number). We use established likelihood testing methods (Helmstetter and others, 2007; Werner and others, 2011) to optimize the neighbor-number, and find that the fourth nearest neighbor produces the optimal smoothed model to match recent spatial patterns of seismicity. The adaptive smoothing is implemented for a single completeness level that maximizes the likelihood parameter. For the WUS catalog, we find that the completeness level giving the highest likelihood is M_w4.0 (since 1963). Differences in the a-grids from the fixed- and adaptive-smoothing methods result from the spatial variation in epicenter density. In more active regions, the adaptive method yields smaller correlation lengths and higher local seismicity rates. Comparisons of the a-grids from the different smoothing methods and the resulting hazard differences are given in figure 36. In the final hazard model, a-grids using fixed and adaptive smoothing are combined with branch weights of 0.60 and 0.40, respectively.

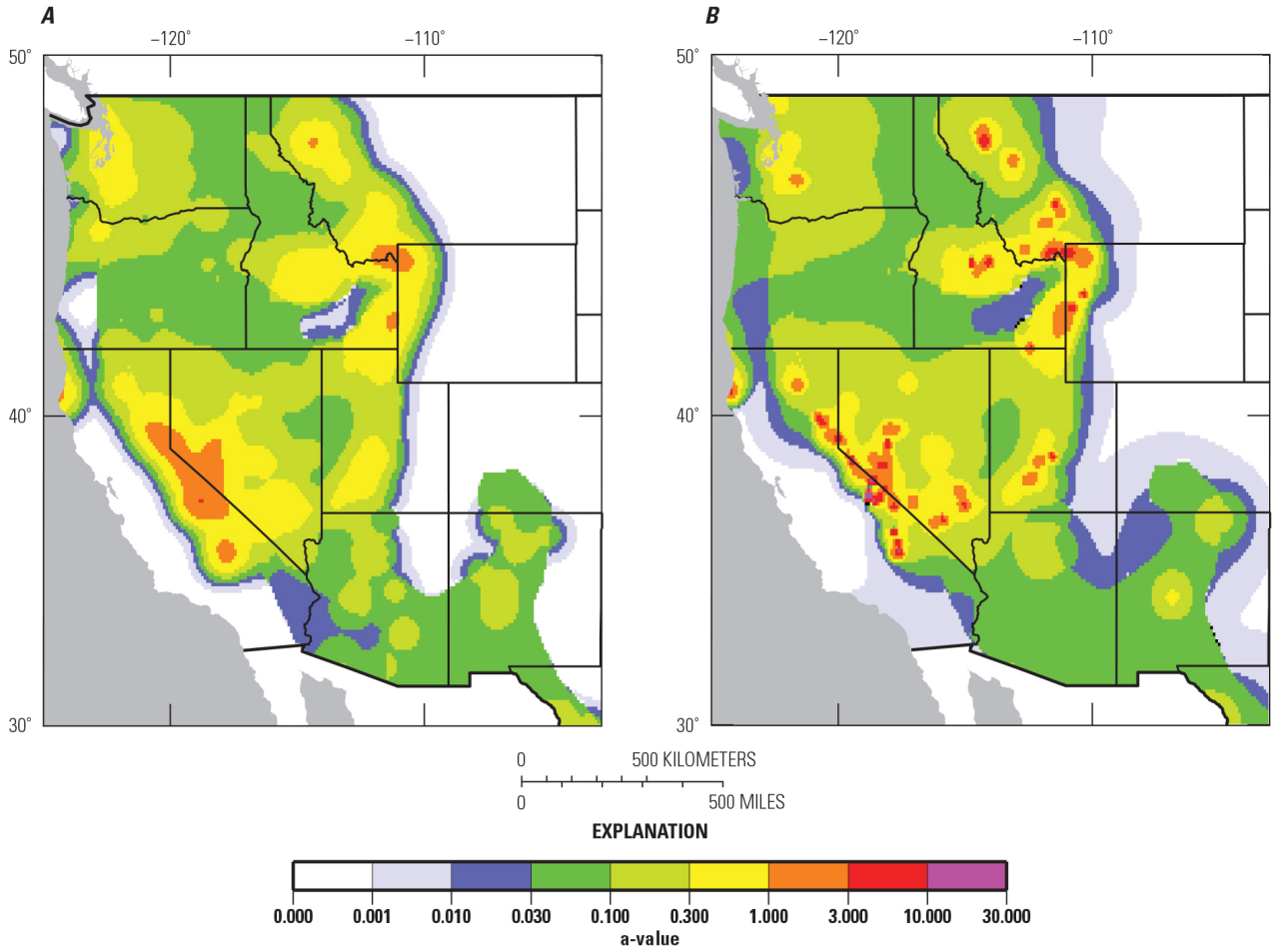

Figure 36. Maps showing incremental seismicity-rate grids from alternative smoothing methods for 5-hertz spectral acceleration. Costal California and Central and Eastern United States seismicity is not included in the grids. *A*, Map of fixed-correlation-length smoothing method and *B*, adaptive-correlation-length smoothing method.

As in past models, separate a-grids are developed from subcatalogs for regions where extensional or nonextensional ground motion relations are used to compute hazard. For the extensional zone, we apply ground motion models with branch weights of 0.667 on normal faulting mechanisms and 0.333 on strike-slip faulting mechanisms to account for variability in future Intermountain West

earthquakes. For the nonextensional zone, we apply branch weights of 0.667 on reverse faulting mechanisms and 0.333 on strike-slip faulting mechanisms to account for the compression and shear in the Pacific Northwest region. These ratios were determined from the geodetic data and are described in section "Combined Geodetic- and Geologic-Based Slip-Rate Models."

Maximum Magnitude for Shallow Crustal Background Seismicity

The 2008 and previous USGS NSHMP maps modeled Mmax 7.0 for background seismicity in most places in the WUS, except in the Central Nevada Seismic Zone (Mmax 7.5) and in geodetic-based shear zones (Mmax 7.6). General consensus in the scientific community is that Mmax should be greater than that assumed in previous models because (1) our inventory of potential sources is incomplete, (2) we have not considered possible linkage of short faults into a long rupture, and (3) we cannot identify locations where possible future rupture on a fault is not or is poorly expressed at the surface, such as the causative fault of the September 2010, M_w7.1, Darfield, New Zealand, earthquake (Quigley and others, 2011). In addition, hazard studies in California and the CEUS have considered magnitudes of M_w7.9 and greater, which is much larger than we have considered in previous models. All known faults are not included in our source model because nearly three-fourths of all known Quaternary faults have insufficient information to characterize recurrence rates of moderate to large earthquakes. The historical record clearly demonstrates that faults that might be considered independent sources (segments) could link up to form larger earthquakes than we have modeled in the past. The longest historical normal surface rupture in North America happened in 1887 in northern Mexico. The Sonora earthquake had an estimated magnitude between M_w7.2 and M_w7.6 and ruptured four distinct faults (Suter, 2006, 2008a, b). Because we are increasing Mmax in surrounding regions and for other reasons previously stated in this section, we cannot identify defensible reasons to exclude them from the Intermountain West or the Pacific Northwest model. Therefore, we selected two Mmax alternatives: one with M_w7.45 (branch weight 0.9), similar to the Sonora, Mexico, earthquake; and one with M_w7.95 (branch weight 0.1), which is consistent with the moment of the geodetic-based velocity data. On the M_w7.45 maximum-magnitude branch the magnitude-frequency distribution is modeled as truncated exponential. On the M_w7.95 maximum-magnitude branch, the magnitude-frequency distribution is modeled with a tapered Kagan (2002) magnitude-frequency distribution, with a corner magnitude of M_w7.5. The maximum magnitude M_w7.45 branch also defines Mmax at a value below the minimum characteristic magnitude of nearby faults; however, the maximum magnitude M_w7.95 branch does not apply this constraint. On this branch, we assume that earthquake ruptures may link up parts of mapped faults and unknown structures in the vicinity. In regions with relatively dense mapped faults, we expect big earthquakes would be associated with significant coseismic slip on several of these neighboring faults. The Wells and Coppersmith (1994) scaling relation for average displacement on normal faults suggests displacements of less than 3.5 meters (m) for M_w7.9 earthquakes.

Modeling Deep or Benioff-Zone Seismicity

In this section we describe the modeling of deep intraslab seismicity. We discuss earthquake rates, maximum magnitude, and a new depth distribution.

Earthquake Rates and Maximum Magnitude

In this update, hazard from deep earthquakes is computed in three separate regions: Washington, Oregon, and northern California. Deep earthquakes (greater than 40 km deep) are modeled with a truncated Gutenberg-Richter magnitude-frequency distribution. The minimum magnitude is M_w5.0 in

California and Washington and is M_w6.5 in Oregon, and the maximum magnitude is M_w7.45 or M_w7.95. In Washington and Oregon, the *b* value is 0.4 up to M_w7.2, whereas in northern California, the *b* value is 0.8.

For deep seismicity with magnitude greater than M_w7.2, the rates are based on a Gutenberg-Richter magnitude-frequency distribution with slope 0.8 in all three regions. Based on steering committee recommendations, we increased the Mmax associated with deep seismicity to M_w7.45 with branch weight 0.5 and to M_w8.0 with branch weight 0.5 from M_w7.2 used in previous USGS NSHMP maps. The current Mmax values are more consistent with worldwide data; a search of the Global Centroid Moment Tensor Project catalog (2013) using a minimum magnitude of M_w7.4, a hypocenter depth range of 40–80 km, and a starting date of 1973 yields the hypocenter set shown in table 7.

Table 7. Global catalog search for large deep earthquakes since 1975. The depth range is 40–80 kilometers.

[°, degrees; km, kilometers; M_b, body-wave magnitude; M_S, surface-wave magnitude; M_w, moment magnitude; UTC, Coordinated Universal Time]

Origin time (UTC)	Latitude (°)	Longitude (°)	Depth (km)	Magnitude	Magnitude type and source
2011-03-11 06:15:40.28	36.281	141.111	42.6	7.9	M_w USGS Preliminary Determination of Epicenters.
2009-10-07 22:03:14.47	–13.006	166.510	45.0	7.7	M_w USGS Preliminary Determination of Epicenters.
2007-11-14 15:40:50.53	–22.247	–69.890	40.0	7.7	M_w USGS Preliminary Determination of Epicenters.
2006-05-03 15:26:40.00	–20.150	–174.100	55.0	8.0	M_w Engdahl, and Villaseñor, 2002.
1999-09-30 16:31:14.00	16.045	–96.869	40.0	7.5	M_S Engdahl, and Villaseñor, 2002.
1995-07-30 05:11:24.00	–23.336	–70.265	40.5	8.0	M_S Engdahl, and Villaseñor, 2002.
1993-08-08 08:34:25.00	12.999	144.872	57.1	7.8	M_S Engdahl, and Villaseñor, 2002.
1993-06-08 13:03:36.00	51.195	157.755	60.5	7.5	M_S Engdahl, and Villaseñor, 2002.
1987-03-05 09:17:05.00	–24.396	–70.099	46.4	7.6	M_S Engdahl, and Villaseñor, 2002.
1985-03-04 00:32:24.00	–33.236	–71.740	40.0	7.4	M_S Engdahl, and Villaseñor, 2002.
1983-04-03 02:50:04.00	8.716	–83.129	57.0	7.5	M_S Engdahl, and Villaseñor, 2002.
1980-07-08 23:19:24.00	–12.485	166.482	55.7	7.5	M_S Engdahl, and Villaseñor, 2002.
1978-06-12 08:14:29.00	38.223	142.022	52.7	7.7	M_S Engdahl, and Villaseñor, 2002.

Table 7. Global catalog search for large deep earthquakes since 1975. The depth range is 40–80 kilometers.—Continued

Origin time (UTC)	Latitude (°)	Longitude (°)	Depth (km)	Magnitude	Magnitude type and source
1977-06-22 12:08:34.00	–22.908	–175.749	64.2	8.1	M_S Engdahl, and Villaseñor, 2002.
1977-04-21 04:24:12.00	–10.007	160.811	43.4	7.4	M_S Engdahl, and Villaseñor, 2002.
1976-11-30 00:40:58.00	–20.548	–68.874	74.4	7.6	M_S Engdahl, and Villaseñor, 2002.
1976-08-16 16:11:11.00	6.292	124.091	58.5	8.0	M_S Engdahl, and Villaseñor, 2002.
1976-01-14 15:56:34.00	–29.212	–177.635	42.2	7.8	M_S Engdahl, and Villaseñor, 2002.
1975-10-31 08:28:04.00	12.537	125.999	51.1	7.5	M_w Engdahl, and Villaseñor, 2002.
1975-07-20 14:37:42.00	–6.612	155.095	61.1	7.5	M_b Engdahl, and Villaseñor, 2002.

In our model, we do not want to overpredict the rate of large deep earthquakes, since we have seen none with magnitude greater than M_w7 in the historical record of the WUS coastal region (an earlier estimate of the 1949 Olympia deep-source earthquake is M_w7.1; however, more recent estimates are lower, Ichinose and others, 2006). To obtain a reasonable rate of large deep earthquakes, we assume the historical rate of M_w4–7 earthquakes, and we constrain the model to have that same cumulative rate. The deep-source (magnitude-rate) distribution in the Puget Sound area is shown in figure 37. The cumulative rate under the black line from M_w4 to 7 equals the cumulative rate under the dashed red line from M_w4 to 7. In Oregon, we used the same approach as is shown in figure 37. That is, we conserved the observed rate of M_w4–7, and used two branches both with truncated Gutenberg-Richter rates, with b=0.8, and with maximum magnitude of M_w7.45 and M_w7.95, respectively. In northern California, we simply increased Mmax; the parameter b was set to 0.8 for all magnitudes in California.

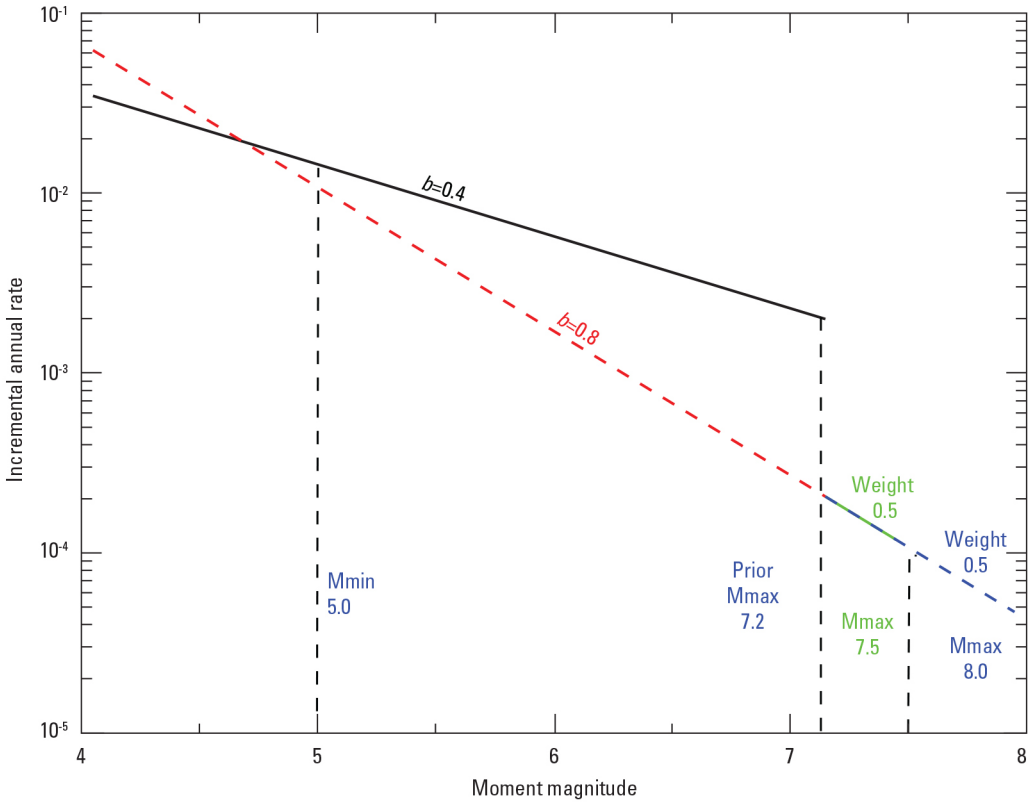

Figure 37. Magnitude-frequency distribution of deep seismicity in the Puget Sound region. Black curve shows the incremental rate of earthquakes up to M_w7.2; bin size equals 0.1-magnitude unit. Two logic-tree branches are used for earthquakes with magnitudes greater than M_w7.2, one having maximum magnitude of M_w7.5 (green curve), the other having maximum magnitude of M_w8.0 (blue curve), each branch weight 0.5.

The deep-focus (Benioff zone) earthquake rates in the 2008 and current models are summarized in table 8. The final two columns show the rates of larger earthquakes not previously considered. For example, the mean annual rate of M_w7.2–7.5 in western Washington is 6.4E-04 for a recurrence time of 1,562 years (branch weight 0.5) or a mean annual rate of 9.9E-04 for a recurrence time of 1,010 years for M_w7.2–8.0 (branch weight 0.5). Similar estimates of deep earthquake rates in Washington and Oregon for the 2014 model compared to that of 2008 are shown in table 8, but a significant decrease of this rate in northern California. The decrease in estimated rate of deep earthquakes in northern California is attributed to two factors: (1) a reclassification of some deep earthquakes as aftershocks that were previously treated as independent earthquakes, and (2) a reclassification of several hypocenters as shallow that previously were listed as deep but were poorly constrained. In the 2014 update, the Washington and California Benioff zone boundaries remain the same as in previous USGS NSHMP maps, but the Oregon Benioff zone has been expanded to cover the entire western part of the State. In 2008, this zone only covered the northwest part of the State. In Oregon, because of the sparseness of deep earthquakes in the catalog, two logic-tree branches on earthquake location are considered for the 2014 update. The first uses Gaussian smoothing with a 50-km smoothing radius around catalog epicenters and the second uses a uniform zone (keeping the rate of deep events per unit area constant). These two logic-tree branches are assigned equal weight.

Table 8. Benioff zone earthquake rates.

[yr, years; M_w, moment magnitude]

Region	2008 mean annual rate	2008 mean return time (yr)	2014 mean annual rate	Mean annual rate M_w7.2–7.5	Mean annual rate M_w7.2–8
N.W. California	4.41E-02	22.7	0.0273	2.1E-04	3.7E-04
W. Oregon	4.0E-03	250	0.00374	1.3E-04	1.6E-04
W. Washington	1.153E-01	8.8	0.1357	6.4E-04	9.9E-04

The Staircase Distribution of Benioff Hypocenters

When computing hazard from deep earthquakes, GMMs are sensitive to depth of the earthquake rupture. This depth parameter not only affects the hypocentral depth, and therefore distance from site, but also affects the ground motion models since the increase of median response increases with focal depth (at the depths considered in this analysis). Intraplate (deep) earthquakes in the Pacific Northwest tend to be confined to a depth band of about 35 to 70 km. In other regions, Benioff zone seismicity extends to greater depths, as much as 600 km or more, but is limited in this study area because of the relative youthfulness of the Juan de Fuca slab (McCrory and others, 2012), which is warmer than other convergent margin slabs.

In all previous NSHMP products, deep seismicity in the Pacific Northwest and California was assigned a fixed depth of 50 km. Although 50 km is a reasonable average depth, an improved model would account for an increasing average depth of focus as the Juan de Fuca slab descends into the Earth's mantle. In the 2014 update, we improve the hazard model by increasing the slab depth towards the east as a set of three steps, with discrete jumps at specific longitudes. Hypocenter data and information about the interface location are used to build the focal-depth model. The two sets of hypocenter data (USGS Advanced National Seismic System, 2014, and the declustered catalog from this study), the Cascadia interface at the latitude of Seattle, and the proposed depths for Benioff seismicity (the "staircase") are shown in figure 38. Longitudes of some cities are shown. Seattle, Wash., is over the deepest step (60 km), Portland, Oreg., is over the middle step (50 km), and Astoria, Oreg., is over the shallowest step (41 km). The shallowest depth on the interface with episodic tremor and slip is at the intersection of the red and green lines, about 35 km depth in figure 38. This location is the deepest interface-event rupture depth on any logic-tree branch. Deep intraplate seismicity, however, extends much farther east. The blue squares in figure 38 are the reported hypocenters of the deep seismicity used to compute the activity grid (C. Mueller, written commun., 2013). The black squares are event hypocenters from the USGS Advanced National Seismic System (2014) catalog, for M_w2.6 and greater sources with depth greater than 35 km and origin times in the period 1990–2013, when hypocenter estimates are believed to be reasonably accurate. The catalog of deep Oregon seismicity is too sparse to provide guidance for defining a staircase depth distribution. The depth distribution shown in figure 38 also is used in Oregon in the 2014 update.

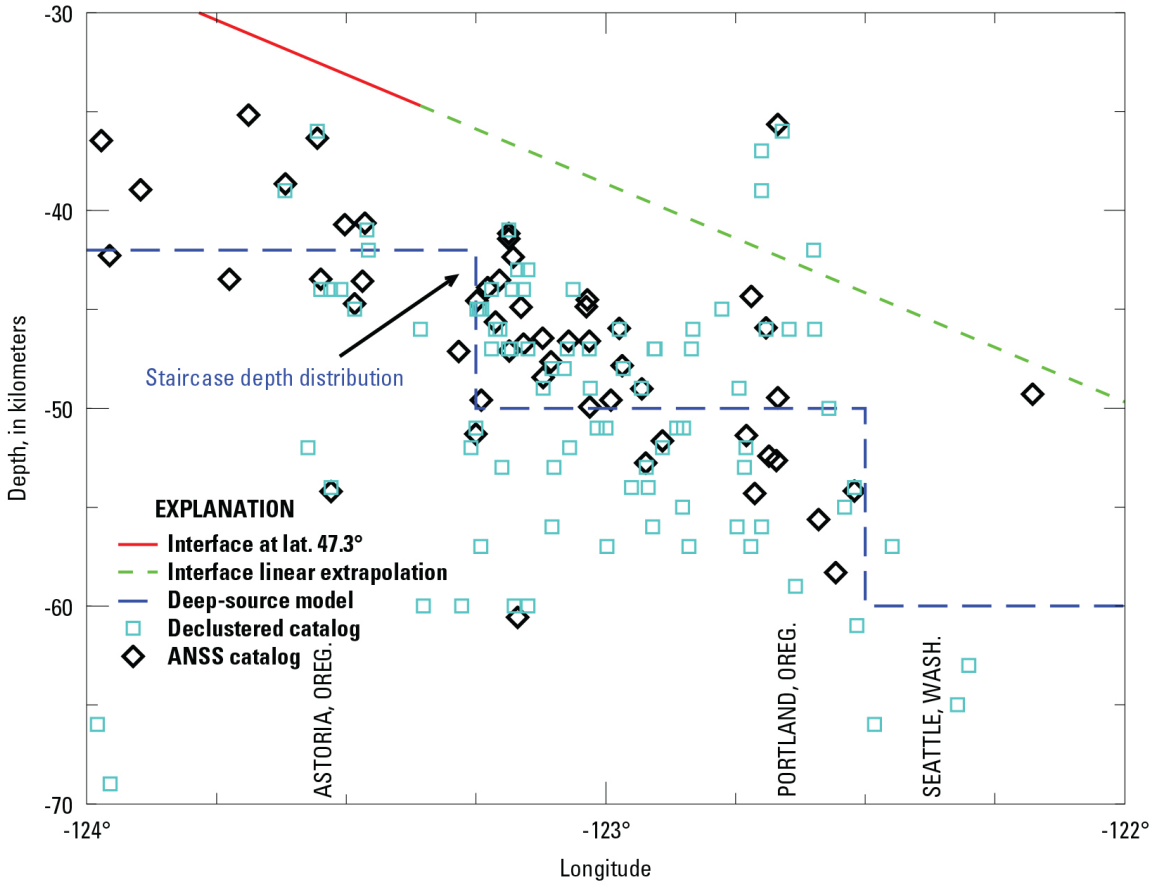

Figure 38. Distribution of deep seismicity beneath the Cascadia interface at lat 47.3˚ N. and modeled depth used for Washington deep seismicity.

The northern California distribution of deep hypocenters, the proposed staircase for modeling these hypocenters, and Cascadia interface projected onto a plane at the lat 41.3°N. are shown on figure 39. Eureka, Calif., is over the shallowest step, at a depth of 39 km, and Redding, Calif., is over the deepest step, at depth –60 km. The top of the zone of episodic tremor and slip is at –30 km in northern California, shown in figure 39 as the point where the red Cascadia (seismically active) interface meets the green (aseismic) Cascadia interface. The shallow step extends farther east, to long 123.05°W., than the corresponding step in Washington and Oregon.

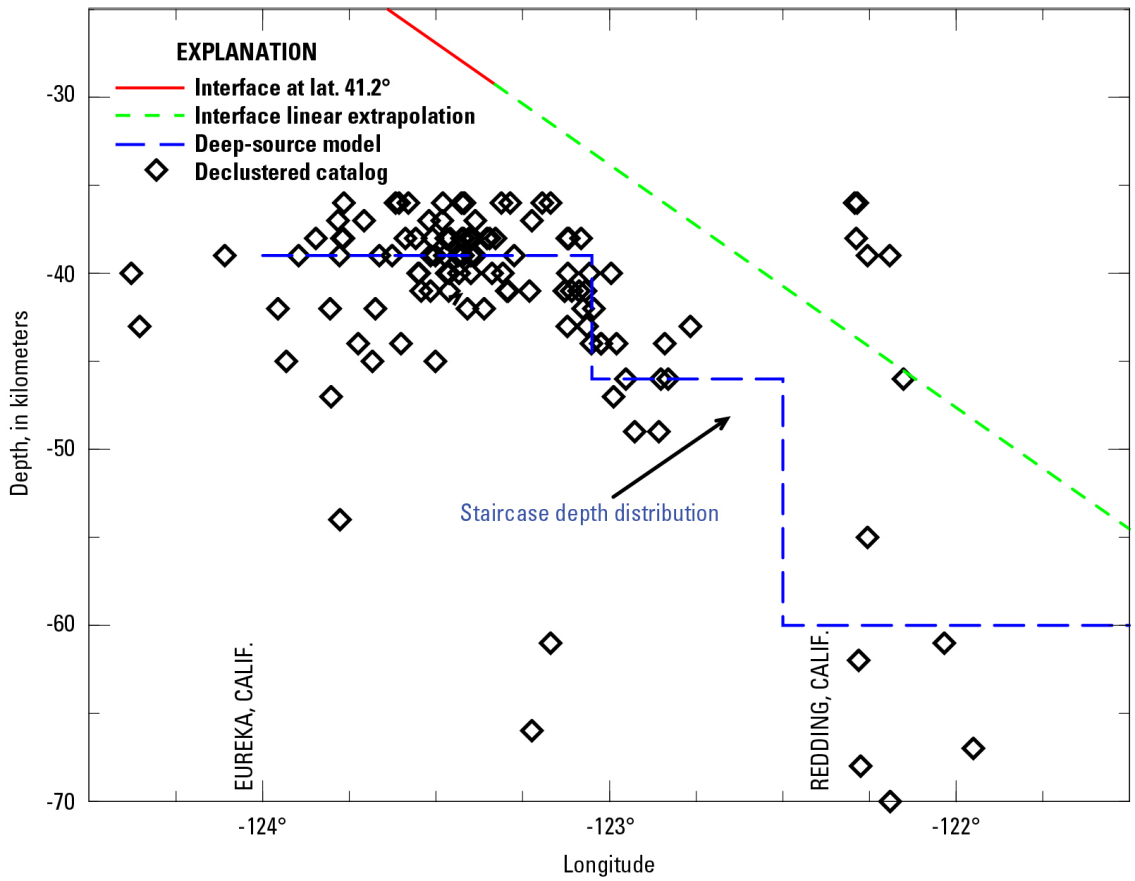

Figure 39. Distribution of deep seismicity beneath the Cascadia interface in northern California and modeled depth used for northern California deep seismicity hazard.

Fault-Based Source Model in the Western United States

Many fault studies show clear evidence of repeated earthquakes of sufficient magnitude to rupture the surface of the Earth. Thus, it is standard practice to include explicit fault sources to augment background sources defined by seismicity, thereby extending the historical record back thousands of years. For each update of the USGS NSHMP maps, we adjust our source characterization to incorporate new published studies in the region. Paleoseismic and geologic data inform the fault-source model regarding the timing, amount of slip per earthquake, and slip rate.

Source characterization improves through better understanding of the region's seismic sources. There are over 2,000 known faults in the WUS that are oriented such that they could relieve regional stress in future earthquakes. Most are poorly understood and characterized only by their location. The NSHMP models include a fault as a source of future earthquakes when the paleoseismic history has been studied sufficiently. These studies provide not only fault location but also evidence of the size, extent of surface rupture, and timing of earthquakes. These site-specific details are required to characterize a source for the purpose of this fault-source model. As a consequence, the fault-source inventory in this model, as in previous models, remains incomplete. Nearly 75 percent of the known faults with Quaternary surface rupture in the region are poorly characterized. Many of these

uncharacterized faults are tens of kilometers to more than 100 km in length and could generate significant earthquakes.

We model potential future earthquakes on the explicit fault sources as those that could rupture the entire fault (full-source rupture) and more numerous smaller magnitude earthquakes (floating partial-source ruptures) that range in magnitude from M_w6.5 to the magnitude of the full-source rupture. The full-source rupture magnitude branch is assigned a branch weight of 0.667 in the Intermountain West and 0.5 in the Pacific Northwest; the partial-source rupture magnitude branch is assigned either 0.333 or 0.5 in the respective regions (fig. 40). Most faults in the WUS are normal fault with possible maximum magnitudes of M_w6.15–7.75 (fig. 41); however, we characterize the longest sources (longer than about 100 km) by floating partial-source ruptures with magnitudes of M_w6.5–7.5. The mode of the maximum magnitude for all normal sources is M_w6.95–7.05. The region contains many fewer strike-slip and thrust sources. Strike-slip fault sources are assigned maximum magnitudes of M_w6.00–7.34 and thrust and reverse fault sources are assigned maximum magnitudes from M_w6.15 to 7.5. Partial-source ruptures allow for smaller earthquakes on a fault.

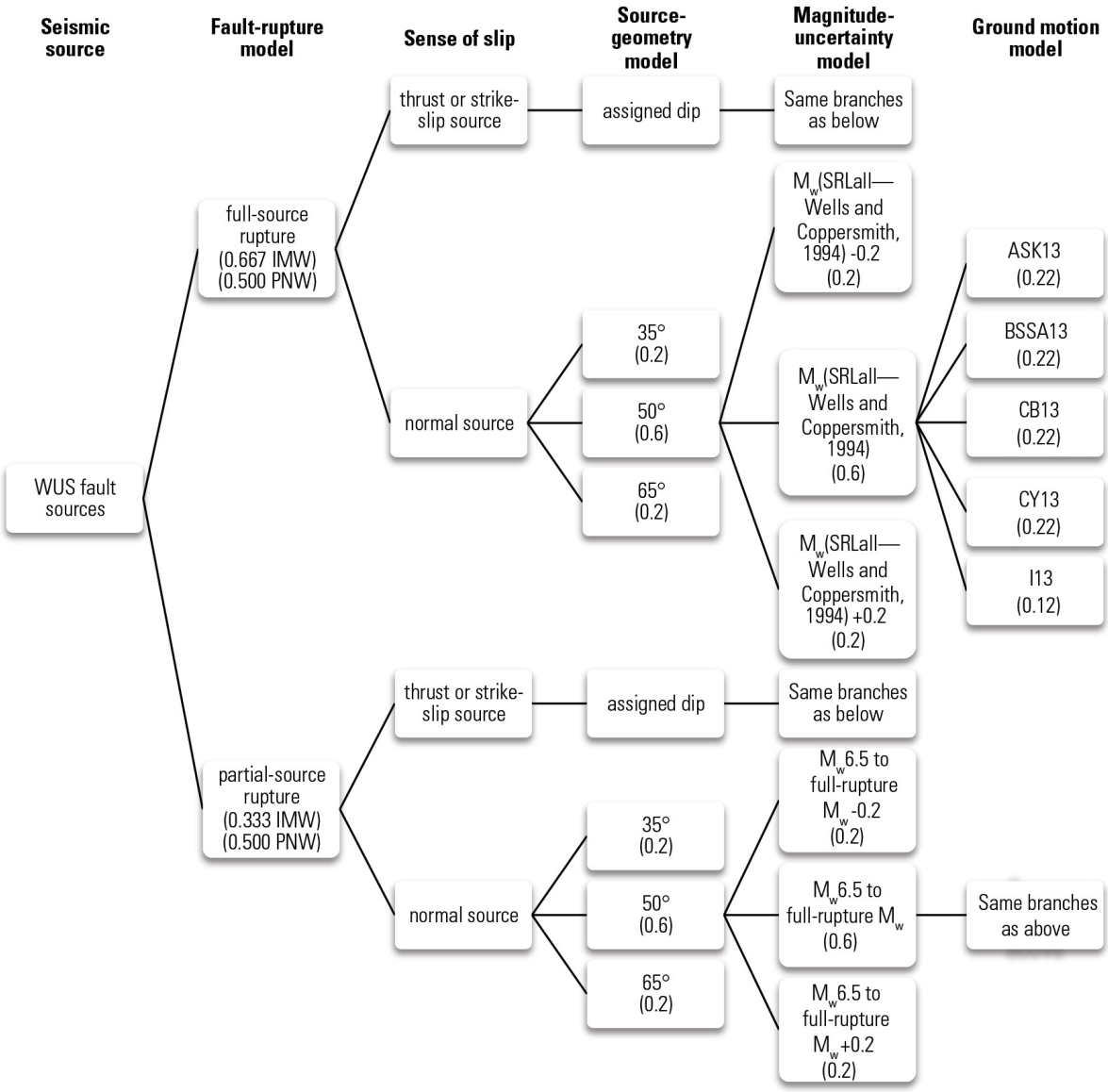

Figure 40. Logic tree for crustal fault sources in the Intermountain West (IMW) and Pacific Northwest (PNW). Assigned branch weight shown in parentheses.

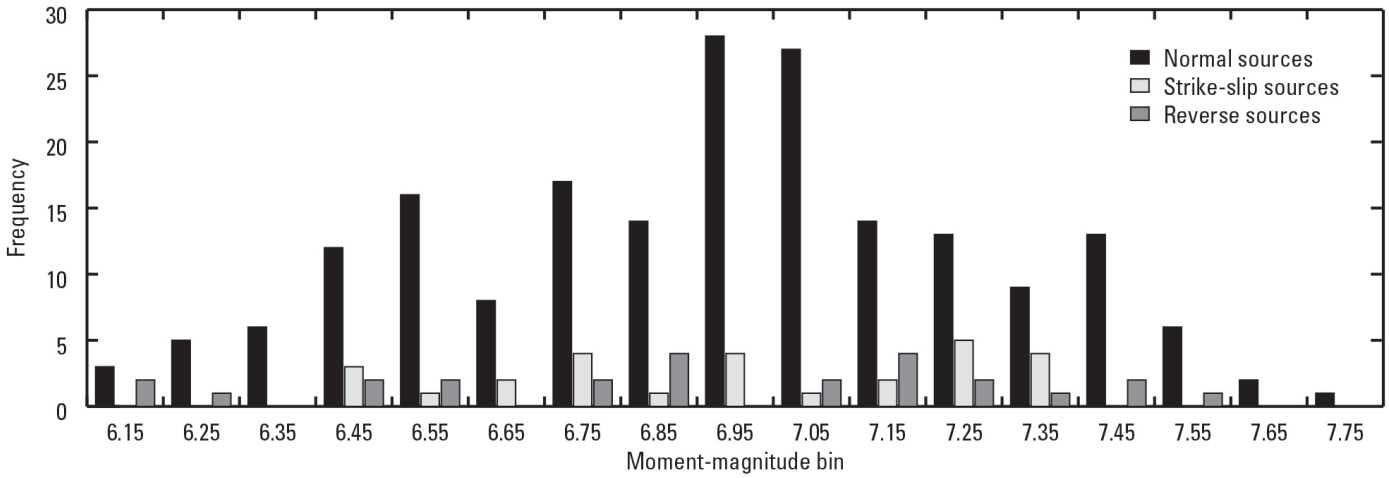

Figure 41. Distribution of assigned full-source rupture magnitude for crustal fault sources in the Intermountain West and Pacific Northwest by sense of slip.

Fault sources in this model are constrained by 40 years of published geologic and paleoseismic studies that characterize activity rate and fault geometry throughout the United States. The model is based on simplified fault geometry that defines its three-dimensional plane in the Earth's crust and one or more parameter(s) to constrain how active the fault is in the model. Typically, the assigned parameter is slip rate; slip rate is the measure of displacement on the fault resolved to the three-dimensional fault plane divided by the appropriate time period. For some fault sources, we constrain the rate of future earthquakes based on the known geologic record when that record does not support the predicted return time of full-source ruptures that would be derived from the assigned slip rate. The dimensions of the fault source constrain its potential maximum magnitude, which along with slip rate determines the frequency of future earthquakes as an annualized rate.

Fault-Source Geometry

The location of fault sources is simplified from the USGS Quaternary fault and fold database (*http://earthquake.usgs.gov/hazards/qfaults/*); faults in this compilation are mapped at scales of either 1:250,000 or 1:100,000. However, the fault sources are accurately located at a scale of 1:1,000,000. Each fault source projects from the Earth's surface to a depth of 15 km, and is assigned a nominal dip based on its sense of slip: strike-slip fault sources dip 90°, thrust fault sources dip 45°, and reverse fault sources dip 60°.

In early versions of the NSHMP maps, normal faults in the WUS were modeled using a single assigned dip of 60° (Frankel and others, 1996, 2002), based on the theory of maximum principal stress for extensional environments (Anderson, 1951) and Byerlee's (1978) law. The previous version of the NSHMP model included dip uncertainty (Petersen and others, 2008). In 2008, normal faults were assigned dips of 40°, 50°, and 60° based on recommendations from the Basin and Range Province Earthquake Working Group (Lund, 2006). In 2012, the working group determined that dip uncertainty was underrepresented based on a global dataset of normal earthquakes. The Basin and Range Province Earthquake Working Group suggested using a default dip of 50±15° for normal faults (Lund, 2012). Implications for hazard are significant: sources with gentler dips are closer to the Earth's surface at

greater distances, the bottom of a 35°-dipping source extends horizontally up to three times the horizontal distance from the surface trace than a 65°-dipping source, and the conversion of vertical displacement to fault-parallel slip is proportional to $(1/\sin(\text{dip}))^2$. These effects all contribute to increased hazard over the shallow-dipping source alternative. Fault-specific dip data are sparse for normal faults in the WUS, but the studies cited below conclude that normal faults dip between 45° and 55°. Locally, the Salt Lake City segment of the Wasatch fault, Utah, may dip 35° (see figure 8 in Bruhn and others, 1992); however, the preferred model for the Wasatch and other nearby faults for analytic stress modeling was pure normal slip on planar rectangular faults dipping 55° (Chang and Smith, 2002; Chang and others, 2006). Historically, normal crustal earthquakes have been shown to nucleate on moderate-to-steeply dipping structures, with a mode of 45° (Molnar and Chen, 1982; Jackson and White, 1989; Thatcher and Hill, 1991; Collettini and Sibson, 2001; Jackson, 2002). Recent data suggest that low-angle normal faults may be located in Papua New Guinea, Greece (the Gulf of Corinth), and Italy (the Apennines) (Collettini, 2011), but the debate regarding the potential of low-angle faults is ongoing (Abers, 2009). Whether or not these recent findings are relevant to the extensional WUS is unknown. This update assigns a default dip to normal sources of 50±15° (fig. 40). No dip uncertainty is assigned to strike-slip, thrust, or reverse fault sources.

We recognized in past models (Frankel and others, 1996, 2002; Petersen and others, 2008) that our results predicted somewhat more full-source ruptures than is represented in the paleoseismic record. The segmentation paradigm in the WUS is based on the observation that long faults do not rupture in their entirety in large-magnitude earthquakes and when they rupture they typically have a similar displacement at any given site. These models often identify changes in fault geometry and timing of past earthquakes to prescribe segments; however, historically geometrical boundaries often are not diagnostic in defining the limits of the surface rupture. The 1887 Sonora earthquake (Suter, 2006, 2008a, b), the 1915 Pleasant Valley earthquake (Wallace, 1984), the 1985 Borah Peak earthquake (Crone and others, 1987), and the 1959 Hebgen Lake earthquake (Witkind, 1964) ruptured through at least one geometrical boundary. To account for this uncertainty in defining segments, we model both full-rupture sources as well as partial segment ruptures to account for a broad range of alternatives. For fault sources longer than about 100 km, we float ruptures along the source with M_w6.5 to M_w7.5.

We model fault segments for only a few fault sources in this model; the remaining faults in the model are allowed to rupture their entire length or rupture shorter parts of the fault (floating ruptures) that do not exaggerate hazard at segment boundaries. The source model is informed both by reported single-event displacement, where large displacement is the best evidence for past large magnitude earthquakes, and earthquake recurrence from the USGS Quaternary fault and fold database and supplemental sources. For most WUS sources, larger magnitudes are calculated from magnitude-length/area scaling relations than is supported by large single-event displacements reported in the literature. We have only used the Wells and Coppersmith (1994) equations for calculating magnitudes and it may be useful to include other scaling relations in the future versions of the map.

Wasatch Fault Zone—Fault Geometry Under Salt Lake City

The Salt Lake City segment of the Wasatch fault zone presents challenges because of uncertainty in the location of the fault plane, especially beneath metropolitan Salt Lake City, Utah. Salt Lake City occupies a large re-entrant in the Wasatch Mountains range front that is bounded on the north by the Salt Lake salient and on the south by the Traverse Mountains. Complex surface faulting is recognized at the latitude of Salt Lake City (fig. 42). Three-dimensional relations between the faults that define the east-dipping West Valley fault zone and the west-dipping Wasatch fault zone are not known but may be illustrated as depicted in figure 43, from right to left: the Wasatch range-front fault, and the East Bench

fault, the Taylorsville scarp and the Granger scarp of the West Valley fault zone. An alternative to this assumption is that the Wasatch range-front fault and the East Bench fault do not merge at depth and independently project to seismogenic depths (15 km), with the West Valley fault(s) truncating at the East Bench fault; however, several alternative models can represent the bifurcation and gap in surface expression of faulting. Geophysical data do not provide conclusive evidence of the location or dip of the fault.

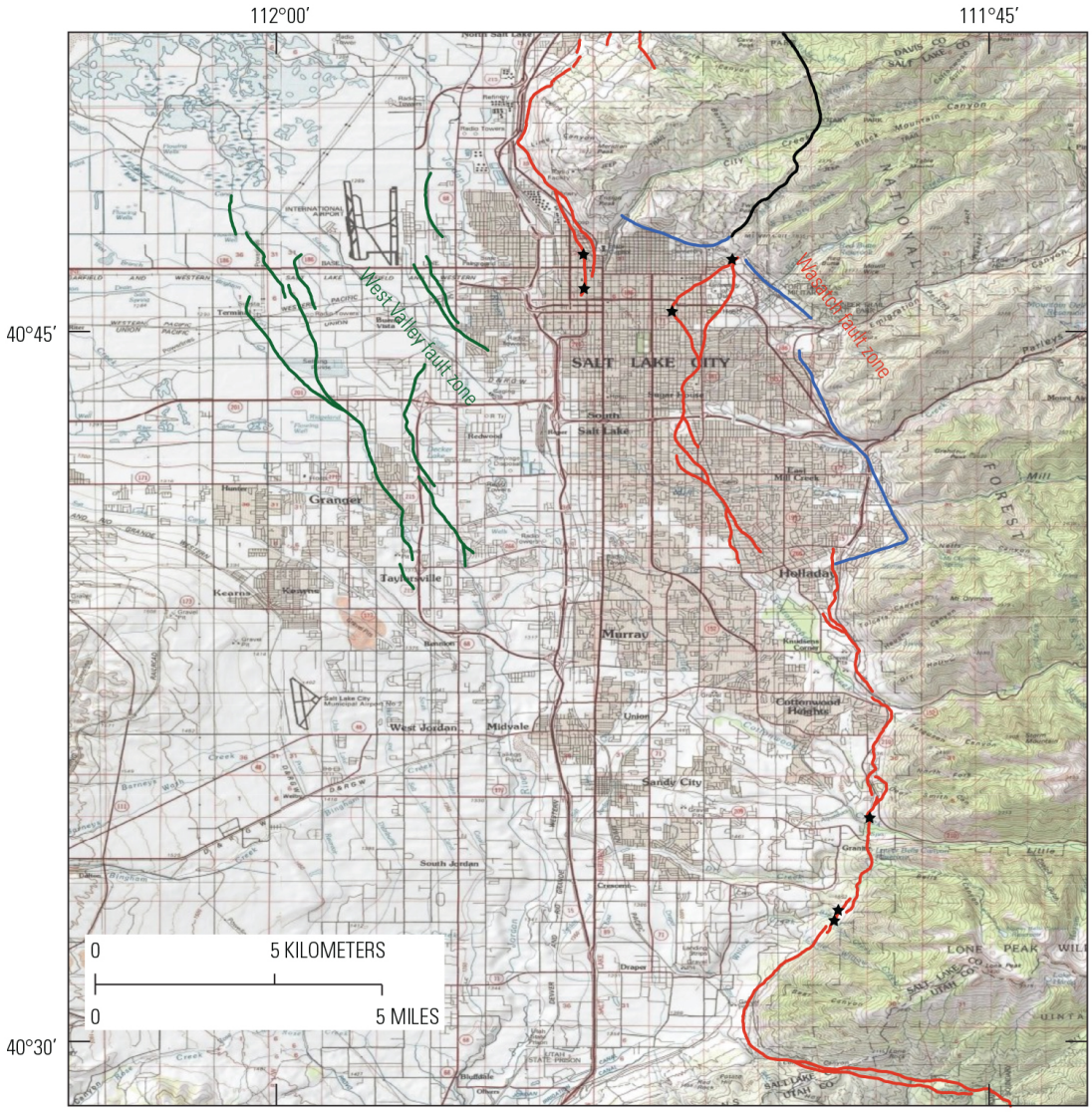

Figure 42. Map of Quaternary faults near Salt Lake City, Utah. The predominantly west-dipping faults with evidence of Holocene activity associated with the Wasatch fault zone are differentiated from those without evidence of Holocene surface rupture. The Holocene West Valley fault zone is antithetic to the Wasatch fault and dips to the east.

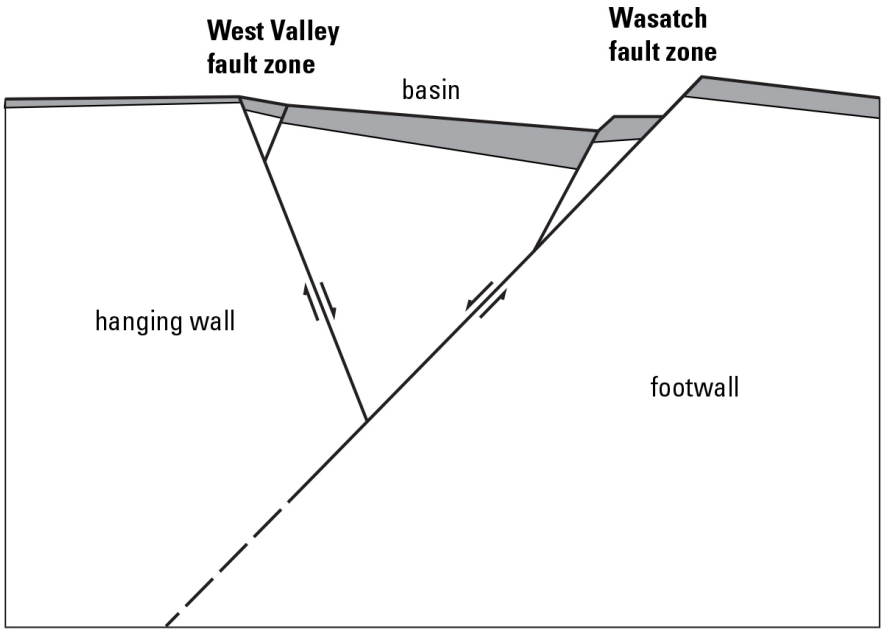

Figure 43. Sketch of spatial relations between a primary fault zone and antithetic fault zone that may reflect the relations between the northern part of the Salt Lake City segment of the Wasatch fault zone and the West Valley fault zone (modified from Bruhn and Schultz, 1996).

The location of the Wasatch fault near Salt Lake City is constrained by nearly continuous, prominent fault scarps at or near the range front from the Traverse Mountains to the Salt Lake salient. Details of surface rupture are further defined at four trench sites: the two southernmost trench sites at South Fork of Dry Creek (Black and others, 1996) and Little Cottonwood Canyon (Swan and others, 1980; McCalpin, 2002), and the northern two on the East Bench fault at Dresdan Place (Machette and others, 1992) and Penrose Drive (DuRoss and Hylland, 2010). Trenches on the Warm Spring fault at Warm Springs Park did not reveal the Wasatch fault (DuRoss and Hylland, 2010); however, evidence of surface rupture was present in a trench in northern Salt Lake City (Robison and Burr, 1991). Thus, the absence of fault scarps between the northern end of the East Bench fault and the Warm Springs fault permits a number of viable options, not all of which are explored here. All the models we present vary in location north of Big Cottonwood Canyon. The magnitude of the full-source rupture is defined by surface-trace length to magnitude-scaling (all) relations of Wells and Coppersmith (1994).

We adopted alternative rupture models in the update of the USGS NSHMP maps: two alternatives break the entire length of the Salt Lake City segment and one alternative breaks two parts of the fault in a short period of time. The mean recurrence interval for full-source ruptures is constrained to 1,300 years (Lund, 2013). Along with the full-source rupture, we model partial rupture of the source with magnitudes M_w6.5–7. The rate of floating partial-source ruptures is constrained by an assigned slip rate of 1.7 mm/yr (based on throw rate of 1.3 mm/yr in Lund, 2013), a dip of 50±15° (Lund, 2012), and b=0.8. Weights assigned to the three dip branches are 0.6, 0.2, and 0.2, respectively. The mean annual slip rate on the fault is constrained to 1.3/sin(50˚) on all three dip branches.

In addition, a floating M_w7.4±0.2 rupture of the Wasatch fault zone from its southern to its northern extremity is included in the model. The floating M_w7.4±0.2 is modified from its characterization in the previous version of the national seismic hazard maps (Petersen and others, 2008).

The modification places a discontinuity in the fault at the north end of the East Bench location and uses a 3-km step when moving this rupture along the fault trace. In the 2008 model, we used a 1-km step.

Model 1

The full-source magnitude for the Salt Lake City segment of the Wasatch Fault source in this alternative model is M_w7.03±0.2. The northern part of this source is constrained by the easternmost branch of the East Bench fault; the source passes through both the Dresdan Place trench site and the Penrose Drive site. The Penrose Drive location is joined to the southern end of the eastern trace of the Warm Springs fault. J. Pechmann (written commun., 2010) provided this two-dimensional geometry based on Roten and others (2011). This model differs from the Roten and others (2011) model by defining a uniform dip along the entire source instead of using variable dip along strike as defined by Bruhn and others (1992). The 5-hertz and 1-hertz spectral acceleration associated with this model (fig. 44) results in maximum ground motion of 1.465 g (acceleration of gravity) and 0.455 g, respectively, at lat 40.705°N., long 111.90°W.

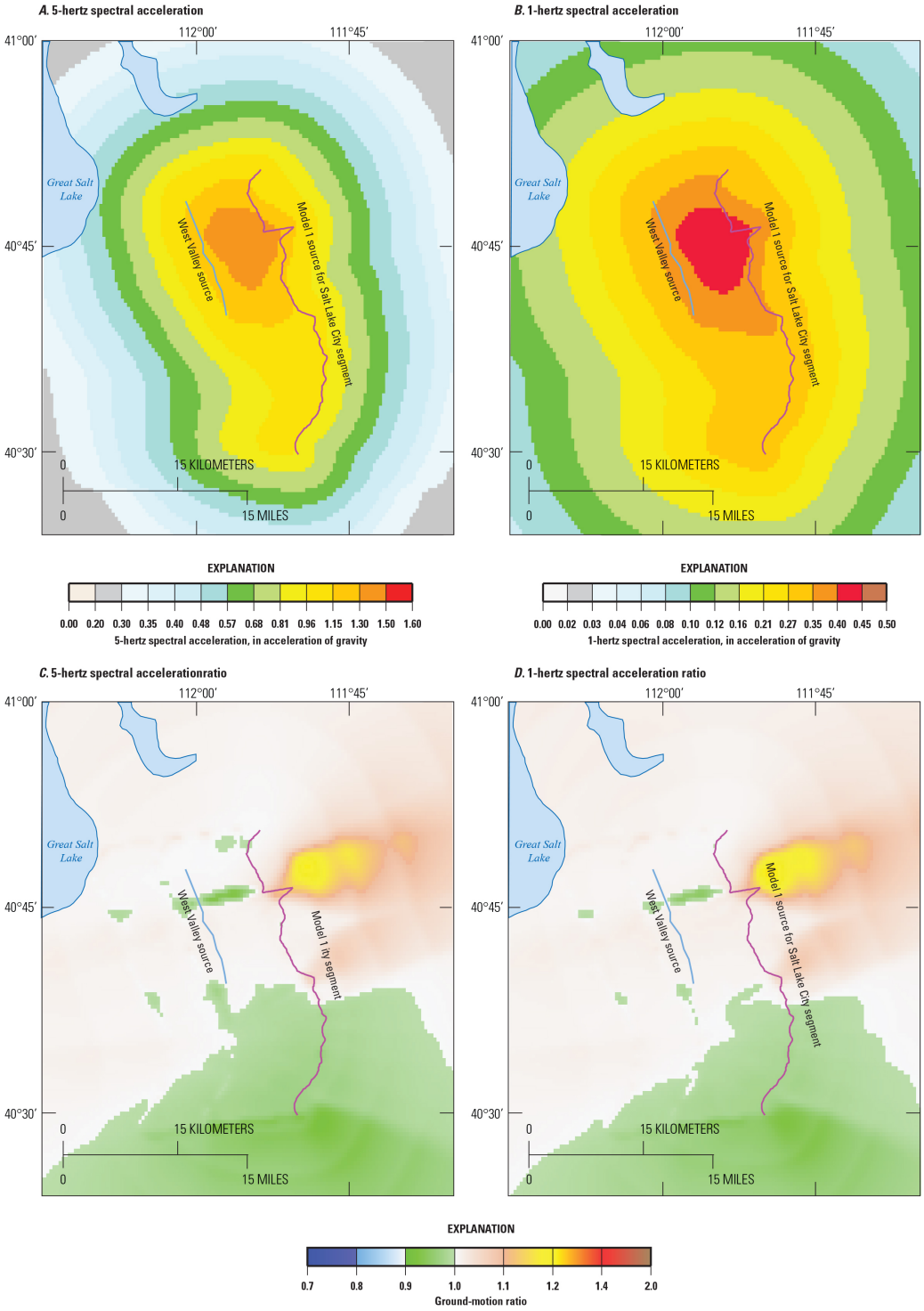

Figure 44. Results of hazard analysis for model 1 based on Roten and others (2011) geometry of the Salt Lake City segment of the Wasatch and the West Valley sources for 5-hertz (0.2-second) and 1-hertz (1-second) spectral acceleration for 2-percent probability of exceedance in 50 years and V_{S30} site condition of 760 meters per second. Maps compare *A*, 5-hertz and *B*, 1-hertz spectral acceleration results; and ratios of the alternative model compared to 2008 source model for *C*, 5-hertz and D, 1-hertz spectral acceleration. Locations of the Warm Springs fault, hypothetical tear fault, and East Bench fault are shown.

Model 2

In this alternative model, we retain the geometry in model 1 and replace the single rupture with three temporally clustered ruptures: an M_w6.9±0.2 rupture on the Cottonwood-East Bench fault, an M_w5.4±0.2 rupture on a hypothetical tear fault (Roten and others, 2011), and an M_w6.7±0.2 rupture on the Warm Springs fault. The sum of moment rates for these three events approximates an M_w7 source on the entire Salt Lake City segment. The clustered-event approach allows us to associate different rupture styles, different fault top and bottom depths, and different fault dips on the three subsources, a degree of flexibility that is not possible if we assume a full-source rupture. In the temporally clustered model, the tear fault is shallow with the top of rupture at 1-km depth and bottom of rupture at 6-km depth; the sense of movement on the tear fault is strike slip. Presumably, the hypothetical strike-slip fault is truncated at depth by the East Bench fault. The partial-source (but nonclustered) rupture branches are the same as those in model 1. In the other models, software limitations require that the same normal-slip fault extends from the surface to 15-km depth everywhere. This model also accommodates the potential west-trending tear fault. The probabilistic motions are shown in figure 45. The maximum 5-hertz and 1-hertz ground motions are 1.57 g and 0.476 g, respectively, at lat 40.765°N. and long 111.90°W.

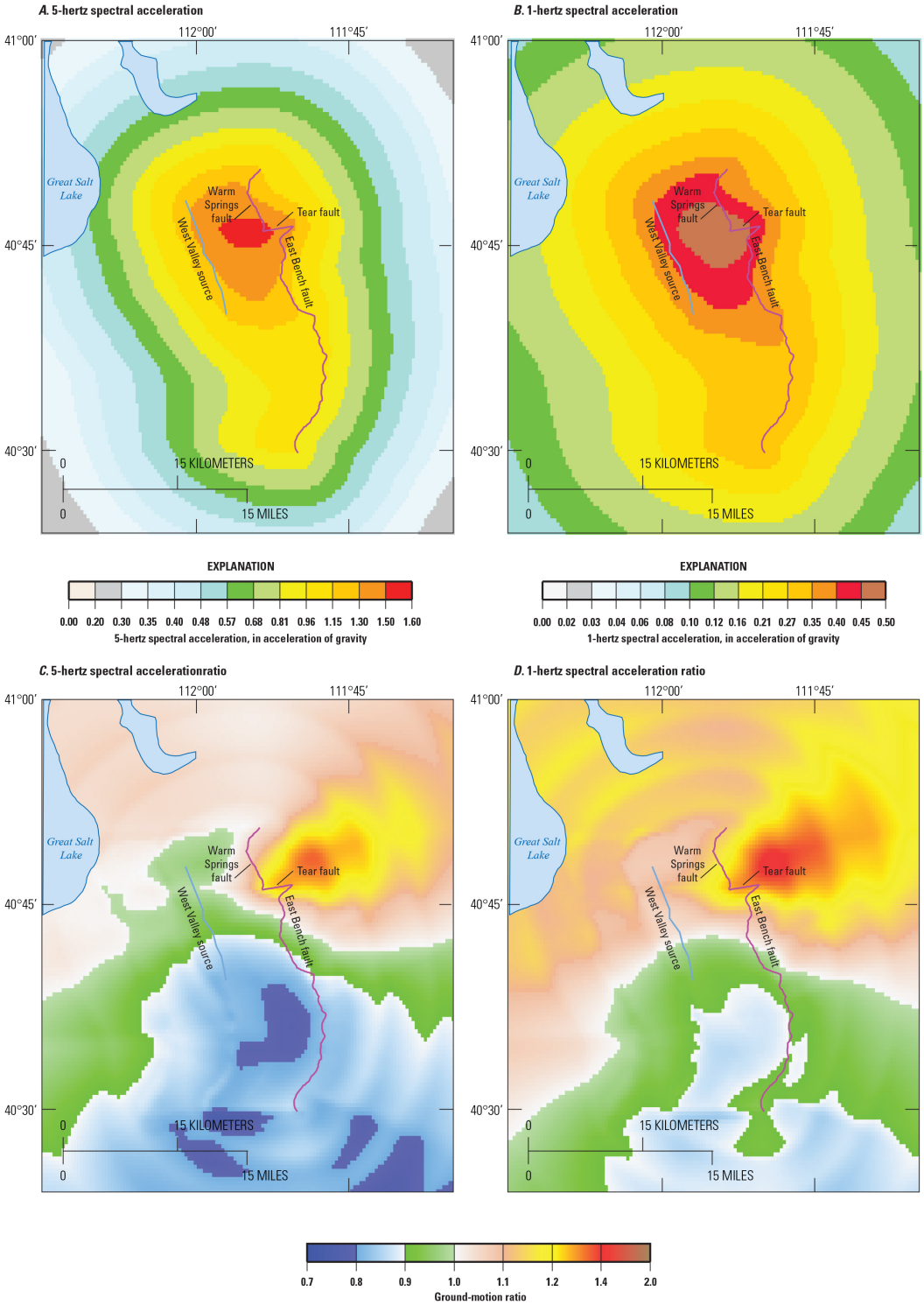

Figure 45. Results of hazard analysis for model 2, the clustered-event model of the Salt Lake City segment of the Wasatch and the West Valley sources for 5-hertz (0.2-second) and 1-hertz (1-second) spectral acceleration for 2-percent probability of exceedance in 50 years and V_{S30} site condition of 760 meters per second. Maps compare *A*, 5-hertz and *B*, 1-hertz spectral acceleration results; and ratios of the alternative model compared to 2008 source model for *C*, 5-hertz and D, 1-hertz spectral acceleration. Locations of the Warm Springs fault, hypothetical tear fault, and East Bench fault are shown.

The temporally clustered-event model produces slightly larger probabilistic motion than several of the other models at sites near the three faults (fig. 46) (that is, parts of downtown Salt Lake City). This is because any of the three ruptures can produce the maximum motion. Although not specified exactly when these three earthquakes would rupture, it is generally assumed that they would happen within minutes to months of one another. Little guidance is available from the limited historical Basin and Range earthquake sequences, but one could consider analogies with the 1954 ruptures in the Central Nevada seismic zone including July, Stillwater; August, Rainbow Mountain; and December, Dixie Valley-Fairview Peak earthquakes or the 1959 Hebgen Lake doublet (Doser, 1985).

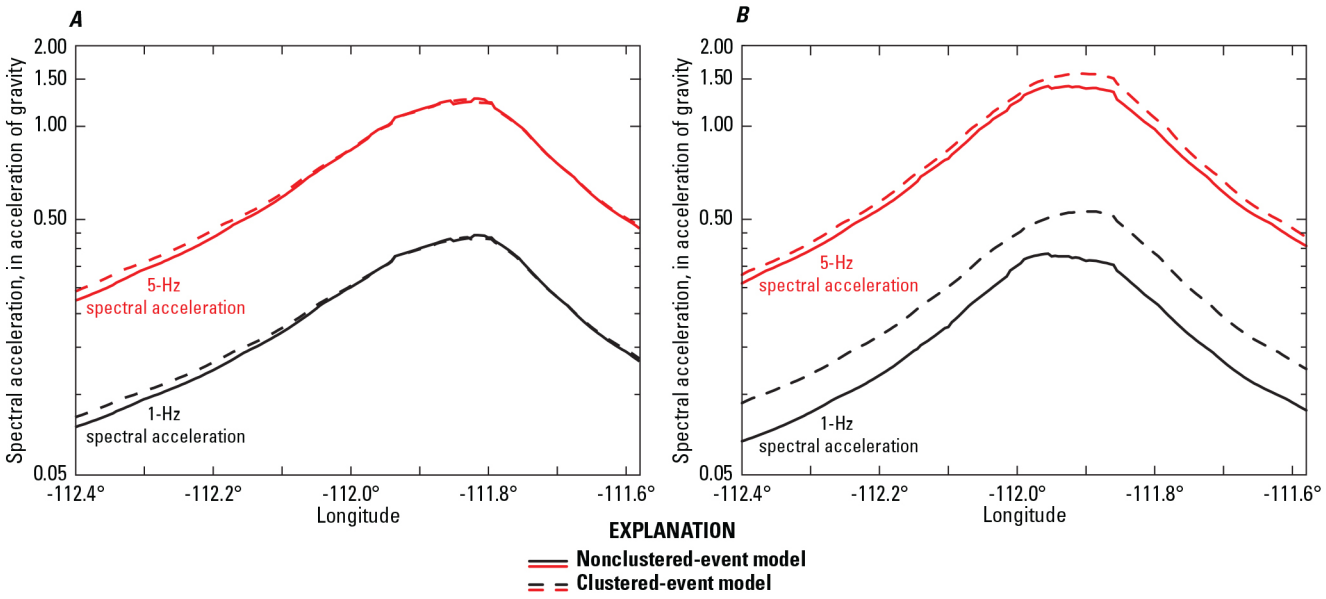

Figure 46. Plots of probabilistic ground motions for 5-hertz and 1-hertz spectral acceleration at 2-percent in 50 years probability of exceedance and V_{S30} site conditions of 760 meters per second along profiles *A*, at lat 40.75°N. and *B*, at lat 40.60°N.

Model 3

The full-source rupture magnitude for the Salt Lake City source in this alternative model is M_w7.05±0.2. The northern part of this source is constrained by the easternmost branch of the East Bench fault; the source passes through the Dresdan Place trench site and the Penrose Drive site. The Penrose Drive locality is joined to the Warm Springs fault following the Virginia Street fault, which is in the footwall of the Warm Springs fault. The part of the Warm Springs fault nearest to and possibly extending into downtown Salt Lake City is not included in this source. The 5-hertz and 1-hertz spectral acceleration associated with this model (fig. 47) results in maximum ground motion of 1.387 g and 0.431 g, respectively, at lat 40.7°N, long 111.90°W.

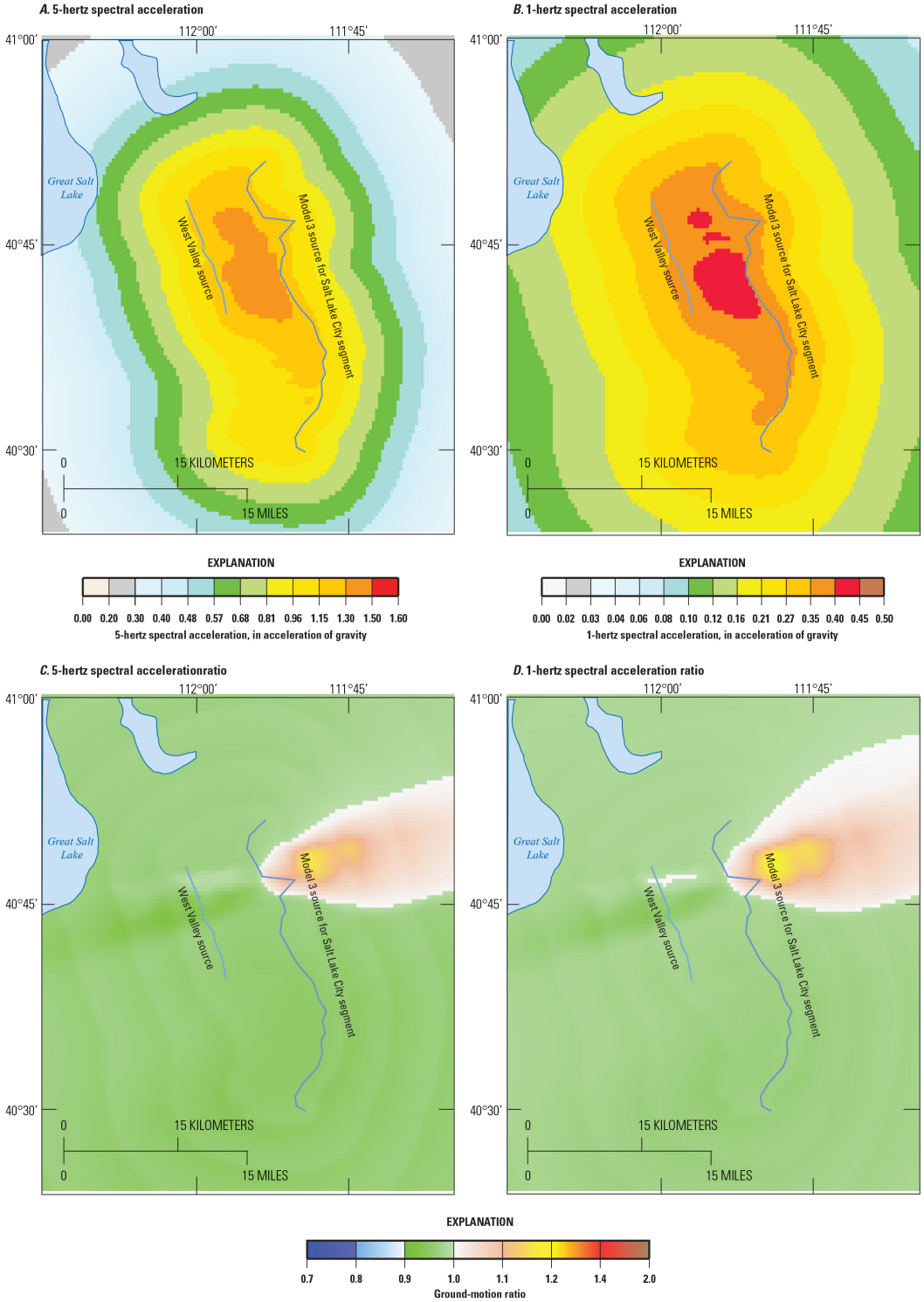

Figure 47. Results of hazard analysis for model 3 of the Salt Lake City segment of the Wasatch and the West Valley sources for 5-hertz (0.2-second) and 1-hertz (1-second) spectral acceleration for 2-percent probability of exceedance in 50 years and V_{S30} site condition of 760 meters per second. Maps compare *A*, 5-hertz and *B*, 1-hertz spectral acceleration results; and ratios of the alternative model compared to 2008 source model for *C*, 5-hertz and D, 1-hertz spectral acceleration. Locations of the Warm Springs fault, hypothetical tear fault, and East Bench fault are shown.

These three models represent epistemic alternatives on the fault geometry and the nature of fault rupture. We assign equal weight (0.24 weight) to each alternative in the final hazard model for full-source ruptures and floating partial-source ruptures of only alternative model 1 (0.18 weight).

Maximum Magnitude for Fault Sources

Regression relations based on the seminal compilation of Wells and Coppersmith (1994) have been used to assign the magnitude of full-source ruptures (M_w with two-sigma uncertainty of ±0.24 magnitude units) for the hundreds of fault sources in the Intermountain West and the Pacific Northwest in the NSHMP model. It typically has been the standard of practice in the industry to apply this scaling equation to estimate magnitude from fault dimensions; the previous versions of the maps used this scaling equation as well. Nevertheless, when these modeled annual frequencies are compared to the paleoseismic record, the modeled rates often are larger than the frequency of paleoseismic earthquakes. A consequence of underestimating magnitudes for full-source ruptures is that higher annual frequencies for all magnitudes are implied. Further studies are required to determine the most appropriate scaling equations for this region. For this update, we continue to apply the Wells and Coppersmith (1994) equations as in previous versions of the maps. We plan to study this effect and determine if alternative magnitude-scaling equations should be applied in future versions of the map.

Constraining Frequency of Future Events

Typically, what is reported as a slip rate is in fact a throw or heave rate that is not resolved to the fault plane at depth. This limited information is reported because the dip of the fault is unknown and, with few exceptions, the dip of the fault at the surface is a poor proxy of its dip at depth. Trenching of historical, normal surface ruptures clearly shows faults at much steeper dips in the near-surface exposure than the modeled fault based on seismological constraints. Therefore, most geologic and paleoseismologic studies report only the horizontal or vertical component of displacement at one or a few point locations along the fault. Few, if any, faults in the WUS are characterized by a sufficient number of randomly distributed sites to yield statistically significant models of earthquake recurrence (Hemphill-Haley and Weldon, 1999). Furthermore, it is rare that investigators describe whether offset at the selected site represents an average displacement or not; however, if the actual extent of the ruptures were known, a general statement of representativeness could be made (for example, Biasi and Weldon, 2006; Wesnousky, 2008). The current methodology accepts these limitations in the data, but there remains considerable uncertainty in the fault-source model. Slip rate as assigned in this model may represent many or all published data or it may reflect only the best-documented data.

Scaling slip rate with dip uncertainty increases the rate of earthquakes modeled on shallow-dipping alternatives and reduces the number of earthquakes at steeper dips; however, the shallow-dipping alternative would contribute most to the hazard if slip rate was scaled to the assigned dip of the source. An unintended consequence of incorporating dip uncertainty into the model is that rates of future earthquakes exceed those observed from the prehistoric record. In order to minimize this effect, we constrain event rate for the alternative dips by the rate from the preferred dip of the source. This method is preferred because calculated event rate then can be compared directly to the known geologic record.

Update of Geologic-Based Fault-Source Parameters

We update the fault-source model based on new literature published since the previous maps (Petersen and others, 2008), which includes our comprehensive review of the key input data for the model.

Faults across the United States were discussed at several of our workshops and we have updated parameters and models (fig. 48, table 9).

- All normal faults have updated three-dimensional geometry
- New sources were added based on recent studies
- Nine sources are modified with additional geologic information
- Fourteen sources have updated slip rate

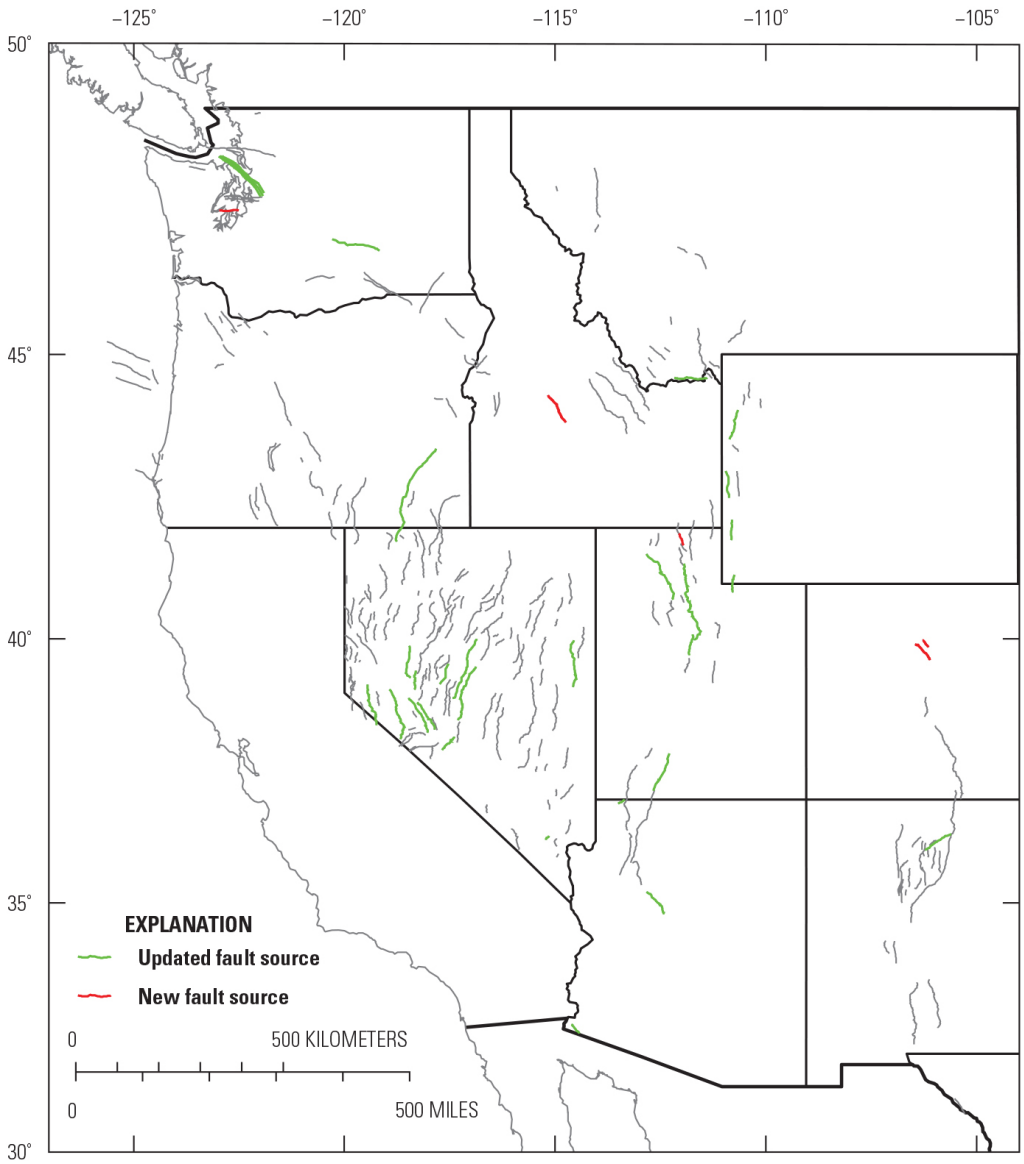

Figure 48. Map of crustal fault sources in the Intermountain West and Pacific Northwest. Fault sources in California are not shown.

Table 9. Changes in Intermountain West and Pacific Northwest crustal fault-source model parameters.

Name	State	Updated parameter	2008 value	2014 value	Reference
Algodones fault zone	Arizona	extend length of source	19.17	26.57	U.S. Bureau of Reclamation (2009).
Big Chino-Little Chino fault	Arizona	extend length of source to include Little Chino fault		64.61	Gootee and others (2010); Ferguson and others (2012); Pearthree and Ferguson (2012).
Gore Range frontal fault	Colorado	new source in 2014			Derouin and others (2010).
Williams Fork Mountains fault	Colorado	new source in 2014			Kirkham (2004).
Sawtooth fault	Idaho	new source in 2014			Thackray and others (2009, 2013); Johnson (2010).
Centennial fault	Montana	throw rate	0.9	0.7	Petrik (2008).
Benton Spring fault	Nevada	heave rate	0.27	0.5	Bell (1995); Wesnousky (2005).
Bettles Well-Petrified Springs fault	Nevada	heave rate		1.3	Wesnousky (2010).
Desatoya Mountains fault zone	Nevada	throw rate	0.1	0.04	Koehler and Wesnousky (2011).
Eglington fault	Nevada	constrain annual rate	0.000066	0.00044	C. dePolo (written commun., 2013).
Lone Mountain fault zone	Nevada	throw rate	0.13	0.2	Hoeft and Frankel (2010).
Rainbow Mountain fault zone	Nevada	heave rate	0.15	0.2	Caskey and others (2004).
Sand Springs Range fault	Nevada	throw rate	0.1	0.2	Bell and others (2004).
Schell Creek Range fault system	Nevada	throw rate	0.01	0.1	Koehler and Wesnousky (2011).
Smith Valley fault	Nevada	throw rate	0.38	0.25	Hayes (1985); Wesnousky and Caffee (2011).
Toiyabe Range fault zone	Nevada	throw rate	0.22	0.06	Koehler and Wesnousky (2011).
Wassuk Range fault zone	Nevada	throw rate	0.55	0.7	Bormann and others (2012).
Western Toiyabe Range fault zone	Nevada	throw rate	0.2	0.07	Koehler and Wesnousky (2011).
Embudo fault	New Mexico	heave rate	0.09	0.13	Bauer and Kelson (2004).
Steens fault zone	Oregon	throw rate	0.3	0.27	Personius and others (2007).

Table 9. Changes in Intermountain West and Pacific Northwest crustal fault-source model parameters.—Continued

Name	State	Updated parameter	2008 value	2014 value	Reference
Great Salt Lake fault zone, Antelope Island section	Utah	constrain annual rate	0.000651	0.000238	Lund (2005, 2013).
Great Salt Lake fault zone, Fremont Island section	Utah	constrain annual rate	0.000746	0.000238	Lund (2005, 2013).
Great Salt Lake fault zone, Promontory section	Utah	constrain annual rate	0.000511	0.000238	Lund (2005, 2013).
Sevier/Toroweap fault zone (northern)	Utah	throw rate	0.36	0.04	Lund and others (2008).
Wasatch fault zone, Nephi section	Utah	constrain annual rate	4.00E-04	1.11E-03	Lund (2013).
Wasatch fault zone, Provo section	Utah	constrain annual rate	4.17E-04	7.69E-04	Lund (2013).
Wasatch fault zone, Salt Lake City section	Utah	location modified			Roten and others (2011).
Wasatch fault zone, Weber section	Utah	constrain annual rate	7.14E-04	7.69E-04	Lund (2013).
West Cache fault, Junction Hills section	Utah	new source in 2014			Lund (2005).
Saddle Mountain fault	Washington	Added 0.25 branch weight to Holocene slip rate		0.5 mm/yr	West and others (1996); West (1997).
Southern Whidbey Island	Washington	extend length of source			Dragovich and others (2007, 2009, 2010); Sherrod and others (2008).
Tacoma fault	Washington	new source in 2014 maps			Sherrod and others (2004).
Bear River fault	Wyoming	constrain annual rate	Not applicable	0.00043	Lund (2013).
Grand Valley fault	Wyoming	throw rate	1.1	0.8	reevaluation of original data.
Rock Creek fault	Wyoming	throw rate	1.7	0.62	Lund (2013).
Teton fault	Wyoming	throw rate	1.3	0.7	O'Connell and others (2003); Hampel and others (2007); White and others (2009).

Wasatch Fault Zone

The Wasatch fault, bounding the eastern side of the Utah urban corridor, is one of the few faults with explicit segmentation in the NSHMP model. The source geometry includes the same dip uncertainty as other Intermountain West normal faults (50±15°), and characteristic magnitudes are based on the surface-rupture length for all styles of faulting (Wells and Coppersmith, 1994).

Much of the model is similar to that in the 2008 USGS NSHMP maps, which is based on a rich paleoseismic record. The Wasatch fault zone is the most studied of any fault in the region; most of the trenches, which are distributed along the central 300 km of the Wasatch fault zone, have evidence of multiple late Quaternary surface ruptures that are constrained by radiometric dating. In this update of the USGS NSHMP maps, we assign a low branch weight (0.1) to floating M_w6.5–7.4 ruptures that are permitted to break through segment boundaries. The rate of these modeled earthquakes is defined by the mean slip rates for each segment in Lund (2013).

The geometry used in the 2008 fault-source model for all segments of the Wasatch fault zone is retained in this update except for the Salt Lake City segment, which is described above. The geometry of the central six fault sources constrains the extent of independent rupture in future earthquakes. The rupture of entire segments is defined by the preferred recurrence interval in Lund (2013); the basis of the recommendation is a reevaluation of radiometric ages from trenching studies that are OxCal calibrated (refer to table 9 for results). The frequency of partial-segment ruptures (M_w6.5 up to the assigned segment magnitude) is constrained by the slip rates in Lund (2013). This 2014 model retains the branch weights used in previous models (fig. 49).

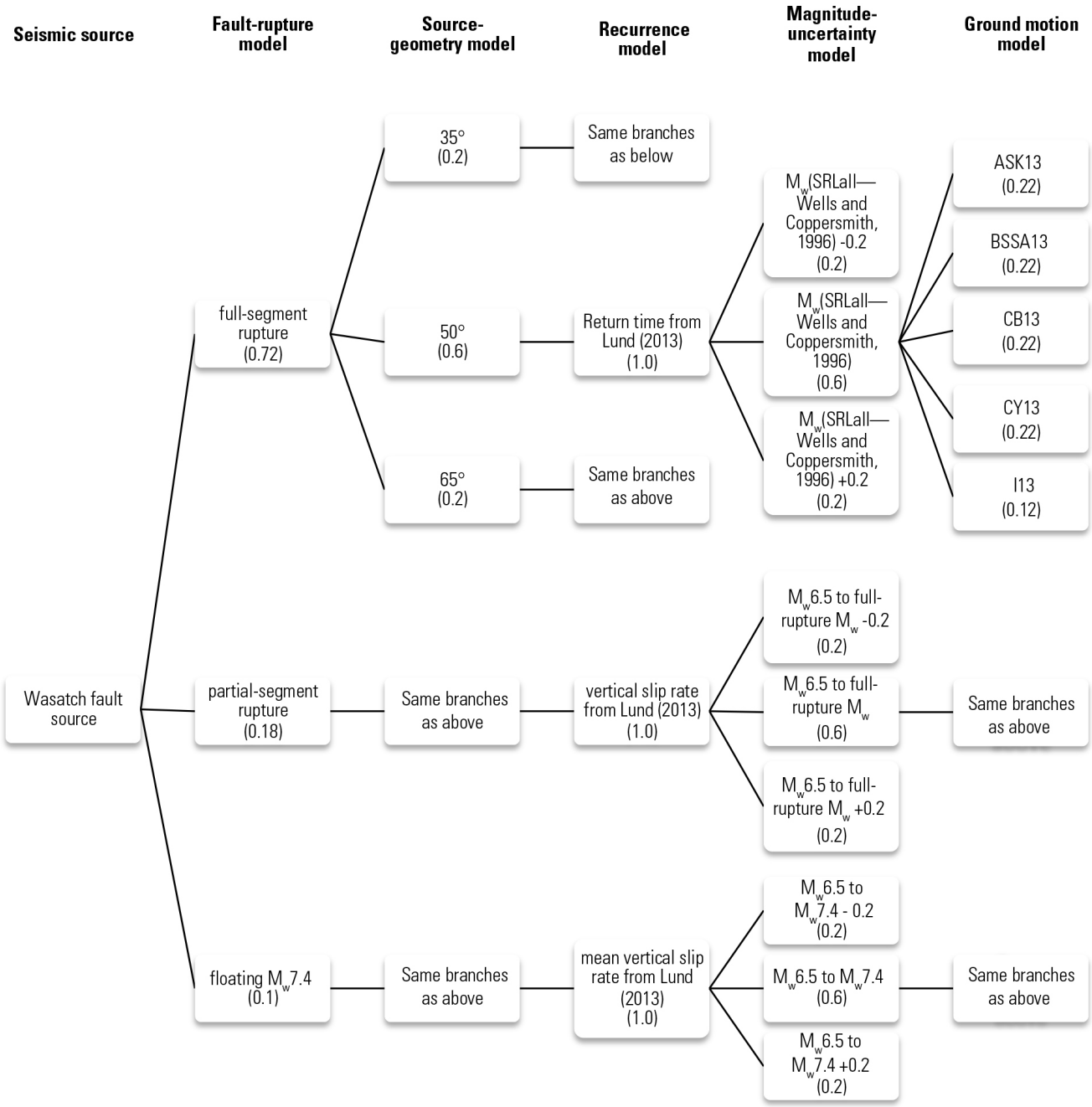

Figure 49. Generic logic tree for Wasatch fault source, Utah. Assigned weight for branches shown in parentheses.

Seattle Fault Zone

For the Seattle fault zone, the recurrence parameters are the same as those used in the 2008 NSHMP maps, the recurrence rates are constrained by paleoseismic studies (Petersen and others, 2008). For the characteristic model, we use a recurrence time of 5,000 years. This is based on the lack of paleoseismologic evidence for coastal uplift comparable to that of the 900 A.D. earthquake for the 5,000 years before 900 A.D. (B. Sherrod, oral commun., 2013). The partial-source rupture model has a recurrence time of 1,000 years for earthquakes greater than or equal to M_w6.5 in the Seattle fault zone.

This rate is similar to the long-term rate of back-thrust earthquakes observed in trenches on Bainbridge Island and the Kitsap Peninsula (Nelson and others, 2003a, b).

Combined Geodetic- and Geologic-Based Slip-Rate Models

An important observation for seismic hazard assessment is that the geologic slip rates, the smoothed seismicity, and the geodetic strain rates are highly correlated. This observation points out the importance of using each of these datasets in assessing seismic hazard; however, these datasets all have limitations and the maturity of the available methodologies for applying these data in hazard assessments varies considerably. For example, the geologic slip rate estimation methods, paleoseismic trenching studies and seismicity studies have been developed extensively over the past century, whereas the geodetic strain rate data and combined geologic and geodetic inversion methods are only recently beginning to be used for hazard assessment. The geodetic data are an important source of information on the activity rates of earthquakes and should be considered in hazard assessments.

In developing previous versions of the maps, we held workshops to determine if there was sufficient GPS strain rate data to apply in the seismic hazard analysis; participants generally decided that the timespan of GPS observations was insufficient for this purpose. Therefore, in developing the 2008 NSHMP maps for the WUS, we relied on geologic slip rates and earthquake recurrence rates from studies of correlated offset Quaternary landforms or deposits. We used the geodetic data for constraining fault slip rates over a broad region and in specific zones located near the eastern California border. These specific zones are known as "shear zones" and are modeled to account for high geodetic strain observations in places where there are few or no fault data to constrain slip rates. Geodetic-based zones were imposed in eastern California and western Nevada to account for earthquakes on faults that are not explicitly included in the model (Frankel and others, 1996, 2002; Petersen and others, 1996, 2008). For these source models, we used 50 percent of the geodetic slip rate and modeled M_w6.5–7.6 earthquakes on evenly spaced line sources that fill the zone. Only 50 percent of the geodetic slip rate was applied because some slip likely does not result in earthquakes and some slip is released in smaller earthquakes or aftershocks that are not considered in the hazard analysis. The geodetic-based models were updated in the 2008 version of the maps by using regional GPS strain-rate models to identify boundaries of regions characterized with high strain rates.

To determine how to use geodetic data in the 2014 NSHMP update, we held two open workshops to discuss new geodetic models and their utility in hazard maps, convened one meeting with modeling teams to coordinate efforts, and formed an expert panel to provide advice on whether or not the models are sufficiently mature for this update. In addition, the UCERF model (ver. 3, Working Group on California Earthquake Probabilities, 2013) convened multiple meetings to discuss how to use combined-inversion slip-rate data for California and issues on the geodetic data, models, and resulting seismic hazard. The participants generally agreed that geodetic data and models would be useful for the 2014 update. In this section, we review the basic information needed for applying geodetic and geologic information in the hazard calculations. For more details on the models and their implications, refer to Petersen and others (2013).

Several new geodetic- and geologic-based kinematic models (combined-inversion models) have been developed over the past few years that can provide new information on locations and rates of future earthquakes, which are discussed in appendixes of Petersen and others (2013). For the 2014 version of the maps, we incorporate new fault-based combined-inversion models with a 20-percent branch weight in the Western United States (WUS) and 70-percent branch weight in California (*http://www.scec.org/ucerf2/*). Three steps were important in constructing the final geodetic- and geologic-based models for the maps: (1) compiling and processing GPS-based velocity data and

entering these data into a new database available for use by all model developers, (2) computing new combined-inversion slip-rate models, and (3) implementing the new models in the hazard analysis.

Data

We use both geologic and geodetic data in assessing seismic hazard in the 2014 update. In this section, we discuss the geologic and geodetic data and their strengths and limitations for use in seismic hazard.

Geologic displacements record long-term average rates (typically over several hundreds or thousands of years) that are essential for assessing the activity rates needed for seismic-hazard analyses. Observations are converted to average slip rates, which are used to forecast the rate of earthquakes on the modeled fault; higher slip rates imply higher activity rates and lower slip rates imply lower activity rates for sources having the same length and width. Paleoseismic trenching studies provide further details that identify earthquake displacements and timing of surface-rupturing earthquakes on faults, so they are direct evidence for past earthquake activity.

Unfortunately, there are several limitations in applying geologic data. First, the slip rates on faults vary from site to site and over different time spans. Therefore, it is difficult to assess which of these rates is most appropriate for a 50-year period for which the maps are made. We typically give more consideration to slip rates that span several of the most recent seismic cycles to assess the future hazard, but this practice may not account for slip rates that vary through time. Second, fault slip rate has substantial uncertainties associated with the measurement of fault displacements and the timing of those displacements, and these uncertainties rarely are documented. Thus, geologically informed slip rate uncertainties can extend over more than a factor of two on poorly studied faults. Third, many faults in the WUS are characterized at only a few sites along the entire length of the fault; in other words, measurements are not a representative sampling of the fault. Fourth, although the paleoseismic data are our most direct estimate of earthquake rates, it is difficult to know if the record of past earthquakes is complete at the site, and this uncertainty can lead to an inaccurate estimate of earthquake rates. Finally, the dip of the fault is required data for calculating slip rate; this input is uncertain and carries with it the greatest impact. These factors are all critical elements in defining the slip-rate uncertainty.

Modern GPS data provide more spatially complete observations on ground deformation, cover a period of 25 years (from 1987–2012), and record the most recent plate-loading rates with submillimeter per year precision, which is more precise than data provided by geologic studies. Geodetic data, in general, are consistent with geologic data but with exceptions that may be important for assessing hazard. These data also have their own limitations for use in hazard analysis. For example, these data do not record the long-term slip rates that we generally need for hazard assessments and the data may include transient strains or aseismic deformation, which are difficult to remove for use in hazard assessment.

The geodetic database, which supported the combined-inversion modeling, was developed by McCaffrey and others (2013) using a variety of sources and by correcting for Cascadia subduction-zone motion. The geologic-based slip-rate model is updated compared to the model applied in the 2008 USGS NSHMP maps (Haller and Wheeler, 2008a, b) and represents expert opinion assessment of all pertinent geologic and paleoseismologic data to inform a single slip rate for each fault source. Geodetic-based models also cannot resolve differences among fault slip rates where faults are closely spaced; resolution of individual fault slip rates in such regions can be poor. In addition, uncertainties are particularly large for the block-type models, which focus deformation only on block boundaries. All of these models consider off-fault or off-block deformation; however, it is unclear how to distribute the

strain rates across the inner parts of the block even though we know that there are many faults distributed within the defined blocks.

We developed strain rate maps using these GPS data, but in these plots we do not eliminate the back-slip motion of the Cascadia subduction zone so that we can view this important component of the hazard. The distribution of maximum shear and dilatation strain rates is shown on figure 50. The maximum shear strain rate map can be considered a proxy for the maximum strain rate. The maps seem similar to the fault slip rate map, the seismicity map, and the previous hazard maps that did not use the geodetic information directly. The dilatation strain rate, on the other hand, provides crucial supporting information on earthquake faulting style in the Western United States. For example, in the Pacific Northwest region, the compressional strain rate dominates the shear strain rate, suggesting higher rate of earthquakes with thrusting mechanisms compared to strike slip mechanisms. In the extensional Intermountain West region, the dilatational strain rate dominates the shear, indicating a higher rate of earthquakes with extensional normal faulting than of strike slip faulting.

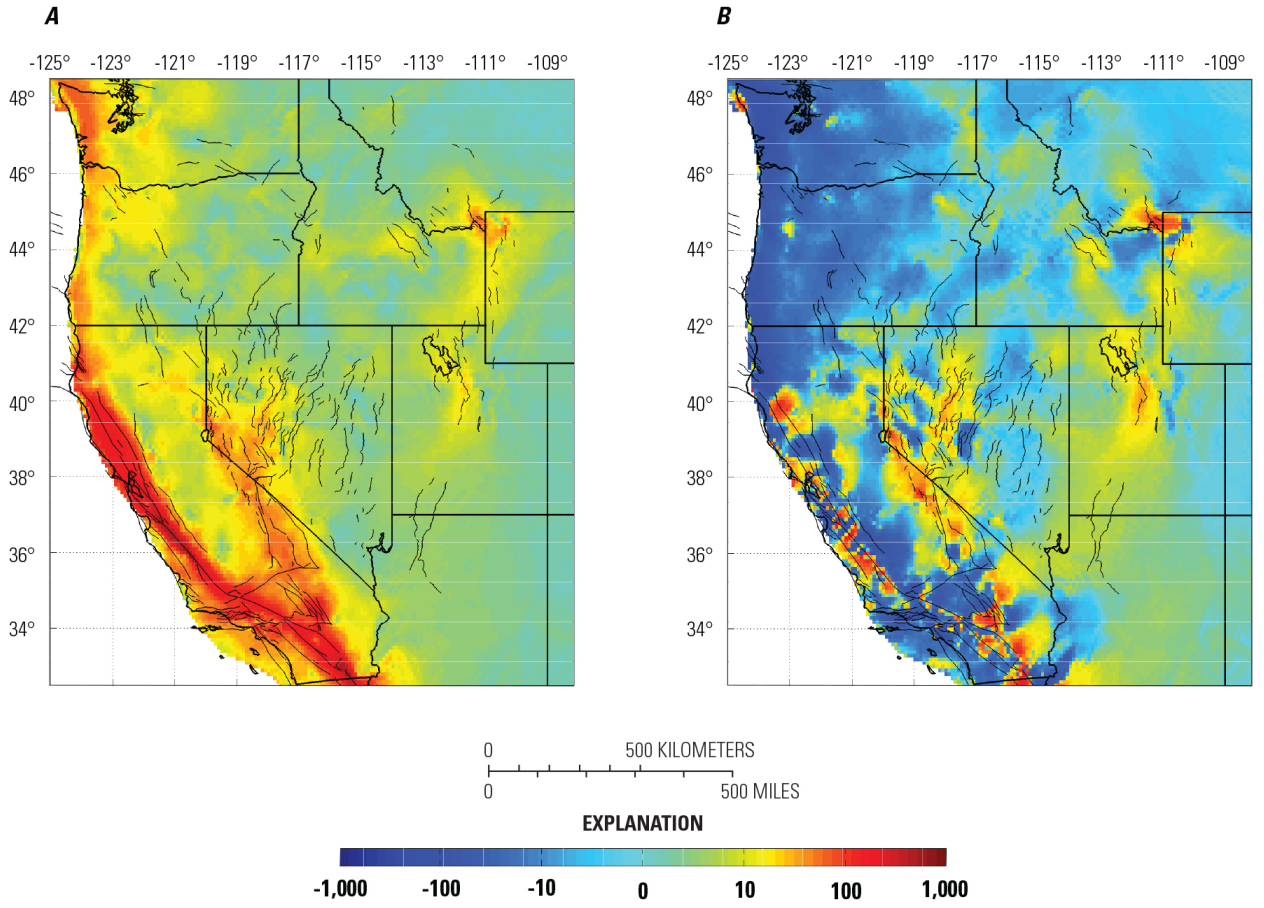

Figure 50. Strain-rate maps of the Western United States calculated using the global positioning system (GPS) dataset collected for the combined-inversion models showing *A*, maximum shear and *B*, dilatational strain. Fault sources are shown (black lines).

Combined Geologic and Geodetic Models

Four modeling teams participated in developing combined geodetic and geologic slip-rate models, and these are described in Petersen and others (2013). The USGS considered combined-inversion slip-rate models for faults in the WUS, including two block models (McCaffrey and others, 2013; Hammond and Bormann, 2013) and two fault-based models (Bird, 2013; and Zeng and Shen, 2013). Each modeling group developed horizontal slip rates using their own inversion methods and these slip rates were then projected onto the preferred fault dip assigned in the NSHMP model by dividing by the cosine of the dip angle.

To implement the geodetic-based models in the hazard analysis, we compared the geologic and the combined-inversion slip rates to identify similarities and differences between the data. Comparisons between the geologic model and combined geologic and geodetic inversion models are shown in figure 51. Some combined-inversion models suggest slip rates that are significantly different from the geologic slip rates. For this analysis, we consider factors of two and one-half of the mean down-dip slip rate (fig. 51) to encompass the 95-percent confidence range for geologic slip rates (Petersen and others, 1996).

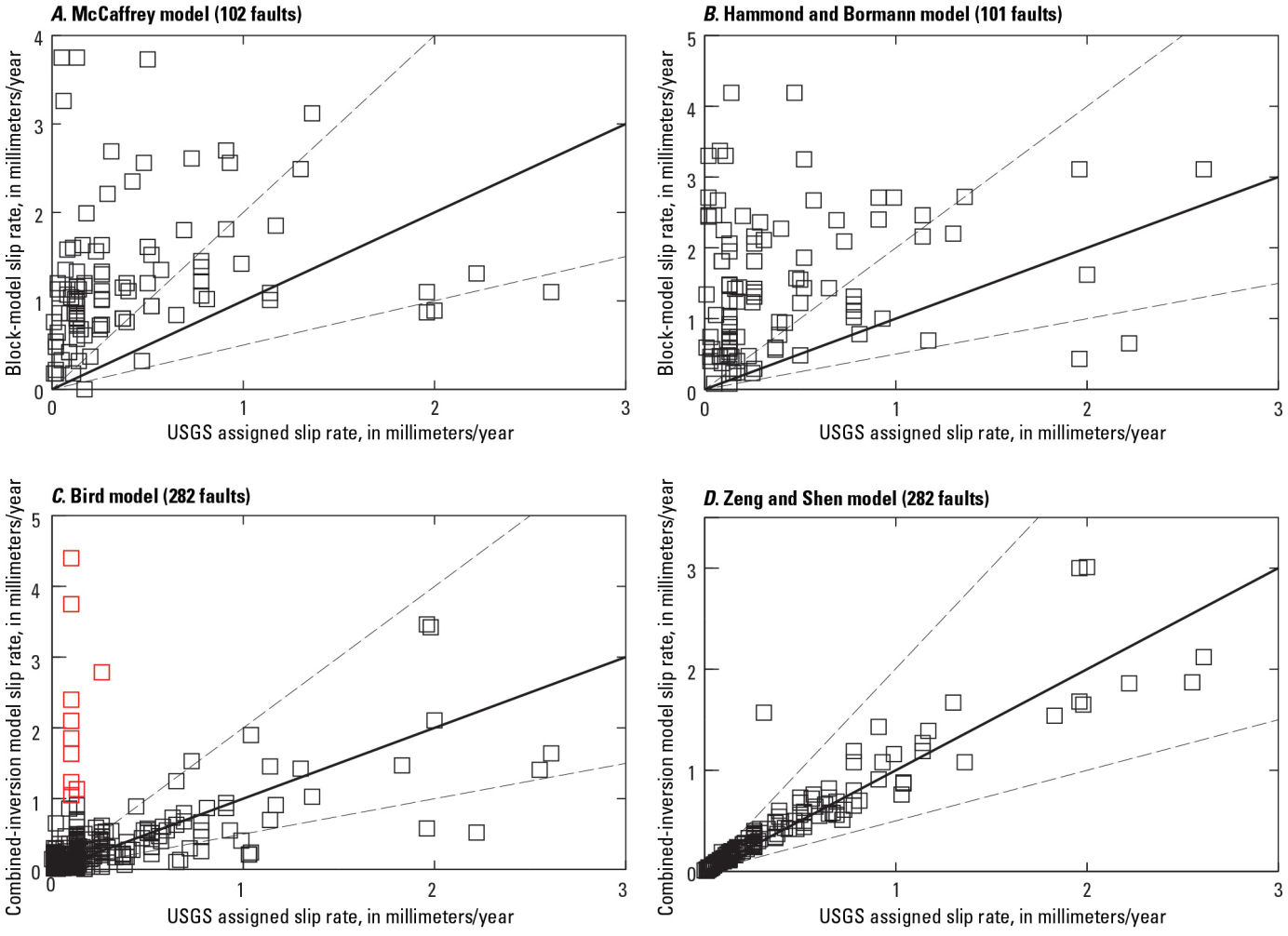

Figure 51. Comparison between the fault-based combined-inversion slip-rate models and the modified 2008 NSHMP assigned slip rates (see Petersen and others, 2013, for modifications to the 2008 model). Solid line

represents equality between the geology and geodesy slip rates, dashed lines represent factors of 2 and ½ compared to the equality line. *A*, Slip rates from McCaffrey and others (2013) and *B*, Hammond and Bormann (2013) block models. *C*, Slip rates from Bird (2013) and *D*, Zeng and Shen (2013) fault-based models. Red symbols on the Bird (2013) graph represent slip rates that were modified in the hazard assessment.

The combined-inversion slip rates of McCaffrey and others (2013) and Hammond and Bormann (2013) generally are higher than the modified 2008 source slip rates (fig. 51). It is important to point out that this comparison does not imply that the slip rates derived from block modeling are right or wrong; we can only conclude that the rates differ from the assigned geologic rates assigned in past hazard maps. The block models use block boundaries that are interpreted from the earthquake data, fault data, and strain rate orientations. Therefore, slip rates in these models are constrained only on the block boundaries, and faults within the blocks are modeled as uniform. The block models only include about one-third of the faults that are in the modified 2008 source model. The modified 2008 source slip rates for the faults included and excluded from the block models are shown in figure 52. About half of the faults that are not included in the block models have slip rates less than 0.3 mm/yr; however, a few of the geologically faster slipping faults also are excluded from the block models because of their locations compared to the block boundaries. For this hazard map implementation, we used slip rates derived from block modeling to assess the general geodetic trends, but did not arrive at consensus on an appropriate method to distribute slip rate within blocks.

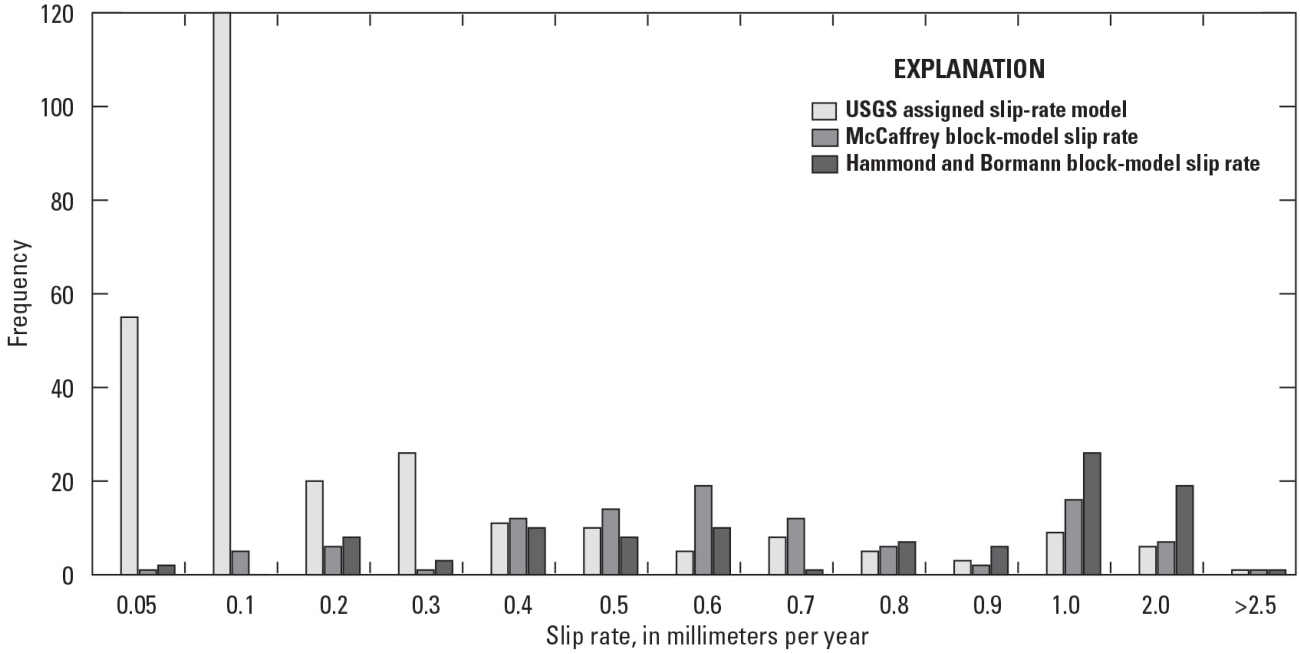

Figure 52. Plot of assigned slip rates in the modified 2008 source model and geodetic-based block models.

The Bird (2013) and the Zeng and Shen (2013) slip-rate models also differ from the modified 2008 source slip rates (fig. 51), though the differences are not as large as they are for the block models. Generally, these two models are more compatible with the modified 2008 source slip rates (fig. 51),

which again does not suggest that they are more correct, but only that they are more similar to the previous slip rates applied in the USGS NSHMP maps.

The Bird (2013) slip-rate model differs significantly (by a factor of two or more) from the modified 2008 source slip rates for some faults (table 10) in western and central Nevada. The modified 2008 source slip rates on these faults are low (about 0.1 mm/yr) and the combined-inversion rates are higher by factors of 10 or more. We model these higher rates in our hazard analysis by using 50 percent of the slip rate indicated by the Bird model and by spreading the reduced slip rate over a region extending about 10 km around the group of faults modeled with high slip rates (fig. 53). We reduce the slip rates on these central Nevada faults because of the first-order differences between the slip rates assigned in the modified 2008 source model and combined geologic-geodetic slip rates, which could be influenced by transient strain or other effects. Further research is required to define the range of acceptable rates before we implement such a major change in the maps that will cause a significant hazard hotspot in the hazard. These faults mostly are located in central Nevada in the vicinity of some past large earthquakes. The region may be influenced by transient deformation (Hammond and others, 2009), groundwater withdrawal, or other nontectonic effects. In addition, the combined-inversion slip rates may not be well resolved and may have large uncertainties. Another possibility is that poorly dated offset features are not reliable and that the geodetic data are more appropriate for hazard in the next 50 years. Additional combined-inversion slip rates in northwestern Oregon also are higher than the modified 2008 source slip rates (fig. 53). Therefore, we also have spread the slip rates for these faults over a zone to account for our uncertainty in the location of future earthquakes in this region.

Table 10. Comparison of assigned slip rate in modified 2008 model and Bird (2013) slip rates where Bird slip rates are greater than two times the slip rate in modified 2008 model.

[km, kilometers ; mm/yr, millimeters per year]

Fault name	State	Modified 2008 assigned slip rate (mm/yr)	Bird (2013) mean slip rate	Predominate sense of slip	Length (km)	Dip (degrees)
Benton Spring fault	Nevada	0.26	1.76	Strike slip	85	90
Bettles Well-Petrified Springs	Nevada	0.1	11.6	Strike slip	71	90
Buffalo Valley fault	Nevada	0.13	0.483	Normal	41	50
Coaldale fault 1	Nevada	0.1	4.33	Strike slip	66	90
Coaldale fault 2	Nevada	0.1	4.33	Strike slip	17	90
Fairview fault	Nevada	0.13	0.0981	Normal	34	50
Faults in Excelsior Mtns	Nevada	0.1		Strike slip	27	90
Hot Springs fault	Nevada	0.13	0.25	Normal	24	50
Huntoon Valley fault	Nevada	0.1		Strike slip	38	90
Rattlesnake fault	Nevada	0.1		Strike slip	15	90
Sand Springs fault	Nevada	0.13	0.25	Normal	42	50
Spanish Springs Peak fault	Nevada	0.1	4.33	Strike slip	5	90
Unnamed faults	Nevada	0.1		Strike slip	40	90

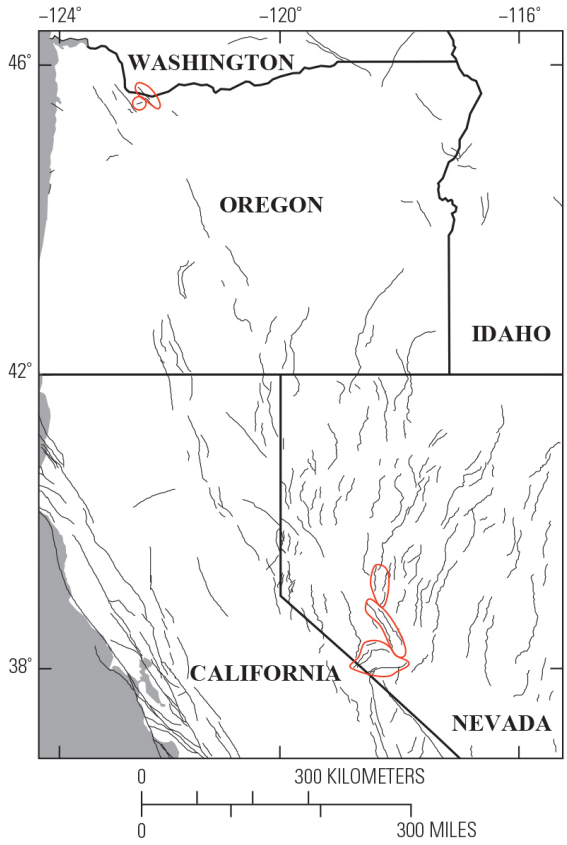

Figure 53. Map showing location of the zones placed around ten fault sources in the Bird (2013) model to smooth the effects of high slip rates on individual fault sources. Slip rates in the two southern Nevada zones are reduced by 50 percent in the hazard model.

A comparison of the on-fault cumulative geologic slip rates and fault-based combined-inversion slip rates of Bird, and Zeng and Shen models along east-west oriented profiles is shown in figure 54, located at 0.1° intervals from 35° to 45° latitude for east (extension, fig. 54*A*) and north (strike slip, fig. 54*B*) motion. Hanging-wall displacements were separated into two components (north and east) and summed along transects to show variability from north to south across the study area; total slip is shown in millimeters per year. The transects show variation of total slip up to 5 mm/yr extension (fig. 54*A*) and less than 4 mm/yr strike-slip component (fig. 54*B*), which is more than a factor of 20 lower than the UCERF3 model for California (Working Group on California Earthquake Probabilities, 2013). For the extensional rates (east), the three models track each other very well in the north, but the Bird (2013) model deviates from the other two near the southern end of the central Nevada seismic zone (latitudes between 38° and 39.5°). This area encompasses the faults for which we have reduced the slip rates. For the strike-slip rates (north), the three models again track each other in the north but deviate from each other near the southern central Nevada seismic zone. The Zeng and Shen (2013) model shows particularly high strike-slip motion in this zone compared to the other two models.

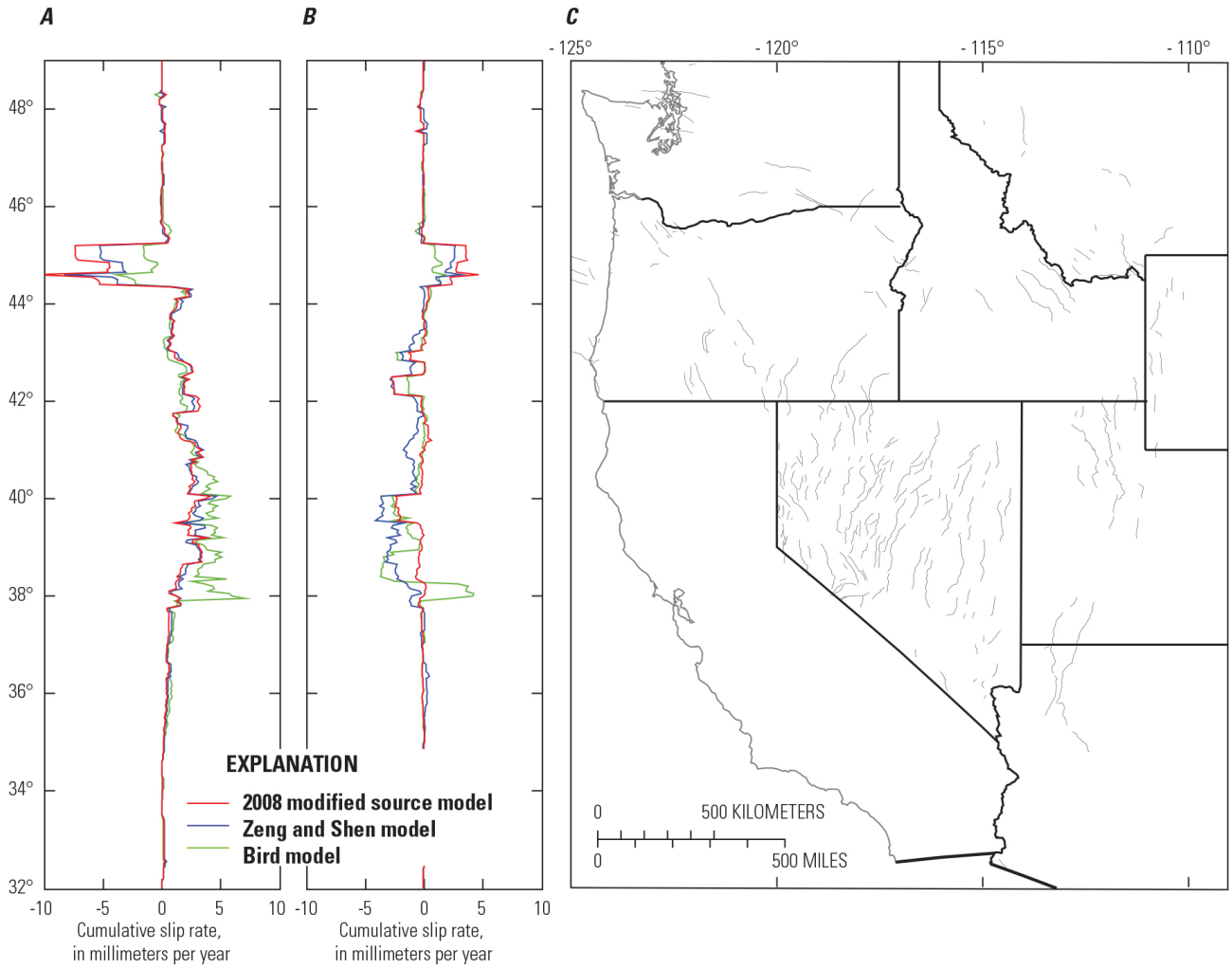

Figure 54. Plot of cumulative on-fault total slip summed along east-west oriented profiles for the 2008 modified source model (Petersen and others, 2013), Bird (2013) model, and Zeng and Shen (2013) model slip rates at 0.1° intervals from lat 32°–48N. for *A*, east (extension) and *B*, north (strike slip) motion. On-fault total slip in California is not included in the sum.

We also considered applying a new off-fault, geodetic-based strain rate as an alternative to the smoothed seismicity model for forecasting M_w5–7 events; however, participants at our workshops and members of our steering committee who reviewed the maps decided that the transient strains and overall off-fault strain rates were not well constrained. In addition, they decided that more work is needed to focus on comparisons between geodetic strain rate tensors and seismicity-based moment tensors before these off-fault models are introduced into the NSHMP maps.

Implementation of Combined-Inversion Models in Hazard Maps

To implement the models in the NSHMP maps, we first examined the combined-inversion model outputs to determine how they differ from the geologic-based slip rates. The Zeng and Shen (2013) model is most similar to the geologic model. Some of our workshop participants have criticized

that the similarity adds little additional information; however, we found important differences between the purely geologic and the Zeng and Shen (2013) models. The differences call attention to high or low slip rates in regions where the geologic data are not well constrained. The Zeng and Shen (2013) model fits the geodetic data equally well as any other geodetic models. The Bird (2013) fault-based, combined-inversion model differs from the geologic model more than the Zeng and Shen model, but in many places the patterns are similar. We modified some of the high slip rates in western and central Nevada in the Bird (2013) model. This modification provides a model that dampens and spreads the hazard in southwestern and central Nevada more than the original Bird model. The block models in the WUS often were significantly different from the geologic-based model as well as the fault-based combined geologic and geodetic inversion models. In addition, the block models did not account for slip rates on all of the faults included in the hazard model. Therefore, these models were not applied directly in the final hazard maps. Further studies will help us understand these discrepancies and determine how to use these models in future applications.

We introduce the combined-inversion fault-based models for the first time into the hazard maps with a low weight (0.2) in the Intermountain West and Pacific Northwest. Project members, the steering committee, and workshop participants recommended low weights for the combined-inversion models since they are new studies that will improve with more research. A higher weight (0.7) is applied in California where the data are more spatially and temporally abundant (*http://www.scec.org/ucerf*). The two fault-based models are weighted equally because we do not favor any particular model. The remaining weight (0.8) is given to the model constrained by expert analysis of geologic data. It should be pointed out that although the geologic-based model receives most of the weight, it also considers the geodetic data implicitly in that the cumulative slip rates across the region are modeled to be consistent with the regional geodetic rates.

In addition, we maintain the geodetic-based shear zones outside of California (from Petersen and others, 2008) to account for additional earthquakes in areas of observed high strain rates (Moschetti and others, 2013). We also include a geodetic zone near Puget Sound (from Petersen and others, 2008) to account for earthquakes located off of the modeled faults. We use the same zones as were applied in the 2008 USGS NSHMP maps. These zones correspond with high off-fault velocities.

Hazard Results

The two fault-based, combined-inversion models for the WUS are similar in many ways, showing similar high- and low-strain rate areas with respect to the purely geologic model. Difference and ratio maps (figs 55, 56, respectively) display changes in hazard assuming the weighted two fault-based, combined-inversion models and the geologic model. Adding the combined-inversion models (0.2 weight) typically elevates the hazard in areas with higher than expected strain rates compared to the hazard resulting from applying only the geologic model. The effect of applying these new models is highest in Nevada, near the southern portion of the Wasatch fault (Utah), near the Rio Grande Rift (Colorado and New Mexico), near the borders between Oregon and Washington, and in Wyoming. The weighted combination of fault-based combined-inversion and geologic models results in about 15–20 percent increases (or about 0.02–0.05 g) compared to the geologic-based model alone in places with observations of high strain rates. The final weighted model results in a hazard map that is similar to previous hazard maps but allows for additional earthquakes in places where higher strain rates have been observed over the past two decades.

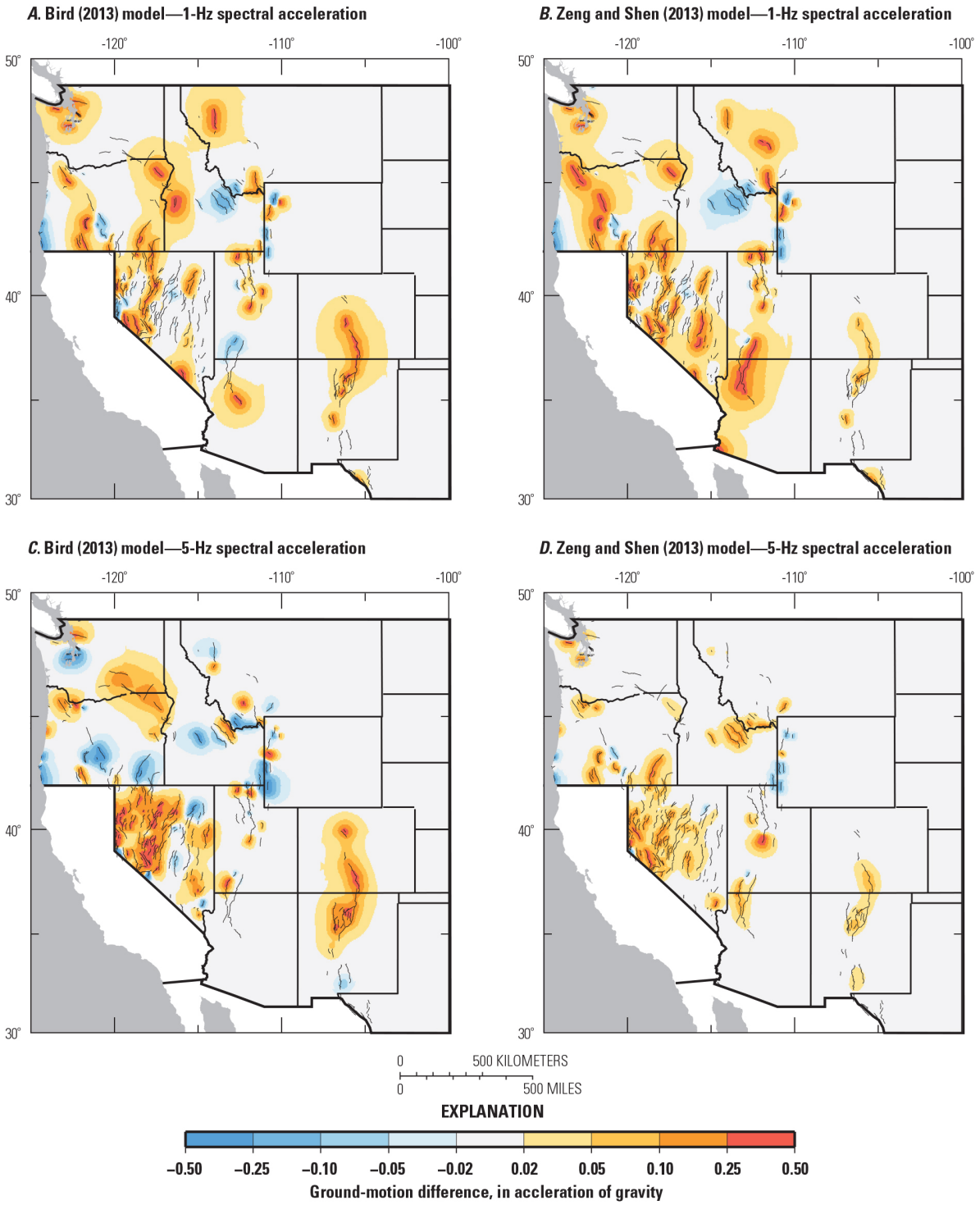

Figure 55. Maps showing difference in 1-hertz (1-second) and 5-hertz (0.2-second) spectral acceleration at 2-percent probability of exceedance in 50 years and V_{S30} site conditions of 760 meters per second. Maps of 1-hertz (1-second) spectral acceleration difference of *A*, fault-based models by Bird (2013) and *B*, Zeng and Shen (2013) and the 2008 modified source model and 5-hertz (0.2-second) spectral acceleration difference of *C*, fault-based models by Bird (2013) and *D*, Zeng and Shen (2013) and the 2008 modified source model respectively. California data not shown.

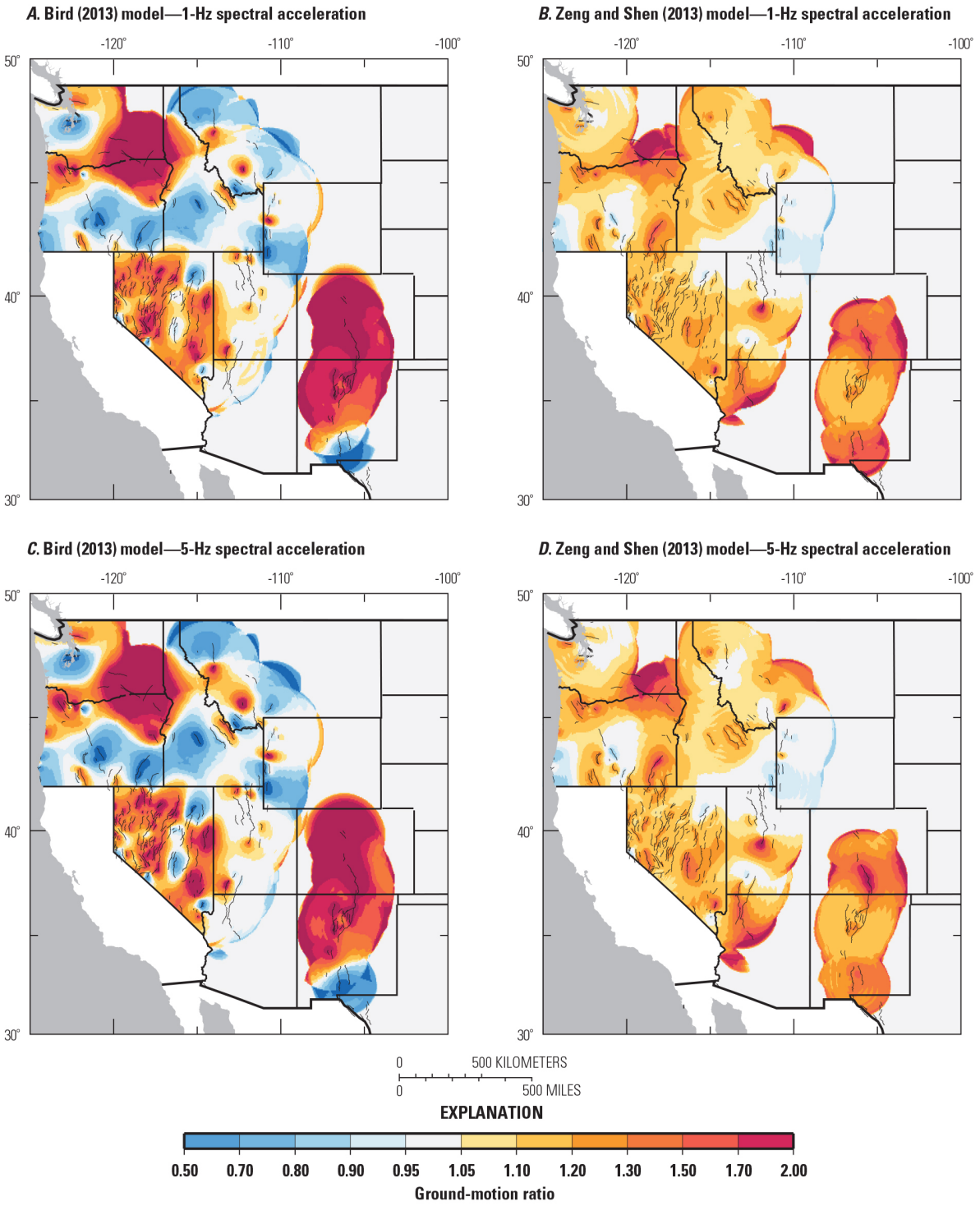

Figure 56. Maps showing ratios of 1-hertz (1-second) and 5-hertz (0.2-second) spectral acceleration at 2-percent probability of exceedance in 50 years and V_{S30} site conditions of 760 meters per second. Ratios of 1-hertz (1-second) spectral acceleration of *A*, fault-based models by Bird (2013) and *B*, Zeng and Shen (2013) and the 2008 modified source model and 5-hertz (0.2-second) spectral acceleration of *C*, fault-based models by Bird (2013) and *D*, Zeng and Shen (2013) and the 2008 modified source model respectively. California data not shown.

The inclusion of these models in this version of the maps demonstrates our recognition that there are advantages to using both the geologic and combined-inversion slip rates. Both datasets have benefits and limitations in constraining the hazard maps. These combined-inversion slip-rate models will continue to evolve and will be more useful in future hazard assessments.

Earthquake Recurrence and Down-Dip Edge of Rupture for the Cascadia Subduction Zone

Logic trees for the recurrence of great earthquakes on the Cascadia subduction zone have been developed from discussions at the November 2010 and March 2012 workshops (Frankel, 2011), which were held for the update of the USGS national seismic hazard maps and for the UCERF3. The location of the down-dip edge of the rupture zones of great Cascadia subduction zone earthquakes was debated in workshops in December 2011 and March 2012 (Frankel, 2011). A logic tree for the position of the down-dip edge also has been developed from these deliberations. For this 2014 update of the NSHMP maps, we considered a broad range of alternative models for the Cascadia subduction zone; however, for this update we did not implement a model based on a proposed temporal correlation of turbidite sediments in marine sediment cores that suggests that the northern San Andreas Fault and Cascadia subduction zone could fail together in north-to-south propagating ruptures (Goldfinger and others, 2008).

Logic Trees for Cascadia Subduction Zone Recurrence

The November 2010 workshop focused on evaluating the analysis and interpretation of turbidites in deep-ocean cores by Goldfinger and others (2012), to constrain the recurrence time and magnitudes of great earthquakes on the Cascadia subduction zone. This workshop is summarized in Frankel (2011). Figure 57 (modified from Goldfinger and others, 2012) shows the great earthquake rupture zones estimated from the 10,000-year turbidite record. During this workshop, the participants accepted the idea of M_w8 earthquakes that rupture only the southern portion of the Cascadia subduction zone. Evidence for these earthquakes is manifested in turbidites (Goldfinger and others, 2008, 2012) and in tsunami deposits found on land at Sixes River (Kelsey and others, 2002) and Bradley Lake (Kelsey and others, 2005; Nelson and others, 2006) in southwestern Oregon. Brian Atwater also presented evidence regarding the possibility of M_w8 earthquakes that only rupture the northern portion of the Cascadia subduction zone, mainly inferred from tsunami deposits at Discovery Bay (Williams and others, 2005).

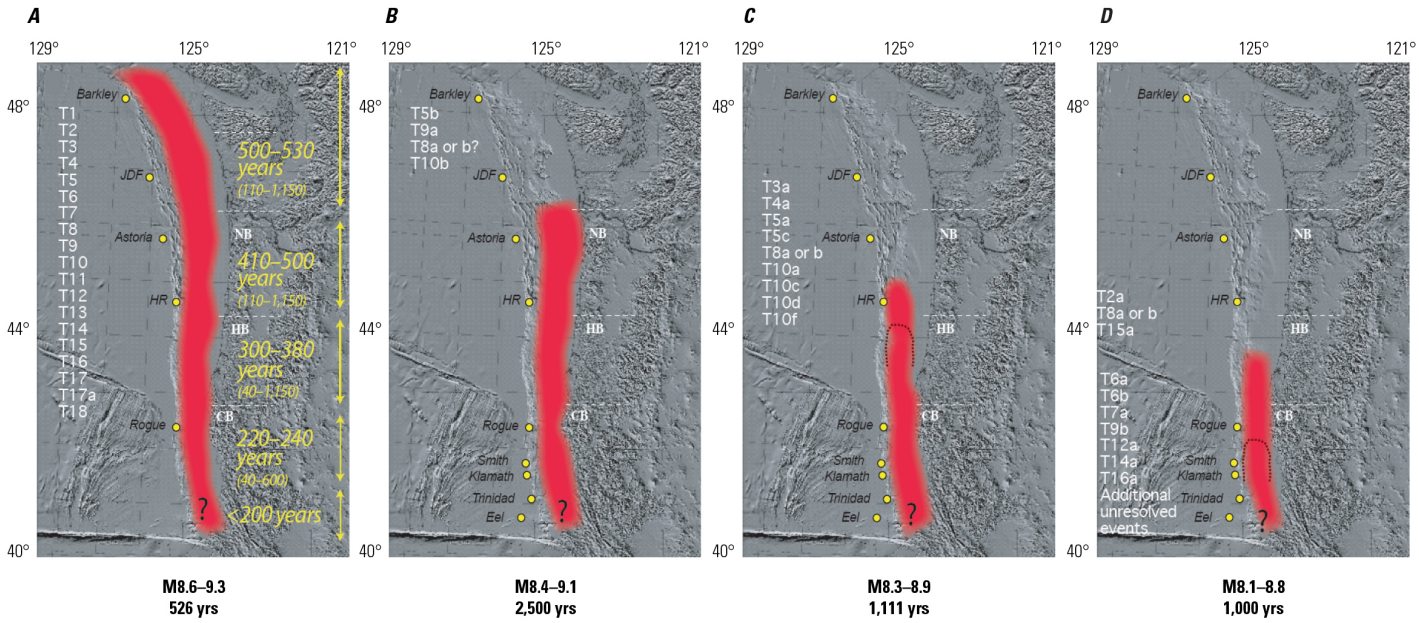

Figure 57. Figure modified from Goldfinger and others (2012) showing rupture zones of great Cascadia earthquakes determined from the turbidite record over the past 10,000 years. Yellow dots are locations of cores. Designation of great earthquakes for each rupture scenario is given on left side of each panel (for example, T1, T5b). Location of Cape Blanco (CB), Heceta Bank (HB), and Nehalem Bank (NB) is shown. The preferred magnitude range and recurrence time used for each rupture scenario in our implementation is shown below each panel. Recurrence times are determined by dividing 10,000 yr by the number of earthquakes in that scenario.

These partial Cascadia subduction zone rupture earthquakes (fig. 57*B*, *C*, *D*) supplement the whole Cascadia subduction zone ruptures with moment magnitudes inferred to be about 9.0 (fig. 57*A*), based on observations and modeling of the tsunami in Japan inferred to have been generated by the 1700 Cascadia earthquake (Satake and others, 1996, 2003). These whole Cascadia subduction zone rupture earthquakes have been well documented from about 5,000 years of evidence of coastal subsidence, tsunami deposits, and liquefaction at numerous sites near the coast of Washington, Oregon, and northern California (Atwater, 1987, 1992; Nelson and others, 1996; Atwater and Hemphill-Haley, 1997; Kelsey and others, 2002, 2005; Witter and others, 2003), as well as from 7,500–10,000 years of turbidites (Adams, 1990; Goldfinger and others, 2003, 2008). Workshop participants agreed that a mean recurrence time of about 500–550 years was appropriate for these whole Cascadia subduction zone ruptures, with an important caveat. They also thought that some of these 500–550-year scenarios may have been a series of M_w8 earthquakes that ruptured the whole Cascadia subduction zone over several years or a couple of decades, similar to what has been observed for the Nankai Trough in Japan (1944 and 1946, Ando, 1975) and along the Columbia-Ecuador coast of South America (1942–1979, Kanamori and McNally, 1982).

The participants of the November 2010 workshop also came to a consensus that the 2014 USGS NSHMP maps and UCERF3 should use a mean recurrence rate of 0.001 per year for M_w8 earthquakes that only rupture the southern portion of the Cascadia subduction zone. This rate is about half the rate for these earthquakes determined by Goldfinger and others (2012). One motivation for this choice was that this rate of partial Cascadia subduction zone ruptures is similar to that observed over certain periods

of time at Sixes River and Bradley Lake (Nelson and others, 1996, 2006). This mean rate was regarded by some workshop participants as a compromise position, pending future research. As new work on the turbidites and other evidence is accomplished, the mean rate for the hazard maps should be reassessed. No consensus on the rate of partial Cascadia subduction zone ruptures in the northern Cascadia subduction zone was reached at the November 2010 workshop. It should be stressed that there is still active debate about the interpretation of the turbidite data (for example, Atwater and Griggs, 2012).

Figure 58 shows the two proposed logic trees for Cascadia subduction zone recurrence. The hazard (frequency of exceeding a specified ground motion) from these two logic trees is additive. For the whole rupture of the Cascadia subduction zone (fig. 58), we consider aleatory uncertainty by having M_w8.8–9.3 earthquakes that rupture the whole Cascadia subduction zone and the possibility of serial M_w8 earthquakes that rupture the entire Cascadia subduction zone over a period of a few decades or less (would be given 20 percent of sequences if implemented). The average recurrence time is 526 years, either for the whole-rupture earthquakes or the series of M_w8s. For the current update of the NSHMP maps, however, we have not implemented the serial M_w8 possibility.

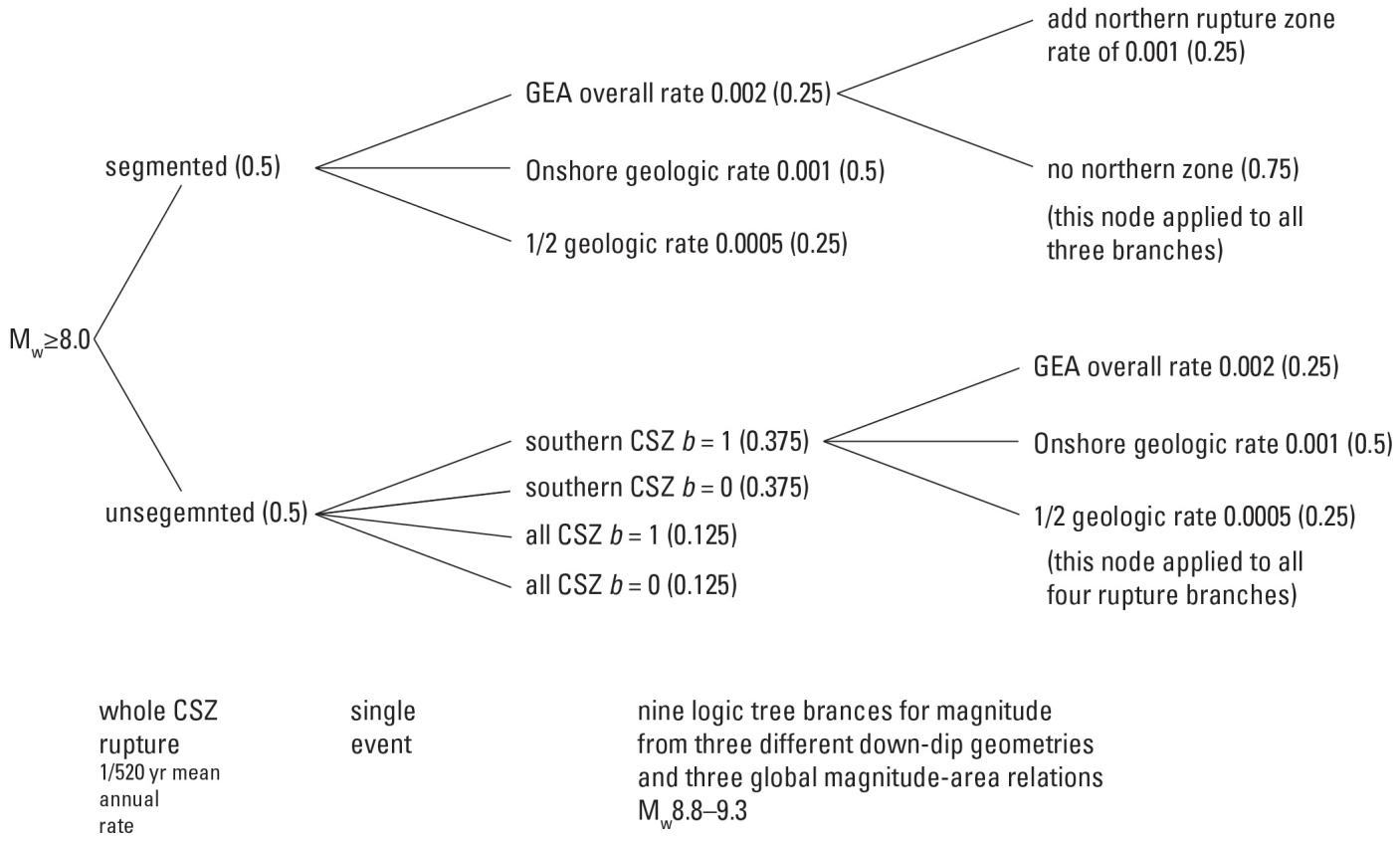

Figure 58. Logic trees for recurrence of great Cascadia subduction zone earthquakes. Note that the hazard (frequency of exceeding any given ground motion) from whole Cascadia subduction zone ruptures (fig. 57*A*) and partial ruptures (fig. 57 *B*, *C*, and *D*) is additive. Goldfinger and others (2012, GEA) rupture rate shown in figure 57. Assigned branch weight shown in parentheses.

The lower probability (would be 20 percent of sequences) for the serial M_w8 rupture reflects many factors. Having an M_w8 earthquake rupture at any location every 500 years, as part of a rupture sequence, would obviously produce less average slip than an M_w9 earthquake rupturing the whole zone every 500 years. The overall plate motion of about 40 mm/yr can be accommodated with M_w9 earthquakes every 500 years with average slip of 20 m per event. This plate rate cannot be accommodated by $M_w8.3–8.5$ earthquakes with a 500-year recurrence time at any one rupture location. This would be a problem if the shallow (less than 30 km depth) part of the subduction interface is highly coupled. Bird and Kagan (2004) found a high coupling factor for a global collection of subduction zones, using a Gutenberg-Richter recurrence model with parameters derived from the observed seismicity; however, it does not seem that earthquakes on the Cascadia subduction zone follow a Gutenberg-Richter magnitude-frequency distribution, given the lack of historically observed earthquakes with magnitudes less than 7 on most of the zone. Pacheco and others (1993) found low coupling factors in many subduction zones, although their results were based on only a 90-year catalog of seismicity. Goldfinger and others (2012) did not indicate evidence of M_w8 serial ruptures in the Cascadia turbidite data. A time-independent hazard calculation for the serial ruptures could be done using the procedure in Toro and Silva (2001), similar to the approach used in the 2008 USGS NSHMP maps for clustering of 1811–1812 type New Madrid earthquakes (Petersen and others, 2008).

To determine the magnitudes of the whole and partial Cascadia subduction zone ruptures, we first calculate the rupture area using a logic tree involving the three down-dip edges of rupture described below. Then we use three global magnitude area relations developed for subduction zone interface earthquakes: Papazachos and others (2004), Murotani and others (2008), and Strasser and others (2010), each with equal weight. Therefore, for each rupture scenario there are nine different values of magnitude used in the hazard calculation. For the whole Cascadia subduction zone ruptures, the magnitudes range from 8.6 to 9.3.

The logic tree shown in the top part of figure 58 characterizes the hazard from individual earthquakes that rupture only a portion of the Cascadia subduction zone. The first node of the partial Cascadia subduction zone rupture logic tree is for segmented as opposed to the unsegmented rupture models, which are given equal weight. Goldfinger and others (2012) presented a rupture model with rupture boundaries approximately chosen at Cape Blanco, Heceta Bank, and Nehalem Bank (fig. 57). This model is used in the “segmented” branch of the logic tree. Participants in the November 2010 workshop decided that Cape Blanco represented a likely segment boundary, for multiple reasons. The age of the incoming subducting plate varies from north to south at that location. Although there is a marked difference in age for the incoming plate at the trench at this latitude, Wilson (2002) found that the age difference is less pronounced in the portion of the plate beneath the coast (P. McCrory, written commun., 2013). Cape Blanco also is near the latitude of the southern edge of the mafic Siletz block on the overriding plate (Burgette and others, 2009). There is more disagreement on whether or not Heceta Bank and Nehalem Bank represent possible segment boundaries. The turbidite data are from a limited number of coring sites and can be interpreted with either segmented or unsegmented rupture models.

An earlier version of these logic trees was described and discussed at a workshop for the update of the Pacific Northwest portion of the USGS NSHMP maps. Some participants suggested that a more formal treatment of the logic tree describing the rate for partial Cascadia subduction zone ruptures should be used. This model has been adopted in the revised logic tree in figure 58. The consensus rate of 0.001 per year for southern Cascadia subduction zone partial ruptures was still advocated by most of the people who expressed an opinion at the workshop.

For the logic tree node for the overall recurrence rate of southern ruptures, we use three branches: (1) the rate from onshore geologic observations (about 0.001 per year), (2) the rate from

Goldfinger and others (2012; about 0.0023 per year), and (3) a rate of 0.0005 per year. The last rate reflects the possibility that some of the onshore and offshore observations may not reflect great earthquakes on the Cascadia subduction zone and also recognizes that there are periods of time in the geologic records at Sixes River and Bradley Lake when the annual rate of inferred partial Cascadia subduction zone rupture events is less than 0.001. Based on the workshop discussion, most participants would assign higher weight to the onshore geologic observations. Assigning weights of 0.5, 0.25, and 0.25, respectively, to these three branches yields a mean rate of 0.0012 per year, very close to the 0.001 rate recommended in the November 2010 workshop.

Figure 59 shows the effect on a seismic hazard map when the Goldfinger and others (2012) rupture model is used full weight, compared to applying the inputs of the 2008 NSHMP model. The magnitudes of the earthquakes were determined from rupture lengths. Peak ground acceleration with 2-percent probability of exceedance in 50 years increase substantially along the Oregon and northern California coasts when the Goldfinger and others (2012) model is used. Figure 60 shows a hazard map with the Goldfinger and others (2012) model for partial Cascadia subduction zone-rupturing earthquakes applied at half weight, but retaining the hazard from whole Cascadia subduction zone ruptures. Applying this half weight is equivalent to using the 0.001 rate reported from the onshore geologic data (Nelson and others, 1996). The hazard values along the southern Oregon and northern California coasts are still significantly higher than those in the 2008 NSHMP model (compare maps left fig. 59*B* and fig. 60*B*).

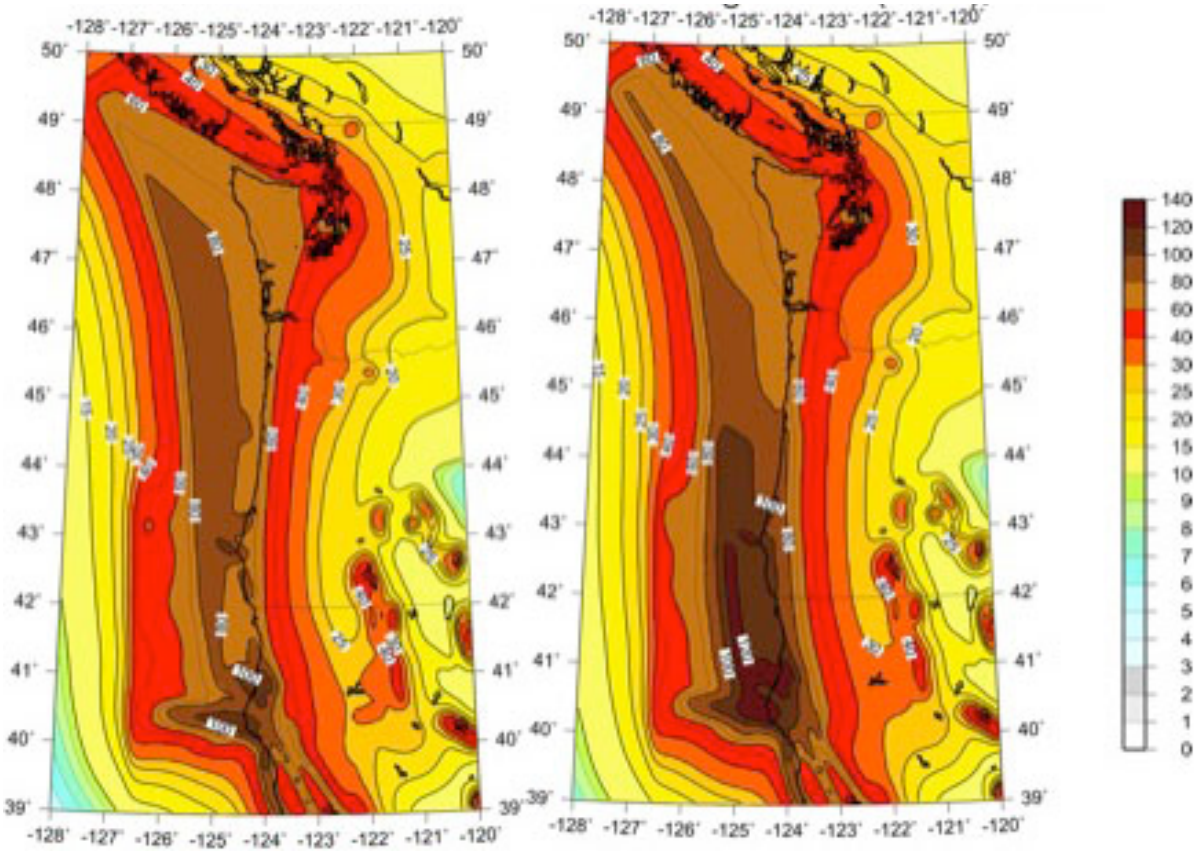

Figure 59. Peak ground acceleration (in percent gravity) at 2-percent probability of exceedance in 50 years and V_{S30} site conditions of 760 meters per second maps for *A*, model that assigns half weight to the partial

Cascadia subduction zone rupture rates from Goldfinger and others (2012) and *B*, adding a northern zone (recurrence rate of 0.001) suggested by Atwater and Griggs (2012). The northern zone extends from the northernmost edge of Goldfinger's zones (Heceta Bank) to the northern end of the Cascadia subduction zone. Hazard from whole Cascadia subduction zone rupture events (about M_w9.0) was included in each figure. Other hazard sources (gridded shallow and deep seismicity, background zones, and crustal faults) included in both maps.

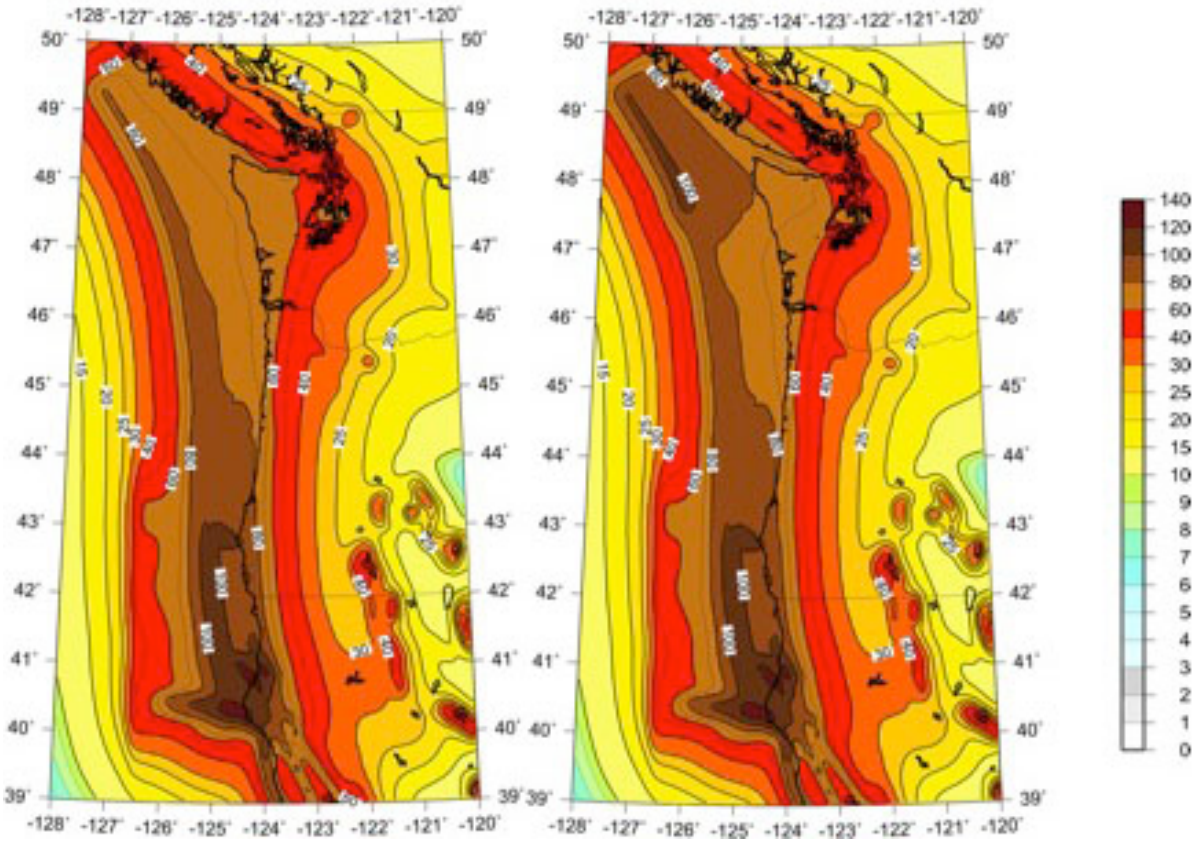

Figure 60. Peak ground acceleration (in percent gravity) at 2-percent probability of exceedance in 50 years and V_{S30} site conditions of 760 meters per second maps for *A*, model that assigns half weight to the partial Cascadia subduction zone rupture rates from Goldfinger and others (2012) and *B*, adding a northern zone (recurrence rate of 0.001) suggested by Atwater and Griggs (2012). The northern zone extends from the northernmost edge of Goldfinger's zones (Heceta Bank) to the northern end of the Cascadia subduction zone. Hazard from whole Cascadia subduction zone rupture events (about M_w9.0) included in each figure. Other hazard sources (gridded shallow and deep seismicity, background zones, and crustal faults) also included in both maps.

The next node of the logic tree (fig. 58) on the segmented model branch is for a northern Cascadia subduction zone rupture, a possibility suggested by Atwater and Griggs (2012), largely from tsunami evidence from Discovery Bay, Wash. (Williams and others, 2005). They argue that the additional tsunamis observed at this location that do not correspond in time with Pacific coastal

evidence of whole Cascadia subduction zone rupture events may indicate M_w8 ruptures on a northern portion of the Cascadia subduction zone. Others at the workshop argue that these deposits may be from local earthquakes under the Strait of Juan de Fuca or the Georgia Straight. One branch is given a recurrence rate of 0.001 per year (Atwater and Griggs, 2012), the other zero. Weights are 0.25 and 0.75, respectively. Note that this possible northern rupture zone is in addition to the more southerly rupture zones specified in Goldfinger and others (2012) that are shown in figure 57. Figure 60*B* shows a hazard map that uses a northern rupture zone along with the southerly rupture zones specified by Goldfinger and others (2012) and whole Cascadia subduction zone ruptures. Note the increase in hazard for northwest Washington and Vancouver Island when a northern rupture zone is added.

The unsegmented branch of the logic tree (fig. 58) entails the use of floating rupture zones. That is, the hazard for each earthquake magnitude is calculated by moving the rupture zone incrementally along the strike of the Cascadia subduction zone until it reaches the other end. The rate of any particular rupture scenario is just the total rate for that magnitude divided by the number of rupture zones for that magnitude. We consider two possibilities for the portion of the Cascadia subduction zone to use for the floating ruptures. The first is for ruptures that cover the area from Cape Mendocino to approximately the latitude of the Washington–Oregon state line. This is the approximate location of the northernmost cores (Astoria) where Goldfinger and others (2012) report evidence of turbidites from southern Cascadia subduction zone earthquakes. The other option is to have floating ruptures over the entire extent of the Cascadia subduction zone, similar to what was used as a scenario for the 1996, 2002, and 2008 USGS NSHMP maps (Frankel and others, 1996, 2002; Petersen and others, 2008).

Trial hazard maps for 2-percent probability of exceedance in 50 years indicate that the segmented rupture model of Goldfinger and others (2012) and models with floating ruptures produce very similar hazard maps for onshore locations, if the models are based on the same total rate of partial rupture earthquakes. Thus, the mean rate of 0.0012 per year is the controlling factor in the hazard maps, rather than the details of the segmentation. The first node of the unsegmented branch describes different models that satisfy the 0.0012 mean annual rate. In this report, we use a Gutenberg-Richter frequency-magnitude distribution from $M_w8.0$ to 8.7. We choose branches with b=1 and b=0. The former represents an average global b value for the Gutenberg-Richter relation. The b=0 branch reflects the unusual nature of the Cascadia subduction zone. Overall, the Cascadia subduction zone does not seem to follow the typical Gutenberg-Richter relation with a b value of one. Given M_w9 earthquakes with a 526-year recurrence time, we do not see M_w7 earthquakes with 5-year recurrence time, at least over the past 150 years of observations. A b value of zero implies equal likelihood of having an $M_w8.0$ or an $M_w8.7$ earthquake. The 2008 USGS NSHMP maps essentially used a b value of about zero for $M_w8.0$–8.7 earthquakes (Petersen and others, 2008); however this scenario represented the hazard from a series of M_w8 earthquakes that fill the Cascadia subduction zone, as an alternative to whole rupture M_w9 earthquakes. In any case, using a b value of one or zero, with an overall rate of $M_w8.0$–8.7 earthquakes of 0.0012 per year, yields very similar seismic hazard maps.

The input models apply alternatives for floating ruptures over the entire Cascadia subduction zone reflect the idea that there could be an $M_w8.0$–8.7 earthquake at any location on the Cascadia subduction zone. This is a reasonable model, given the uncertainties and the possibility that onshore sites and offshore cores may not have recorded all of the M_w8 earthquakes on the Cascadia subduction zone. It is problematic to choose a rate for these branches with floating rupture over the entire Cascadia subduction zone. We use the logic tree of rates applied only to the southern ruptures (fig. 58), multiplied by the length ratio of the whole Cascadia subduction zone to the southern rupture zone (fig. 57*B*), to maintain the logic tree rate in the southern Cascadia subduction zone (relative to the case with only southern ruptures) and to account for the possibility of ruptures in the northern portion.

A time-dependent hazard calculation would be straightforward for the whole Cascadia subduction zone rupture scenarios (M_w8.6–9.3 or a series of M_w8s), given a 526-year average recurrence time and the time since the 1700 earthquake (Petersen and others, 2002). Calculating time-dependent hazard maps for the M_w8.0–8.7 partial rupture scenarios would be problematic given the variability of the rupture scenarios.

Logic Tree for Down-Dip Edge of Rupture

The location of the down-dip edge of the rupture zones of great Cascadia earthquakes (fig. 61) can have substantial effect on the seismic hazard estimates for certain areas. This location is used to determine the closest distance of rupture to a site for the GMMs used in the seismic hazard calculation. One important issue is how the developers of GMMs use empirical data to identify the edge of a rupture zone. This edge often is determined by slip distributions derived from inversions of strong motion data or teleseismic data. Thus, it corresponds to the location where the coseismic slip is a small fraction of the peak slip on the plate interface during a great earthquake.

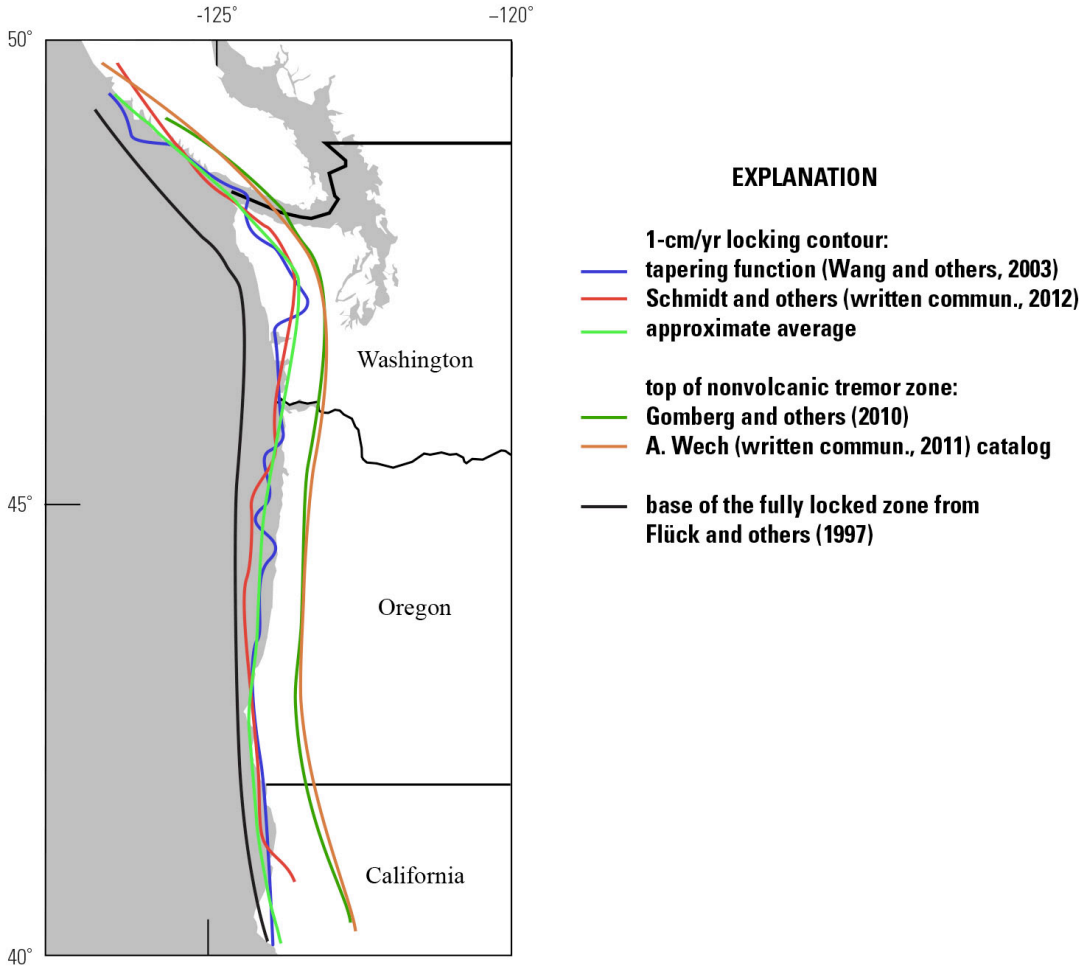

Figure 61. Alternative locations of down-dip edge of Cascadia rupture. We use the midpoint of the updated version of the fully locked zone from Flück and others (1997) and the average of the 1-cm/yr locking contours as the seaward branch in the logic tree.

In the December 2011 workshop, participants had favorable views of procedures that used modeling of GPS and uplift data to constrain the interseismic locking on the Cascadia subduction zone. Participants also wanted to use the top of the tremor zone as one model for the location of the down-dip edge of rupture. There were suggestions from participants to give low weight to a model with the down-dip edge at the midpoint of the tremor zone. We have not implemented this suggestion.

For the March 2012 workshop, we presented a logic tree based on three branches (fig. 62): (1) the average of the 1 centimeter per year (cm/yr) locking contours from McCaffrey and others (written commun., 2012) and Schmidt and others (written commun., 2012), based on modeling GPS and uplift data and applying a down-dip tapering function derived in Wang and others (2003); (2) the top of tremor zone based on the compilation of Gomberg and others (2010) and Aaron Wech from *http://tunk.ess.washington.edu/map_display/* (Pat McCrory and Luke Blair, written commun., 2012), and (3) the base of the locked zone from Flück and others (1997), based on thermal modeling and uplift data. Figure 61 shows a map with these possibilities.

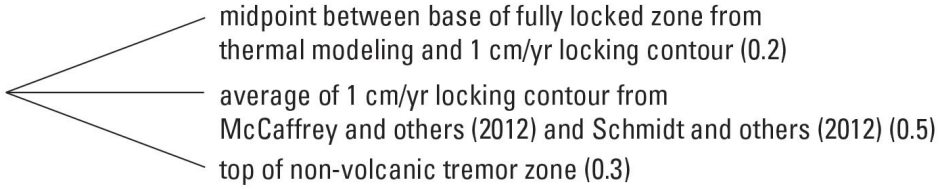

Figure 62. Logic tree for down-dip edge of rupture zones of great Cascadia earthquakes. Assigned branch weight shown in parentheses.

The March 2012 workshop participants clearly stated that the 1-cm/yr locking contour was a reasonable center of mass of opinion for the location of the down-dip edge. This depth corresponds to the location on the fault plane with a coupling factor of approximately 0.25. Given the observation that the down-dip portion of the rupture zone of the 2011 M_w9.0 Tohoku earthquake that generated significant strong ground motions had a coseismic slip much lower than the peak slip determined for the rupture (Frankel, 2013), workshop participants thought that using the 1-cm/yr locking contour (about 25 percent locking) for the consensus estimate of the downdip edge was a reasonable strategy.

The March 2012 workshop participants did not have a consensus on the model to use for the most seaward logic-tree branch. Participants did express the view that applying the base of the Flück and others (1997) locked zone was too far seaward. As an interim solution, we propose the seaward branch to be located at the midpoint of the base of the locked zone from the updated equivalent of Flück and others (1997) and the 1-cm/yr locking contour from the recent GPS and uplift modeling.

The logic tree for the down-dip edge is shown in figure 62. We assigned weights of 0.5, 0.3, and 0.2, respectively, to the 1-cm/yr locking contour determined from GPS and uplift modeling, the top of nonvolcanic tremor, and the midpoint between the base of the fully locked zone and the 1-cm/yr contour (fig. 61).

Magnitude-Frequency Distribution and Along Strike Earthquake Rate

Figure 63 presents a summary logic tree that combines the rate logic trees (fig. 58), the down-dip edge logic tree (fig. 62), and magnitude scaling and ground motion model choices. Note that the three

magnitude-area scaling relations are applied to full Cascadia subduction zone ruptures and the segmented model of partial Cascadia subduction-zone ruptures. The three down-dip edge options combined with three magnitude-area scaling relations yield a total of nine magnitudes for the full Cascadia subduction-zone rupture and for each of the four partial rupture scenarios in the segmented model. The magnitude ranges for these scenarios are given in table 11, along with logic tree mean rate for individual rupture scenarios and model weights. Table 11 also lists magnitude range and rate for the unsegmented model. Figure 64 shows the total cumulative and incremental rates for all ruptures for the entire Cascadia subduction zone. The incremental magnitude-frequency distributions are for binned magnitudes with a bin width of 0.1 magnitude units and rates are given at the center of each bin. The Cascadia subduction zone cumulative magnitude-frequency distribution implies an effective recurrence time of about 300 years for earthquakes with M_w8.0 and greater.

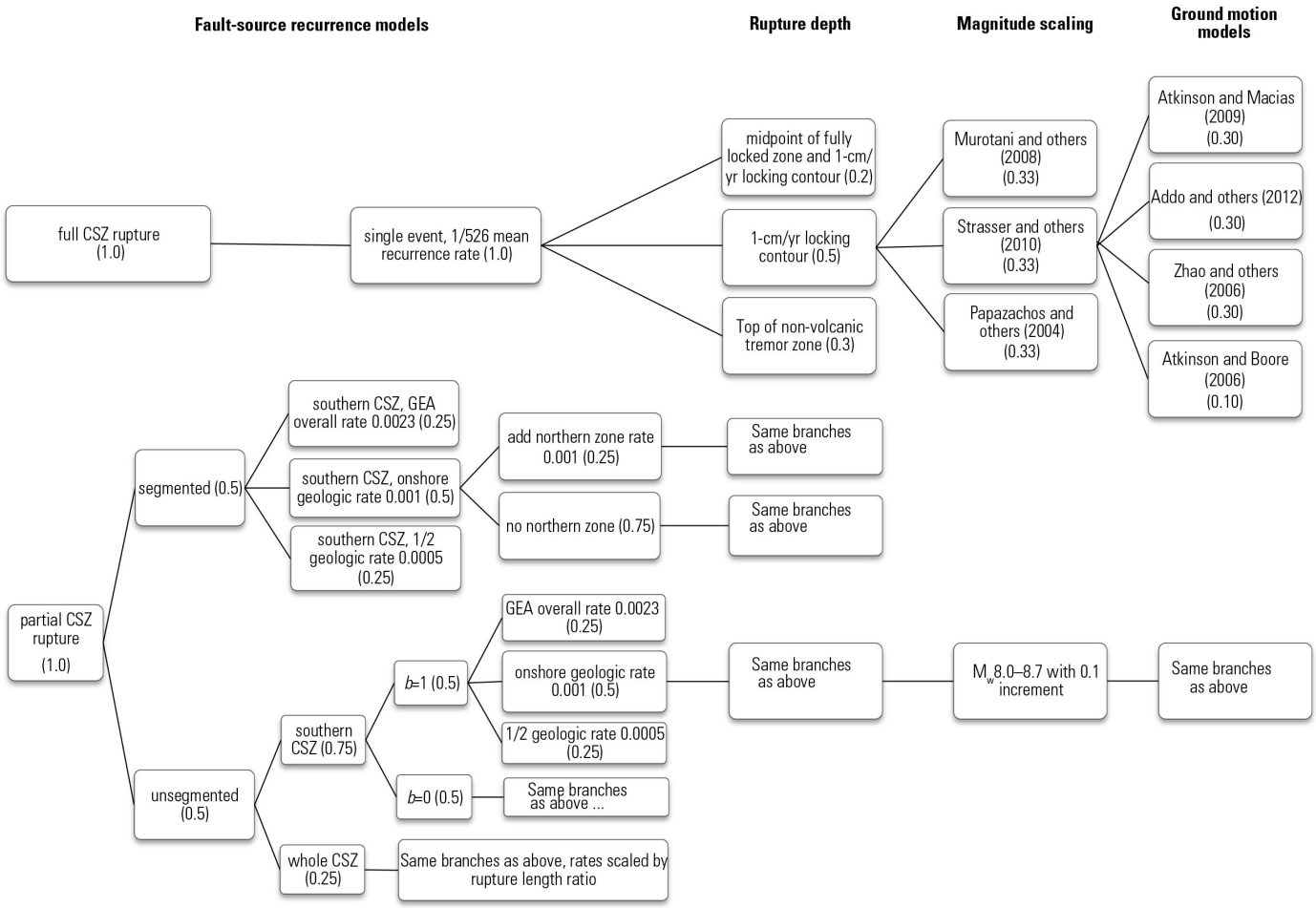

Figure 63. Cascadia subduction zone (CSZ) summary logic tree. Note that the hazard (frequency of exceeding any given ground motion) from full Cascadia subduction zone ruptures and partial ruptures is additive. Assigned weight for branches shown in parentheses. The magnitude scaling branches apply to all three rupture-depth branches. Ground motion model branches apply to all magnitude-scaling branches as well as all branches in the unsegmented model. GEA denotes the Goldfinger and others (2012) rupture rate (fig. 57).

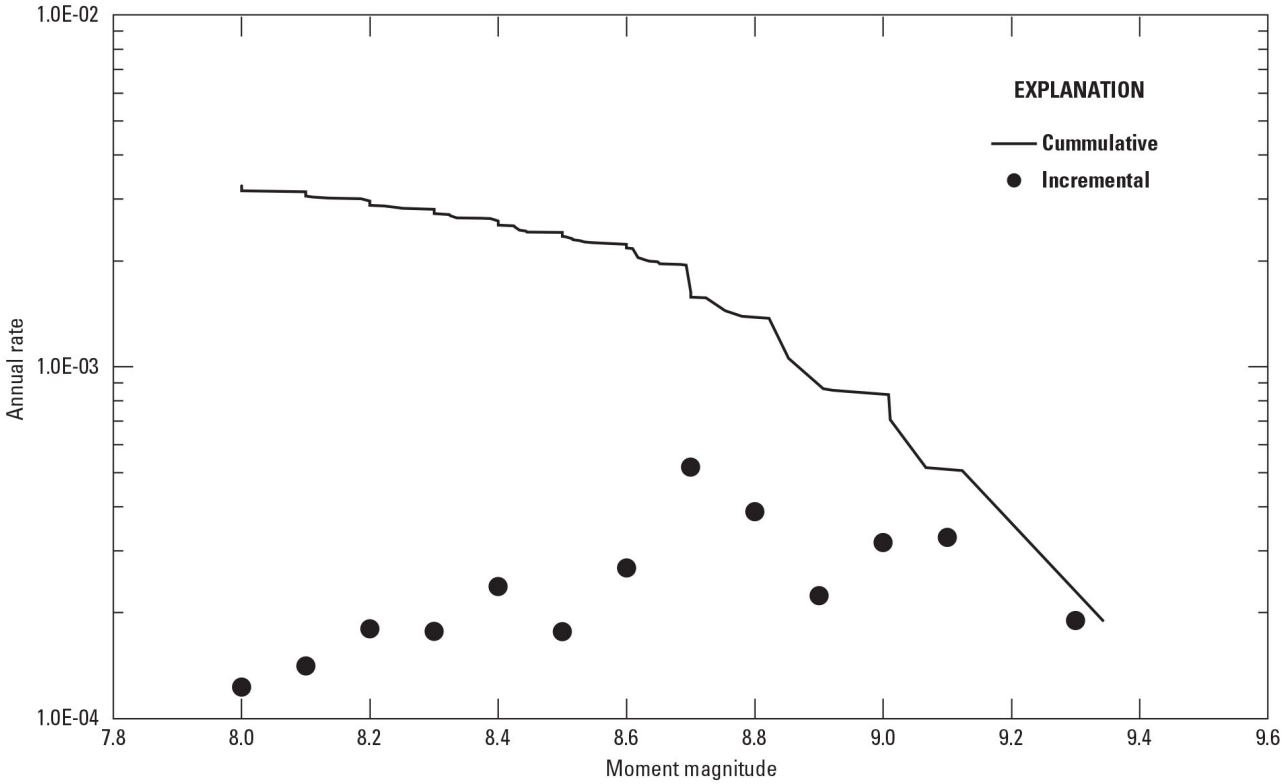

Figure 64. Total cumulative and binned incremental magnitude-frequency distributions for all rupture scenarios for the Cascadia subduction zone.

Table 11. Event rates for Cascadia subduction zone.

Rupture cases			M_w	Mean rate for individual rupture (per year)	Weight
Characteristic (segmented)	Full Cascadia subduction zone [1] (all four segments)		8.6–9.3	0.00190	1.0
	Partial rupture	Case B[2] (southern three segments)	8.4–9.1	0.00021	0.5
		Case C[2] (southern two segments)	8.3–8.9	0.00047	
		Case D[2] (southernmost segment)	8.1–8.8	0.00052	
		Northern zone	8.3–8.9	0.001	0.1
Gutenberg-Richter (floating rupture)		Full Cascadia subduction zone[3]	8.0–8.7	0.0012	0.1
		Southern zone[4]	8.0–8.7	0.0012	0.4

[1]Full Cascadia subduction zone, southern three segments, southern two segments, and southernmost segment rupture cases correspond to Goldfinger and others (2012), cases A, B, C, and D (fig. 57), respectively. The northern zone extends from the northernmost edge of Case B to the northern end of Cascadia subduction zone.

[2]Rates were determined in a way that maintains the relative rates observed by Goldfinger and others (2012) while honoring the logic tree mean rate of 0.0012 per year (along the southernmost segment). Goldfinger and others (2012) rates for Cases B, C, and D were obtained by dividing the number of events for each case by 10,000 years. Hazard from these events is additive.

[3]Rate is scaled from logic tree mean rate of 0.0012 per year by the ratio of full Cascadia subduction zone length to the length of the southern zone.

[4]Rupture floats over the southern part of Cascadia subduction zone only, identical to the extent of Case B (fig. 57*B*).

Earthquake rates along the Cascadia subduction zone are dominated by the full characteristic Cascadia subduction zone ruptures, with 1 event in 526 years. We also added additional partial Cascadia subduction zone ruptures that are more numerous in the south. Figure 65 shows the contributions to the earthquake rates from each of the models and how the rates vary along the fault. For example, in the far south (adjacent to California) the large earthquake rate is about 1 event in 315 years, whereas in the far north (adjacent to Washington) the rate is lower, about 1 event in 460 years.

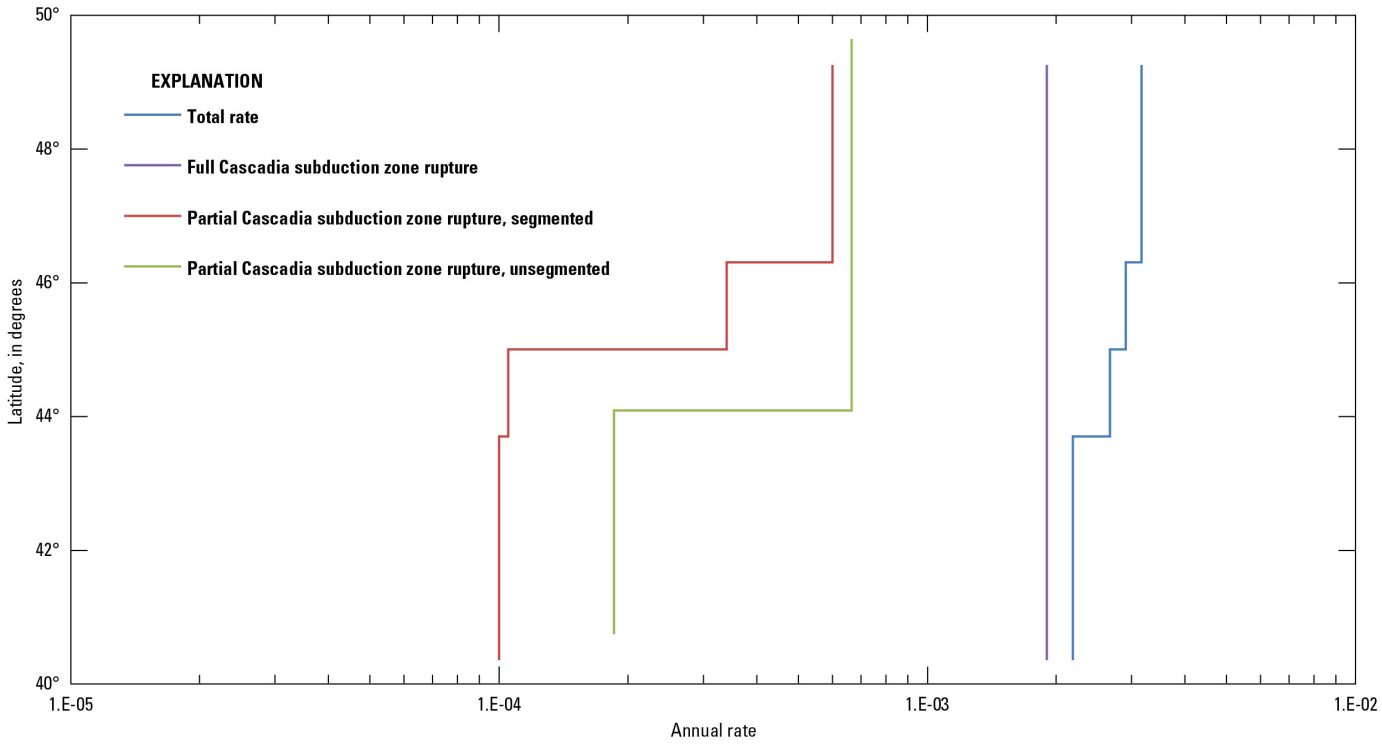

Figure 65. Variation of earthquake rates for each of the input model along the Cascadia subduction zone.

California

The California portion of the 2014 USGS NSHMP maps is based on the long-term, time-independent component of the UCERF3 developed by the Working Group on California Earthquake Probabilities (2013). The two primary goals of this earthquake-rate model are to relax fault-segmentation assumptions and include multifault ruptures, both of which were limitations of the previous model (UCERF2). To accomplish this, UCERF3 leverages a newly developed "grand inversion" platform, which solves for the rate of all earthquakes simultaneously (fig. 66), while also using a broader range of data constraints (fig. 67). This approach eliminates the apparent UCERF2 overprediction of M_w6.5–M_w7 earthquake rates and permits inclusion of multifault ruptures similar to those recently observed in nature (for example, the 2002 M_w7.9 Denali, Alaska earthquake rupture, Schwartz and others, 2012).

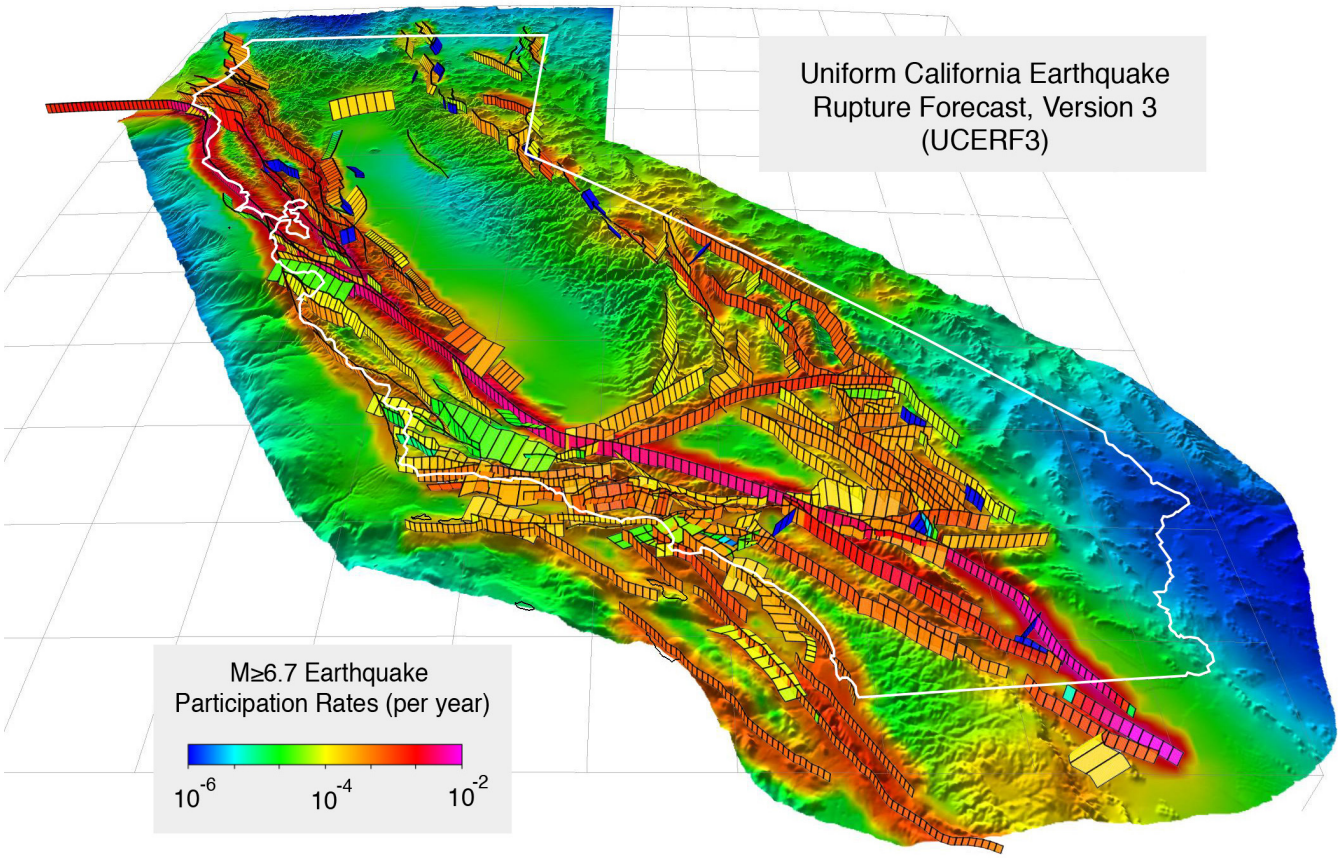

Figure 66. Map of earthquake participation rate for the Uniform California Earthquake Rupture Forecast, ver. 3.3 (UCERF3) model. For the purpose of this illustration, faults are projected above the earth's surface.

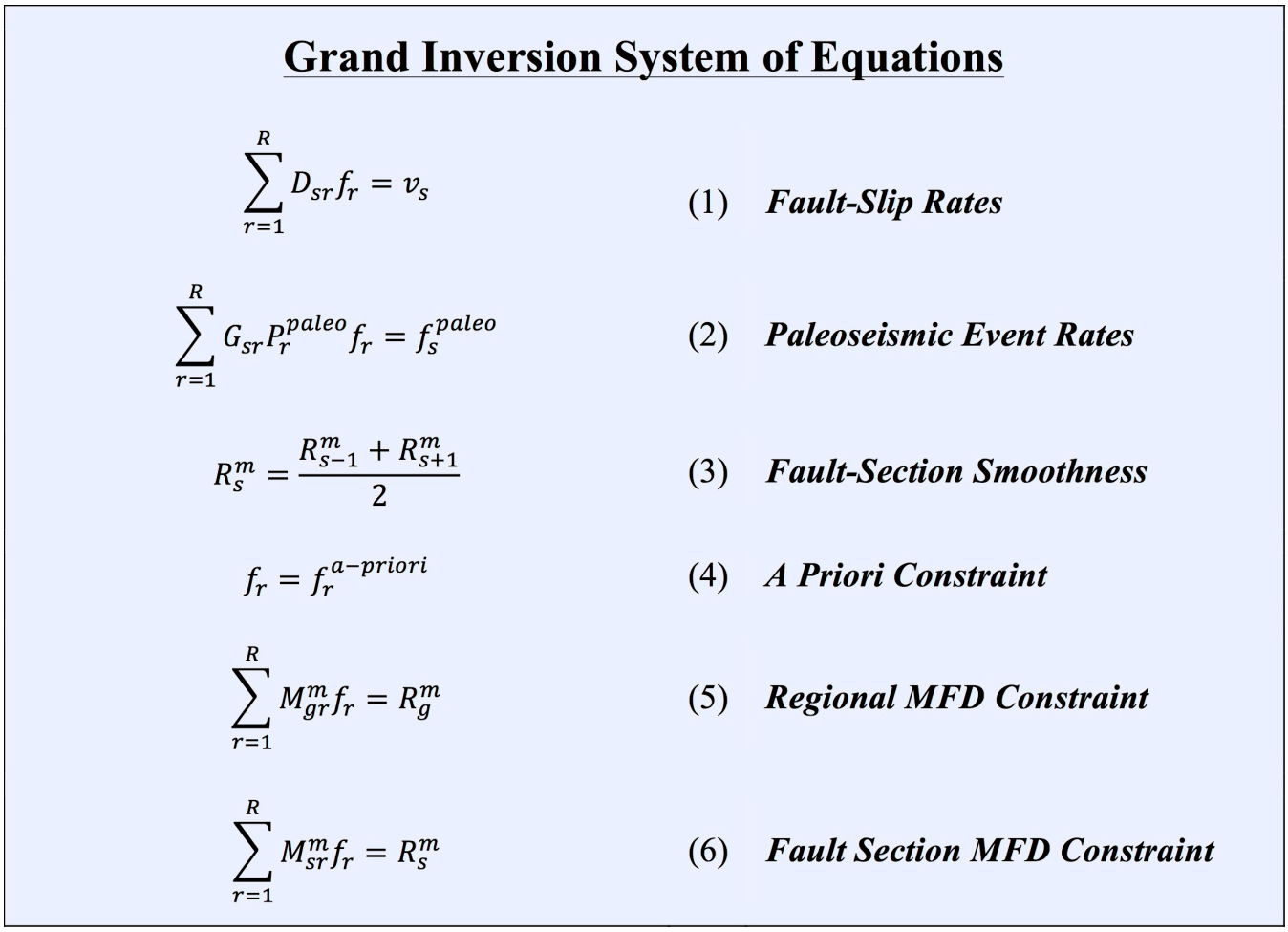

Figure 67. The grand inversion system of equations used in solving for the long-term rate of fault-based ruptures.

The inversion approach conceptually is simple and extensible with respect to adding other constraints. Without invoking segmentation, however, the problem inherently is underdetermined in terms of solving for the rate of every possible rupture (solutions are nonunique). The inversion calculation therefore uses a multithreaded simulated-annealing algorithm, which samples the null space efficiently and samples a range of models given overall data uncertainties. This approach is more derivative than the prescriptive nature of previous models (magnitude-frequency distributions are now derived rather than assumed). Individual solutions are more difficult to understand, necessitating the development of a variety of analysis tools.

While building UCERF3, the WGCEP updated almost all datasets from UCERF2 and developed a number of new key components. These include four new deformation models, which provide fault slip rates: one based on pure geologic data, and three kinematically consistent models that also incorporate geodetic data. These models provide slip rates on faults where none previously existed, thereby producing some of the largest hazard changes relative to UCERF2. The deformation models also constitute one of the largest epistemic uncertainties, with the other important contributors being a new smoothed-seismicity algorithm, two new scaling equations, and alternative values for the total regional rate of M_w5 and larger events. All of these influential options are new, so UCERF3 represents a

considerable broadening of epistemic uncertainties, with the complete set yielding 1,440 alternative models (logic-tree branches; fig. 68). The large number of models, coupled with a need to sample the null space of each, required the use of supercomputers. Extensive hazard calculations not only quantify the influence of each epistemic uncertainty, but also show that those associated with model nonuniqueness are negligible in comparison.

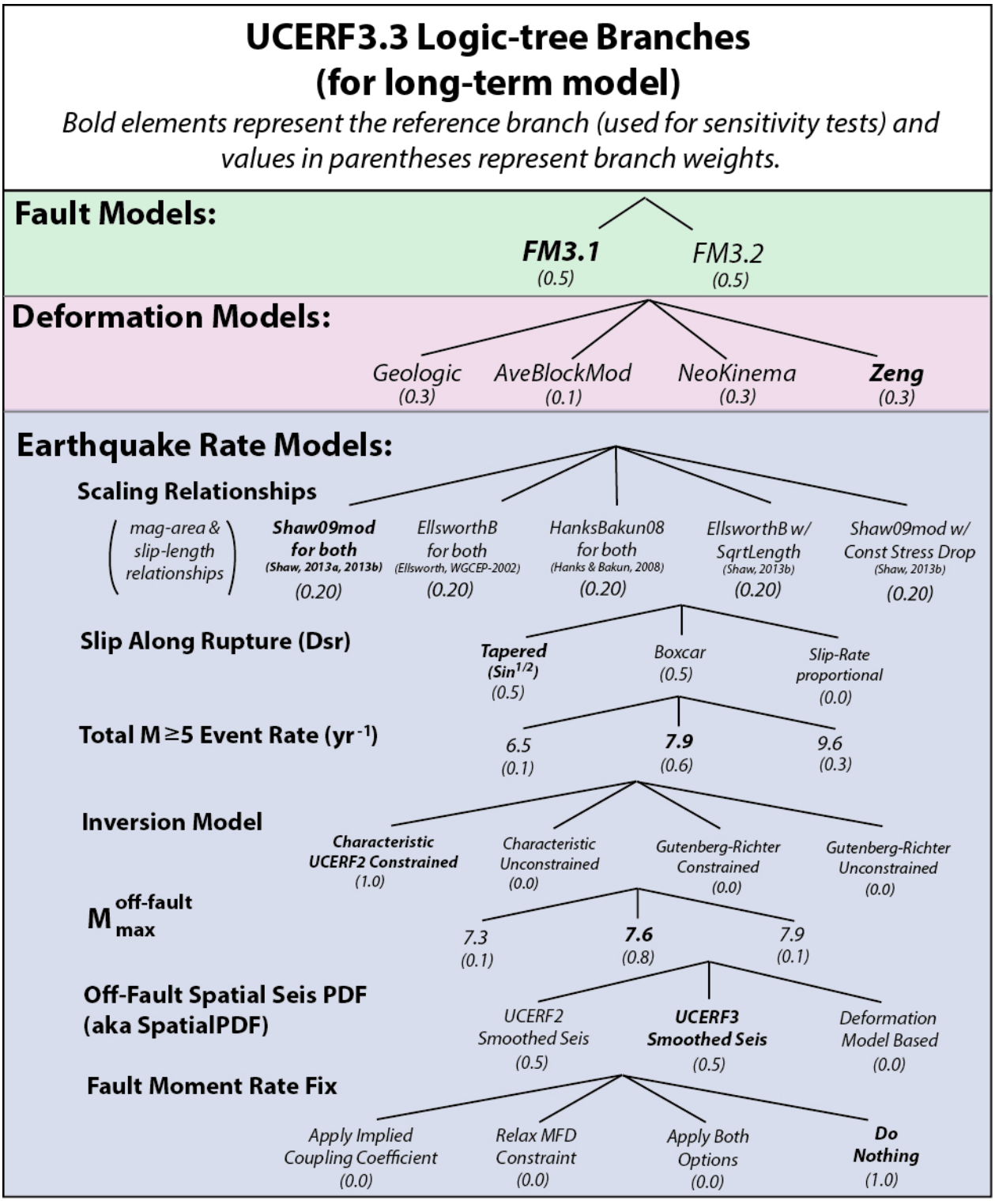

Figure 68. Logic tree for the Uniform California Earthquake Rupture Forecast, ver. 3.3 (UCERF3) model. Assigned branch weights shown in parentheses. Fault models (FM) version 3.1 and 3.2 are assigned equal weight. PDF refers to probability density function, MFD to magnitude-frequency distribution, and UCERF2 to version 2 of the Uniform California Earthquake Rupture Forecast.

Before inverting for fault-based earthquake rates, UCERF3 faults are discretized into approximately 7-km subsections. Each subsection is allowed to rupture with any other subsection located within 5 km, subject to static-stress based geometric compatibility rules, and ruptures must span at least two subsections. These constraints allow approximately 250,000 unique fault ruptures across California, some that are much larger than previously considered. Geodetic and geologic slip rates, as well as paleoseismic recurrence data, are then inverted to solve for the rate of each unique rupture, subject to a variety of additional constraints, including along fault (rate) smoothness, regional and fault-specific magnitude-frequency distributions (MFDs), and a-priori rates (for example, at Parkfield; see Working Group on California Earthquake Probabilities (2013) for more details. Once fault-based rates have been computed, the total fault-based MFD is subtracted from the statewide MFD, and the remainder is distributed across the state using spatial probability density functions (PDFs) derived from models of smoothed seismicity. Two spatial PDFs are considered, one based on the fixed radius Gaussian smoothing kernel of UCERF2, and a second that uses adaptive smoothing (where the smoothing radius is a function of the density of M_w greater than 2.6 earthquakes). In this way, fault-based and gridded, or background, earthquake rates are coupled across all branches of the UCERF3 logic tree, and do not exceed the historical statewide rate dictated by the "M_w greater than or equal to 5 rate" branch of the logic tree.

As with prior California earthquake rate models, UCERF3 is an approximation of the system and represents a limited range of models. For example, inversions are explicitly constrained to stay as close as possible to UCERF2, and rules are applied with respect to whether ruptures can jump between faults. This means that, although UCERF3 is demonstrably better than UCERF2 overall, there may be areas that warrant further site-specific investigations. To this end, the entire framework is available on an open-source platform. The grand inversion is not free of expert judgment; it provides a system-level framework for testing hypotheses and formally balancing the influence of different experts. For example, significant challenges are posed by the inversion when applying the Gutenberg-Richter hypothesis to individual faults, which may indicate that the hypothesis should be rejected. A time-dependent UCERF3 model also is under development and will be published separately in the near future. Please refer to the Working Group on California Earthquake Probabilities (2013) documentation for a comprehensive description of UCERF3 methodology, key assumptions, and potential improvements.

Ground Motion Models

Ground motion models (GMMs) are equations that express the ground motion intensity in terms of characteristics of the earthquake source, propagation path of the seismic waves, and the site conditions. The ground motion intensity is quantified by the mean and standard deviation of an assumed normal probability density function for the horizontal spectral acceleration (SA) in the logarithmic scale. Median and logarithmic standard deviations typically are expressed as functions of spectral period, earthquake magnitude, source-to-site distance, and other parameters characterizing the earthquake source, path, and site conditions.

Ground motion models used in the USGS NSHMP maps are categorized into three groups based on their tectonic settings: (1) those developed for earthquakes in stable continental regions, which are used in the Central and Eastern United States (CEUS) region; (2) those for shallow crustal earthquakes in active tectonic regions, which are used in the Western United States (WUS) region; and (3) those for earthquakes in subduction zones (including both interface and intraslab), which are used in the Pacific Northwest region.

In the CEUS and for subduction interface earthquakes, we calculate ground motions from sources that are up to 1,000 km from the site. In the WUS and for deep intraslab earthquakes, ground motions are calculated for distances less than 300 km from the site. For CEUS sources, we cap and truncate ground motions to avoid unacceptably large values. Capping and truncation do not significantly affect the results at probability levels of 2-percent probability or greater of exceedance in 50 years. Median ground motions are capped at 1.5 g for peak ground acceleration (PGA) and at 3.0 g for the 0.2-second (5-hertz) spectral acceleration. The ground motion distribution for PGA is truncated at 3 g and for 0.2-second spectral acceleration at 6 g when these values are less than the 3-sigma cutoff, where sigma represents the logarithmic standard deviation of the ground motion model (GMM). In addition, we truncate the distribution of ground motions at three standard deviations above the median for PGA and SA for all GMMs.

Ground Motion Model Selection Criteria

For the 2014 update of the USGS NSHMP maps, the steering committee suggested that the USGS produce a set of criteria for selecting GMMs from the collection of all available GMMs. Although these criteria have been considered in the past updates of the USGS NSHMP maps in a general sense, they have not been formally introduced. Using Bommer and others (2010) as a guideline and based on the expertise and advice of the steering committee members and the NSHMP members, USGS has developed the following set of criteria. As advised in Cotton and others (2006), the following criteria are designed not to be excessively specific at the time of writing, but rather sufficiently flexible to be adaptable to the continuing growth of the global strong motion database and the continued evolution of GMMs.

General Requirements

1. **Basic**—The GMM must provide, as a minimum, equations for the median and aleatory uncertainty of the horizontal component for peak ground acceleration and spectral acceleration at 0.2- and 1-second spectral periods (5-hertz and 1-hertz frequencies). The GMM must be applicable to one of the tectonic regions relevant to the United States.
2. **Publication—**The GMM must be published in the form of a journal paper, open-file report, or similar publicly accessible publication. The publication should summarize the database, reasonably describe the modeling procedure, demonstrate the scaling characteristics with parameters in the model over the parameter ranges of applicability, and provide justification for the fit of the model to data. The database used in development of the model must be accessible to the public as to allow the work to be reproduced and validated by others.
3. **Implementation—**GMM modelers are required to provide source codes (currently in Fortran language), verification tables, or validation plots to the USGS NSHMP team members, and be available to discuss and provide guidance on the implementation of their models.
4. **Uniqueness—**Because USGS uses a weighted combination of published GMMs, each GMM should be a statistically independent model. If a GMM is a combination of other GMMs, it should include models not already used in the USGS weighted combination to avoid double counting.

Ground Motion Model Database

5. **Data—**A recorded or simulated database should be processed using uniform criteria and procedures that account for noise. Database also must be accessible to the public.

Ground Motion Model Parameters and Applicability Range

6. **Magnitude—**The GMM must have magnitude dependence (also see items 11–13 on functional form). The magnitude applied must be based on moment magnitude. The model must be applicable or reasonably extrapolated to a magnitude range of 5.0 to 8.2 for shallow crustal earthquakes in the WUS and 4.7 to 8.2 for stable continental earthquakes in the CEUS. The GMMs for subduction earthquakes should be applicable or reasonably extrapolated to a magnitude range of 5.0 to 8.0 for intraslab and 8.0 to 9.3 for interface earthquakes.
7. **Distance—**The GMM must have distance dependence (also see items 12–13 on functional form). Distance should be measured from the rupture source or from the surface projection of the rupture source. The GMM should be applicable or reasonably extrapolated to a distance of 300 km for shallow crustal and intraslab subduction earthquakes, and 1,000 km for stable continental and interface subduction earthquakes.
8. **Faulting style—**Shallow crustal GMMs for the WUS need to account for strike-slip, reverse, and normal faulting mechanisms.
9. **Hanging wall—**Shallow crustal GMMs for the WUS need to have physically reasonable behavior in close proximity of faults over the hanging wall and footwall.
10. **Site conditions—**GMMs must include a term for V_{S30} (currently for WUS GMMs), or be accompanied by other relations that transfer their equations to a V_{S30} of 760 meters per second (m/s) (currently for CEUS and subduction interface and deep intraslab GMMs). For use in softer soil hazard maps, GMMs should account for nonlinear soil effects.

Ground Motion Model Functional Form and Modeling Procedure

11. The GMM should have nonlinear magnitude dependence and a source corner frequency or source spectral shape that is magnitude dependent.
12. The GMM should include magnitude saturation for close distances through the use of an appropriate finite-fault distance measure or fictitious depth term or both. The GMM should have a magnitude-dependent distance decay to reasonably extrapolate across the magnitude and distance range of interest.
13. The GMM should include an exponential decay with distance term to account for frequency dependent attenuation (that is, Q).
14. GMMs should balance model complexity and either data constraints or constraints based on ground motion simulation as decided by the NSHMP team and Steering Committee.
15. GMMs should not display any substantial biases or trends in the between-event (inter-event) or within-event (intra-event) residuals with respect to distance, magnitude, soil conditions such as V_{S30}, and other parameters included in the model.
16. When applicable, standard deviations should distinguish between within-event (intra-event) and between-event (inter-event) components of variability.

Central and Eastern United States

For the CEUS, ground motion models and their weights are updated. In this section we discuss the changes that contribute to the new weighting scheme, including the important parameters and applicability limits of each model.

2008 Models and Weights

The 2008 hazard maps (Petersen and others, 2008) used seven GMMs with two different weighting schemes, one for RLMEs such as the New Madrid seismic zone and the Charleston seismic zone, and the other for background-gridded sources (GridSrc). These GMMs and their corresponding weights are listed in table 12. Most GMMs developed for the CEUS are based on simulated ground motions because of the scarcity of recordings for large magnitude events in this region. In 2008, we categorized the models based on the type of their simulated databases, which is shown as the model "Type" in table 12 and was the basis for assigning weights.

Models by Frankel and others (1996), Toro (2002) for the midcontinent region, and Silva and others (2002) with constant stress drop and magnitude saturation are categorized as single-corner frequency models, with the first representing a point source model and the last two representing finite fault models. Two versions of the model by Atkinson and Boore (2006) are dynamic-corner frequency models, one with a stress drop of 140 bars and the other with a stress drop of 200 bars. Models by Campbell (2003) and Tavakoli and Pezeshk (2005) are categorized as hybrid models, translating WUS empirical data and models to the CEUS for assumed parameter ratios between the two regions. Finally, the model by Somerville and others (2001) for nonrift regions is based on full-waveform simulations. Weight assignments were based on model types and will be discussed later in the Weight section below in more detail.

Table 12. Central and Eastern United States ground motion models and weights in the 2008 hazard maps.

[GMM, ground motion model; GridSrc, background-gridded sources; RLME, regional large-magnitude earthquake]

	2008 GMM	Abbreviation	Type	Weight	
				RLME	GridSrc
1.	Frankel and others (1996)	F96	Single corner–point source	0.1	0.125
2.	Toro and others (1997), Toro (2002)	T02	Single corner–finite fault	0.2	0.25
3.	Silva and others (2002)	S02	Single corner–finite fault	0.1	0.125
4.	Atkinson and Boore (2006)				
	• 140 bar stress drop	AB06	Dynamic corner	0.1	0.125
	• 200 bar stress drop			0.1	0.125
5.	Campbell (2003)	C03	Hybrid	0.1	0.125
6.	Tavakoli and Pezeshk (2005)	TP05	Hybrid	0.1	0.125
7.	Somerville and others (2001)	S01	Full-waveform simulation	0.2	0

2014 Models—Major Changes Since 2008

The 2014 hazard maps include two new models that were not available in 2008: Atkinson (2008'), which refers to the Atkinson (2008) model as updated in Atkinson and Boore (2011), and Pezeshk and others (2011). Both of these models use WUS empirical strong motion models and adjust them for use in the CEUS by assuming certain differences between the ground motion characteristics in the two regions. Pezeshk and others (2011) is similar in methodology to the models by Campbell (2003) and Tavakoli and Pezeshk (2005) and is categorized as a hybrid model. Atkinson (2008') is placed under a separate category in the logic tree, namely the "reference empirical" branch, because it uses a slightly different approach in modeling than hybrid GMMs (that is, it uses regional ground motion

observations to develop scaling factors for a WUS GMM and does not use a stochastic or seismological model). Due to this modeling approach, Atkinson (2008') follows a different geometric spreading (GS) than the hybrid models mentioned above, which will be discussed in more detail in the next section. In the 2014 update, we also replace the dynamic corner frequency model by Atkinson and Boore (2006) with their 2011 update, referred to as the Atkinson and Boore (2006'). This updated model has a magnitude-dependent stress drop and therefore covers only one branch of the logic tree. The final list of GMMs used in the 2014 hazard maps is given in table 13.

Table 13. Central and Eastern United States ground motion models and weights in the 2014 hazard maps.

[GMM, ground motion model; GS, geometric spreading; km, kilometers; NA, not applicable; RLME, regional large-magnitude earthquake; >, greater than]

2014 GMM	Abbreviation	Type	Kappa* (hard to firm rock)	GS	Weight**		
					RLME	GridSrc	>500 km
1. Frankel and others (1996)	F96	Single corner	0.01	R^{-1}	0.06	0.06	0.16
2. Toro and others (1997), Toro (2002)	T02	Single corner	0.01	R^{-1}	0.11	0.13	0
3. Silva and others (2002)	S02	Single corner	0.01	R^{-1}	0.06	0.06	0
4. Campbell (2003)	C03	Hybrid	0.01	R^{-1}	0.11	0.13	0.17
5. Tavakoli and Pezeshk (2005)	TP05	Hybrid	0.01	R^{-1}	0.11	0.13	0.17
6. Atkinson and Boore (2006')	AB06'	Dynamic corner	0.02	$R^{-1.3}$	0.22	0.25	0.3
7. Pezeshk and others (2011)	P11	Hybrid	0.02	$R^{-1.3}$	0.15	0.16	0.2
8. Atkinson (2008')	A08'	Reference Empirical	0.02	NA	0.08	0.08	0
9. Somerville and others (2001)	S01	Full waveform	0.01	NA	0.10	0	0

* Hard rock and firm rock, respectively, refer to V_{S30} greater than about 1500 and about 760 meters per second

** Rounded to two decimal places

In previous USGS NSHMP maps, all CEUS GMMs were used up to a 1,000 km distance. In the 2014 update, we use two weighting schemes, one for distances shorter than 500 km and one for distances between 500 and 1,000 km, to improve the maps. Table 13 shows the weights for selected GMMs. For distances longer than 500 km, we remove the models that are not applicable at very large distances and redistribute the weights among the remaining models. The median ground motions for the selected models for distances shorter than 500 km are shown in figure 69 at peak ground acceleration, 0.2-second (5-hertz) spectral acceleration, and 1-second (1-hertz) spectral acceleration for a moment magnitude of 7. In these figures, GMMs are color coded by the model type. In the 2014 update, weight assignments are not only based on the model type, but also on the CEUS parameters, which are discussed below.

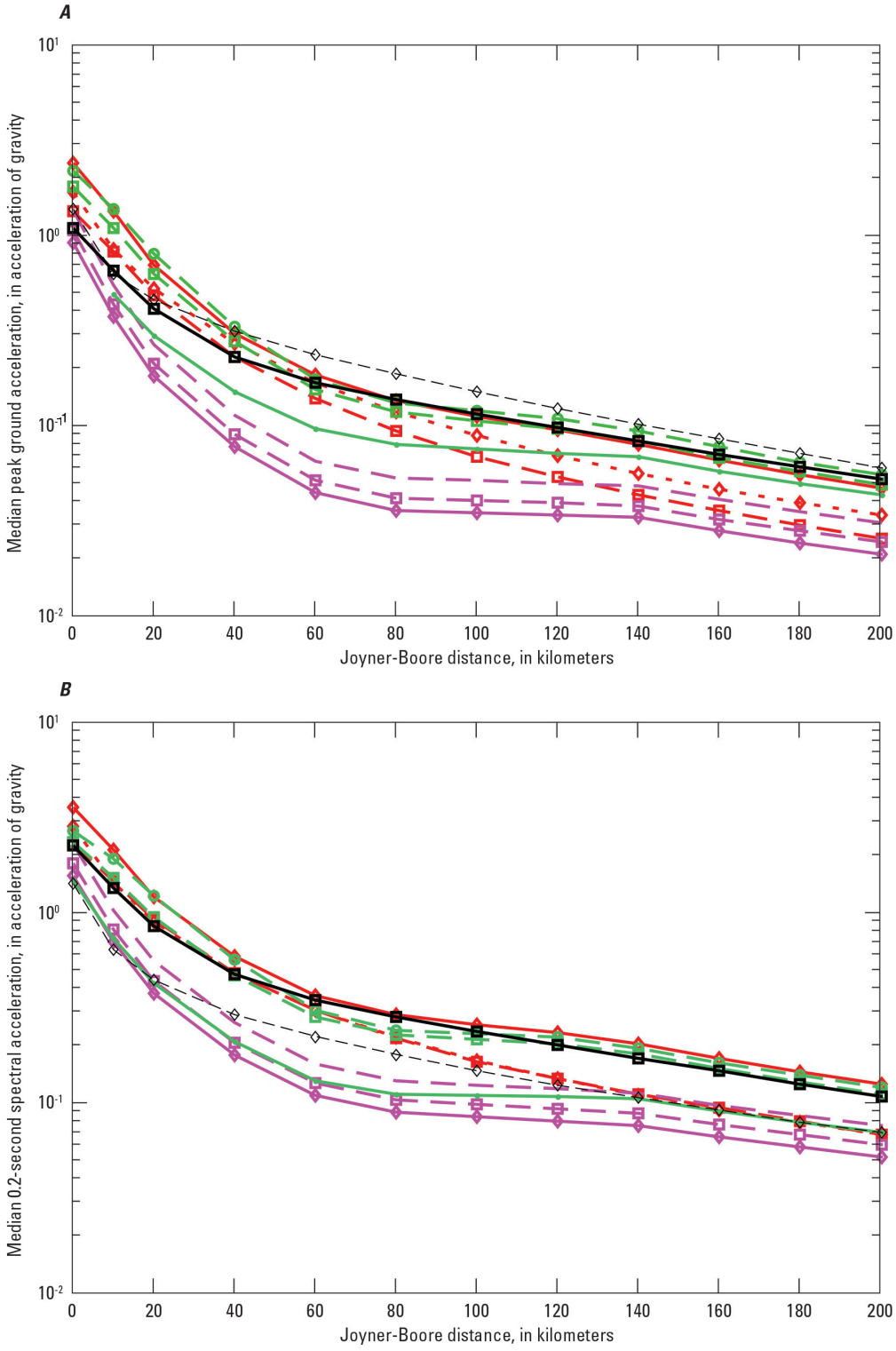

Figure 69. Comparison of Central and Eastern United States median ground motion models by model type. Graphs show ground motion versus distance for *A*, peak ground acceleration; *B*, 0.2-second spectral acceleration; and *C*, 1-second spectral acceleration for an earthquake with moment magnitude of 7 and V_{S30} site conditions of 760 meters per second. Ground motion model abbreviations are defined in table 13.

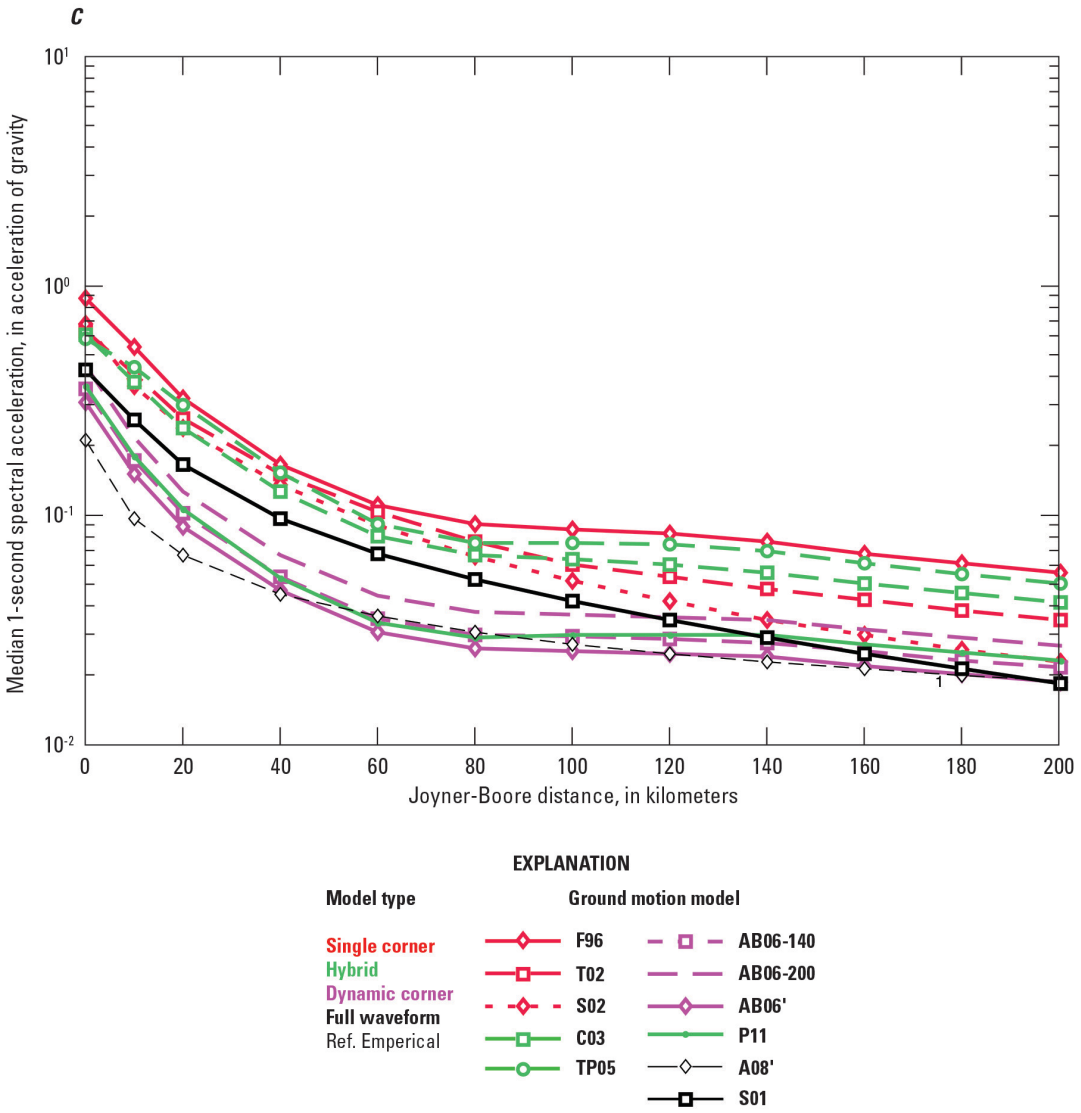

Figure 69. Comparison of Central and Eastern United States median ground motion models by model type. Graphs show ground motion versus distance for *A*, peak ground acceleration; *B*, 0.2-second spectral acceleration; and *C*, 1-second spectral acceleration for an earthquake with moment magnitude of 7 and V_{S30} site conditions of 760 meters per second. Ground motion model abbreviations are defined in table 13.—Continued

Important Parameters for the Central and Eastern United States Ground Motion Models

Two important parameters in modeling of ground motions for the CEUS are Kappa and geometric spreading (GS). Assumptions for these parameters are listed in table 13 for each model. Kappa defines the high-frequency, near-surface site attenuation of the ground motion. Geometric spreading usually has been represented by the inverse of distance from the source (R^{-1}) but in some

recent models developers have preferred $R^{-1.3}$ for distances out to 70 km. In December 2012, the USGS held a workshop on ground motion models where valid reasons/ranges for both R^{-1} and $R^{-1.3}$ were presented. Empirical validation is difficult because of the scarcity of large magnitude events in the region; therefore, we use both types of models for representing epistemic uncertainty. These parameters are considered in addition to the model type to assign our weights in 2014. Figure 70 shows the median ground motions for selected models coded by color based on their geometric spreading.

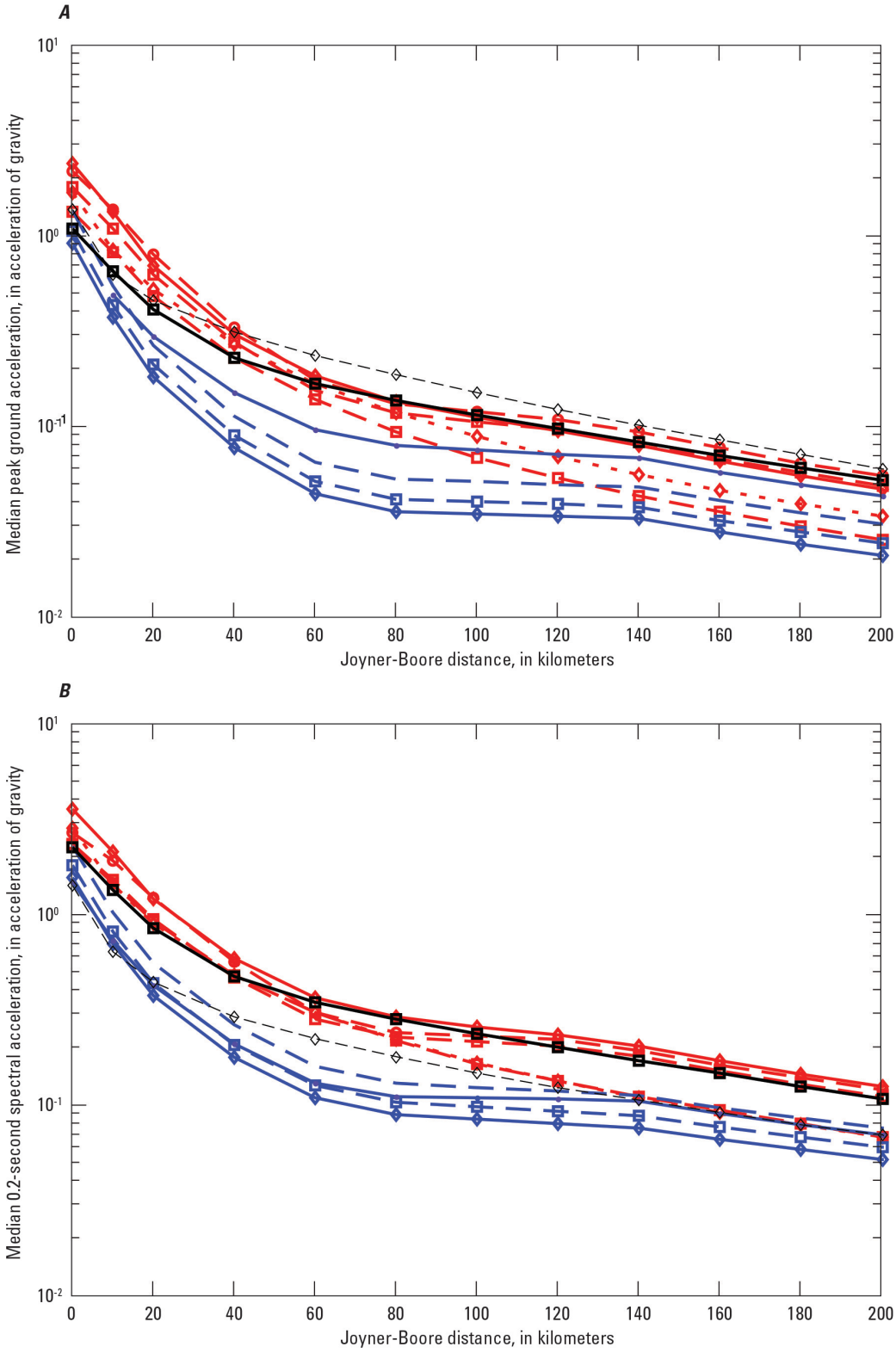

Figure 70. Comparison of Central and Eastern United States median ground motion models by category. Graphs show ground motion versus distance for *A*, peak ground acceleration; *B*, 0.2-second spectral acceleration; and *C*, 1-second spectral acceleration for an earthquake with moment magnitude of 7 and V_{S30} site conditions of 760 meters per second. Ground motion model abbreviations are defined in table 13.

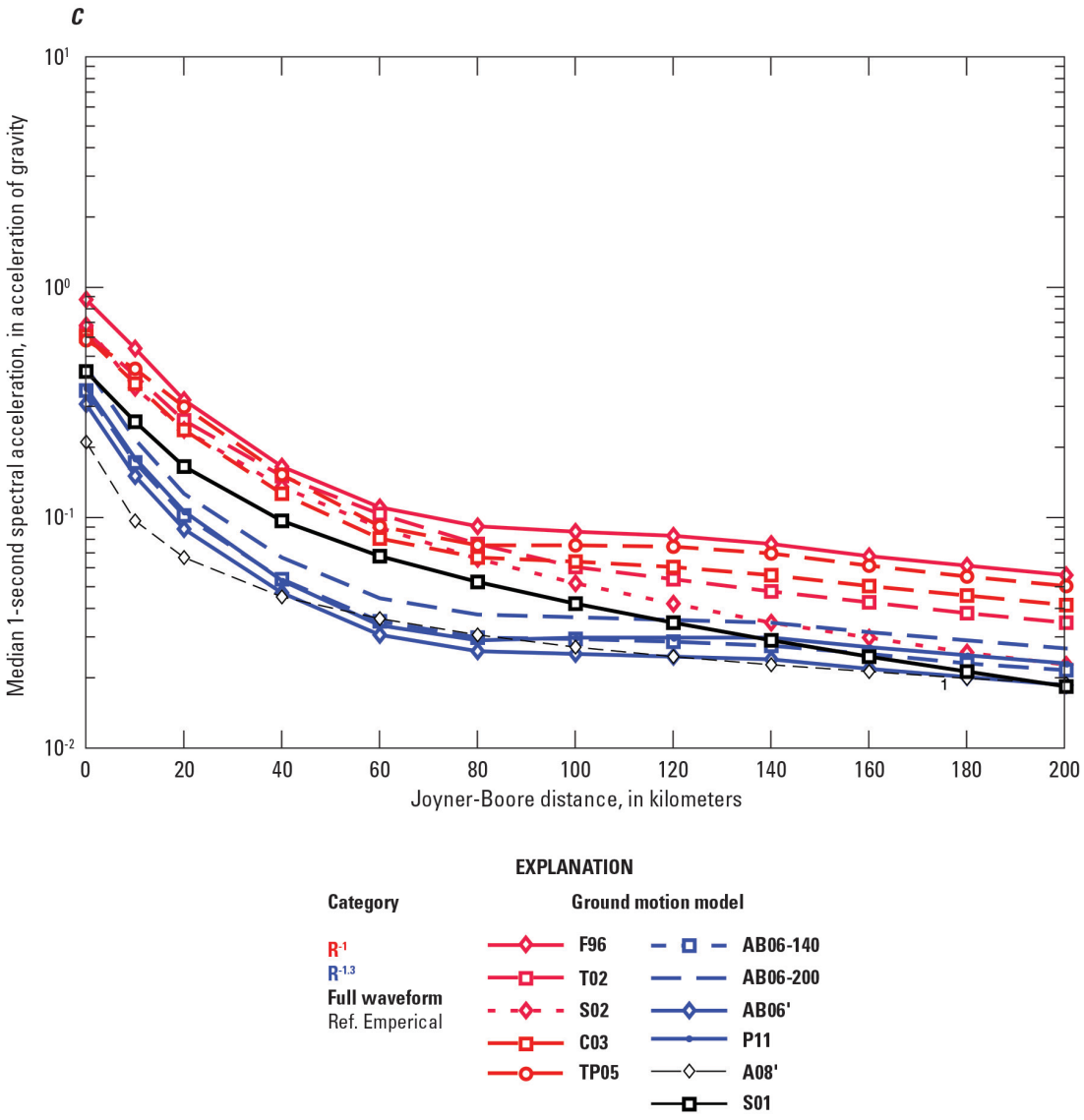

Figure 70. Comparison of Central and Eastern United States median ground motion models by category. Graphs show ground motion versus distance for *A*, peak ground acceleration; *B*, 0.2-second spectral acceleration; and *C*, 1-second spectral acceleration for an earthquake with moment magnitude of 7 and V_{S30} site conditions of 760 meters per second. Ground motion model abbreviations are defined in table 13.—Continued

In the 2014 update, even though Pezeshk and others (2011) is considered an update of Tavakoli and Pezeshk (2005), we do not remove Tavakoli and Pezeshk (2005) based on our discussions with the developer. This decision was made because the two models use two different assumptions on the CEUS parameters, Kappa and GS. Including both models in the hazard maps represents epistemic uncertainty; however, the Tavakoli and Pezeshk (2005) model is given lower weight because of its use of outdated empirical data and models.

Applicability Limits of Models (Magnitude, Distance, Soil Condition)

The applicable range of each model considered for the CEUS varies. The model by Somerville and others (2001) is applicable only for earthquakes with magnitudes greater than 6.0. Therefore, this model is used only for RLME sources. For background seismicity (that is, GridSrc in table 13), this model is removed and the weights for other models are re-normalized.

Recommendations on the applicable distance range varies from modeler to modeler; however, as previously mentioned, for simplicity, in the past USGS NSHMP maps used all CEUS models up to a distance of 1,000 km. In the 2014 update, we improve the maps by removing Toro and others (1997), Toro (2002), Silva and others (2002), Atkinson (2008'), and Somerville and others (2001) for distances between 500 and 1,000 km. The maximum distance recommended by the authors of the mentioned GMMs were 500, 400, 700, and 500 km, respectively.

The CEUS GMMs typically are developed for hard rock conditions (National Earthquake Hazards Reduction Program, NEHRP; Building Seismic Safety Council 2009, site class A, with time-averaged shear wave velocity in the upper 30 m of the crust of $V_{S30} \geq 1{,}500$ m/s); however, the national seismic hazard maps are prepared for a reference site condition on firm rock representing the boundary between NEHRP site classes B and C and specified by $V_{S30}=760$ m/s. Therefore, a conversion from hard to firm rock (NEHRP site class A to BC) is required. Two models provide frequency-dependent conversion factors (table 14). Frankel and others (1996) developed factors using a Kappa of 0.01 for BC site class and 0.006 for A site class. Atkinson and Boore (2011) developed their factors using a Kappa of 0.02 for BC site class and 0.005 for A site class. The factors by Atkinson and Boore (2011) are applied to models with geometric spreading of $R^{-1.3}$ (that is, Atkinson and Boore, 2006'; Pezeshk and others, 2011), Atkinson (2008') is based on a WUS GMM and uses V_{S30} directly as an input parameter, and factors by Frankel and others (1996) are applied to all other models for conversion to firm rock. As can be seen in table 14, differences between the two models are greater at lower spectral periods and smaller at longer periods. As noted in Atkinson and Boore (2011), there is considerable uncertainty in these crude correction factors, and they may greatly underestimate the actual amplifications for CEUS sites, because of the prevalence of soils overlying very hard rock, which sets up resonance conditions in this region.

Table 14. Frequency-dependent factors to convert from hard rock (NEHRP site class A) to firm rock (NEHRP site class BC).

[PGA, peak ground acceleration]

Spectral period	Frankel and others (1996)	Atkinson and Boore (2011)
PGA	1.52	1.04*
0.1 second	1.74	1.04
0.2 second	1.76	1.31
0.3 second	1.72	1.41
0.5 second	1.58	1.40
1.0 second	1.34	1.27
2.0 second	1.20	1.26

*The amplification factor at PGA can be distance dependent as noted in Atkinson (2008). The value listed is from Atkinson and Boore (2011) and is applicable to distances near 10 kilometers.

Weights

The weighting scheme for the GMMs in 2008 was based on their model types. The single-corner models received a weight of 0.4, with finite-fault models and point-source models each receiving weights of 0.3 and 0.1, respectively. Dynamic-corner models, hybrid models, and full-waveform simulation based models each received a weight of 0.2. Each type of model has certain advantages and takes into account ground motion features that others do not; therefore, this kind of weighting accounts for epistemic uncertainty in modeling. Figure 69 shows the models grouped by type. In 2008, most GMMs incorporated R^{-1} geometric spreading; however, the Atkinson and Boore (2006) models received 20-percent weight and applied alternative stress drops of 140 and 200 bars and $R^{-1.3}$ geometric spreading.

In 2014, in addition to the model type, we also consider geometric spreading and Kappa to distribute the weights. Weights are developed based on the logic tree shown in figure 71. Based on workshop discussions and the results of some external studies (that is, residual analysis and EPRI study described below), the group of models with $R^{-1.3}$ geometric spreading receive a larger weight relative to 2008. Consequently, proportional weights are assigned to the two alternative Kappa models. Figure 70 shows the models grouped by their geometric spreading. In general, $R^{-1.3}$ models have lower median ground motions than R^{-1} models. Therefore, the combined median model for 2014 is lower than that in 2008, as shown in figure 72, for moment magnitudes of 6.5, 7.0, and 7.5, and distances of 20 and 100 km on hard rock site conditions. Figure 73 shows the attenuation of the combined median model with distance at a moment magnitude of 7.0 on firm rock site conditions for peak ground acceleration, 0.2-second (5-hertz) spectral acceleration, and 1-second (1-hertz) spectral acceleration. Although it is not shown on figure 73, in general, the 2014 combination is closer to the 2008 combination for smaller magnitudes (see fig. 72).

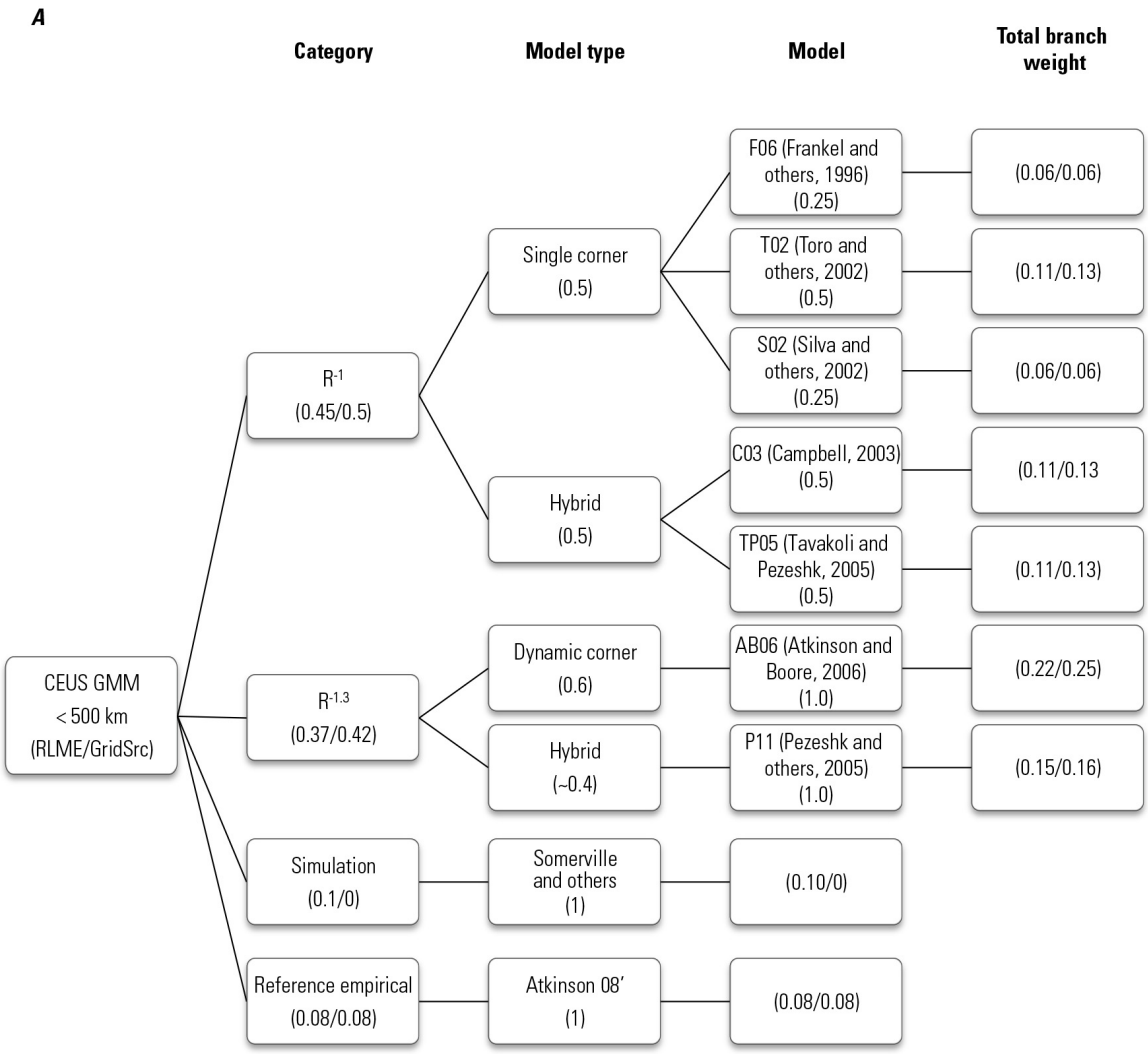

Figure 71. Logic trees for ground motion models in the Central and Eastern United States (CEUS GMM) at distances *A*, less than or equal to 500 kilometers and *B*, greater than 500 kilometers. Assigned branch weight shown in parentheses.

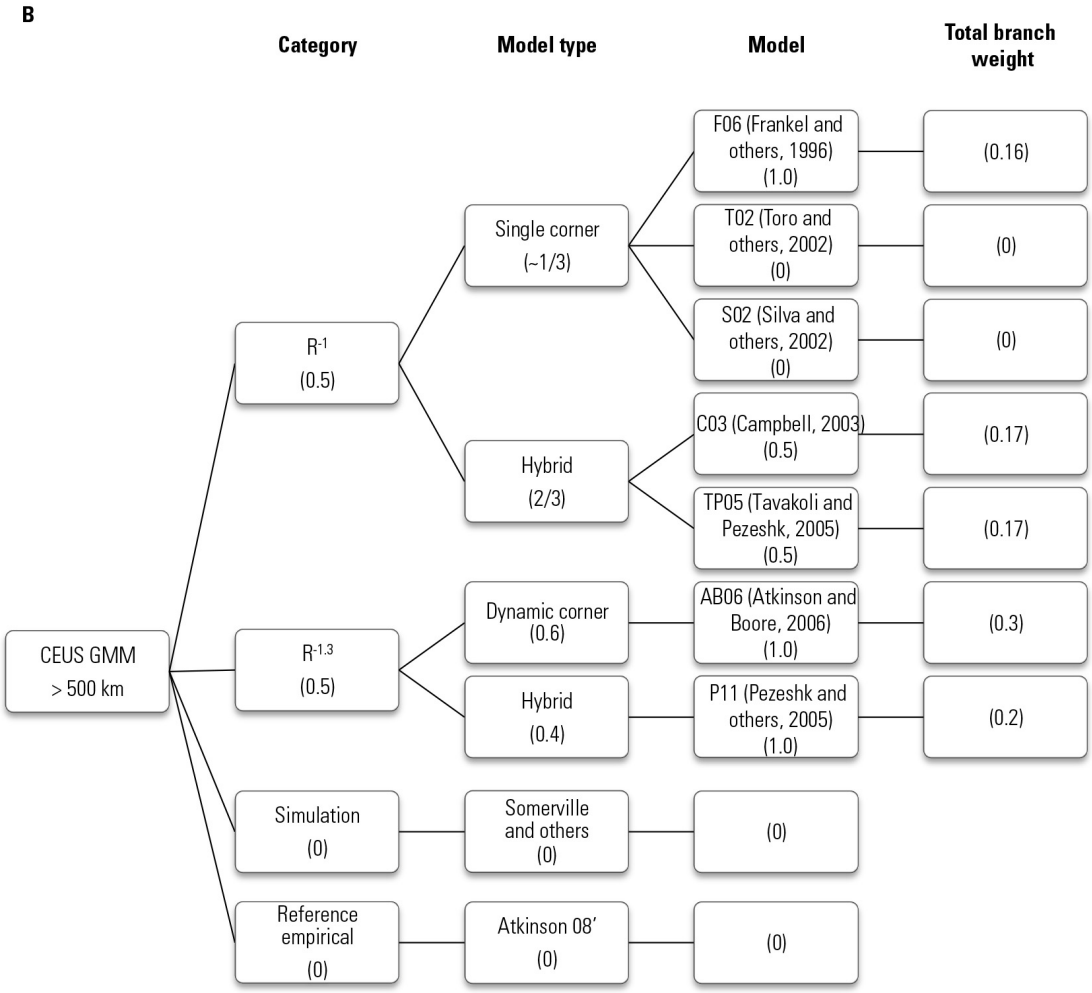

Figure 71. Logic trees for ground motion models in the Central and Eastern United States (CEUS GMM) at distances *A*, less than or equal to 500 kilometers and *B*, greater than 500 kilometers. Assigned branch weight shown in parentheses.—Continued

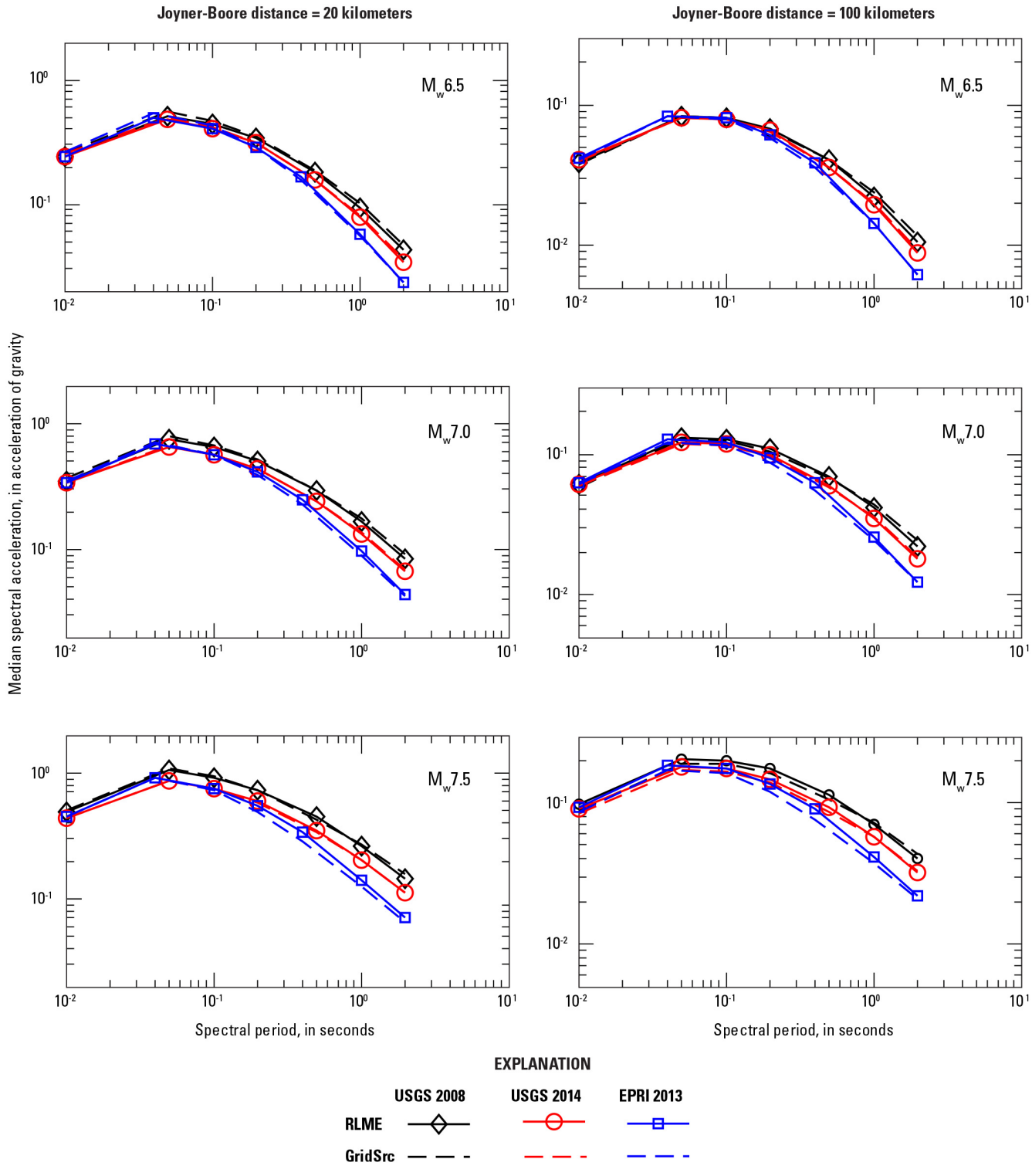

Figure 72. Comparison of median spectral acceleration for 2008 and 2014 USGS, and 2013 EPRI ground motion models. Graphs show results of combined median ground motion models for three magnitudes at two distances and V_{S30} site conditions of 760 meters per second.

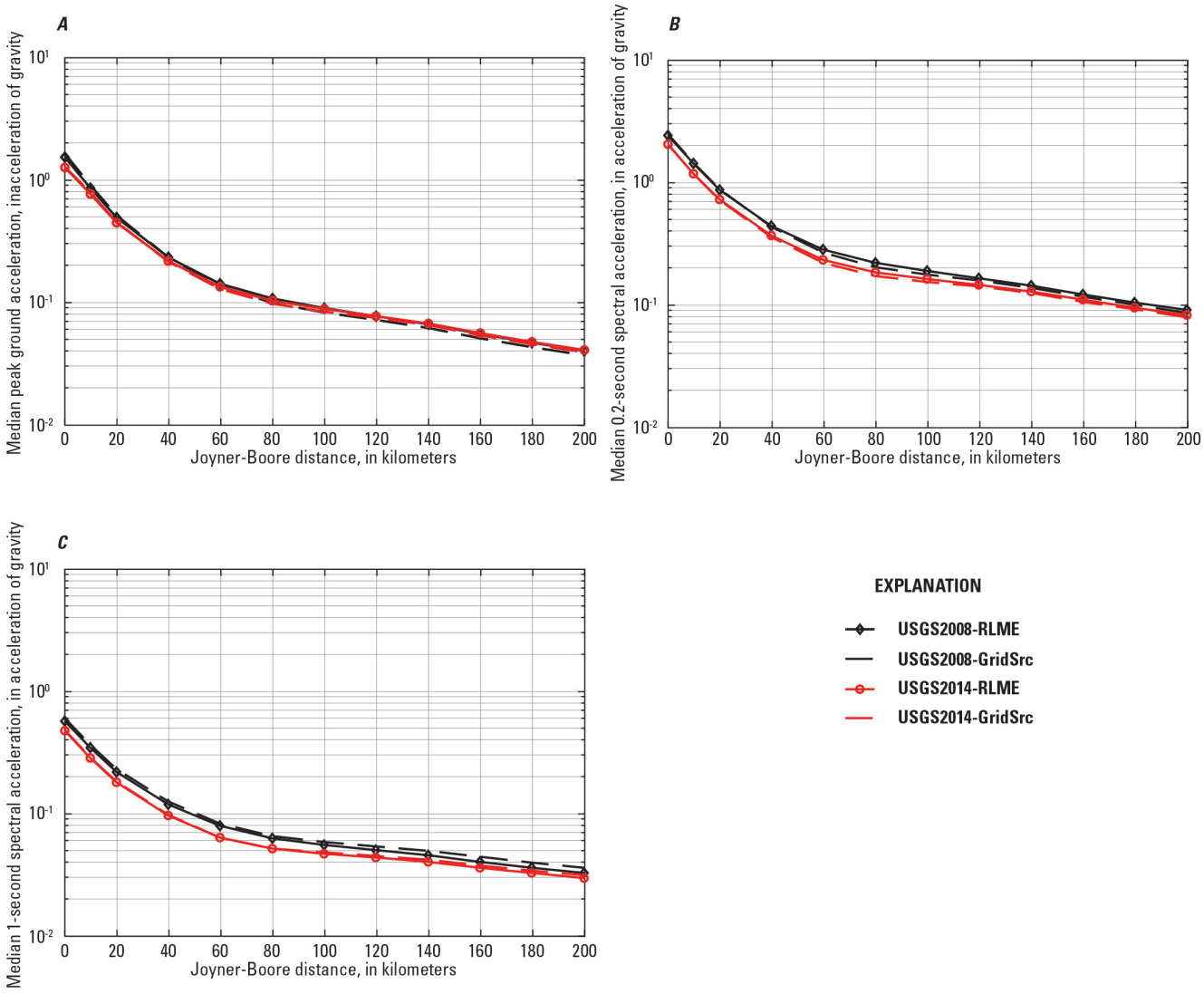

Figure 73. Comparison of combined Central and Eastern United States ground motion models versus distance for V_{S30} site conditions of 760 meters per second for an earthquake with moment magnitude of 7. Graphs show *A*, peak ground acceleration, *B*, 0.2-second (5-hertz) spectral acceleration, and *C*, 1-second (5-hertz) spectral acceleration for Central and Eastern United States sources using ground motion models for the 2008 and 2014 version of the maps.

Additional considerations in assigning the weights came from external studies comparing GMM equations to CEUS earthquake data (written commun., Christine Goulet and Chris Cramer; Electrical Power Research Institute, 2013). We did not use these studies directly, but rather considered their results as additional guidelines and tools. Two external studies (personal commun., Christine Goulet and Chris Cramer; Electrical Power Research Institute, 2013) utilized the NGA-East preliminary database of ground motions for the CEUS to perform residual analyses for each of the GMMs. One study examined total residuals and, by averaging over various scenarios and over the three spectral periods used by the USGS, proposed bias factors to rank the fit of individual models to data. Another study used mixed-effects residuals, separating residuals into between-event and within-event terms and looking at patterns

with magnitude and distance separately. This study qualitatively evaluated each model within and outside its applicability range. Both studies offer useful comparisons, but suffer from the disadvantage of data scarcity for moderate to large magnitudes that have significant contribution to hazard. Therefore, we use these residual studies only as guidelines in our decision making but not as direct ranking tools.

Another external study that we considered was that of the Electric Power Research Institute (EPRI) project on assessing CEUS ground motions (Electrical Power Research Institute, 2013). The EPRI model categorizes the CEUS GMMs into different classes, and assigns weights to each class based on the confidence in models and their fit to available data. Their classes are also based on the R^{-1} and $R^{-1.3}$ geometric spreading models. The EPRI model was not available in final form by May 2013 for this update; however, the steering committee encouraged the use of the EPRI model in establishing GMM weights. We compared our weighted combination of GMMs to that of Electrical Power Research Institute (2013). Figure 72 shows examples of this comparison at magnitudes 6.5, 7, and 7.5, for two distance measures of 20 and 100 km, on hard rock conditions. In general, even though our 2014 model is lower than our 2008 model, it is closer to that of Electrical Power Research Institute (2013). At 0.2 and 1 second, the model by Electrical Power Research Institute (2013) is slightly lower than our 2014 weighted combination.

To show the difference in median ground motion since 2008, the ground motion combinations according to the 2008 USGS model (table 12) and the 2014 USGS model (table 13) are plotted versus distance in figure 73 for peak ground acceleration, 0.2-second (5-hertz) spectral acceleration, and 1-second (1-hertz) spectral acceleration, for a magnitude of 7.0 on firm rock site conditions. The subplots in this figure are for distances up to 200 km where ground motions are of significant amplitudes. In general, at short to moderate distance ranges the new 2014 combination is lower than the 2008 combination (lower at 1-second and 0.2-second spectral acceleration than at PGA). Although not shown in figure 73, at longer distances (greater than 500 km), the 2014 combination is a little higher than that of 2008 because of changes mentioned previously; however, these ground motions at such long distances are very small, around 0.01 g, and consequently their contribution to hazard is minimal.

Central and Eastern United States Difference and Ratio Maps—Comparing 2014 and 2008 Ground Motion Models

In this section, we discuss the changes in the 2014 hazard maps caused by GMMs for the CEUS by showing difference and ratio maps for 2-percent probability of exceedance in 50 years on a uniform firm rock site condition at peak ground acceleration, 0.2-second (5-hertz) spectral acceleration, and 1-second (1-hertz) spectral acceleration with 5-percent damping. These maps illustrate a deaggregation of the hazard and show the relative contribution of an individual GMM to the overall hazard. The difference maps demonstrate the difference between the probabilistic ground motions obtained using the 2014 seismic source model and an individual 2014 GMM, and the probabilistic ground motions obtained using the 2014 seismic source model and the weighted combination of all nine 2014 GMMs. The ratios also use the 2014 source model and are made by dividing the probabilistic ground motions from an individual GMM by the probabilistic ground motions from the weighted combination of all nine GMMs.

Probabilistic seismic hazard difference and ratio maps for Frankel and others (1996, F96), Toro (2002, T02), Silva and others (2002, S02), Atkinson and Boore (2006, AB06'), Atkinson (2008, A08'), Campbell (2003, C03), Tavakoli and Pezeshk (2005, TP05), Pezeshk and others (2011, P11), and Somerville and others (2001, S01) GMMs are shown in figures 74–79. Earthquakes on faults and within background sources in the CEUS are modeled with magnitudes ranging from M_w4.7 to 8.0 and the mechanisms are not specified CEUS earthquakes.

Ratio maps show variability among the 2014 GMMs ranging from below 0.5 up to a factor of 2, and the differences range within about ±0.5 g. Note that most significant differences between GMMs shown in figures 74–79 are seen at very close proximity of the faults in regions with higher activity rates. Models with $R^{-1.3}$ attenuation have lower ground motions than models with R^{-1} attenuation. The Somerville and others (2001) and the Atkinson (2008') models are more variable, sometimes higher than average and sometimes lower.

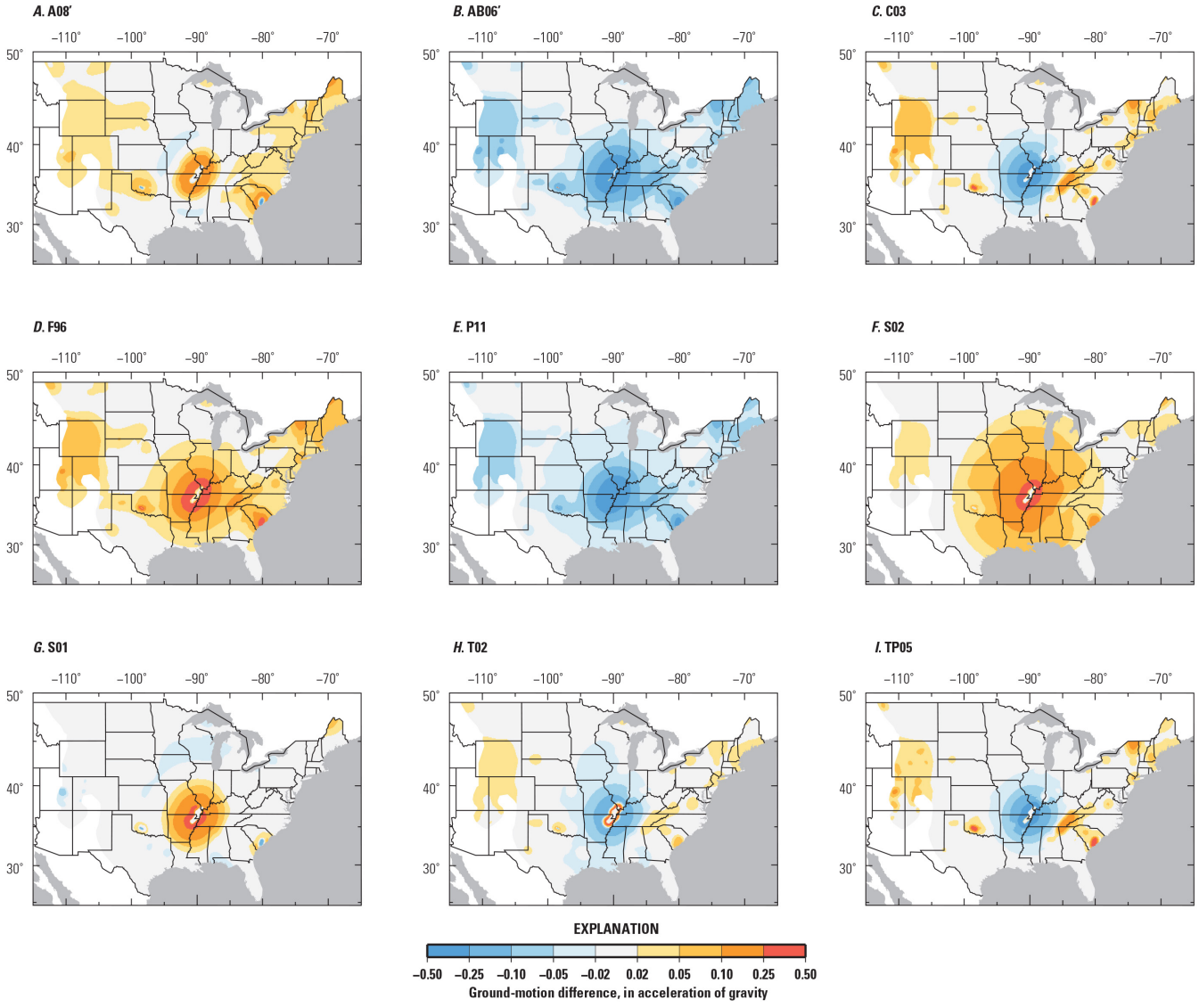

Figure 74. Maps showing difference in peak ground acceleration from individual ground motion models in the Central and Eastern United States compared to the 2008 model at 2-percent in 50 years probability of exceedance and V_{S30} site conditions of 760 meters per second. *A*, A08' (Atkinson, 2008); *B*, AB06' (Atkinson and Boore, 2006); *C*, C03 (Campbell, 2003); *D*, F96 (Frankel and others, 1996); *E*, P11 (Pezeshk and others, 2011); *F*, S02 (Silva and others, 2002); *G*, S01 (Somerville and others, 2001); *H*, T02 (Toro, 2002); and *I*, TP05 (Tavakoli and Pezeshk, 2005). Western United States sources are not included.

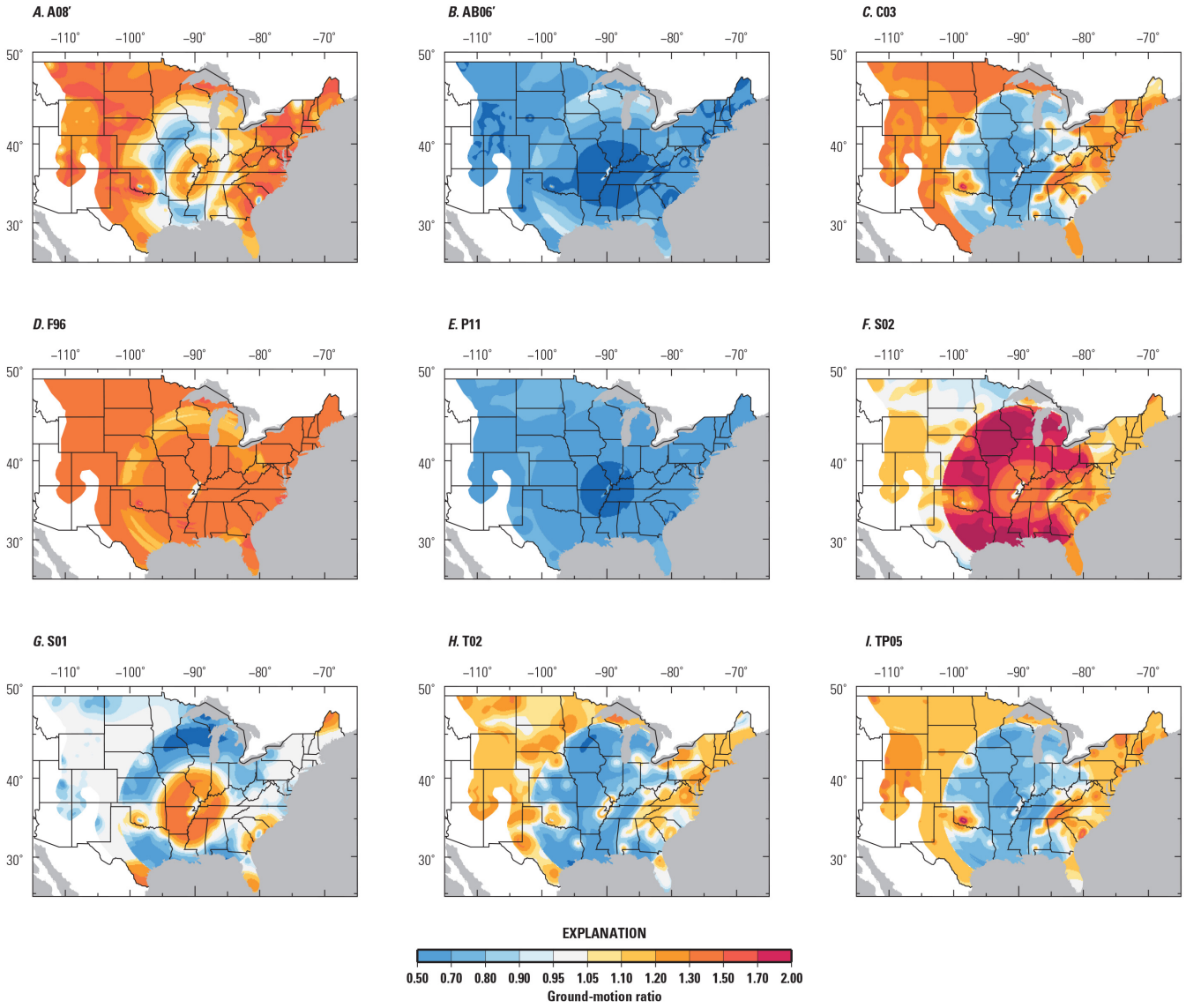

Figure 75. Maps showing ratio of peak ground acceleration from individual ground motion models in the Central and Eastern United States compared to the 2008 model at 2-percent in 50 years probability of exceedance and V_{S30} site conditions of 760 meters per second. *A*, A08' (Atkinson, 2008); *B*, AB06' (Atkinson and Boore, 2006); *C*, C03 (Campbell, 2003); *D*, F96 (Frankel and others, 1996); *E*, P11 (Pezeshk and others, 2011); *F*, S02 (Silva and others, 2002); *G*, S01 (Somerville and others, 2001); *H*, T02 (Toro and others, 2002); and *I*, TP05 (Tavakoli and Pezeshk, 2005). Western United States sources are not included.

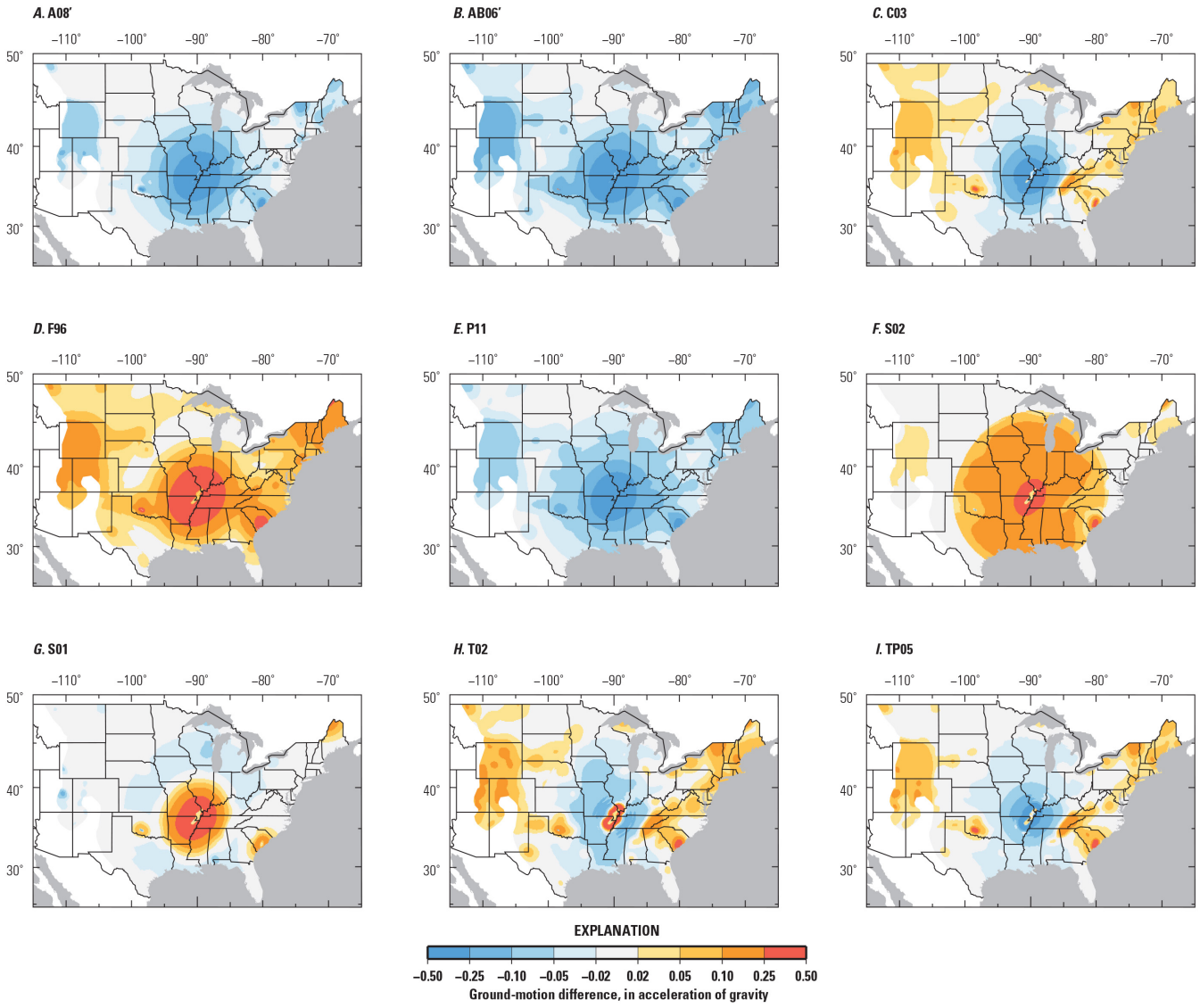

Figure 76. Maps showing difference in 0.2-second (5-hertz) spectral acceleration from individual ground motion models in the Central and Eastern United States compared to the 2008 model at 2-percent in 50 years probability of exceedance and V_{S30} site conditions of 760 meters per second. *A*, A08' (Atkinson, 2008); *B*, AB06' (Atkinson and Boore, 2006); *C*, C03 (Campbell, 2003); *D*, F96 (Frankel and others, 1996); *E*, P11 (Pezeshk and others, 2011); *F*, S02 (Silva and others, 2002); *G*, S01 (Somerville and others, 2001); *H*, T02 (Toro and others, 2002); and *I*, TP05 (Tavakoli and Pezeshk, 2005). Western United States sources are not included.

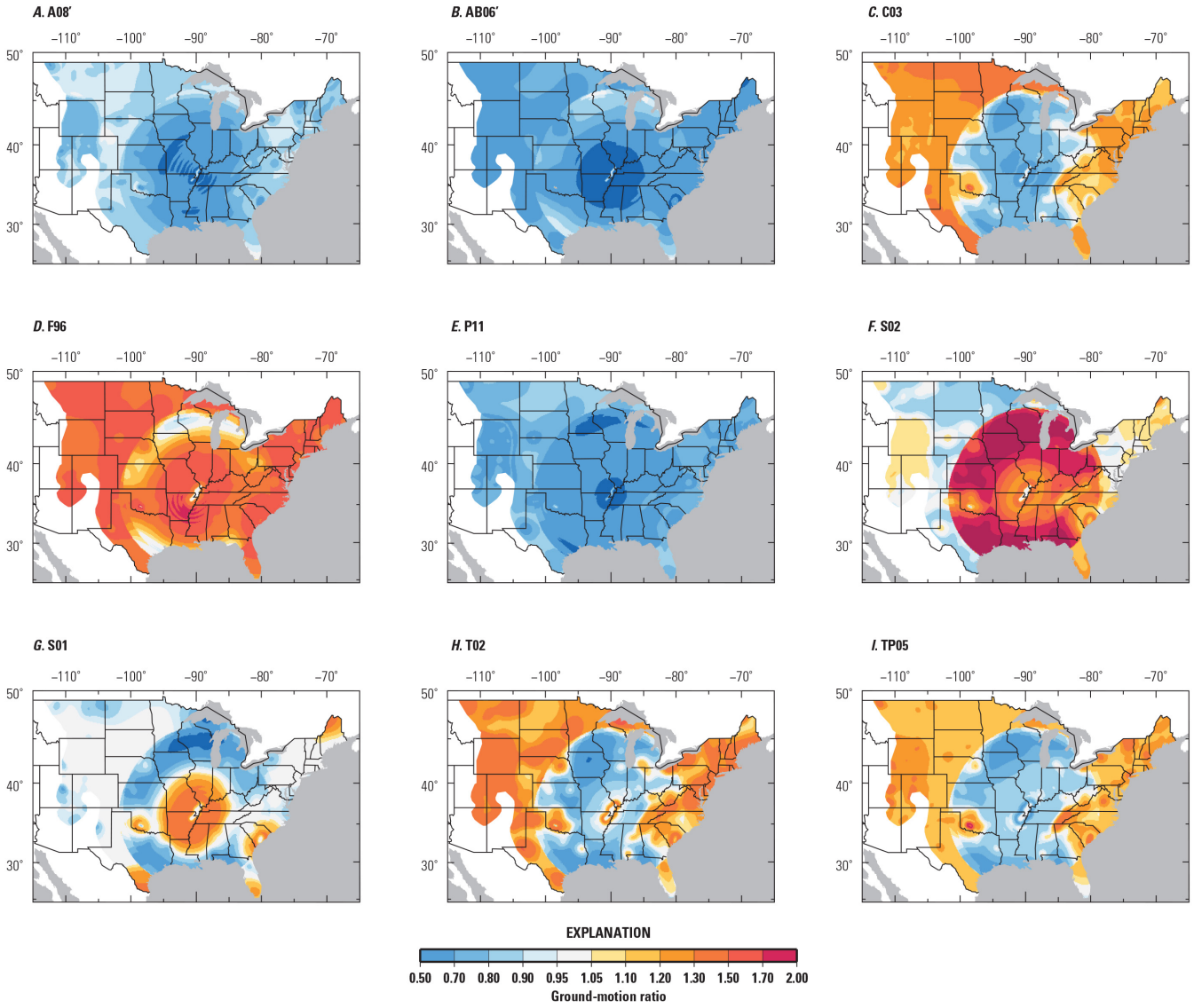

Figure 77. Maps showing ratio of 0.2-second (5-hertz) spectral acceleration from individual ground motion models in the Central and Eastern United States compared to the 2008 model at 2-percent in 50 years probability of exceedance and V_{S30} site conditions of 760 meters per second. *A*, A08' (Atkinson, 2008); *B*, AB06' (Atkinson and Boore, 2006); *C*, C03 (Campbell, 2003); *D*, F96 (Frankel and others, 1996); *E*, P11 (Pezeshk and others, 2011); *F*, S02 (Silva and others, 2002); *G*, S01 (Somerville and others, 2001); *H*, T02 (Toro and others, 2002); and *I*, TP05 (Tavakoli and Pezeshk, 2005). Western United States sources are not included.

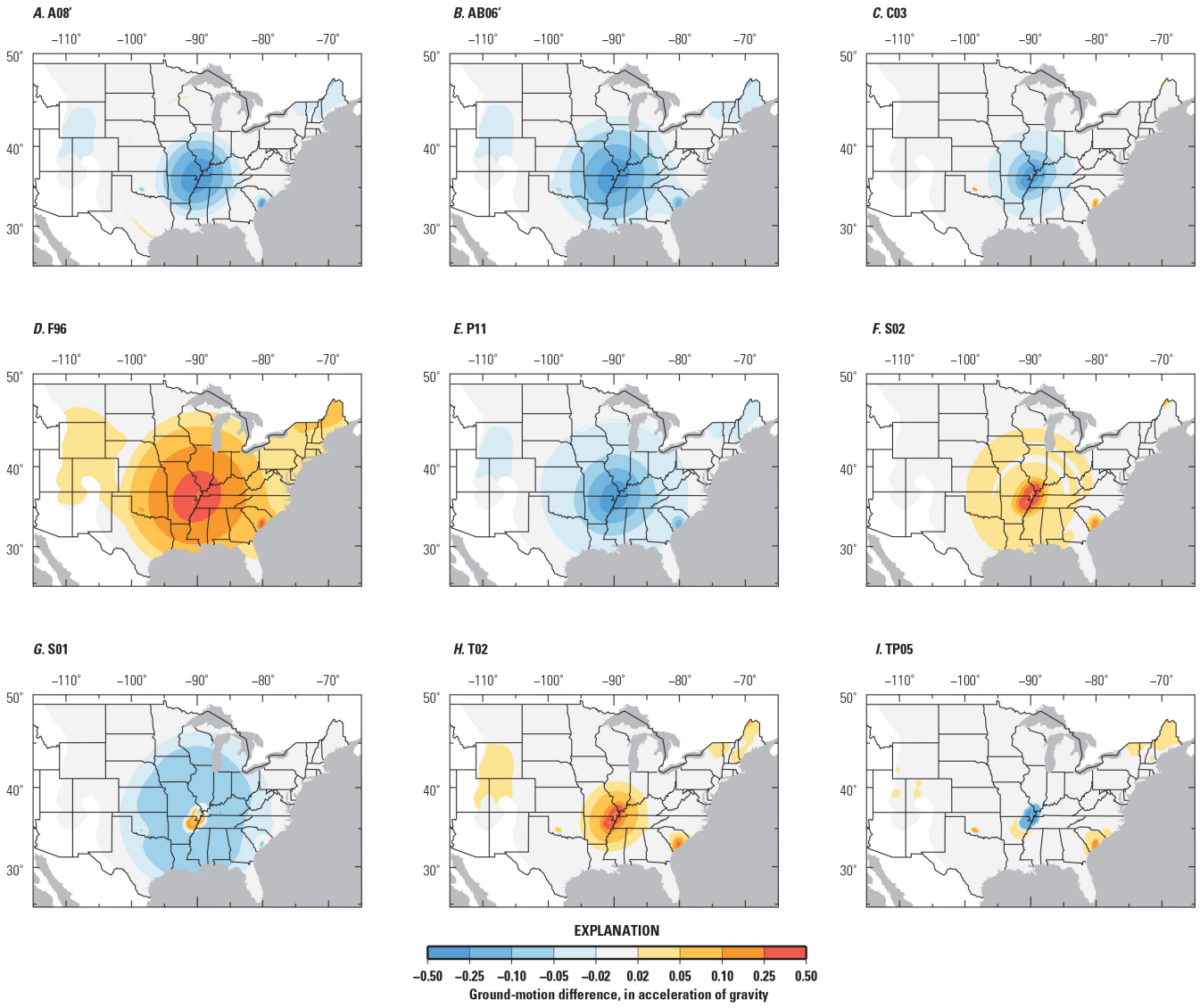

Figure 78. Maps showing difference in 1-second (1-hertz) spectral acceleration from individual ground motion models in the Central and Eastern United States compared to the 2008 model at 2-percent in 50 years probability of exceedance and V_{S30} site conditions of 760 meters per second. *A*, A08' (Atkinson, 2008); *B*, AB06' (Atkinson and Boore, 2006); *C*, C03 (Campbell, 2003); *D*, F96 (Frankel and others, 1996); *E*, P11 (Pezeshk and others, 2011); *F*, S02 (Silva and others, 2002); *G*, S01 (Somerville and others, 2001); *H*, T02 (Toro and others, 2002); and *I*, TP05 (Tavakoli and Pezeshk, 2005). Western United States sources are not included.

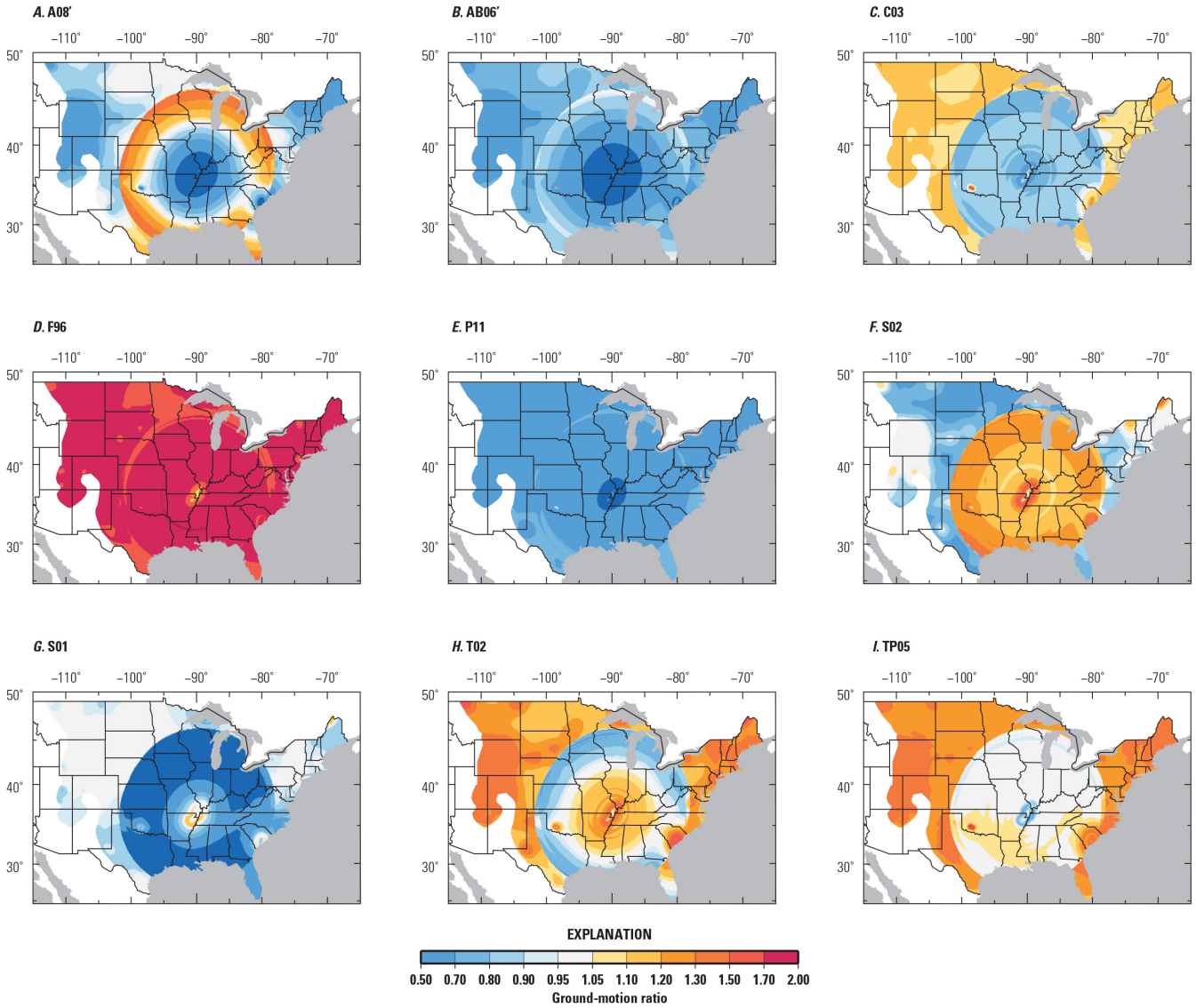

Figure 79. Maps showing ratio of 1-second (1-hertz) spectral acceleration from individual ground motion models in the Central and Eastern United States compared to the 2008 model at 2-percent in 50 years probability of exceedance and V_{S30} site conditions of 760 meters per second. *A*, A08' (Atkinson, 2008); *B*, AB06' (Atkinson and Boore, 2006); *C*, C03 (Campbell, 2003); *D*, F96 (Frankel and others, 1996); *E*, P11 (Pezeshk and others, 2011); *F*, S02 (Silva and others, 2002); *G*, S01 (Somerville and others, 2001); *H*, T02 (Toro and others, 2002); and *I*, TP05 (Tavakoli and Pezeshk, 2005). Western United States sources are not included.

Western United States

For the WUS, all ground motion models are updated. In this section we discuss the new models and their assigned weights.

2008 Models and Weights

In 2008, three of the NGA relations (Power and others, 2008) were implemented in the national seismic hazard maps. The NGA project was coordinated by the PEER center and developed a global strong motion database containing 173 earthquakes and 5 new GMMs for shallow crustal earthquakes in active tectonic regions. For 2008, the USGS selected three of the NGA models and used V_{S30} as an input parameter to generate the maps for reference site conditions. Each of the modelers used a different subset of the global database to develop and constrain their models. The models were weighted equally and additional epistemic uncertainty was added based on the database used by two of the GMMs to account for the close interactions between modelers. The models used in 2008 are listed in table 15.

Table 15. Western United States ground motion models and weights in the 2008 hazard maps.
[GMM, ground motion model; NGA, Next Generation Attenuation project]

2008 GMM	Abbreviation	Source	Weight
1. Boore and Atkinson (2008)	BA08	NGA	1/3
2. Campbell and Bozorgnia (2008)	CB08	NGA	1/3
3. Chiou and Youngs (2008)	CY08	NGA	1/3

2014 Model Updates

In 2010, PEER started phase 2 of the NGA project (NGA-West2). Tasks related to the horizontal component of ground motion concluded in 2013, with final PEER reports published and posted on May 15, 2013 (Bozorgnia and others, 2014). We started interactions with NGA-West2 modelers in 2012, implementing preliminary models in stages, looking at their individual effects on the hazard maps, and providing feedback to the developers. The NGA-West2 project updated the NGA (hereafter referred to as "NGA-West1") database for small, moderate, and large magnitude events, as well as the five GMMs for horizontal component of ground motion. Thousands of ground motions recorded worldwide since 2003 have been uniformly processed and added, resulting in the NGA-West2 database (see figure 80 for magnitude-distance distribution), which is more than a factor of two larger than that of the NGA-West1. The new database includes ground motions recorded during the 2003 Bam (Iran), 2004 Parkfield (Calif.), 2007 Niigata Chuetsu-oki (Japan), 2008 magnitude 7.9 Wenchuan (China), 2009 L'Aquila (Italy), 2010 Darfield (New Zealand), 2011 Christchurch (New Zealand), and more small-magnitude data from California (Bozorgnia and others, 2014).

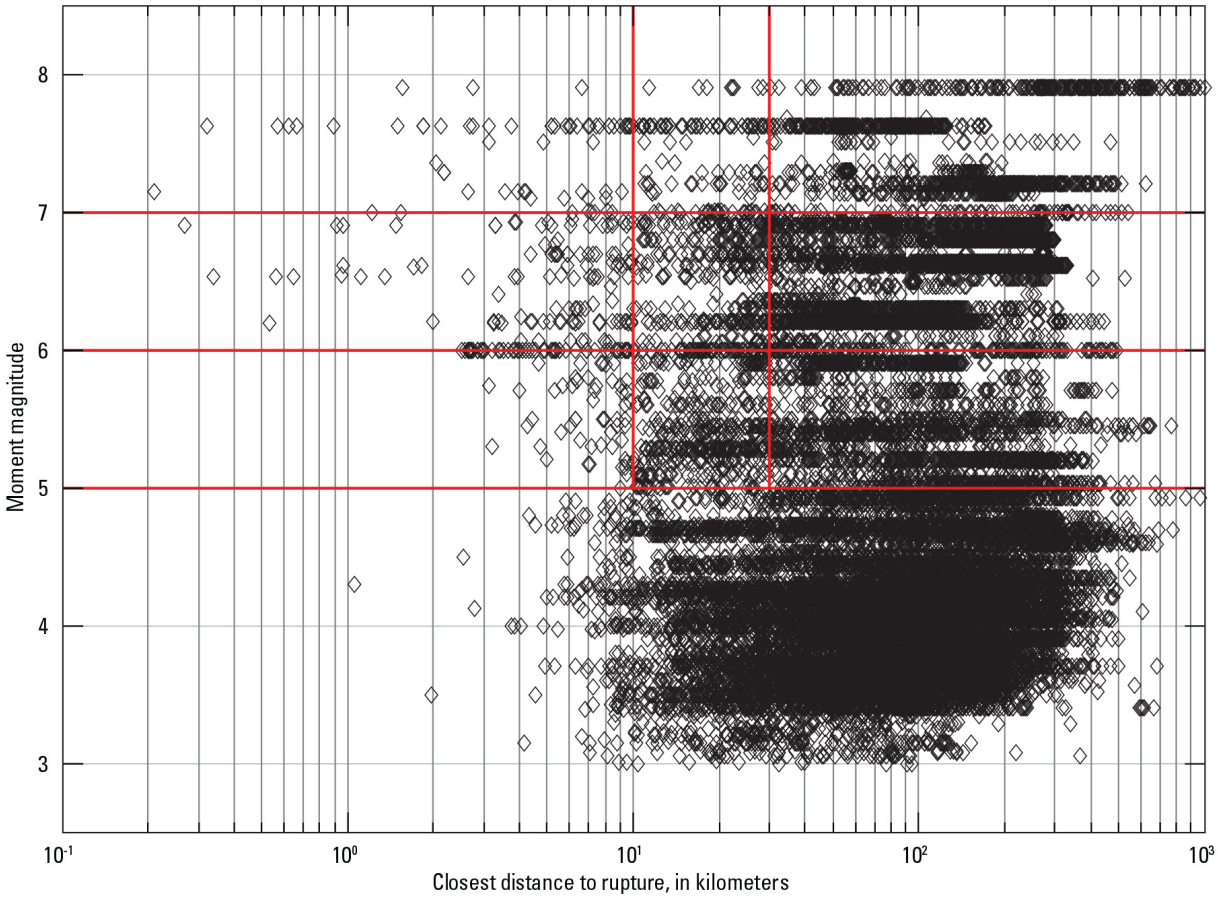

Figure 80. Magnitude-distance distribution of records in phase 2 of the Next Generation Attenuation project (NGA-West2) database.

Changes in the five NGA-West2 GMMs are not only due to the extended database, but also caused by other modeling features that represent significant advances compared to NGA-West1 models. We also show the changes in the median and standard deviations of each model for certain scenarios (see figs. 81–84). In general, compared to the 2008 models, NGA-West2 models have lower median ground motions for small magnitude events, significant changes in hanging wall terms due to better modeling of this feature using additional simulations, and higher standard deviations, especially at smaller magnitudes caused by the extended database. All five NGA-West2 models are included in the 2014 USGS NSHMP maps for the reference firm site conditions of V_{S30}=760 m/s.

All GMMs used for the WUS and their assigned weights are shown in table 16. In addition to the NGA-West2 models, other GMMs (for example, an updated version of Graizer and Kalkan, 2011) also were considered; however, due to late publication or failure to satisfy our GMM selection criteria, they were not incorporated in the 2014 update of the USGS NSHMP maps. The model by Idriss (2013) lacks nonlinear soil modeling and cannot be used for maps of soft soil conditions, but inclusion of this model for the reference firm rock site condition maps provides epistemic uncertainty. The weights are distributed evenly between all GMMs with the exception of the Idriss (2013) model, which is assigned a

lower weight because it does not have as many detailed modeling features (for example, the lack of distinction between normal and strike-slip fault mechanisms, hanging wall term, and basin depth term).

Table 16. Western United States ground motion models and weights in the 2014 hazard maps.
[GMM, ground motion model; NGA, Next Generation Attenuation project]

	2014 GMM*	Abbreviation	Source	Weight
1.	Abrahamson and others (2013, 2014)	ASK13	NGA-West2	0.22
2.	Boore and others (2013, 2014)	BSSA13	NGA-West2	0.22
3.	Campbell and Bozorgnia (2013, 2014)	CB13	NGA-West2	0.22
4.	Chiou and Youngs (2013, 2014)	CY13	NGA-West2	0.22
5.	Idriss (2013, 2014)	I13	NGA-West2	0.12

*References are based on May 2013 PEER reports, but the final models implemented in the USGS NSHMP maps are based on the modelers' Earthquake Spectra publications appearing in 2014, listed in the references.

Figures 81–83 show the median values of the GMMs used in 2008 and 2014 hazard maps at peak ground acceleration, 0.2-second (5-hertz) spectral acceleration, and 1-second (1-hertz) spectral acceleration. Two magnitudes, 5.0 (left subplots) and 7.0 (right subplots), are displayed. Figure 81 is for an example of a strike-slip fault, whereas figures 82 and 83 show an example over the hanging wall side of a normal fault and a reverse fault, respectively. Figure 84 shows how standard deviation (commonly known as "sigma") varies with magnitude for the selected GMMs at 0.2-second and 1-second spectral acceleration. More detailed comparison of NGA-West2 models can be found in Gregor and others (2014).

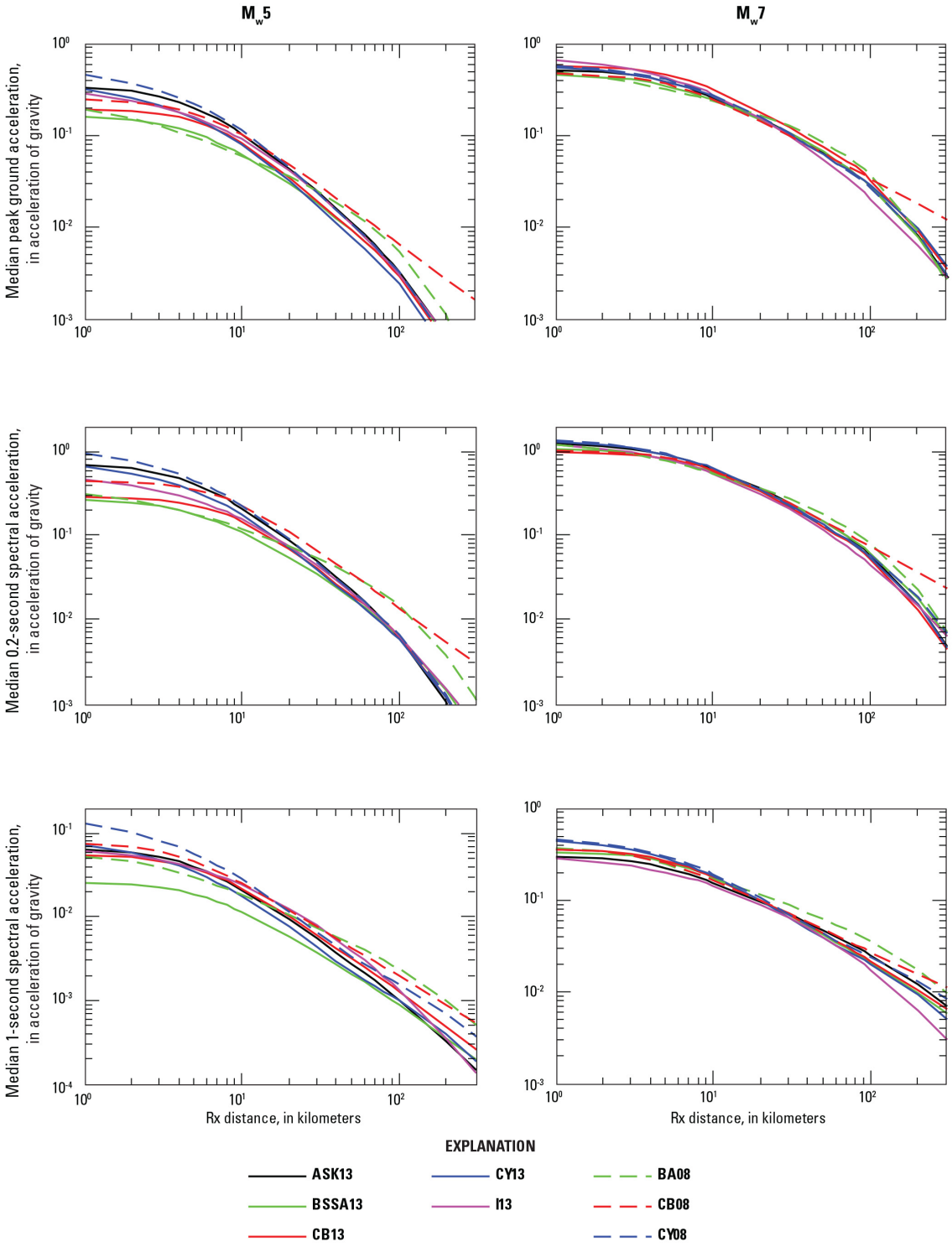

Figure 81. Comparison of median ground motion versus distance for a strike slip fault at three periods and two magnitudes and V_{S30} site conditions of 760 meters per second. *A*, Peak ground acceleration for moment magnitude 5 earthquake; *B*, peak ground acceleration for moment magnitude 7 earthquake; *C*, 0.2-second (5-hertz) spectral acceleration for moment magnitude 5 earthquake; *D*, 0.2-second (5-hertz) spectral acceleration for moment magnitude 7 earthquake; *E*, 1-second (1-hertz) spectral acceleration for moment magnitude 5 earthquake; and *F*, 1-second (1-hertz) spectral acceleration for moment magnitude 7 earthquake.

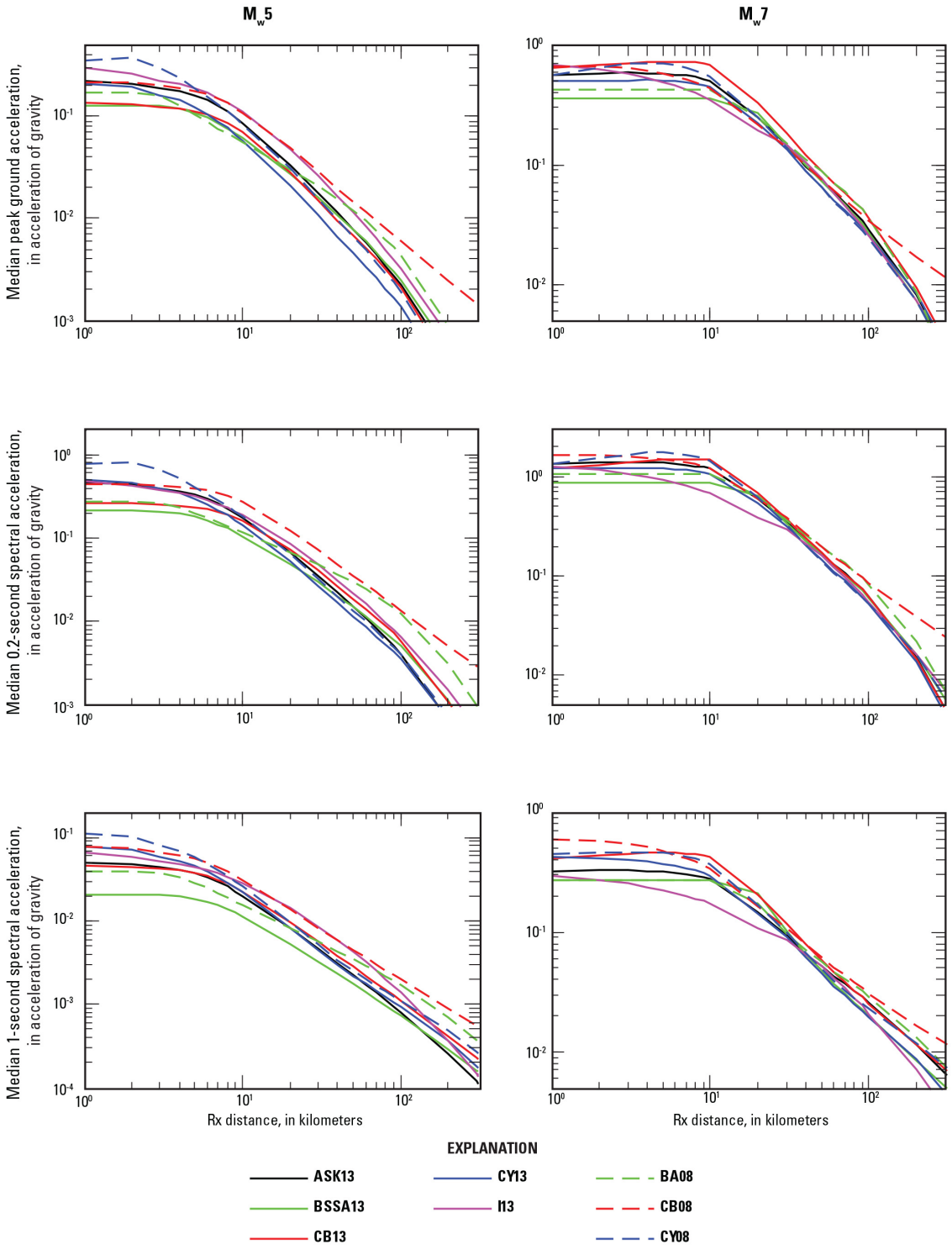

Figure 82. Comparison of median ground motion versus distance on the hanging wall of a normal fault at three periods and two magnitudes and V_{S30} site conditions of 760 meters per second. *A*, Peak ground acceleration for moment magnitude 5 earthquake; *B*, peak ground acceleration for moment magnitude 7 earthquake; *C*, 0.2-second (5-hertz) spectral acceleration for moment magnitude 5 earthquake; *D*, 0.2-second (5-hertz) spectral acceleration for moment magnitude 7 earthquake; *E*, 1-second (1-hertz) spectral acceleration for moment magnitude 5 earthquake; and *F*, 1-second (1-hertz) spectral acceleration for moment magnitude 7 earthquake.

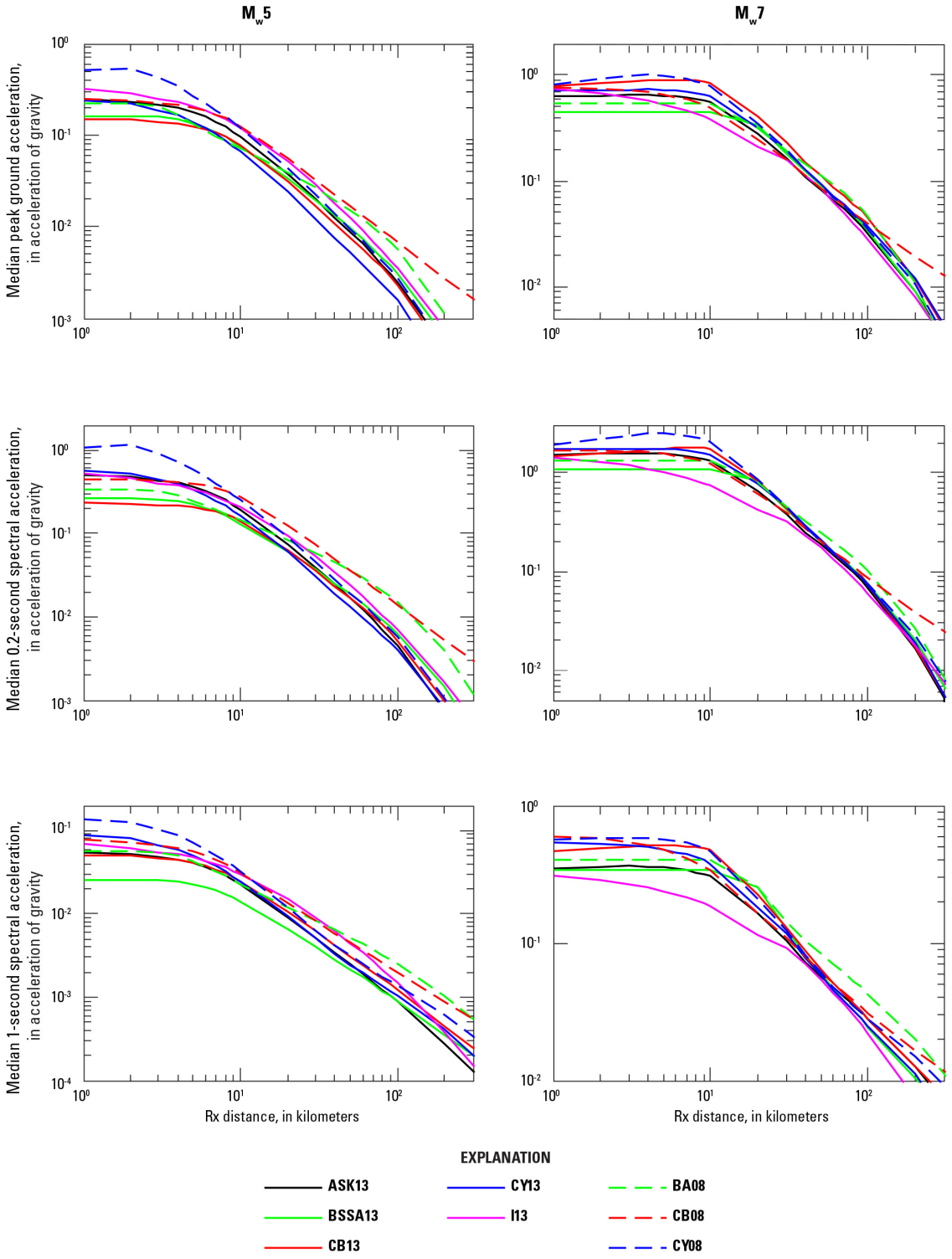

Figure 83. Comparison of median ground motion versus distance on the hanging wall of a reverse fault at three periods and two magnitudes and V_{S30} site conditions of 760 meters per second. *A*, Peak ground acceleration for moment magnitude 5 earthquake; *B*, peak ground acceleration for moment magnitude 7 earthquake; *C*, 0.2-second (5-hertz) spectral acceleration for moment magnitude 5 earthquake; *D*, 0.2-second (5-hertz) spectral

acceleration for moment magnitude 7 earthquake; *E*, 1-second (1-hertz) spectral acceleration for moment magnitude 5 earthquake; and *F*, 1-second (1-hertz) spectral acceleration for moment magnitude 7 earthquake.

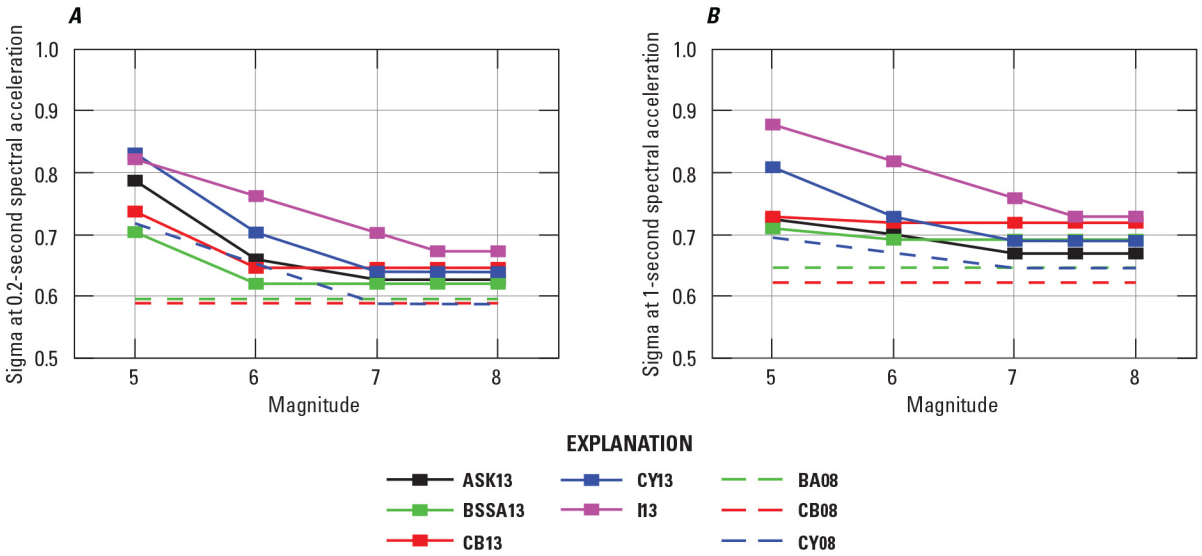

Figure 84. Standard deviation (sigma) versus magnitude for Central and Eastern United States ground motion models for *A*, 0.2-second (5-hertz) and *B*, 1-second (1-hertz) spectral acceleration.

Figures 85–99 show weighted combinations of WUS GMMs for five different faulting scenarios: strike slip fault (figs. 85–87), normal fault over the hanging wall (figs. 88–90), normal fault over the footwall (figs. 91–93), reverse fault over the hanging wall (figs. 94–96), and reverse fault over the footwall (figs. 97–99). In each group of figures, the first, second and third figures, respectively, correspond to peak ground acceleration, 0.2-second (5-hertz) spectral acceleration, and 1-second (1-hertz) spectral acceleration. In each figure, weighted combinations of the median and 84th-percentile ground motions (that is, plus one sigma) are given for magnitudes 6.5, 7.0, and 7.5. Black dashed lines labeled “combo-08” are based on table 15 with three GMMs and solid red lines labeled “combo-13” correspond to table 16 with five GMMs.

At large distances, the 2014 combination attenuates at a faster rate than the 2008 combination in almost all the figures. This effect can be observed in the ratio maps of 2014 hazard to 2008 hazard presented in the Results section.

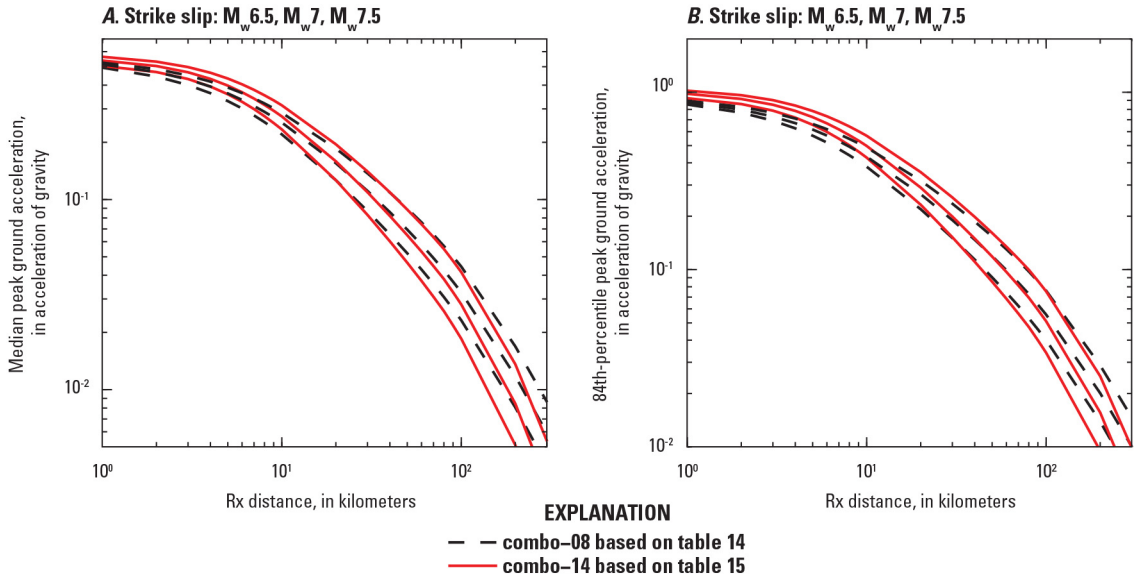

Figure 85. Comparison of 2008 and 2014 combined ground motion models for peak ground acceleration versus distance for a strike slip fault in the Western United States at three magnitudes and V_{S30} site conditions of 760 meters per second. Graphs show *A*, median and *B*, 84th percentile.

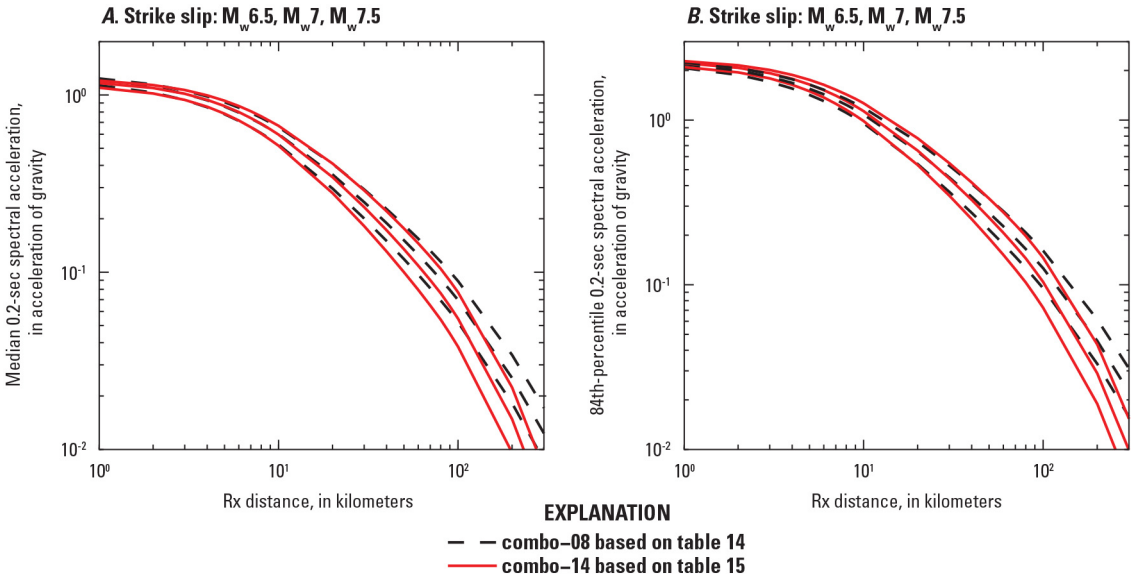

Figure 86. Comparison of 2008 and 2014 combined ground motion models for 0.2-second (5-hertz) spectral acceleration versus distance for a strike slip fault in the Western United States at three magnitudes and V_{S30} site conditions of 760 meters per second. Graphs show *A*, median and *B*, 84th percentile.

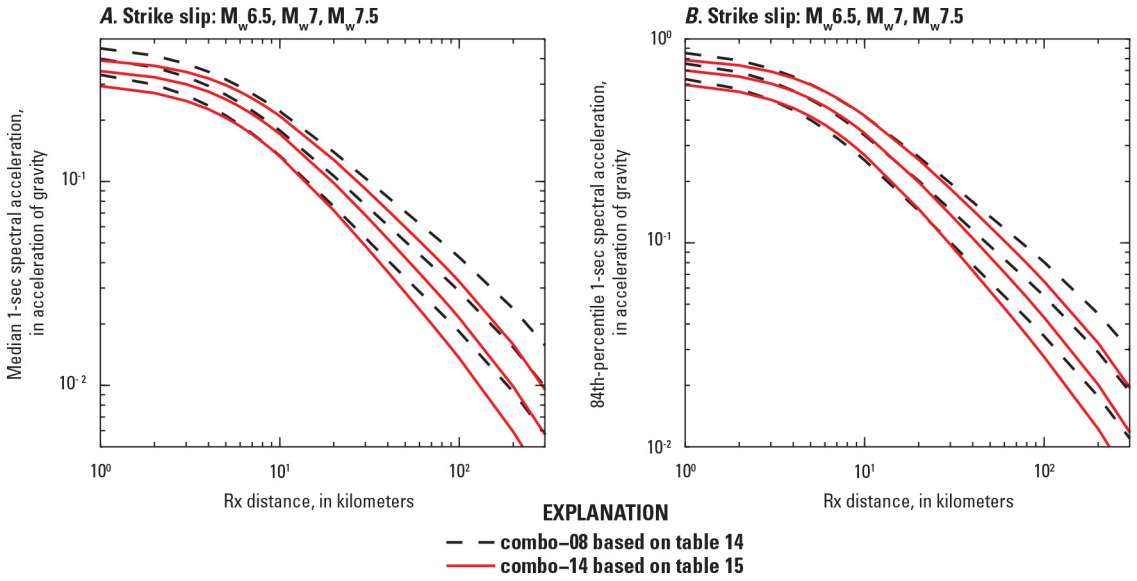

Figure 87. Comparison of 2008 and 2014 combined ground motion models for 1-second (1-hertz) spectral acceleration versus distance for a strike slip fault in the Western United States at three magnitudes and V_{S30} site conditions of 760 meters per second. Graphs show *A*, median and *B*, 84th percentile.

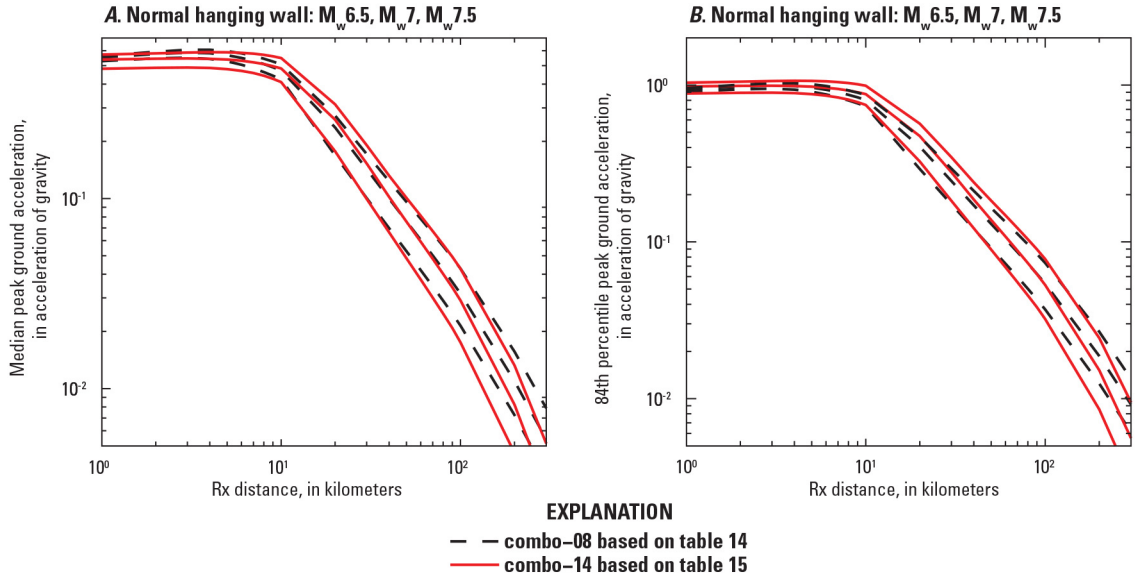

Figure 88. Comparison of 2008 and 2014 combined ground motion models for peak ground acceleration versus distance for the hanging wall of a normal fault in the Western United States at three magnitudes and V_{S30} site conditions of 760 meters per second. Graphs show *A*, median and *B*, 84th percentile.

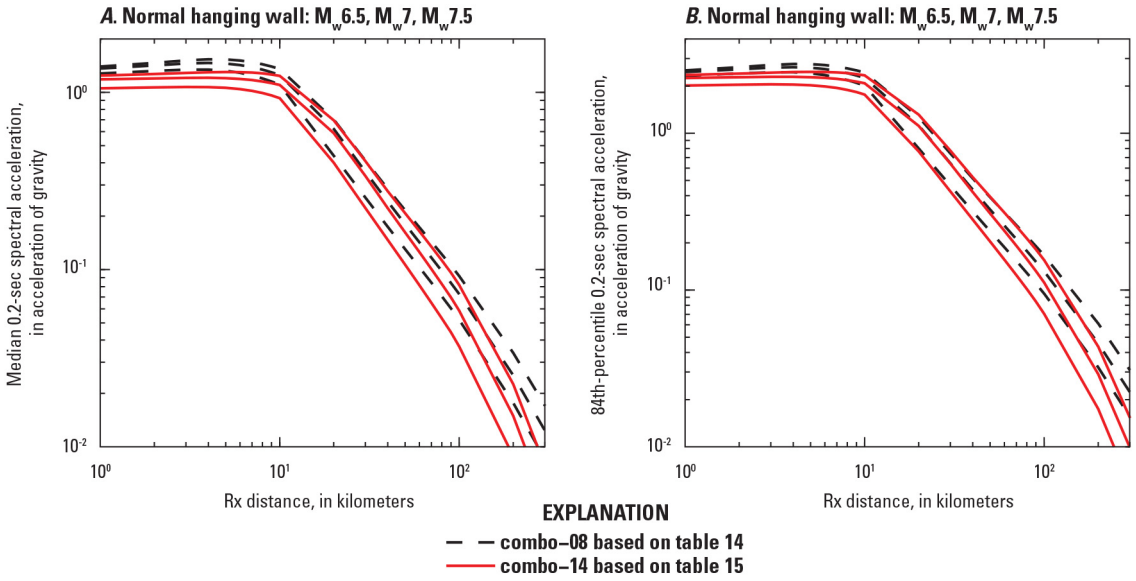

Figure 89. Comparison of 2008 and 2014 combined ground motion models for 0.2-second (5-hertz) spectral acceleration versus distance for the hanging wall of a normal fault in the Western United States at three magnitudes and V_{S30} site conditions of 760 meters per second. Graphs show *A*, median and *B*, 84th percentile.

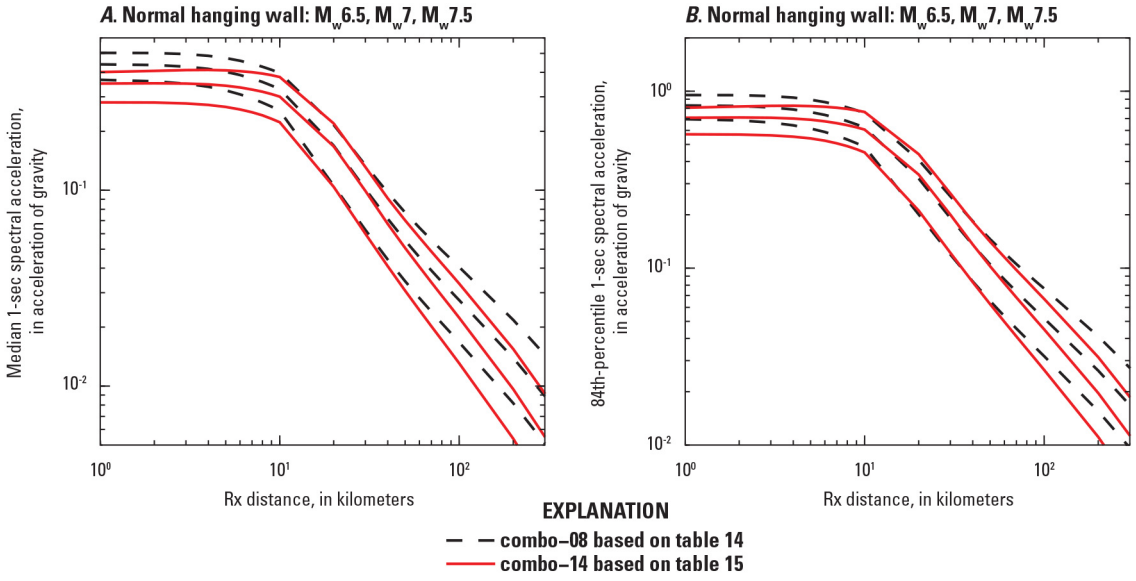

Figure 90. Comparison of 2008 and 2014 combined ground motion models for 1-second (1-hertz) spectral acceleration versus distance for the hanging wall of a normal fault in the Western United States at three magnitudes and V_{S30} site conditions of 760 meters per second. Graphs show *A*, median and *B*, 84th percentile.

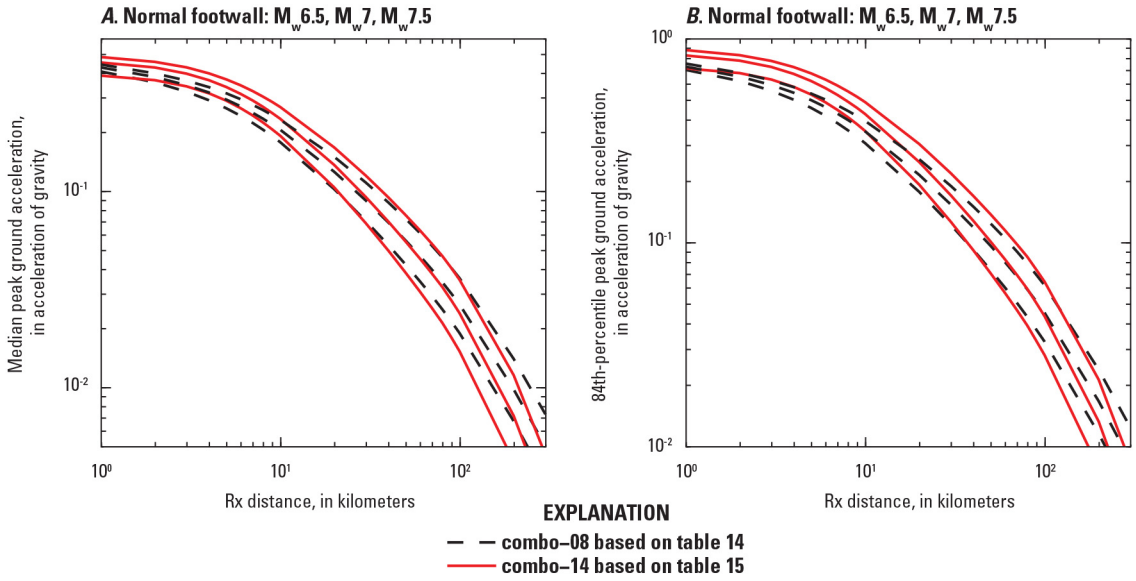

Figure 91. Comparison of 2008 and 2014 combined ground motion models for peak ground acceleration versus distance for the footwall of a normal fault in the Western United States at three magnitudes and V_{S30} site conditions of 760 meters per second. Graphs show *A*, median and *B*, 84th percentile.

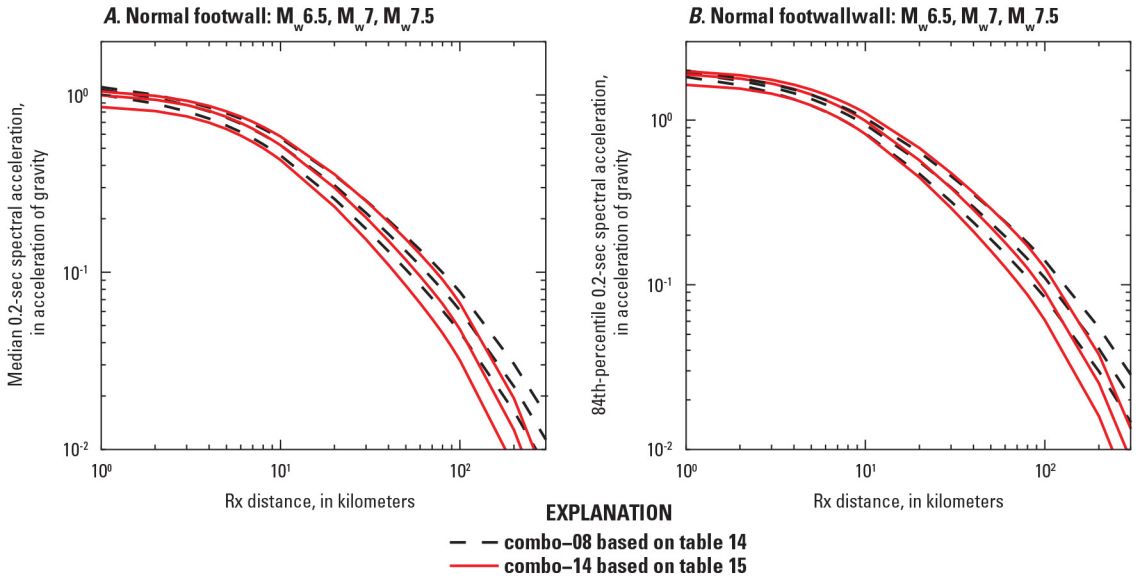

Figure 92. Comparison of 2008 and 2014 combined ground motion models for 0.2-second (5-hertz) spectral acceleration versus distance for the footwall of a normal fault in the Western United States at three magnitudes and V_{S30} site conditions of 760 meters per second. Graphs show *A*, median and *B*, 84th percentile.

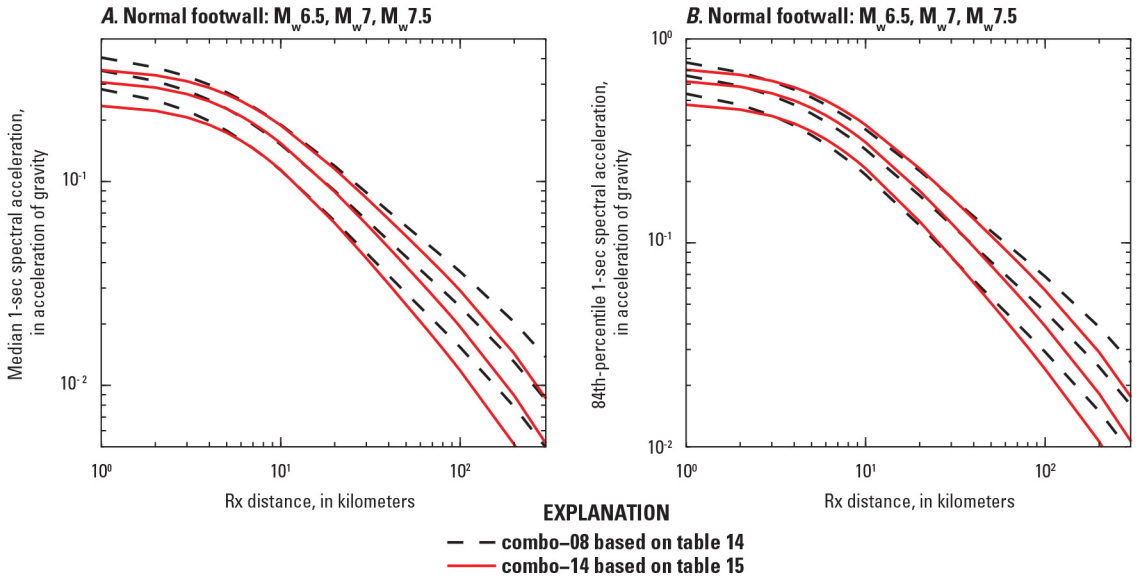

Figure 93. Comparison of 2008 and 2014 combined ground motion models for 1-second (1-hertz) spectral acceleration versus distance for the footwall of a normal fault in the Western United States at three magnitudes and V_{S30} site conditions of 760 meters per second. Graphs show *A*, median and *B*, 84th percentile.

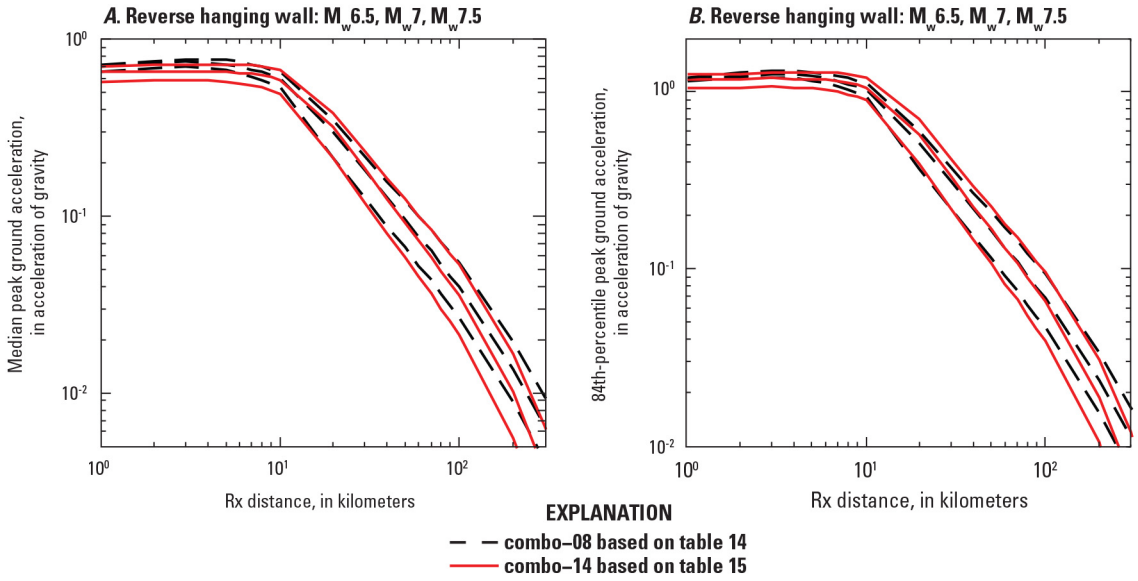

Figure 94. Comparison of 2008 and 2014 combined ground motion models for peak ground acceleration versus distance for the hanging wall of a reverse fault in the Western United States at three magnitudes and V_{S30} site conditions of 760 meters per second. Graphs show *A*, median and *B*, 84th percentile.

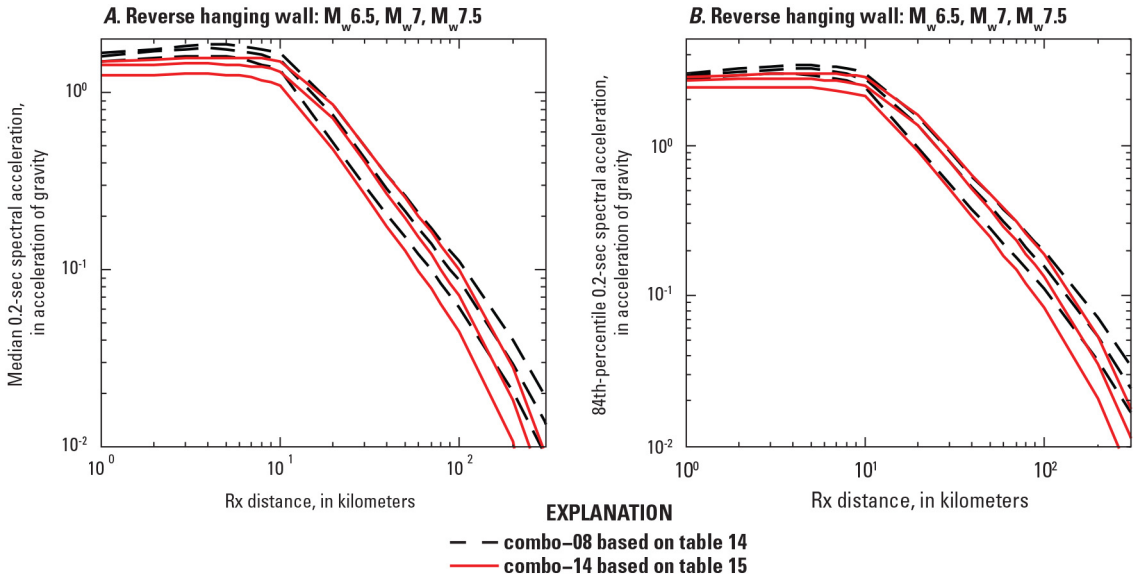

Figure 95. Comparison of 2008 and 2014 combined ground motion models for 0.2-second (5-hertz) spectral acceleration versus distance for the hanging wall of a reverse fault in the Western United States at three magnitudes and V_{S30} site conditions of 760 meters per second. Graphs show *A*, median and *B*, 84th percentile.

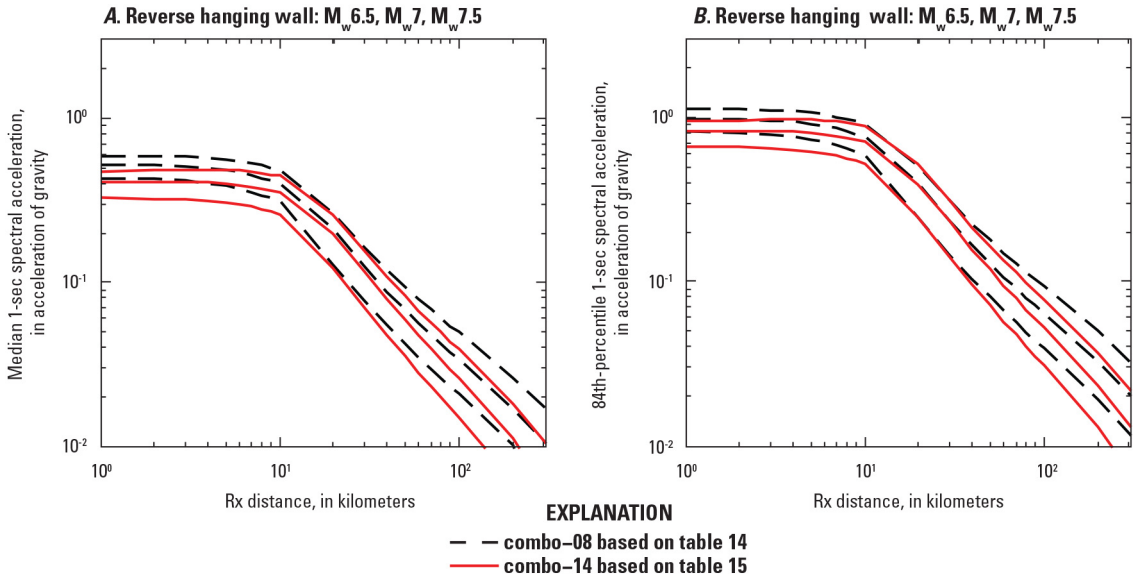

Figure 96. Comparison of 2008 and 2014 combined ground motion models for 1-second (1-hertz) spectral acceleration versus distance for the hanging wall of a reverse fault in the Western United States at three magnitudes and V_{S30} site conditions of 760 meters per second. Graphs show *A*, median and *B*, 84th percentile.

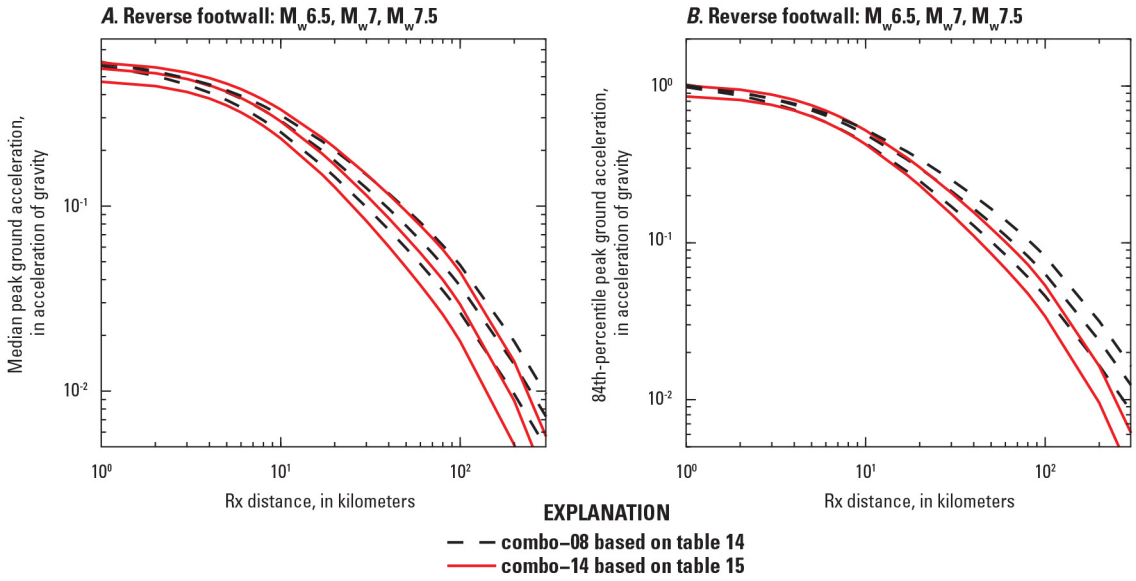

Figure 97. Comparison of 2008 and 2014 combined ground motion models for peak ground acceleration versus distance for the footwall of a reverse fault in the Western United States at three magnitudes and V_{S30} site conditions of 760 meters per second. Graphs show *A*, median and *B*, 84th percentile.

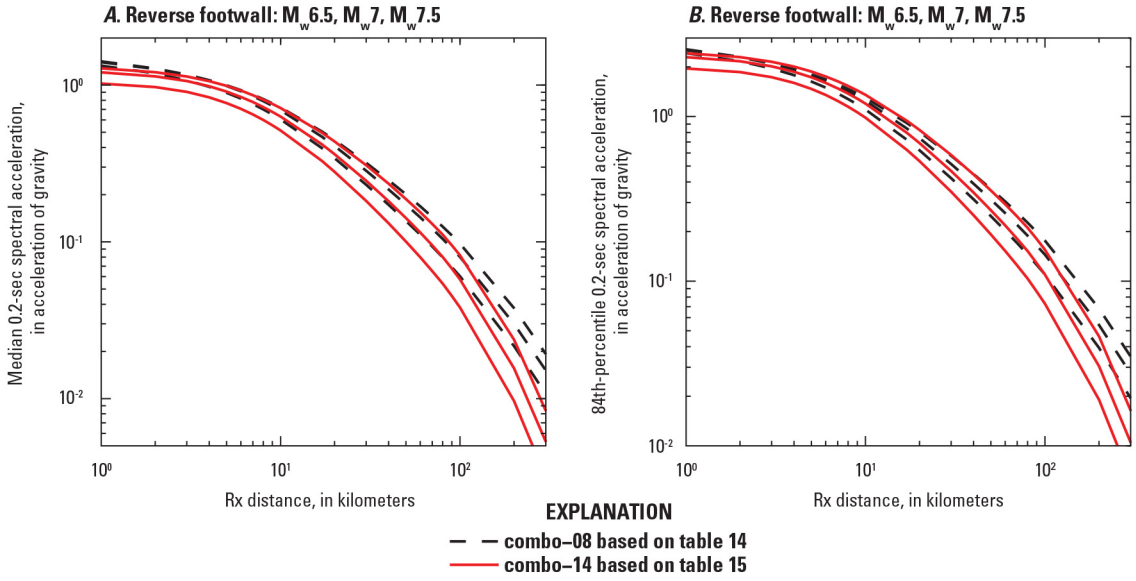

Figure 98. Comparison of 2008 and 2014 combined ground motion models for 0.2-second (5-hertz) spectral acceleration versus distance for the footwall of a reverse fault in the Western United States at three magnitudes and V_{S30} site conditions of 760 meters per second. Graphs show *A*, median and *B*, 84th percentile.

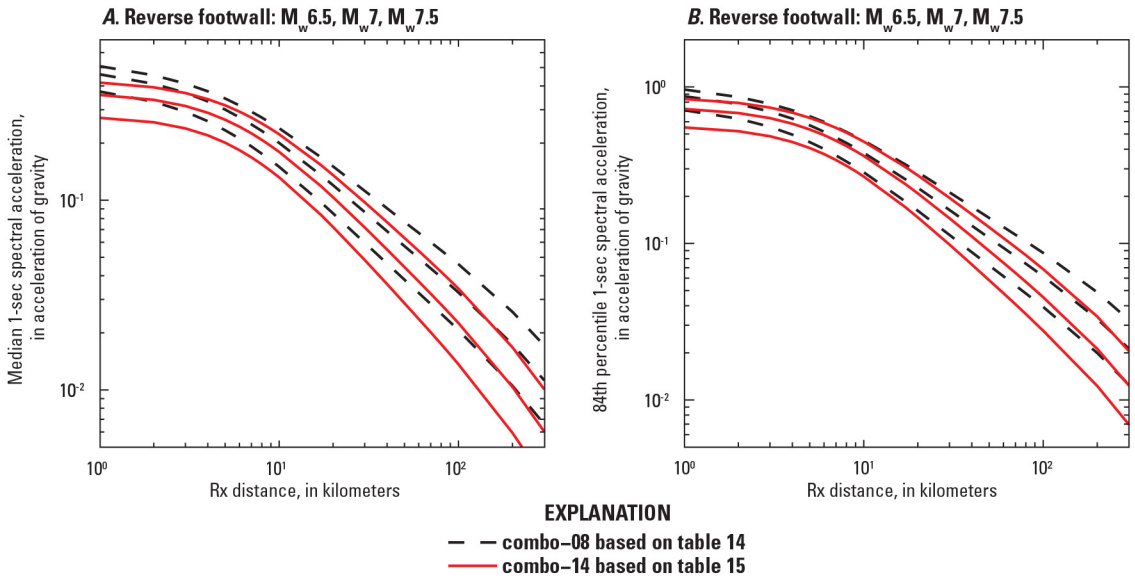

Figure 99. Comparison of 2008 and 2014 combined ground motion models for 1-second (1-hertz) spectral acceleration versus distance for the footwall of a reverse fault in the Western United States at three magnitudes and V_{S30} site conditions of 760 meters per second. Graphs show *A*, median and *B*, 84th percentile.

Additional Epistemic Uncertainty

We acknowledge that inclusion of all five NGA-West2 models in the maps has increased the epistemic uncertainty in the WUS; however, we still follow the square-root rule used in 2008 to estimate the additional epistemic uncertainty based on the number of earthquakes used in modeling. In 2008, the ground motion uncertainty was assumed to be 50 percent for M_w7 and larger events, and R_{rup} less than 10 km, where R_{rup} represents the closest distance to rupture. This assumption remains unchanged in 2014, which translates to an additive factor of 0.4 in the log-space (90-percent confidence limits). Epistemic uncertainty for other magnitude-distance bins (table 17) was calculated based on $Dgnd=0.4\times\sqrt{(n/N)}$, where N is the number of earthquakes recorded in the given magnitude-distance bin, and n is the number of earthquakes in the M_w7 and larger and R_{rup} less than 10 km bin. Two databases were used in 2008 (those of CB08 and CY08) and the results were averaged. In 2014, we use databases from ASK13, BSSA13, CB13, and CY13 to update the 2008 values. The results are shown in table 17. Similar to 2008, this uncertainty (that is, Avg Dgnd, which stands for the average difference in ground motion) is applied symmetrically, with the unmodified model (that is, gnd, which stands for the ground motion prediction) weighting 0.63, and the "gnd±Avg Dgnd" models weighting 0.185.

Table 17. Additional epistemic uncertainty for use in the 2014 hazard maps. *N* is the number of earthquakes recorded in the given magnitude-distance bin used by the given ground motion model. $Dgnd=0.4\times\sqrt{(n/N)}$.

[M, moment magnitude, R_{rup}, distance measure used in ground motion models; ≤, less than or equal to]

M and R_{rup} range	*N* ASK13	Dgnd ASK13	*N* BSSA13	Dgnd BSSA13	*N* CB13	Dgnd CB13	*N* CY13	Dgnd CY13	Avg Dgnd 2013
$5\leq M<6$, $R_{rup}<10$ km	19	0.29	13	0.33	7	0.48	10	0.38	0.37
$5\leq M<6$, $10\leq R_{rup}<30$	49	0.18	32	0.21	24	0.26	27	0.23	0.22
$5\leq M<6$, $30\leq R_{rup}$	43	0.19	69	0.14	29	0.23	14	0.32	0.22
$6\leq M<7$, $R_{rup}<10$	29	0.23	19	0.28	26	0.25	24	0.24	0.25
$6\leq M<7$,$10\leq R_{rup}<30$	33	0.22	25	0.24	32	0.22	26	0.24	0.23
$6\leq M<7$, $30\leq R_{rup}$	32	0.22	31	0.22	34	0.22	19	0.28	0.23
$M\geq 7$, $R_{rup}<10$	10	0.40	9	0.40	10	0.40	9	0.40	0.40
$M\geq 7$, $10\leq R_{rup}<30$	12	0.37	10	0.38	13	0.35	11	0.36	0.36
$M\geq 7$, $30\leq R_{rup}$	12	0.37	13	0.33	18	0.30	13	0.33	0.33

Western United States Difference and Ratio Maps—Comparing 2014 and 2008 Ground Motion Models

In this section, we discuss changes in the 2014 hazard maps for the WUS by showing difference and ratio maps for 2-percent probability of exceedance in 50 years on a uniform firm rock site condition for peak ground acceleration, 0.2-second (5-hertz) spectral acceleration, and 1-second (1-hertz) spectral acceleration with 5-percent damping.

Intermountain West and Crustal Sources in the Pacific Northwest

Here we discuss changes to the seismic hazard compared to the 2008 maps for the Western United States outside of California. These maps illustrate a deaggregation of the hazard showing the relative contribution of an individual GMM to the overall hazard. The difference maps demonstrate the difference between the probabilistic ground motions obtained using the 2014 source model and one 2014 GMM, and the probabilistic ground motion obtained using the 2014 source model and the weighted combination of all five 2014 GMMs. The ratios also use the 2014 source model and are made by dividing the probabilistic ground motions from one GMM by the probabilistic ground motion from the weighted combination of all five GMMs.

Figures 100–105 show probabilistic seismic hazard difference maps and ratio maps for the Abrahamson and others (2013 and 2014, ASK13), Boore and others (2013 and 2014, BSSA13), Campbell and Bozorgnia (2013 and 2014, CB13), Chiou and Youngs (2013 and 2014, CY13), and Idriss (2013 and 2014, I13) GMMs. Most faults contained in the Intermountain West region have normal, or in a few cases strike slip mechanisms, with magnitudes ranging from around 6.5 to 7.5. Crustal faults in the Pacific Northwest region typically are reverse faults with some strike-slip motion and are characterized with magnitudes ranging from about 6.5 to 7.5. Background earthquakes included in the 2014 model are combinations of strike slip and normal (Intermountain West region) or strike slip and reverse (Pacific Northwest region) and range from M_w5 to 7.95.

Observe that most significant differences in these figures are seen at very close proximity to the faults, which likely is due to the differences in modeling of hanging wall and footwall effects in various GMMs. There is complexity for individual GMMs because of effects of fault mechanism and earthquake rate.

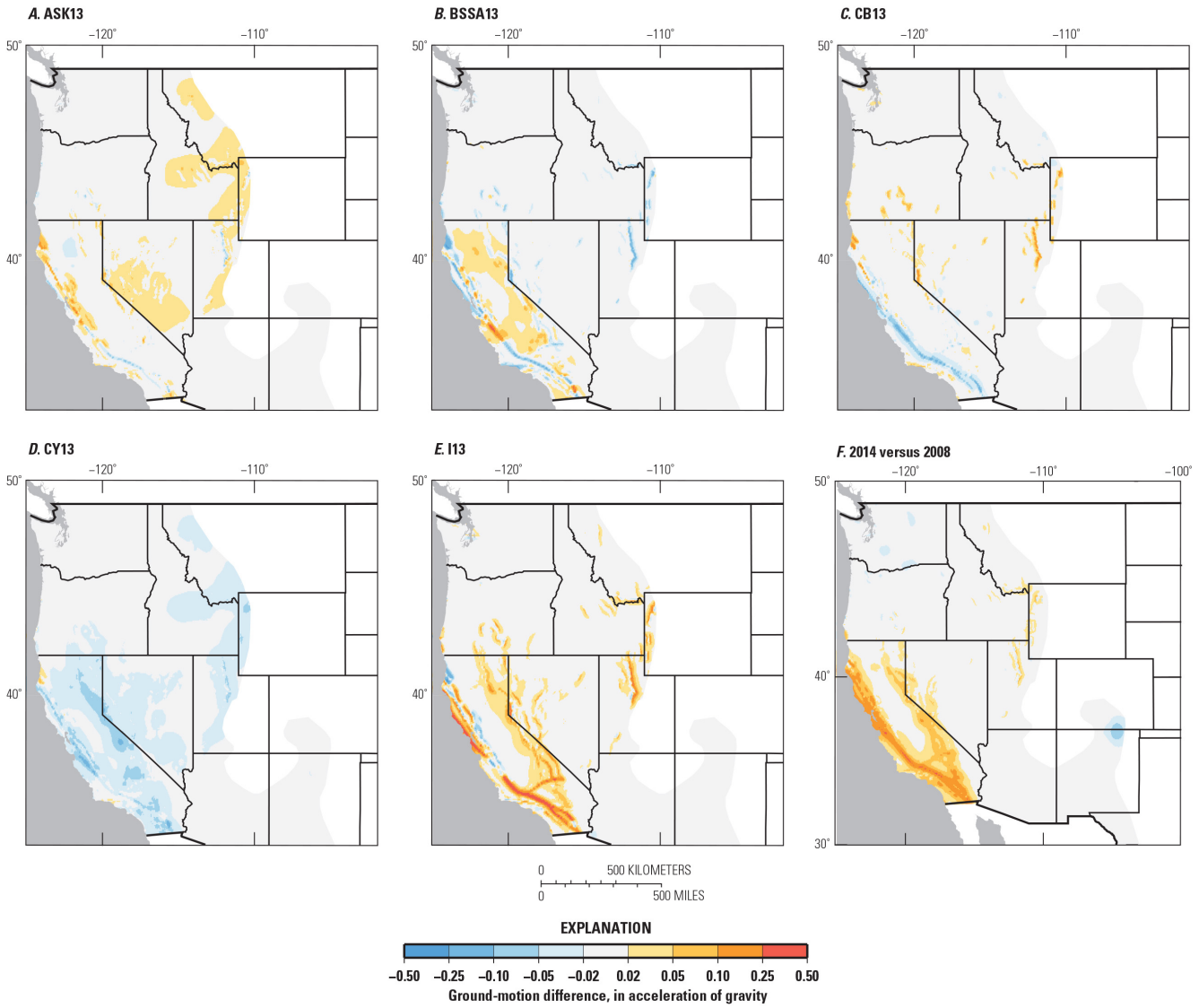

Figure 100. Maps showing difference in peak ground acceleration from individual ground motion models in the Western United States compared to the 2008 model at 2-percent in 50 years probability of exceedance and V_{S30} site conditions of 760 meters per second. *A*, ASK13 (Abrahamson and others, 2013, 2014); *B*, BSSA13 (Boore and others, 2013, 2014); *C*, CB13 (Campbell and Bozorgnia, 2013, 2014); *D*, CY13 (Chiou and Youngs, 2013, 2014); *E*, I13, Idriss (2013, 2014); and *F*, 2014 combined ground motion models. Central and Eastern United States sources are not shown.

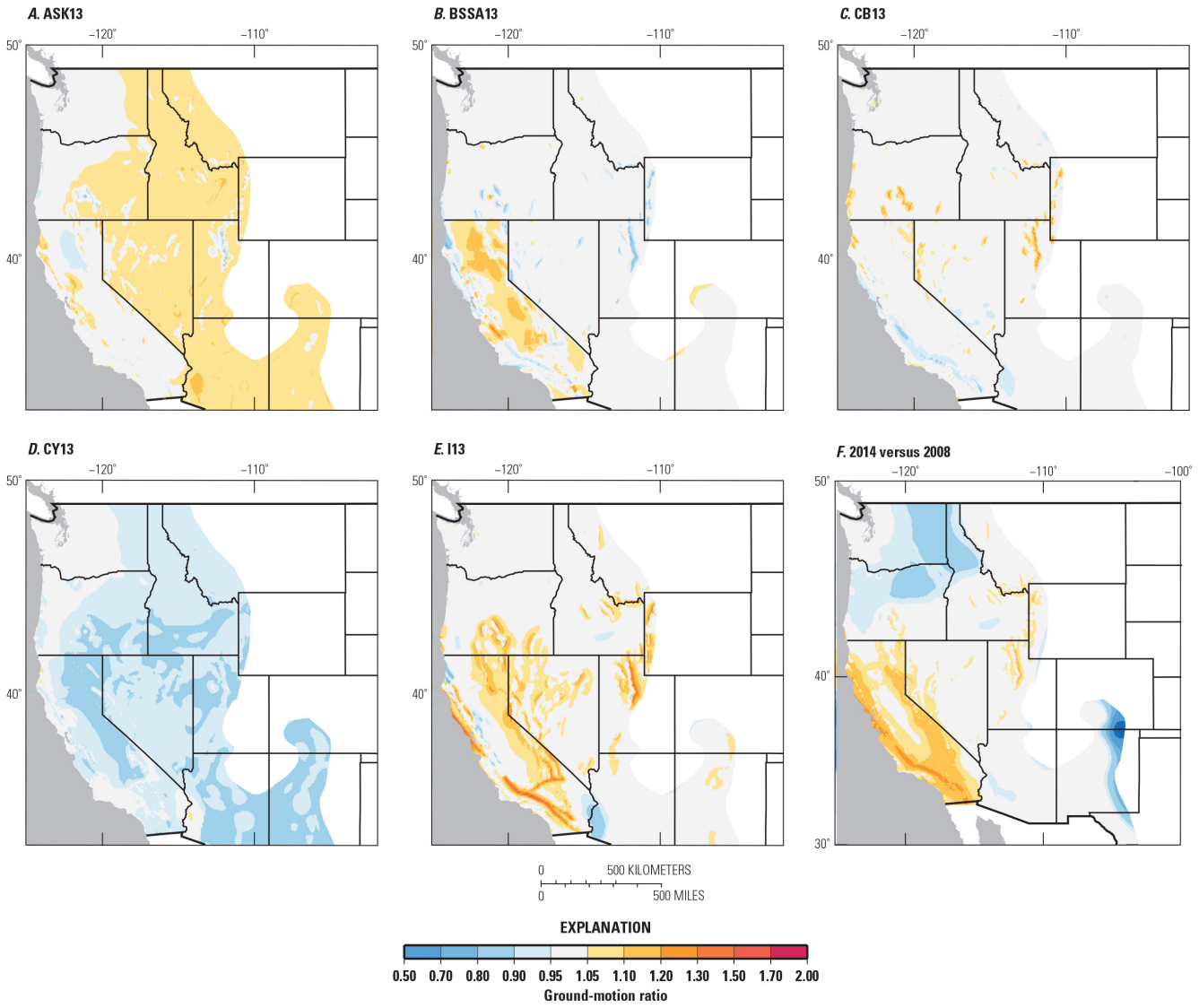

Figure 101. Maps showing ratio of peak ground acceleration from individual ground motion models in the Western United States compared to the 2008 model at 2-percent in 50 years probability of exceedance and V_{S30} site conditions of 760 meters per second. *A*, ASK13 (Abrahamson and others, 2013, 2014); *B*, BSSA13 (Boore and others, 2013, 2014); *C*, CB13 (Campbell and Bozorgnia, 2013, 2014); *D*, CY13 (Chiou and Youngs, 2013, 2014); *E*, I13, Idriss (2013, 2014); and *F*, 2014 combined ground motion models. Central and Eastern United States sources are not shown.

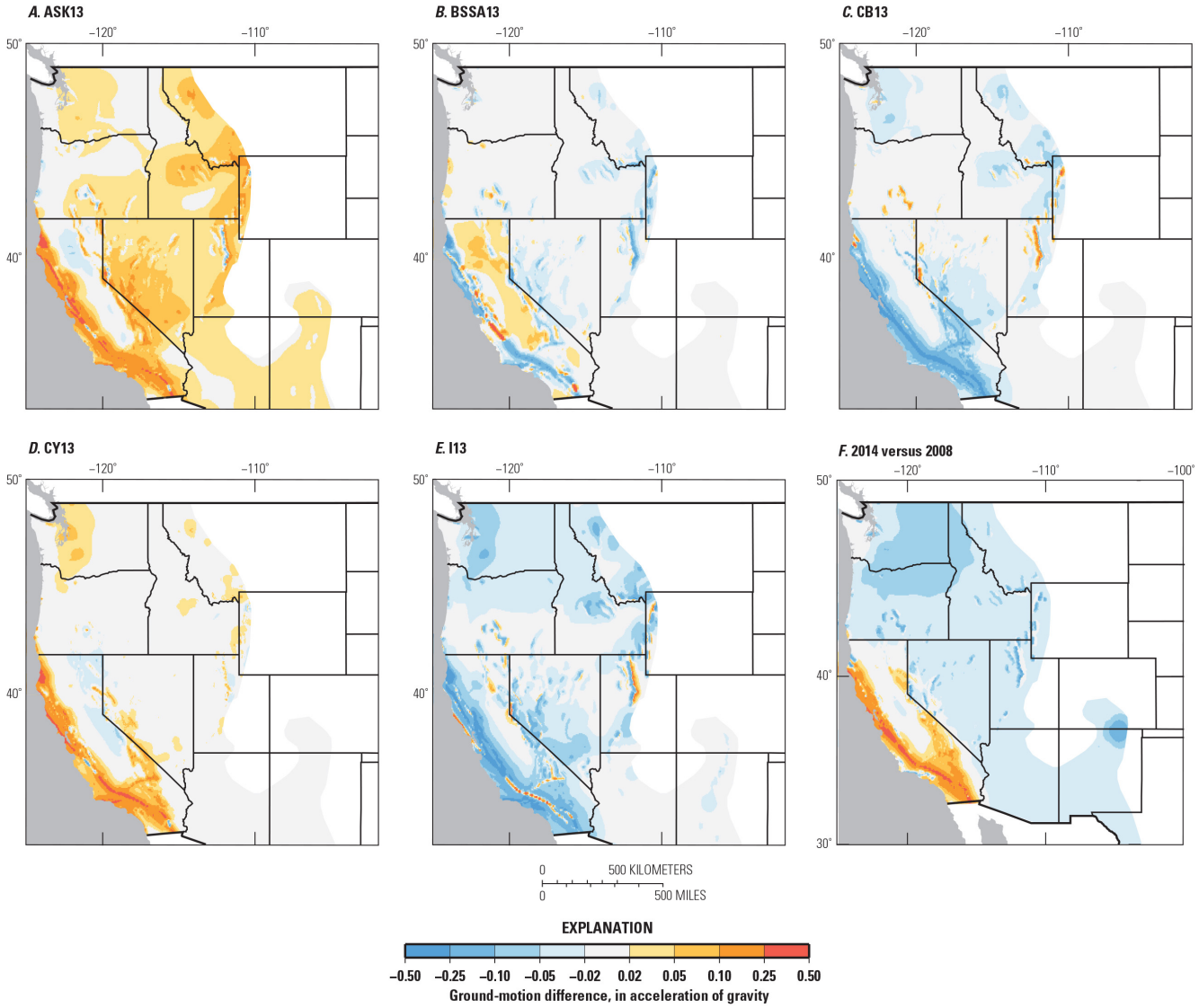

Figure 102. Maps showing difference in 0.2-second (5-hertz) spectral acceleration from individual ground motion models in the Western United States compared to the 2008 model at 2-percent in 50 years probability of exceedance and V_{S30} site conditions of 760 meters per second. *A*, ASK13 (Abrahamson and others, 2013, 2014); *B*, BSSA13 (Boore and others, 2013, 2014); *C*, CB13 (Campbell and Bozorgnia, 2013, 2014); *D*, CY13 (Chiou and Youngs, 2013, 2014); *E*, I13, Idriss (2013, 2014); and *F*, 2014 combined ground motion models. Central and Eastern United States sources are not shown.

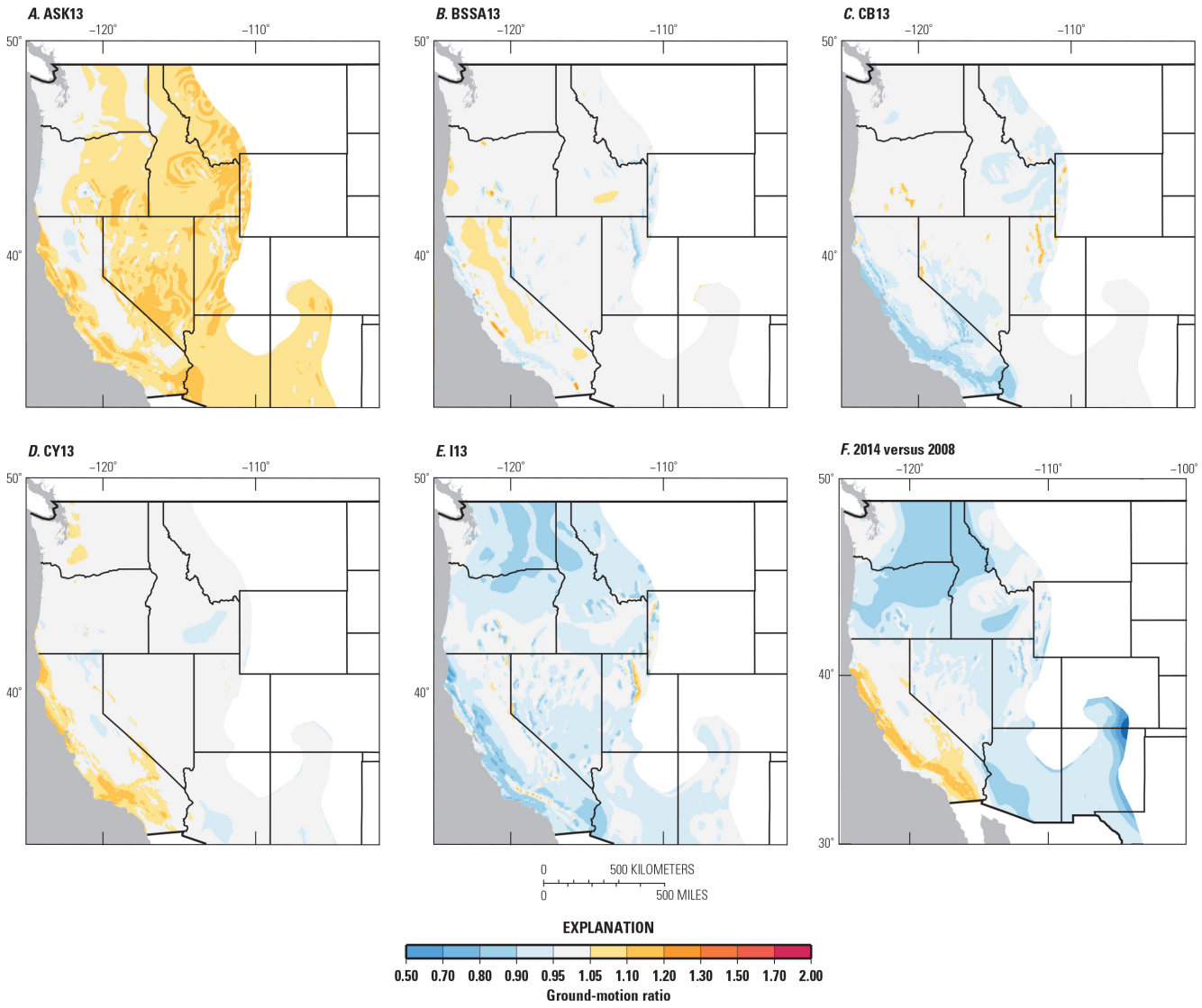

Figure 103. Maps showing ratio of 0.2-second (5-hertz) spectral acceleration from individual ground motion models in the Western United States compared to the 2008 model at 2-percent in 50 years probability of exceedance and V_{S30} site conditions of 760 meters per second. *A*, ASK13 (Abrahamson and others, 2013, 2014); *B*, BSSA13 (Boore and others, 2013, 2014); *C*, CB13 (Campbell and Bozorgnia, 2013, 2014); *D*, CY13 (Chiou and Youngs, 2013, 2014); *E*, I13, Idriss (2013, 2014); and *F*, 2014 combined ground motion models. Central and Eastern United States sources are not shown.

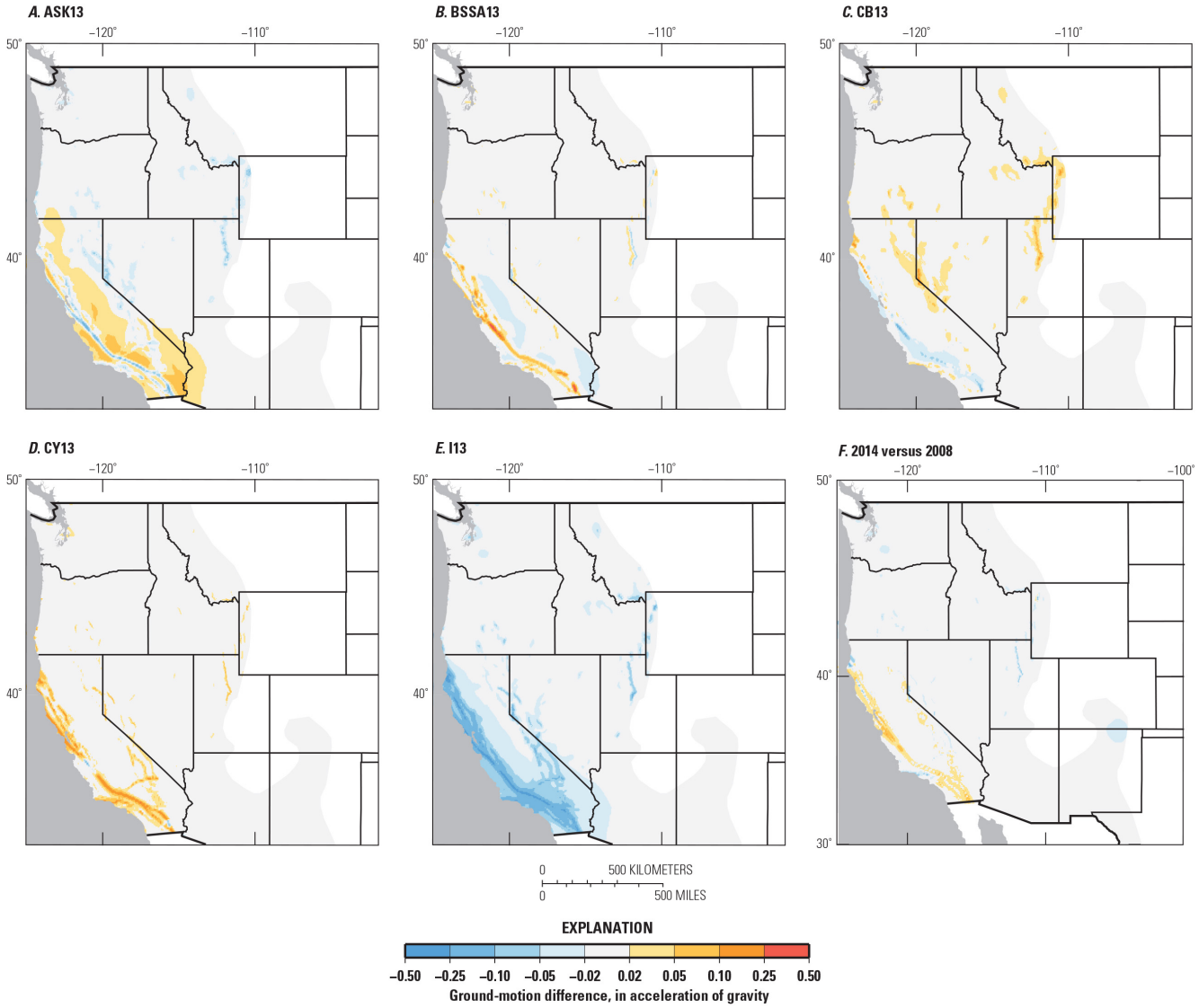

Figure 104. Maps showing difference in 1-second (1-hertz) spectral acceleration from individual ground motion models in the Western United States compared to the 2008 model at 2-percent in 50 years probability of exceedance and V_{S30} site conditions of 760 meters per second. *A*, ASK13 (Abrahamson and others, 2013, 2014); *B*, BSSA13 (Boore and others, 2013, 2014); *C*, CB13 (Campbell and Bozorgnia, 2013, 2014); *D*, CY13 (Chiou and Youngs, 2013, 2014); *E*, I13, Idriss (2013, 2014); and *F*, 2014 combined ground motion models. Central and Eastern United States sources are not shown.

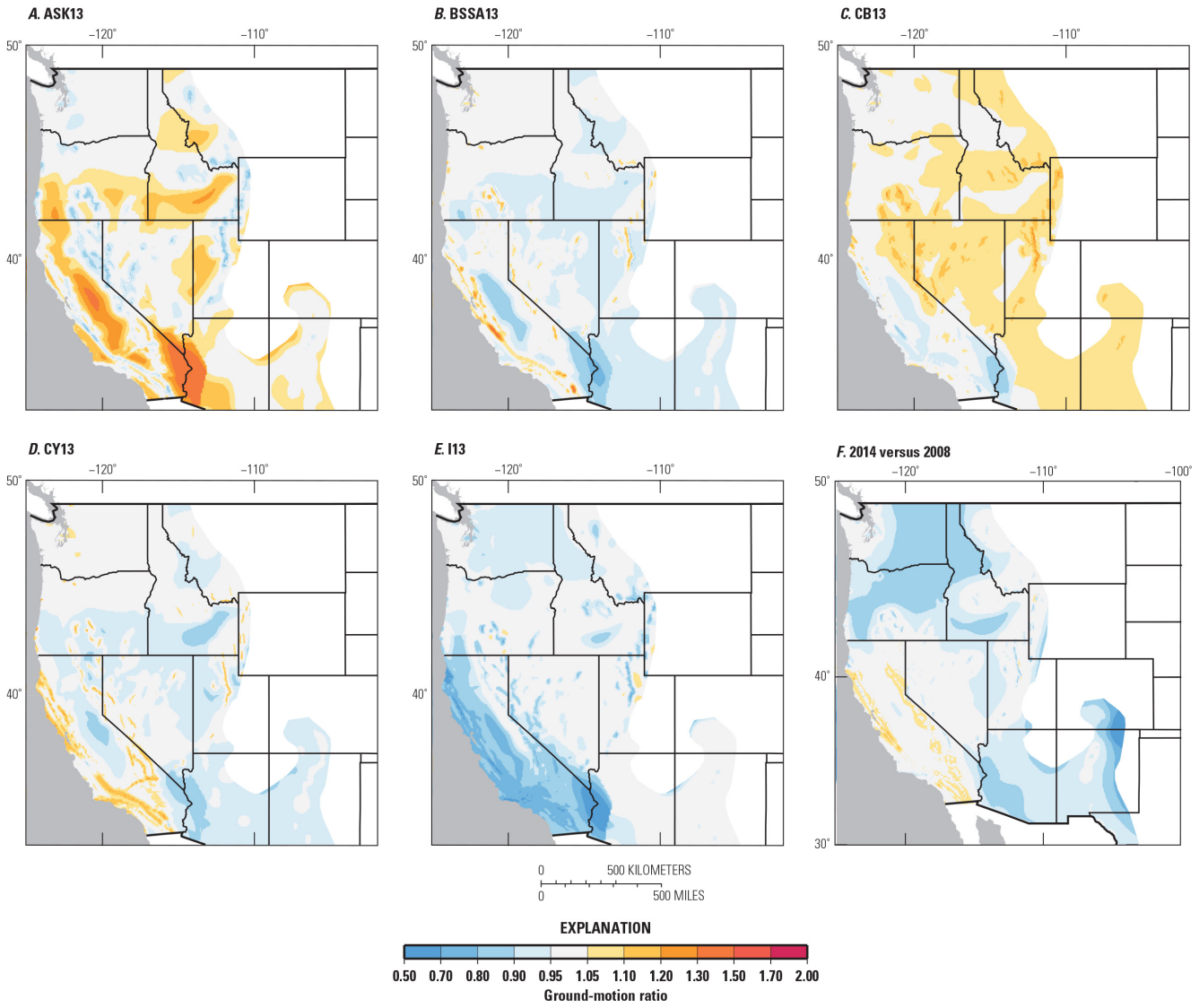

Figure 105. Maps showing ratio of 1-second (1-hertz) spectral acceleration from individual ground motion models in the Western United States compared to the 2008 model at 2-percent in 50 years probability of exceedance and V_{S30} site conditions of 760 meters per second. *A*, ASK13 (Abrahamson and others, 2013, 2014); *B*, BSSA13 (Boore and others, 2013, 2014); *C*, CB13 (Campbell and Bozorgnia, 2013, 2014); *D*, CY13 (Chiou and Youngs, 2013, 2014); *E*, I13, Idriss (2013, 2014); and *F*, 2014 combined ground motion models. Central and Eastern United States sources are not shown.

California

Difference and ratio maps for California are shown for similar hazard levels as were applied for the rest of the WUS in figures 106–111. These maps illustrate the relative contribution of each individual GMM to the overall hazard. The difference maps demonstrate the difference between the probabilistic ground motions obtained using the 2014 source model and one GMM, and the probabilistic ground motion obtained using the 2014 source model and the weighted combination of all five GMMs.

The ratios also use the 2014 source model and are made by dividing the ground motion from one GMM by the ground motion from the weighted combination of all five GMMs: Abrahamson and others (2013 and 2014, ASK13), Boore and others (2013 and 2014, BSSA13), Campbell and Bozorgnia (2013 and 2014, CB13), Chiou and Youngs (2013 and 2014, CY13), and Idriss (2013 and 2014, I13). Each plot also includes a comparison of the 2014 and 2008 combined GMMs (ratio: 2014/2008 or difference: 2014–2008) using the 2014 source model. Note that in these latter maps (2014 compared to 2008), the 2014 source model does not include gridded seismicity sources outside the state.

Most faults in California are strike slip but the eastern part of California also contains normal faults, and the Transverse Ranges and northwest portions contain reverse faults. Magnitudes on faults range from 6 to higher than 8 and on background sources range from 5 to 7.9. Ground motions for PGA are lower when applying the Chiou and Youngs (2013, 2014) compared to the others, but they are lower for 0.2-second and 1-second spectral acceleration when applying the Idriss (2013, 2014) model, especially over the San Andreas fault system. The California ground motions from Abrahamson and others (2013, 2014) and Chiou and Youngs (2013, 2014) are higher than average at 0.2-second and 1-second spectral acceleration over the active faults. Individual GMMs show complexity due to variable magnitude scaling and mechanism. Because activity rates are higher in California than in the rest of the WUS, higher epsilons often are observed (that is, difference between ground motion at 2-percent probability of exceedance in 50 years often are higher than the median ground motion for a particular magnitude and distance).

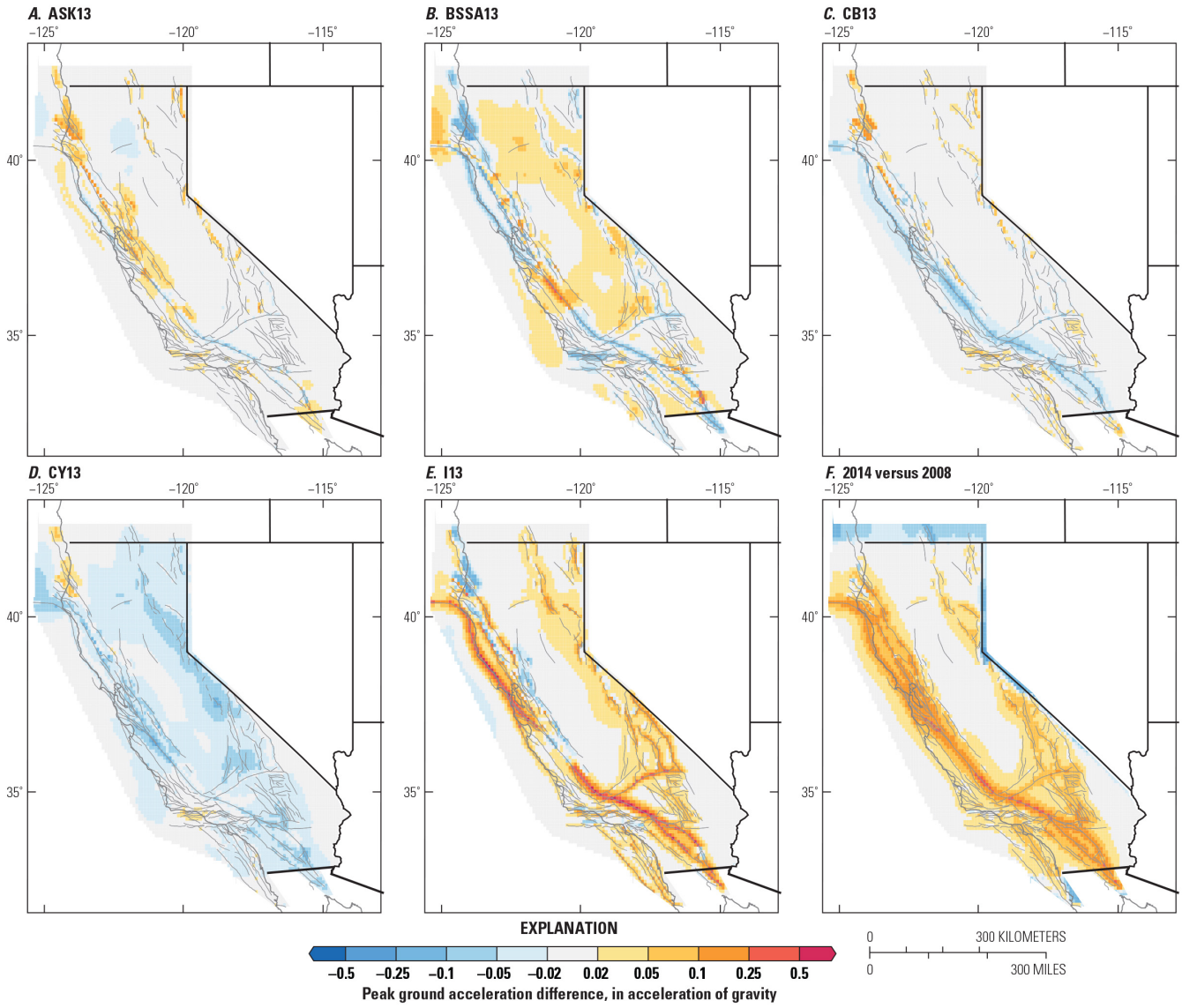

Figure 106. Maps showing difference in peak ground acceleration from individual ground motion models in California compared to the 2008 model at 2-percent in 50 years probability of exceedance and V_{S30} site conditions of 760 meters per second. *A*, ASK13 (Abrahamson and others, 2013, 2014); *B*, BSSA13 (Boore and others, 2013, 2014); *C*, CB13 (Campbell and Bozorgnia, 2013, 2014); *D*, CY13 (Chiou and Youngs, 2013, 2014); *E*, I13, Idriss (2013, 2014); and *F*, 2014 combined ground motion models.

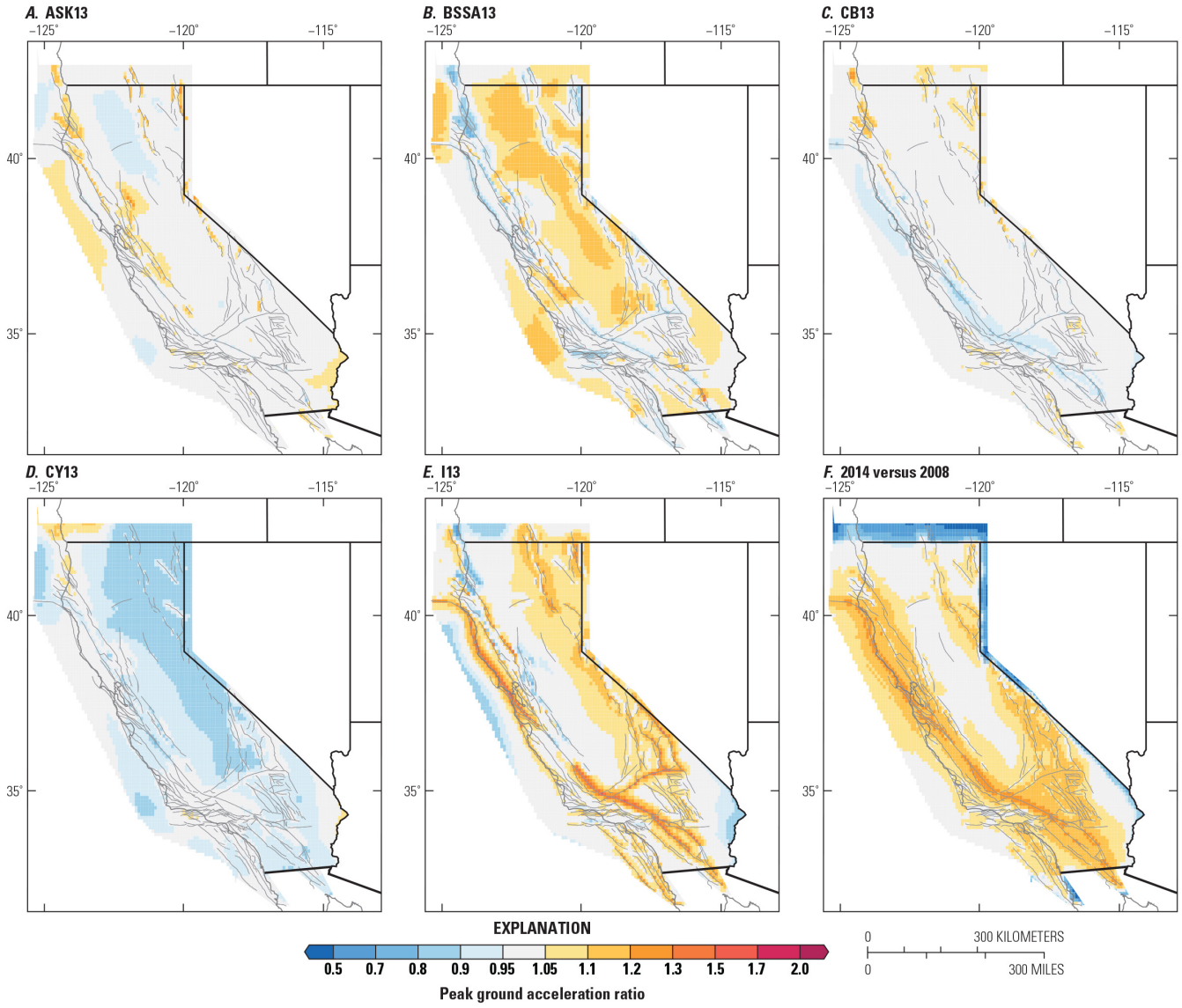

Figure 107. Maps showing ratio of peak ground acceleration from individual ground motion models in California and the 2008 model at 2-percent in 50 years probability of exceedance and V_{S30} site conditions of 760 meters per second. *A*, ASK13 (Abrahamson and others, 2013, 2014); *B*, BSSA13 (Boore and others, 2013, 2014); *C*, CB13 (Campbell and Bozorgnia, 2013, 2014); *D*, CY13 (Chiou and Youngs, 2013, 2014); *E*, I13, Idriss (2013, 2014); and *F*, 2014 combined ground motion models.

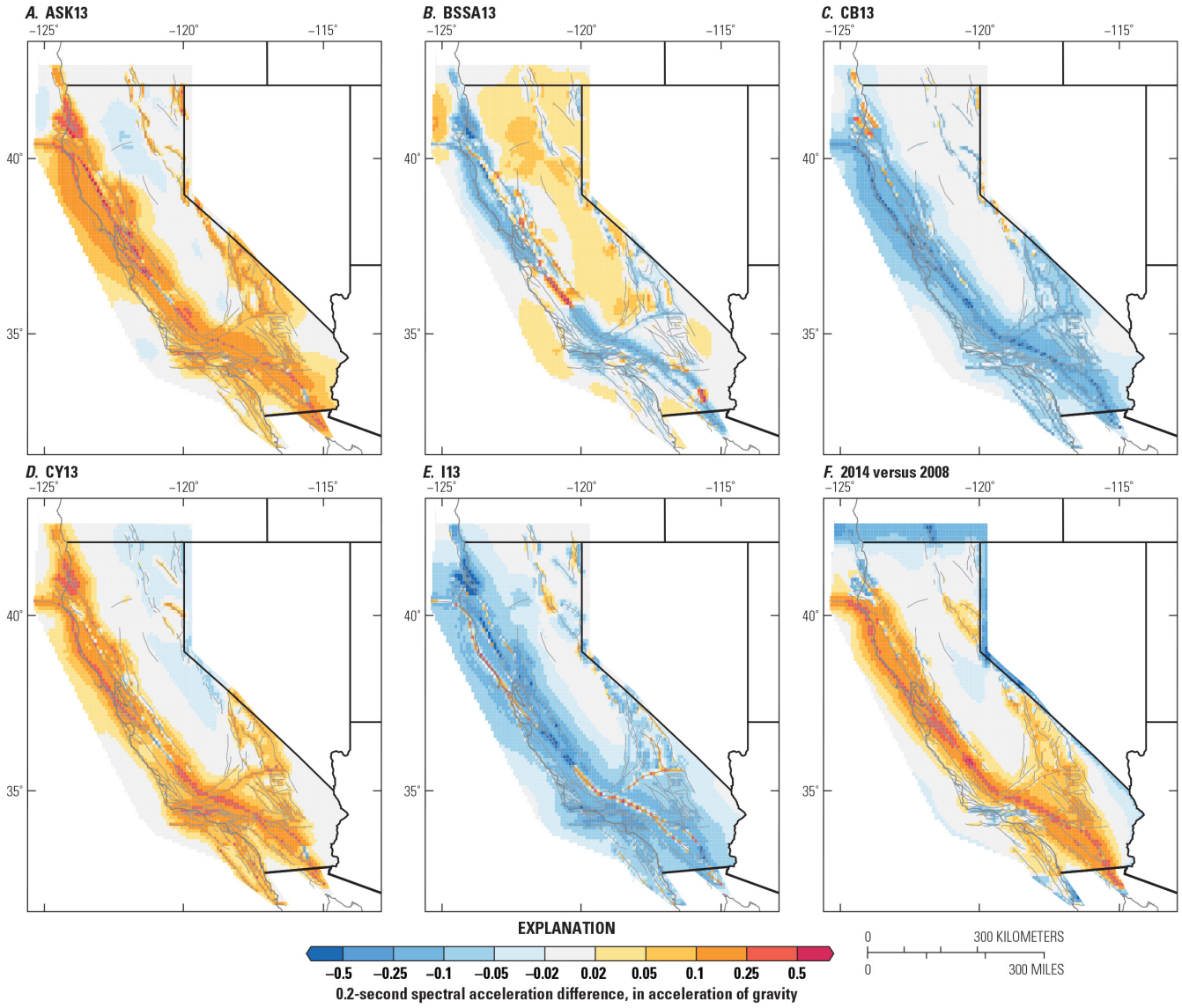

Figure 108. Maps showing difference in 0.2-second (5-hertz) spectral acceleration from individual ground motion models in California compared to the 2008 model at 2-percent in 50 years probability of exceedance and V_{S30} site conditions of 760 meters per second. *A*, ASK13 (Abrahamson and others, 2013, 2014); *B*, BSSA13 (Boore and others, 2013, 2014); *C*, CB13 (Campbell and Bozorgnia, 2013, 2014); *D*, CY13 (Chiou and Youngs, 2013, 2014); *E*, I13, Idriss (2013, 2014); and *F*, 2014 combined ground motion models.

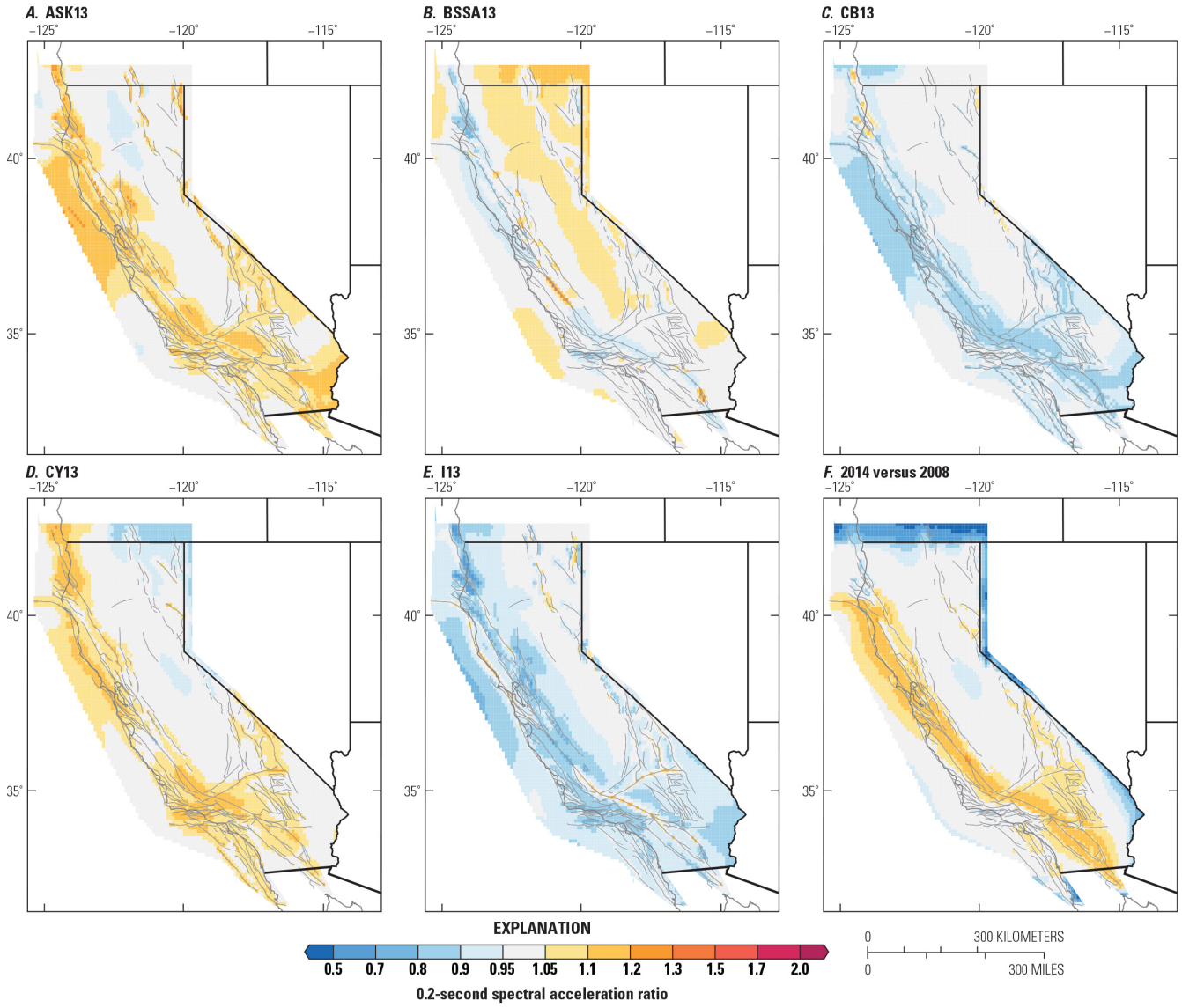

Figure 109. Maps showing ratio of 0.2-second (5-hertz) spectral acceleration from individual ground motion models in California and the 2008 model at 2-percent in 50 years probability of exceedance and V_{S30} site conditions of 760 meters per second. *A*, ASK13 (Abrahamson and others, 2013, 2014); *B*, BSSA13 (Boore and others, 2013, 2014); *C*, CB13 (Campbell and Bozorgnia, 2013, 2014); *D*, CY13 (Chiou and Youngs, 2013, 2014); *E*, I13, Idriss (2013, 2014); and *F*, 2014 combined ground motion models.

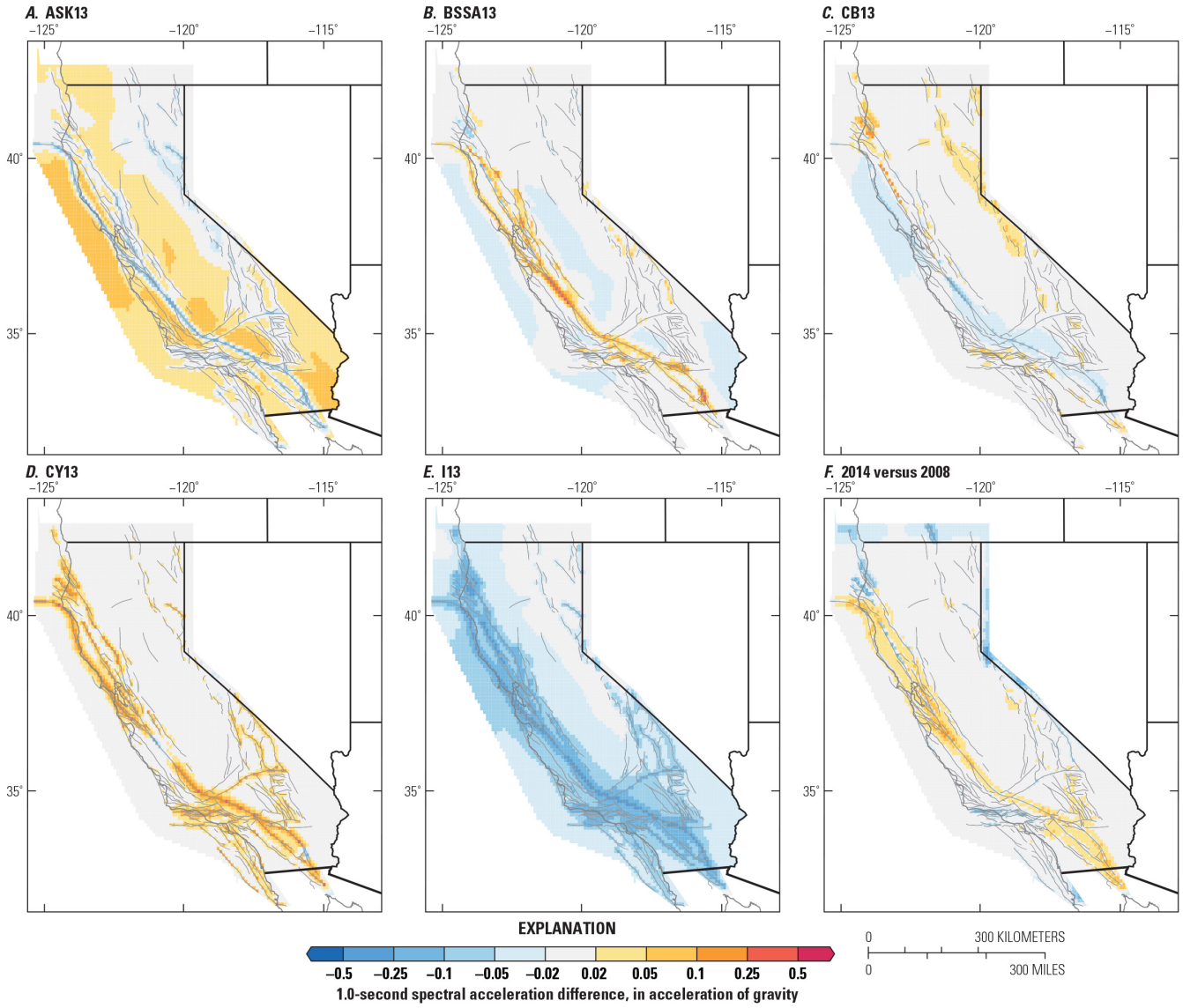

Figure 110. Maps showing difference in 1-second (1-hertz) spectral acceleration from individual ground motion models in California compared to the 2008 model at 2-percent in 50 years probability of exceedance and V_{S30} site conditions of 760 meters per second. *A*, ASK13 (Abrahamson and others, 2013, 2014); *B*, BSSA13 (Boore and others, 2013, 2014); *C*, CB13 (Campbell and Bozorgnia, 2013, 2014); *D*, CY13 (Chiou and Youngs, 2013, 2014); *E*, I13, Idriss (2013, 2014); and *F*, 2014 combined ground motion models.

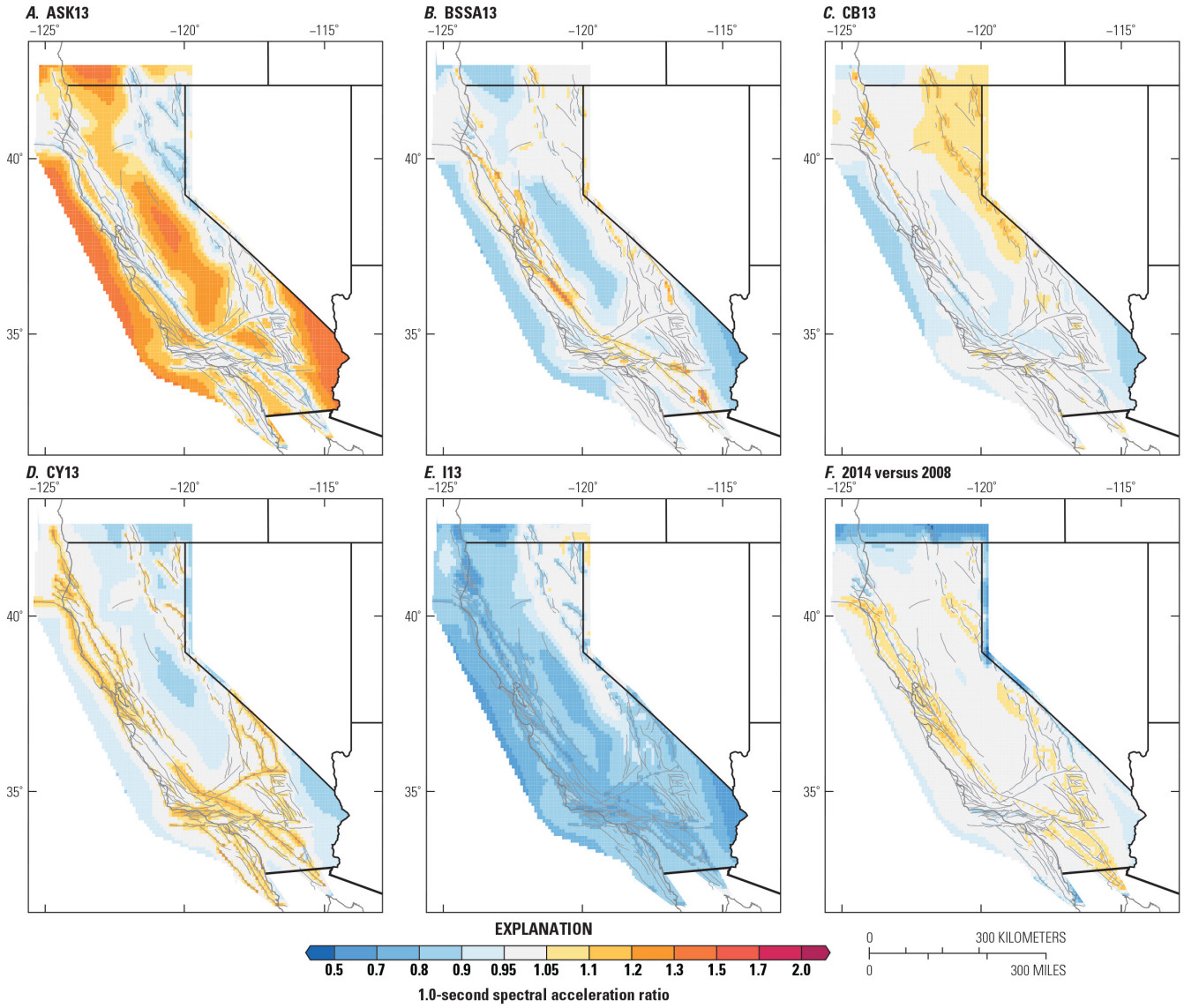

Figure 111. Maps showing ratio of 1-second (1-hertz) spectral acceleration from individual ground motion models in California and the 2008 model at 2-percent in 50 years probability of exceedance and V_{S30} site conditions of 760 meters per second. *A*, ASK13 (Abrahamson and others, 2013, 2014); *B*, BSSA13 (Boore and others, 2013, 2014); *C*, CB13 (Campbell and Bozorgnia, 2013, 2014); *D*, CY13 (Chiou and Youngs, 2013, 2014); *E*, I13, Idriss (2013, 2014); and *F*, 2014 combined ground motion models.

Ground Motion Models for Subduction Interface Earthquakes

The 2008 and 2014 GMMs for subduction interface earthquakes and their weights are given in table 18. Figure 112 displays the spectral acceleration from the models used in 2014 at a site 110 km from the nearest point on the rupture surface from an interface earthquake of magnitude 9. Figures 113 and 114 display the decay with distance of median 0.2-second and 1-second spectral acceleration, respectively, from a magnitude 9 subduction source. These figures include the Youngs and others

(1997) model that was used in the 2008 hazard maps for reference. The Youngs and others (1997) model was removed from the 2014 hazard maps per the authors' request.

The Atkinson and Boore (2003) global model is retained with a lower weight because the possibility of gentle decay with distance of the intermediate- to long-period motion cannot be rejected. This model may need some modifications for periods beyond 1 hertz (1 second). The other models exhibit steeper decay with distance but are influenced strongly by Tohoku, Japan, data, which may not be representative of behavior in the Pacific Northwest region. Beyond the distance of 400 km recommended by the authors, this model is simply extrapolated with distance for spectral periods below and including 1-second. For longer periods, however, extrapolation to larger distances (beyond 400 km) results in unlikely high ground motion values. This is due to the zero anelastic attenuation at spectral periods greater than 1-second, which is built in the model regardless of the distance. Based on communications with the authors and comparisons with the available long-period data from large earthquakes at long distances (for example, earthquakes in Tohoku, Japan, and Maule, Chile), the model is modified slightly to include an anelastic attenuation term for distances beyond 400 km and periods greater than 1 second (s). For 2-second and 3-second spectral acceleration maps, the term $-0.001\times(R-400)$ is added to account for the anelastic attenuation beyond 400 km, where R represents the distance in km. For 1.5-second spectral acceleration maps, the cut-off distance is reduced to 200 km and the term $-0.001\times(R-200)$ is used instead to ensure that the anelastic attenuation is less than that of 1 second, but more than what is used at 2 second.

Table 18. Subduction interface ground motion models and weights in 2008 and 2014 hazard maps.

	Interface GMM	2008 weights	2014 weights
1.	Geomatrix (Youngs and others, 1997)	0.25	0
2.	Atkinson and Boore (2003) global model	0.25	0.10
3.	Zhao and others (2006)	0.5	0.30
4.	Atkinson and Macias (2009)	0	0.30
5.	BC Hydro (Addo and others, 2012)	0	0.30

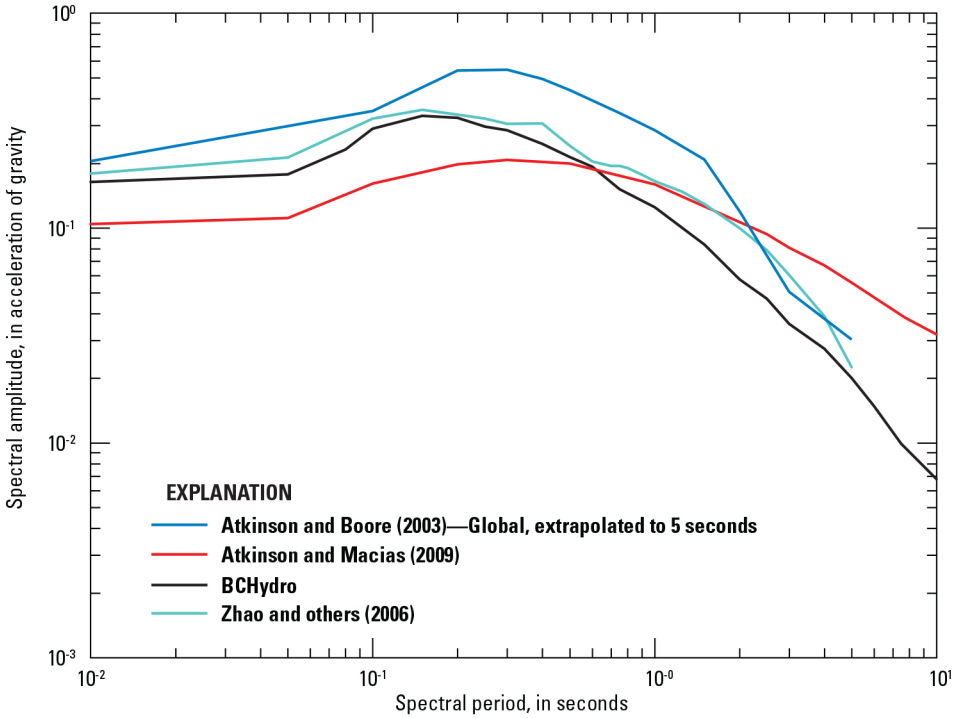

Figure 112. Plot of subduction-interface ground motion models versus period for an earthquake with moment magnitude of 9 at a distance of 110 kilometers for V_{S30} site conditions of 760 meters per second.

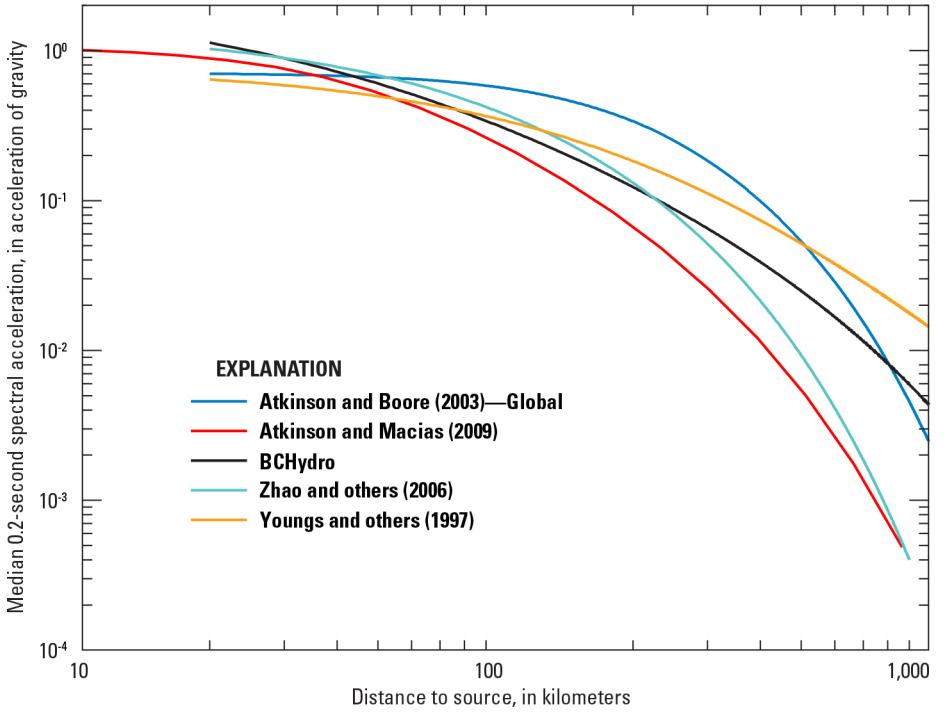

Figure 113. Plot of median 0.2-second spectral acceleration for subduction-interface ground motion models versus distance for an earthquake with moment magnitude of 9 and V_{S30} site conditions of 760 meters per second.

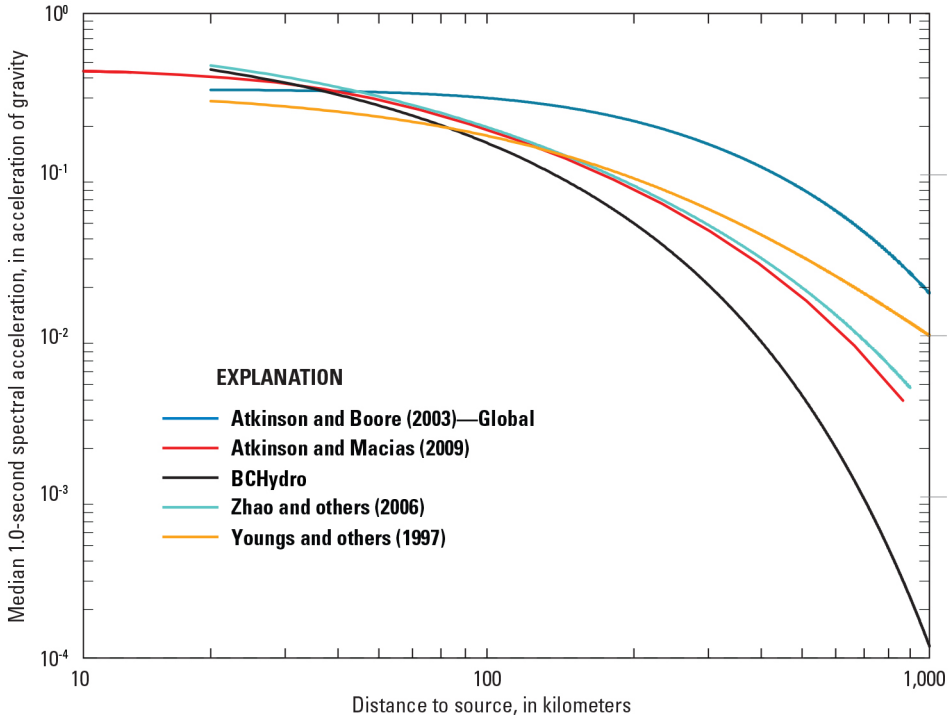

Figure 114. Plot of median 1-second spectral acceleration for subduction-interface ground motion models versus distance for an earthquake with moment magnitude of 9 and V_{S30} site conditions of 760 meters per second.

Figures 115–120 show comparisons of the individual subduction interface GMMs and the weighted average of the suite of GMMs used in the 2014 maps. These comparisons are made for peak ground acceleration, 0.2-second (5-hertz) spectral acceleration, and 1-second (1-hertz) spectral acceleration; AB03-GL, which represents the Atkinson and Boore (2003) global model; AM09, which represents the Atkinson and Macias (2009) model; BCHYDRO, which represents the Addo and others (2012) model; and ZHAO, which represents the Zhao and others (2006) model. The individual GMM is subtracted with or divided by the 2014 weighted average to obtain the difference and ration maps. Hot colors (red, yellow) represent ground motions higher than average, whereas cold colors (blues) represent motions lower than average.

For sites located near the Cascadia subduction zone, the BC Hydro and Zhao and others (2006) models typically are higher than the others, whereas for sites located farther away, the Atkinson and Boore (2003) model typically is higher than the others. The Atkinson and Macias (2009) model typically is lower than the others for all three periods.

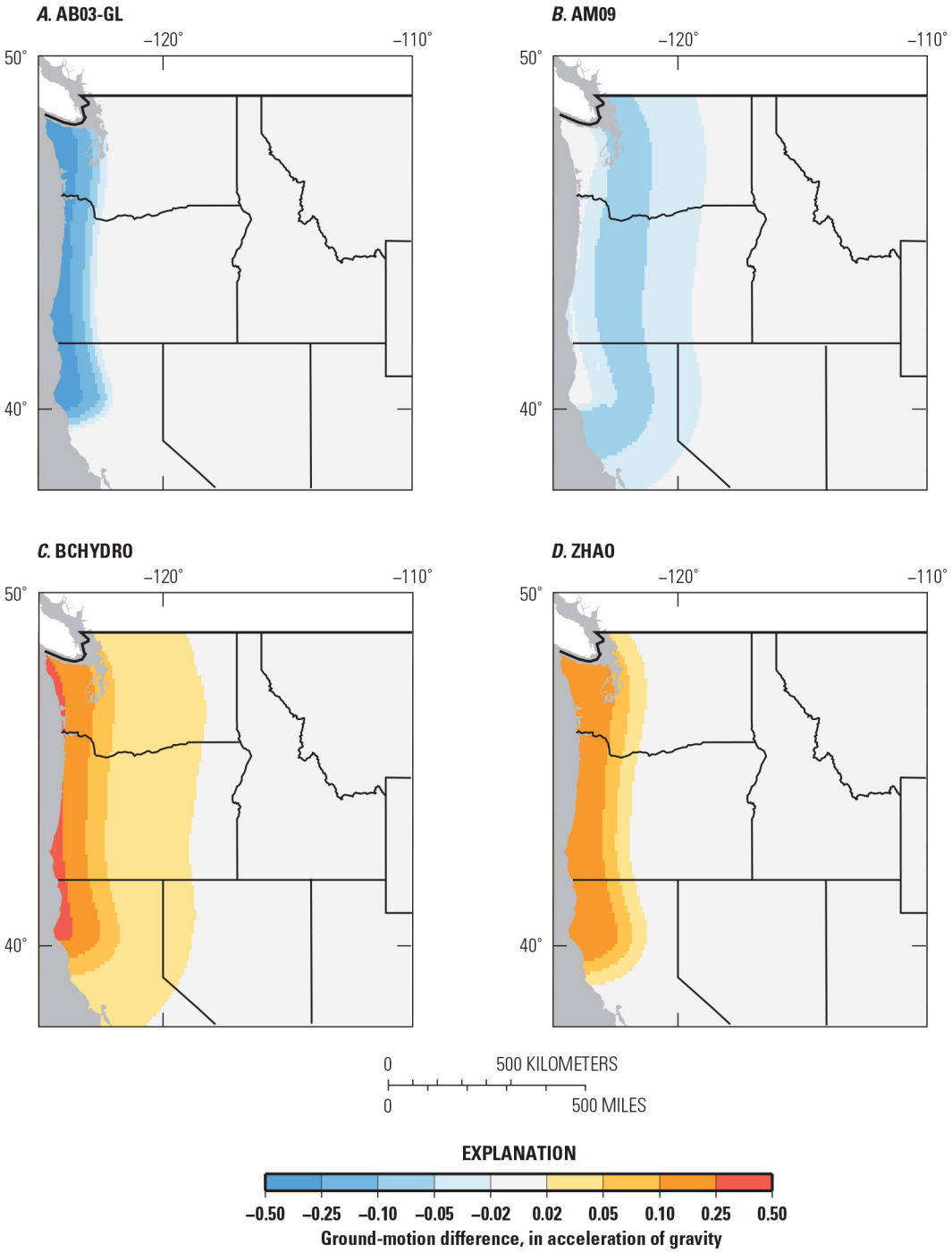

Figure 115. Maps showing difference in peak ground acceleration from individual subduction-interface ground motion models compared to the 2008 model at 2-percent in 50 years probability of exceedance and V_{S30} site conditions of 760 meters per second. *A*, AB03-GL (Atkinson and Boore, 2003) global model; *B*, AM09 (Atkinson and Macias, 2009); *C*, BCHYDRO (Addo and others, 2012); and *D*, ZHAO (Zhao and others, 2006) models.

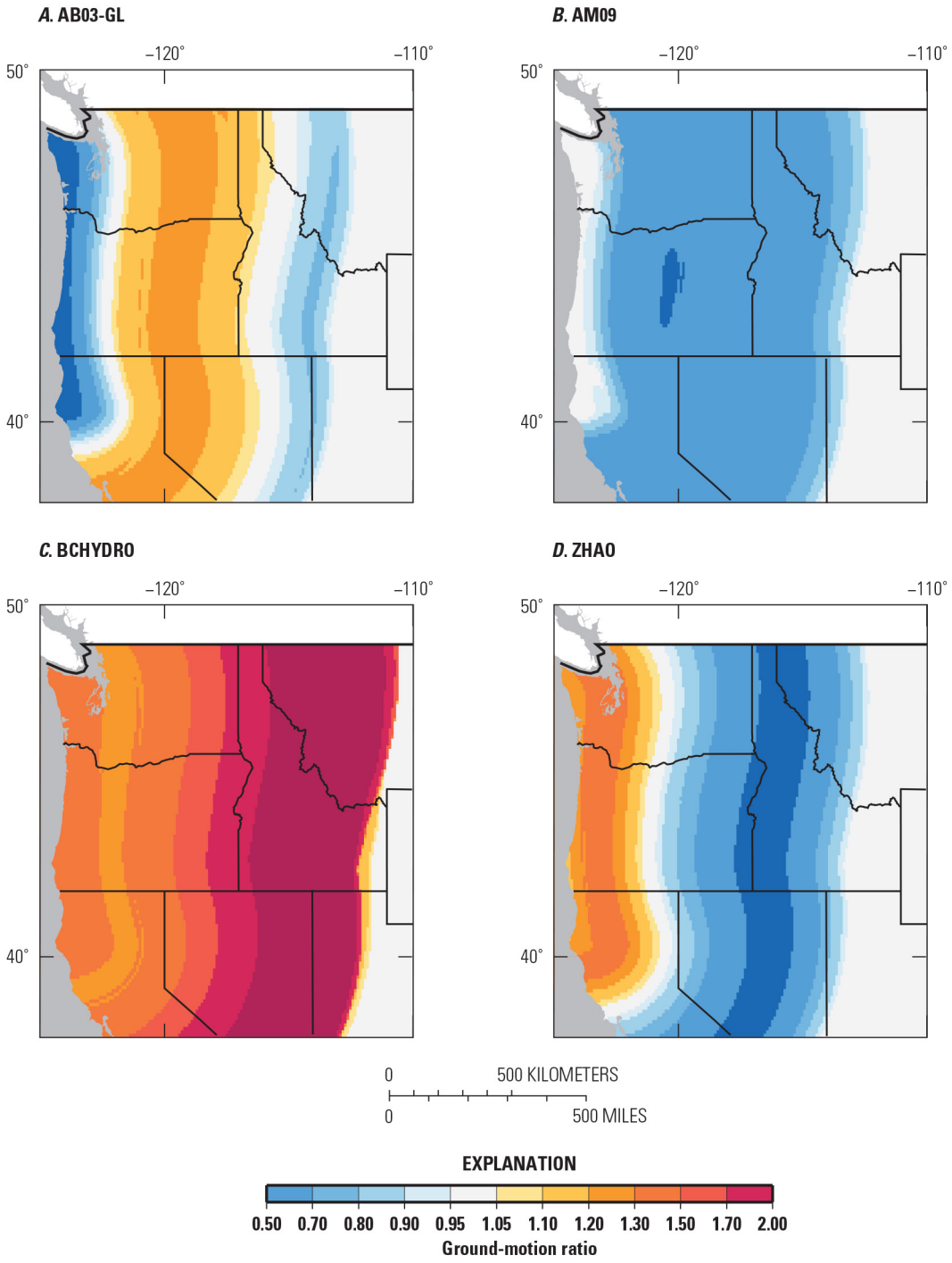

Figure 116. Maps showing ratios of peak ground acceleration from individual subduction-interface ground motion models and the 2008 model at 2-percent in 50 years probability of exceedance and V_{S30} site conditions of 760 meters per second. *A*, AB03-GL (Atkinson and Boore, 2003) global model; *B*, AM09 (Atkinson and Macias, 2009); *C*, BCHYDRO (Addo and others, 2012); and *D*, ZHAO (Zhao and others, 2006) models.

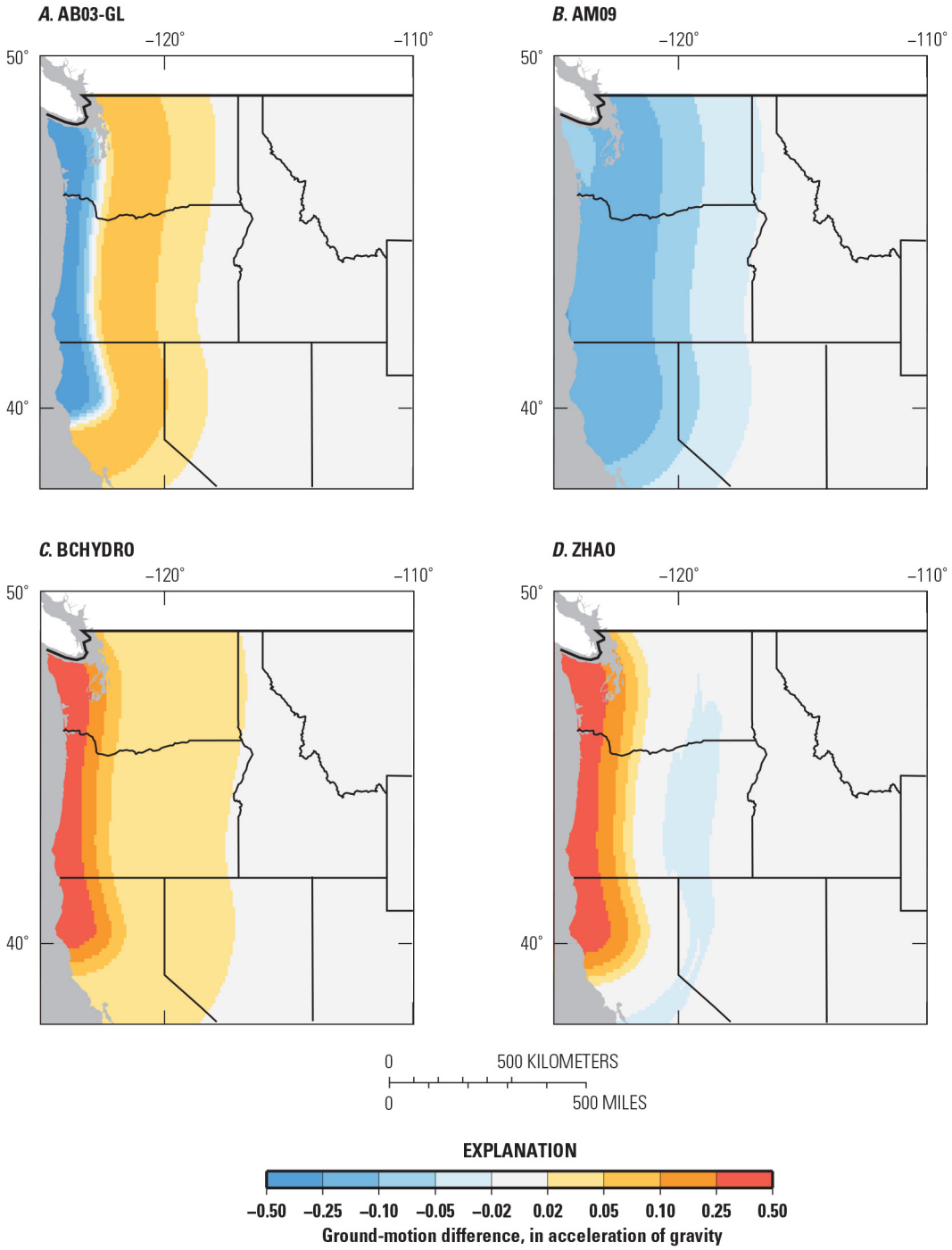

Figure 117. Maps showing difference in 0.2-second (5-hertz) spectral acceleration from individual subduction-interface ground motion models compared to the 2008 model at 2-percent in 50 years probability of exceedance and V_{S30} site conditions of 760 meters per second. *A*, AB03-GL (Atkinson and Boore, 2003) global model; *B*, AM09 (Atkinson and Macias, 2009); *C*, BCHYDRO (Addo and others, 2012); and *D*, ZHAO (Zhao and others, 2006) models.

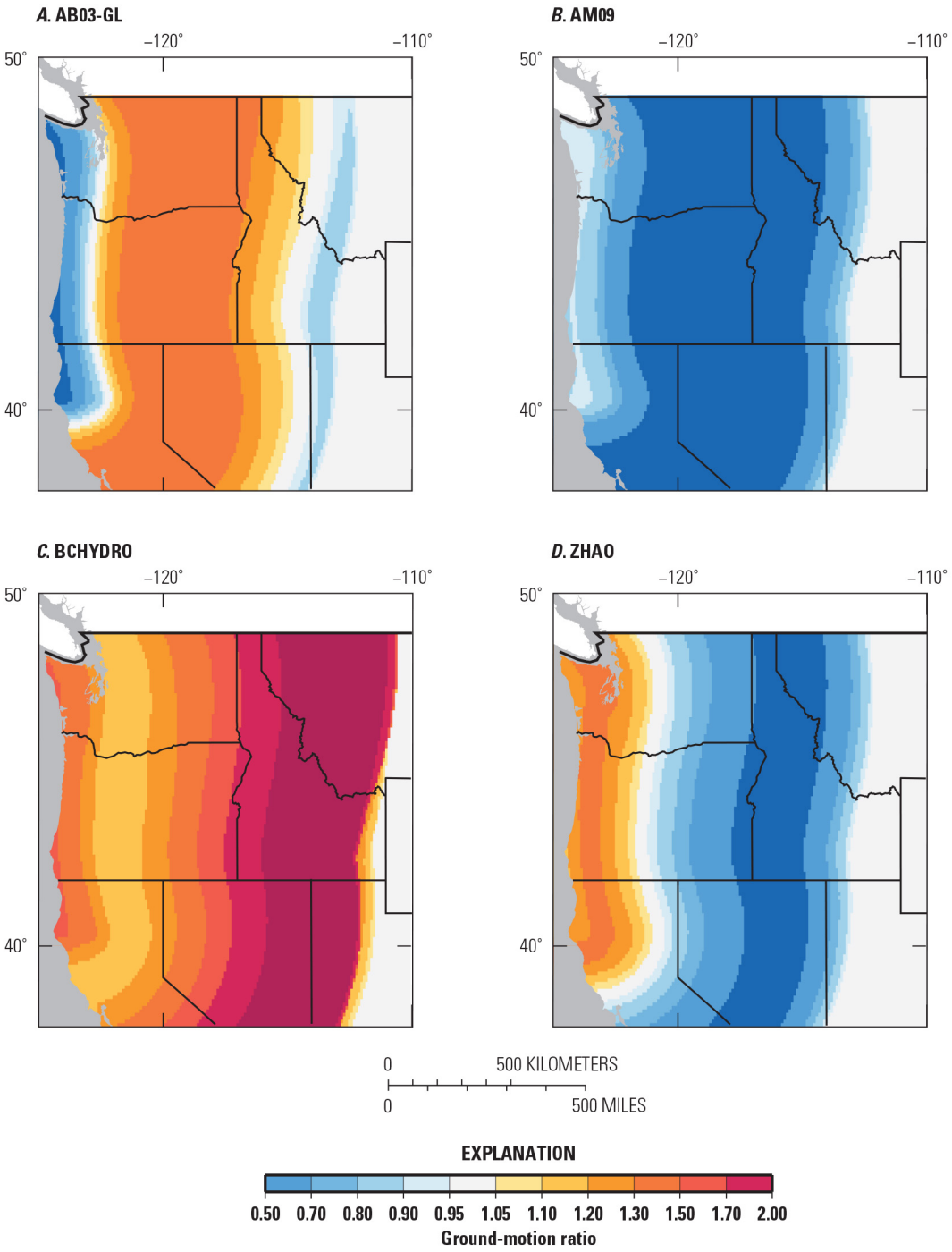

Figure 118. Maps showing ratios of 0.2-second (5-hertz) spectral acceleration from individual subduction-interface ground motion models and the 2008 model at 2-percent in 50 years probability of exceedance and V_{S30} site conditions of 760 meters per second. *A*, AB03-GL (Atkinson and Boore, 2003) global model; *B*, AM09 (Atkinson and Macias, 2009); *C*, BCHYDRO (Addo and others, 2012); and *D*, ZHAO (Zhao and others, 2006) models.

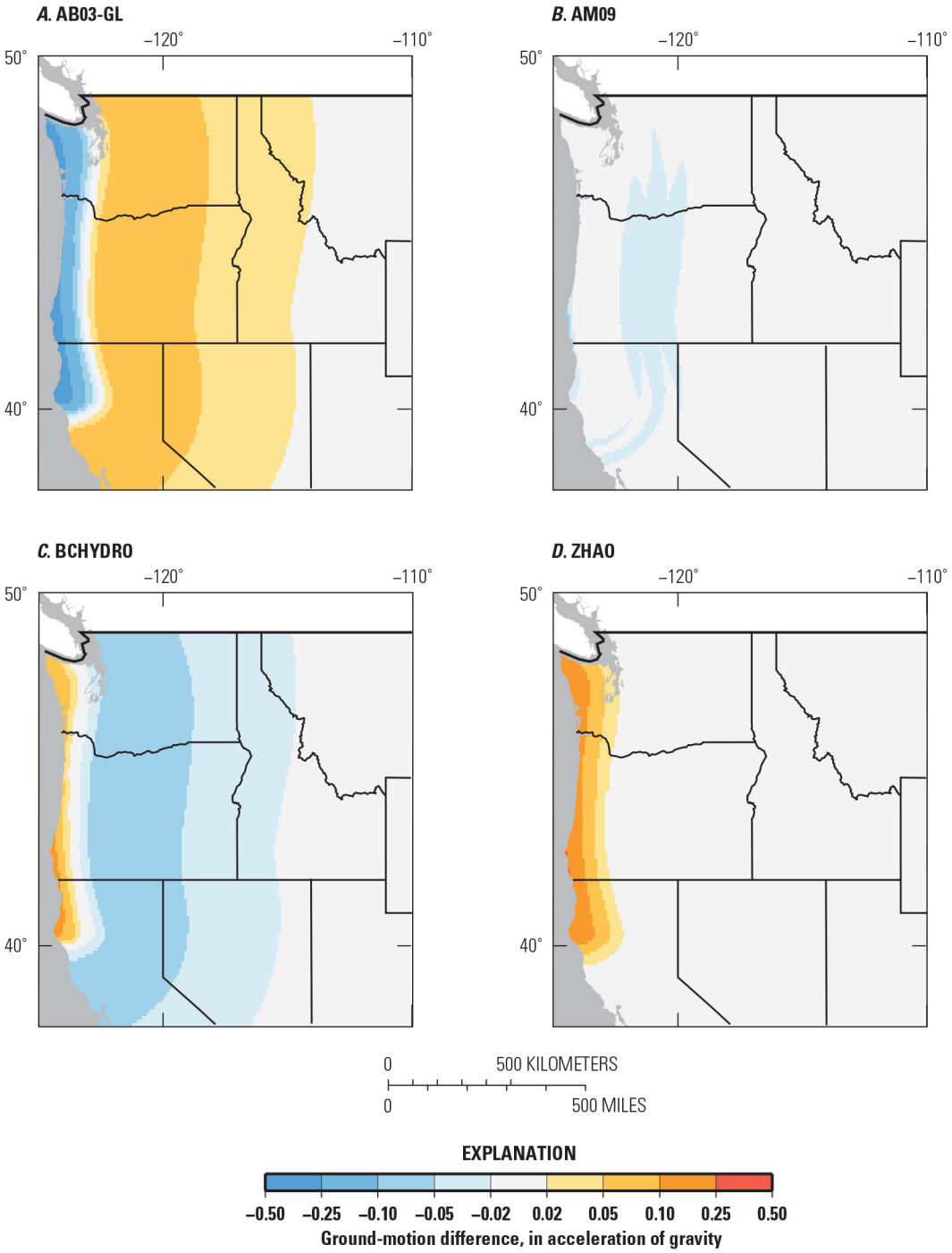

Figure 119. Maps showing difference in 1-second (1-hertz) spectral acceleration from individual subduction-interface ground motion models compared to the 2008 model at 2-percent in 50 years probability of exceedance and V_{S30} site conditions of 760 meters per second. *A*, AB03-GL (Atkinson and Boore, 2003) global model; *B*, AM09 (Atkinson and Macias, 2009); *C*, BCHYDRO (Addo and others, 2012); and *D*, ZHAO (Zhao and others, 2006) models.

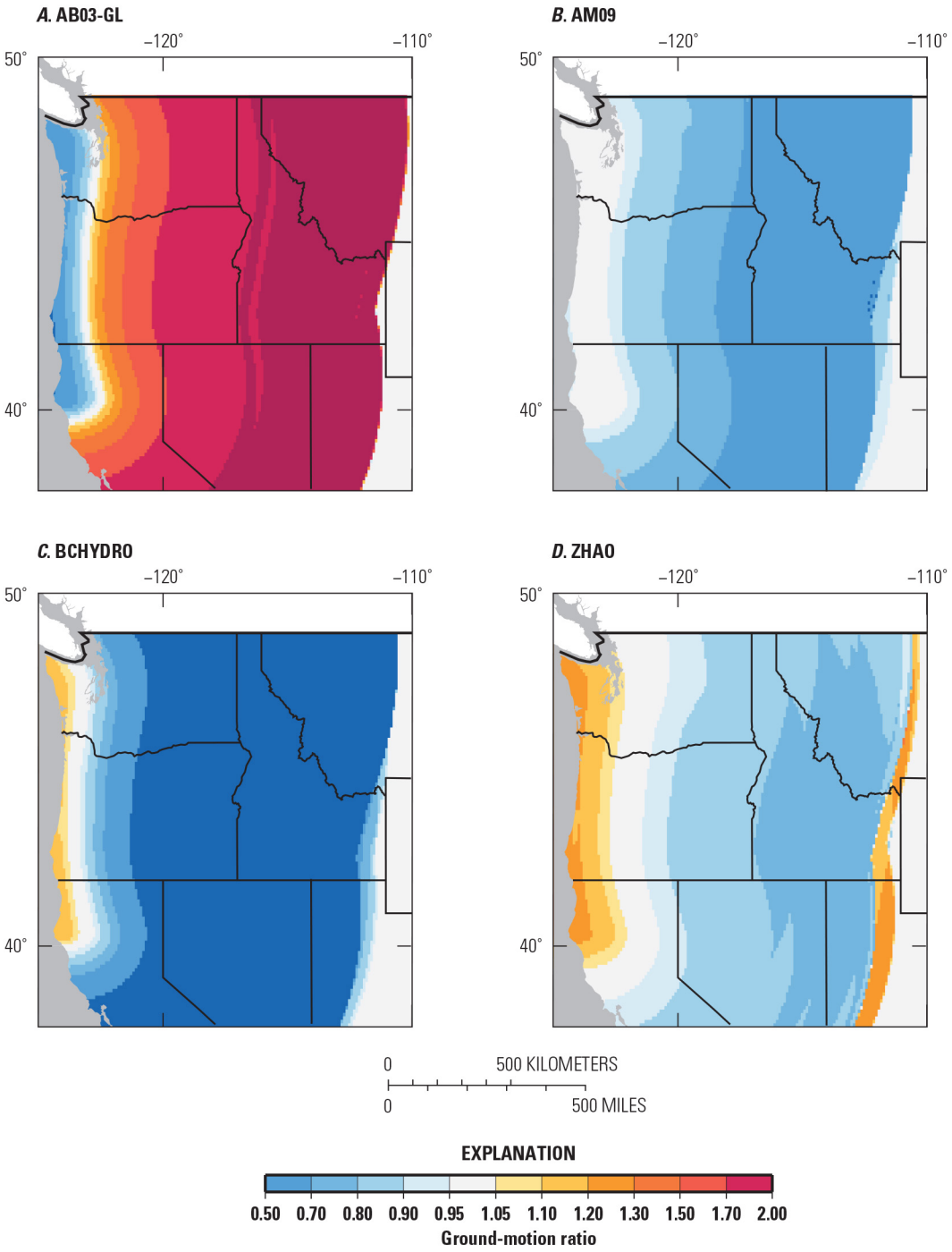

Figure 120. Maps showing ratios of 1-second (1-hertz) spectral acceleration from individual subduction-interface ground motion models and the 2008 model at 2-percent in 50 years probability of exceedance and V_{S30} site conditions of 760 meters per second. *A*, AB03-GL (Atkinson and Boore, 2003) global model; *B*, AM09 (Atkinson and Macias, 2009); *C*, BCHYDRO (Addo and others, 2012); and *D*, ZHAO (Zhao and others, 2006) models.

Ground Motion Models for Subduction Intraslab Earthquakes (Deep Seismicity)

In the 2008 hazard maps, we used three GMMs to model ground vibration from deep-focus earthquakes: the Youngs and others (1997) model with 0.5 weight, and two Atkinson and Boore (2003) models, one for global source (0.25 weight) and one for the Cascadia source (0.25 weight). By depth and location, most of these are associated with the Benioff zone of the subducting slab. The modifications to the GMMs from 2008 to 2014 maps are listed in table 19 with inclusion of two new models, Zhao and others (2006) and BC Hydro (Addo and others, 2012). The Atkinson and Boore equations have been retained to sample epistemic uncertainty in ground motion from deep earthquakes. The Youngs and others (1997) equation was dropped in the 2014 update per developers' recommendation.

Zhao and others (2006) was truncated to saturate the ground motions above M_w7.8. The effect of capping magnitude at 7.8 is to limit the median ground motion to the following values: (1) truncation for 0.2-second spectral acceleration and 50-km distance (closest distance to rupture, Rcd) at 1.5 g and 100-km distance at 0.52 g, (2) truncation is applied for 1-second spectral acceleration and 50-km distance at 0.4 g and 100-km distance at 0.14 g, and (3) truncation is applied for PGA and 50-km distance at 0.7 g and 100-km distance at 0.22 g. The probabilistic ground motion is limited to the median plus three sigma.

Figures 121*A* and *B* show median GMMs for deep sources associated with table 19 for 0.2-second spectral acceleration (5 hertz frequency) and 1 second spectral acceleration (1 hertz frequency), respectively. Figure 121*B* shows the four 2014 GMMs and figure 121*A* also includes Youngs and others (1997) for comparison. The medians are shown for sources of magnitudes of 6.2 and 7.2 with a depth of 50 km. The newer GMMs tend to predict larger short period motion and lower long period motion than the earlier models.

Table 19. Pacific Northwest intraslab (deep) ground motion models and weights in 2008 and 2014 hazard maps.
[GMM, ground motion model]

	Intraslab (deep) GMM	2008 weights	2014 weights
1.	Geomatrix (Youngs and others, 1997)	0.5	0
2.	Atkinson and Boore (2003) global model	0.25	0.1667
3.	Atkinson and Boore (2003) Cascadia model	0.25	0.1667
4.	Zhao and others (2006)	0	0.33
5.	BC Hydro (Addo and others, 2012)	0	0.33

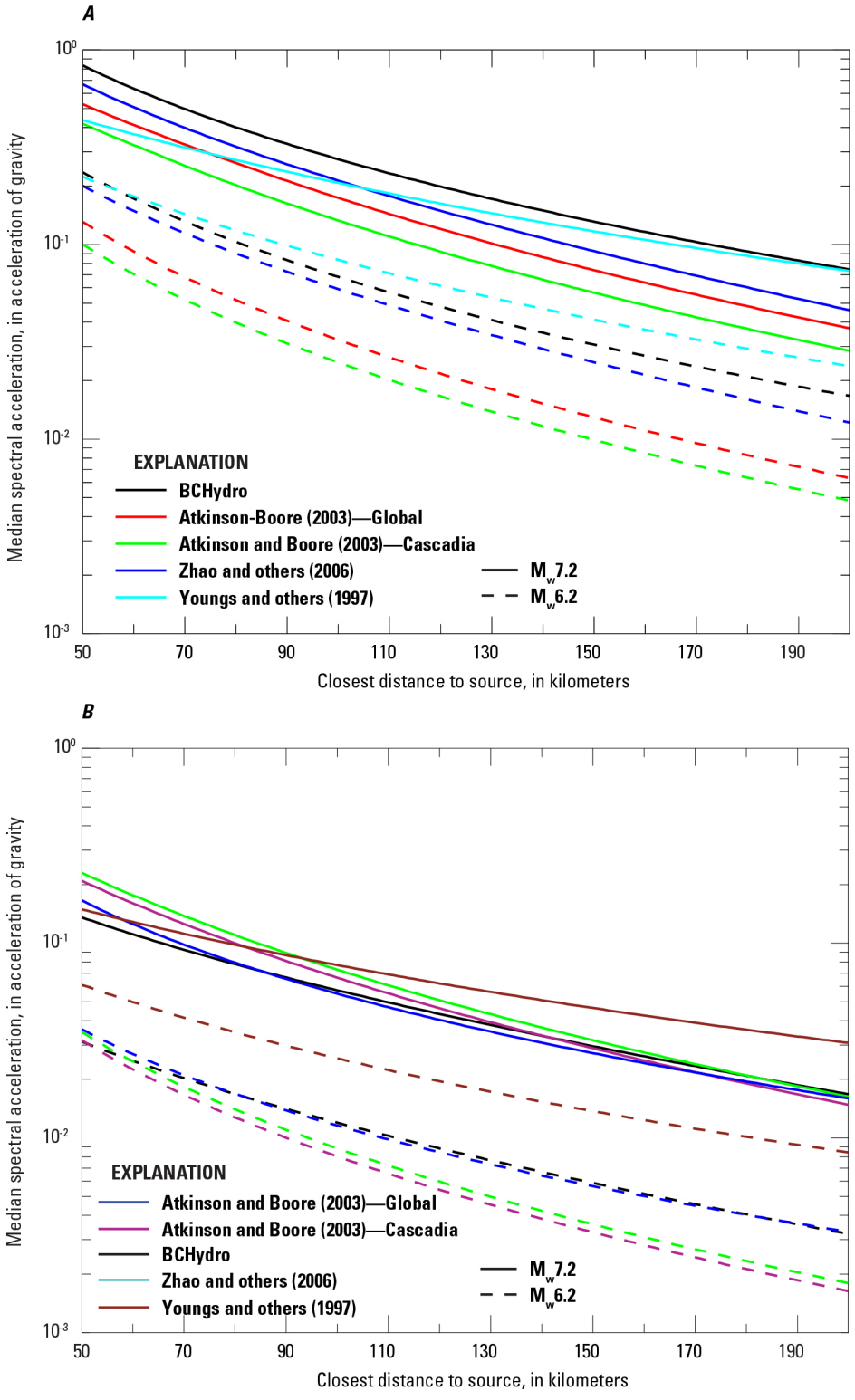

Figure 121. Plots of subduction intraslab (deep) ground motion models versus distance for *A*, 0.2-second spectral acceleration, and *B*, 1-second spectral acceleration.

Figures 122–127 show comparisons of the individual deep intraslab GMMs and the weighted average of the suite of GMMs used in the 2014 maps. These comparisons are made for peak ground acceleration, 0.2-second (5-hertz) spectral acceleration, and 1-second (1-hertz) spectral acceleration; AB03-GL, which represents the Atkinson and Boore (2003) global and Cascadia models; BCHYDRO, which represents the Addo and others (2012) model; AM09, which represents the Atkinson and Macias (2009) model, and ZHAO, which represents the Zhao and others (2006) model. The individual GMM is subtracted from or divided by the 2014 weighted average to obtain the difference and ration maps. Hot colors (red, yellow) represent ground motions higher than average, whereas cold colors (blues) represent motions lower than average.

For sites located near deep seismicity in the Pacific Northwest, the BC Hydro and Zhao and others (2006) models for peak ground acceleration and 0.2-second (5-hertz) spectral acceleration are typically higher than the others whereas the Atkinson and Boore (2003) models are both typically lower than average. The trend is opposite for 1-second (1-hertz) spectral acceleration with the Atkinson and Boore models having a little higher ground motions than average.

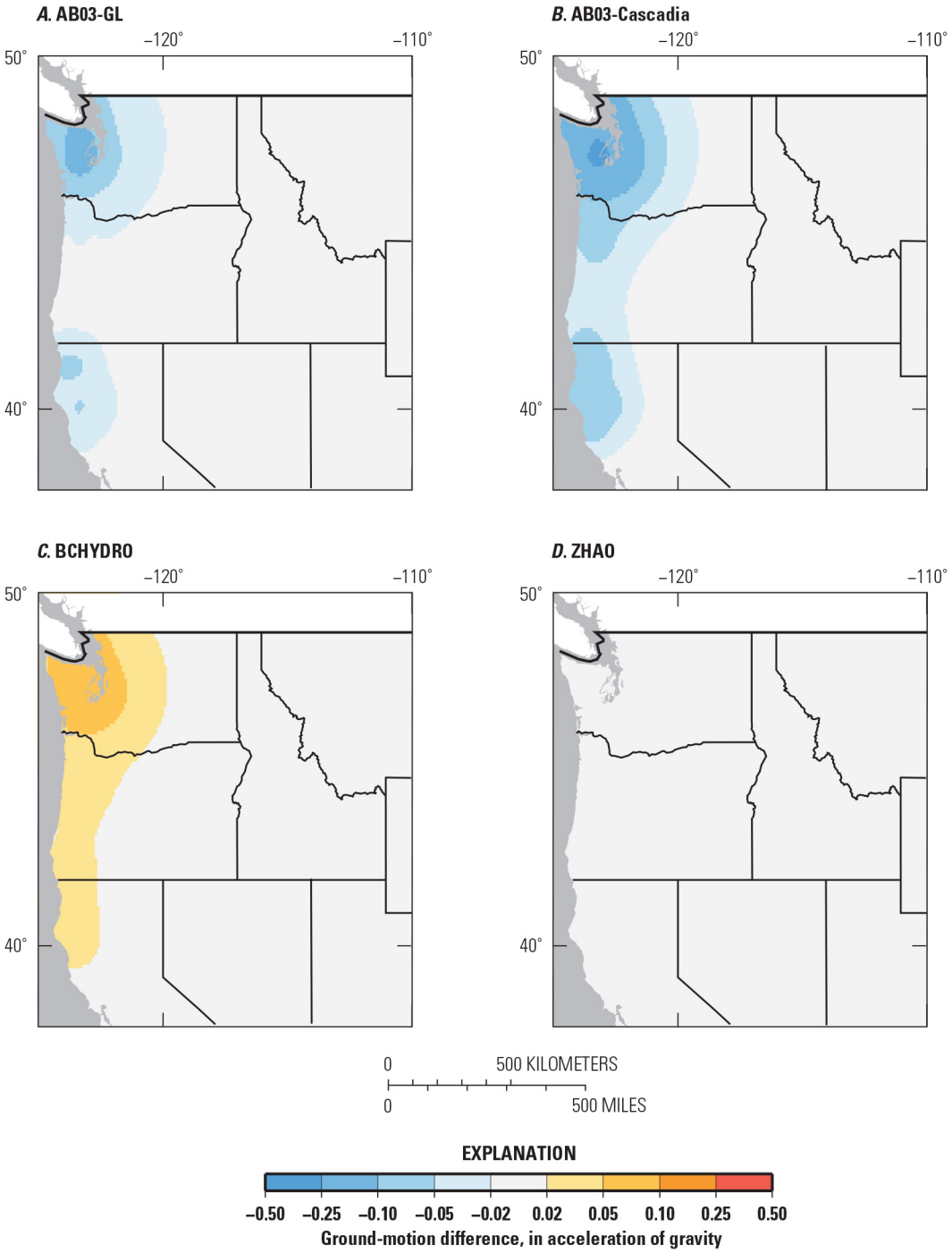

Figure 122. Maps showing difference in peak ground acceleration from individual deep-intraslab ground motion models compared to the 2008 model at 2-percent in 50 years probability of exceedance and V_{S30} site conditions of 760 meters per second. *A*, AB03-GL (Atkinson and Boore, 2003) global model; *B*, AB03-Cascadia (Atkinson and Boore, 2003) Cascadia model; *C*, BCHYDRO (Addo and others, 2012); and *D*, ZHAO (Zhao and others, 2006) models. Changes in the Zhao and others (2006) model is close to the mean; differences are close to zero.

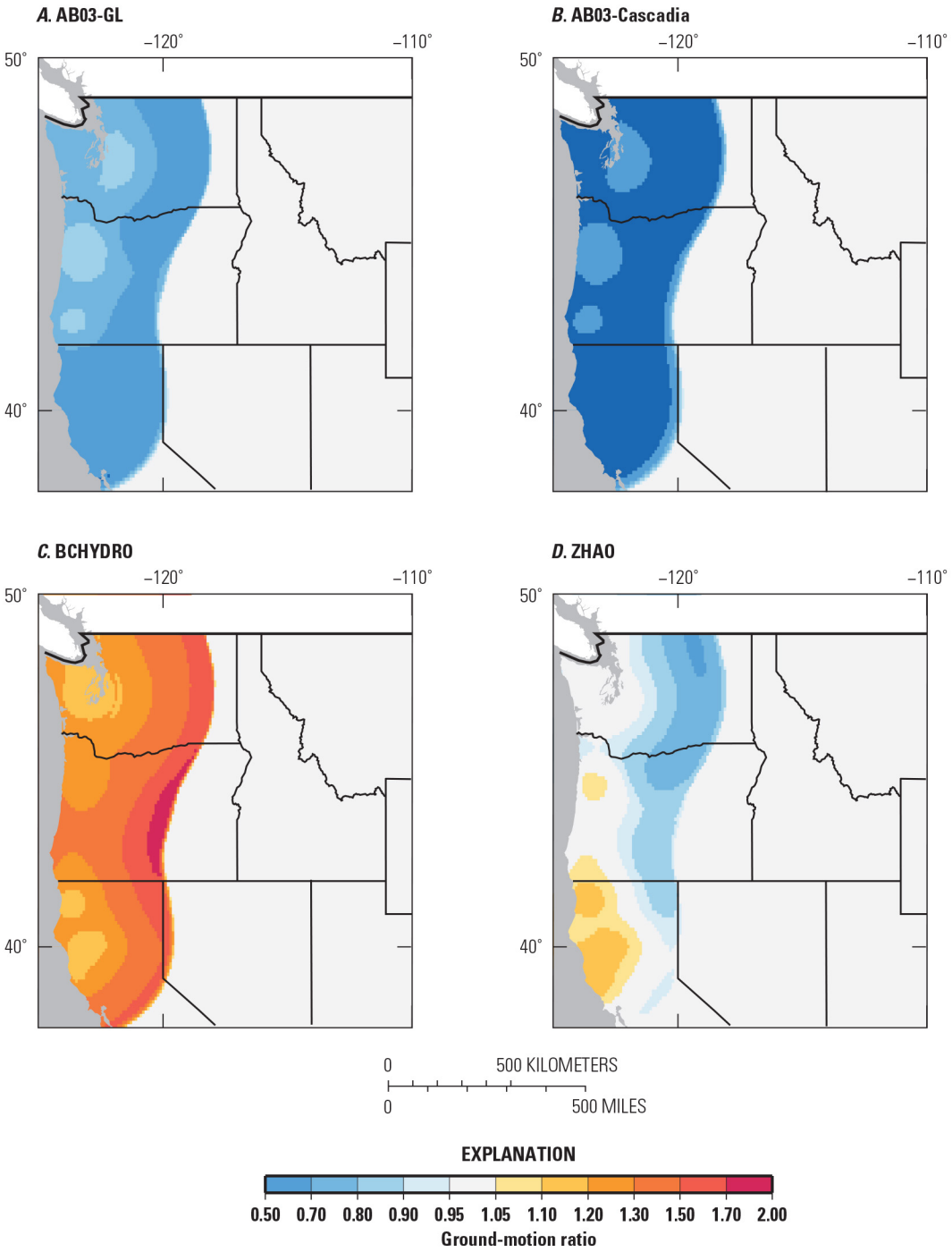

Figure 123. Maps showing ratios of peak ground acceleration from individual deep-intraslab ground motion models and the 2008 model at 2-percent in 50 years probability of exceedance and V_{S30} site conditions of 760 meters per second. *A*, AB03-GL (Atkinson and Boore, 2003) global model; *B*, AB03-Cascadia (Atkinson and Boore, 2003) Cascadia model; *C*, BCHYDRO (Addo and others, 2012); and *D*, ZHAO (Zhao and others, 2006) models.

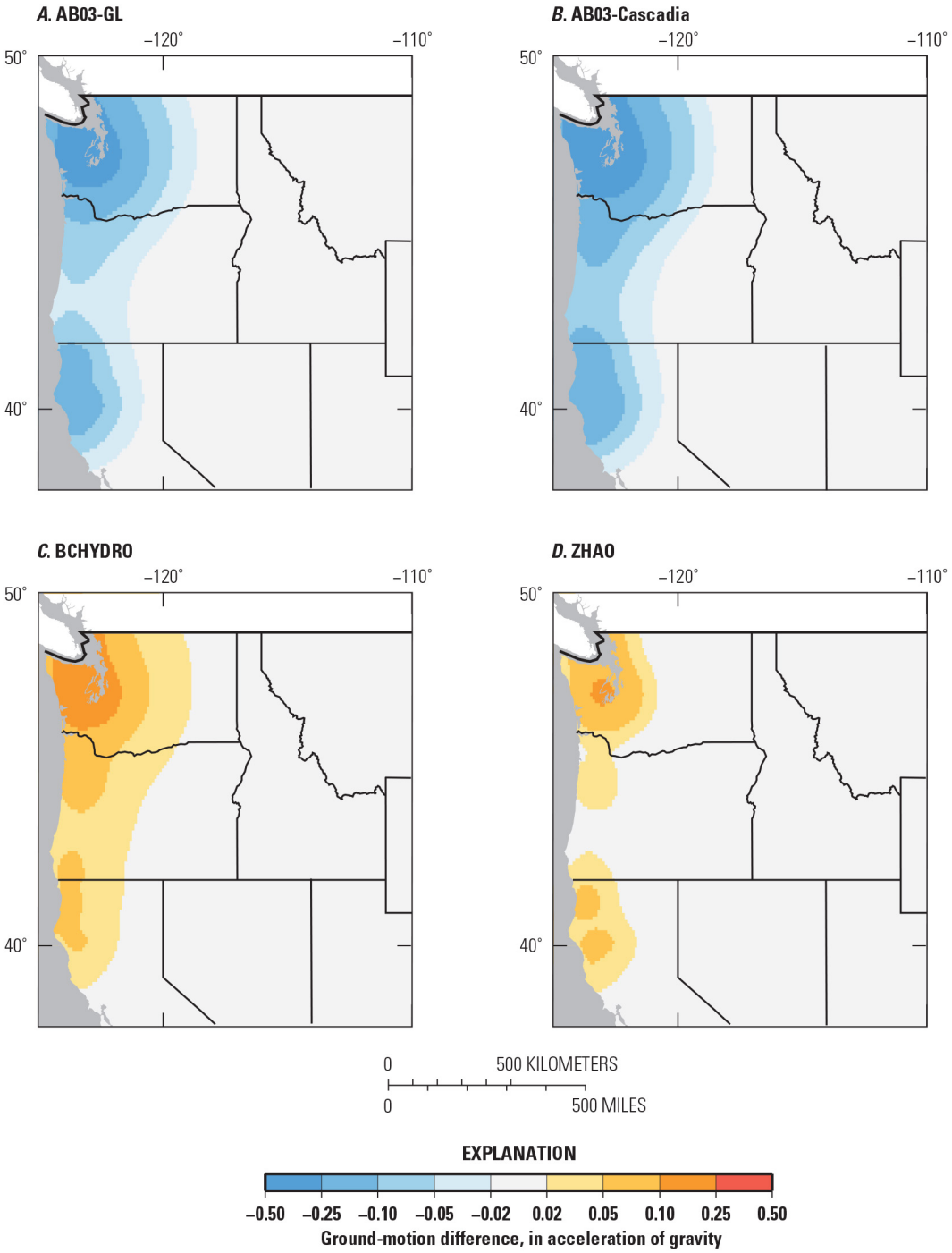

Figure 124. Maps showing difference in 0.2-second (5-hertz) spectral acceleration from individual deep-intraslab ground motion models compared to the 2008 model at 2-percent in 50 years probability of exceedance and V_{S30} site conditions of 760 meters per second. *A*, AB03-GL (Atkinson and Boore, 2003) global model; *B*, AB03-Cascadia (Atkinson and Boore, 2003) Cascadia model; *C*, BCHYDRO (Addo and others, 2012); and *D*, ZHAO (Zhao and others, 2006) models.

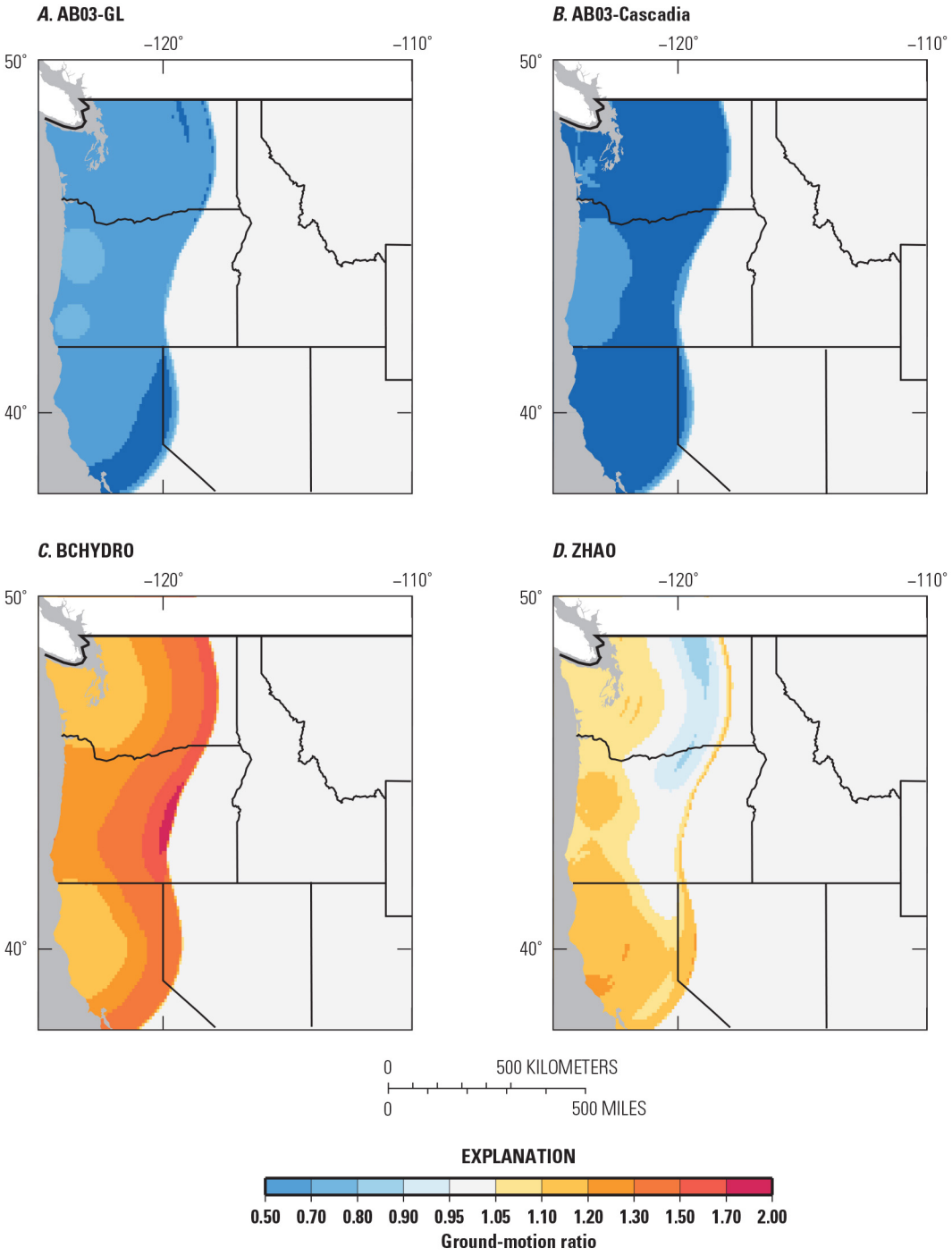

Figure 125. Maps showing ratios of 0.2-second (5-hertz) spectral acceleration from individual deep-intraslab ground motion models and the 2008 model at 2-percent in 50 years probability of exceedance and V_{S30} site conditions of 760 meters per second. *A*, AB03-GL (Atkinson and Boore, 2003) global model; *B*, AB03-Cascadia (Atkinson and Boore, 2003) Cascadia model; *C*, BCHYDRO (Addo and others, 2012); and *D*, ZHAO (Zhao and others, 2006) models.

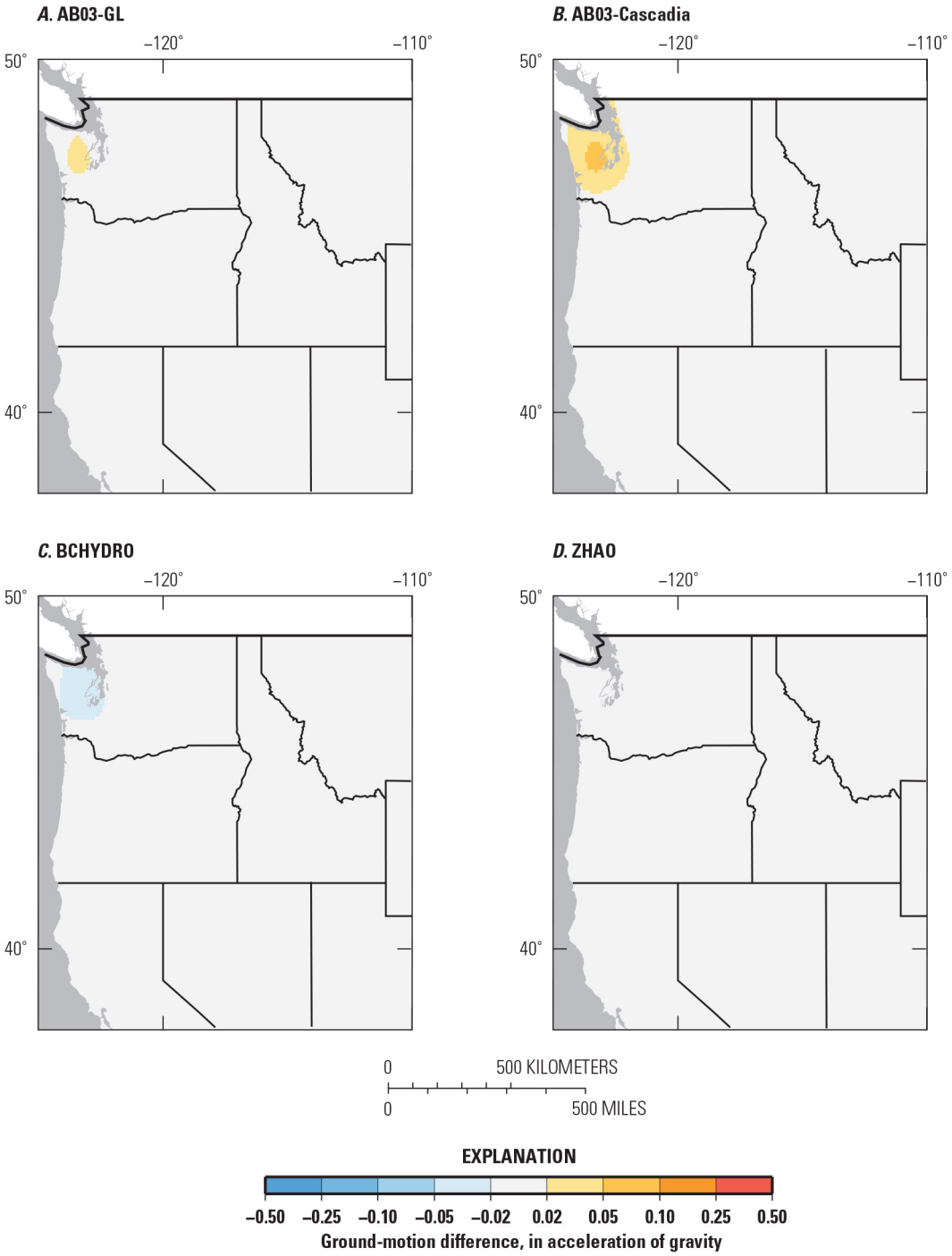

Figure 126. Maps showing difference in 1-second (1-hertz) spectral acceleration from individual deep-intraslab ground motion models compared to the 2008 model at 2-percent in 50 years probability of exceedance and V_{S30} site conditions of 760 meters per second. *A*, AB03-GL (Atkinson and Boore, 2003) global model; *B*, AB03-Cascadia (Atkinson and Boore, 2003) Cascadia model; *C*, BCHYDRO (Addo and others, 2012); and *D*, ZHAO (Zhao and others, 2006) models. Changes in the Zhao and others (2006) model is close to the mean; differences are close to zero.

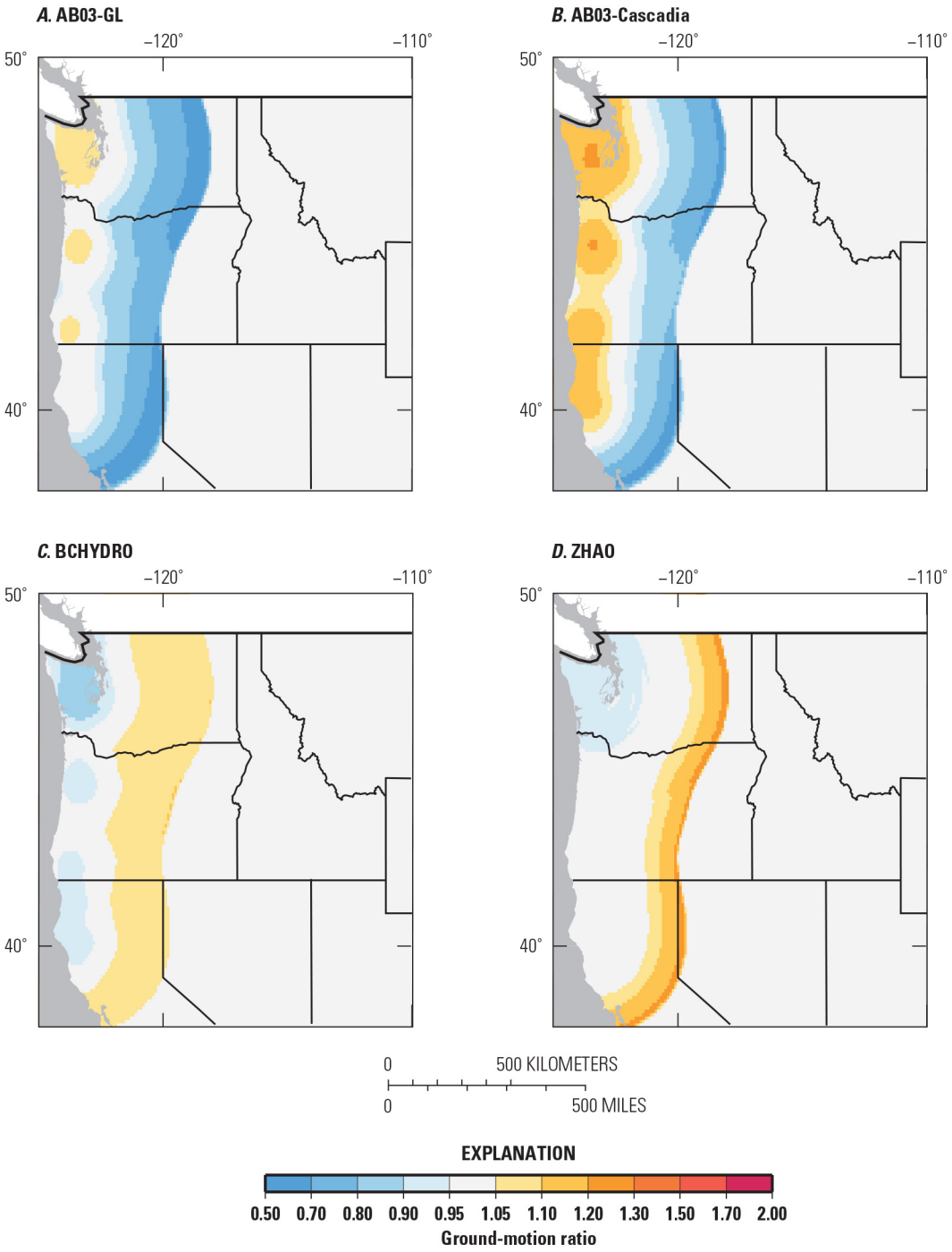

Figure 127. Maps showing ratios of 1-second (1-hertz) spectral acceleration from individual deep-intraslab ground motion models and the 2008 model at 2-percent in 50 years probability of exceedance and V_{S30} site conditions of 760 meters per second. *A*, AB03-GL (Atkinson and Boore, 2003) global model; *B*, AB03-Cascadia (Atkinson and Boore, 2003) Cascadia model; *C*, BCHYDRO (Addo and others, 2012); and *D*, ZHAO (Zhao and others, 2006) models.

Results

The 2014 USGS NSHMP maps incorporate significant source and ground motion modifications that create complex patterns of hazard changes across the United States. Updates of the earthquake catalog, rates, and smoothed seismicity methods; fault rupture models using geologic and geodetic information; and ground motion models have resulted in changes to ground motions in nearly all of the conterminous United States. In this section we concentrate our discussion on the building code type hazard maps that are computed for 2-percent probability of exceedance in 50 years and a uniform firm rock (V_{S30}=760 m/s) site condition for PGA and spectral response acceleration at 1-hertz (1-second spectral acceleration) and 5-hertz (0.2-second spectral acceleration) for 5-percent damping. We have examined other ground shaking types such as for longer periods that will be considered in future reports.

In the following sections, we present the changes to the USGS NSHMP maps, relative to the 2008 USGS NSHMP maps, and discuss the contributing factors that result in probabilistic ground motion differences. To examine the causes of the differences between the 2014 and 2008 USGS NSHMP maps, we show difference (2014 probabilistic ground motions minus 2008 ground motions) and ratio maps (2014 probabilistic ground motions divided by 2008 ground motions) for the WUS, CEUS, California, and subduction related earthquakes. In addition to the total changes in ground motions at PGA and 1-hertz and 5-hertz spectral acceleration between the 2014 and 2008 USGS NSHMP maps, we show separately the influence of changes caused by updated fault-source models, seismicity-based background-source models, and ground motion models.

Central and Eastern United States

Differences between the 2008 NSHMP maps and the 2014 NSHMP maps are complex across the CEUS with hazard varying locally (figs. 128–133). These changes mainly are caused by (1) updated GMMs; (2) updated seismicity rate calculations and smoothing methods; and (3) modified fault models for New Madrid (Missouri) seismic zone and surrounding area, Charleston (S.C.) seismic zone, new Charlevoix (eastern Canada) fault and areal source zones, and the Meers (Oklahoma) and Cheraw (Colo.) faults (fig. 21).

The updated GMMs and their weights have the overall effect of reducing ground motions for all sources and at all ground motion spectral periods. The reason for this is that the 2014 models are weighted more heavily with the equations that decay more quickly with distance than the models applied in 2008. These hazard decreases, in general, are more significant for moderate distances and larger magnitudes.

Earthquake catalog and rate changes in the gridded-seismicity model cause many of the local differences across the CEUS (especially for shorter periods). Regional changes in hazard across the CEUS are caused by a new catalog and newly adopted treatment of the seismicity rates; the 2014 NSHMP model incorporates seismicity-rate adjustments for observed and converted magnitudes following the CEUS–SSCn (2013), applies a new catalog with modified completeness criteria, and applies partial weight to seismicity rate distributions calculated from new adaptive-smoothing techniques. As in 2008, we have omitted earthquakes suspected to be related to mining or industrial fluid injection/extraction processes. Some changes in the seismicity rate and treatment of these events cause local differences in the maps (such as Fashing, Tex., central Oklahoma, and the Raton Basin, Colo. and N. Mex.). Methods to account for the hazard from these deleted events in a consistent manner are under development in the seismological community.

Fault sources affect ground shaking hazard at a large range of distances; for example, changes in the model near New Madrid, Mo., and Charleston, S. C., are clear on both the difference and ratio maps.

Ground motions have changed near Charlevoix due to the addition of a new fault source. The ground motion maps clearly show the influence of the New Madrid seismic zone out to 1,000 km where concentric patterns are observed (figs. 128–133).

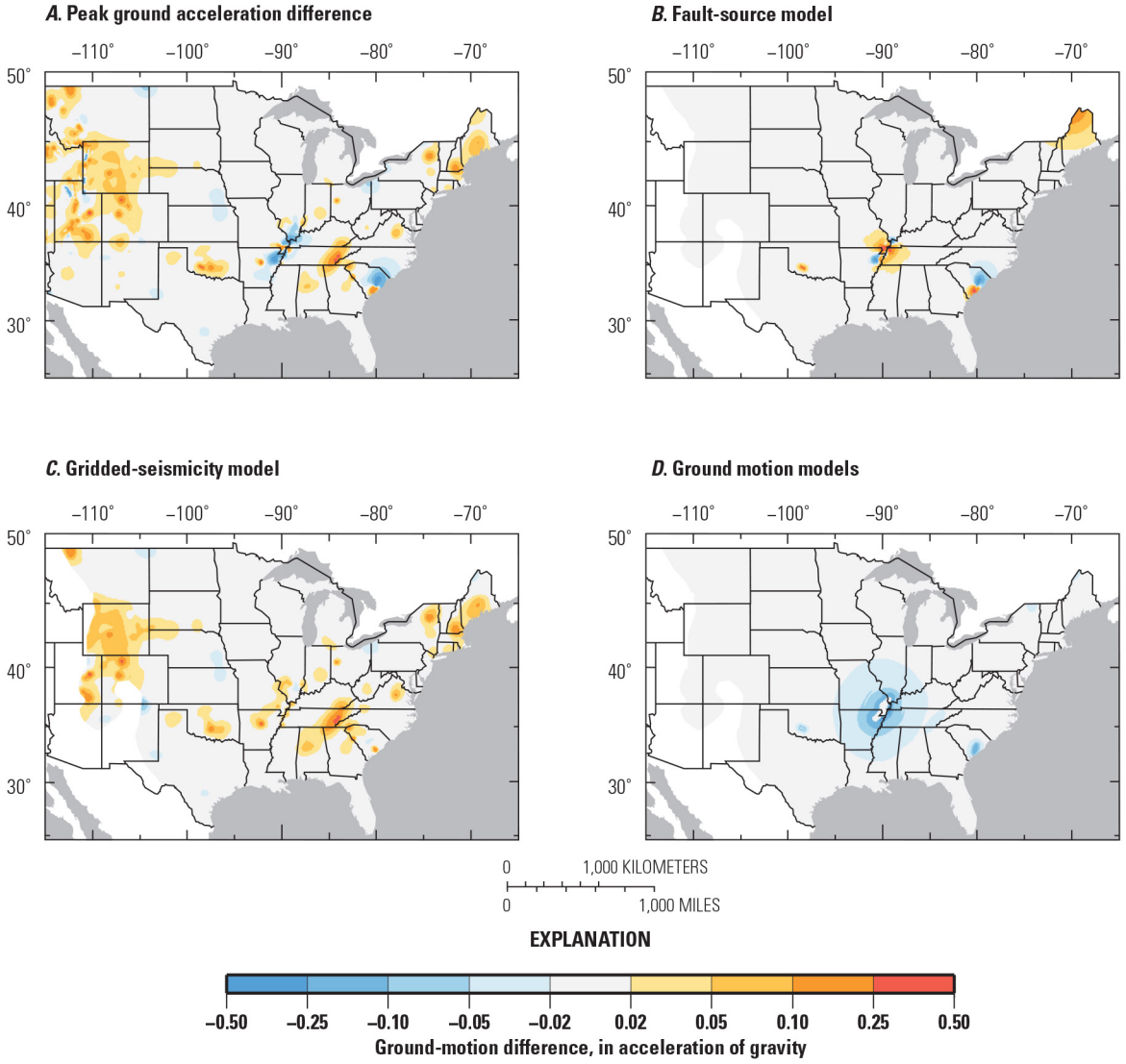

Figure 128. Maps showing difference in peak ground acceleration in the Central and Eastern United States at 2-percent in 50 years probability of exceedance and V_{S30} site conditions of 760 meters per second. Differences in ground motion due to *A*, updates to the 2014 model compared to the 2008 model; *B*, changes in fault-source model; *C*, changes in background seismicity rates; and *D*, changes in ground motion models. *A* includes Western United States sources and the other panels do not.

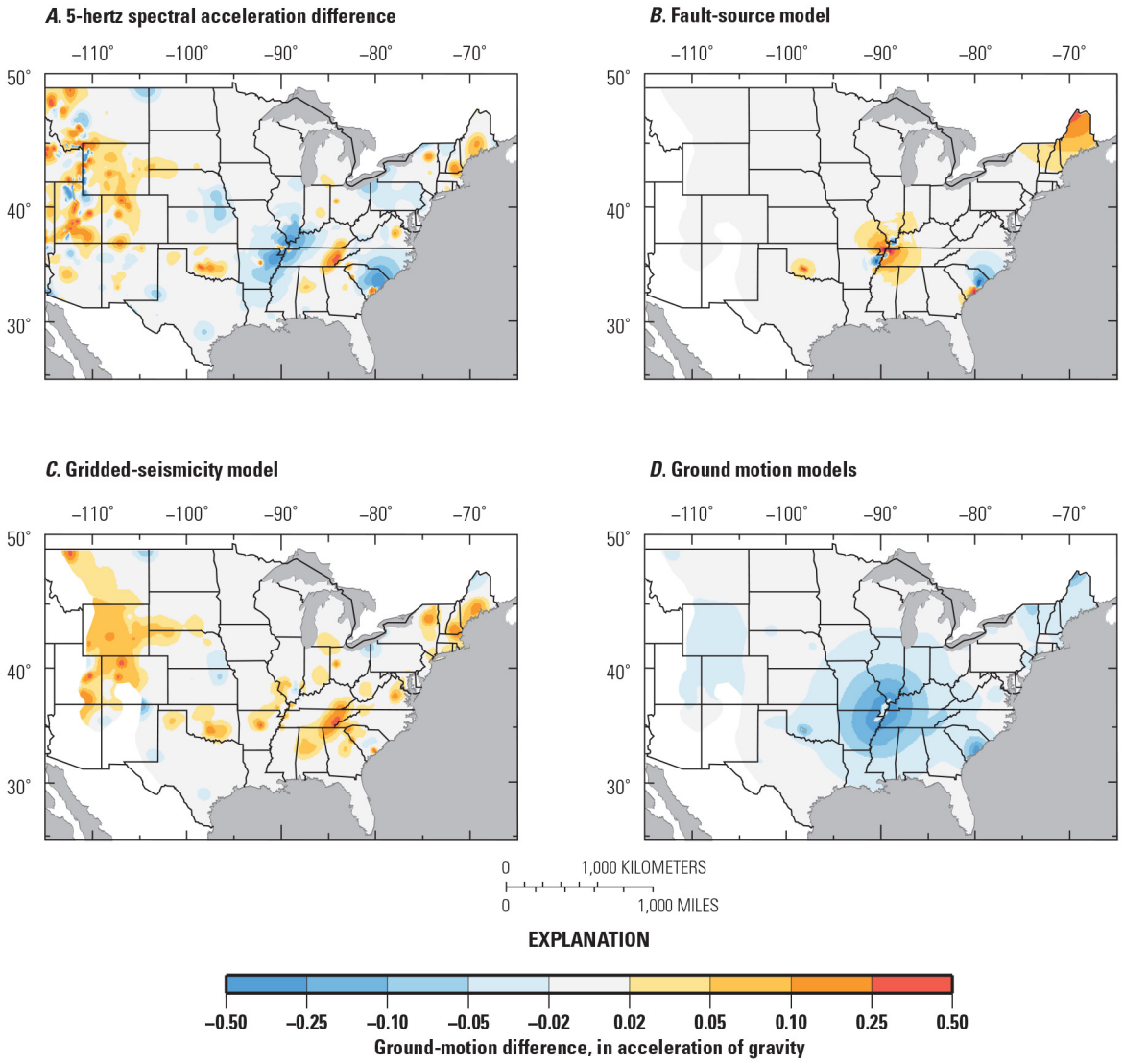

Figure 129. Maps showing difference in 5-hertz (0.2-second) spectral acceleration in the Central and Eastern United States at 2-percent in 50 years probability of exceedance and V_{S30} site conditions of 760 meters per second. Differences in ground motion due to *A*, updates to the 2014 model compared to the 2008 model; *B*, changes in fault-source model; *C*, changes in background seismicity rates; and *D*, changes in ground motion models. *A* includes Western United States sources and the other panels do not.

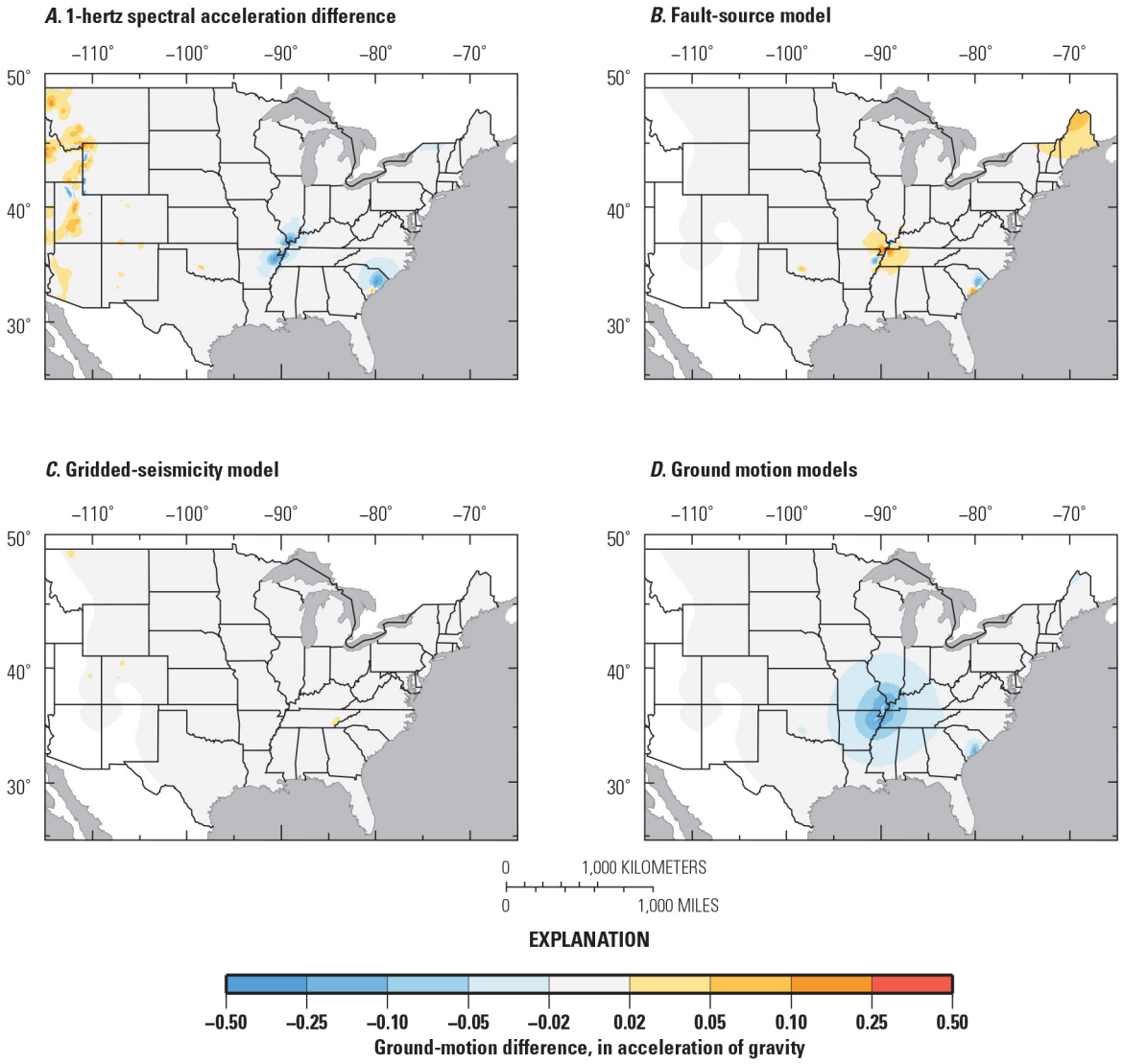

Figure 130. Maps showing difference in 1-hertz (1-second) spectral acceleration in the Central and Eastern United States at 2-percent in 50 years probability of exceedance and V_{S30} site conditions of 760 meters per second. Differences in ground motion due to *A*, updates to the 2014 model versus the 2008 model; *B*, changes in fault-source model; *C*, changes in background seismicity rates; and *D*, changes in ground motion models. *A* includes Western United States sources and the other panels do not.

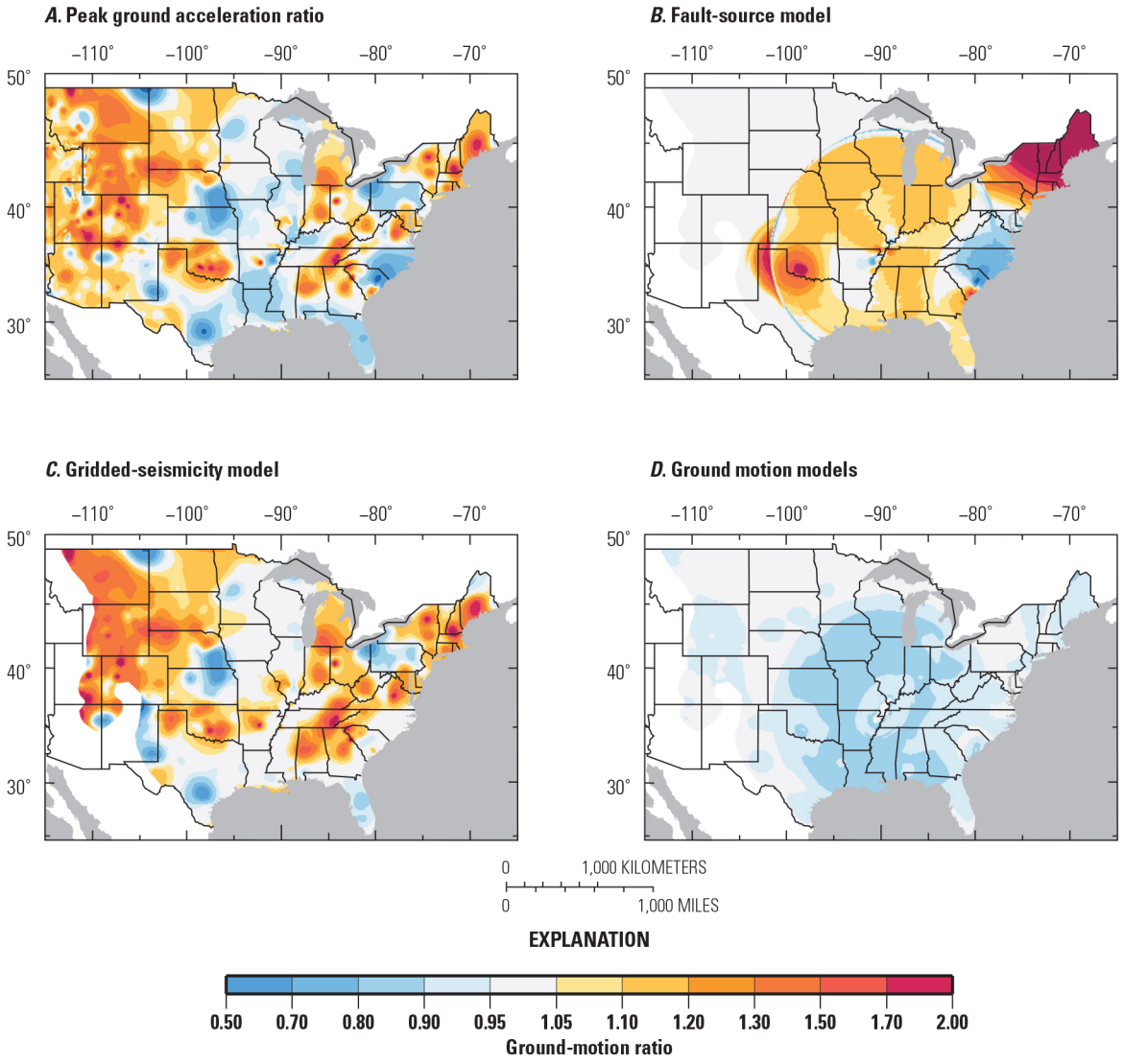

Figure 131. Maps showing ratios of peak ground acceleration in the Central and Eastern United States at 2-percent in 50 years probability of exceedance and V_{S30} site conditions of 760 meters per second. Changes in ground motion shown include *A*, updates to the 2014 model versus the 2008 model; *B*, changes in fault-source model; *C*, changes in background seismicity rates; and *D*, changes in ground motion models. *A* includes Western United States sources and the other panels do not.

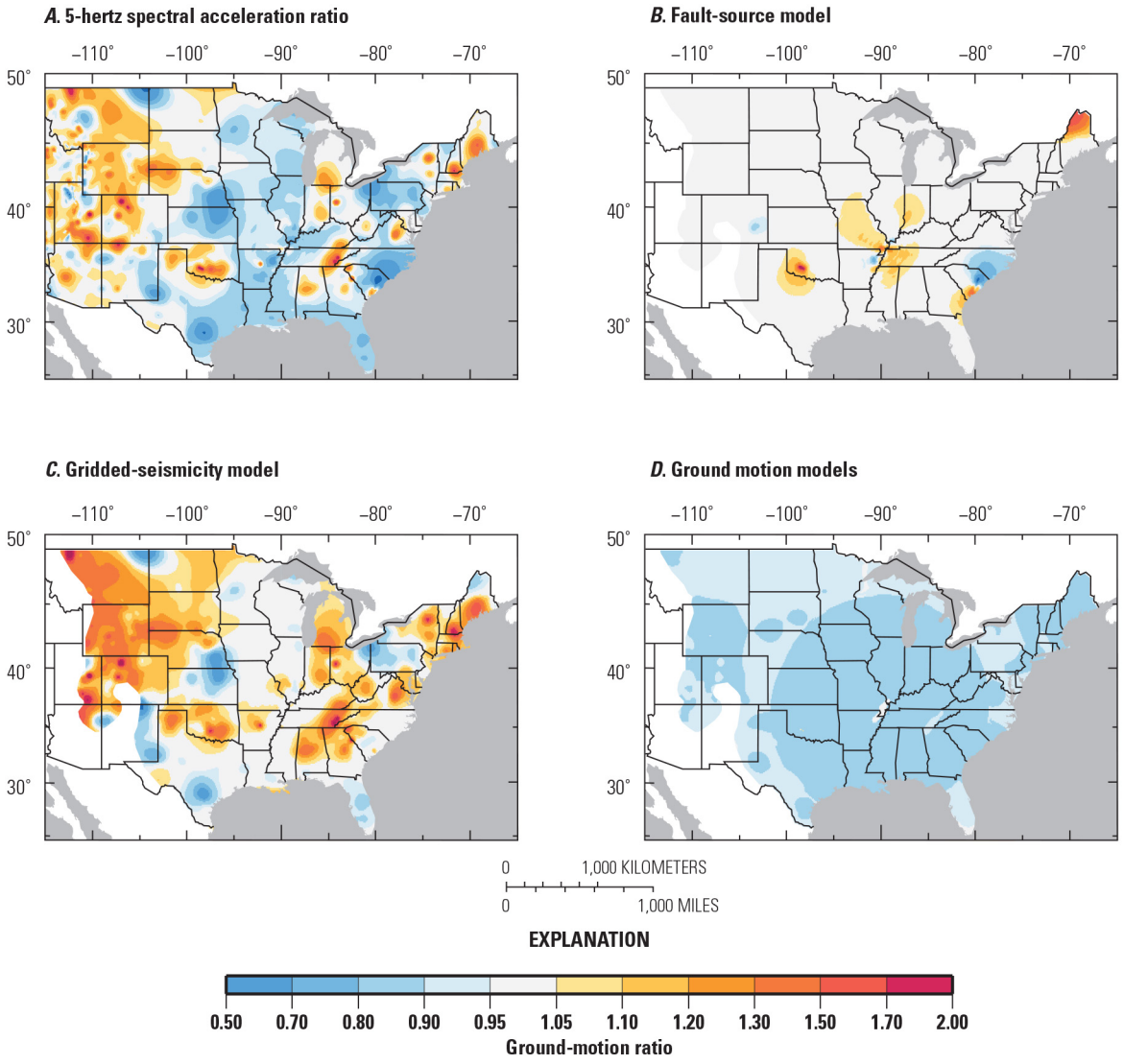

Figure 132. Maps showing ratios of 5-hertz (0.2-second) spectral acceleration in the Central and Eastern United States at 2-percent in 50 years probability of exceedance and V_{S30} site conditions of 760 meters per second. Changes in ground motion shown include *A*, updates to the 2014 model compared to the 2008 model; *B*, changes in fault-source model; *C*, changes in background seismicity rates; and *D*, changes in ground motion models. *A* includes Western United States sources and the other panels do not.

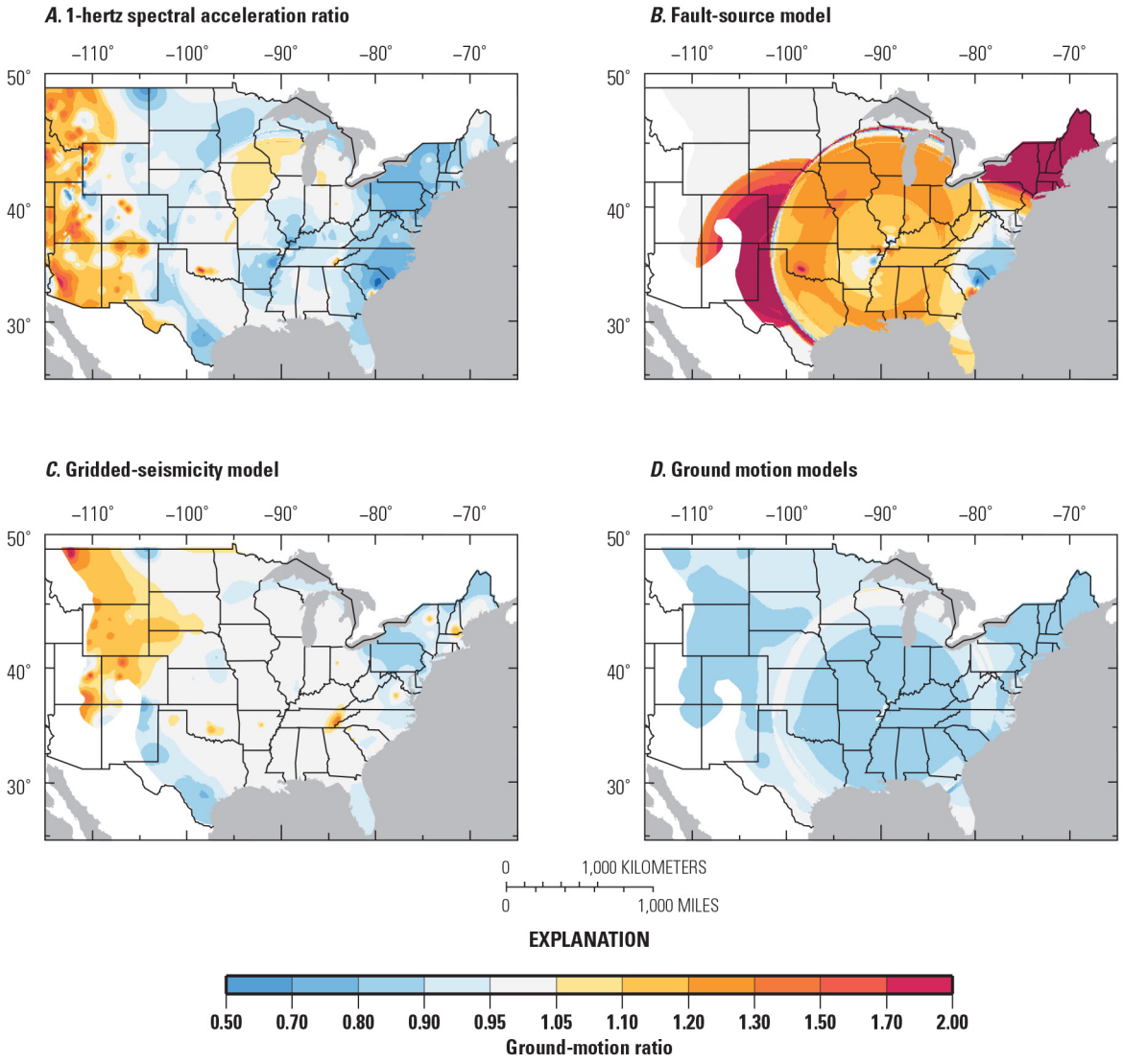

Figure 133. Maps showing ratios of 1-hertz (1-second) spectral acceleration in the Central and Eastern United States at 2-percent in 50 years probability of exceedance and V_{S30} site conditions of 760 meters per second. Changes in ground motion shown include *A*, updates to the 2014 model compared to the 2008 model; *B*, changes in fault-source model; *C*, changes in background seismicity rates; and *D*, changes in ground motion models. *A* includes Western United States sources and the other panels do not.

Western United States

In this section we discuss the hazard sensitivity from the shallow crustal earthquakes, subduction interface earthquakes, deep intraslab earthquakes, and California earthquakes. We look at the effects of seismicity-based models, fault-based models, and ground motion models on the total hazard.

Intermountain West and Pacific Northwest Shallow Crustal Earthquake Hazard

Figures 134–139 show difference and ratio maps comparing 2014 to 2008 probabilistic ground motions in the WUS for PGA (figs. 134 and 137), 5-hertz (0.2-second; figs. 135 and 138) and 1-hertz (1-second; figs. 136 and 139) spectral acceleration with a 2-percent probability of exceedance in 50-year level on firm rock site condition. The 2014 maps in the WUS depict a complicated hazard pattern across a broad area compared to the 2008 maps. Changes in hazard are due to (1) changes in the GMMs, (2) changes in the earthquake catalog and seismicity rate changes for shallow crustal earthquakes, and (3) changes in the crustal fault models.

The shallow crustal GMMs are composed of the NGA-West2 updated equations (Bozorgnia and others, 2014). The GMMs for shallow crustal faults cause increases in hazard over several major faults for peak ground acceleration, decreases for 0.2-second (5-hertz) spectral acceleration, and minor changes for 1-hertz spectral acceleration. Strike-slip ground motions and aleatory uncertainties for large earthquakes with high recurrence rates typically are higher than in 2008, whereas dip slip ground motions vary with period. This partially is accounted for by a reduced hanging-wall effect for normal faulting earthquakes. The ratio maps (figs. 137–139) show that with respect to distance, GMMs fall off faster than in older models. This is consistent with the attenuation with distance shown in the previous section. Ratios show changes up to ±30 percent; nevertheless, the differences can be very small and only range within about ±0.05 g away from faults and about ±0.15 g over faults.

Earthquake catalog and rate changes as well as smoothing algorithms cause changes in hazard across the WUS. Due to the addition of the adaptive smoothing model, ground motions often increase over a seismicity cluster but decrease at larger distances.

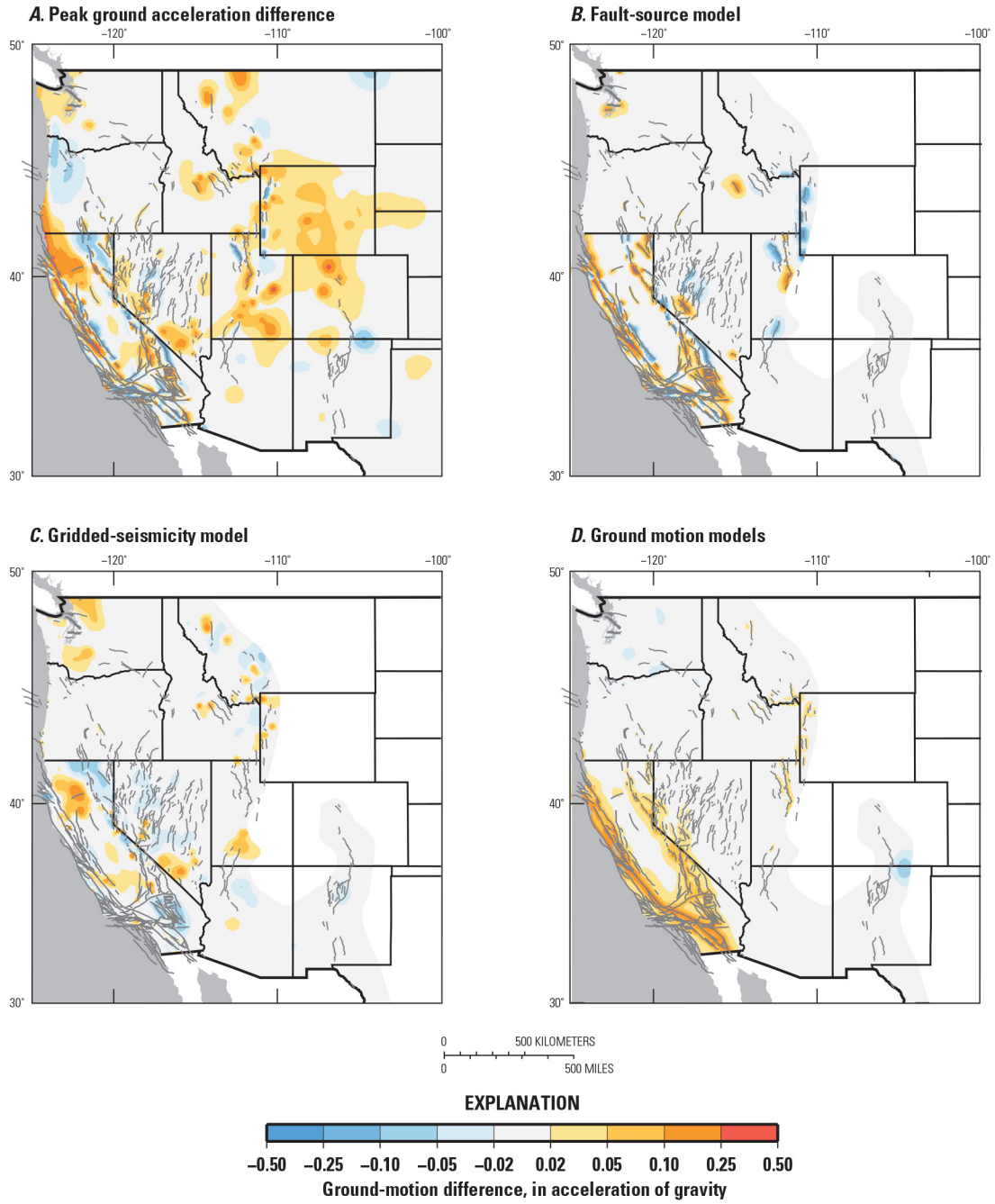

Figure 134. Maps showing difference in peak ground acceleration in the Western United States at 2-percent in 50 years probability of exceedance and V_{S30} site conditions of 760 meters per second. Differences in ground motion are due to *A*, updates to the 2014 model compared to the 2008 model; *B*, changes in fault-source model; *C*, changes in background seismicity rates; and *D*, changes in ground motion models. *A* includes Central and Eastern United States sources and the other panels do not.

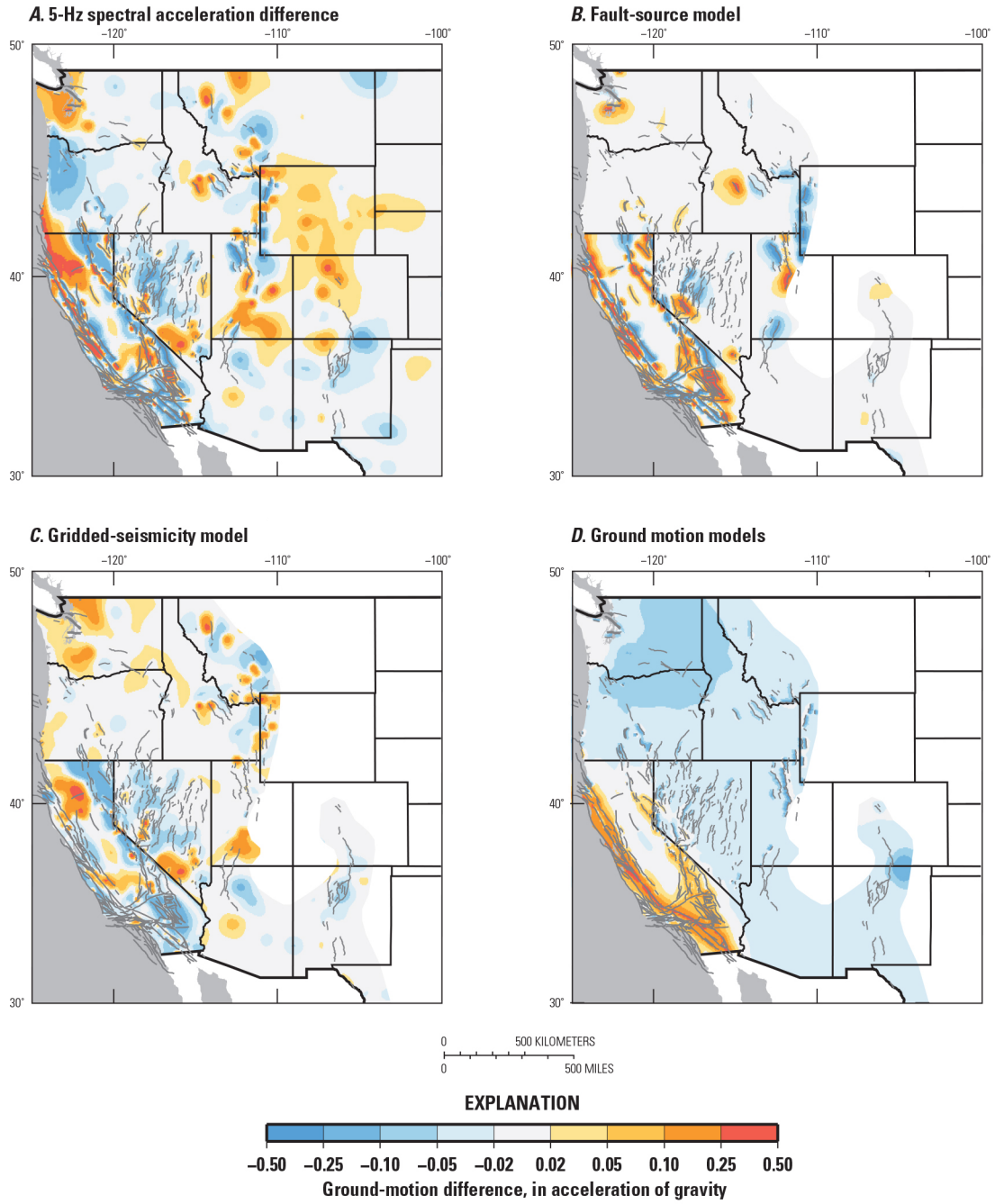

Figure 135. Maps showing difference in 5-hertz (0.2-second) spectral acceleration in the Western United States at 2-percent in 50 years probability of exceedance and V_{S30} site conditions of 760 meters per second. Differences in ground motion are due to *A*, updates to the 2014 model compared to the 2008 model; *B*, changes in fault-source model; *C*, changes in background seismicity rates; and *D*, changes in ground motion models. *A* includes Central and Eastern United States sources and the other panels do not.

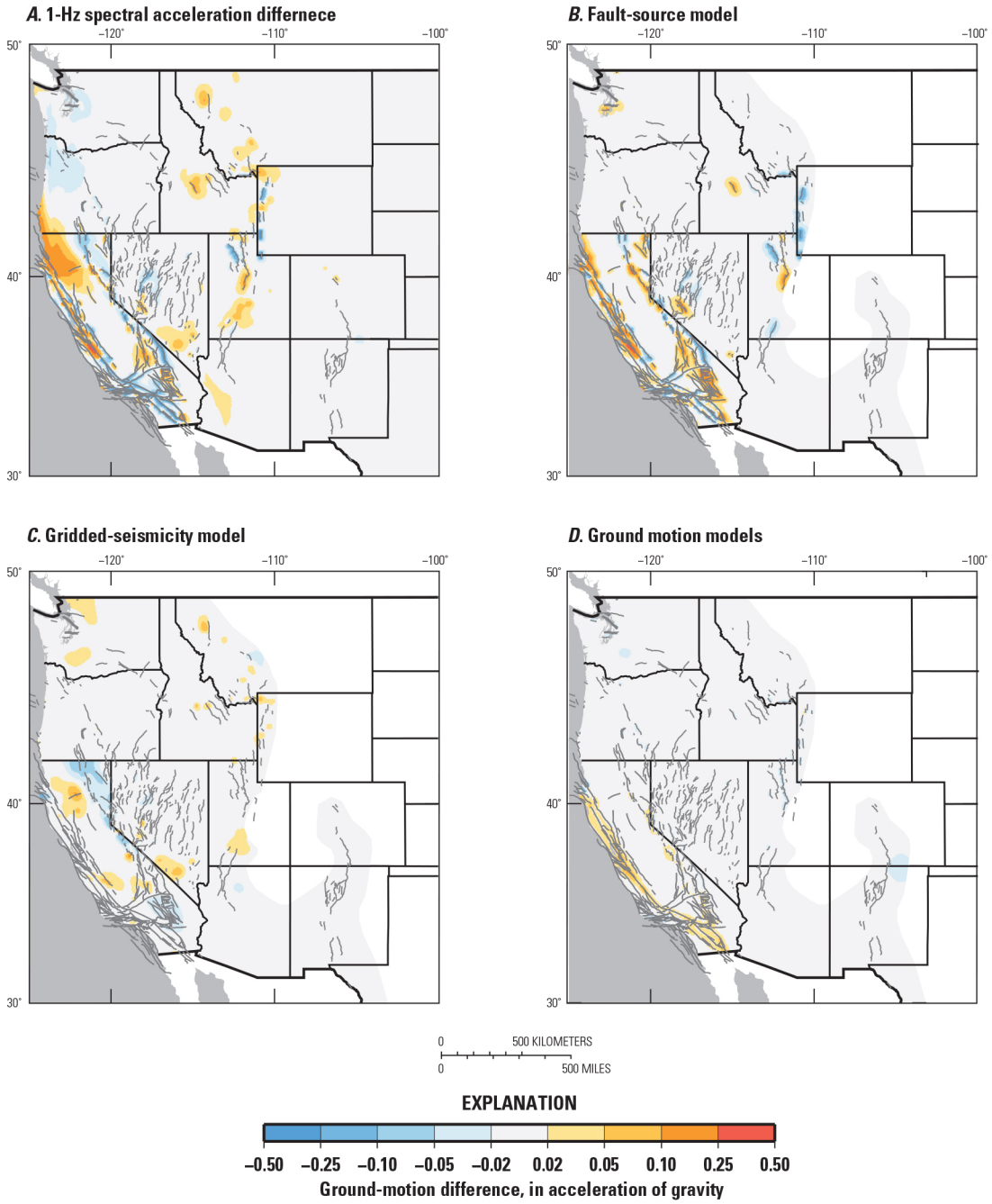

Figure 136. Maps showing difference in 1-hertz (1-second) spectral acceleration in the Western United States at 2-percent in 50 years probability of exceedance and V_{S30} site conditions of 760 meters per second. Differences in ground motion are due to *A*, updates to the 2014 model compared to the 2008 model; *B*, changes in fault-source model; *C*, changes in background seismicity rates; and *D*, changes in ground motion models. *A* includes Central and Eastern United States sources and the other panels do not.

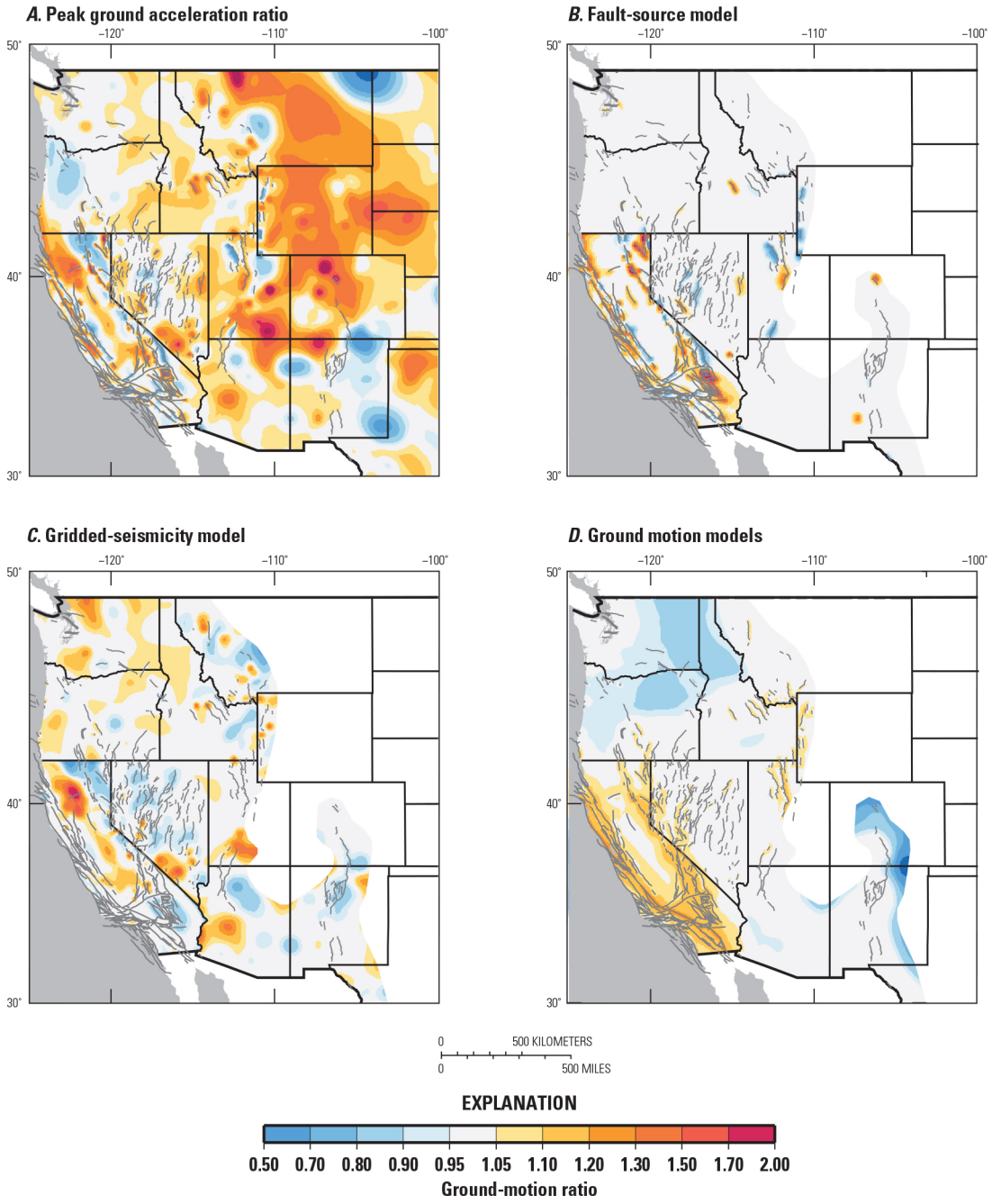

Figure 137. Maps showing ratios of peak ground acceleration in the Western United States at 2-percent in 50 years probability of exceedance and V_{S30} site conditions of 760 meters per second. Changes in ground motion shown include *A*, updates to the 2014 model compared to the 2008 model; *B*, changes in fault-source model; *C*, changes in background seismicity rates; and *D*, changes in ground motion models. *A* includes Central and Eastern United States sources and the other panels do not.

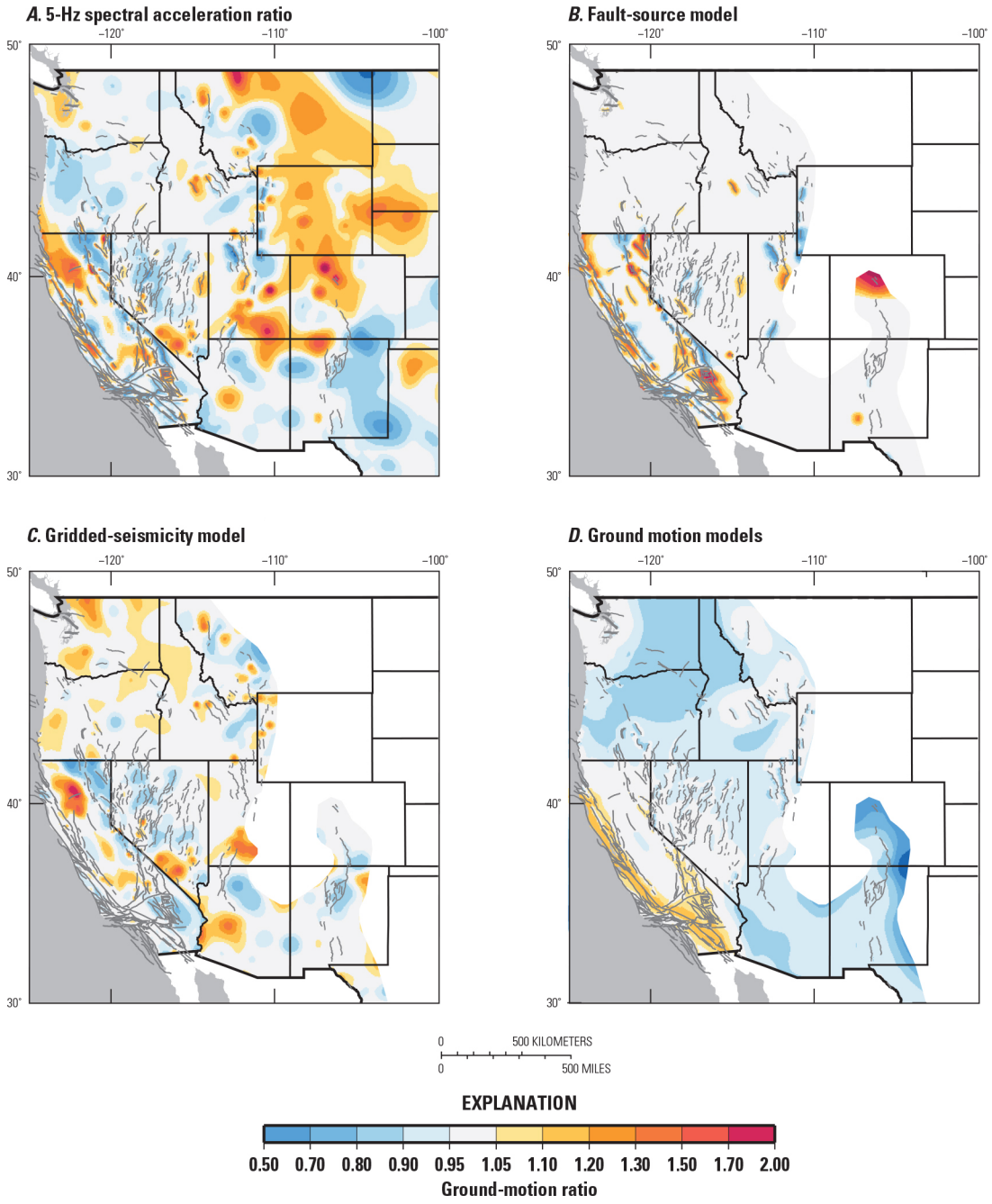

Figure 138. Maps showing ratios of 5-hertz (0.2-second) spectral acceleration in the Western United States at 2-percent in 50 years probability of exceedance and V_{S30} site conditions of 760 meters per second. Changes in ground motion shown include *A*, updates to the 2014 model compared to the 2008 model; *B*, changes in fault-source model; *C*, changes in background seismicity rates; and *D*, changes in ground motion models. *A* includes Central and Eastern United States sources and the other panels do not.

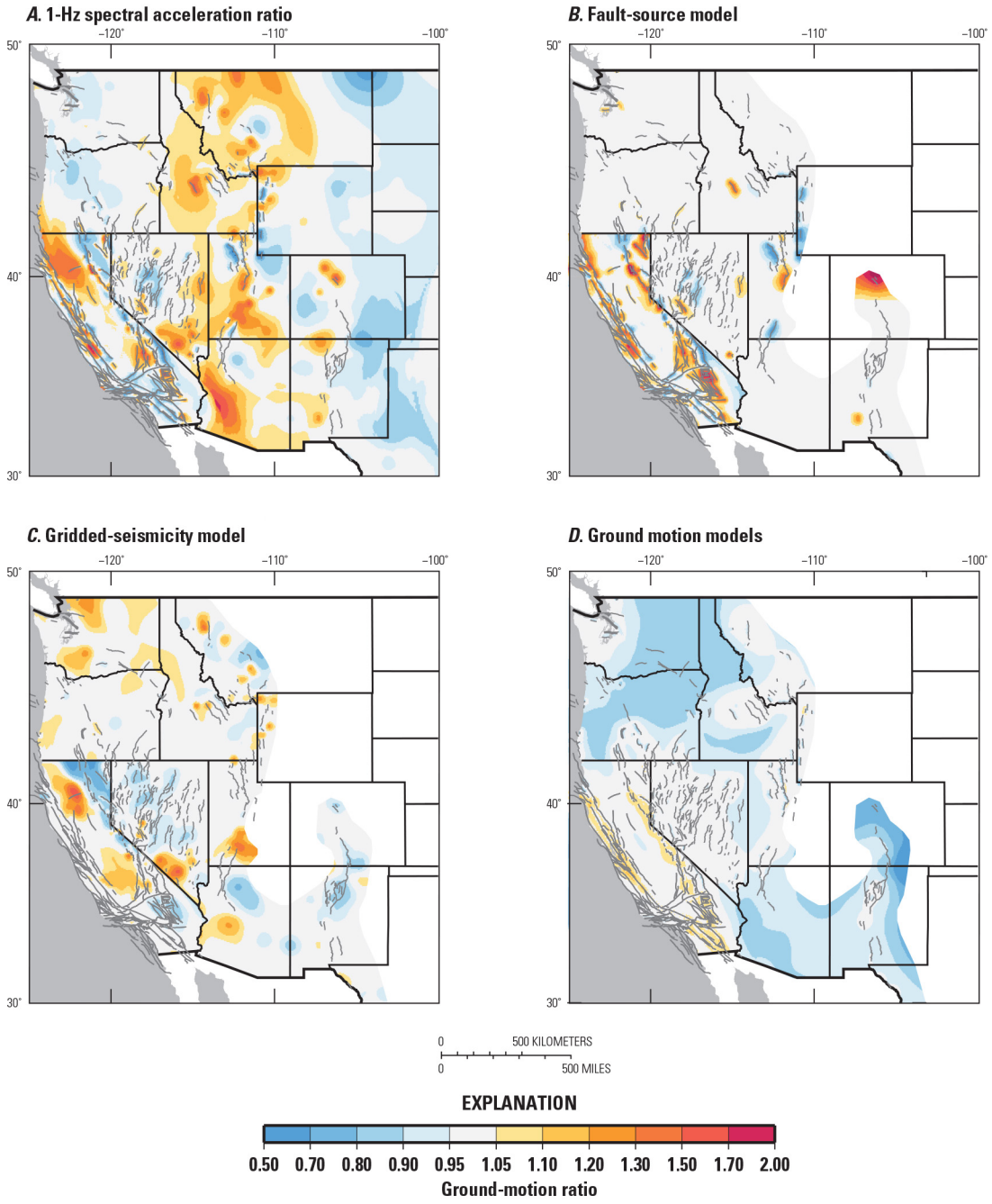

Figure 139. Maps showing ratios of 1-hertz (1-second) spectral acceleration in the Western United States at 2-percent in 50 years probability of exceedance and V_{S30} site conditions of 760 meters per second. Changes in ground motion shown include *A*, updates to the 2014 model compared to the 2008 model; *B*, changes in fault-source model; *C*, changes in background seismicity rates; and *D*, changes in ground motion models. *A* includes Central and Eastern United States sources and the other panels do not.

Fault model changes are due to using geodetic/geologic combined-inversion models, adding new or modifying existing fault sources, and calculating rates based on the 50° dip on normal faults. In particular, several new faults have been added or modified in the 2014 NSHMP maps.

Important changes near Salt Lake City, Utah; Reno, Nev.; Las Vegas, Nev.; and Seattle, Wash., are described below. Hazard near the Salt Lake City segment of the Wasatch fault zone has changed due to a new logic tree on fault geometry beneath Salt Lake City. The hazard on the southern Wasatch fault has increased due to changes in the geologic and geodetic fault models. Sites in Salt Lake City have reduced hazard for several reasons: (1) Great Salt Lake fault is characterized by reduced event rates (Lund, 2013), (2) lower partial-source rupture rates due to lower event rates on shallow-dipping source, (3) lower ground motions on the hanging-wall of the fault. Hazard near Reno, Nev., has decreased due to lower event rates on shallow dipping Carson Range and Kings Canyon fault system. Ground motions have increased near Las Vegas, Nev. because of the modification of the slip rate on the Eglington fault. Important changes in Washington are related to the addition of the Tacoma fault and changes to the South Whidbey Island fault. The Seattle region hazard has not changed significantly because we use a very similar model for the Seattle fault as was applied in 2008. We have not modified this fault using the geodetic model.

Changes to probabilistic ground motion at 2-percent probability of exceedance in 50 years for Intermountain West and Pacific Northwest crustal fault sources are apparent only for the most active faults in the region. Tables 20 and 21 identify maximum ground motion changes at 5-hertz spectral acceleration (figs. 135*B* and 138*B*) due to the 2014 update to fault-source parameters.

Table 20. Intermountain West and Pacific Northwest fault sources that contribute to ground motion increases at 5-hertz (0.2-second) spectral acceleration.

[g, gravitational acceleration constant equal to 9.81 meters per second squared; GM, ground motion; <, less than]

Fault source	State	Notes
Gore Range frontal fault	Colorado	new source increases GM <0.05 g.
Williams Fork Mountains fault	Colorado	new source increases GM <0.05 g.
Sawtooth fault	Idaho	new source increases GM <0.5 g.
Benton Spring fault	Nevada	slip rate change increases GM <0.5 g.
Bettles Well-Petrified Springs fault	Nevada	slip rate change increases GM <0.5 g.
Eglington fault	Nevada	annual rate and slip rate change increases GM <0.5 g.
Lone Mountain fault zone	Nevada	slip rate change increases GM <0.25 g.
Smith Valley fault	Nevada	slip rate change increases GM <0.25 g.
Wassuk Range fault zone	Nevada	slip rate change increases GM <0.25 g.
Steens fault zone	Oregon	slip rate change increases GM <0.1 g.
Wasatch fault zone, Nephi section	Utah	annual rate and slip rate change increases GM <0.5 g.
Wasatch fault zone, Provo section	Utah	annual rate and slip rate change increases GM <0.5 g.
Wasatch fault zone, Salt Lake City section	Utah	location modified locally increases GM.
Wasatch fault zone, Weber section	Utah	annual rate and slip rate change increases GM <0.1 g.
West Cache fault, Junction Hills section	Utah	new source increases GM <0.1 g.
Saddle Mountain fault	Washington	added 0.25 branch weight to Holocene slip rate increases GM <0.05 g.
Southern Whidbey Island	Washington	length of source extended, which locally increases GM.
Tacoma fault	Washington	new source increases GM <0.5 g.

Table 21. Intermountain West and Pacific Northwest fault sources that contribute to ground motion decreases at 5-hertz (0.2-second) spectral acceleration.

[g, gravitational acceleration constant equal to 9.81 meters per second squared; GM, ground motion; <, less than]

Fault source	State	Notes
Centennial fault	Montana	slip rate change decreases GM <0.1 g.
Desatoya Mountains fault zone	Nevada	slip rate change decreases GM <0.05 g.
Sand Springs Range fault	Nevada	slip rate change decreases GM <0.25 g.
Toiyabe Range fault zone	Nevada	slip rate change decreases GM <0.25 g.
Western Toiyabe Range fault zone	Nevada	slip rate change decreases GM <0.25 g.
Steens fault zone	Oregon	slip rate.
Great Salt Lake fault zone, Antelope Island section	Utah	constrained annual rate change decreases GM <0.5 g.
Great Salt Lake fault zone, Fremont Island section	Utah	constrained annual rate change decreases GM <0.5 g.
Great Salt Lake fault zone, Promontory section	Utah	constrained annual rate change decreases GM <0.5 g.
Sevier/Toroweap fault zone (northern)	Utah	slip rate change decreases GM <0.25 g.
Wasatch fault zone, Salt Lake City section	Utah	location modified locally decreases GM.
Bear River fault	Wyoming	constrained annual rate change decreases GM <0.5 g.
Grand Valley fault	Wyoming	slip rate change decreases GM <0.25 g.
Rock Creek fault	Wyoming	slip rate change decreases GM <0.5 g.
Teton fault	Wyoming	slip rate change decreases GM <0.5 g.
Southern Whidbey Island	Washington	length of source extended, which locally decreases GM.

Cascadia Subduction Interface Contributions

Figures 140–145 show difference and ratio maps for the total 2014 model with respect to the 2008 model, the contribution from the 2014 Cascadia subduction interface sources compared to the 2008 seismic sources, and the contribution from the 2014 compared to the 2008 subduction interface GMMs. These comparisons are made for peak ground acceleration, 0.2-second (5-hertz) spectral acceleration, and 1-second (1-hertz) spectral acceleration for 760 m/s V_{S30}.

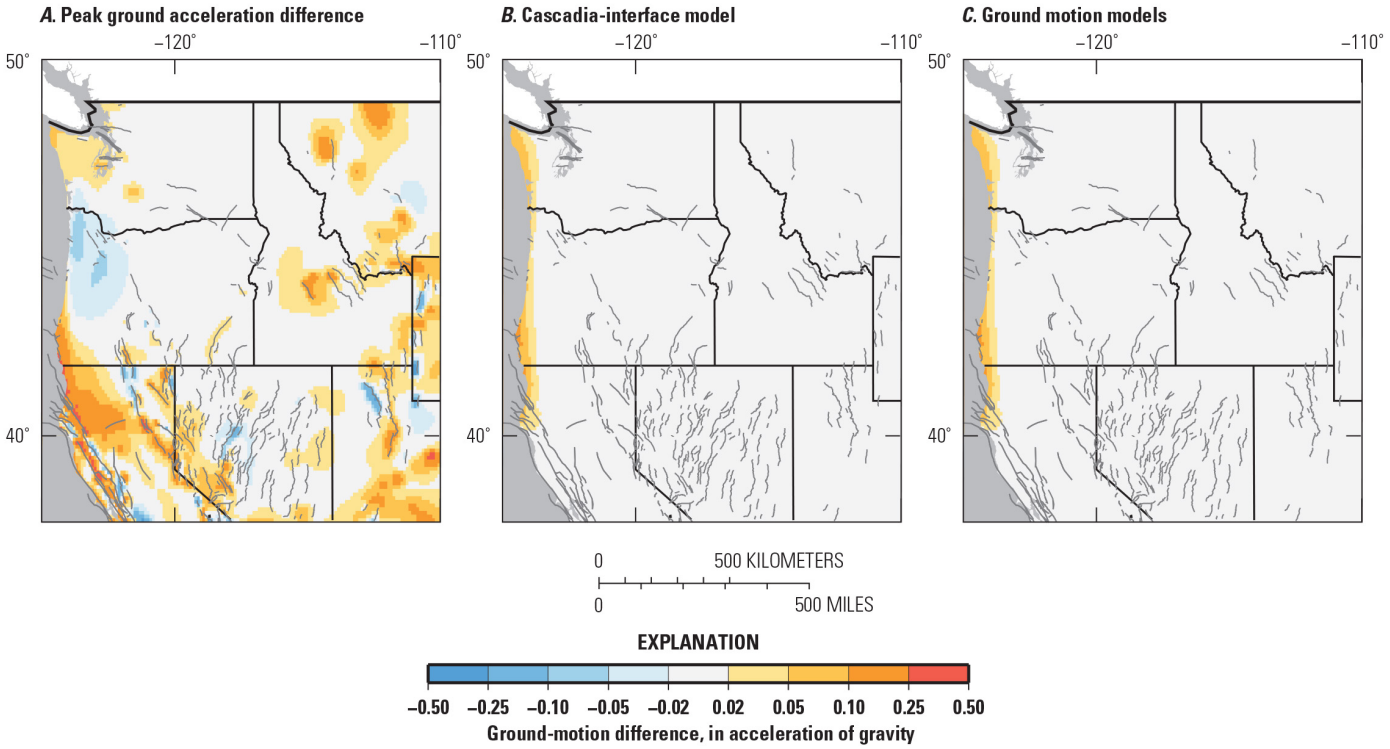

Figure 140. Maps showing difference in peak ground acceleration for the Cascadia subduction zone at 2-percent in 50 years probability of exceedance and V_{S30} site conditions of 760 meters per second. Differences in ground motion are due to *A*, updates to the 2014 model compared to the 2008 model; *B*, changes in fault-source model; and *C*, changes in ground motion models.

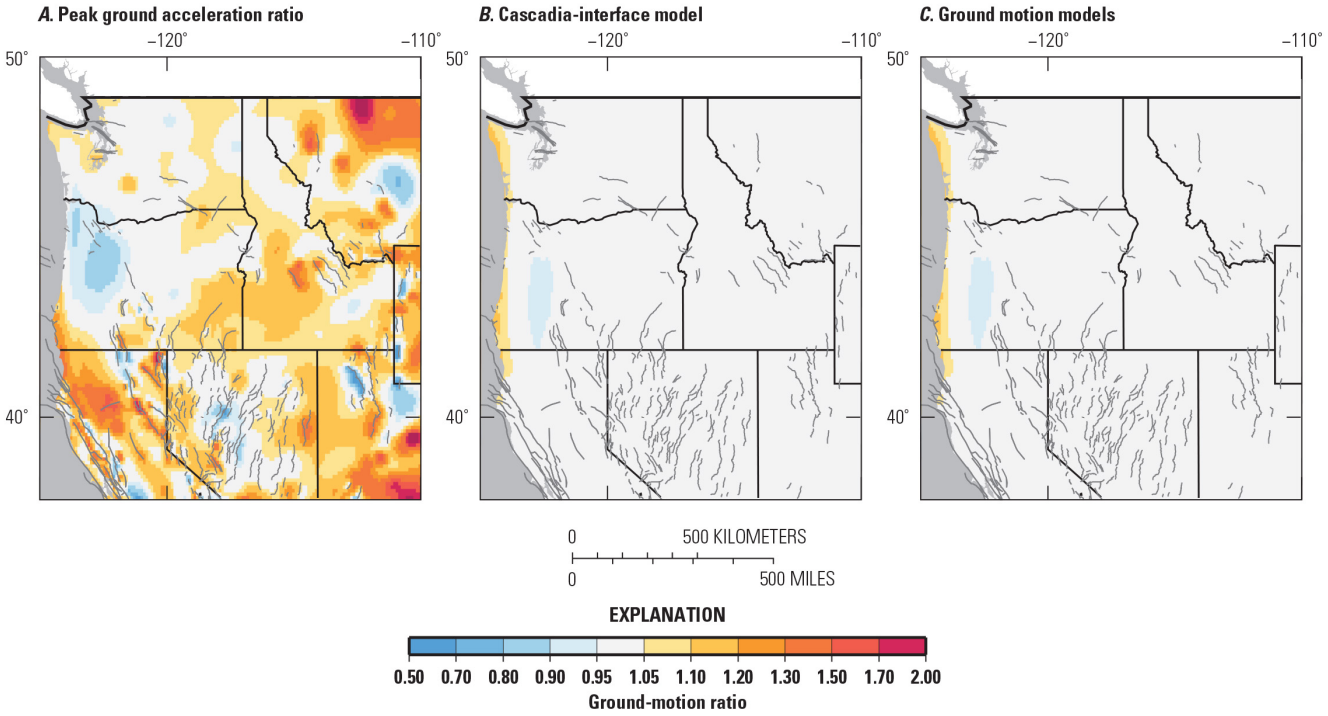

Figure 141. Maps showing ratios of peak ground acceleration for the Cascadia subduction zone at 2-percent in 50 years probability of exceedance and V_{S30} site conditions of 760 meters per second. Changes in ground motion shown include *A*, updates to the 2014 model compared to the 2008 model; *B*, changes in fault-source model; and *C*, changes in ground motion models.

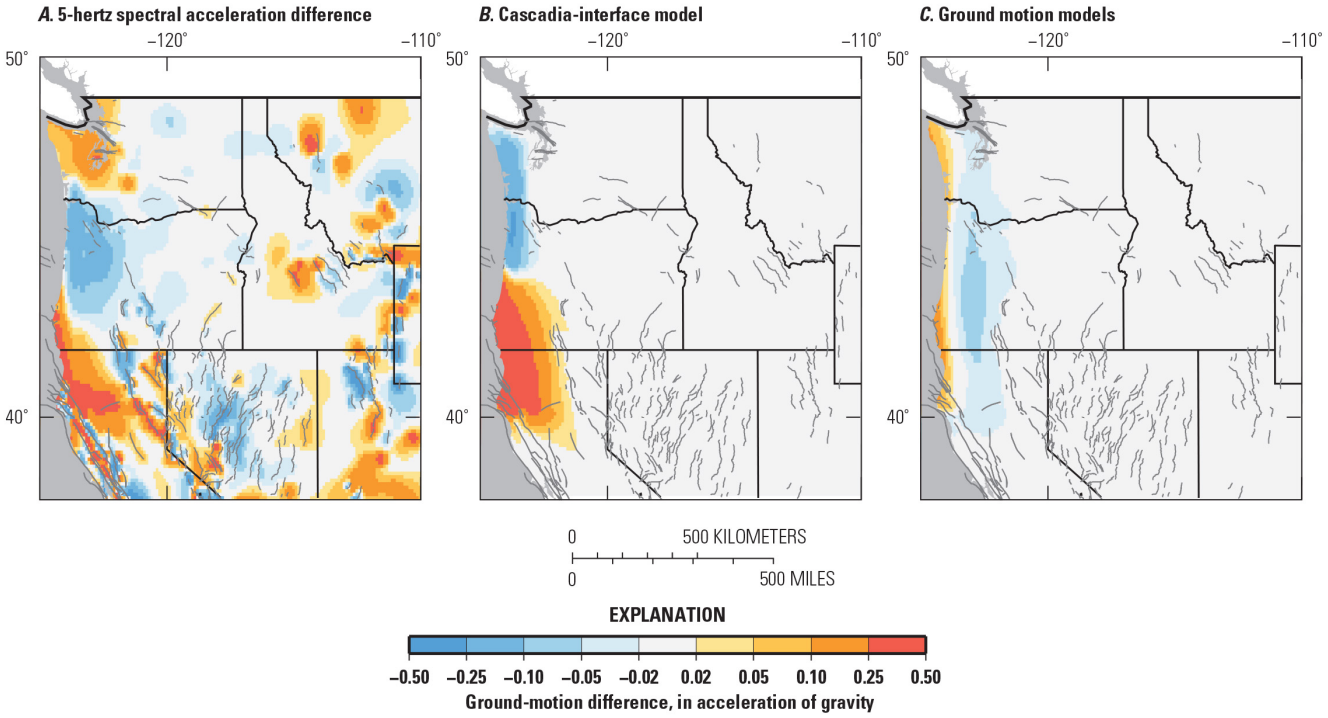

Figure 142. Maps showing difference in 5-hertz (0.2-second) spectral acceleration for the Cascadia subduction zone at 2-percent in 50 years probability of exceedance and V_{S30} site conditions of 760 meters per second. Differences in ground motion are due to *A*, updates to the 2014 model compared to the 2008 model; *B*, changes in fault-source model; and *C*, changes in ground motion models.

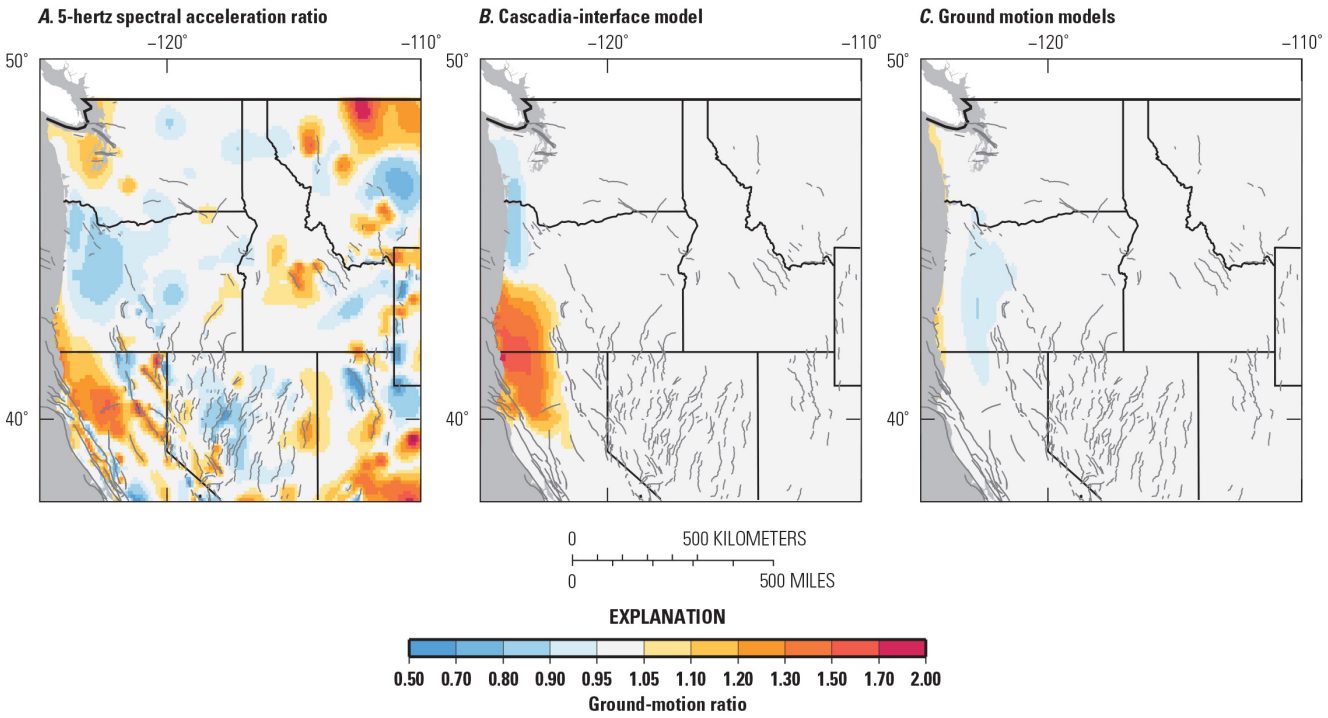

Figure 143. Maps showing ratios of 5-hertz (0.2-second) spectral acceleration for the Cascadia subduction zone at 2-percent in 50 years probability of exceedance and V_{S30} site conditions of 760 meters per second. Changes in ground motion shown include *A*, updates to the 2014 model compared to the 2008 model; *B*, changes in fault-source model; and *C*, changes in ground motion models.

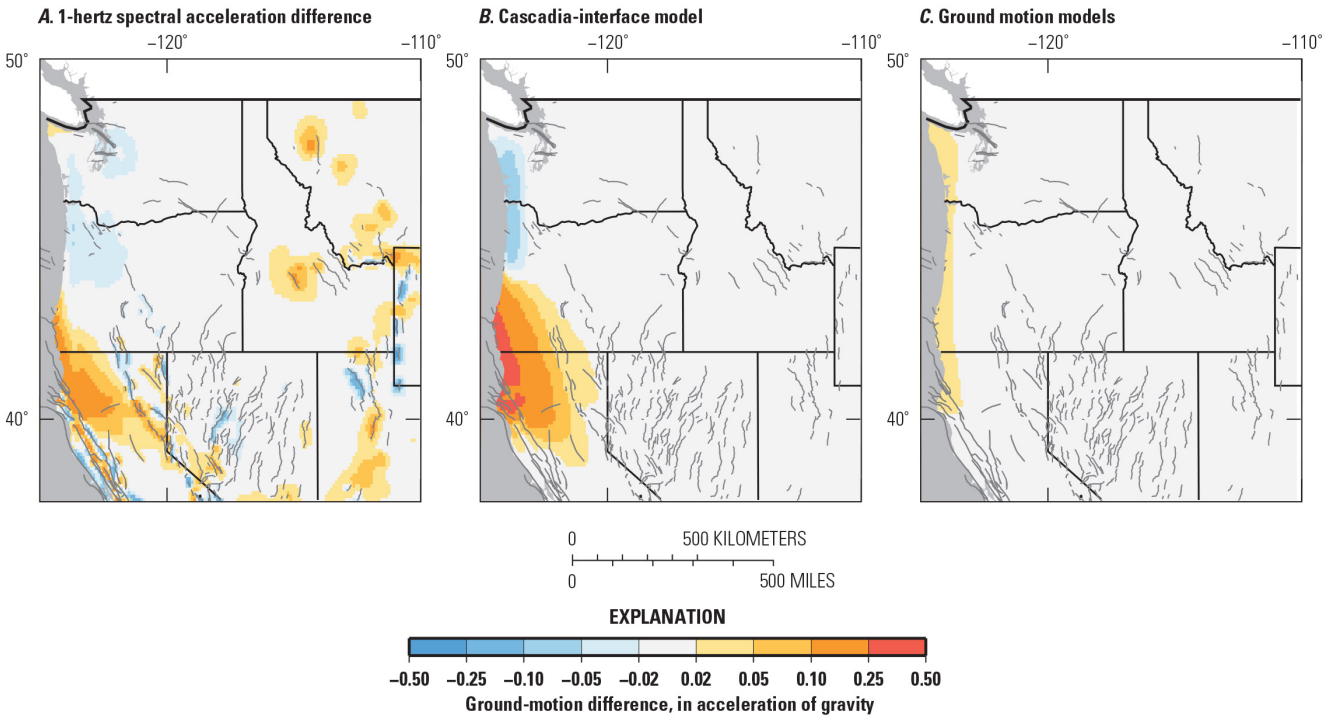

Figure 144. Maps showing difference in 1-hertz (1-second) spectral acceleration for the Cascadia subduction zone at 2-percent in 50 years probability of exceedance and V_{S30} site conditions of 760 meters per second. Differences in ground motion are due to *A*, updates to the 2014 model compared to the 2008 model; *B*, changes in fault-source model; and *C*, changes in ground motion models.

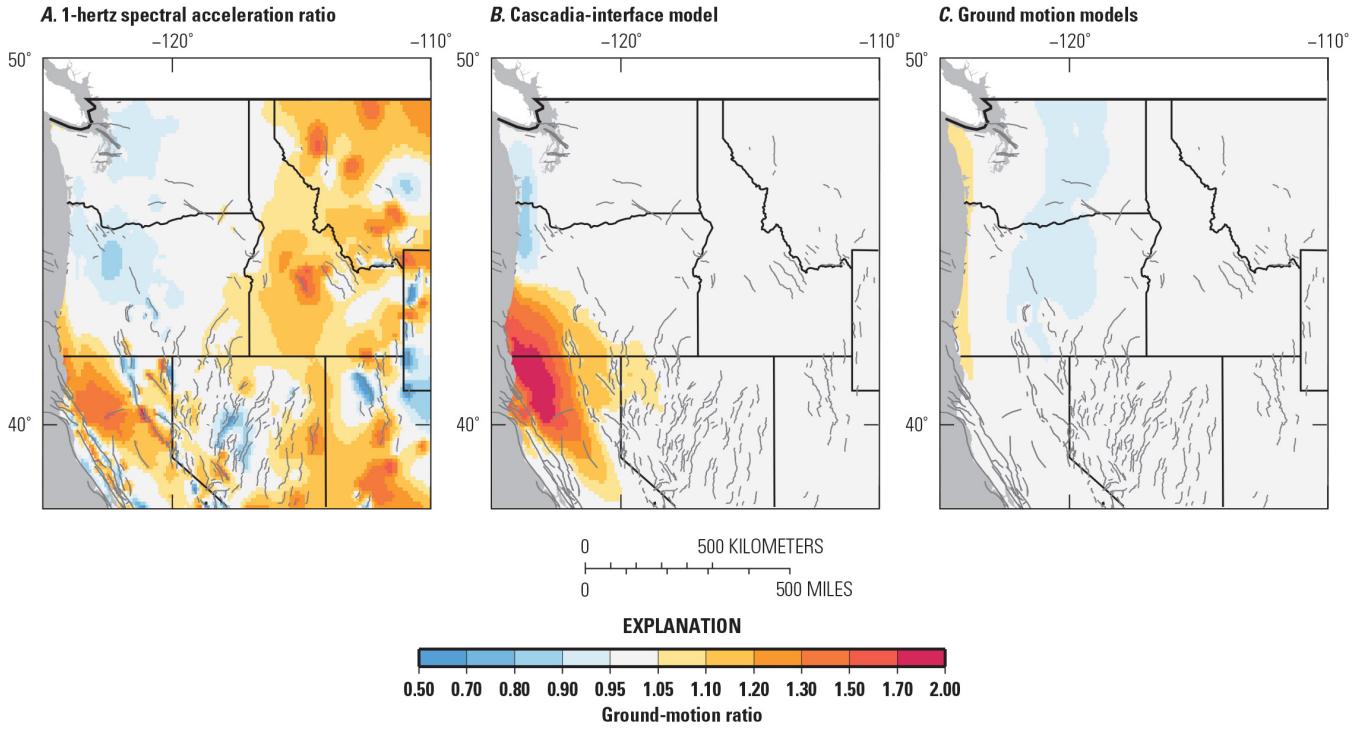

Figure 145. Maps showing ratios of 1-hertz (1-second) spectral acceleration for the Cascadia subduction zone at 2-percent in 50 years probability of exceedance and V_{S30} site conditions of 760 meters per second. Changes in ground motion shown include *A*, updates to the 2014 model compared to the 2008 model; *B*, changes in fault-source model; and *C*, changes in ground motion models.

The 2014 maps along the Cascadia subduction zone depict a complicated hazard pattern across a broad area compared to the 2008 maps. Changes in hazard are due to (1) changes in the ground motion models and (2) changes in the Cascadia subduction zone source models.

For the 2014 NSHMP maps, two new GMMs for subduction interface earthquakes were added and the weights were redistributed. The new subduction-interface ground motions are higher close to the source and decay faster with greater distances than in the 2008 models. The updated ground motion models mostly affect coastal Washington, Oregon, and California.

The Cascadia source model contains a higher rate of earthquakes in the south based on new data described in "Earthquake Recurrence and Down-Dip Edge of Rupture for the Cascadia Subduction Zone" section which increases hazard in the southern half of the zone. The Cascadia subduction source and GMM changes have caused an increase in ground shaking hazard along northwestern Washington and California and along the southwestern Oregon coastlines for all three periods. Ground shaking hazard generally is lower in northwestern Oregon due to changes in the rate of large subduction interface earthquakes on the northern Cascadia. Ground shaking tends to be a little lower at sites farther from the subduction zone because the ground motion models generally fall off faster than in previous models.

Cascadia Deep Intraslab Contributions

Figures 146–151 show difference and ratio maps for the total 2014 model with respect to the 2008 model, the contribution from the 2014 deep intraslab sources compared to the 2008 seismic sources, and the contribution from the 2014 deep intraslab GMMs compared to the 2008 GMMs. These comparisons are made for peak ground acceleration, 0.2-second (5-hertz) spectral acceleration, and 1-second (1-hertz) spectral acceleration for 760 m/s V_{S30}.

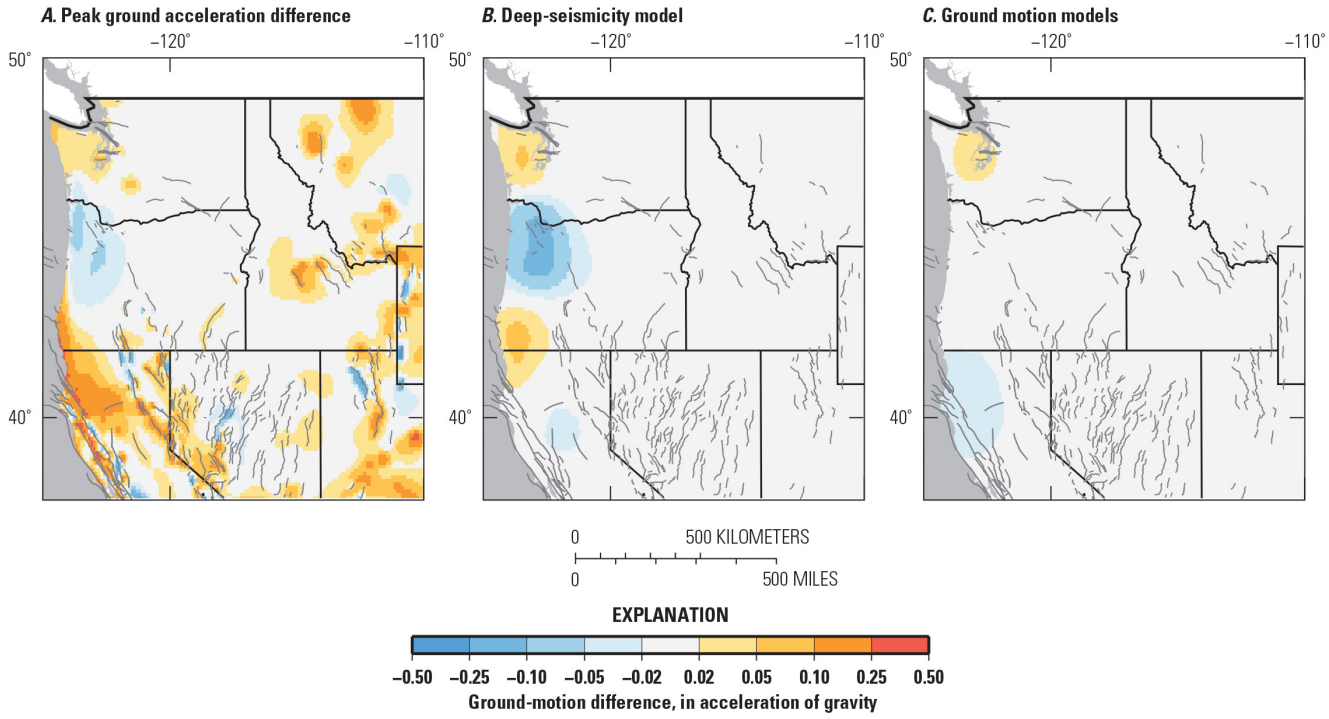

Figure 146. Maps showing difference in peak ground acceleration for deep intraslab seismic sources at 2-percent in 50 years probability of exceedance and V_{S30} site conditions of 760 meters per second. Differences in ground motion are due to *A*, updates to the 2014 model compared to the 2008 model; *B*, changes in deep-seismicity model; and *C*, changes in ground motion models.

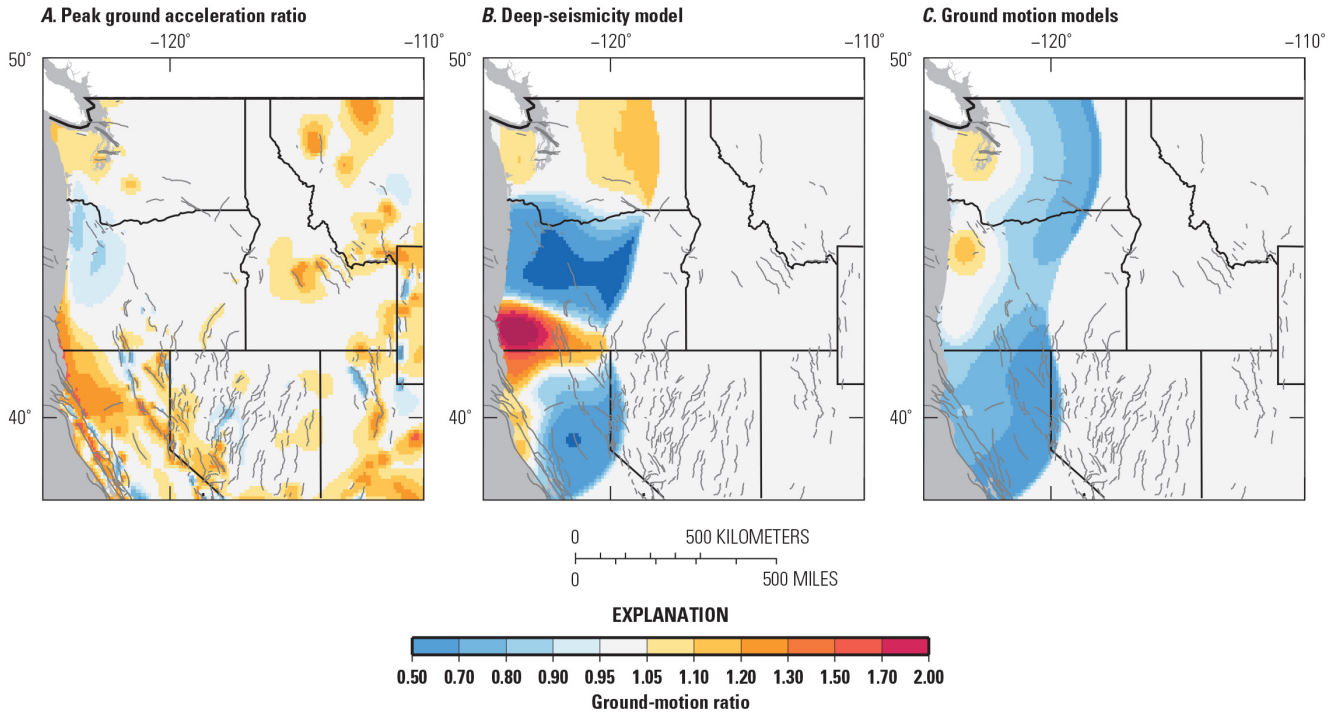

Figure 147. Maps showing ratios of peak ground acceleration for deep intraslab seismic sources at 2-percent in 50 years probability of exceedance and V_{S30} site conditions of 760 meters per second. Changes in ground motion shown include *A*, updates to the 2014 model compared to the 2008 model; *B*, changes in deep-seismicity model; and *C*, changes in ground motion models.

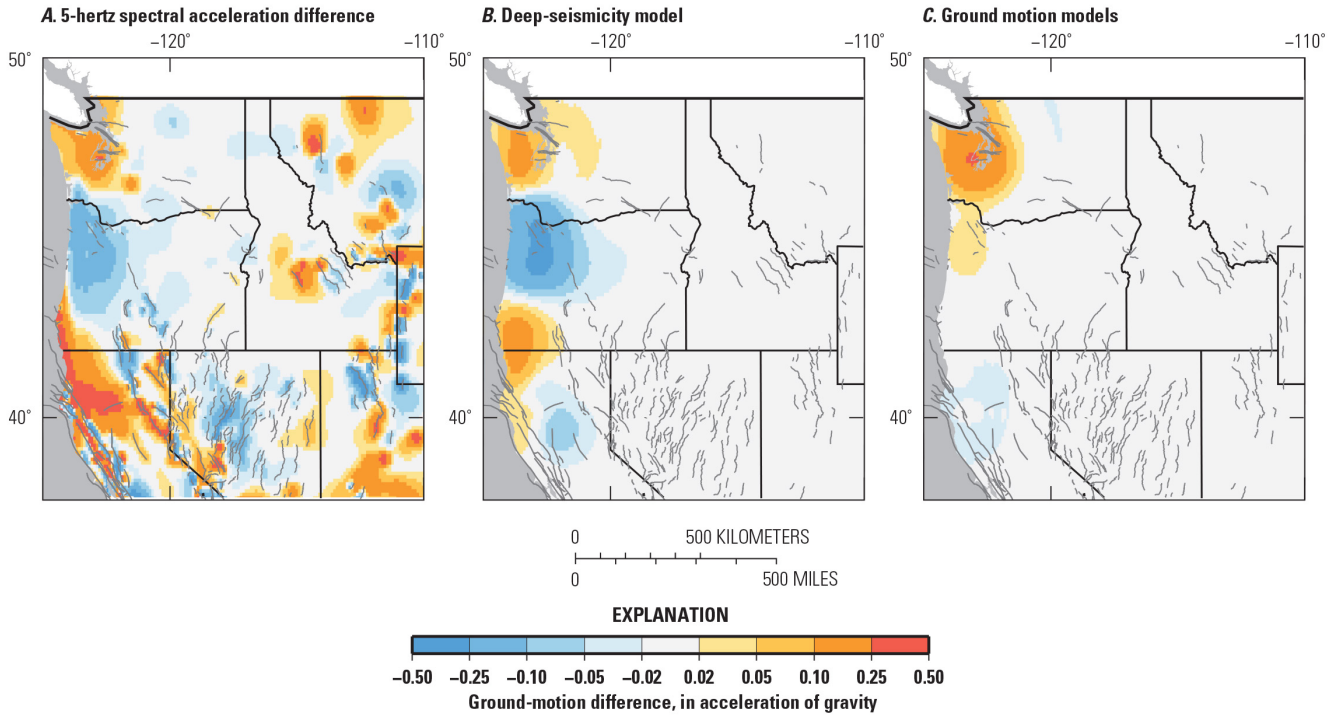

Figure 148. Maps showing difference in 5-hertz (0.2-second) spectral acceleration for deep intraslab seismic sources at 2-percent in 50 years probability of exceedance and V_{S30} site conditions of 760 meters per second. Differences in ground motion are due to *A*, updates to the 2014 model compared to the 2008 model; *B*, changes in deep-seismicity model; and *C*, changes in ground motion models.

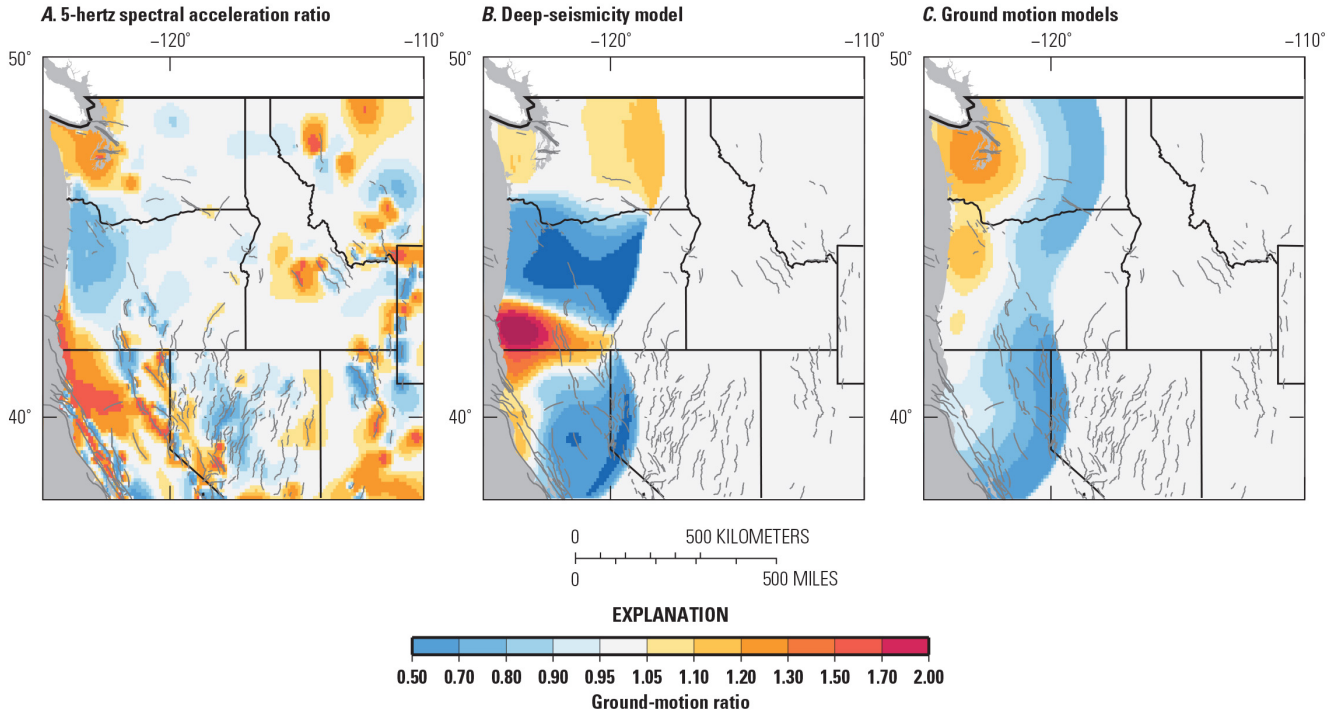

Figure 149. Maps showing ratios of 5-hertz (0.2-second) spectral acceleration for deep intraslab seismic sources at 2-percent in 50 years probability of exceedance and V_{S30} site conditions of 760 meters per second. Changes in ground motion shown include *A*, updates to the 2014 model compared to the 2008 model; *B*, changes in deep-seismicity model; and *C*, changes in ground motion models.

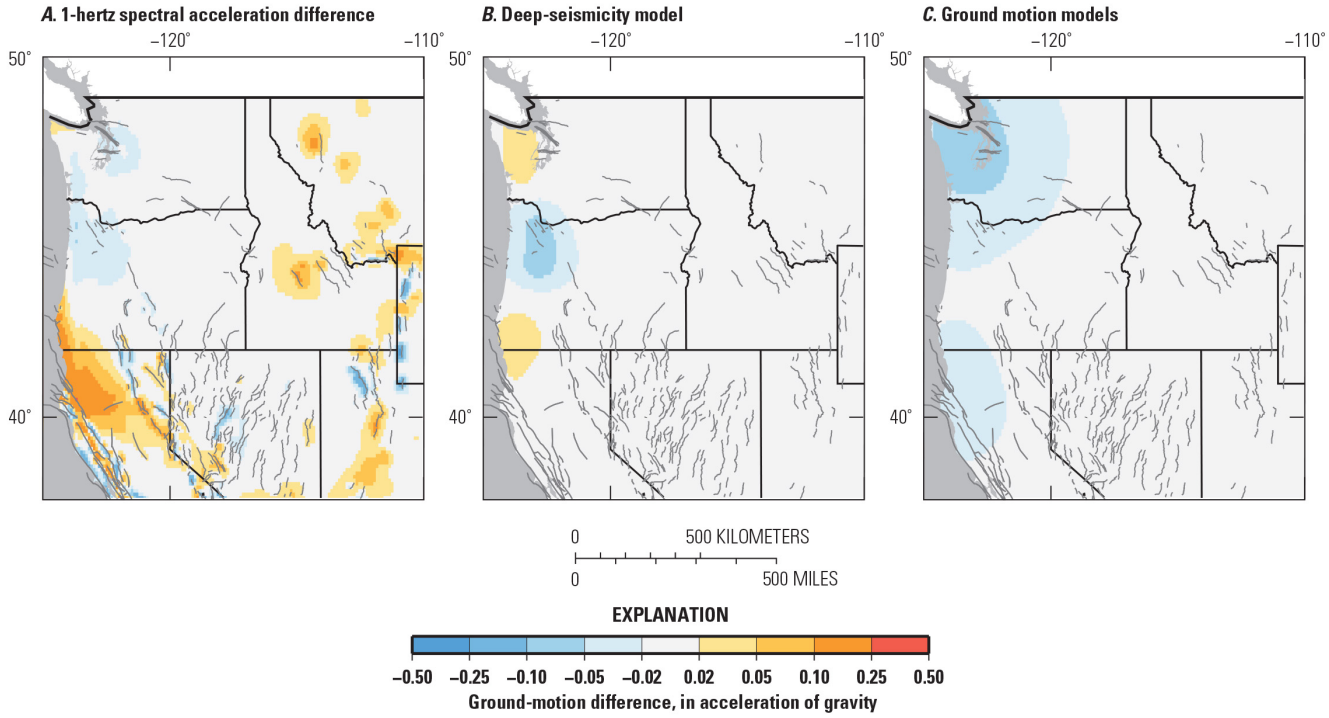

Figure 150. Maps showing difference in 1-hertz (1-second) spectral acceleration for deep intraslab seismic sources at 2-percent in 50 years probability of exceedance and V_{S30} site conditions of 760 meters per second. Differences in ground motion are due to *A*, updates to the 2014 model compared to the 2008 model; *B*, changes in deep-seismicity model; and *C*, changes in ground motion models.

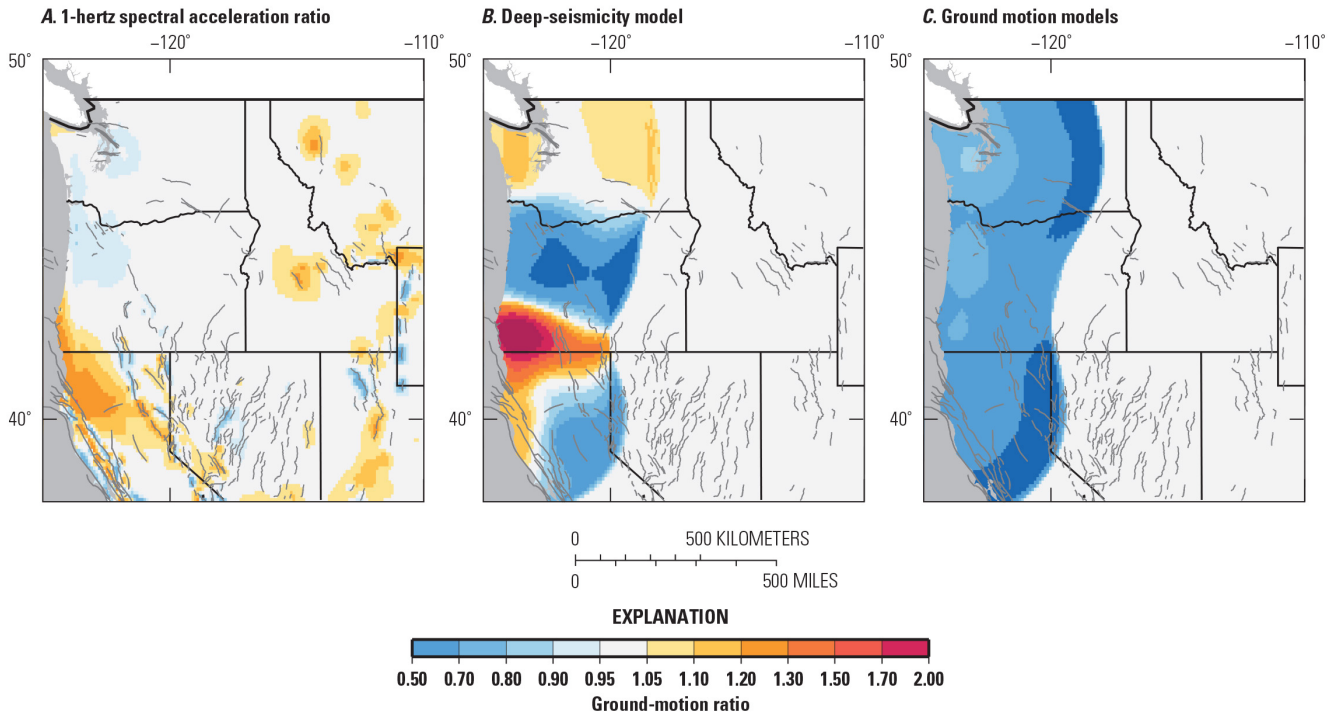

Figure 151. Maps showing ratios of 1-hertz (1-second) spectral acceleration for deep intraslab seismic sources at 2-percent in 50 years probability of exceedance and V_{S30} site conditions of 760 meters per second. Changes in ground motion shown include *A*, updates to the 2014 model compared to the 2008 model; *B*, changes in deep-seismicity model; and *C*, changes in ground motion models.

The 2014 maps for deep intraslab earthquakes are quite different from the 2008 maps. Changes in hazard are due to (1) changes in the GMMs and (2) changes in the earthquake catalog and seismicity rate changes for deep intraslab earthquakes, (3) the Mmax distribution, the depth distribution (staircase), and (4) the deep source zone beneath Washington and Oregon. Figures 146–151 show sensitivity of the hazard model to proposed changes in the seismic sources and ground motion models.

The GMMs for deep intraslab earthquakes cause large increases to the hazard for 5-hertz and lower hazard at 1-hertz spectral acceleration in the Puget Sound region, Wash. Figures 146*C* and 147*C* show the effect on probabilistic peak ground acceleration in western Washington, Oregon, and northwest California of changing ground motion models, using the 2014 source model in the numerator and denominator. Near the Washington and Oregon source, peak ground acceleration increases about 10 percent. At greater distances, peak ground acceleration decreases. In California, however, peak ground acceleration decreases over 20 percent near the source. The difference between source characterizations explains this behavior. In California, the mean magnitude is relatively small due to a larger *b* value (0.8), whereas in Washington and Oregon, the mean magnitude is relatively large due to a smaller *b* value (0.4). The updated GMMs tend to reduce the median peak ground acceleration for smaller intraplate sources but tend to raise the median peak ground acceleration for larger intraplate sources. Figures 148*C* and 149*C* show the effect on probabilistic 0.2-second (5-hertz) spectral acceleration in the same region. The 0.2-second (5-hertz) spectral acceleration increases about 20 percent near the Washington and Oregon source, but decreases 10 percent near the California source. Again, this

different behavior is attributed to lower mean magnitude of deep sources in the California part of the hazard model. At greater distances from the deep source, the 5-hertz spectral acceleration decreases everywhere in the 2014 model. Figures 150*C* and 151*C* show the effect on probabilistic 1-hertz spectral acceleration in the same region. The 1-hertz spectral acceleration decreases everywhere. This change is larger in California, up to 50 percent lower than in the 2008 model; in Washington and Oregon, up to a 30-percent decrease is more typical. Newer GMMs tend to greatly reduce the median 1-hertz spectral acceleration for smaller sources but tend to only slightly reduce the median 1-hertz spectral acceleration for larger sources, compared to the 2008 suite of GMMs.

The combined effects of source model, including new activity grids, higher Mmax, and the use of a staircase depth distribution, are shown in figures 146*B*–151*B*. Effects of the SSC and GMMs are shown in the left panel. In Washington, the new ground motions at 5-hertz frequency are slightly larger (fig. 148*A*), due to combined effects of increased Mmax (fig. 148*B*) and ground motions (fig. 148*C*). The new ground motions at 1-hertz frequency are slightly lower (fig. 150*A*) at Washington sites because the decrease in median motion (fig. 150*C*) dominates the increase due to larger Mmax (fig. 150*B*). In northern Oregon, probabilistic ground motion decreases for peak ground acceleration, 5-hertz, and 1-hertz frequency (fig. 146*A*–151*A*), but in southern Oregon it increases due to the new seismic source model, which spreads out hazard over the entire western one-half of the state in the 2014 NSHMP maps. In northern California, the overall hazard is dominated by the subduction interface ground motions. Lower activity rates and ground motions from intraslab GMMs decrease the hazard relative to the 2008 model. At coastal sites, the decrease is less pronounced because the depth of seismicity has been reduced from 50 km (the default value in 2008) to 39 km. The shallower focal depth tends to increase predicted motion at sites directly over these events.

California Shallow Crustal Earthquake Hazard

Proposed changes to probabilistic ground motions in California arise from the adoption of the new UCERF3 developed by the WGCEP (Working Group on California Earthquake Probabilities, 2013) and the use of new GMMs for shallow crustal seismic sources (see "Ground Motion Models" section). The following figures and text summarize the significant changes in hazard implied by these new models, relative to the 2008 USGS NSHMP maps by (1) examining changes due broadly to the earthquake source models and GMMs, and (2) examining source model specific changes at the statewide and local levels (that is, San Francisco and Los Angeles) and explaining all the areas where calculated ground motions are expected to change more than 10 percent. The probabilistic seismic hazard, difference, and ratio maps presented in this section are for 2-percent probability of exceedance in 50 years on firm rock (V_{S30}=760 m/s) uniform site condition for PGA and spectral acceleration at 0.2 second (5 hertz) and 1.0 second (1 hertz). Note that the figures and explanatory text do not identify every change; however, the largest changes are identified and addressed, and the many numerous small changes (such as those spanning a few pixels in the accompanying statewide maps) fall into the broad categories identified herein. The higher resolution local maps offer insight as to the causes of smaller changes.

Earthquake Source and Ground Motion Model Changes

In this section we present the total model and the contributions of the source and ground motion models.

Total Model

Figures 152–154 (peak ground acceleration, 1-hertz spectral acceleration, and 5-hertz spectral acceleration, respectively) show comparisons of the 2008 USGS NSHMP maps (*A* in each figure) to the new 2014 maps (*B* in each figure). Note that these maps include Cascadia subduction interface events and deep subduction intraslab events in the northwest part of the State that mask contributions from some shallow crustal sources present in the UCERF3 earthquake rate model. Broadly speaking, the hazard maps at each period are similar, but the accompanying ratio (*C* in each figure) and difference (*D* in each figure) maps reveal significant variation between the two. Across the three periods examined, the spatial distribution of differences is similar; causes of changes that exceed ±10 percent are detailed in the following section.

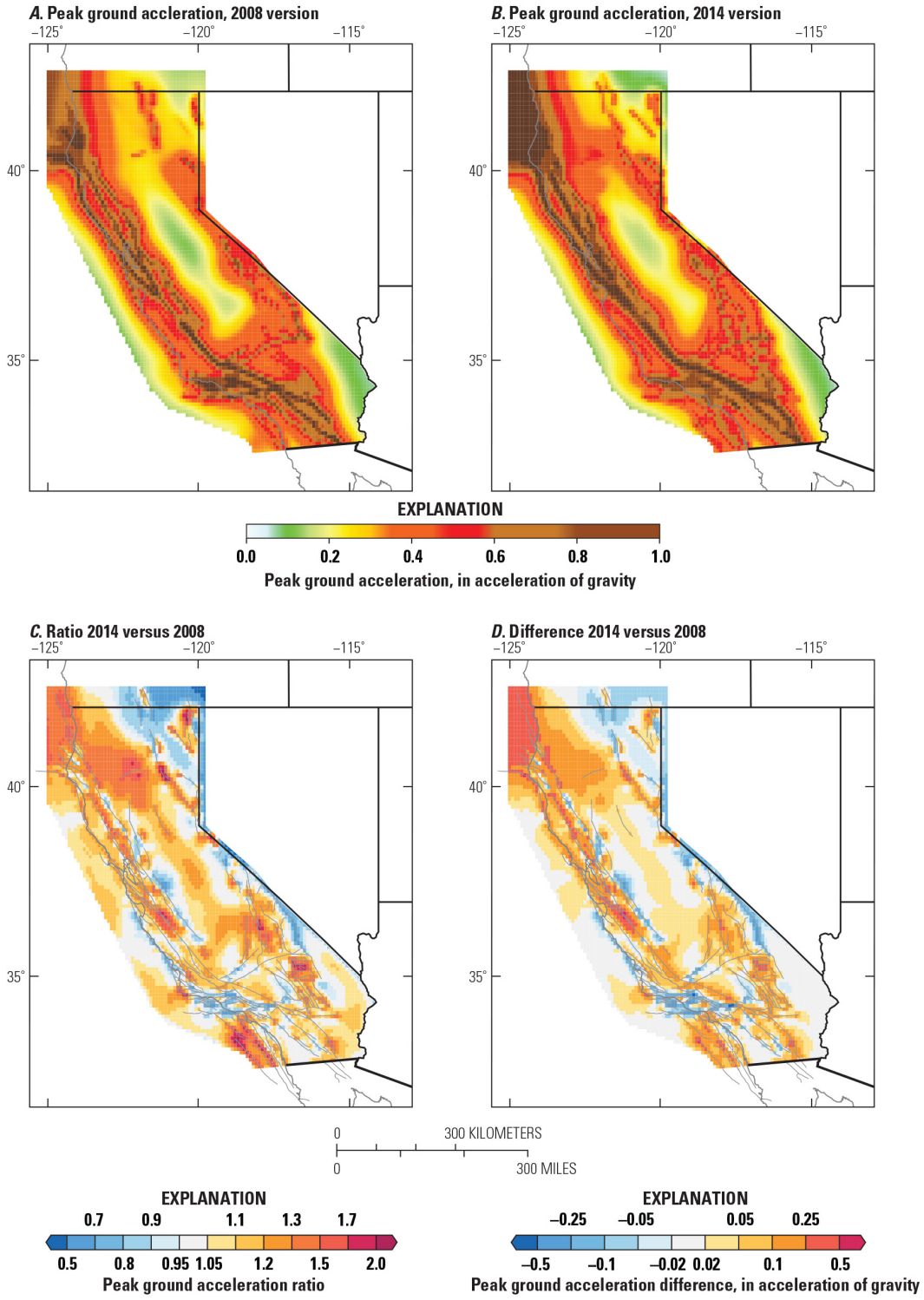

Figure 152. Maps showing changes in peak ground acceleration in California at 2-percent in 50 years probability of exceedance and V_{S30} site conditions of 760 meters per second. *A*, 2008 map of peak ground acceleration in California, and *B*, 2014 map. These maps include Cascadia subduction interface and intraslab sources in the northwest part of the state. *C*, shows the ratio of and *D*, the difference between the results shown in *A* and *B*. Note that the ratio scale spans a factor of two and that light gray masks changes within ±5 percent. Sources entirely outside of California are not included.

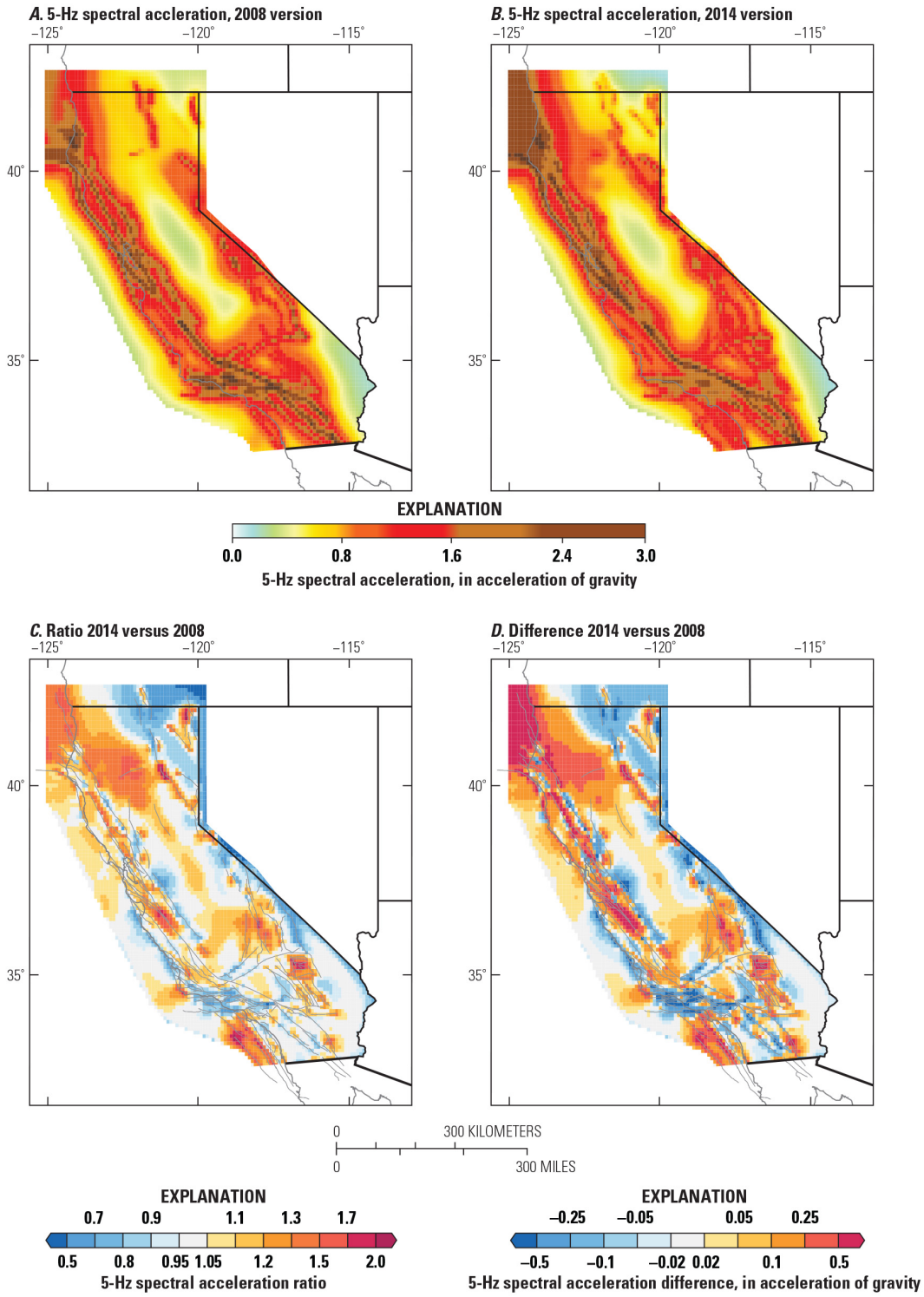

Figure 153. Maps showing changes in 5-hertz (0.2-second) spectral acceleration in California at 2-percent in 50 years probability of exceedance and V_{S30} site conditions of 760 meters per second. *A*, 2008 map of peak ground acceleration in California, and *B*, 2014 map. These maps include Cascadia subduction interface and intraslab sources in the northwest part of the state. *C*, shows the ratio of and *D*, the difference between the results shown in *A* and *B*. Note that the ratio scale spans a factor of two and that light gray masks changes within ±5 percent. Sources entirely outside of California are not included.

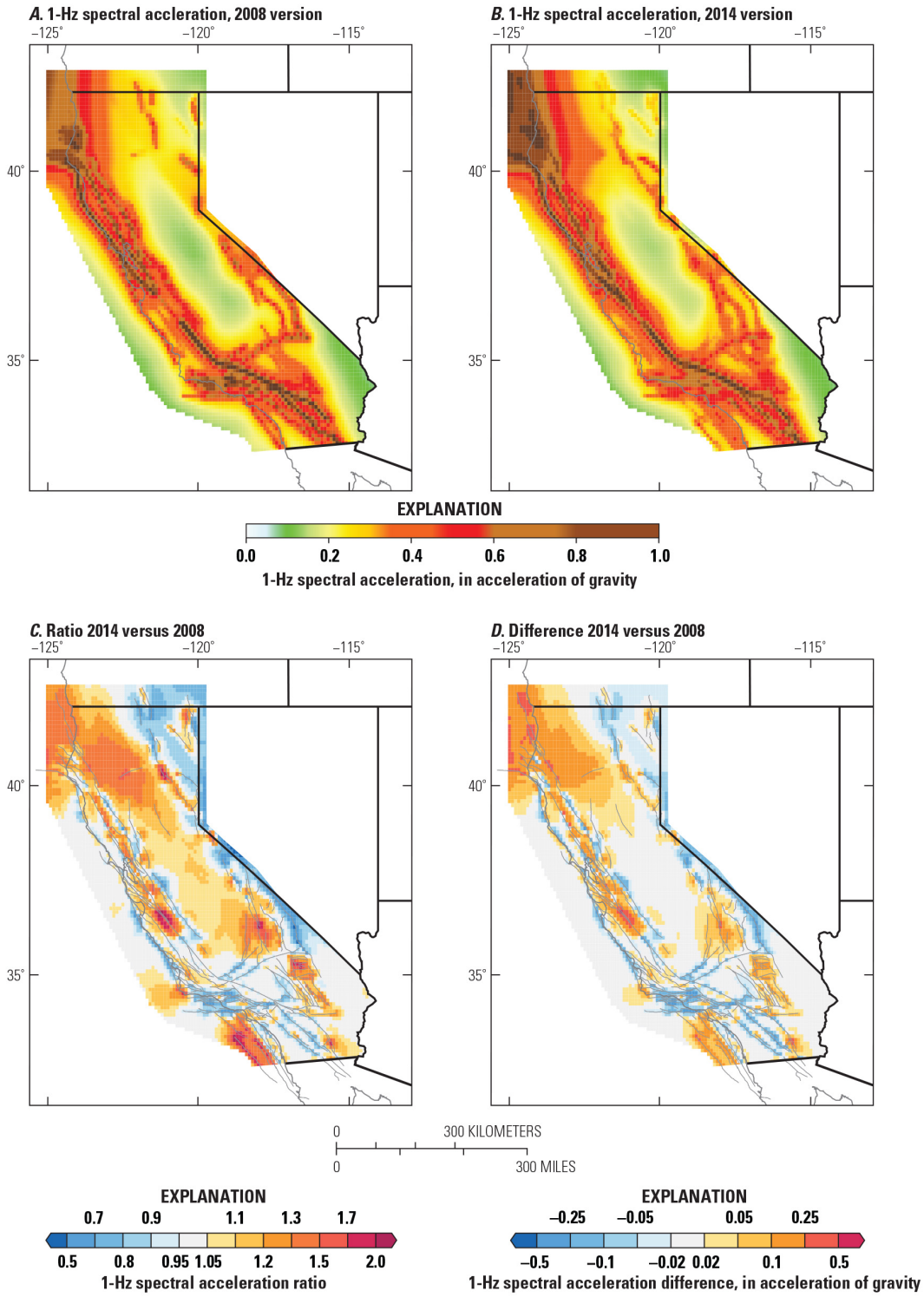

Figure 154. Maps showing changes in 1-hertz (1-second) spectral acceleration in California at 2-percent in 50 years probability of exceedance and V_{S30} site conditions of 760 meters per second. *A*, 2008 map of peak ground acceleration in California, and *B*, 2014 map. These maps include Cascadia subduction interface and intraslab sources in the northwest part of the state. *C*, shows the ratio of and *D*, the difference between the results shown in *A* and *B*. Note that the ratio scale spans a factor of two and that light gray masks changes within ±5 percent. Sources entirely outside of California are not included.

Contributions From Fault and Gridded Seismicity Sources

Figures 155–157 (peak ground acceleration, and 5-hertz and 1-hertz spectral acceleration, respectively) show ratios (*A* and *B* in each figure) and differences (*C* and *D* in each figure) between the 2008 and 2014 USGS NSHMP maps decomposed into contributions from fault (*A* in each figure) and background (or gridded seismicity) sources (*B* in each figure). Note that these maps do not include subduction interface and intraslab sources as in figures 152–154. Comparison with figures 152–154 shows that most of the changes in probabilistic ground motions at all periods of interest are due to the UCERF3 fault-source model, which is examined in more detail in the following section. The UCERF3 logic tree includes two gridded seismicity source branches, one that approximates the 2008 USGS NSHMP model and another that uses a tighter smoothing kernel, each receiving 50-percent weight. The branch with the tighter smoothing kernel concentrates grid sources in areas of high instrumental seismicity, resulting in spikes (orange dots) of increased probabilistic ground motions across the State. The complementary effects of these increases are light blue halos of decreased ground motion around the spikes (see for example, fig. 157*D*, along the California–Nevada border). It is also worth noting that the branch with the tighter smoothing kernel was generated using a declustered catalog that included events down to M_w2.5, giving rise to additional spatial variations in modeled earthquake rates. Again, although the amplitude of the differences between 2008 and 2014 vary, the spatial distribution of changes implied by fault and grid sources is similar across the periods examined.

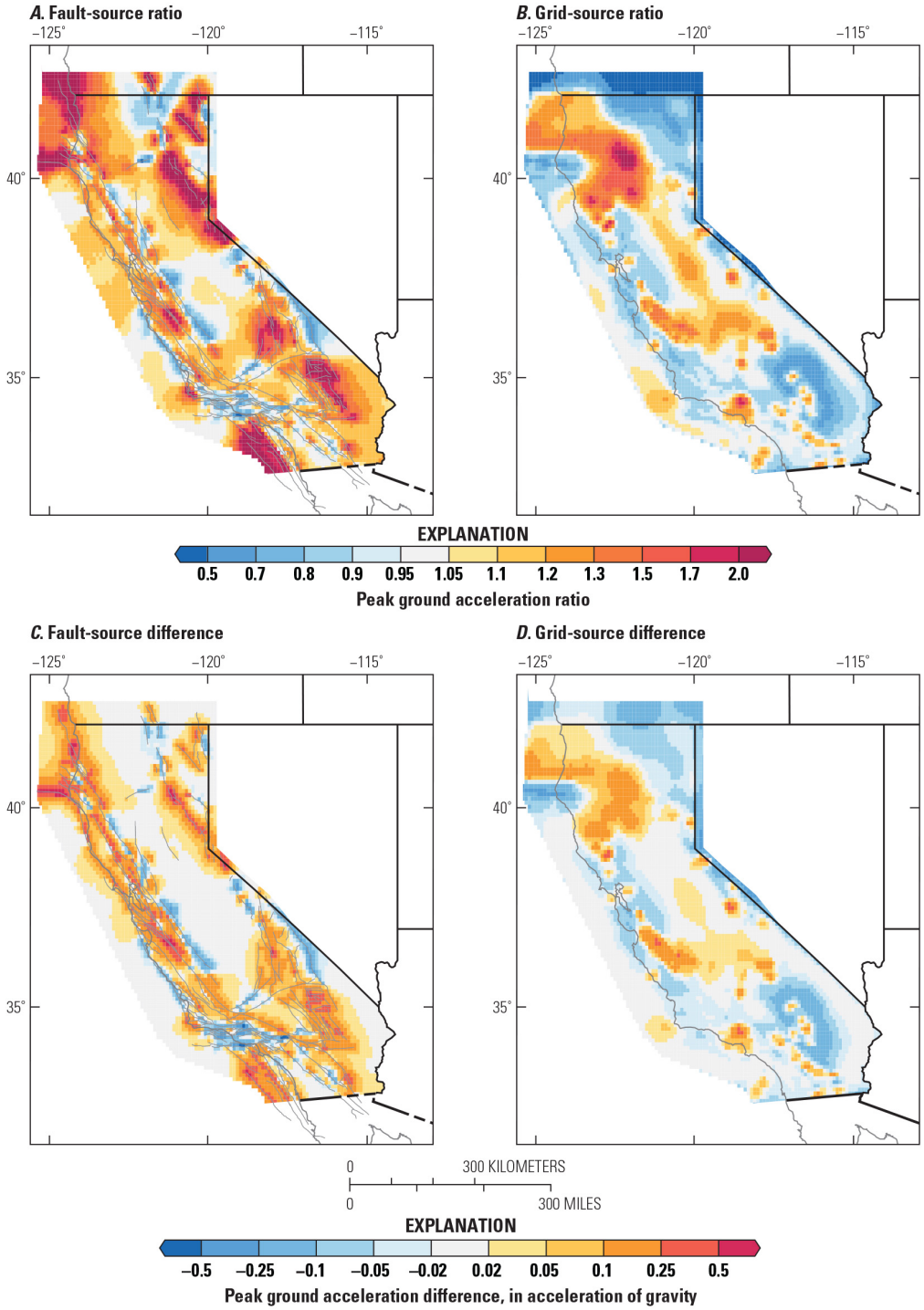

Figure 155. Maps showing changes in peak ground acceleration in California at 2-percent in 50 years probability of exceedance and V_{S30} site conditions of 760 meters per second. Maps do not include subduction interface and intraslab sources in the northwest part of the state. Changes in ground motion shown include *A*, ratio of the 2014 fault-source model compared to the 2008 model; *B*, ratio of the 2014 background seismicity rates compared to that in the 2008 model; *C*, difference between the 2014 fault-source model and the 2008 model; and *D*, difference between the 2014 background seismicity rates and the 2008 model. Sources entirely outside of California are not included.

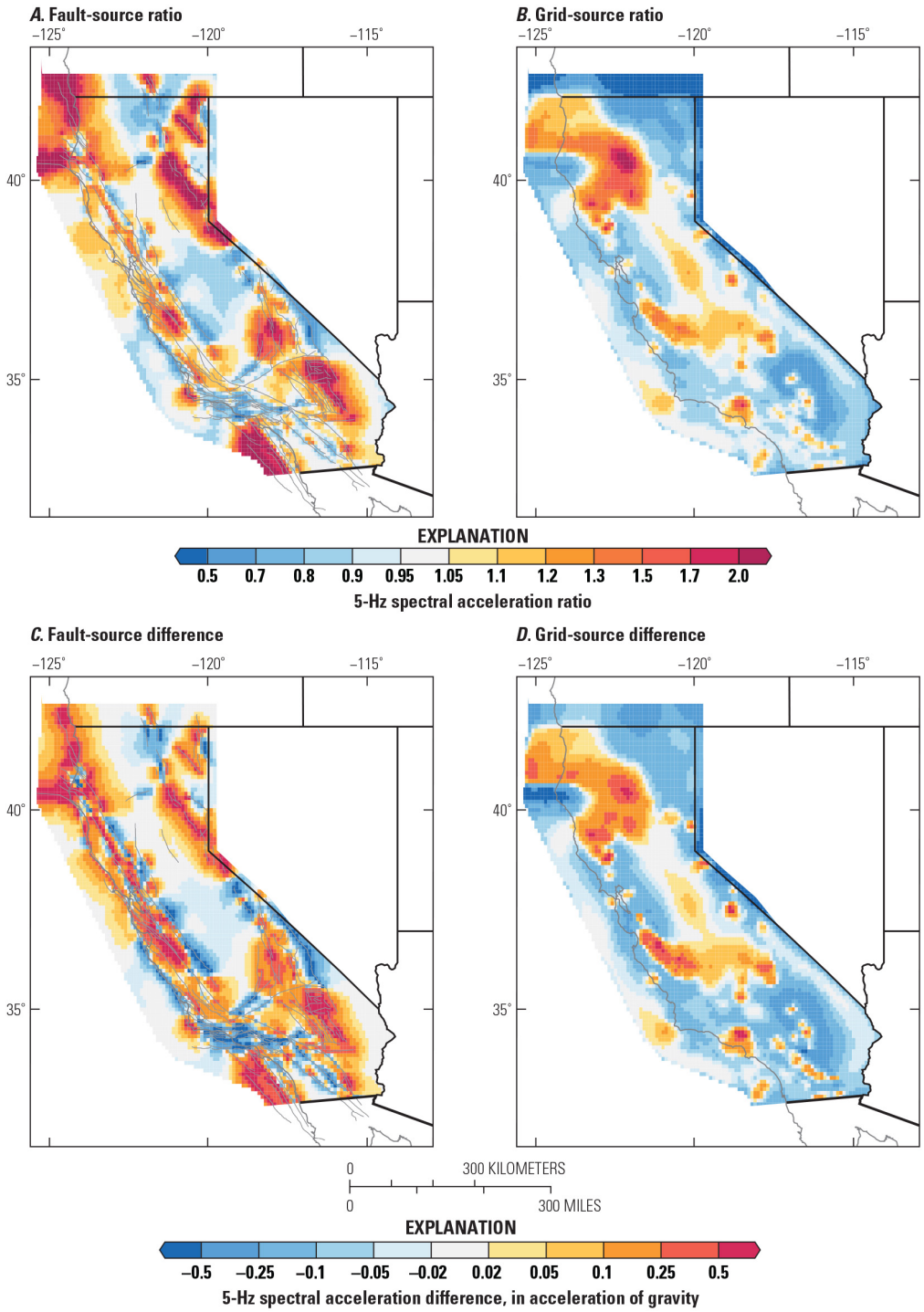

Figure 156. Maps showing changes in 5-hertz (0.2-second) spectral acceleration in California at 2-percent in 50 years probability of exceedance and V_{S30} site conditions of 760 meters per second. Maps do not include subduction interface and intraslab sources in the northwest part of the state. Changes in ground motion shown include *A*, ratio of the 2014 fault-source model compared to the 2008 model; *B*, ratio of the 2014 background seismicity rates compared to that in the 2008 model; *C*, difference between the 2014 fault-source model and the 2008 model; and *D*, difference between the 2014 background seismicity rates and the 2008 model. Sources entirely outside of California are not included.

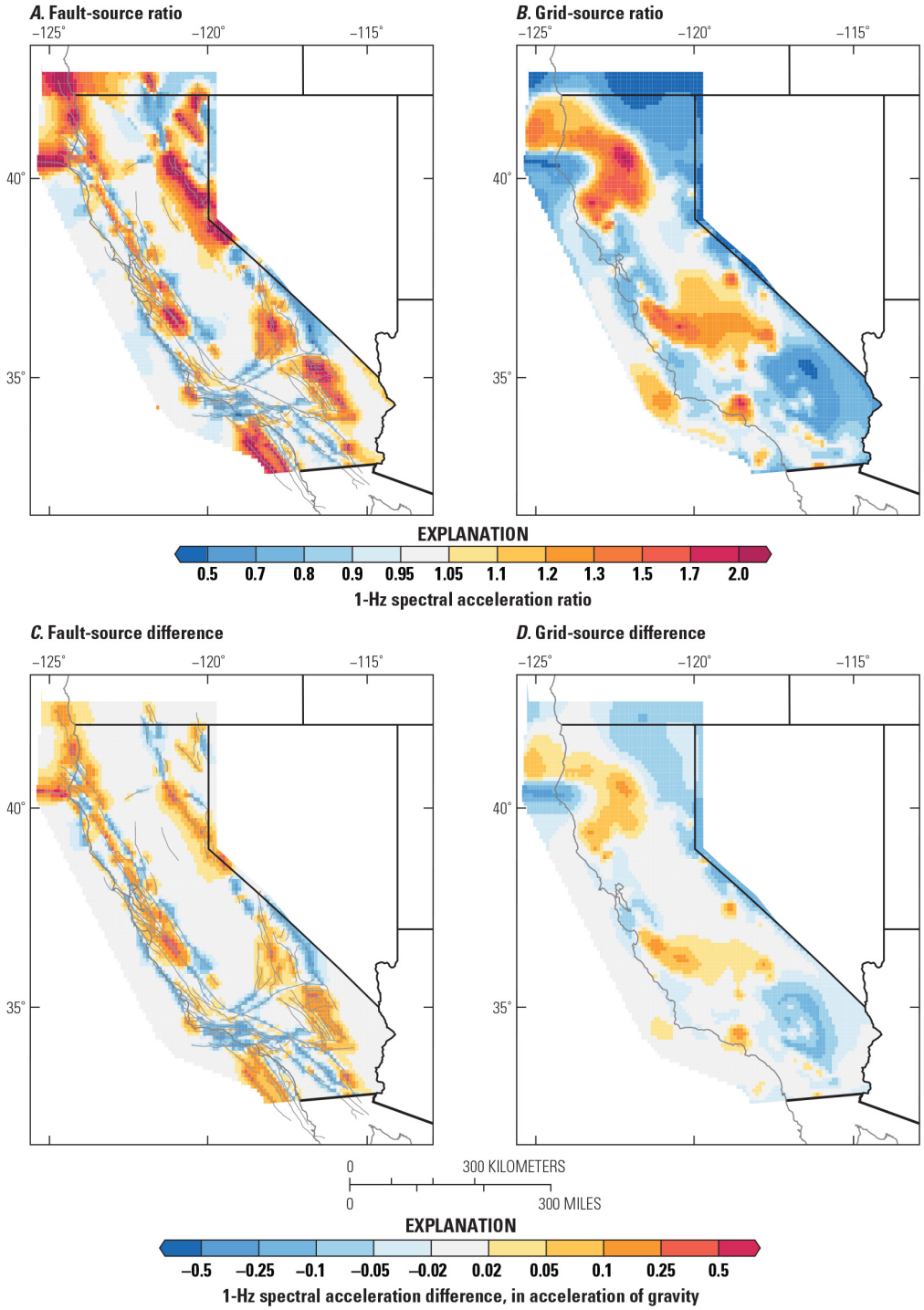

Figure 157. Maps showing changes in 1-hertz (1-second) spectral acceleration in California at 2-percent in 50 years probability of exceedance and V_{S30} site conditions of 760 meters per second. Maps *do not* include subduction interface and intraslab sources in the northwest part of the state. Changes in ground motion shown include *A*, ratio of the 2014 fault-source model compared to the 2008 model; *B*, ratio of the 2014 background seismicity rates compared to that in the 2008 model; *C*, difference between the 2014 fault-source model and the 2008 model; and *D*, difference between the 2014 background seismicity rates and the 2008 model. Sources entirely outside of California are not included.

Earthquake-Source Model Versus Ground Motion Model

Figures 158–160 (peak ground acceleration, and 5-hertz and 1-hertz spectral acceleration, respectively) show the total difference (*D* in each figure) between the 2008 and 2014 USGS NSHMP maps (considering only crustal fault and gridded seismicity sources), and its decomposition into contributions from UCERF3 (*B* in each figure) and the new ground motion models (*A* and *C* in each figure). These figures show that across the three periods of interest, most of the proposed ground motion changes arise from adoption of UCERF3 as the source model of the USGS NSHMP maps. Only where increases implied by the 2014 ground motion models are highest (for instance, along the San Andreas corridor) do ground motions further increase above that implied by the change in source model.

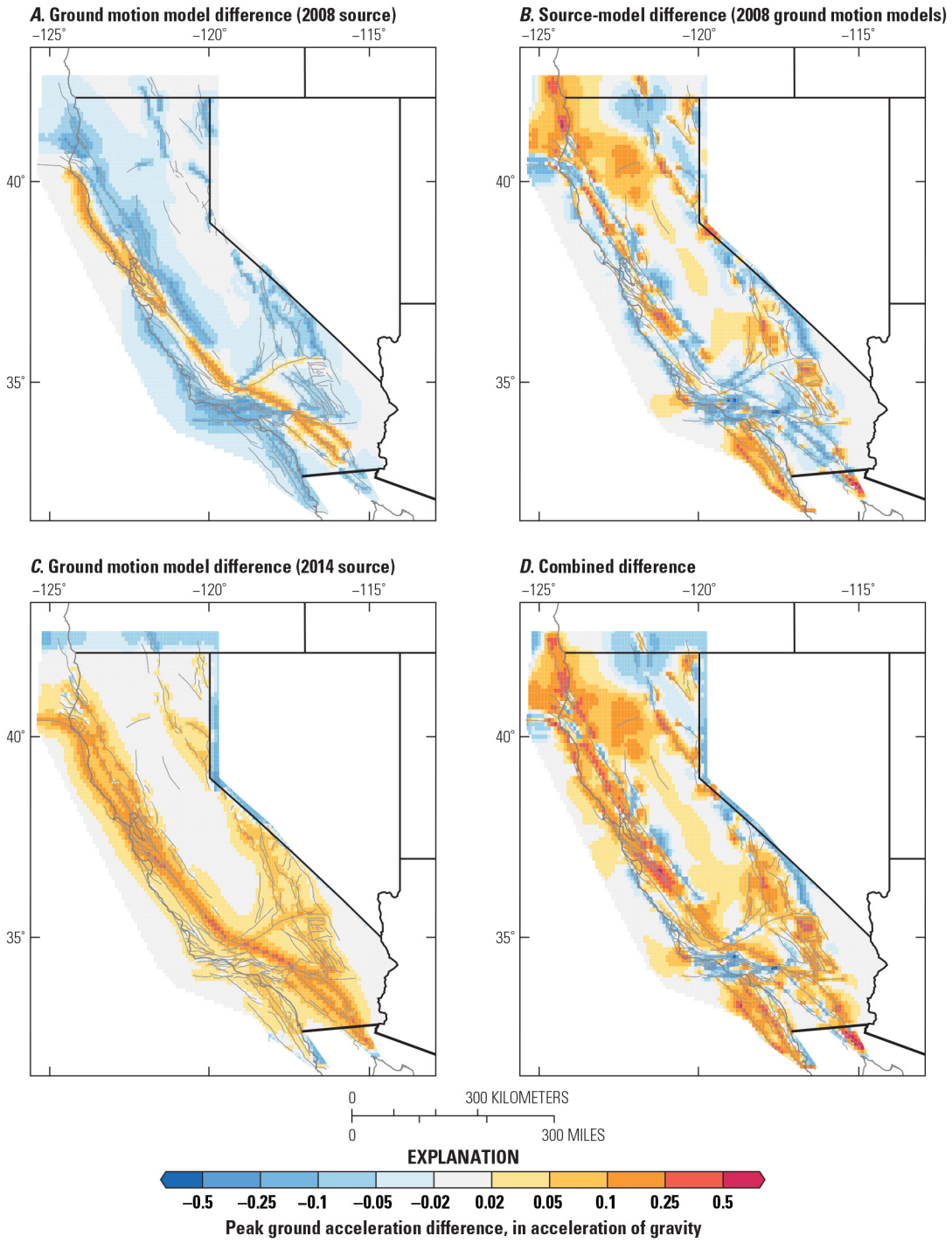

Figure 158. Maps showing difference in peak ground acceleration in California at 2-percent in 50 years probability of exceedance and V_{S30} site conditions of 760 meters per second. Differences are due to changes in the ground motion models using the *A*, 2008 source models; and *C*, 2014 source model; and *B*, changes in the fault-source model; and *D*, the total difference between the 2014 model compared to the 2008 model. Sources entirely outside of California are not included.

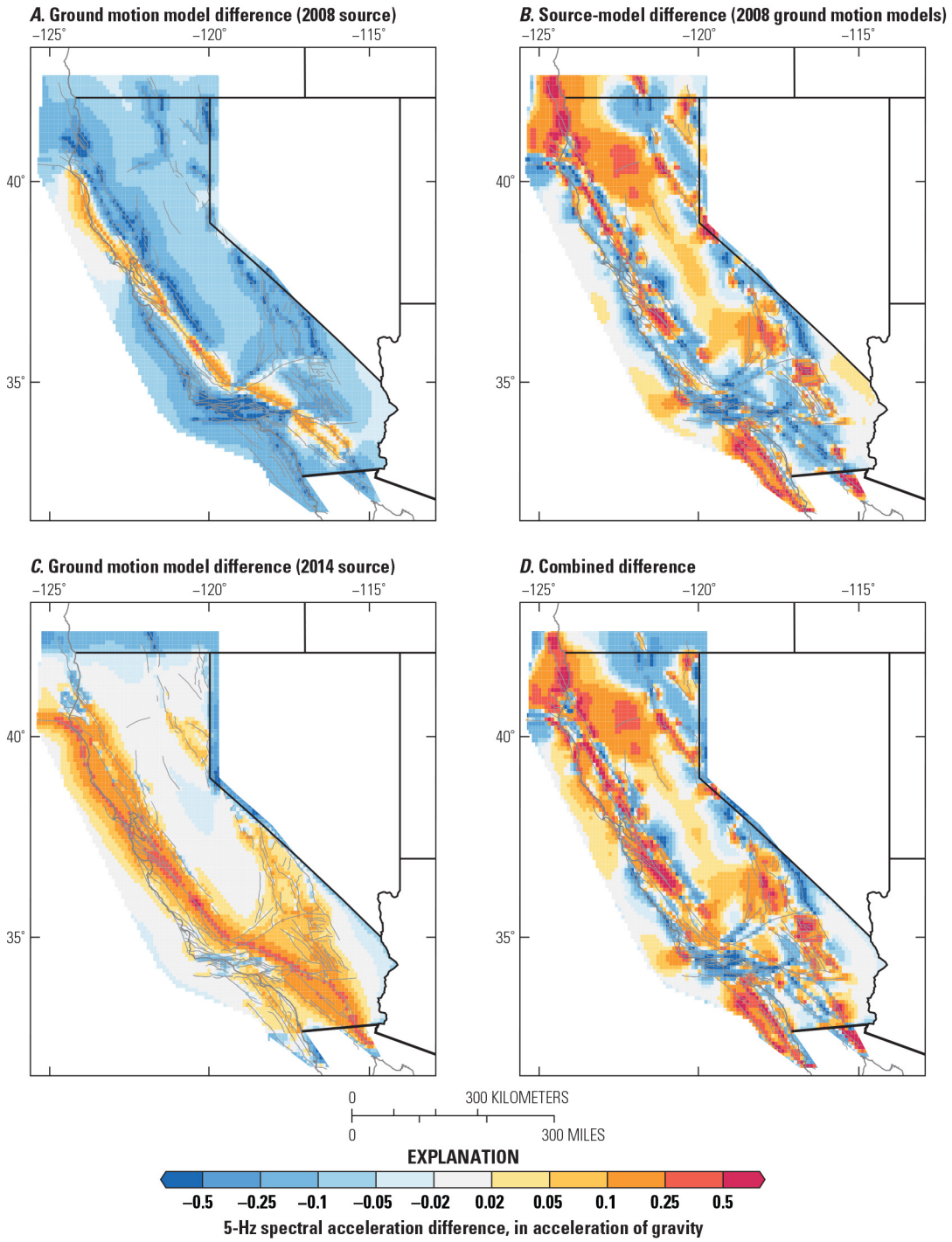

Figure 159. Maps showing difference in 5-hertz (0.2-second) spectral acceleration in California at 2-percent in 50 years probability of exceedance and V_{S30} site conditions of 760 meters per second. Differences are due to changes in the ground motion models using the *A*, 2008 source models; and *C*, 2014 source model; and *B*, changes in the fault-source model; and *D*, the total difference between the 2014 model compared to the 2008 model. Sources entirely outside of California are not included.

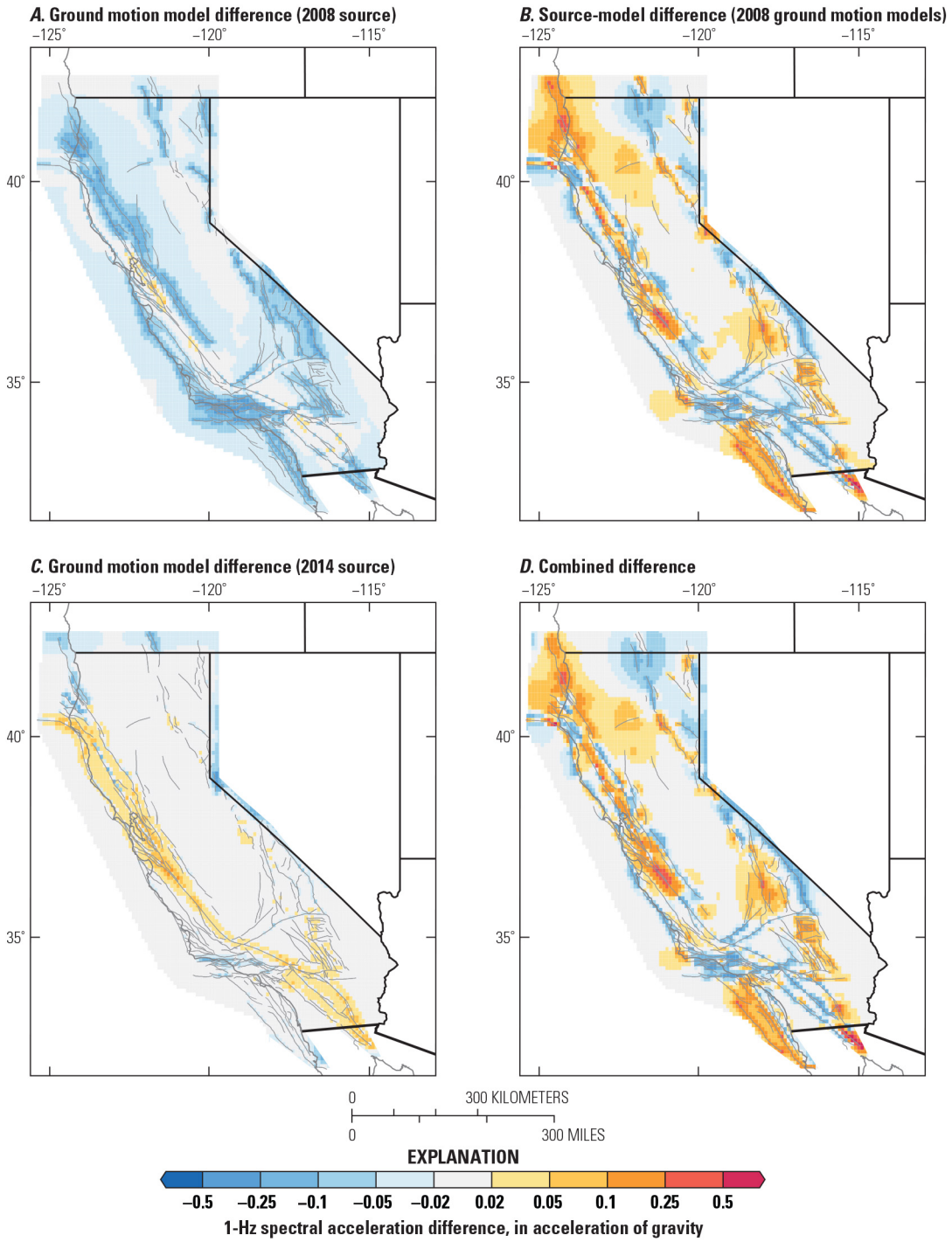

Figure 160. Maps showing difference in 1-hertz (1-second) spectral acceleration in California at 2-percent in 50 years probability of exceedance and V_{S30} site conditions of 760 meters per second. Differences are due to changes in the ground motion models using the *A*, 2008 source models; and *C*, 2014 source model; and *B*, changes in the fault-source model; and *D*, the total difference between the 2014 model compared to the 2008 model. Sources entirely outside of California are not included.

To compute the source model differences the 2008 USGS NSHMP ground motions were subtracted from those computed using the UCERF3 source model with the 2008 GMMs. The GMM differences were computed by subtracting the ground motions implied by the 2008 GMMs from those implied by the 2014 GMMs using both the 2008 (top-left) and 2014 (bottom-left) source models. In these latter maps, it is interesting to note the sensitivity of the 2014 GMMs to source model rate changes at different magnitudes and for specific focal mechanisms. In both cases, the 2014 GMMs further increase computed ground motions along the strike-slip faults of the San Andreas corridor; however, when using the 2014 source model, the increase at peak ground acceleration and 5-hertz spectral acceleration extends across most faults in the State. Using the 2008 source model implies we would expect broad decreases in ground motions in the vicinity of normal and reverse faults; however, the inclusion of multifault ruptures with much larger magnitudes in UCERF3 indicates the opposite is true.

Changes Caused by UCERF3

The following section outlines the specific ±10-percent changes in ground motion in the 2014 USGS NSHMP maps that arise from adoption of UCERF3 as the NSHMP earthquake source model. The previous section showed that the spatial distribution of changes are consistent across the three spectral periods of interest, and so only peak ground acceleration with a 2-percent probability of exceedance in 50 years is examined in detail. Note that the ground motion maps used to derive the figures accompanying this section do not include Cascadia subduction interface and intraslab sources, which tend to dominate hazard in the northwest part of the State.

Gridded Source Contributions

Many changes (mostly increases) in probabilistic ground motion are due to the use of the "UCERF3 smoothed seismicity" model for background sources. Although this background source model only receives 50-percent weight (a model based on UCERF2 smoothed seismicity receives the other half), it uses a tighter, adaptive smoothing kernel, which gives rise to spikes in ground motion over small areas. The locations of the most significant grid source contributions to hazard are circled in figure 161*B*. Comparison with figures 155–157 show that there are numerous locations where it is difficult to resolve if a ground motion increase is due exclusively to changes in the 2014 smoothed seismicity model.

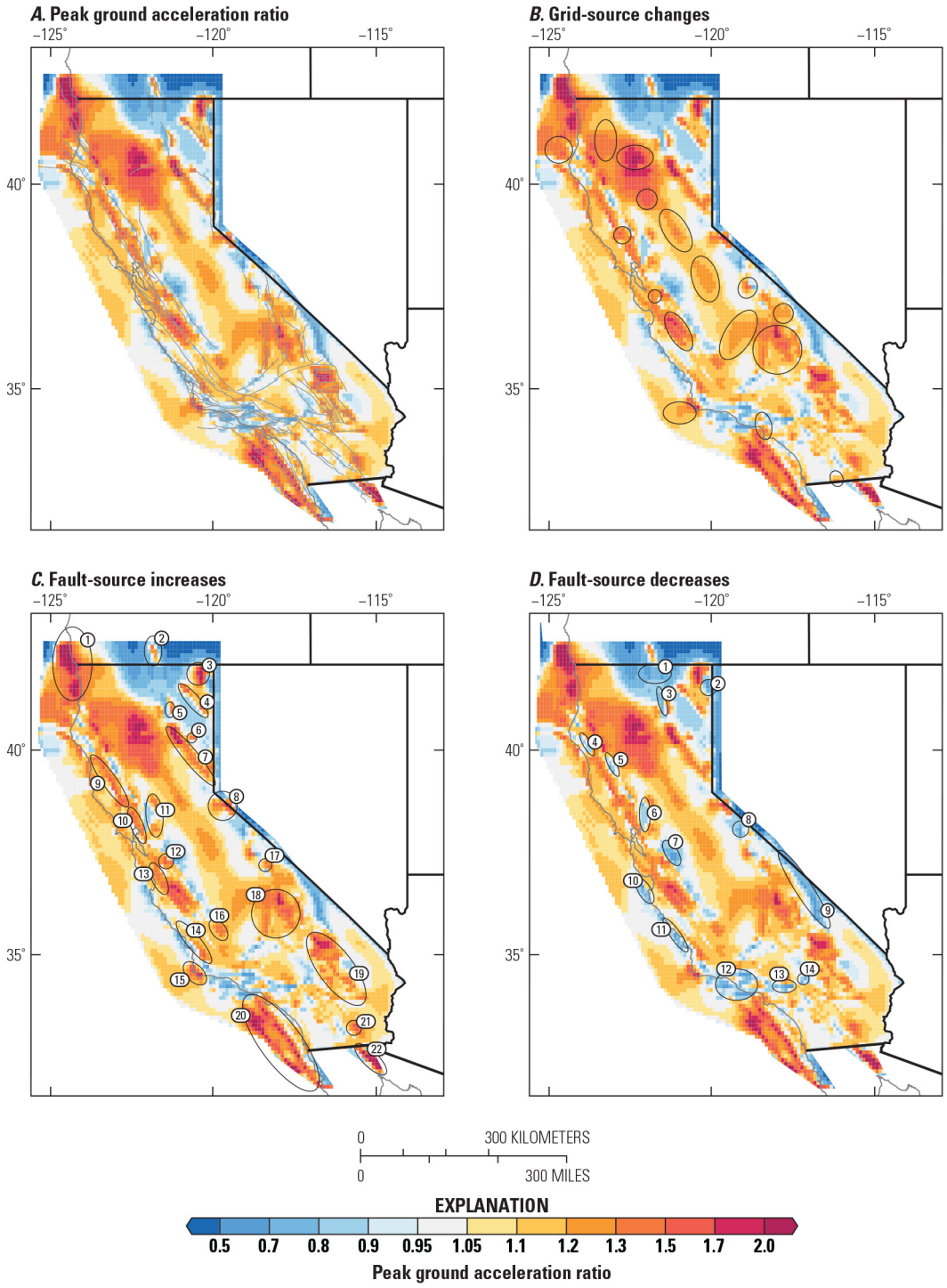

Figure 161. Maps showing ratios of peak ground acceleration for California at 2-percent in 50 years probability of exceedance and V_{S30} site conditions of 760 meters per second. Maps do not include Cascadia subduction sources. Changes in ground motion include *A*, updates to the 2014 model compared to the 2008 model; *B*, changes in background seismicity rates; and maps that highlight *C* and *D*, increases and decreases arising from changes to the fault-source model, respectively (numbers correspond to descriptions in tables 22 and 23). Sources entirely outside of California are not included.

Fault-Source Contributions

The remaining changes to probabilistic ground motion arise from (1) slip- or moment-rate changes on existing 2008 USGS NSHMP faults, (2) geometric changes to existing faults, (3) the introduction of new faults, and (4) fault participation in multifault ruptures. Although the rates of large multifault events generally are quite low, they consume a significant portion of the statewide moment budget and do not contribute significantly to 2-percent probability of exceedance in 50 years PGA ground motions, resulting in a general decrease in ground motion along the major California fault zones. Figure 161*C* and *D* highlight the significant increases and decreases, respectively, in ground motion implied by UCERF3; see tables 22 and 23 for explanations of each numbered item in figure 161.

Table 22. California fault sources that contribute to ground motion increases (see fig. 161*C*).

[ABM, average block model; UCERF2, Uniform California Earthquake Rupture Forecast, ver. 2]

ID	Fault source	Notes
1	Big Lagoon–Bald Mountain fault	Extended north approximately 60 km and has 8x moment rate for ABM deformation model.
2	South Klamath Lake West fault	New fault.
3	Goose Lake, Fitzhugh Creek, Jess Valley, and Davis Creek faults	New faults.
4	Likely fault	Moment rate doubled.
5	Pittville fault	New fault.
6	Honey Lake fault	Fault extended to west.
7	Almanor, Walker Spring, Keddie Ridge, Skinner Flat, Mohawk Valley, Dog Valley, Polaris, and Incline Village faults	Seven new faults.
8	West Tahoe and Antelope Valley faults	New fault and southern extension of West Tahoe fault.
9	Maacama fault	20-percent increase in moment rate.
10	West Napa fault	3.5x increase in moment rate, mostly due to ABM deformation model.
11	Great Valley 03, 05, and 06, and Los Medanos–Roe Island faults	New and alternate fault models.
12	Greenville South and Ortigalita faults	Ortigalita: geometric and moment-rate changes; Greenville South extended further south.
13	Silver Creek, Monte Vista–Shannon, and Sargent faults	New or extension of existing (Monte Vista–Shannon) faults.
	Zayante–Vergeles fault	Moment-rate increase (x9 increase for reverse fault representation)
14	Oceanic–West Hausna faults	New fault with high moment rate.
15	Los Alamos, Santa Ynez River, Santa Ynez West, and Hosgri Extension faults	New faults.

Table 22. California fault sources that contribute to ground motion increases (see fig. 161*C*).—Continued

ID	Fault source	Notes
16	Lost Hills fault	New fault.
17	Fish Slough, Independence, and Owens Valley faults	Fault geometry change (Fish Slough) and moment-rate increases on all three faults.
18	Sierra Nevada (N. extension) and White Wolf Extension Faults; Scodie and Lake Isabella Seismicity lineaments	New faults commingled with gridded seismicity sources.
19	15+ new faults	Many new faults added in the eastern Mojave desert; some were present in UCERF2 with 0 zero slip rate; others are entirely new (for example, Cleghorn Pass and Lake Faults).
20	San Clemente, San Diego Trough, Santa Cruz Catalina Ridge, Oceanside, and San Pedro Basin faults	Multiple new offshore faults.
21	Elmore Ranch fault	Moment-rate increase.
22	Cerro Prieto fault	New fault.

Table 23. California fault sources that contribute to ground motion decreases (see fig. 161*D*)

ID	Fault Source	Notes
1	Gillem–Big Crack & Cedar Mtn.–Mahogany Mtn. faults	Lower slip rates.
2	Surprise Valley Fault	Moment-rate decrease.
3	Hat Creek–McArthur–Mayfield fault	Moment-rate decrease.
4	Maacama fault	High slip-rate fault shortened at northern end.
5	Bartlett Springs fault	Trace geometry changes.
6	Great Valley 03, 04 faults	Moment-rate decrease.
7	Great Valley 08 (Orestimba) fault	60-percent decrease in moment rate; participation in multifault ruptures.
8	Mono Lake fault	Moment-rate decrease.
9	Death Valley North, South, and Black Mtn. Frontal faults	40-percent decrease in moment rate; participation in multifault ruptures.
10	San Gregorio South	Fault geometry and slip/event rate change.
11	Hosgri fault	Down dip width increase and participation in multifault ruptures contributes to lower hazard although total moment rate has changed little.
12	San Cayetano, Anacapa–Dume, Oak Ridge Offshore, and Channel Islands Deep Ramp faults	New faults and moment-rate increases on existing.
13	Cucamonga fault	Methodological difference; Cucamonga participates in multifault ruptures rather than by itself in high-rate "characteristic" events. Down dip width also increased.
14	North Frontal and Cleghorn faults	Moment-rate decreases.

Local Changes

Comparisons of local changes in probabilistic ground motion for the San Francisco Bay and Los Angeles areas implied by the use of UCERF3 as the USGS NSHMP earthquake source model are shown in figures 162 and 163, respectively. These comparisons are improved by using higher resolution computational grids (0.02 and 0.05 degrees per pixel, as opposed to 0.1 degree per pixel in the statewide comparisons). As with the statewide comparisons, most changes in ground motion arise from updates to existing faults (slip- or moment-rate, or geometry) or the introduction of new faults. A number of such changes are identified in figures 162 and 156, and explanations of each are provided in tables 24 and 25. The higher resolution map and scale reveal how sensitive hazard is to slight changes in geometry (for example, a once vertical fault that now has a slight dip picks up a hanging-wall effect). Another contribution to changes in hazard that stands out at the local scale is the presence of segment boundaries in the 2008 USGS NSHMP fault model, across which slip-rate changes are common. As with the previous section, these comparisons are all for 2-percent probability of exceedance in 50-year PGA ground motion.

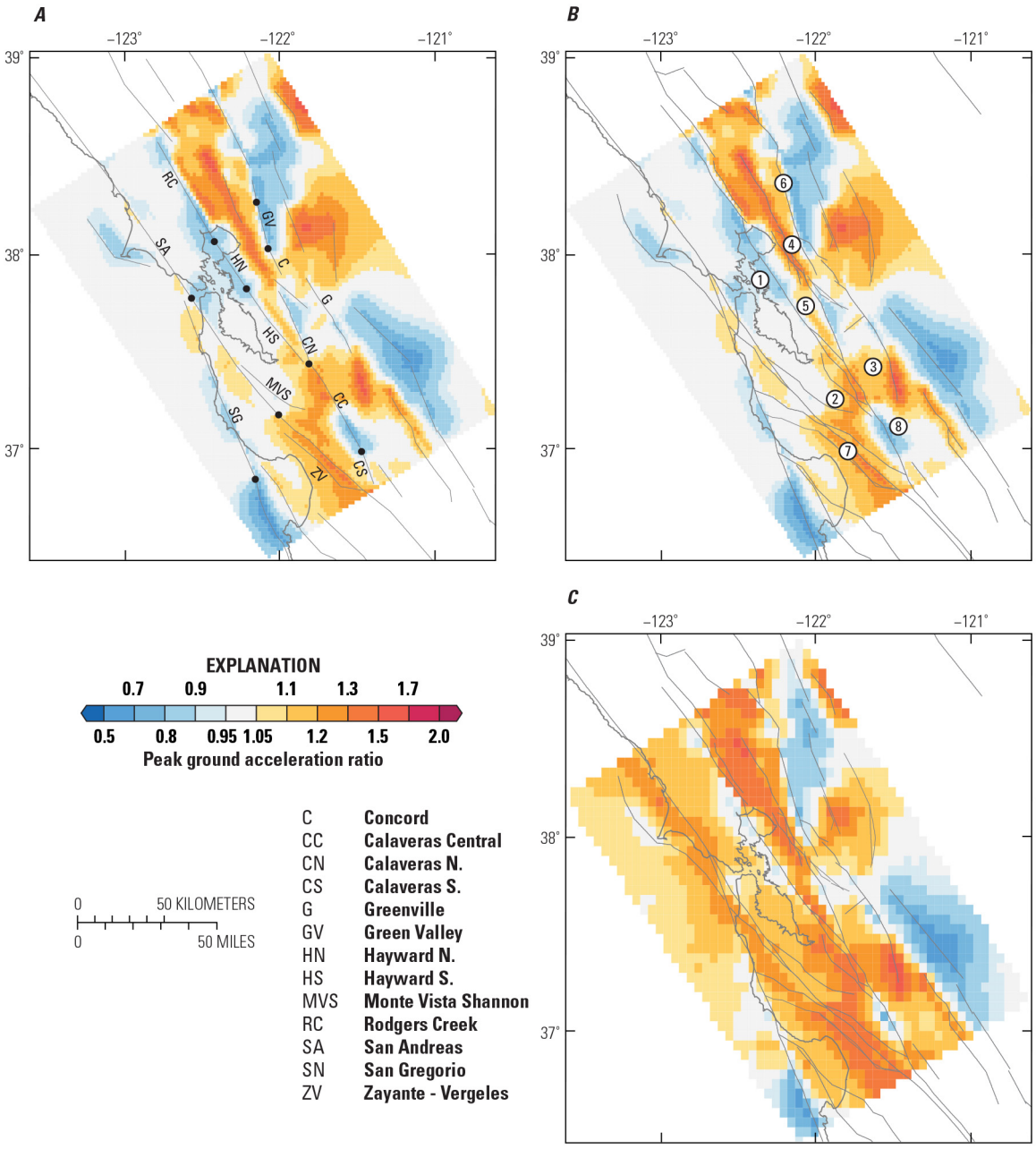

Figure 162. Maps showing ratios of peak ground acceleration in the San Francisco Bay area at 2-percent in 50 years probability of exceedance and V_{S30} site conditions of 760 meters per second implied by the Uniform California Earthquake Rupture Forecast, ver. 3 (UCERF3) source model to that of the 2008 fault-source model (maps do not consider new ground motion models). *A*, 2008 version of the fault-source model (black dots mark significant 2008 modeled segment boundaries); *B*, shows UCERF3 faults (all fault models, refer to table 24 for explanations of ground motion variation at the numbered locations); and *C,* ratio of 2014 model compared to the 2008 model.

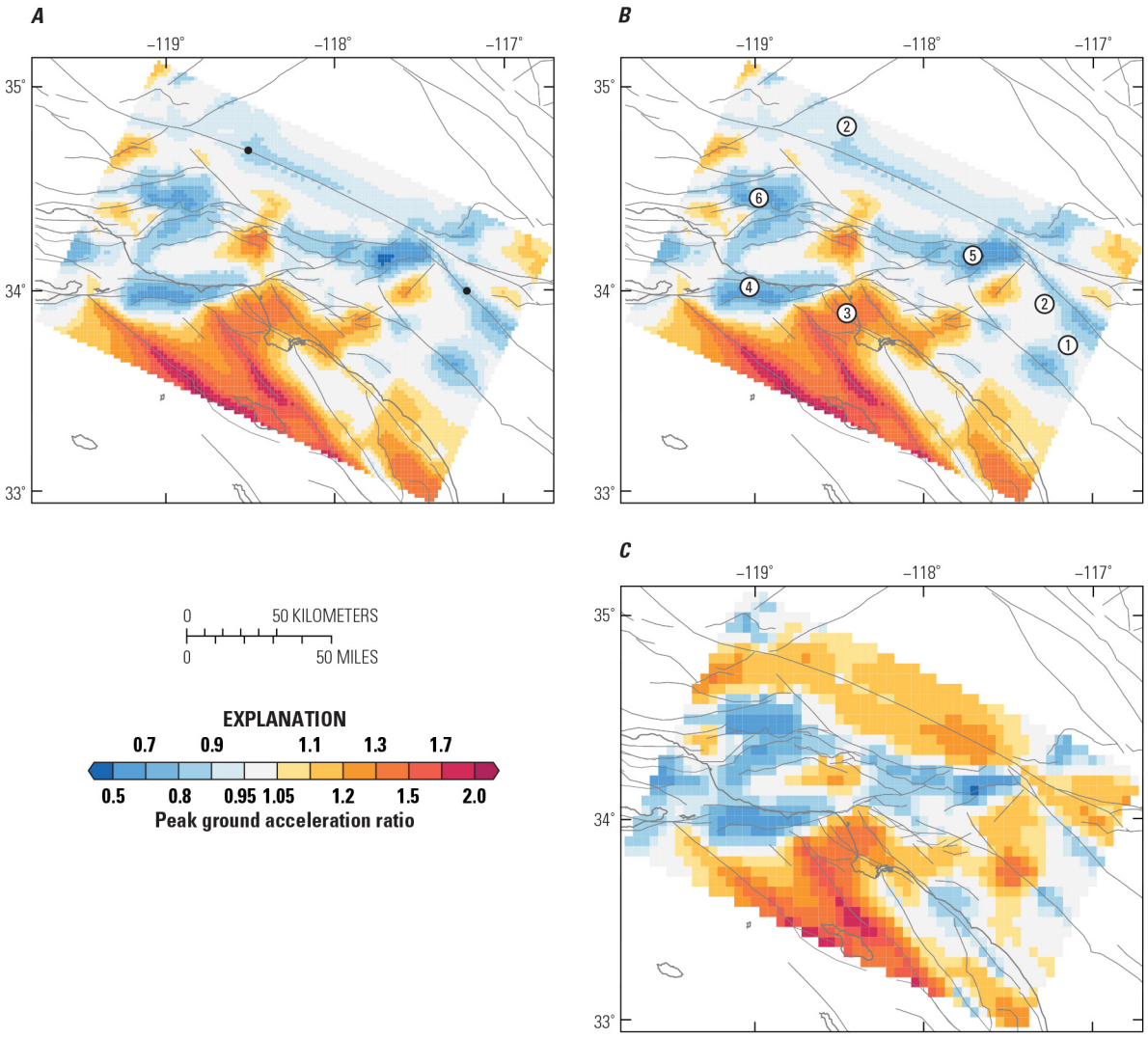

Figure 163. Maps showing ratios of peak ground acceleration in the Los Angeles area at 2-percent in 50 years probability of exceedance and V_{S30} site conditions of 760 meters per second implied by the Uniform California Earthquake Rupture Forecast, ver. 3 (UCERF3) source model to that of the 2008 fault-source model (maps do not consider new ground motion models). *A*, 2008 USGS NSHMP faults (black dots mark significant 2008 modeled segment boundaries); *B*, shows UCERF3 faults (all fault models, refer to table 25 for explanations of ground motion variation at the numbered locations); and *C,* ratio of 2014 model compared to the 2008 model.

Table 24. San Francisco Bay area ground motion changes (see fig. 162).

[mm/yr, millimeters per year]

ID	Notes
1	Oakland—Hazard decrease due to the Hayward fault as a whole participating in multifault ruptures and the presence of the Hayward N.–Hayward S. segment (slip-rate change) boundary in the 2008 USGS NSHMP source model (UCERF2).
2	Numerous new fault and updated fault geometries Monte Vista–Shannon extension Hayward S. Extension addition Silver Creek addition.
3	New fault: Greenville S.
4	Numerous Contra Costa Faults connecting Calaveras N. and West Napa.
5	Increased hazard between Calaveras N. and Hayward South due to change in fault geometry. Both faults dip towards each other, whereas they were both vertical in UCERF2, thereby increasing hanging-wall effects.
6	Green Valley relocated slightly to west but also now dipping to the west thereby significantly reducing hazard on what is now the footwall (east) side of the fault trace.
7	Increased hazard in vicinity of Zayante–Vergeles (ZV) and San Andreas (at Santa Cruz; SAF). To the west of ZV, the broad area of increased hazard is due to one fault model (3.1) representing ZV as a west-dipping reverse fault. The area of high increase between ZV and SAF is due to the Santa Cruz section having a 79-degree west dip, whereas it was vertical in UCERF2. High hazard to the east of the SAF is due to the inclusion of the Sargent fault in UCERF3.
8	The large drop in hazard on the southern part of the central Calaveras primarily is due to the drop in slip rate on the central Calaveras (15 mm/yr to approximately 11.5 mm/yr). On the northern one-half of the fault, this drop is overwhelmed by the rapidly slipping, east dipping south Hayward Extension. The loss of the south-central Calaveras segment boundary also contributes to lower hazard.

Table 25. Los Angeles area ground motion changes (see fig. 163).

ID	Notes
1	Conversion from independent overlapping faults to “stepovers” on both the San Jacinto and Elsinore faults.
2	(Note: there are two number 2 markers in figure.) Decreased hazard due to presence of segment boundaries in 2008 model (UCERF2).
3	Multiple new faults considered that had 0 mm/yr slip rates in the 2008 USGS NSHMP maps. Although rates generally are low (approximately 1 mm/yr) (for example, Compton, San Pedro escarpment), these significantly increase 2 percent in 50-year ground motions.
4	Anacapa-Dume; 7-percent reduction in moment.
5	Cucamonga methodological change; now participates with other faults.
6	San Cayetano; 10-percent reduction in moment.

Considering the 2014 GMMs in conjunction with UCERF3, probabilistic ground motions generally increase in a manner consistent with what was observed at the statewide scale. In the case of PGA, probabilistic ground motions increase most dramatically along strike-slip faults of the San Andreas corridor and exhibit little or no change in the vicinity of reverse faults. For example, in the Bay Area (fig. 162*C*), there is a marked increase in probabilistic ground motion along the San Andreas Fault and broader areas of increased ground motion about the faults of the East Bay (such as the Calaveras-Hayward system among others). Near Los Angeles (fig. 163*C*), probabilistic ground motion along the Mojave section of the San Andreas Fault is increased, whereas when considering the UCERF3 source model alone, ground motion had decreased.

Conclusions and Future Directions

The 2014 national seismic hazard maps apply the best available science as determined by project scientists, workshop participants, and the National Seismic Hazard Mapping Project (NSHMP) steering committee that provided critical review and guidance. Many new input datasets, models, and methods were implemented in this update, including the following: the Central and Eastern U.S. Seismic Source Characterization for Nuclear Facilities (CEUS–SSCn, 2012) project developed a new Central and Eastern U.S. (CEUS) source model; Electric Power Research Institute reevaluated weights for CEUS ground motion models; the Basin and Range Province Earthquake Working Group and the Working Group on Utah Earthquake Probabilities models provided new information for the Intermountain West region faults; a working group combined geologic and geodetic inversion slip rates to update the fault sources across the Western United States (WUS); the Cascadia working groups developed new models for fault geometry and earthquake recurrence; the Uniform California Earthquake Rupture Forecast model provided new multisegment rupture models; and the Next Generation Attenuation group (Pacific Earthquake Engineering Research Center, PEER) provided new ground motion models for WUS crustal earthquakes. In addition, many other scientists and engineers participated in workshops, a Tiger Team committee, and numerous meetings and discussions of earthquake sources and ground motions that were implemented in this analysis. The new seismic hazard models benefitted from the advice of many hundreds of experts across the country.

The 2014 updated hazard maps differ from the 2008 maps in complex ways. The new ground motions vary locally depending on complicated changes in the underlying models. In the CEUS, the new earthquake catalog, completeness models, smoothing algorithms, magnitude uncertainty adjustments, and fault models change the hazard, and the new ground motion model-weighting scheme generally lowers the ground motions. The resulting maps for the CEUS can differ by ±20 percent over broad areas, with larger changes locally, compared to the 2008 maps due to complicated interactions between the various parts of the models. In the Intermountain West region, the combined geologic and geodetic inversion models increase the hazard along the Wasatch fault and central Nevada region, but the new NGA-West2 ground motions tend to lower the hazard on the hanging walls of normal faults with respect to the 2008 USGS NSHMP maps. These counteracting effects can result in complicated patterns of changes which are about ± 20 percent over broad portions of the region compared to the previous hazard maps. In the Pacific Northwest, the new Cascadia source model causes the hazard to increase by up to 40 percent in the southern Cascadia subduction zone due to the addition of possible M_w8 and greater earthquakes, but causes the hazard to decrease slightly along the northern Cascadia subduction zone because of reduced earthquake rates relative to the 2008 NSHMP model. Subduction ground motions from the new models fall off faster with distance than motions in previous models, but they also tend to be higher near fault ruptures. In California, the new UCERF3 model accounts for earthquakes that rupture multiple faults yielding larger magnitudes than applied in the previous model;

however, the new maps also include new ground motion models, new slip rates from combined geodetic-geologic inversions, new faults, and an adaptive smoothing seismicity model that can locally increase the hazard compared to the previous model. The overall changes are often less than ±20 percent across most of California. At a specific site, it is important to examine all model changes to determine why the ground motions may have increased or decreased.

Several issues still need to be addressed in future versions of the maps. For example, we have not finalized a model for the treatment of hazard from earthquakes suspected of being caused by fluid injection (potentially induced earthquakes). This is a very complex problem and alternatives will, most likely, be considered as a series of logic-tree branches in future models. The users of the hazard maps should consider additional hazard from potentially induced events. Another issue involves the time-dependence of hazard displayed in these maps. The current hazard model is a time-independent model and does not consider the elapsed time since the last earthquakes on faults. These maps do not vary in time, which is a desirable feature in building code maps; however, other users want to consider time dependence. As source models are updated and new ground motion models are developed for the CEUS (NGA-East project) and for subduction zones (NGA-Subduction project), such models will better define the potential ground motions and associated uncertainty for these earthquakes. We will continue to examine the sensitivity and uncertainty in ground motions from all logic-tree branches included in this 2014 NSHMP model. Maps for alternative site conditions, alternative probabilities, and alternative ground motion parameters and frequencies are also important products that will have many uses. Scenario hazard maps and urban seismic hazard maps will help guide urban planning and development. In addition, new updates for Alaska, Hawaii, and Puerto Rico seismic hazard are currently under revision. We welcome comments on these maps and encourage discussions on how to improve future updates of the USGS NSHMP maps.

Acknowledgments

We wish to thank the hundreds of workshop, working group, review, and other participants who made valuable suggestions for revising the 2014 USGS national seismic hazard maps and models. We especially thank members of the National Seismic Hazard Mapping Project steering committee (John Anderson (chair), Norm Abrahamson, Ken Campbell, Martin Chapman, Michael Hamburger, William Lettis, Nilesh Shome, Ray Weldon, Chris Wills), who reviewed the documentation, data, methods, and models, and provided excellent feedback that helped us to improve the quality of this product. We thank the National Earthquake Hazard Reduction Program (NEHRP) for funding the development of the maps. Many groups and organizations are discussed in the documentation and we appreciate all of their cooperation in working on strict timelines to make the maps available to the Building Seismic Safety Council for their consideration in the building code process. In addition we appreciate the efforts of Stephanee R. Walker who served as editor of this report and Janet L. Slate who reviewed the document for content and policy issues.

References Cited

Abers, G.A., 2009, Slip on shallow-dipping normal faults: Geology, v. 37, p. 767–768.

Abrahamson, Norman, and Silva, Walter, 2008, Summary of the Abrahamson & Silva NGA ground-motion relations: Earthquake Spectra, v. 24, p. 67–97.

Abrahamson, N.A., Silva W.J., and Kamai, Ronnie, 2013, Update of the AS08 ground-motion prediction equations based on the NGA-West2 data set: Berkeley, University of California, Pacific Earthquake Engineering Research Center PEER Report 2013/04, 143 p.

Abrahamson, N.A., Silva, W.J., and Kamai, R., 2014, Summary of the Abrahamson, Silva, and Kamai NGA-West2 ground-motion relations for active crustal regions: Earthquake Spectra, in press.
Adams, John, 1990, Paleoseismicity of the Cascadia subduction zone—Evidence from turbidites off the Oregon-Washington margin: Tectonics, v. 9, p. 569–583.
Addo, Kofi, Abrahamson, Norman, and Youngs, Robert, (BC Hydro), 2012, Probabilistic seismic hazard analysis (PSHA) model—Ground motion characterization (GMC) model: Report E658, published by BC Hydro.
Algermissen, S.T., and Perkins, D.M., 1976, A probabilistic estimate of the maximum acceleration in rock in the contiguous United States: U.S. Geological Survey Open-File Report 76–416, 45 p., 2 plates, scale 1:7,500,000.
Anderson, E.M., 1951, The dynamics of faulting: Edinburgh, Oliver and Boyd, 206 p.
Ando, Masataka, 1975, Source mechanisms and tectonic significance of historical earthquakes along the Nankai trough, Japan: Tectonophysics, vol. 27, p. 119–140.
Atkinson, G.M., 2004a, Empirical attenuation of ground-motion spectral amplitudes in southeastern Canada and the northeastern United States: Bulletin of the Seismological Society of America, v. 94, p. 1,079–1,095.
Atkinson, G.M., 2004b, Erratum to "Empirical attenuation of ground-motion spectral amplitudes in southeastern Canada and the northeastern United States": Bulletin of the Seismological Society of America, v. 94, p. 2,419–2,423.
Atkinson, G.M., 2008, Ground-motion prediction equations for eastern North America from a referenced empirical approach—Implications for epistemic uncertainty: Bulletin of the Seismological Society of America, v. 98, p. 1,304–1,318, doi:10.1785/0120070199.
Atkinson, G.M., and Boore, D.M., 2003, Empirical ground-motion relations for subduction-zone earthquakes and their application to Cascadia and other regions: Bulletin of the Seismological Society of America, v. 93, p. 1,703–1,729.
Atkinson, G.M., and Boore, D.M., 2006, Earthquake ground-motion prediction equations for eastern North America: Bulletin of the Seismological Society of America, v. 96, p. 2,181–2,205, doi:10.1785/0120050245.
Atkinson, G.M., and Boore, D.M., 2011, Modifications to existing ground-motion prediction equations in light of new data: Bulletin of the Seismological Society of America, v. 101, p. 1,121–1,135, doi:10.1785/0120100270.
Atkinson, G.M., and Macias, M., 2009, Predicted ground motions for great interface earthquakes in the Cascadia subduction zone: Bulletin of the Seismological Society of America, v. 99, p. 1,552–1,578.
Atwater, B.F., 1987, Evidence for great Holocene earthquakes along the outer coast of Washington state: Science, v. 236, p. 942–944.
Atwater, B.F., 1992, Geologic evidence for earthquakes during the past 2000 years along the Copalis River, southern coastal Washington: Journal of Geophysical Research-Solid Earth, v. 97, p. 1,901–1,919.
Atwater, B.F., and Hemphill-Haley, E., 1997, Recurrence intervals for great earthquakes of the past 3,500 years at northeastern Willapa Bay, Washington: U.S. Geological Survey Professional Paper 1576, 108 p. (Also available at *http://pubs.usgs.gov/pp/1576/*.)
Atwater, B.F., and Griggs, G.B., 2012, Deep-sea turbidites as guides to Holocene earthquake history at the Cascadia subduction zone—Alternative views for a seismic-hazard workshop: U.S. Geological Survey Open-File Report 2012–1043, 58 p. (Also available at *http://pubs.usgs.gov/of/2012/1043/.)*

Bakun, W.H., and Hopper, M.G., 2004a, Magnitudes and locations of the 1811–1812 New Madrid, Missouri, and the 1886 Charleston, South Carolina, earthquakes: Bulletin of the Seismological Society of America, v. 94, p. 64–75.

Bakun, W.H., and Hopper, M.G., 2004b, Catalog of significant historical earthquakes in the Central United States: U.S. Geological Survey Open-File Report 2004–1086, 57 p. (Also available at *http://pubs.er.usgs.gov/publication/ofr20041086*.)

Bakun, W.H., Johnston, A.C., and Hopper, M.G., 2003, Estimating locations and magnitudes of earthquakes in eastern North America from Modified Mercalli intensities: Bulletin of the Seismological Society of America, v. 93, p. 190–202.

Bauer, P.W., and Kelson, K.I., 2004, Rift extension and fault slip rates in the southern San Luis basin, New Mexico, *in* Brister, B.S., Bauer, P.W., Read, A.S., and Lueth, V.W., eds., Geology of the Taos region: New Mexico Geological Society Guidebook, 55th Field Conference, p. 172–180.

Bell, J.W., 1995, Quaternary geologic map of the Mina quadrangle, Nevada: Nevada Bureau of Mines and Geology Field Studies Map 10, scale 1:24,000.

Bell, J.W., Caskey, S.J., Ramelli, A.R., and Guerrieri, Luca, 2004, Pattern and rates of faulting in the central Nevada seismic belt, and paleoseismic evidence for prior beltlike behavior: Bulletin of the Seismological Society of America, v. 94, p. 1,229–1,254.

Biasi, G.P., and Weldon, R.J., II, 2006, Estimating surface rupture length and magnitude of paleoearthquakes from point measurements of rupture displacement: Bulletin of the Seismological Society of America, v. 96, p. 1,612–1,623.

Bird, Peter, 2013, Estimation of fault slip rates in the conterminous Western United States with statistical and kinematic finite-element programs, Appendix C, *in* Petersen, M.D., Zeng, Yuehua, Haller, K.M., McCaffrey, Robert, Hammond, W.C., Bird, Peter, Moschetti, Morgan, and Thatcher, Wayne, Geodesy- and geology-based slip-rate models for the Western United States (excluding California) national seismic hazard maps: U.S. Geological Survey Open-File Report 2013-1293, p. 48–57.

Bird, Peter, and Kagan, Y.Y., 2004, Plate-tectonic analysis of shallow seismicity—Apparent boundary width, beta, corner magnitude, coupled lithosphere thickness, and coupling in seven tectonic settings: Bulletin of the Seismological Society of America, v. 94, p. 2,380–2,399.

Black, B.D., Lund, W.R., Schwartz, D.P., Gill, H.E., and Mayes, B.H., 1996, Paleoseismology of Utah, volume 7—Paleoseismic investigation on the Salt Lake City segment of the Wasatch fault zone at the South Fork Dry Creek and Dry Gulch sites, Salt Lake County, Utah: Utah Geological Survey Special Study 92, 22 p.

Boatwright, John, 1994, Regional propagation characteristics and source parameters of earthquakes in northeastern North America: Bulletin of the Seismological Society of America, v. 84, p. 1–15.

Bommer, J.J., Douglas, John, Scherbaum, Frank, Cotton, Fabrice, Bungum, Hilmar, and Faeh, Donat, 2010, On the selection of ground-motion prediction equations for seismic hazard analysis: Seismological Research Letters, v. 81, p. 783–793.

Boore, D.M., and Atkinson, G.M., 2008, Ground-motion prediction equations for the average horizontal component of PGA, PGV, and 5%-damped PSA at spectral periods between 0.01 s and 10.0 s: Earthquake Spectra, v. 24, p. 99–138.

Boore, D.M., Stewart, J.P., Seyhan, Emel, and Atkinson, G.A., 2013, NGA-West2 equations for predicting response spectral accelerations for shallow crustal earthquakes: University of California, Berkeley, Pacific Earthquake Engineering Research Center PEER Report 2013/05, 134 p.

Boore, D.M., Stewart, J.P., Seyhan, Emel, and Atkinson, G.A., 2014, NGA-West2 equations for predicting response spectral accelerations for shallow crustal earthquakes: Earthquake Spectra, in press.

Bormann, J.M., Surpless, B.E., Caffee, M.W., and Wesnousky, S.G., 2012, Holocene earthquakes and late Pleistocene slip-rate estimates on the Wassuk Range fault zone, Nevada: Bulletin of the Seismological Society of America, v. 102, p. 1,884–1,891.

Boyd, O.S., Mueller, C.S., and Rukstales, K.S., 2007, Preliminary probabilistic seismic hazard map for Afghanistan: U.S. Geological Survey Open-File Report 2007–1137, 29 p. (Also available at *http://pubs.usgs.gov/of/2007/1137/*.)

Bozorgnia, Yousef, Abrahamson, N.A., Al Atik, Linda, Ancheta, T.D., Atkinson, G.M., Baker, J.W., Baltay, Annemarie, Boore, D.M., Campbell, K.W., Brian S.-J. Chiou, Darragh, Robert , Day, Steve , Donahue, Jennifer, Graves, R.W., Gregor, Nick, Hanks, Thomas, Idriss, I.M., Kamai, Ronnie, Kishida, Tadahiro, Kottke, Albert, Mahin, S.A., Rezaeian, Sanaz, Rowshandel, Badie, Seyhan, Emel, Shahi, Shrey, Shantz, Tom, Silva, Walter, Spudich, Paul, Stewart, J.P., Watson-Lamprey, Jennie, Wooddell, Kathryn, and Youngs, Robert, 2014, NGA-West2 research project: Earthquake Spectra, in press.

Bruhn, R.L., and Schultz, R.A., 1996, Geometry and slip distribution in normal fault systems—Implications for mechanics and fault-related hazards: Journal of Geophysical Research-Solid Earth, v. 101, p. 3,401–3,412, doi:10.1029/95JB03253.

Bruhn, R.L., Gibler, P.R., Houghton, W., and Parry, W.T., 1992, Structure of the Salt Lake segment, Wasatch normal fault zone—Implications for rupture propagation during normal faulting, *in* Gori, P.L., and Hays, W.W., eds., Assessment of regional earthquake hazards and risk along the Wasatch front, Utah: U.S. Geological Survey Professional Paper 1500, p. H1–H25.

Building Seismic Safety Council, 2009, NEHRP recommended seismic provisions for new buildings and other structures, 2009 edition: FEMA report P-750. (Also available at *http://www.fema.gov/media-library/assets/documents/18152?id=4103*.)

Burgette, R.J., Weldon, R.J., and Schmidt, D.A., 2009, Interseismic uplift rates for western Oregon and along-strike variation in locking on the Cascadia subduction zone: Journal of Geophysical Research-Solid Earth, v. 114, doi:10.1029/2008JB005679.

Byerlee, J., 1978, Friction of rocks: Pure and Applied Geophysics, v. 116, p. 615–626.

Calais, Eric, and Stein, Seth, 2009, Time-variable deformation in the New Madrid seismic zone: Science, v. 323, p. 1,442.

Campbell, K.W., 2003, Prediction of strong ground motion using the hybrid empirical method and its use in the development of ground motion (attenuation) relations in eastern North America: Bulletin of the Seismological Society of America, v. 93, p. 1,012–1,033.

Campbell, K.W., and Bozorgnia, Yousef, 2008, NGA ground motion model for the geometric mean horizontal component of PGA, PGV, PGD and 5% damped linear-elastic response spectra for periods ranging from 0.01 and 10.0 s: Earthquake Spectra, v. 24, p. 139–171.

Campbell, K.W., and Bozorgnia, Yousef, 2013, *NGA*-West2 Campbell-Bozorgnia Ground Motion Model for the horizontal components of PGA, PGV, and 5%-damped elastic pseudo-acceleration response spectra for periods ranging from 0.01 to 10 s: University of California, Berkeley, Pacific Earthquake Engineering Research Center PEER Report 2013/06, 238 p.

Campbell, K.W., and Bozorgnia, Yousef, 2014, Campbell-Bozorgnia NGA-West2 ground motion model for the average horizontal components of PGA, PGV, and 5%-damped linear response spectra: Earthquake Spectra, in press.

Caskey, S.J., Bell, J.W., Ramelli, A.R., and Wesnousky, S.G., 2004, Historic surface faulting and paleoseismicity in the area of the 1954 Rainbow Mountain-Stillwater earthquake sequence, central Nevada: Bulletin of the Seismological Society of America, v. 94, p. 1,255–1,275.

CEUS–SSCn, 2012, Central and Eastern United States seismic source characterization for nuclear facilities: Palo Alto, California, EPRI, U.S. DOE, and U.S. NRC, [variously paged]. (Also available at *http://www.ceus-ssc.com/Report/Downloads.html*.)

Chang, W.-L., and Smith, R.B., 2002, Integrated seismic-hazard analysis of the Wasatch Front, Utah: Bulletin of the Seismological Society of America, v. 92, p. 1,904–1,922, doi:10.1785/0120010181.

Chang, W.-L., Smith, R.B., Meertens, C.M., and Harris, R.A., 2006, Contemporary deformation of the Wasatch Fault, Utah, from GPS measurements with implications for interseismic fault behavior and earthquake hazard—Observations and kinematic analysis: Journal of Geophysical Research-Solid Earth, v. 111, B11405, doi:10.1029/2006JB004326.

Chiou, B.S.J., and Youngs, R.R., 2008, An NGA model for the average horizontal component of peak ground motion and response spectra: Earthquake Spectra, v. 24, p. 173–215.

Chiou, B.S.J., and Youngs, R.R., 2013, Update of the Chiou and Youngs NGA ground motion model for average horizontal component of peak ground motion and response spectra: University of California, Berkeley, Pacific Earthquake Engineering Research Center PEER Report 2013/07, 76 p.

Chiou, B.S.-J., and Youngs, R.R., 2014, Update of the Chiou and Youngs NGA ground motion model for average horizontal component of peak ground motion and response spectra: Earthquake Spectra, in press.

Collettini, Cristiano, 2011, The mechanical paradox of low-angle normal faults—Current understanding and open questions: Tectonophysics, v. 510, p. 253–268.

Collettini, Cristiano, and Sibson, R.H., 2001, Normal faults, normal friction?: Geology, v. 29, p. 927–930.

Cotton, Fabrice, Scherbaum, Frank, Bommer, J.J., and Bungum, Hilmar, 2006, Criteria for selecting and adjusting ground-motion models for specific target applications—Applications to Central Europe and rock sites: Journal of Seismology, v. 10, p. 137–156.

Crone, A.J., and Luza, K.V., 1990, Style and timing of Holocene surface faulting on the Meers fault, southwestern Oklahoma: Geological Society of America Bulletin, v. 102, p. 1–17.

Crone, A.J., Machette, M.N., Bonilla, M.G., Lienkaemper, J.J., Pierce, K.L., Scott, W.E., and Bucknam, R.C., 1987, Surface faulting accompanying the Borah Peak earthquake and segmentation of the Lost River fault, central Idaho: Bulletin of the Seismological Society of America, v. 77, p. 739–770.

Crone, A.J., Machette, M.N., Bradley, L.-A., and Mahan, S.A., 1997, Late Quaternary surface faulting on the Cheraw fault, southeastern Colorado: U.S. Geological Survey Miscellaneous Geologic Investigations Series Map I-2591, 7 p. pamphlet, 1 pl., scale 1:250,000.

Derouin, S.A., Piety, L.A., and Feng, Su, 2010, Evaluation of the Gore Range frontal fault and revised probabilistic seismic hazard analysis for Green Mountain Dam, Colorado: Bureau of Reclamation Seismotectonic Report 2010-01, 89 p.

Doser, D.I., 1985, Source parameters and faulting processes of the 1959 Hebgen Lake, Montana, earthquake sequence: Journal of Geophysical Research-Solid Earth, v. 90, p. 4,537–4,555.

Dragovich, J.D., Anderson, M.L., Walsh, T.J., Johnson, B.L., and Adams, T.L., 2007, Geologic map of the Fall City 7.5-minute quadrangle, King County, Washington: Washington Division of Geology and Earth Resources Geologic Map GM-67, 16 p. pamphlet, scale 1:24,000.

Dragovich, J.D., Littke, H.A., Anderson, M.L., Hartog, Renate, Wessel, G.R., DuFrane, S.A., Walsh, T.J., MacDonald J.H., Jr., Mangano, J.F., and Caker, Recep, 2009, Geologic map of the Snoqualmie

7.5-minute quadrangle, King County, Washington: Washington Division of Geology and Earth Resources Geologic Map GM–75, scale 1:24,000.
Dragovich, J.D., Littke, H.A., Anderson, M.L., Wessel, G.R., Koger, C.J., Saltonstall, J.H., MacDonald, J.H., Jr., Mahan, S.A., and DuFrane, S.A., 2010, Geologic map of the Carnation 7.5-minute quadrangle, King County, Washington: Washington Division of Geology and Earth Resources Open-File Report 2010–1, scale 1:24,000.
DuRoss, C.B., and Hylland, M.D., 2010, Paleoseismic investigation to compare surface chronologies of the West Valley fault zone and Sale Lake City segment of the Wasatch fault zone, Salt Lake City, Utah: U.S. Geological Survey External Grant Award Number G10AP00068, 148 p. (Also available at *http://earthquake.usgs.gov/research/external/reports/G10AP00068.pdf*.)
Dziewonski, A.M., Chou, T.-A., and Woodhouse, J.H., 1981, Determination of earthquake source parameters from waveform data for studies of global and regional seismicity: Journal of Geophysical Research-Solid Earth, v. 86, p. 2,825–2,852.
Ekström, Göran, Nettles, Meredith, and Dziewonski, A.M., 2012, The global CMT project 2004–2010—Centroid-moment tensors for 13,017 earthquakes: Physics of the Earth and Planetary Interiors, v. 200, p. 1–9. (Also available at http://*www.globalcmt.org*, accessed February 2013.)
Electric Power Research Institute (EPRI), 2013, EPRI (2004, 2006) ground-motion model (GMM) review project: Electric Power Research Institute Technical Report, Product ID 3002000717. (Also available at *http://www.epri.com/abstracts/Pages/ProductAbstract.aspx?ProductId=000000003002000717*.)
Ellsworth, W.L., 2013, Injection-induced earthquakes: Science, v. 341, p. 142–149.
Engdahl, E.R., and Rinehart, W.A., 1991, Seismicity map of North America project, *in* Slemmons, D.B., Engdahl, E.R., Zoback, M.D., and Blackwell, D.B., eds., Neotectonics of North America—Decade Map Volume 1: Boulder, Colo., Geological Society of America, p. 21–27.
Engdahl, E.R., and Villaseñor, A., 2002, Global seismicity: 1900–1999, *in* Lee, W.H.K., Kanamori, Hiroo, Jennings, P.C., and Kisslinger, Carl, eds., International handbook of earthquake and engineering seismology: International Association of Seismology and Physics of the Earth's Interior (IASPEI), p. 665–690.
Felzer, K.R., 2008, Appendix I, Calculating California seismicity rates, *in* Working Group on California Earthquake Probabilities, The uniform California earthquake rupture forecast, version 2 (UCERF 2): U.S. Geological Survey Open-File Report 2007–1437–I, 41 p. (Also available at *http://pubs.usgs.gov/of/2007/1437/*.)
Felzer, K.R., and Cao, Tianqing, 2008, Appendix H, WGCEP historical California earthquake catalog, *in* Working Group on California Earthquake Probabilities, The uniform California earthquake rupture forecast, version 2 (UCERF 2): U.S. Geological Survey Open-File Report 2007–1437–H. (Also available at *http://pubs.usgs.gov/of/2007/1437/*.)
Ferguson, C.A., Gootee, B.F., Pearthree, P.A., and Cook, J.P., 2012, Geologic map of the Paulden 7 1/2' quadrangle, Yavapai County, Arizona: Arizona Geological Survey Digital Geologic Map 91, ver. 1.0, 1 sheet, scale 1:24,000.
Flück, P., Hyndman, R.D., and Wang, Kelin, 1997, Three-dimensional dislocation model for great earthquakes of the Cascadia subduction zone: Journal of Geophysical Research-Solid Earth, v. 102, p. 20,539–20,550, doi:10.1029/97JB01642.
Frankel, Arthur, 1995, Mapping seismic hazard in the Central and Eastern United States: Seismological Research Letters, v. 66, p. 8–21.
Frankel, A.D., 2011, Summary of November 2010 meeting to evaluate turbidite data for constraining the recurrence parameters of great Cascadia earthquakes for the update of the national seismic hazard

maps: U.S. Geologic Survey Open-File Report 2011–1310, 13 p. (Also available at *http://pubs.usgs.gov/of/2011/1310/*.)
Frankel, A., 2013, Rupture history of the 2011 M 9 Tohoku Japan earthquake determined from strong-motion and high-rate GPS recordings—Subevents Radiating Energy in Different Frequency Bands, Bulletin of the Seismological Society of America, v. 103, p. 1,290–1,306, doi: 10.1785/0120120148.
Frankel, Arthur, Mueller, Charles, Barnhard, Theodore, Perkins, David, Leyendecker, E.V., Dickman, Nancy, Hanson, Stanley, and Hopper, Margaret, 1996, National seismic hazard maps—Documentation June 1996: U.S. Geological Survey Open-File Report 96-532, 110 p.
Frankel, A.D., Petersen, M.D., Mueller, C.S., Haller, K.M., Wheeler, R.L., Leyendecker, E.V., Wesson, R.L., Harmsen, S.C., Cramer, C.H., Perkins, D.M., and Rukstales, K.S., 2002, Documentation for the 2002 update of the national seismic hazard maps: U.S. Geological Survey Open-File Report 2002–420, 39 p.
Frankel, Arthur, Smalley, Robert, and Paul, Jonathan, 2012, Significant motions between GPS sites in the New Madrid region—Implications for seismic hazard: Bulletin of the Seismological Society of America, v. 102, p. 479–489.
Frohlich, Cliff, 2012, Two-year survey comparing earthquake activity and injection-well locations in the Barnett Shale, Texas: Proceedings of the National Academy of Sciences, v. 109, p. 13,934–13,938.
Frohlich, Cliff, and Brunt, Michael, 2013, Two-year survey of earthquakes and injection/production wells in the Eagle Ford Shale, Texas, prior to the M_w4.8 20 October 2011 earthquake: Earth and Planetary Science Letters, v. 379, p. 56–63.
Gardner, J.K., and Knopoff, L., 1974, Is the sequence of earthquakes in southern California, with aftershocks removed, Poissonian?: Bulletin of the Seismological Society of America, v. 64, p. 1,363–1,367.
Geological Survey of Canada, *http://www.earthquakescanada.nrcan.gc.ca/index-eng.php*, accessed 30 January 2013.
Global Centroid Moment Tensor Project catalog, http:// *www.globalcmt.org*, accessed April 2013.
Goldfinger, Chris, Nelson, C.H., Johnson, J.E., and Shipboard Scientific Party, 2003, Holocene earthquake records from the Cascadia subduction zone and northern San Andreas Fault based on precise dating of offshore turbidites: Annual Reviews of Earth and Planetary Sciences, v. 31, p. 555–577.
Goldfinger, Chris, Grijalva, Kelly, Burgmann, Roland, Morey, A.E., Johnson, J.E., Nelson, C.H., Gutiérrez-Pastor, Julia, Ericsson, Andrew, Karabanov, Eugene, Chaytor, J.D., Patton, Jason, Gràcia, Eulàlia, 2008, Late Holocene rupture of the northern San Andreas Fault and possible stress linkage to the Cascadia subduction zone: Bulletin of the Seismological Society of America, v. 98, p. 861–889.
Goldfinger, Chris, Nelson, C.H., Morey, A.E., Johnson, J.E., Patton, J.R., Karabanov, Eugene, Gutiérrez-Pastor, Julia, Eriksson, A.T., Gràcia, Eulàlia, Dunhill, Gita, Enkin, R.J., Dallimore, Audrey, and Vallier, Tracy, 2012, Turbidite event history—Methods and implications for Holocene paleoseismicity of the Cascadia subduction zone: U.S. Geological Survey Professional Paper 1661–F, 170 p. (Available at *http://pubs.usgs.gov/pp/pp1661f/*.)
Gomberg, Joan, Bedrosian, B., Bodin, P., Bostock, M., Brudzinski, M., Creager, K., Dragert, H., Egbert, G., Ghosh, A., Henton, J., Houston, H., Kao, H., McCrory, P., Melbourne, T., Peacock, S., Roeloffs, E., Rubinstein, J., Schmidt, D., Trehu, A., Vidale, J., Wang, Kelin, and Wech, A., 2010, Slow-slip phenomena in Cascadia from 2007 and beyond—A review: Geological Society of America Bulletin, v. 122, p. 963–978.

Gootee, B.F., Ferguson, C.A., Spencer, J.E., and Cook, J.P., 2010, Geologic map of the Chino Valley North 7 1/2' quadrangle, Yavapai County, Arizona, v. 1.0: Arizona Geological Survey Geologic Map DGM-80, 42 p.
Graizer, Vladimir, and Kalkan, Erol, 2011, Modular filter-based approach to ground motion attenuation modeling: Seismological Research Letters, v. 82, p. 21–31.
Gregor, Nick, Abrahamson, N.A., Atkinson, G.M., Boore, D.M., Bozorgnia, Yousef, Campbell, K.W., Chiou, B.S.-J., Idriss, I.M., Kamai, Ronnie, Seyhan, Emel, Silva, Walter, Stewart, J.P., and Youngs, Robert, 2014, Comparison of NGA-West2 GMPEs: Earthquake Spectra, in press.
Gutenberg, Beno, and Richter, C.F., 1944, Frequency of earthquakes in California: Bulletin of the Seismological Society of America, v. 34, p. 185–188.
Hajic, E.R., Wiant, M.D., and Oliver, J.J., 1995, Distribution and dating of prehistoric earthquake liquefaction in southeastern Illinois, Central U.S.: Final technical report submitted to the U.S. Geological Survey National Earthquake Hazards Reduction Program under Contract 1434-93-G-2359, 33 p.
Haller, K.M., and Wheeler, R.L., 2008a, Parameter for faults in the Intermountain West, *in* Petersen, M.D., Frankel, A.D., Harmsen, S.C., Mueller, C.S., Haller, K.M., Wheeler, R.L., Wesson, R.L., Zeng, Yuehua, Boyd, O.S., Perkins, D.M., Luco, Nicolas, Field, E.H., Wills, C.J., and Rukstales, K.S., Documentation for the 2008 update of the United States national seismic hazard maps: U.S. Geological Survey Open-File Report 2008–1128, p. G-1–18.
Haller, K.M., and Wheeler, R.L., 2008b, Parameter for faults in the Pacific Northwest, *in* Petersen, M.D., Frankel, A.D., Harmsen, S.C., Mueller, C.S., Haller, K.M., Wheeler, R.L., Wesson, R.L., Zeng, Yuehua, Boyd, O.S., Perkins, D.M., Luco, Nicolas, Field, E.H., Wills, C.J., and Rukstales, K.S., Documentation for the 2008 update of the United States national seismic hazard maps: U.S. Geological Survey Open-File Report 2008–1128, p. H-1–6.
Hammond, W.C., Kreemer, Corné, and Blewitt, Geoffrey, 2009, Geodetic constraints on contemporary deformation in the northern Walker Lane—3, Central Nevada seismic belt postseismic relaxation, *in* Oldow, J.S., and Cashman, P.H., eds., Late Cenozoic structure and evolution of the Great Basin–Sierra Nevada transition: Geological Society of America Special Paper 447, p. 33–54.
Hammond, W.C., and Bormann, Jayne, 2013, A block model of Western United States tectonic deformation for the 2014 national seismic hazard maps from GPS and geologic data, Appendix B, *in* Petersen, M.D., Zeng, Yuehua, Haller, K.M., McCaffrey, Robert, Hammond, W.C., Bird, Peter, Moschetti, Morgan, and Thatcher, Wayne, Geodesy- and geology-based slip-rate models for the Western United States (excluding California) national seismic hazard maps: U.S. Geological Survey Open-File Report 2013-1293, p. 39–47.
Hampel, Andrea, Hetzel, Ralf, and Densmore, A.L., 2007, Postglacial slip-rate increase on the Teton normal fault, northern Basin and Range province, caused by melting of the Yellowstone ice cap and deglaciation of the Teton Range?: Geology, v. 35, p. 1,107–1,110.
Hayes, G.F., 1985, Late Quaternary deformation and seismic risk in the southern Sierra Nevada Great Basin boundary zone near the Sweetwater Mountains, California and Nevada: Reno, University of Nevada, unpublished M.S. thesis, 135 p.
Helmstetter, Agnés, Kagan, Y.Y., and Jackson, D.D., 2007, High-resolution time-independent grid-based forecast for $M \geq 5$ earthquakes in California: Seismological Research Letters, v. 78, p. 78–86.
Hemphill-Haley, M.A., and Weldon, R.J., II, 1999, Estimating prehistoric earthquake magnitude from point measurements of surface rupture: Bulletin of the Seismological Society of America, v. 89, p. 1,264–1,279.
Herrmann, R.B., 1977, Recurrence relations: Earthquake Notes, v. 48, p. 47–49.

Herrmann, R.B., 2013, *http://www.eas.slu.edu/eqc/eqc.html*, accessed 2013.
Hoeft, J.S., and Frankel, K.L., 2010, Temporal variations in extension rate along the Lone Mountain fault and strain partitioning in the eastern California shear zone-Walker Lane: Geosphere, v. 6, p. 917–936.
Holbrook, John, Autin, W.J., Rittenour, T.M., Marshak, Stephen, and Goble, R.J., 2006, Stratigraphic evidence for millennial-scale temporal clustering of earthquakes on a continental-interior fault—Holocene Mississippi River floodplain deposits, New Madrid seismic zone, USA: Tectonophysics, v. 420, p. 431–454.
Horton, Steven, 2012, Disposal of hydrofracking waste fluid by injection into subsurface aquifers triggers earthquake swarm in central Arkansas with potential for damaging earthquake: Seismological Research Letters, v. 83, p. 250–260, doi:10.1785/gssrl.83.2.250.
Hough, S.E., Armbruster, J.G., Seeber, Leonardo, and Hough, J.F., 2000, On the Modified Mercalli intensities and magnitudes of the 1811–1812 New Madrid earthquakes: Journal of Geophysical Research-Solid Earth, v. 105, p. 23,839–23,864.
Hough, S.E., and Martin, Stacey, 2002, Magnitude estimates of two large aftershocks of the 16 December 1811 New Madrid earthquake: Bulletin of the Seismological Society of America, v. 92, p. 3,259–3,268.
Hough, S.E., and Page, M., 2011, Toward a consistent model for strain accrual and release for the New Madrid seismic zone, central United States: Journal of Geophysical Research-Solid Earth, v. 116, B03311, doi:*10.1029/2010JB007783*.
Hough, S.E., Martin, Stacey, Bilham, Roger, and Atkinson, G.M., 2002, The 26 January 2001 M 7.6 Bhuj, India, earthquake—Observed and predicted ground motions: Bulletin of the Seismological Society of America, v. 92, p. 2,061-2,079.
Ichinose, G.A., Thio, H.K., Somerville, P.G., 2006, Moment tensor and rupture model for the 1949 Olympia, Washington, earthquake and scaling relations for Cascadia and global intraslab earthquakes: Bulletin of the Seismological Society of America, v. 96, p. 1,029-1,037.
Idriss, I.M., 2013, NGA-West2 model for estimating average horizontal values of pseudo-absolute spectral accelerations generated by crustal earthquakes: University of California, Berkeley, Pacific Earthquake Engineering Research Center PEER Report 2013/08, 31 p.
Idriss, I.M., 2014, NGA-West2 model for estimating average horizontal values of pseudo-absolute spectral accelerations generated by crustal earthquakes: Earthquake Spectra, Accepted for NGA-West2 special issue.
Independent Expert panel on New Madrid Seismic Zone Earthquake Hazards, 2011, *http://earthquake.usgs.gov/aboutus/nepec/reports/NEPEC_NMSZ_expert_panel_report.pdf*, accessed April 2014.
Jackson, J.A., 2002, Using earthquakes for continental tectonic geology, *in* Lee, W.H.K., Kanamori, Hiroo, Jennings, P.C., and Kisslinger, Carl, eds., International handbook of earthquake and engineering seismology, v. 81A: London, Academic Press, p. 491–504.
Jackson, J.A., and White, N.J., 1989, Normal faulting in the upper continental-crust—Observations from regions of active extension: Journal of Structural Geology, v. 11, p. 15–36.
Johnson, E.M., 2010, Lacrustine evidence of seismic events on the Sawtooth fault in Redfish Lake drainage, Sawtooth Mountains, central Idaho: Pocatello, Idaho State University, unpublished M.S. thesis, 125 p.
Johnston, A.C., 1989, The seismicity of 'stable continental interiors', *in* Gregersen, Søren, and Basham, P.W., eds., Earthquakes at North-Atlantic passive margins—Neotectonics and postglacial rebound: Kluwer Academic Publishers, NATO ASSI Series, v. 266, p. 299–327.

Johnston, A.C., 1994, Seismotectonic interpretations and conclusions from the stable continental region seismicity database, *in* Johnston, A.C., Coppersmith, K.J., Kanter, L.R., and Cornell, C.A., eds., The earthquakes of stable continental regions, v. 1: Palo Alto, California, Electric Power Research Institute, p. 4-1–4-103.

Johnston, A.C., 1996, Seismic moment assessment of earthquakes in stable continental regions—1. Instrumental seismicity: Geophysical Journal International, v. 124, p. 381–414.

Johnston, A.C., Coppersmith, K.J., Kanter, L.R., and Cornell, C.A., 1994, The earthquakes of stable continental regions: Palo Alto, California, Electric Power Research Institute, 5 volumes, 2,519 p., 16 plates.

Kagan, Y.Y., 2002, Seismic moment distribution revisited—I. Statistical results: Geophysical Journal International, v. 148, p. 520–541.

Kammerer, A.M., and Ake, J.P., 2012, Practical implementation guidelines for SSHAC Level 3 and 4 hazard studies: U.S. Nuclear Regulatory Commission NUREG-2117, rev. 1, 235 p.

Kanamori, Hiroo, and McNally, K.C., 1982, Variable rupture mode of the subduction zone along the Ecuador-Colombia coast: Bulletin of the Seismological Society of America, vol. 72, p, 1,241–1,253.

Kelsey, H.M., Witter, R.C., and Hemphill-Haley, Eileen, 2002, Plate-boundary earthquakes and tsunamis of the past 5500 years, Sixes River estuary, southern Oregon: Geological Society of America Bulletin, v. 114, p. 298–314.

Kelsey, H.M., Nelson, A.R., Hemphill-Haley, Eileen, and Witter, R.C., 2005, Tsunami history of an Oregon coastal lake reveals a 4,600 years record of great earthquakes on the Cascadia subduction zone: Geological Society of America Bulletin, v. 17, p. 1,009–1,032.

Kelson, K.I., and Swan, F.H., 1990, Paleoseismic history of the Meers fault, southwestern Oklahoma, and implications for evaluations of earthquake hazards in the Central and Eastern United States, *in* Weiss, A.J., ed., Seventeenth water reactor safety information meeting: Proceedings of the U.S. Nuclear Regulatory Commission NUREG/CP-0105, v. 2, p. 341–365.

Kirkham, R.M., 2004, Quaternary faulting in the Williams Fork valley graben, north-central Colorado, and comparison with late Quaternary deformation near Spinney Mountain, central Colorado: Technical report to U.S. Geological Survey, Reston, Virginia, under Contract 02HQGR0102, 46 p. (Also available at *http://earthquake.usgs.gov/research/external/reports/02HQGR0102.pdf*.)

Koehler, R.D., and Wesnousky, S.G., 2011, Late Pleistocene regional extension rate derived from earthquake geology of late Quaternary faults across the Great Basin, Nevada, between 38.5 degrees N and 40 degrees N latitude: Geological Society of America Bulletin, v. 123, p. 631–650.

Lund, W.R., 2005, Consensus preferred recurrence interval and vertical slip rate estimates—Review of Utah paleoseismic-trenching data by the Utah Quaternary Fault Parameters Working Group: Utah Geological Survey Bulletin 134, 109 p.

Lund, W.R., ed., 2006, Basin and Range Province Earthquake Working Group seismic-hazard recommendations to the U.S. Geological Survey National Seismic Hazard Mapping Program: Utah Geological Survey Open-File Report 477, 23 p.

Lund, W.R., ed., 2012, Basin and Range Province Earthquake Working Group II—Recommendations to the U.S. Geological Survey National Seismic Hazard Mapping Program for the 2014 update of the national seismic hazard maps: Utah Geological Survey Open-File Report 591, 16 p.

Lund, W.R., comp., 2013, Working Group on Utah Earthquake Probabilities—Preliminary fault characterization parameters for faults common to the working groups study area and the U.S. national seismic hazard maps—Data provided to the U.S. Geological Survey for use in the 2014 update of the national seismic hazard maps in Utah: Utah Geological Survey Open-File Report 611, 6 p.

Lund, W.R., Knudsen, T.R., and Vice, G.S., 2008, Paleoseismic reconnaissance of the Sevier fault, Kane and Garfield Counties, Utah: Utah Geological Survey Special Study 122, 31 p.
Machette, M.N., Personius, S.F., and Nelson, A.R., 1992, Paleoseismology of the Wasatch fault zone—A summary of recent investigations, interpretations, and conclusions, *in* Gori, P.L., and Hays, W.W., eds., Assessment of regional earthquake hazards and risk along the Wasatch front, Utah: U.S. Geological Survey Professional Paper 1500, p. A1–A71.
McCaffrey, Robert, Bird, Peter, Bormann, Jayne, Haller, K.M., Hammond, W.C., Thatcher, Wayne, Wells, R.E., and Zeng, Yuehua, 2013, NSHMP block model of Western United States active tectonics, Appendix A, *in* Petersen, M.D., Zeng, Yuehua, Haller, K.M., McCaffrey, Robert, Hammond, W.C., Bird, Peter, Moschetti, Morgan, and Thatcher, Wayne, Geodesy- and geology-based slip-rate models for the Western United States (excluding California) national seismic hazard maps: U.S. Geological Survey Open-File Report 2013–1293, p. 27–38.
McCalpin, J.P., 2002, Paleoseismology of Utah, volume 10—Post-Bonneville paleoearthquake chronology of the Salt Lake City segment, Wasatch fault zone, from the 1999 "megatrench" site: Utah Geological Survey Miscellaneous Publication 02–7, 37 p.
McCrory, P.A., Blair, J.L., Waldhauser, Felix, Oppenheimer, D.H., 2012, Juan de Fuca slab geometry and its relation to Wadati-Benioff zone seismicity: Journal of Geophysical Research-Solid Earth, v. 117, B09306, doi:10.1029/2012JB009407.
McGarr, Arthur, 2002, Control of strong ground motion of mining-induced earthquakes by the strength of the seismogenic rock mass: Journal of the South African Institute of Mining and Metallurgy, v. 102, p. 225–229.
Molnar, Peter, and Chen, W.-P., 1982, Seismicity and mountain building, *in* Hsu, K.J., ed., Mountain building processes: London, Academic Press, p. 41–57.
Moschetti, M.P., Petersen, M.D., and Zeng, Yuehua, 2013, Consideration of the use of off-fault strain rates from combined inversions of geodetic (GPS) and geologic data for the national seismic hazard maps, Appendix E, *in* Petersen, M.D., Zeng, Yuehua, Haller, K.M., McCaffrey, Robert, Hammond, W.C., Bird, Peter, Moschetti, Morgan, and Thatcher, Wayne, Geodesy- and geology-based slip-rate models for the Western United States (excluding California) national seismic hazard maps: U.S. Geological Survey Open-File Report 2013–1293, p. 69–80.
Macherides, Anastasia, 2002, The development of a moment-magnitude based earthquake catalog for the Northeastern United States: Chestnut Hill, Mass., Boston College, unpublished M.S. thesis, 81 p.
Mueller, Charles, Hopper, Margaret, and Frankel, Arthur, 1997, Preparation of earthquake catalogs for the national seismic hazard maps—Contiguous 48 States: U.S. Geological Survey Open-File Report 97–464, 36 p.
Murotani, Satoko, Miyake, Hiroe, Koketsu, Kazuki, 2008, Scaling of characterized slip models for plate-boundary earthquakes: Earth, Planets, and Space, v. 60, p. 987–981.
Nelson, A.R., Shennan, Ian, and Long, A.J., 1996, Identifying coseismic subsidence in tidal-wetland stratigraphic sequences at the Cascadia subduction zone of western North America: Journal of Geophysical Research-Solid Earth, v. 101, p. 6,115–6,135.
Nelson, A.R., Johnson, S.Y., Kelsey, H.M., Sherrod, B.L., Wells, R.E., Okumura, Koji, Bradley, L.-A., Bogar, Robert, and Personius, S.F., 2003a, Field and laboratory data from an earthquake history study of the Waterman Point fault, Kitsap County, Washington: U.S. Geological Survey Miscellaneous Field Studies Map MF-2423, scale 1:3,000. (Also available at *http://pubs.usgs.gov/mf/2003/mf-2423/*.)
Nelson, A.R., Johnson, S.Y., Kelsey, H.M., Wells, R.E., Sherrod, B.L., Pezzopane, S.K., Bradley, L.-A., Koehler, R.D., and Bucknam, R.C., 2003b, Late Holocene earthquakes on the Toe Jam Hill fault,

Seattle fault zone, Bainbridge Island, Washington: Geological Society of America Bulletin, v. 115, p. 1,388–1,403.
Nelson, A.R., Kelsey, H.M., and Witter, R.C., 2006, Great earthquakes of variable magnitude at the Cascadia subduction zone: Quaternary Research, v. 65, p. 354–365.
Nuttli, O.W., 1973, Seismic wave attenuation and magnitude relations for eastern North America: Journal of Geophysical Research, vol. 78, p. 876–885.
Obermeier, S.F., 1998, Liquefaction evidence for strong earthquakes of Holocene and latest Pleistocene ages in the states of Indiana and Illinois, USA: Engineering Geology, v. 50, p. 227–254.
O'Connell, D.R.H., Wood, C.K., Ostenaa, D.A., Block, L.V., and LaForge, R.C., 2003, Ground motion evaluation for Jackson Lake Dam, Minidoka Project, Wyoming: U.S. Bureau of Reclamation Seismotectonic Report 2003-2.
Pacheco, J.F., Sykes, L.R., and Scholz, C.H., 1993, Nature of seismic coupling along simple plate boundaries of the subduction type: Journal of Geophysical Research-Solid Earth, v. 98, p. 14,133–14,159.
Pancha, Aasha, Anderson, J.G., and Kreemer, Corné, 2006, Comparison of seismic and geodetic scalar moment rates across the Basin and Range province: Bulletin of the Seismological Society of America, v. 96, p. 11–32.
Papazachos, B.C., Scordilis, E.M., Panagiotopoulos, D.G., Papazachos, C.B., and Karakaisis, G.F., 2004, Global relations between seismic fault parameters and moment magnitudes of earthquakes: Bulletin of the Geological Society of Greece, v. 36, p. 1,482–1,489.
Pearthree, P.A., and Ferguson, C.A., 2012, Geologic map of the Wineglass Ranch 7 1/2' quadrangle, Yavapai County, Arizona: Arizona Geological Survey Digital Geologic Map DGM-90, 1 sheet, scale 1:24,000.
Personius, S.F., Crone, A.J., Machette, M.N., Mahan, S.A., Kyung, J.B., Cisneros, Hector, and Lidke, D.J., 2007, Late Quaternary paleoseismology of the southern Steens fault zone, northern Nevada: Bulletin of the Seismological Society of America, v. 97, p. 1,662–1,678.
Petersen, M.D., Bryant, W.A., Cramer, C.H., Cao, Tianqing, Reichle, Michael, Frankel, A.D., Lienkaemper, J.J., McCrory, P.A., and Schwartz, D.P., 1996, Probabilistic seismic hazard assessment for the State of California: California Division of Mines and Geology Open-File Report 96–08 and U.S. Geological Survey Open-File Report 96–706, 33 p. (Also available at *http://pubs.er.usgs.gov/publication/ofr96706*.)
Petersen, M.D., Cramer, C.H., and Frankel, A.D., 2002, Simulations of seismic hazard for the Pacific Northwest of the United States from earthquakes associated with the Cascadia subduction zone: Pure and Applied Geophysics, v. 159, p. 2,147–2,168.
Petersen, M.D., Frankel, A.D., Harmsen, S.C., Mueller, C.S., Boyd, O.S., Luco, Nicolas, Wheeler, R.L., Rukstales, K.S., and Haller, K.M., 2012, The 2008 U.S. Geological Survey national seismic hazard models and maps for the central and eastern United States, *in* Cox, R.T., Tuttle, M.P., Boyd, O.S., and Locat, Jacques, eds., Recent advances in North American paleoseismology and neotectonics east of the Rockies: Geological Society of America Special Paper 493, p. 243–257, doi: 10.1130/2012.2493(12).
Petersen, M.D., Frankel, A.D., Harmsen, S.C., Mueller, C.S., Haller, K.M., Wheeler, R.L., Wesson, R.L., Zeng, Yuehua, Boyd, O.S., Perkins, D.M., Luco, Nicolas, Field, E.H., Wills, C.J., and Rukstales, K.S., 2008, Documentation for the 2008 update of the United States national seismic hazard maps: U.S. Geological Survey Open-File Report 2008–1128, 128 p.
Petersen, M.D., Zeng, Yuehua, Haller, K.M., McCaffrey, Robert, Hammond, W.C., Bird, Peter, Moschetti, Morgan, and Thatcher, Wayne, 2013, Geodesy- and geology-based slip-rate models for the

Western United States (excluding California) national seismic hazard maps: U.S. Geological Survey Open-File Report 2013-1293, 80 p.
Petrik, F.E., 2008, Scarp analysis of the Centennial normal fault, Beaverhead County, Montana and Fremont County, Idaho: Bozeman, Montana State University, unpublished M.S. thesis, 287 p.
Pezeshk, Sharam, Zandieh, Arash, and Tavakoli, Behrooz, 2011, Hybrid empirical ground-motion prediction equations for eastern North America using NGA models and updated seismological parameters: Bulletin of the Seismological Society of America, v. 101, p. 1,859–1,870, doi:10.1785/0120100144.
Power, Maurice, Chiou, Brian, Abrahamson, Norman, Bozorgnia, Yousef, Shantz, Thomas, and Roblee, Clifford, 2008, An overview of the NGA project: Earthquake Spectra, v. 24, p. 3–21.
Quigley, M., Van Dissen, R., Litchfield, N., Villamor, P., Duffy, B., Barrell, D., Furlong, K., Stahl, T., Bilderback, E., and Noble, D., 2011, Surface rupture during the 2010 M_w7.1 Darfield (Canterbury) earthquake—Implications for fault rupture dynamics and seismic-hazard analysis: Geology, v. 40, p. 55–58, doi:10.1130/G32528.1.
Robison, R.M., and Burr, T.N., 1991, Fault-rupture hazard analysis using trenching and borings—Warm Springs fault, Salt Lake City, Utah, *in* McCalpin, J.P., ed., Proceedings of the 27th Symposium on Engineering Geology and Geotechnical Engineering: Boise, Idaho Department of Transportation, p. 26-1–26-13.
Roten, Daniel, Olsen, K.B., Pechmann, J.C., Cruz-Atienza, V.M., and Magistrale, Harold, 2011, 3D simulations of M_w7 earthquakes on the Wasatch fault, Utah, Part I—Long-period (0–1 Hz) ground motion: Bulletin of the Seismological Society of America, v. 101, p. 2,045–2,063.
Satake, Kenji, Shimazaki, Kunihiko, Tsuji, Yoshinobu, and Ueda, Kazue, 1996, Time and site of a giant earthquake in Cascadia inferred from Japanese tsunami records of January 1700: Nature, v. 379, p. 246–249.
Satake, Kenji, Wang, Kelin, and Atwater, B.F., 2003, Fault slip and seismic moment of the 1700 Cascadia earthquake inferred from Japanese tsunami descriptions: Journal of Geophysical Research-Solid Earth, v. 108, 2535, doi:10.1029/2003JB02521.
Schwartz, D.P. and Coppersmith, K.J., 1984, Fault behavior and characteristic earthquakes—Examples from the Wasatch and San Andreas fault zones: Journal of Geophysical Research-Solid Earth, vol. 89, p. 5,681–5698.
Schwartz, D.P., Haeussler, P.J., Seitz, G.G., and Dawson, T.E., 2012, Why the 2002 Denali fault rupture propagated onto the Totschunda fault—Implications for fault branching and seismic hazards: Journal of Geophysical Research-Solid Earth, 117, B11304, doi:10.1029/2011JB008918.
Seeber, Leonardo, and Armbruster, J.G., 1991, NCEER-91 earthquake catalog—Improved intensity-based magnitudes and recurrence relations for U.S. earthquakes east of New Madrid: National Center for Earthquake Engineering Research Technical Report NCEER-91-0021, 110 p., *http://folkworm.ceri.memphis.edu/catalogs/html/cat_nceer.html*, accessed March 2006 (Also available at http://mceer.buffalo.edu/publications/catalog/reports/NCEER-91-Earthquake-Catalog-Improved-Intensity-based-Magnitudes-and-Recurrance-Relations-for-U-S-Earthquakes-East-of-New-Madrid-NCEER-91-0021.html).
Sherrod, B.L., Blakely, R.J., Weaver, C.S., Kelsey, H.M, Barnett, Elizabeth, Liberty, Lee, Meagher, K.L., and Pape, Kristin, 2008, Finding concealed active faults—Extending the southern Whidbey Island fault across the Puget Lowland, Washington: Journal of Geophysical Research-Solid Earth, v. 113, B05313.

Sherrod, B.L., Brocher, T.M., Weaver, C.S., Bucknam, R.C., Blakely, R.J., Kelsey, H.M., Nelson, A.R. and Haugerud, R., 2004, Holocene fault scarps near Tacoma, Washington, USA: Geology v. 32, p. 9–12.

Silva, Walter, Gregor, Nick, and Darragh, Robert, 2002, Development of regional hard rock attenuation relations for central and eastern North America: Pacific Engineering and Analysis Technical Report, 57 p. (Also available at *http://www.pacificengineering.org/CEUS/Development%20of%20Regional%20Hard_ABC.pdf*.)

Sipkin, S.A., 2003, A correction to body-wave magnitude m_b based on moment magnitude M_w: Seismological Research Letters, v. 74, p. 739–742.

Somerville, Paul, Collins, Nancy, Abrahamson, Norman, Graves, Robert, and Saikia, Chandan, 2001, Ground motion attenuation relations for the Central and Eastern United States—Final report, June 30, 2001: Technical report to U.S. Geological Survey, Reston, Virginia, under Contract 99HQGR0098, 38 p.

Stover, C.W., and Coffman, J.L., 1993, Seismicity of the United States, 1568–1989 (revised): U.S. Geological Survey Professional Paper 1527, 418 p.

Stover, C.W., Reagor, B.G., and Algermissen, S.T., 1984, United States earthquake data file: U.S. Geological Survey Open-File Report 84–225, 123 p.

Strasser, F.O., Arango, M.C., and Bommer, J.J., 2010, Scaling of the source dimensions of interface and intraslab subduction-zone earthquakes with moment magnitude: Seismological Research Letters, v. 81, p. 941–950.

Suter, Max, 2006, Contemporary studies of the 3 May 1887 M_w7.5 Sonora, Mexico (Basin and Range province) earthquake: Seismological Research Letters, v. 77, p. 134–147.

Suter, Max, 2008a, Structural configuration of the Otates fault (southern Basin and Range province) and its rupture in the 3 May 1887 M_w7.5 Sonora, Mexico, earthquake: Bulletin of the Seismological Society of America, v. 98, p. 2,879–2,893.

Suter, Max, 2008b, Structural configuration of the Teras fault (southern Basin and Range province) and its rupture in the 3 May 1887 M_w7.5 Sonora, Mexico earthquake: Revista Mexicana De Ciencias Geologicas, v. 25, p. 179–195.

Swan, F.H., III, Schwartz, D.P., and Cluff, L.S., 1980, Recurrence of moderate to large magnitude earthquakes produced by surface faulting on the Wasatch fault zone, Utah: Bulletin of the Seismological Society of America, v. 70, p. 1,431–1,462.

Tavakoli, Behrooz, and Pezeshk, Shahram, 2005, Empirical-stochastic ground-motion prediction for eastern North America: Bulletin of the Seismological Society of America, v. 95, p. 2,283–2,296.

Thackray, G.D., Rodgers, D.W., Johnson, E.M., and Shapley, M.D., 2009, Preliminary evaluation of a newly discovered Holocene scarp on the Sawtooth fault, central Idaho: Geological Society of America Abstracts with Programs, v. 41, p. 55.

Thackray, G.D., Rodgers, D.W., and Streutker, David, 2013, Holocene scarp on the Sawtooth fault, central Idaho, USA, documented through lidar topographic analysis: Geology, v. 41, p. 639–642, doi:10.1130/G34095.1.

Thatcher, Wayne, and Hill, D.P., 1991, Fault orientations in extensional and conjugate strike-slip environments and their implications: Geology, v. 19, p. 1,116–1,120.

Toro, G.R., 2002, Modification of the Toro et al. (1997) attenuation equations for large magnitudes and short distances: Risk Engineering Technical Report, 10 p. (Also available at *http://www.ce.memphis.edu/7137/PDFs/attenuations/Toro_2001_(modification_1997).pdf*.)

Toro, G.R., Abrahamson, N.A., and Schneider, J.F., 1997, Model of strong ground motions from earthquake in central and eastern North America—Best estimates and uncertainties: Seismological Research Letters, v. 68, p. 41–57.
Toro, G.R., and Silva, W.J., 2001, Scenario earthquakes for Saint Louis, MO, and Memphis, TN, and seismic hazard maps for the Central United States region including the effect of site condition: Technical report to U.S. Geological Survey under Contract 1434-HQ-97-GR02981, 248 p. (Also available at *http://www.riskeng.com/downloads/scen_ceus_rept.)*
Tuttle, M.P., and Atkinson, G.M., 2010, Localization of large earthquakes in the Charlevoix seismic zone, Quebec, Canada, during the past 10,000 years: Seismological Research Letters, v. 81, p. 140–147.
U.S. Bureau of Reclamation, 2009, Ground water elevations—Seepage and groundwater investigations Yuma area: U.S. Bureau of Reclamation map, 1 sheet. (Also available at *http://www.usbr.gov/lc/yuma/programs/YAWMS/Groundwater/YA122008-72dpi.pdf*.)
U.S. Geological Survey Advanced National Seismic System, 2014, *http://earthquake.usgs.gov/monitoring/anss/*, accessed, April 2014.
U.S. Geological Survey Comprehensive Catalog, *http://earthquake.usgs.gov/*, accessed April 2013.
U.S. Geological Survey Preliminary Determination of Epicenters (PDE) online catalog, *http://neic.usgs.gov/neis/epic/epic_global.html*, accessed April 2007 and January 2013.
Utsu, Tokuji, 2002, Relationships between magnitude scales, *in* Lee, W.H.K., Kanamori, Hiroo, Jennings, P.C., and Kisslinger, Carl, eds., International handbook of earthquake and engineering seismology: International Association of Seismology and Physics of the Earth's Interior (IASPEI), p. 733–746. (Also available at *http://www.sciencedirect.com/science/bookseries/00746142/81/part/PA*.)
Wallace, R.E., 1984, Fault scarps formed during the earthquakes of October 2, 1915, in Pleasant Valley, Nevada, and some tectonic implications, *in* Faulting related to the 1915 earthquakes in Pleasant Valley, Nevada: U.S. Geological Survey Professional Paper 1274–A, 33 p. (Also available at *http://pubs.usgs.gov/pp/1274a-b/report.pdf*.)
Wang, Kelin, Wells, Ray, Mazzotti, Stephane, Hyndman, R.D., and Sagiya, Takeshi, 2003, A revised dislocation model of interseismic deformation of the Cascadia subduction zone: Journal of Geophysical Research—Solid Earth, vol. 108, 2026, doi:10.1029/2001JB001227.
Weichert, D.H., 1980, Estimation of the earthquake recurrence parameters for unequal observation periods for different magnitudes: Bulletin of the Seismological Society of America, v. 70, p. 1,337–1,346.
Wells, D.L., and Coppersmith, K.J., 1994, New empirical relationships among magnitude, rupture length, rupture width, and surface displacements: Bulletin of the Seismological Society of America, v. 84, p. 974–1,002.
Werner, M.J., Helmstetter, Agnes, Jackson, D.D., and Kagan, Y.Y., 2011, High-resolution long-term and short-term earthquake forecasts for California: Bulletin of the Seismological Society of America, v. 101, p. 1,630–1,648.
Wesnousky, S.G., 2005, Active faulting in the Walker Lane: Tectonics, v. 24, p. 1–35, TC3009, doi:10.1029/2004TC001645.
Wesnousky, S.G., 2008, Displacement and geometrical characteristics of earthquake surface ruptures—Issues and implications for seismic-hazard analysis and the process of earthquake rupture: Bulletin of the Seismological Society of America, v. 98, p. 1,609–1,632.
Wesnousky, Steve, 2010, Neotectonics, active faults, fluvial processes, soils, ancient lakes, paleoseismology, tectonic geomorphology, and other stuff in the central Walker Lane: Friends of the

Pleistocene, Pacific Cell, field-trip guidebook, 99 p. (Also available at *http://www.fop.cascadiageo.org/pacific_cell/2010/FOP2010.html*.)
Wesnousky, S.G., and Caffee, Marc, 2011, Range-bounding normal fault of Smith Valley, Nevada—Limits on age of last surface-rupture earthquake and late Pleistocene rate of displacement: Bulletin of the Seismological Society of America, v. 101, p. 1,431–1,437.
West, M.W., 1997, A continuation of a "pilot" study of Quaternary surface deformation, Saddle Mountains anticline, northern Pasco Basin, Washington: Technical report to U.S. Geological Survey, Reston, Virginia, under Contract 1434-HQ-97-GR-02999, 33 p.
West, M.W., Ashland, F.X., Busacca, A.J., Berger, G.W., and Shaffer, M.E., 1996, Late Quaternary deformation, Saddle Mountains anticline, south-central Washington: Geology, v. 24, p. 1,123–1,126.
Wheeler, R.L., 1995, Earthquakes and the cratonward limit of Iapetan faulting in eastern North America: Geology, v. 23, p. 105–108.
White, B.J.P., Smith, R.B., Husen, Stephan, Farrell, J.M., and Wong, Ivan, 2009, Seismicity and earthquake hazard analysis of the Teton–Yellowstone region, Wyoming: Journal of Volcanology and Geothermal Research, v. 188, p. 277–296.
Williams, H.F.L., Hutchinson, Ian, and Nelson, A.R., 2005, Multiple sources for late-Holocene tsunamis at Discovery Bay, Washington State, USA: The Holocene, v. 15, p. 60–73, doi:10.1191/0956683605hl784rp.
Wilson, D.S., 2002, The Juan de Fuca plate and slab—Isochron structure and Cenozoic plate motions, *in* Kirby, Stephen, Wang, Kelin, and Dunlop, Susan, eds., The Cascadia subduction zone and related subduction systems: U.S. Geological Survey Open-File Report 02–328, p. 9–12. (Also available at *http://pubs.usgs.gov/of/2002/0328/pdf/OF02-328.pdf*.)
Witkind, I.J., 1964, Reactivated faults north of Hebgen Lake, *in* The Hebgen Lake, Montana, earthquake of August 17, 1959: U.S. Geological Survey Professional Paper 435–G, p. 37–50.
Witter, R.C., Kelsey, H.M., and Hemphill-Haley, Eileen, 2003, Great Cascadia earthquakes and tsunamis of the past 6700 years, Coquille River estuary, southern coastal Oregon: Geological Society of America Bulletin, v. 115, p. 1,289–1,306.
Working Group on California Earthquake Probabilities (WGECP), 2013, Uniform California earthquake rupture forecast, version 3 (UCERF3)—Time-independent model: U.S. Geological Survey Open-File Report 2013–1165, 97 p. (Also available at http://pubs.er.usgs.gov/publication/ofr20131165.)
Youngs, R.R., Chiou, S.J., Silva, W.J., and Humphrey, J.R., 1997, Strong ground motion attenuation relationships for subduction zone earthquakes: Seismological Research Letters, v. 68, p. 58–73.
Zeng, Yuehua, and Shen, Zhengkang, 2013, A fault-based model for crustal deformation in the Western United States, Appendix D, *in* Petersen, M.D., Zeng, Yuehua, Haller, K.M., McCaffrey, Robert, Hammond, W.C., Bird, Peter, Moschetti, Morgan, and Thatcher, Wayne, Geodesy- and geology-based slip-rate models for the Western United States (excluding California) national seismic hazard maps: U.S. Geological Survey Open-File Report 2013-1293, p. 58–68. (Also available at *http://pubs.er.usgs.gov/publication/ofr20131293*.)
Zhao, J.X., Zhang, Jian, Asano, Akihiro, Ohno, Yuki, Oouchi, Taishi, Takahashi, Toshimasa, Ogawa, Hiroshi, Irikura, Kojiro, Thio, H.K., Somerville, P.G., Fukushima, Yasuhiro, and Fukushima, Yoshimitsu, 2006, Attenuation relations of strong ground motion in Japan using site classification based on predominant period: Bulletin of the Seismological Society of America, v. 96, p. 898–913.

ISSN: 2331-1258 (online)
http://dx.doi.org/10.3133/ofr20141091